University of Durham

A helium, oxygen and rhenium-osmium isotope study of some intraplate magmatism

James Martin Dines Day

A thesis submitted in partial fulfilment of the requirements for the degree of Doctor of Philosophy

Department of Earth Sciences
The University of Durham
United Kingdom

September 2004

Declaration

I declare that this thesis, which I submit for the degree of Doctor of Philosophy at the University of Durham, is my own work. No part of the material presented in this thesis has previously been submitted by me or any other person for a degree in this or any other university. In all cases the material from the work of others has been duly acknowledged.

James Martin Dines Day

University of Durham, United Kingdom

September 2004

Abstract: A helium, oxygen and rhenium-osmium isotope study of some intraplate magmatism

James M.D. Day *Department of Earth Sciences, University of Durham, UK*

Intraplate magmatism provides important constraints on the evolution, dynamics and composition of the Earth's mantle. Uncertainties remain, however, in understanding the mantle sources related to intraplate magmatism. For example, the influence or existence of mantle stratification, core-mantle interaction and recycling of subducted components are poorly understood. The extent to which geochemical signatures of intraplate magmas are modified during melt transportation, eruption and emplacement also requires better definition. This thesis employs He, O and Re-Os isotope systematics on selected volcanic and intrusive rocks from a number of oceanic and continental intraplate settings to address some of these key issues.

New constraints on the effect of syn-eruptive degassing and post-emplacement mobility processes on intraplate magmas are presented. Ocean Island Basalts (OIB) from the Western Canary Islands and Coppermine Continental Flood Basalts (CFB) suggest that Re degassing for both modern and ancient alkaline and tholeiitic sub-aerially erupted lavas are similar in extent. Crustal contamination is shown to explain some low $\delta^{18}O$ ($\leq 5‰$) in central Icelandic lavas and low $^{3}He/^{4}He$ ($< 8R_A$) in Western Canary Island and central Iceland lavas. Study of the Mackenzie large igneous province (LIP) also reveals that relatively limited (2-4%) crustal contamination can generate large $^{187}Os/^{188}Os$ isotopic variation ($\geq$ 80 γOs units) in high Os concentration cumulate rocks. This finding provides direct support for the role of crustal contamination in the formation of stratiform chromitite reefs in the Muskox Intrusion. By inference, contamination by ancient ($\geq$ 0.5Ga) continental crust might also explain coupled ^{186}Os-^{187}Os enrichments in some continental intraplate magmas.

He isotope ratios of intraplate magmas have been used to infer mantle stratification with both shallow and deep mantle origins proposed for a long-lived, primordial, high $^{3}He/^{4}He$ reservoir. In this work the continental lithospheric mantle, especially Archaean peridotite and eclogite, are shown to possess low $^{3}He/^{4}He$

(<4R_A). This observation, combined with low $^3He/^4He$ (6±1R_A) of continental intraplate alkaline volcanics (CIAV), derived from the lithosphere-asthenosphere boundary, provides evidence that a long-lived primordial He component does not exist in the shallow upper mantle.

Low $\delta^{18}O$ (< 0.9‰) and high $^{187}Os/^{188}Os$ (γOs = +8 to +37) for high Os concentration (> 50 ppt) Western Canary OIB indicate that recycled oceanic crust forms part of the mantle source for these basalts, a theme also common to low $\delta^{18}O$ measured in central Icelandic glasses with $^3He/^4He$ ratios similar to those of mid ocean ridge basalts. Decoupling of lithophile (Sr, Nd, Pb) and siderophile (Os) isotope tracers from He in both settings provides evidence for ^3He-recharge with $^3He/^4He$ up to 11.8R_A for the Western Canary Islands and 34.3R_A for central Icelandic lavas.

There is evidence in Western Canary Island lavas, and in OIB globally, that a common or 'universal' mantle component is present with a near-chondritic $^{187}Os/^{188}Os$ (≥0.127), mantle-like $\delta^{18}O$ (~5.2‰) and elevated $^{206}Pb/^{204}Pb$ (≥19.1) with respect to the depleted mantle; the so-called FOZO (Focus Zone), PHEM (Primary He mantle), or C (Common) components. Coppermine Re-Os isochron ages (1284 ± 13 Ma) are within error of the accepted 1270 ± 4 Ma U-Pb age for the Muskox Intrusion. γOs initials derived from both the Coppermine CFB (+2.0) and Muskox Intrusion (+1.3) lie on an enstatite or ordinary chondritic Os isotopic evolution curve for the Earth's mantle indicating derivation from a source similar to the universal component recognised in modern-day OIB.

These results can be interpreted in the context of a veined or banded peridotite-pyroxenite mantle. Small amounts of partial melting of a heterogeneous mantle source leads to great isotopic variability whilst larger degrees of partial melting will lead to more homogeneous mantle-derived compositions. Pyroxenite sources might also explain the correlated isotopic and elemental compositions, including the possibility of ^{186}Os-^{187}Os enrichment in OIB through high Re/Os and Pt/Os ratios. Ultimately, a universal mantle component appears to be present in all intraplate magmatism. This universal component is not always related to high $^3He/^4He$ and appears to provide an endmember component to all intraplate mantle melting signatures from the Archaean to the present-day.

Table of Contents

List of Figures

List of tables

List of abbreviations

Inevitably, because of the complex issues of chemical geodynamics and isotope geochemistry the published nomenclature is somewhat cluttered with acronyms and abbreviations. In order to alleviate some of the pain in reading this thesis a list of abbreviations, terms and acronyms are provided here. Some of these abbreviations are used widely in the literature, whilst others are less common or have, scandalously, been developed during the course of this thesis. Where terms can be accredited to a particular paper or to this thesis they are duly referenced.

AHIGL	-	Arthur Holmes Isotope Geology Laboratory
BSE	-	Bulk Silicate Earth
C	-	Common component *(Hanan and Graham, 1996)*
CAMP	-	Central Atlantic Magmatic Province
CFB	-	Continental Flood Basalt
CFE	-	Cliff Forming Eruptions *(Carracedo et al., 1998)*
CIAV	-	Continental Intraplate Alkaline Volcanics *(this work)*
CLM	-	Continental Lithospheric Mantle
CMB	-	Core-Mantle Boundary
CMV	-	Coppermine Volcanics (CFB) *(this work)*
CC	-	Continental Crust (this work)
DMM	-	Depleted Mid-Ocean Ridge Basalt Mantle
DTM	-	Department of Terrestrial Magmatism (Carnegie, Washington)
EM1	-	Enriched Mantle type 1
EM 2	-	Enriched Mantle type 2
FCC	-	Freemans Cove Complex *(this work)*
FOZO	-	Focus Zone *(Hart et al., 1992)*
HFSE	-	High Field Strength Elements
HIMU	-	High μ
HSE	-	Highly Siderophile Element
HRDM	-	Helium Recharged Depleted Mantle *(Stuart et al., 2003)*
ICP-MS	-	Inductively Coupled Plasma Mass Spectrometry
ID	-	Isotope Dilution

LILE	-	Large Ion Lithophile Elements
LIP	-	Large Igneous Province
LMI	-	Layered Mafic (Ultramafic) Intrusion
LONU	-	Low ν *(Anderson, 1998)*
LVC	-	Low Velocity Zone *(Hoernle et al., 1995)*
MAR	-	Mid-Atlantic Ridge
MARID	-	Mica-Amphibole-Rutile-Ilmenite-Diopside association
MORB	-	Mid-Ocean Ridge Basalt
NAEM	-	North Atlantic End-Member *(Ellam and Stuart, 2000)*
NAIP	-	North Atlantic Igneous Province
NBW	-	Namqualand-Bushmanland-Warmbad *(Janney et al., 2003)*
N-TIMS	-	Negative Thermal Ionisation Mass Spectrometry
OFB	-	Oceanic Flood Basalt
OIB	-	Ocean Island Basalt
OIAV	-	Oceanic Intraplate Alkaline Volcanics *(this work)*
PFE	-	Platform Forming Eruptions *(Carracedo et al., 1998)*
PGE	-	Platinum Group Element
PHEM	-	Primary Helium Mantle *(Farley et al.,1992)*
PIC	-	Phlogopite-Ilmenite-Clinopyroxene (minor rutile) association
PIMMS	-	Plasma Ionisation Multi-collector Mass Spectrometry
PM	-	Primitive Mantle
PPM	-	Parts Per Million (1×10^{-6})
PPB	-	Parts Per Billion (1×10^{-9})
PPT	-	Parts Per Trillion (1×10^{-12})
REE	-	Rare Earth Elements (Light, Middle and Heavy)
ROC	-	Recycled Oceanic Crust *(this work)*
ROL	-	Recycled Oceanic Lithosphere *(this work)*
UMCP	-	University of Maryland, College Park
WCMP	-	Western Cape Melilitite Province *(Janney et al., 2002)*
XRF	-	X-Ray Fluorescence

Acknowledgements

I would like to thank my supervisors Graham Pearson and Colin Macpherson for their considerable patience and speedy return of comments to me in the last few weeks of writing this thesis. Individually, I would like to thank Graham for his instruction in all things Os and Colin for partially funding and arranging time in Royal Holloway and Scripps Institution of Oceanography for me. I believe that Graham and Colin have made me a more focussed, competent and thicker-skinned scientist.

On the all-important money front I would like to acknowledge receipt of a NERC PhD studentship (NER/S/A/2000/03304). I would especially like to thank Keith Ray at NERC for arranging some extra dosh after my unfortunate incident with a random female Japanese exchange-student and a rugby ball. I have also benefited from a Mineralogical Society Postgraduate Travel Bursary and an American Association of Petroleum Geology grant-in-aid to visit Scripps and a Society of Economic Geologists grant for continuing work on the Muskox Intrusion. The Skene Bursary from University College, Durham, a IAVCEI student hardship reprieve, the Edgar Pam Fellowship 2004 from the Institute of Materials, Minerals and Mining and a travel bursary from VMSG have all contributed to travel, registration and field trips at the IAVCEI general assembly in Chile where I will present work from this thesis later on in 2004.

The Arthur Holmes Isotope Geology Laboratory would not operate without the efforts of Geoff Nowell and Chris Ottley. I would like to thank both Geoff and Chris for their labours and especially Geoff for accommodating my hectic data collection schedule in the last few weeks of August 2004. At Royal Holloway, Dave Lowry, Dave Mattey, Nathalie Grassineau and Stuart Grimes are thanked for making work in the lab there a real pleasure. At Scripps, Dave Hilton, Alison Shaw, Lillie Jaffe, Justin Kulungoski and Diana de Leeuw made lab work in the Californian beach side setting even better than it already was. I greatly appreciate Dave Hilton's enthusiasm and constructive advice both as Scripps and to the present and only hope that his MAP-215 has stopped mourning my departure and is working once again. I also had a series of constructive discussions with Alison about how best to work the word 'sexy' into her thesis; sadly, we never discussed how to work it into mine.....

Because I spent a significant amount of time seemingly chained to the N-TIMS, making concoctions in the clean lab, or drinking concoctions in the 'Vic' with Rich and Dave at Durham, I never got around to visiting all the field areas discussed in this thesis. I am therefore grateful to Larry Hulbert and Bruce Kjarsgaard (Geological Survey of Canada) for providing me with bits of Canada, making me feel welcome in Ottawa and passing data and discussion my way throughout the genesis of this thesis. Phil Janney (Chicago Field Museum), Chris Harrison (GSC), Tim Elliott (University of Bristol) and Fin Stuart (Scottish Universities Reactor and Research Centre) are all thanked for bits of South Africa, Canada, the Canary Islands and Scotland/East Greenland, respectively.

Despite my pasty features blending in with the shiny mass spectrometers and lab at Durham I did manage some field work in the sunny Canary Islands. I find it difficult to imagine a better trip than the one I had there. The geological information and maps Juan Carlos Carracedo provided me with

and the first rate logistics and Spanish 'I need a lift to...' signs Pauline Agnew supplied made for three weeks of 'fieldwork heaven' on El Hierro and La Palma. I would like to express my gratitude to Juan-Carlos and Pauline for making me feel at home on Tenerife. I do, however, have to admit to them that I am not that keen on battered Moray eel. I would also like to thank 'Neddy', 'Dobbin' and 'Manuel' for saving me and sizeable chunks of the Western Canaries from the dreaded elevator in Los Gigantos.

There are some excellent researchers at Durham (more are arriving daily!) and I would like to thank Henry Emeleus, Dougal Jerram, Brian Turner and many others for discussion, reading of chapters, or just superb tutorial drinks in the Castle. Some of the friendships forged whilst in the Dept. of Earth Sciences at Durham are likely to last a lifetime. I would like to thank Rich Single, Dave Dowall, Darren Chertkoff, Dougal Jerram, Nicola DePaola, Phil Hall, Adrian White, Woody Wilson, Tom Sinclair, Richard 'Bones' Jones, Dan Morgan, Kirstin Lemon, Graham Thompson, Shaz Jeffries, Heather Handley, John Collins, Abi Bralee, Jens Lamping and Jules Wright for making good times here at Durham; I wish them and those I have doubtless forgotten all the best for their future endeavours. I would especially like to thank Rich for helping me to spend most of my money in Klute in the summer of 2002, Dave for battering me about in Klute on occasion whilst 'cutting some serious shapes' on the dance floor, Nic for persuading us to 'talk about it' and Darren and Dan for providing me with brunch subsequent to finding me kipping on their sofa. Of late Bones has had to suffer insanity, singing and occasional whoops of delight in the wee small hours of the open-plan loony asylum – sorry mate.

Field trips to the Western US and Namibia were made all the more special because of some of the previously mentioned rogues. Special thanks to Roger Jerram for cleaning up after Dougal, Darren and I and for the delightful wake-up calls in Namibia. Special credit also to Mt. St. Helens for reinvigorating my interest in planetary volcanism and to Jon Davidson, Clarence Hall and the UCLA gang for arranging a fantastic trip. Elsewhere in Durham, Kay and the 64 Whinney Hill inmates have all provided me with distractions and kept me on the straight and narrow.

Janice Clark has been an indispensable and valued friend in the last six months of writing-up and data collection and has subsidised some fantastic meals in Durham, Bamburgh and the Lakes - she even took me to St. James' Park! Thank you lv and my love to you yss!

It is difficult to express the gratitude I wish to convey to my family. My sister, Clare is a constant source of inspiration to me and her enthusiasm to get out and see more of the world has driven me to do likewise. My mother, Gill and father, Nigel, have supported me unfailingly throughout my life and have always been there for me. I am exceptionally lucky to have Nigel and Gill Day for my parents - I dedicate this thesis to them.

Chapter 1: Introduction

1.1 Study objectives

A major goal in the Earth Sciences is to understand the dynamic and complex interplay of magmatism in the increasingly well-defined paradigm of plate tectonics. This thesis considers a number of case studies of intraplate magmatism – the type of magmatism whose origin is the most controversial and poorly understood. Geochemical studies of intraplate magmatism offer insights into the composition of the Earth's mantle and provide a record of source characteristics and melting processes. Intraplate magmas record interaction with the mantle and crust during transport, storage and, in the case of volcanic rocks, eruption at the Earth's surface. The development of melts into multiphase systems (e.g., melting, crystallisation, degassing) and contact with crustal and mantle lithologies during transport to the Earth's surface provide great scope for elemental and isotopic variations to be developed in intraplate magmas. Geochemical investigations of intraplate magmatism have wider ramifications as they provide the ground truths for geophysical models of mantle convection and evolution. However, key questions remain, in particular (Fig. 1.1):

- The extent to which crustal processes such as magmatic degassing, post-emplacement alteration and crustal contamination mask the chemical signatures of the mantle sources of melts.
- The depth in the mantle from which intraplate magmatism originates and what this implies about structure, especially mantle stratification.
- The source components which are involved in intraplate magmatism and the extent to which they involve core-mantle interaction, primitive mantle components, and recycled oceanic, continental crustal and lithospheric material.
- The extent to which study of intraplate magmatism can contribute towards better understanding the evolution of the Earth's mantle, its heterogeneity and overall composition.

This thesis considers four case studies which have been selected because of the potential solutions they provide to some of these key problems (Fig. 1.1). The studies investigate intraplate magmatism from (i) central Iceland and the North

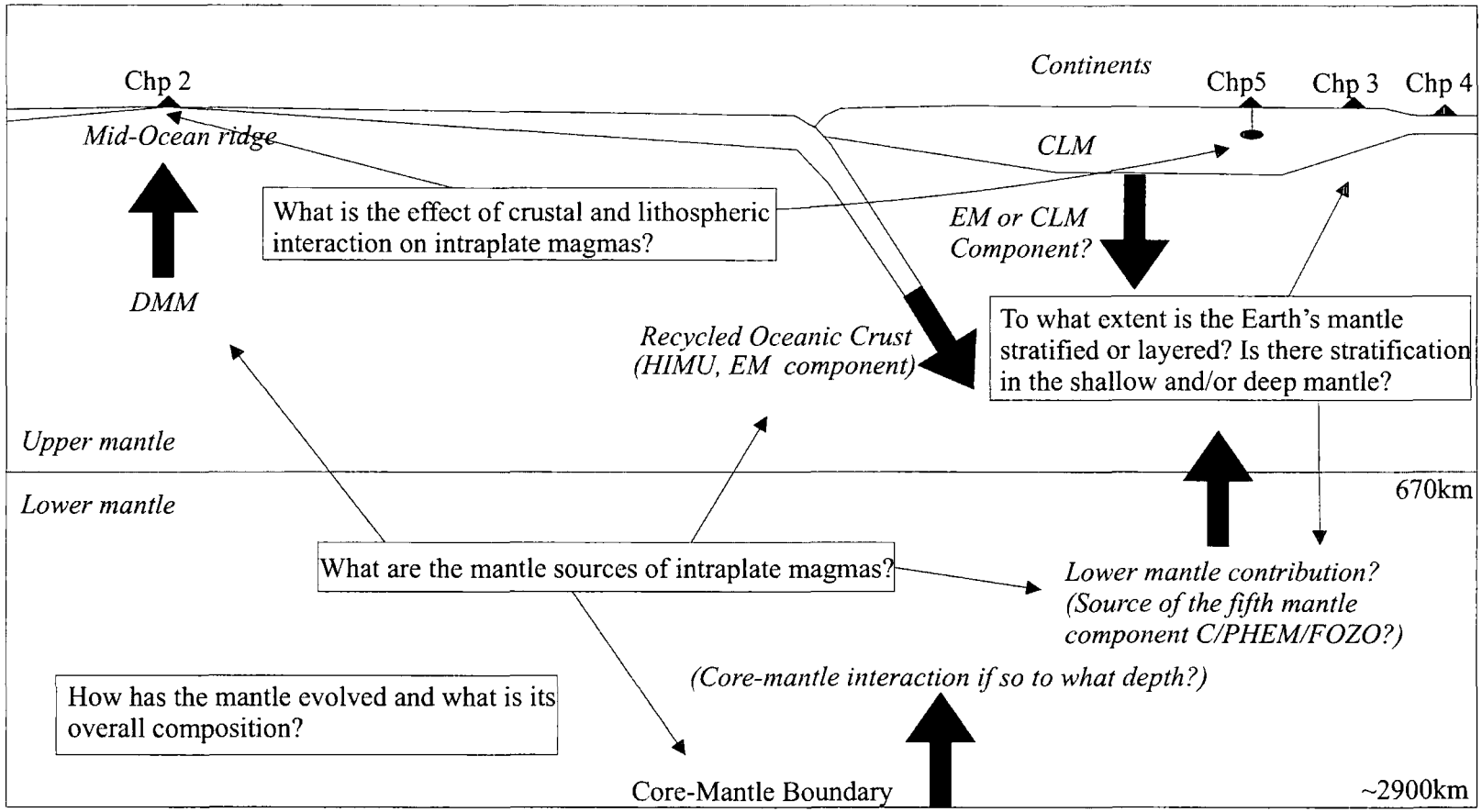

Fig. 1.1: Schematic diagram of the Earth's mantle annotated with some questions key to understanding intraplate magmatism and possible questions that can be answered regarding the compositions, stratification and evolution of the Earth's mantle from study of intraplate magmas. Thick black arrows correspond to potential mantle fluxes relating to intraplate magmatism. Locations of intraplate magmas presented in chapters from this study are shown relative to plate boundary conditions.

Atlantic Igneous Province, (ii) Continental Intraplate Alkaline Volcanics (CIAV) from Uganda, South Africa and Canada, (iii) the Western Canary Islands of El Hierro and La Palma and (iv) the Mackenzie Large Igneous Province (LIP) (the Coppermine continental flood basalts and Muskox Intrusion). Individually and combined, these case studies provide new insights into the Earth's mantle and the origins of intraplate magmatism.

1.2 Definitions of intraplate magmatism

Intraplate magmatism can broadly be defined as the eruption or intrusion of lavas and magmas away from major plate tectonic boundaries, or where anomalous magmatism occurs and persists at plate margins associated with incipient rifting prior to major ocean basin formation (e.g., Iceland; Chapter 2). Intraplate magmatism can be classified according to (i) its location (i.e., within oceanic or continental lithosphere), (ii) its extent (i.e., temporal and volume considerations) and (iii) in the case of ancient examples, the chemical and petrographic characteristics of magmatism. On the oceanic plates the degrees of melting and temporal evolution of magmatism generate two major styles of magmatism: oceanic volcanic plateaux which are volumetrically massive (>0.1-5.8 $\times$ 10^7 km^3; Coffin and Elderholm, 1994) and oceanic islands which are volumetrically much smaller edifices ($1\times10^{4\text{-}5}$ km^3; Chapter 4). Both are composed predominantly of basalt (Oceanic Flood Basalts (OFB) and Oceanic Island Basalts (OIB)), and can often be related temporally and spatially to other forms of intraplate magmatism. In the case of OIB, many show age progressive evolution in the form of hotspot tracks such as Hawaii (Wilson, 1963). Within oceanic islands, Oceanic Intraplate Alkaline Volcanics (OIAV) may also occur and include carbonatitic, melilititic and nephelitic magma compositions (e.g., Clague and Frey, 1982; Wilson *et al.*, 1995).

Similar styles of intraplate magmatism can also be found on the continents. These include Continental Flood Basalt (CFB) provinces which, like OFB constitute parts of LIPs (Chapter 5). CFB are predominantly composed of basalt, but can also retain voluminous silicic magmatism within their stratigraphy or be composed predominantly of silicic magmatic products (e.g., Chon Aike, South America; Whitsunday, Australia). No obvious equivalents for OIB can be found on the continents, although some less voluminous CFB may represent the continental

manifestation of OIB. Volumetrically small, but nevertheless important types of intraplate magmatism located on the continents are Continental Intraplate Alkaline Volcanics (CIAV; Chapter 3) that are preserved as linear chains of volcanism or as incipient rift related magmatism. The term CIAV encompasses kimberlites, lamprophyres, alnöites, melilitites, alkali basalts and ultrapotassic equivalents.

The different styles of intraplate magmatism offer opportunities for understanding different aspects of mantle geochemistry. Small-degree partial melts (CIAV, Oceanic-IAV or OIAV) provide an opportunity to investigate processes that occur between the convecting and conducting parts of the mantle where these melts are proposed to originate (e.g., Brooks *et al.*, 1976; Hawkesworth *et al.*, 1990; Wilson *et al.*, 1995; Janney *et al.*, 2002, 2003). OIB provide insight into the composition of the mantle directly beneath oceanic plates and are the records of modern-day intraplate magmatism. LIP offer a longer-term view of the evolution of the mantle because they span much of geological history and because their huge volumes of melting may provide a bulk estimate for the composition of the Earth's mantle. This thesis examines different examples of these styles of magmatism to address the key questions presented in section 1.1.

1.3 He, O and Re-Os isotopes in magmatic systems

The helium, oxygen and osmium isotope systems have provided powerful constraints on models for mantle evolution and structure (Shirey and Walker, 1998; Eiler, 2001; Hilton and Porcelli, 2003). He, O and Os behave very differently in terms of both elemental and isotopic fractionation processes and can therefore be used to recognise different mantle source components and crustal and lithospheric modification processes acting upon intraplate magmas.

1.3.1 Helium

Helium has three important attributes which make it a sensitive tracer of mantle processes (Hilton and Porcelli, 2003). First, it has two isotopes: ^{3}He, which is primordial, and ^{4}He, predominantly created by α-particle decay of members of the ^{238}U, ^{235}U and ^{232}Th decay series. Modification of primordial $^{3}He/^{4}He$ ratios is therefore the result of radioactive decay and high $^{3}He/^{4}He$ ratios originate from a source which has preserved a significant proportion of its primordial He content.

Second, He is chemically inert so that it passes easily into the gas phase and is effectively lost from the solid Earth. Finally, this inertness is implicitly linked to He being a highly incompatible element (Brooker *et al.,* 2003). Whilst there is evidence that diffusive fractionation can cause some deviations in $^{3}He/^{4}He$ ratios because of its isotopic 'lightness' (e.g., the relative mass difference of ^{3}He to ^{4}He, or $\Delta M/M$), this process is insignificant when compared with radiogenic decay processes (Burnard, 2004). The attributes of He make it a powerful tracer of reservoirs with different time integrated $^{3}He/(U+Th)$ in the Earth's mantle.

1.3.2 Oxygen

Oxygen is the most abundant element on Earth and with silicon, forms the basis for most mineral phases found in the mantle and crust. There are three stable isotopes of O (^{16}O, ^{17}O and ^{18}O) and these isotopes are fractionated in nature by either equilibrium fractionation caused by the mass dependence of chemical bonding or the effect of mass differences on processes such as diffusion, or physio-chemical fractionation (Hoefs, 1973). Because oxygen is isotopically 'light' the mass differences are sufficient to cause noticeable fractionation in nature compared with isotopically heavier elements (e.g., Sr, Nd, Hf, Os, Pb). The use of such light stable isotope systems may overcome some of the limitations inherent in using radiogenic isotopes as tracers of crustal recycling processes (Eiler *et al.,* 1995; 1996; 1997; Harmon and Hoefs, 1995; Lassiter and Hauri, 1998). This is because the $^{18}O/^{16}O$ ratio of a protolith is not affected by aging in the mantle or by high temperature metamorphic processes (Garlick *et al.,* 1971) and because the abundance of oxygen between mantle and crustal reservoirs does not vary significantly. This makes oxygen a powerful indicator of crustal contamination and recycling of oceanic crust. Oxygen isotope ratios of volcanic rocks can be used in conjunction with isotopic ratios of radiogenic daughter elements (He, Sr, Nd, Hf, Os, Pb) to investigate open system behaviour of magmas such as incorporation of crust and the contributions from different mantle reservoirs.

Stable isotopic fractionations are temperature dependant such that different terrestrial reservoirs fractionate O to different degrees (e.g., mantle, crust, hydrosphere). As such O can provide constraints on mixing between these reservoirs and mass transfer within the Earth as a whole. Crustal and atmospheric processing

leads to the development of large scale oxygen isotope heterogeneity at crustal levels where low temperature fractionation (<300°C) causes large variations in $^{18}O/^{16}O$. Re-introducing crustal material into the Earth or interaction between mantle-derived melts and crustal materials during transport may be reflected in the oxygen isotope variations in intraplate magmas.

1.3.3 Rhenium-osmium

There are two geochemically important long-lived osmium isotope decay schemes which are characterised by the fact that both parent and daughter isotopes are Highly Siderophile Elements (HSE). The ^{187}Re-^{187}Os system is based on the β^- transition of ^{187}Re to ^{187}Os with a half life of 42Ga (Giga annums or 1×10^9 yrs) and a decay constant of 1.6662×10^{-11} a^{-1} (Smoliar *et al.*, 1996). The ^{190}Pt-^{186}Os system is based upon the α transition of ^{190}Pt to ^{186}Os with a half life of ~470Ga and a decay constant of $\sim1.415\times10^{-12}$ a^{-1} (Cook *et al.*, 2004).

Because of their preferential association with metal or sulphide relative to silicate phases, the HSE Re, Pt and Os are considered to have been almost totally extracted from the terrestrial mantle during core segregation (Shirey and Walker, 1998). Large differences in the Re/Os and Pt/Os ratio between melts and their melt residues can be generated because of the different partitioning of incompatible Re and Pt from compatible Os during partial melting (Reisberg *et al.*, 1993; Hauri and Hart, 1993; Shirey and Walker, 1998; Schaefer *et al.*, 2002; Pearson *et al.*, 2004b). Because of the large differences in compatibility of Re and Os, the Re-Os system can generate substantial isotopic heterogeneity in relatively short intervals of time making the Re-Os isotopic system a powerful tracer of recycled crustal components and continental lithospheric mantle (Shirey and Walker, 1998; Hauri, 2002). As such the Re-Os and Pt-Os isotope systems can provide unique insights into the origin and evolution of the mantle and intraplate magmas compared to other long-lived radiogenic isotope systems that are lithophile and partition preferentially into silicate phases (e.g., Rb-Sr, Sm-Nd, Lu-Hf, U-Th-Pb).

In combination, O, He, Os and other isotopic and elemental information have the potential to reveal the origin of intraplate magmas and the nature and evolution of their mantle sources. In the following section the structure of this thesis is

outlined, as are the current problems and paradigms relevant to the examples of intraplate magmatism investigated here.

1.4 Thesis outline

A common introduction to geochemical observations and problems in intraplate magmatism as well as individual case studies considered in this thesis are presented below.

1.4.1 Mantle components and intraplate magmas

The composition of mantle sources are often inferred from the isotopic signatures of basaltic lavas erupted at the Earth's surface. In particular, the isotopic systematics of OIB have been used as the primary source of evidence that there are long-lived chemical heterogeneities in the mantle (Zindler and Hart, 1986). Correlations in Sr-Nd-Pb isotope ratios require the existence of mantle reservoirs that are isotopically and chemically long-lived and distinct from MORB. These variably enriched mantle reservoirs (EMI, EMII, HIMU, Zindler and Hart, 1986) have been attributed to:

- Oceanic crust and sediment (e.g., Hofmann and White, 1982; White, 1985; Weaver, 1991a,b; Hart *et al.*, 1992).
- Metasomatised oceanic lithosphere (Niu and O'Hara, 2003)
- Continental lithospheric mantle (McKenzie and O'Nions, 1983)
- The result of sampling upon melting and averaging - the central limit theorem (Meibom and Anderson, 2003)
- The 'prevalent mantle' component (also individually referred to as FOZO, C, PHEM or LVC), a primordial mantle source (Hart, 1984; Hart *et al.*, 1992; Farley *et al.*, 1992; Hoernle *et al.*, 1995; Hanan and Graham, 1996; Hilton *et al.*, 1999).

Regardless of the components involved in OIB petrogenesis, one aspect is clear; globally these basalts come from chemically and isotopically distinct mantle reservoirs of variable age and provenance.

As well as exhibiting a range in Sr-Nd-Pb isotope ratios, OIB also have variable $^{3}He/^{4}He$ ratios ranging from 30 to $38R_A$ at Hawaii and Iceland (Kurz *et al.*, 1983; Hilton *et al.*, 1999) to ~5 to $7R_A$ at Tristan da Cuhna, Gough, St Helena, Tubuaii and

Mangaia (Kurz *et al.*, 1982; Graham *et al.*, 1992; Hanyu and Kaneoka, 1997). This suggests that mantle sources for OIB contain helium with both less and more time-integrated radiogenic isotopic components, respectively, than the source of mid-oceanic ridge basalts (MORB, ~8R_A; Graham, 2002; Hilton and Porcelli, 2003). General consensus is that elevated $^3He/^4He$ ratios measured in OIB and CFB indicate large-scale stratification of the mantle and derivation of high $^3He/^4He$ from the lower mantle or core-mantle boundary (e.g., Craig and Lupton, 1976; Kellogg and Wasserburg, 1990; Porcelli and Wasserburg, 1995; Farley and Neroda, 1998; Porcelli and Halliday, 2001; Graham, 2002; Hilton and Porcelli, 2003). So-called low-^3He hotspots are thought to contain one or more recycled components (Kurz *et al.*, 1982; Graham *et al.*, 1992; Hanyu and Kaneoka, 1997) but have $^3He/^4He$ ratios that are higher than expected for pure recycled components. The higher $^3He/^4He$ ratios of low-^3He hotspots are thought to be due either due to diffusive exchange (Hanyu and Kaneoka, 1998), or through mixing with a high-^3He source (Hilton *et al.*, 2000a).

Two distinct classes of model have been proposed to account for mantle with higher time-integrated $^3He/(U+Th)$ than the DMM. The first calls for large-scale stratification of the mantle with preservation of high $^3He/^4He$ in the lower mantle (e.g., Kurz *et al.*, 1983; Porcelli and Wasserburg, 1995; Graham, 2002; Hilton and Porcelli, 2003), or possibly even the core (Macpherson *et al.*, 1998; Porcelli and Halliday, 2001). Coupling of high $^3He/^4He$ values with solar-like Ne isotope ratios (Honda *et al.*, 1993) indicate that this is a primordial volatile component. A lower mantle that has been isolated from the upper mantle is consistent with the noble gas mass balance of the DMM and continental crust (Porcelli and Wasserburg, 1995). Tomographic images of long, narrow, seismically "fast" structures in the lower mantle, which can be mapped to sites of present-day plate convergence at the Earth's surface, also suggest that upper mantle material is transported below the mantle transition zone (van der Hilst *et al.*, 1997). If material is emplaced into the lower mantle, mass balance of these two reservoirs requires that there is return flow from the lower to the upper mantle.

The alternative class of model suggests that the high $^3He/(U+Th)$ reservoir resides in the shallow mantle. In these models, there exists a shallow and volatile-rich mantle characterised by low U and Th relative to DMM, due to ancient melt

extraction events (Anderson, 1998). This shallow mantle contains He-rich mineral phases that have captured and preserved high $^{3}He/^{4}He$ fluids over extended periods ($>1\times10^{9}$ years; Natland, 2003; Meibom *et al.*, 2003). The essential pre-requisites for this class of model is that the source maintains: (1) low $^{238}U/^{3}He$ (NU) for a given U/Th ratio, i.e., the LONU component (Anderson, 1998), resulting in low ^{4}He production and consequent preservation of high $^{3}He/^{4}He$ and, (2) residence in the shallow mantle where it would be effectively sampled by low-degree partial melts formed through incipient rifting of continents (e.g., Anderson, 1995; 1998; 2000). LONU mantle can be envisaged as residual and refractory mantle (Anderson, 1998), existing within the 'perisphere', a hypothesised shallow mantle reservoir between the lithosphere and asthenosphere (Anderson, 1995; 2000). Such a model would allow shallow origins for both CFB (e.g., King and Anderson, 1995) and OIB that have high $^{3}He/^{4}He$ signatures.

In addition to OIB, the mantle source compositions of LIPs are highly contentious with proposed endmembers including primitive mantle, continental lithospheric mantle (CLM), mixtures of various mantle derived melts with continental crust, recycled oceanic crust or lithosphere, or deep mantle and possible core-mantle region contributions (Carlson *et al.*, 1981a, b; Hawkesworth *et al.*, 1983; DePaolo, 1988; Campbell and Griffiths, 1990; Carlson, 1991; Walker *et al.*, 1994; Shirey, 1997; Schaefer *et al.*, 2000). LIPs may sample the same reservoirs as OIB, at different extents of melting and hence may provide complementary constraints on mantle dynamics because, through geological time, they provide a different perspective on mantle evolution. LIPs are also important due to their speculative impact on climate forcing and biotic mass extinctions (Rampino and Stothers, 1988; Wignall, 2001). In addition, they represent the addition of large volumes of juvenile crust over short periods of time (Cox, 1980; Rampino and Stothers, 1988; Hill *et al.*, 1992) and so provide information on crustal evolution. LIP host some of the largest economic deposits of precious metals on Earth and so geochemical constraints on LIP also provide important information on the genesis of these ore deposits (e.g., Arndt *et al.*, 2003).

Much of the geochemical and isotopic data available for LIPs either originates solely from their associated CFB or from large layered mafic-ultramafic intrusions. However, geological and geochemical studies seldom examine these integral

structural parts in conjunction. Provided that both the co-genetic CFB and associated layered mafic-ultramafic intrusions are exposed and well preserved, then their valuable joint-study will yield information on the styles and timing of mantle melting and magma separation as well as fractional crystallisation and crustal melting processes. This information includes insight into CFB-dyke-layered mafic-ultramafic intrusion relationships, LIP time-scales, the role of concomitant crustal assimilation and fractional crystallisation and the extent of CLM interaction. Ultimately the relative proportions of mantle-derived magmas sourcing LIP and their primitive compositions may be ascertained.

1.4.2 Uncertainties in intraplate magmas: crustal and lithospheric contamination

A curious aspect of available OIB data sets is that some islands have restricted He-Sr-Nd-Pb isotope compositions whilst others show a large range (e.g., Chaffey *et al.*, 1989; Graham *et al.*, 1992a; Kurz *et al.*, 1982; Le Roux *et al.*, 1990; Graham *et al.*, 1990, Barling *et al.*, 1994; Hilton *et al.*, 1995; Woodhead *et al.*, 1993; Thirlwall *et al.*, 2004; Chapter 2). These differences could be related to the length-scales (commonly cited as 10^2 to 10^5km) of mantle heterogeneity such that Ocean Islands with limited isotopic variability tap a more homogeneous source than islands with a wider isotopic range. However, there remain several areas of uncertainty in these interpretations that are considered below.

1.4.2.1 Crustal contamination

First, there is the effect of high-level crustal interaction. This process has been shown to affect Sr-O and He isotope systematics of Icelandic lavas (Condomines *et al.*, 1983; Hemond *et al.*, 1988; Chapter 2) and has also been shown to affect the Re-Os, Sr-Nd-Pb, O and He isotope systematics in OIB (Reisberg *et al.*, 1993; Marcantonio *et al.*, 1995; Hilton *et al.*, 1995; Thirlwall *et al.*, 1997; Widom *et al.*, 1999; Harris *et al.*, 2000). These datasets have resulted in shallow level crustal contamination being proposed as an alternative to mantle source heterogeneity for basalts in Iceland (Hemond *et al.*, 1993; Eiler *et al.*, 2000c; Chapter 2), Hawaii (Eiler *et al.*, 1996; Garcia *et al.*, 1998), Gran Canaria (Thirlwall *et al.*, 1997), Tristan da Cuhna (Harris *et al.*, 2000), and Heard Island (Hilton *et al.*, 1995).

Extreme examples where crustal contamination can obscure primary compositions in mantle-derived magmas come from the geochemical and isotopic signatures of CFB and LIP. Crustal contamination has been recognised as potentially complicating attempts to use the chemical signatures of CFB suites as probes of their mantle source regions (e.g., Carlson *et al.*, 1981a,b) and may also be important in the generation of precious metal mineralization in layered mafic-ultramafic intrusions (Irvine, 1975) and Cu-Ni-PGE side-wall deposits (e.g., Keays, 1995; Lesher and Stone, 1996; Lambert *et al.*, 1998; Ripley *et al.*, 1998). Indeed, the overwhelming majority of lithophile element investigations of CFB and layered mafic-ultramafic intrusions have pointed to significant contributions from the crust to mantle-derived melts feeding LIPs (e.g., Carlson *et al.*, 1981a,b; Thompson *et al.*, 1983; Ripley *et al.*, 1998; Tepley and Davidson, 2003; McBirney and Creaser, 2003; Arndt *et al.*, 2003). By understanding and removing the observed effects of crustal contamination to CFB lavas and cumulate layered mafic-ultramafic intrusive rocks, an appraisal of potential mantle source contributions becomes more realistic.

1.4.2.2 Lithospheric mantle contamination

Second, lithospheric mantle contributions may influence the generation of OIB and CFB/LIP. Trace element studies of Grand Comore and Oahu lavas require hydrous mineral phases in their mantle source which suggests oceanic lithosphere may be a significant source in the generation of some OIB magmas (Class and Goldstein, 1997). Hf-Nd isotope analysis of Oahu lithospheric xenoliths has subsequently revealed extensive interaction between Honolulu volcanics and Pacific mantle lithosphere (Bizimis *et al.*, 2003). Additionally, Os isotope studies of OIB have shown that oceanic lithosphere contributions are an integral part of the OIB source (see review by Hauri, 2002). Numerous studies of CFB and LIP have cited the CLM as a potential source for these continental intraplate magmas on the basis of elemental, lithophile (Sr, Nd, Pb; e.g., Turner *et al.*, 1995; Hawkesworth *et al.*, 1999) and Re-Os isotopes (Ellam *et al.*, 1992; Horan *et al.*, 1995). Lithospheric interaction is a process that requires careful consideration in understanding the geochemical signatures of intraplate magmas.

1.4.2.3 The possibility of a fifth mantle component

Finally, if crustal or lithospheric mantle interaction is unable to explain the isotopic variations seen in OIB, then the extent to which their isotopic variations reflect mantle mixing processes between isotopically distinct sources becomes a key determinant. So does the way in which all forms of intraplate magmas relate to one another in terms of a common mantle component. The question then, is whether such mixing can explain and account for the FOZO, C, or PHEM component and whether these represent a genuine 5^{th} mantle component. These questions, in conjunction with the possible role of the lower mantle or core (e.g., Brandon *et al.*, 1999) and the relative proportions and roles of recycled oceanic and continental materials into the asthenospheric mantle remain the greatest uncertainties when using intraplate magmas as probes of the Earth's mantle.

1.4.3 Thesis overview

Chapter 2 presents new oxygen and helium isotope data for glasses and phenocryst phases from the recent lavas of the central Icelandic rift zones and Palaeogene NAIP magmatism. Its primary goals are to investigate how modification in the Icelandic or Hebridean/East Greenland crust impacts primary source signatures in basaltic magmas with elevated $^{3}He/^{4}He$ and whether there is $^{3}He/^{4}He$ and $^{18}O/^{16}O$ heterogeneity in the modern Icelandic and Palaeogene NAIP mantle source.

In Chapter 3, new He and O isotope data are presented for a Roberts Victor eclogite as well as olivines from the Namaqualand-Bushmanland-Warmbad and Western Cape Melilitite provinces from the African continent. New He and O isotope data, major and trace element data as well as ^{40}Ar-^{39}Ar derived age dates are also provided for the Freemans Cove Complex, Nunavut, Canada. Chapter 3 presents two tests of the hypothesis that a high $^{3}He/^{4}He$ component resides in the shallow mantle. First the helium isotope composition and heterogeneity of the CLM is assessed and described. Second, an appraisal of the helium isotope composition and heterogeneity of CIAV formed by low degree partial melting of the mantle is conducted to assess whether a high time-integrated $^{3}He/(U+Th)$ component can exist and remain within the CLM or the convecting upper mantle from which CIAV are derived.

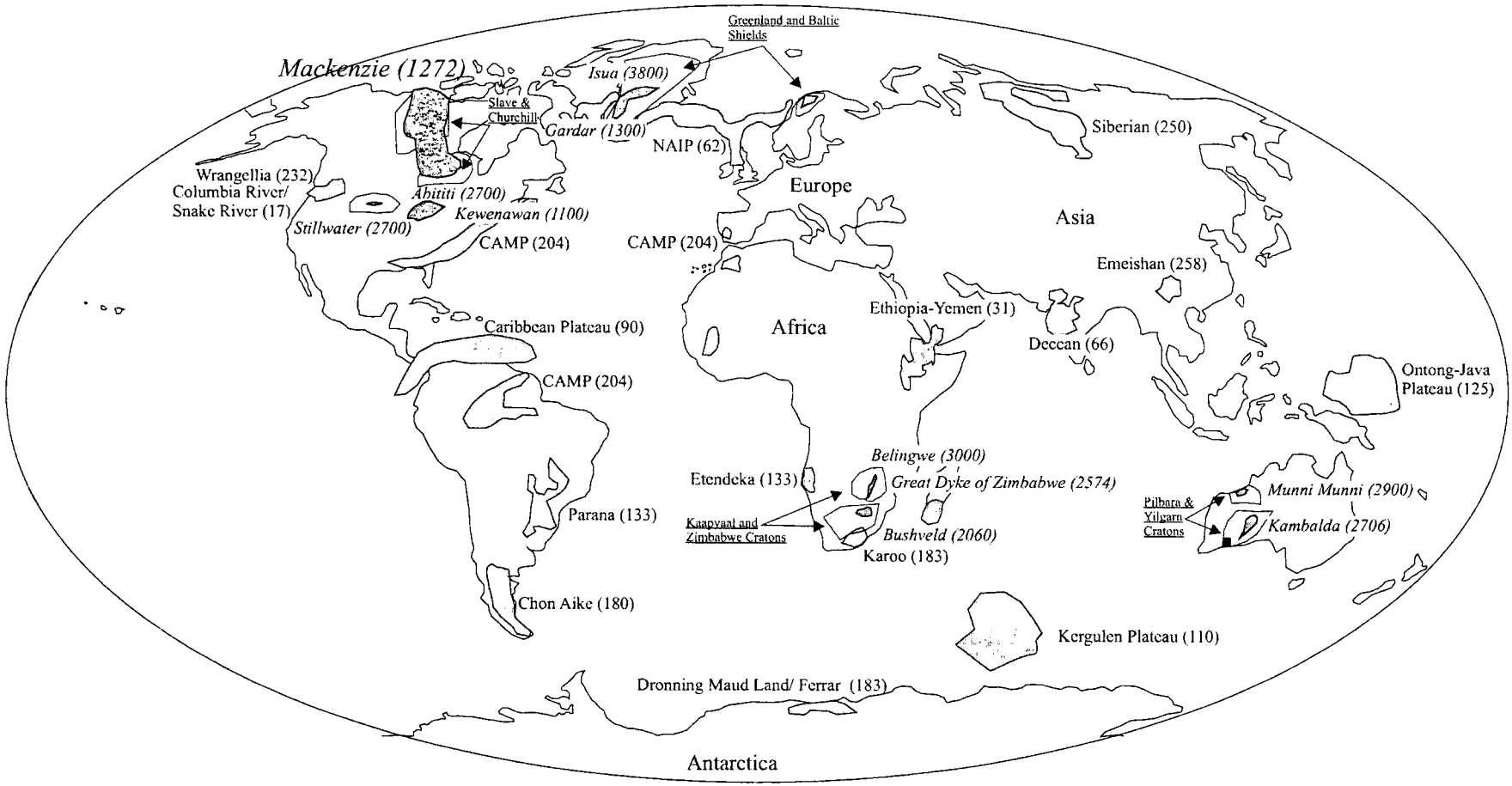

Figure 1.2: Mercator projection of the Earth showing selected large igneous provinces and their maximum measured ages (in parentheses as Ma). LIPs older than the Phanerozoic are indicated by italicised writing. Cratonic areas shown as unfilled solid outlines and encompass Proterozoic and Archaean LIPs. For the Mackenzie LIP the cratonic areas shown are the Slave and Churchill shields. Current plate boundaries and magmatic environments are not shown. Age information obtained from http://www.largeigneousprovinces.org.

Chapter 4 presents new He, O, Sr, Nd, Re-Os, Pb isotope, major and trace element results for the two westernmost Canary Islands, El Hierro and La Palma. The chapter considers the partial melting and crustal modification processes affecting lavas from these two islands and considers the mantle sources responsible for the large isotopic variation measured in Western Canary Island lavas. Ultimately this large data set is considered in the context of models for mantle structure and dynamics based upon geochemical information from OIB.

Chapter 5 examines a mid-Proterozoic example of preserved co-genetic CFB-layer mafic-ultramafic intrusion relationships; the Coppermine CFB and Muskox intrusion. There are a number of reasons for studying the Coppermine CFB and Muskox Intrusion. First the combined giant Mackenzie dyke swarm, Coppermine CFB and large (>3500km^3) ultramafic-mafic Muskox intrusion are well preserved making geochemical analysis and stratigraphic interpretation easier than more structurally deformed equivalents. The Muskox intrusion also has the highest ratio of ultramafic to mafic layers of all large layered mafic-ultramafic intrusions recognised on the planet and hosts potentially economic deposits of Cu-Ni-PGE. Picritic lavas have been recently recognised in the Coppermine CFB allowing comparison with Re-Os studies of picritic lavas from other CFB. These high MgO basaltic to picritic rocks also imply large degree melting of the mantle beneath the Canadian Shield at ~1.27Ga. Finally the Mackenzie magmatic event shows a number of similarities to Proterozoic and Phanerozoic LIPs (Fig. 1.2) and represents one of the largest singular post-Archaean intraplate magmatic events to have occurred on Earth. In this chapter, new trace element and Re-Os isotope data for the Muskox Intrusion, Keel dyke and Coppermine CFB are presented. Preliminary objectives of this study are to examine the age relationships of the Coppermine CFB and Muskox intrusion and to place constraints on crustal modification processes. The ultimate objective is to recognise the mantle sources responsible for Mackenzie LIP magmatism and to provide further constraints on the Re-Os isotope evolution of Earth's mantle, examining evidence for possible core contributions to continental magmatic events.

Chapter 6 presents the main observations and conclusions made from the intraplate magmatism case studies presented in chapters 2, 3, 4 and 5 and discusses how He, O and Os isotope constraints can solve key questions (section 1.1) in intraplate magmatism.

Chapter 2: $^{18}O/^{16}O$ compositions of central Icelandic and North Atlantic Igneous Province magmatism; source mixing versus crustal contamination for the origin of extreme $^{3}He/^{4}He$ variation in volcanic rocks

2.1 Introduction

The Palaeogene North Atlantic Igneous Province (NAIP) represents a large intraplate magmatic event associated with continental break-up. The NAIP Palaeocene to modern-day legacy is the creation of Iceland and its continuing magmatism. Palaeogene NAIP and Icelandic magmatism share similar isotopic characteristics. Extreme $^{3}He/^{4}He$ ratios have been measured in Palaeogene (e.g., Stuart *et al.*, 2003) and Icelandic lavas (Hilton *et al.*, 1999) and common Sr-Nd-Pb isotope attributes have been recognised in all forms of NAIP and Icelandic magmatism (Ellam and Stuart, 2000). However, the different settings for magmatism (continental versus oceanic) mean that any mantle Sr-Nd-Pb-Os isotope variations in NAIP magmatism is complicated by the effects of ancient continental crustal and lithospheric contamination. For Iceland, which lies on the mid-Atlantic ridge, such effects are insignificant.

Icelandic magmatism displays significant Sr, Nd and Pb isotope variation which can be explained through contributions from several components that are incompatible element enriched and depleted compared to normal mid-ocean ridge basalts (MORB; e.g., Schilling *et al.*, 1982; Elliott *et al.*, 1991; Hemond *et al.*, 1993; Thirlwall *et al.*, 2004). The age of the Icelandic crust limits the degree to which Sr, Nd and Pb isotopic variation can be generated through *in situ* radioactive ingrowth and crustal assimilation processes, and requires distinct mantle domains beneath Iceland (Thirlwall *et al.*, 2004). In this chapter new O isotope data on Icelandic and NAIP magmatism are presented together with supporting He isotope and trace element data for central Icelandic lavas. The aims are:

- To examine the effects of crustal contamination on the NAIP and central Icelandic rocks suites and the effects this may have on $^{3}He/^{4}He$ ratios.

- To assess isotopic heterogeneity in the mantle sources of Icelandic and NAIP magmatism and the initial $^{3}He/^{4}He$ and $\delta^{18}O$ ratios of these domains.
- To consider the reasons for extreme variation of $^{3}He/^{4}He$ ratios measured in central Icelandic and NAIP basalts.
- To comment on the possible implications this study may have for interpretation and assessment of mantle sources in intraplate magmatism.

2.2 Geological setting

The opening of the North Atlantic ~60Ma was associated with wide-spread basaltic magmatism stretching from the Canadian Arctic to the British Isles and Arctic Norway, forming a Continental Flood Basalt (CFB) province with an estimated volumes in excess of $(6\text{-}10)\times10^{6}$ km^{3} (Saunders *et al.*, 1997). The volumes and extent of Palaeogene NAIP magmatism cannot be explained by simple adiabatic melting of the convecting mantle and so require a mechanism which enabled excess melting around the Atlantic margins. Parental magmas containing in excess of 18-19 wt. % MgO have been inferred for picritic tholeiite magmatism in East and West Greenland and Baffin Island (Gill *et al.*, 1992; Brown *et al.*, 1996). West Greenland picrites also contain high concentrations of Os (Schaefer *et al.*, 2000a), suggesting high degrees (>25%) of partial melting due to anomalous mantle temperatures (potential temperatures >1540°C). Alternative origins for increased melting have been proposed from high water contents measured in Mg-rich olivines from the NAIP (Jamveit *et al.*, 2001).

This 'hotspot' or 'wetspot' has persisted until the present day, where, with respect to typical plate boundary spreading centres, excess magmatism at the junction between the Reykjanes and Kolbeinsey ridges has resulted in the formation of Iceland. In this manner, the geological histories of both Iceland and the NAIP are intrinsically linked.

2.2.1 Geochemical setting for the Palaeogene NAIP CFB

The NAIP is probably the best studied large igneous province (LIP) in the world. As such, the NAIP geochemical and geophysical properties are well characterised (e.g., Saunders *et al.*, 1997). Magmatism along the Atlantic margins is consistent with rifting (chron 24) and subsequent oceanic lithosphere formation at ~56Ma. CFB

magmatism began at 60.5-62.8Ma (Pearson *et al.*, 1996; Hamilton *et al.*, 1998; Saunders *et al.*, 1997), when transitional alkaline to tholeiitic magmatism occurred approximately synchronously in Baffin Island, West and East Greenland, the Faeroe Islands and the British Isles.

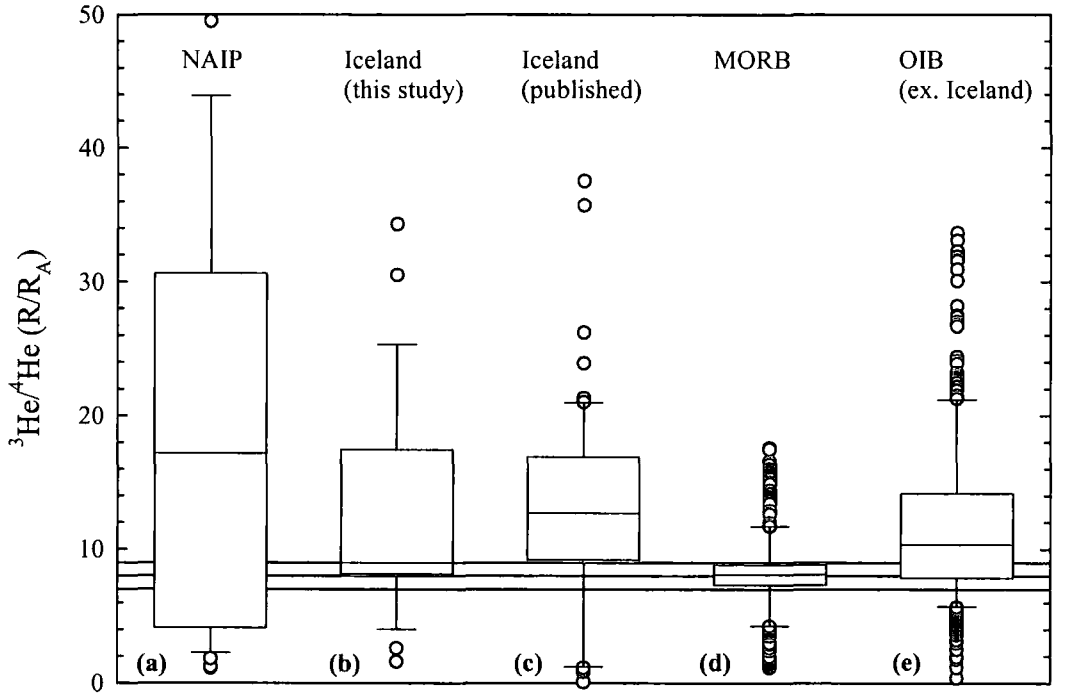

Fig. 2.1: Box plot of $^3He/^4He$ ratios (R/R_A notation) of phenocrysts and glasses analysed by crushing in vacuo. (a) NAIP phenocrysts = 19.2±15.1R_A (1 S.D; n=38); (b) central Iceland lavas (this study) = 12.6±7.9R_A (1.S.D; n= 25); (c) published Icelandic data = 13.1±7.5R_A (1.S.D; n= 61); (d) compiled MORB data (including Reykjanes and Kolbeinsey ridge data) = 8.2±2.9R_A (1.S.D; n= 403); (e) OIB (excluding Iceland) = 11.9±6.0R_A (1.S.D; n= 448). Solid lines are MORB average (8±1R_A) from Hilton and Porcelli (2003). Data for NAIP from Stuart et al. (2000; 2003), Ellam and Stuart (2000), Graham et al. (1998), Marty et al. (1998), Peate et al. (2003). Data for Iceland, OIB and MORB listed in Graham (2002). The box plot illustrates measures of distribution and dispersion of the chosen analyte. Box represents interquartile range (25^{th} to 75^{th} percentiles) and error bars represent 10^{th} and 90^{th} percentiles with outliers plotted as single points. A line within the box represents the mean of the data.

NAIP basaltic lavas exhibit substantial ranges in Sr, Nd and Pb isotope ratios (Saunders *et al.*, 1997; Ellam and Stuart. 2000). Variable Sr, Nd and Pb isotope ratios require mixing between DMM and Archaean amphibolite and granulite (Saunders *et al.*, 1997). Ellam and Stuart (2000) used Pb isotopes to define a common depleted North Atlantic End-Member (NAEM) composition relative to MORB, in addition to a recognised Icelandic component (Hilton *et al.*, 1999), in the genesis of NAIP magmas. To date, the most extreme, unaltered terrestrial $^3He/^4He$

ratios have been measured in NAIP lavas and more recent Icelandic lavas (Fig. 2.1). $^3He/^4He$ greater than MORB have been measured in Palaeogene lavas from Baffin Island (49.5R_A; Stuart *et al.*, 2003), West Greenland (30.7R_A; Graham *et al.*, 1998), NE Greenland (21.2R_A; Marty *et al.*, 1998), East Greenland (18.1R_A; Peate *et al.*, 2003) and Western Scotland (22.1R_A; Stuart *et al.*, 2000). These results are comparable with $^3He/^4He$ measured in a Palaeocene ankaramite from NW Iceland (37.7R_A; Hilton *et al.*, 1999) and lavas from the recent Central Icelandic rift zones (up to 34.3R_A; this study). As well as high $^3He/^4He$ ratios, extreme variation in $^3He/^4He$ (1.6-49.5R_A) exists for NAIP and Icelandic lavas. The purpose of this study is to constrain the origins of both high $^3He/^4He$ and the extreme variability in $^3He/^4He$.

The geochemical identity of the NAIP on the basis of chronostratigraphic, elemental abundances and isotopic ratios appears to be from a persistent (>60Ma) mantle anomaly with high time-integrated $^3He/(U+Th)$, relatively depleted Sr and enriched Nd and Pb isotope signatures, that has variably mixed with asthenospheric mantle (e.g., Stuart *et al.*, 2003). This study examines NAIP magmatism which occurred in East Greenland and Skye, Scotland (appendix A). East Greenland samples are from the Prinsen af Wales Bjerge Formation, a thick pile of tholeiitic to alkali basalt lavas erupted ~53-56 Ma (Peate *et al.*, 2003). Samples from Skye are from the main Cuillin peridotite complex, the Skye dyke swarm, the Little Minch Sill Complex and from the Skye Main Lava series; a thick tholeiitic to transitional alkali basalt lava pile erupted ~58-61 Ma (Hamilton *et al.*, 1998). All samples have been described previously for their elemental and He, Sr, Nd, Pb isotope characteristics (Brown *et al.*, 1996; Ellam and Stuart, 2000; Stuart *et al.*, 2000).

2.2.2 Iceland

Iceland is a geologically young (<15 Ma) sub-aerial section of the Mid-Atlantic Ridge (MAR), distinguished by anomalously thick crust (e.g., Darbyshire *et al.*, 2000; Kaban *et al.*, 2002). Volcanism occurs primarily along neo-volcanic zones; sub-aerial extensions of the MAR. The neo-volcanic zones of Iceland can be subdivided into the western and northern branches which erupt tholeiitic lavas and a south-eastern branch which produces mainly Fe-Ti basalts and alkali basalts.

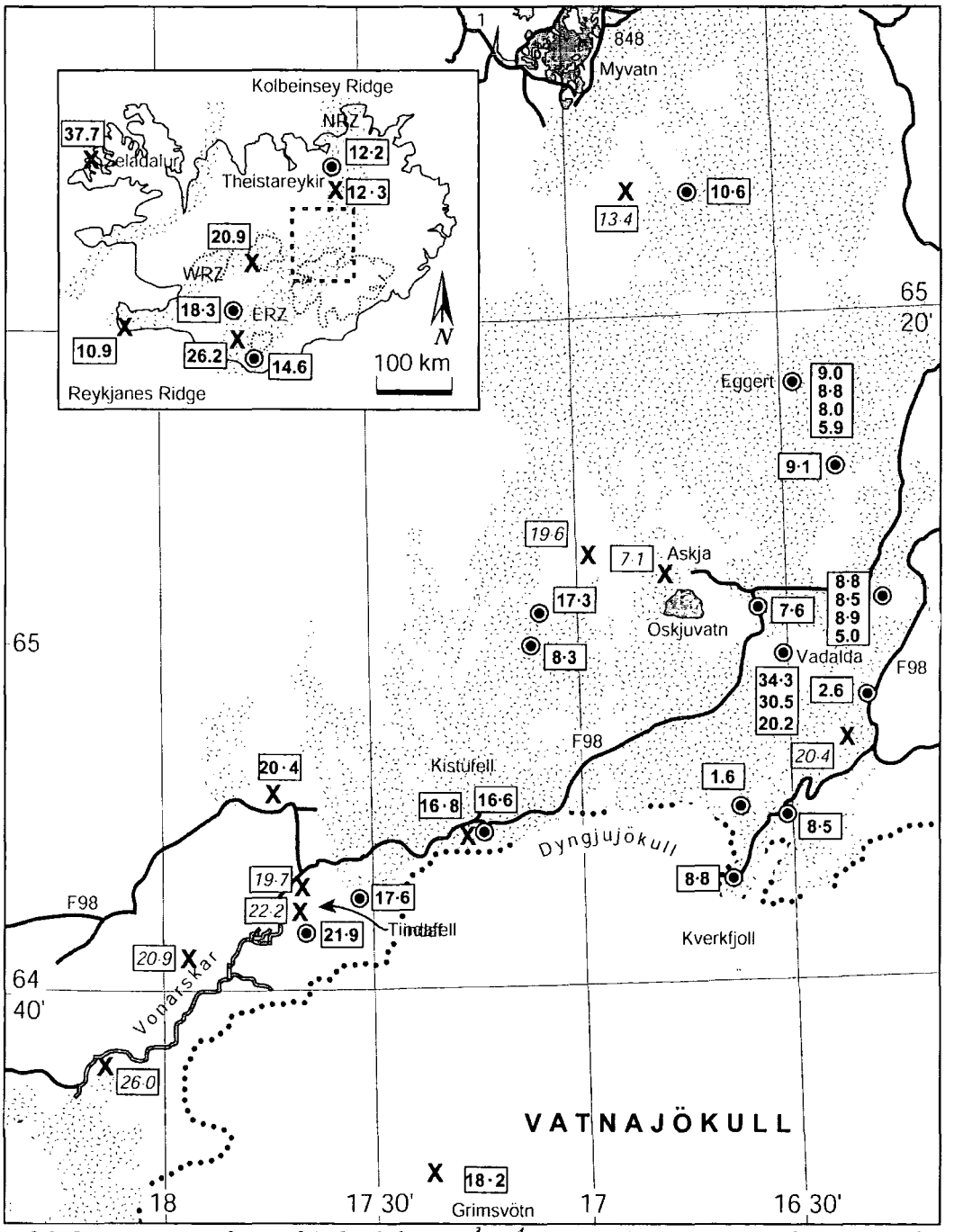

Fig. 2.2: Location map of central Iceland showing $^3He/^4He$ ratios (R/R_A notation) of present work and published values from Kurz et al. (1985), Hilton et al. (1990), Poreda et al. (1992) and Breddam et al. (2000). Samples include hyaloclastic glasses, phenocrysts and geothermal fluids. Motif represents historical or post-glacial lava flows.

This study focuses on sub-glacial glasses and sub-aerial olivine basaltic lava flows from central Iceland – at the convergence of the northern (NRZ) and western rift zones (WRZ; Fig. 2.2). Volcanism in central Iceland is characterised by different eruptive styles with fissure-fed, central edifice and monogenetic sub-glacial volcanoes all being sampled in this study. Optically fresh glasses were collected

from sub-glacial pillow lavas, some of which contain olivine phenocrysts. The lava flows generally contain abundant olivine phenocrysts set in a fine-grained plagioclase, pyroxene and glass matrix. NAL 625 contains augite phenocrysts, as does NAL 626, which also contains abundant (~30%) plagioclase phenocrysts that are glomerophyric and/or complexly zoned. The central Iceland samples are supplemented by glasses and lavas from the NRZ (Th-29) and Eastern Rift Zone (ERZ; Sal-575 and PJOR). Details of samples can be found in appendix A.

2.3 Results

Olivine phenocrysts from East Greenland and Skye magmatism were provided by F. Stuart for oxygen isotope analysis. For these samples He-Pb ± Sr ± Nd isotope analyses have been described elsewhere (Ellam and Stuart, 2000; Stuart *et al.*, 2000) and will not be re-described here. For central Iceland samples Sr and Nd isotope analyses were kindly provided by B. Seth and M. Thirlwall. O isotope analyses on all central Iceland and NAIP samples were obtained by the author. He and trace element analyses were obtained jointly by the author, D. Hilton and C. Macpherson and have been presented by Day *et al.* (2002). Description of analytical techniques for trace elements and oxygen and helium isotopes can be found in appendices B and C and major and trace element data for central Iceland can be found in appendix E.

2.3.1 Major and trace elements for central Icelandic basalts

All Central Iceland samples included in this study are tholeiitic in composition. The glasses display a restricted range of compositions with MgO contents varying from 12.5 to 5.0 wt. % (Appendix E). Trace elements are enriched relative to primitive mantle by factors up to 40 times in the high field strength elements (HFSE) Nb and Ta, 25 times in light rare earth elements (LREE) and 8 times in heavy rare earth elements (HREE) (Fig. 2.3). The glasses are relatively enriched in some large ion lithophile elements (LILE) such as Rb, Ba, Sr but not in Cs, K and Pb; they also show depletions in HFSE, U and Th. The glasses are enriched in incompatible elements compared with highly magnesium lavas from Theistareykir (NRZ) or Reykjanes (WRZ; Skovgaard *et al.*, 2001). The whole rock picro-basalts and basaltic lavas have >7 wt. % MgO and fall into LREE-depleted (Th-29, NAL-688) and enriched groups (NAL-626, NAL-625, NAL-611, Pjor).

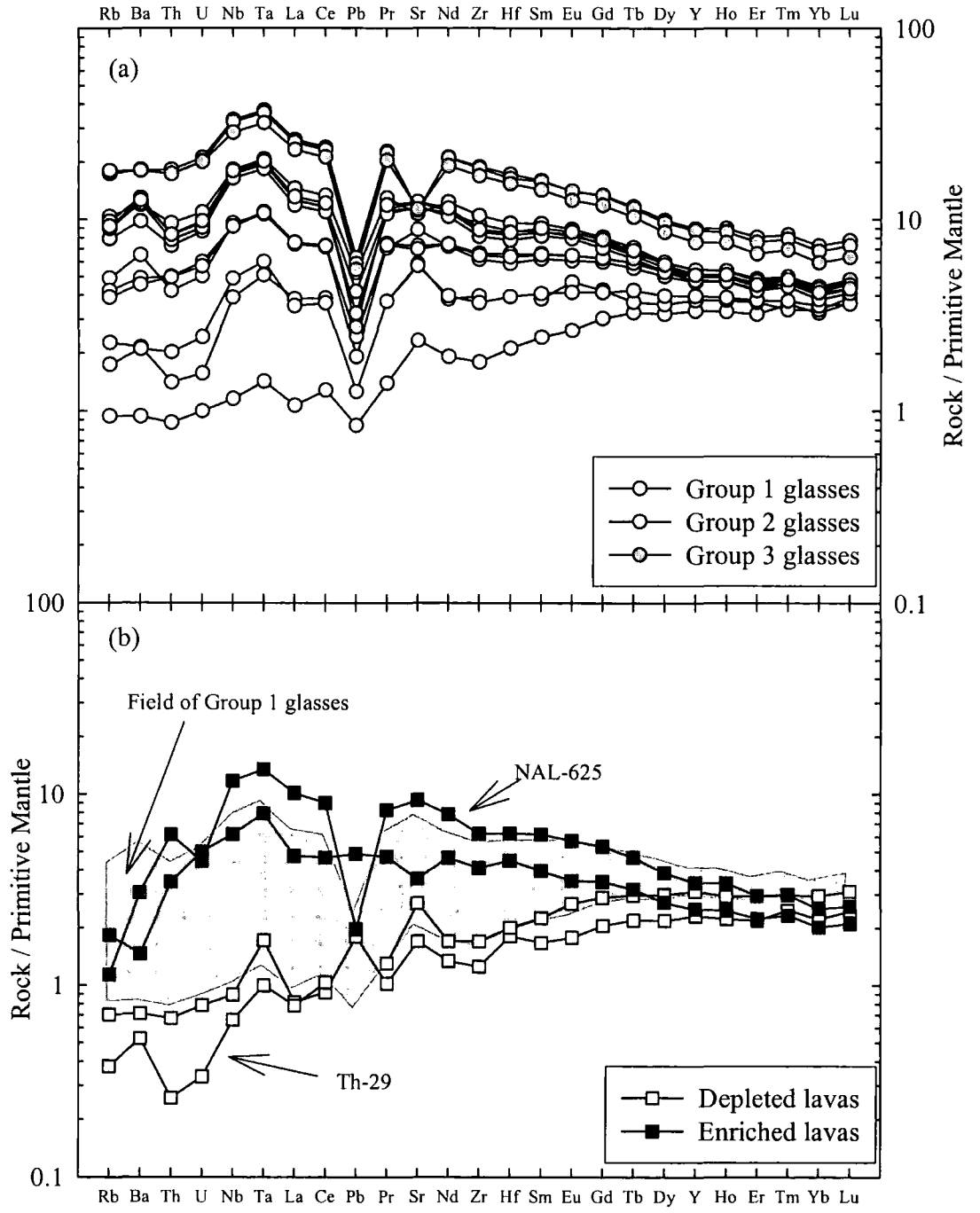

Fig. 2.3: Primitive mantle normalised trace element patterns of (a) sub-glacial glasses and (b) sub-aerial picro-basalts and basalts from central Iceland. Trace elements are normalised to primitive mantle (Sun and McDonough, 1989). Data for Th-29 and NAL-611 (Group 1 glass) are from Skovgaard et al. (2001) and Breddam (2002) respectively.

Based upon their REE profiles and trace element concentrations (Fig. 2.3), central Iceland glasses can be assigned to three groups. Group 1 range from pronounced LREE depletion to mild LREE enrichment ($(La/Yb)_n$ = 0.33-1.77, $(La/Sm)_n$ = 0.44-

1.12, $(Sm/Yb)_n$ = 0.75-1.51). Group 2 glasses have similar HREE contents to Group 1 glasses but more elevated LREE ($(La/Yb)_n$ = 2.82-3.36, $(La/Sm)_n$ = 1.44-1.53, $(Sm/Yb)_n$ = 1.96-2.20). Group 3 glasses have the highest concentrations of REE but have overall patterns that are similar to Group 2 ($(La/Yb)_n$ = 3.58-3.89, $(La/Sm)_n$ = 1.60-1.64, $(Sm/Yb)_n$ = 2.19-2.40). All glasses display relative enrichment of Ta and Nb (all have positive ΔNb (Fitton *et al.*, 1997)) and depletion in Pb, with respect to neighbouring elements. Group 1 glasses generally display positive Ba and Sr anomalies. Positive Ba anomalies also appear in Group 2 but without the Sr anomaly, while in Group 3 the Ba anomaly is absent and Sr is depleted relative to neighbouring elements (Fig 2.3).

The picro-basalt lava samples are distinct from the glass groups on the basis of their trace element patterns, due to their mineral-accumulative or -fractionated nature. They can be split into two groups (Fig. 2.3), those that are LREE-enriched (NAL-625 and PJOR), with $(La/Yb)_n$ = 2.36-4.02, $(La/Sm)_n$ = 1.20-1.64 and $(Sm/Yb)_n$ = 1.97-2.34, and those that are LREE-depleted (Th-29, NAL-688) with $(La/Yb)_n$ = 0.27-0.37, $(La/Sm)_n$ = 0.35-0.43 and $(Sm/Yb)_n$ = 0.75-0.77. The LREE-enriched picro-basalts show similar enrichment in the HFSE Nb and Ta to the glasses but lower concentrations of LILE (Cs, Rb, Ba). The LREE-enriched picro-basalts have greater fractionation in their REE patterns than the glasses and lower HREE which probably indicates a greater degree of partial melting in the presence of residual garnet. To a first approximation, Th-29 resembles the most depleted Group 1 glass and enriched PJOR also falls with the range of Group 1 lavas (Fig 2.3). The trace element patterns of the picrites are comparable with previously published data (e.g., Breddam, 2002 and Skovgaard *et al.*, 2001).

2.3.2 $^{87}Sr/^{86}Sr$ and $^{143}Nd/^{144}Nd$ isotope results for Icelandic basalts

Sr and Nd isotope data for central Iceland lavas are presented in Seth *et al.* (2004) and in Table 2.1. Sr and Nd isotope variations for Iceland glasses correspond to glass groupings with Group 1 glasses exhibiting the least radiogenic $^{87}Sr/^{86}Sr$ (0.703100-0.703194) and most radiogenic $^{143}Nd/^{144}Nd$ (0.513079-0.513040) (Fig. 2.4). Group 2 and 3 glasses possess more radiogenic $^{87}Sr/^{86}Sr$ (up to 0.703326) and more unradiogenic $^{143}Nd/^{144}Nd$ (up to 0.512003). Group 1 glasses lie close to the range of previously analysed glasses from Kistufell (Breddam, 2002), however, Group 2 and

3 glasses possess the most radiogenic $^{87}Sr/^{86}Sr$ for a given $^{143}Nd/^{144}Nd$ compared to Reykjanes ridge glasses that have comparable $^{87}Sr/^{86}Sr$ (Thirlwall *et al.*, 2004). Picrite Th-29 has the least radiogenic $^{87}Sr/^{86}Sr$ (0.702928) and most radiogenic $^{143}Nd/^{144}Nd$ (0.513155) of the samples analysed and is typical of lavas from Theistareykir (Elliott *et al.*, 1991). Picro-basalt NAL-625 possesses radiogenic $^{87}Sr/^{86}Sr$ (0.703463) and unradiogenic $^{143}Nd/^{144}Nd$ (0.512986) and in this respect is very similar to the Palaeocene ankaramite SEL-97 (Hilton *et al.*, 1999).

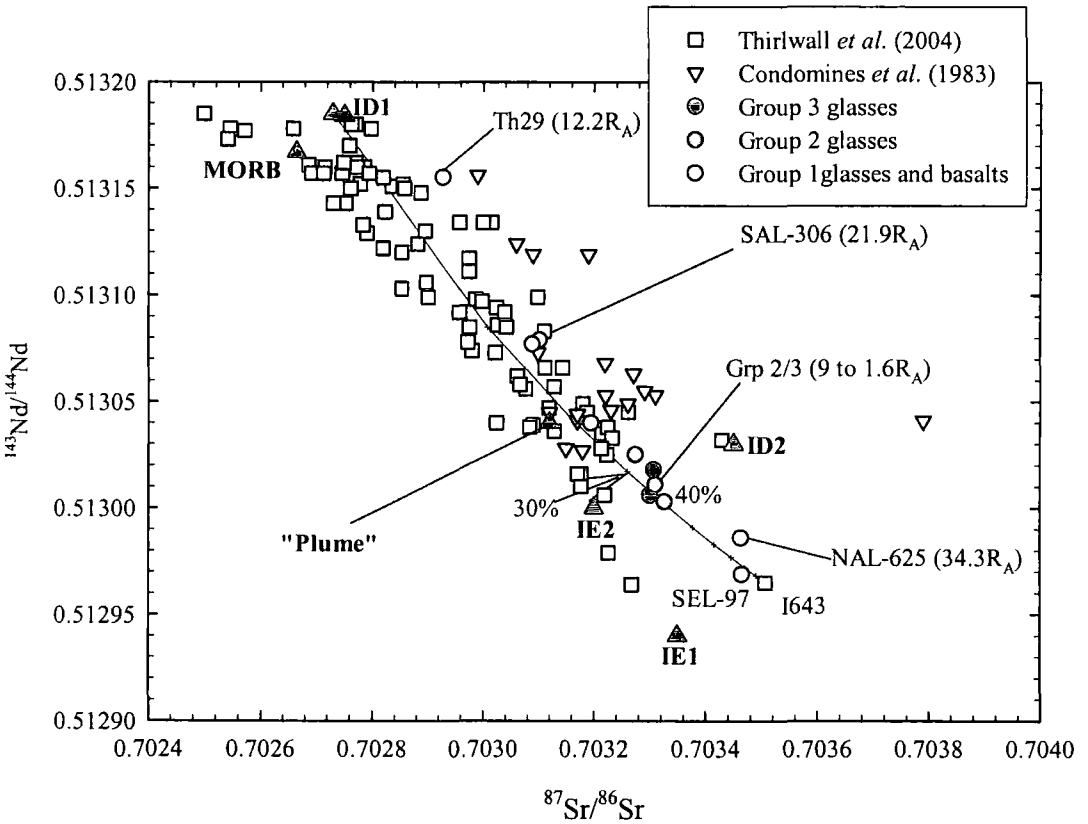

Fig. 2.4: $^{87}Sr/^{86}Sr$ versus. $^{143}Nd/^{144}Nd$ for Icelandic lavas with data from Condomines et al. (1983), Thirlwall et al. (2004) and Seth et al. (2004). Groupings for central Icelandic samples and some $^{3}He/^{4}He$ ratios denoted for samples presented in Table 2.1. End-members (▲) from Thirlwall et al. (2004). Curve denotes bulk mixing trajectory between ID1 component and Landmannalauger rhyolite sample I643 showing 30% and 40% addition of rhyolite brackets Group 2 and 3 central Iceland glasses. See Fig. 2.10 for modelling parameters.

Extrapolated mantle end-members defined by Thirlwall *et al.* (2004) have been plotted on Fig. 2.4. Th-29 plots close to Iceland depleted component ID1, which is very similar to typical MORB, but has slightly more radiogenic $^{87}Sr/^{86}Sr$. Like Kistufell glasses (Breddam, 2002), Group 1 central Iceland glasses plot close to a hypothesised 'plume' component whilst Group 2 and 3 glasses trend towards an enriched component not recognised by Thirlwall *et al.* (2004) but which corresponds closely to the compositions of picrites NAL-625 and SEL-97 as well as a

Landmannalauger rhyolite, I643. The variations seen in Sr and Nd for the glasses are similar to the degree of Pb isotope variation (Seth *et al.*, 2004) in the same samples and extend and overlap East Rift Zone arrays defined by Thirlwall *et al.* (2004).

Table 2.1 - Central Iceland lava He, O, Sr, Nd isotope data

Sample[1] (& phase)	$\delta^{18}O$ (‰)[2]	Wt. (g)	R/R_A	(1σ) ±	[He][3]	$^{87}Sr/^{86}Sr$ (± 2 σ)		$^{143}Nd/^{144}Nd$ (± 2 σ)		Group
Northern Iceland Rift Zone										
Th-29 olivine	4.70 (0.03)[4]	0.65	12.2	0.3	1.3	0.702928	16	0.513155	5	
Central Iceland Rift Zone										
NAL-239 olivine[5]	4.01	0.94	10.6	0.3	7	0.703274	10	0.513024	4	2
NAL-688 glass	4.82 (0.06)	0.50	9.0	0.2	127	*n.d.*		*n.d.*		1
NAL-688 gl.(dup)	"	0.12	8.8	0.2	85	"		"		1
NAL-688 ol.GR[6]	4.38	1.20	8.0	0.4	1.3	"		"		1
NAL-688 ol.CC[6]	5.08 (0.27)	1.08	5.9	0.3	1.3	"		"		1
Herdubreid glass	4.46	0.50	9.1	0.2	44.5	0.703194	10	0.513040	4	1
#9613 olivine	*n.d.*	1.58	7.6	0.8	1.2	*n.d.*		*n.d.*		
NAL-626 glass	3.51 (0.11)[7]	0.52	17.3	0.3	17.4	*n.d.*		*n.d.*		
NAL-355 glass	3.96	0.11	8.8	0.5	31	0.703310	10	0.513011	4	2
NAL-356 glass	4.04 (0.01)	0.11	8.5	0.3	58.2	0.703326	10	0.513003	4	2
NAL-355/6 glass	4.07	0.59	8.9	0.2	22.3	*n.d.*		*n.d.*		2
NAL-357 glass	4.07	0.59	5.0	0.7	0.61	0.703300	11	0.513006	4	3
NAL-625 olivine	4.16 (0.23)	1.10	34.3	4.0	0.35	0.703463	11	0.512986	4	
NAL-625 ol (dup)	"	3.04	30.5	3.0	0.19	"		"		
NAL-625 cpx	4.64	0.62	20.2	5.0	0.41	"		"		
TRO-53 olivine	*n.d.*	2.77	8.3	5.0	0.25	*n.d.*		*n.d.*		
KVK-147 glass	3.82 (0.05)	0.54	2.6	0.9	0.78	*n.d.*		*n.d.*		3
NAL-611 olivine	4.27	2.36	16.6	2.0	1	*n.d.*		*n.d.*		
NAL-496 glass	4.28	0.11	17.6	5.0	2.5	0.703102	10	0.513079	4	1
KVK-168 glass	3.31 (0.01)	0.50	1.6	0.2	3.8	0.703307	10	0.513018	4	3
KVK-169 glass	3.98	0.51	8.5	0.3	8.9	*n.d.*		*n.d.*		2
SAL-306 glass	4.56 (0.21)	0.10	21.9	3.0	8.8	0.703100	9	0.513077	5	1
Southern Iceland Rift Zone										
SAL575 glass	*n.d.*	0.87	14.6	3.1	1.5	*n.d.*		*n.d.*		1
PJOR olivine	4.68	1.61	18.3	0.6	3.2	*n.d.*		*n.d.*		

1. For locations and latitude and longitude of samples see Appendix A
2. Numbers in parenthesis are standard deviations of replicate analyses
3. ± 5% based upon reproducibility of standard, as nccSTP/g
4. from Eiler *et al.* (2000a)
5. O isotope and trace element analysis performed on glass aliquot
6. GR = glass rim; CC = crystalline centre
7. O isotope analysis performed on olivine

2.3.3 $^3He/^4He$ and [He] results for Icelandic basalts

Helium isotope ratios ($^3He/^4He$) and concentrations ([He]) are reported in Table 2.1 with locations of samples and their helium isotope ratios shown in Fig. 2.2. Glasses and phenocrysts samples from central Iceland are characterised by a wide range in $^3He/^4He$ ratios encompassing high-^3He hotspot ratios (>>$8R_A$), through MORB-like

values ($8\pm1R_A$*) to values considerably lower than MORB indicating a significant contribution from radiogenic He in those lavas.

The highest value measured in this work is $34.3R_A$ for Vadalda (NAL-625), just north of the Vatnajökull Icecap (Fig. 2.2), is significantly greater than any other reported He isotope ratio for the Icelandic neovolcanic zones (previous highs are $26R_A$ for Koldukvislarbotner and $26.2R_A$ for Thrihyrngur in central Iceland and ERZ respectively; Kurz *et al.*, 1985 and Poreda *et al.*, 1992). The $^3He/^4He$ of Vadalda is comparable with the highest value of older volcanic successions at Seladalur, northwest Iceland ($37.7R_A$ Hilton *et al.*, 1999) and is higher than those of olivines from Tertiary lavas throughout the North Atlantic Magmatic Province (Graham *et al.*, 1998; Stuart *et al.*, 2000; Peate *et al.*, 2003) except for Baffin Island picrites (Stuart *et al.*, 2003). The $^3He/^4He$ ratio of this sample is also comparable to lavas from Loihi seamount, Hawaii and the Galapagos Islands, the only other modern day OIB to register helium isotope ratios greater than $25R_A$ (Kurz *et al.*, 1983; Graham *et al.*, 1993; Kurz and Geist, 1999).

Notably, the $^3He/^4He$ ratio of clinopyroxene phenocrysts from the same Vadalda sample are lower than the ratio observed in olivines ($20.2R_A$ versus $34.3R_A$). Such an effect has been observed previously and attributed to preferential capture of radiogenic He in the pyroxene lattice (Hilton *et al.*, 1995). However, the clinopyroxene $^3He/^4He$ is still higher than most of the samples presented in this study, as well as previously analysed samples from central Iceland (Breddam *et al.*, 2000) corroborating the high $^3He/^4He$ inferred for this particular locality.

High $^3He/^4He$ hotspot values were found at five further sites in Central Iceland: Ketildyngja ($10.6R_A$), Fjallsendi ($17.3R_A$), Kistufell ($16.6R_A$), Gaesahruiker ($17.6R_A$) and Bardarbunga ($21.9R_A$). These samples lie towards the northern and western parts of the study area. The values obtained for the Bardarbunga glass compares well with other reported values in the immediate area ($22.2R_A$ for Innsta-Blakafell and $19.7R_A$ for Tindafell; Kurz *et al.*, 1985). This study also reports high $^3He/^4He$ values for the Theistareykir NRZ lava Th-29 ($12.2R_A$) and the SRZ lavas from Solheimajökull ($14.6R_A$) and Pjorsardalur ($18.3R_A$). Four of these high $^3He/^4He$ values were obtained from glass, and with the exception of Fjallsendi for

* Using $^3He/^4He$ MORB compilation of Hilton and Porcelli (2003)

which no group-defining data is available, each samples is classified as a Group 1 glass or LREE-depleted lava.

MORB-like $^3He/^4He$ ratios characterises six of the central Icelandic localities investigated in this study: Herdubried, Odadahraun, Upptyppingar, Trolladyngja, Jardfraedingaslod and Eggert. Notably, both high [He] glass samples and low [He] olivines contained MORB-like $^3He/^4He$ signatures and span nearly the entire range of [He] reported in this study (Fig. 2.5). These locations all lie immediately north of Vatnajökull and cluster around the most elevated $^3He/^4He$ sample from Vadalada (Fig 2.1). The glasses contain the greatest He concentration (up to 1.3×10^{-7} cm^3STP/g) but some low He concentration olivine (e.g., TRO-53) also contain MORB-like He. Two glass samples with MORB-like He belong to Group 1 (Herduibred, Eggert), five to Group 2 (although 3 are samples from the same flow: NAL-355, NAL-356, NAL-355/356), and the two remaining lavas are ungrouped (#9613, TRO-53).

He isotope ratios lower than MORB were found for four samples: glasses from Upptyppingar, Hvannalindir and Jardfraedingaslod and olivine phenocrysts from the centre of a pillow lava from Eggert. The three low $^3He/^4He$ glasses comprise all of Group 3 and have low [He] (Fig. 2.5). Upptyppingar and Hvannalindir glasses have [He] $<1 \times 10^{-9}$ cm^3STP/g and the Jardfraedingaslod glass KVK-168 has discernibly lower [He] than MORB-like KVK-169 which is from the same locality. Like Group 2, the Group 3 glasses occur immediately north of Vatnajökull (Fig 2.1).

Olivines from the centre of an Eggert pillow lava (NAL-688) have a lower $^3He/^4He$ ratio ($5.9R_A$) compared with olivine separated from the glass rim ($8.0R_A$) and the glass itself ($8.9R_A$). A similar degree of isotopic heterogeneity has also been observed in the $\delta^{18}O_{olivine}$ of Theistareykir flows (Eiler *et al.*, 2000a); this feature may also be reflected in the variable $\delta^{18}O_{olivine}$ measured in some of the samples presented here (Table 2.1). This observation can be interpreted in one of two ways: capture of some xenocrystic olivine in this sample or, possible cosmogenic implantation of ^3He on the outer surface of the flow. Based upon the heterogeneity of $\delta^{18}O_{olivine}$, the recent de-glaciation in the area and the difficulty in releasing trapped cosmogenic ^3He during crush experiments, the former interpretation is preferred.

Table 2.2 - Skye and East Greenland O, He, Pb isotope data

Sample[1]	$\delta^{18}O$ (‰)[2]	R/R_A[3]	(1σ) ±	[He][4]	$^{206}Pb/^{204}Pb$ (± 2 σ)		$^{207}Pb/^{204}Pb$ (± 2 σ)		$^{208}Pb/^{204}Pb$ (± 2 σ)	
Skye Main Lava Series, Isle of Skye										
SK 266	5.14	3.5	0.7	0.6	17.226	10	15.321	12	37.140	20
BB1	5.13	18.4	2.1	0.6	18.043	7	15.476	5	37.730	14
LL1	4.85	22.1	3.6	0.9	16.286	8	15.079	8	36.050	14
SK 291		1.2	0.6	1.1	16.839	10	15.200	10	36.850	30
Little Minch Sill Complex, Isle of Skye										
INV 1	5.17	2.3	0.4	0.6	16.787	7	15.209	6	36.880	20
BH 1	5.16	4.1	0.8	1.3	17.558	13	15.399	14	37.580	35
Drum	5.04									
SR 81	5.26	2.5	1.3	0.9	17.678	5	15.397	4	37.850	11
Skye Dyke Swarm, Isle of Skye										
SK 056	4.69	2.9	0.1	12	17.534	15	15.361	19	37.040	33
SK 057	4.69	8	0.4	1.9	17.378	5	15.355	5	37.070	11
SK 204	2.72	6.6	0.3	0.7	17.377	6	15.452	5	37.530	14
SK 204	3.70	6.6	0.3	0.7	17.377	6	15.452	5	37.530	14
Cuillin Complex, Isle of Skye										
SK 208	4.64	1.1	0.0	9.6	16.806	6	15.244	6	37.270	15
Prinsen af Wales Fm. East Greenland										
EG 2240	5.62	9.7	0.8		17.551	8	15.149	7	37.309	18
	5.47	9.7	0.8		17.551	8	15.149	7	37.309	18
EG 2244	4.84	1.8	0.8		14.733	4	14.620	5	35.741	11
EG 3359	4.83	10.5	1.0		18.328	6	15.352	5	38.409	15

1. For locations and latitude and longitude of samples see Appendix A
2. O analysed by laser fluorination on olivine
3. Measured $^3He/^4He$ (R/R_A notation) (Data from Stuart *et al.* 2000; Ellam and Stuart, 2000)
4. He abundance as nccSTP/g
5. Pb isotopes analysed on VG54E mass spectrometer (in Stuart *et al.* 2000; Ellam and Stuart, 2000)

2.3.4 $^{18}O/^{16}O$ isotope results for Icelandic and NAIP basalts

For this study 13 NAIP olivines, 20 central Iceland glasses, olivines and a clinopyroxene have been analysed for their $\delta^{18}O$ isotope signatures (total of 46 analyses including replicates); data are presented in Tables 2.1 and 2.2 with errors quoted in Appendix C.2. A visual comparison between CFB olivines, Icelandic lavas, lithospheric mantle olivine and OIB is shown in Fig. 2.6. Prinsen af Wales Bjerge Formation lavas possess $\delta^{18}O$ values in the range of +4.83 to +5.62‰. Skye Main lava series possess $\delta^{18}O$ values in the range of +4.95 to +5.23‰ while three dolerite sills from Skye exhibit $\delta^{18}O$ values similar to the upper end of the lava range (+5.23±0.10, 2.S.D., n=3).

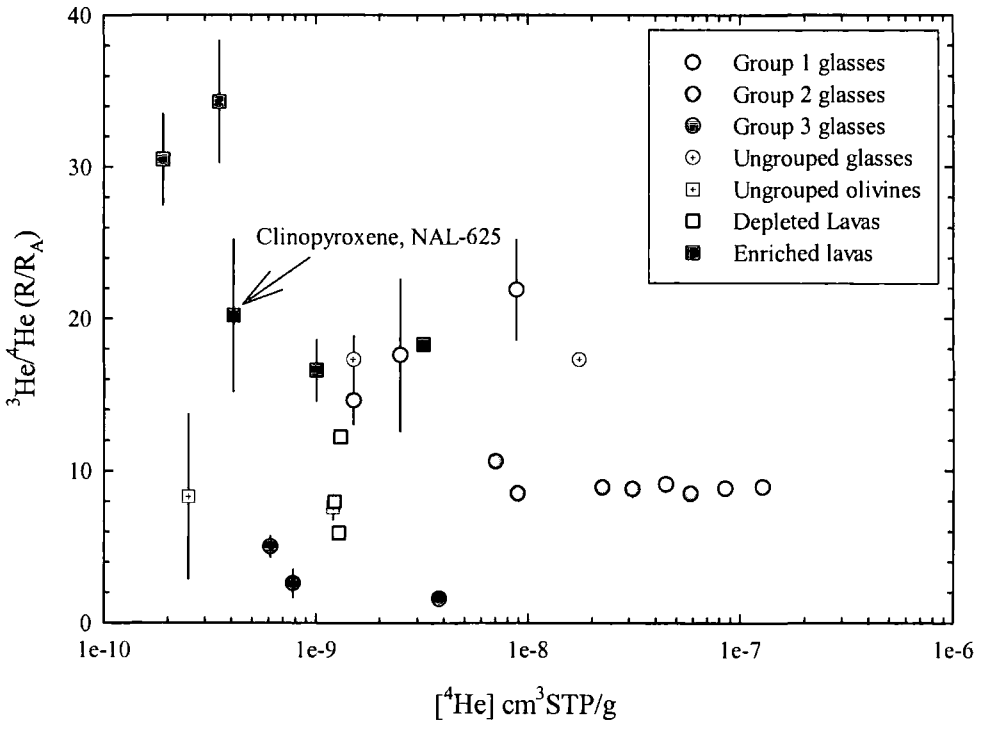

Fig. 2.5: Plot of $^3He/^4He$ (R/R_A notation) versus helium concentration ([He]). 2σ errors are shown or are smaller than symbols. Groupings of lavas and glasses are shown.

The Skye dyke swarm and Cuillin complex peridotite possess a range of lower $\delta^{18}O$ (+2.72 to +4.79‰), compared with Skye lavas and Little Minch sills, the most extreme being dyke SK204 which shows oxygen isotope heterogeneity similar to or greater than that measured in lavas from central and northern Iceland (Eiler *et al.*, 2000c; this chapter). Compared with other CFB provinces, measured $^{18}O/^{16}O$ of NAIP olivines extend to lighter $\delta^{18}O_{Ol}$ (+2.72 to +5.62‰) compared with the olivines from Miocene Yemen CFB (+5.12 to +6.15‰; Baker *et al.*, 2000), the only other CFB lavas to be studied in detail for $\delta^{18}O$ values of their mafic minerals. The $\delta^{18}O$ of studied CFB partly overlap the range of peridotite olivine (Mattey *et al.*, 1994) or compilations of MORB or OIB olivine (Eiler *et al.*, 1997; chapter 4) (Fig. 2.6), but extend to significantly lower values.

Central Icelandic glasses possess $\delta^{18}O$ values in the range of +3.31 to +4.82‰ (Fig. 2.6). The $\delta^{18}O$ values of glasses are lower than those of basaltic glasscs from arc-volcanics (Eiler *et al.*, 2000b), back-arc basins (Macpherson and Mattey, 1998;

Macpherson *et al.*, 2000), and mid-ocean ridges (Eiler *et al.*, 2000a), but their upper limit is similar to four glasses previously obtained from central Iceland (Breddam, 2002). Oxygen isotope ratios in olivine ($\delta^{18}O_{ol}$) phenocrysts vary between +3.51 to +5.08‰. The olivine values are lower than those typically observed for ocean islands (Eiler *et al.*, 1996; Eiler *et al.*, 1997), arc volcanics (Eiler *et al.*, 2000b), mantle peridotites (Mattey *et al.*, 1994), or MORB (Eiler et al., 2000c). Results are similar to, or lower than, values reported for the Reykjanes peninsula (Gee *et al.*, 1998; Skovgaard *et al.*, 2001) and Theistareykir (Eiler *et al.*, 2000a; Skovgaard *et al.*, 2001). One clinopyroxene phenocryst from NAL-625 was analysed and possessed $\delta^{18}O$ signature of +4.64‰. $\delta^{18}O$ values are generally lower than expected if glass was in equilibrium with olivine from NRZ and WRZ lavas (Macpherson and Mattey, 1998, Eiler *et al.*, 2000b). At magmatic temperatures olivine will possess $\delta^{18}O$ *ca.* 0.4‰ lower than the melt from which it crystallised (Eiler *et al.*, 2000b).

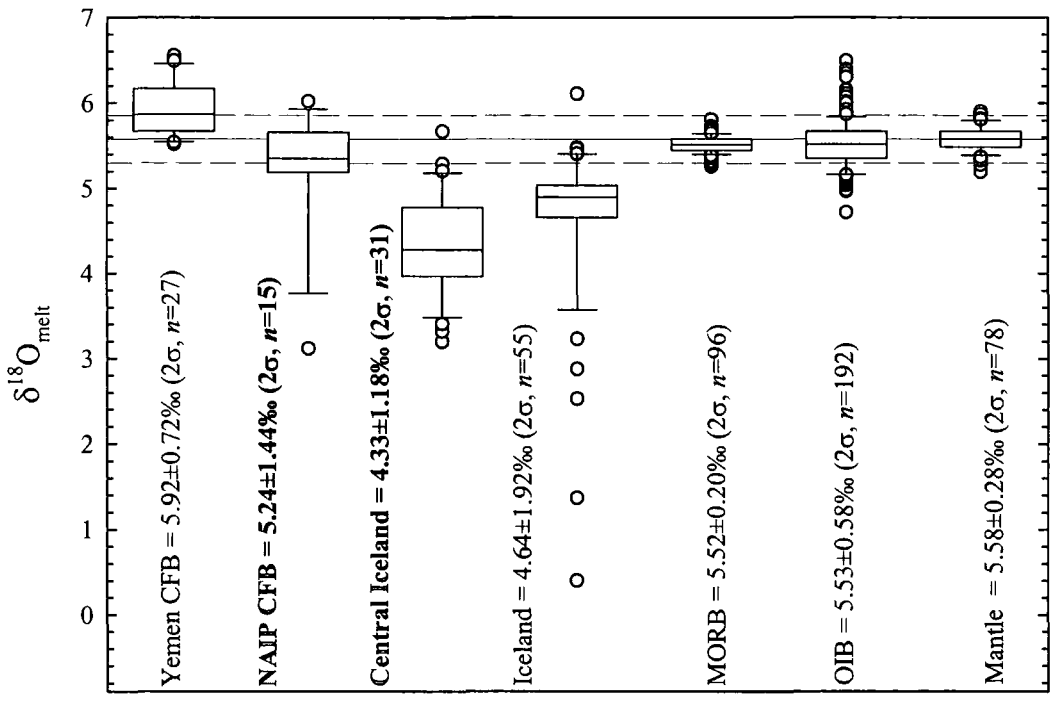

Fig. 2.6: Box plot of oxygen isotope ratios analysed by laser fluorination for phenocrysts and glasses from different volcanic environments expressed as melt compositions. Melt compositions for olivine derived assuming a $\Delta^{18}O_{mineral\text{-}melt} = -0.4$ after Eiler et al. (2000b). Data from this study (NAIP, central Iceland), Mattey et al. (1994), Eiler et al. (1995; 1996; 1997), Gee et al. (1998), Garcia et al. (1998), Baker et al. (2000), Harris et al. (2000), Eiler et al. (2000c), Eiler et al. (2000a), Breddam (2002), Widom and Farquhar (2003), Cooper et al. (2004). See Fig. 2.1 for explanation of statistical distribution and dispersion.

2.4 Discussion

This study presents the highest measured $^{3}He/^{4}He$ ratio from the central Icelandic rift zones. This study also highlights the existence of both $^{3}He/^{4}He$ (1.6 to 34.3R_A) and oxygen isotope heterogeneity in central Iceland lavas. The sampled helium and oxygen isotopic heterogeneity is also observed in Palaeogene NAIP rocks (1.1-22.1R_A). Central Icelandic lavas and Palaeogene lavas and intrusive rocks from Skye and East Greenland trend from mantle-like to low $\delta^{18}O$ (5.6 to 2.7‰). In the following sections, the cause of helium and oxygen isotope variation in central Iceland and the Palaeogene NAIP and the implications for the mantle sources of these basalts are considered. The discussion initially focuses on the processes of coupled crustal assimilation and fractional crystallisation (AFC) and the role of He-degassing. The discussion then considers the cause of the high $^{3}He/^{4}He$ component seen in central Iceland and the possibility of heterogeneous $^{3}He/^{4}He$ and $\delta^{18}O$ isotope mantle domains. The possibility of a low-$\delta^{18}O$ component in the mantle beneath Iceland and the relationship $^{3}He/^{4}He$ and $\delta^{18}O$ have with Sr-Nd-Pb isotope systematics are discussed. The findings lead to a critical examination of employing helium isotope datasets to discuss mantle reservoir chemistry without first considering the variable effects of degassing and crustal interaction experienced by magmas. Based upon these data advice is given as to how He isotope datasets should be applied to geochemical problems.

2.4.1 Intra-crustal processes in central Icelandic and NAIP magmas

Relic magmatism of Skye and East Greenland, as well as lavas from central Iceland possess $\delta^{18}O$ that is typically lower than expected for typical mantle melts (e.g., Ito *et al.*, 1987; Eiler *et al.*, 1996, 1997; Harris, 2000; Widom and Farquhar, 2002; chapter 4). This observation has been made previously for Icelandic lavas (e.g., Condomines *et al.*, 1983; Hemond *et al.*, 1993; Gee *et al.*, 1998; Eiler *et al.*, 2000a) and explained either by assimilation of Icelandic crust with low $^{18}O/^{16}O$ due to hydrothermal alteration (Gautason and Muehlenbachs, 1998), or to the presence of low $\delta^{18}O$-domains in the Icelandic mantle (Thirlwall *et al.*, 1999; Seth *et al.*, 2004). These arguments might similarly be extended to the low $\delta^{18}O$ signatures measured in lavas and intrusive magmatic rocks from Skye and East Greenland. Convincing

evidence for the role of crustal contamination is given by different relationships between the NAIP and Iceland data sets.

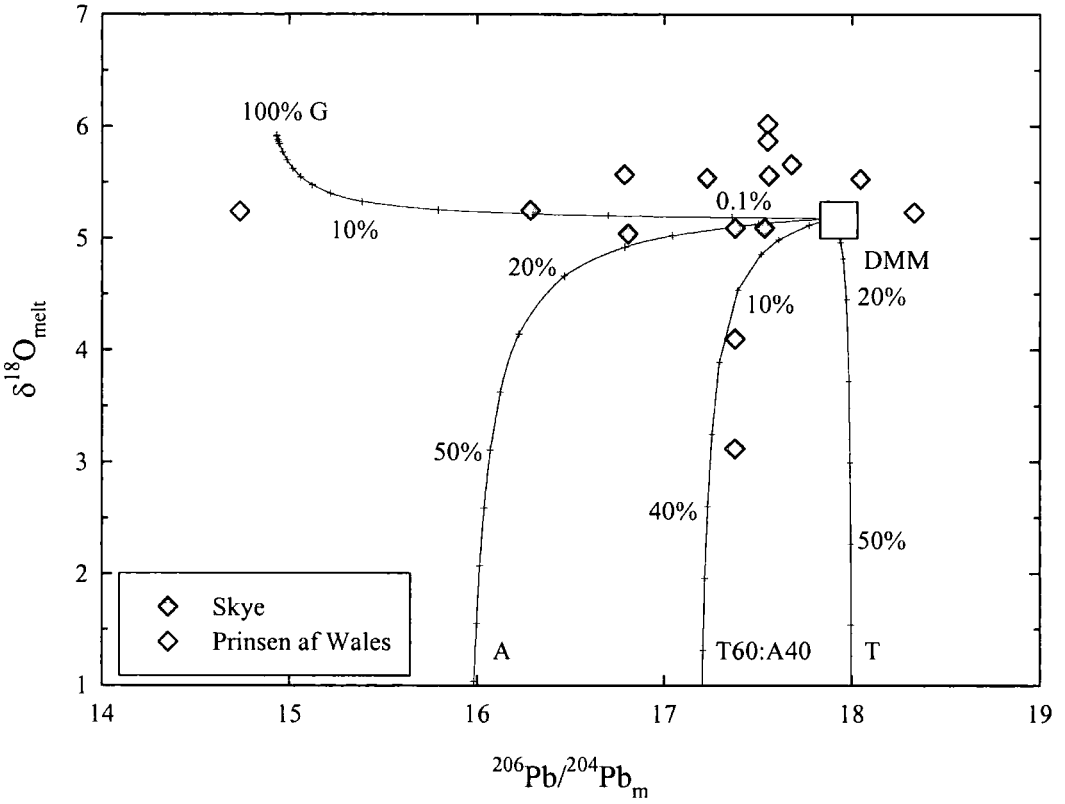

Fig. 2.7: $^{206}Pb/^{204}Pb_m$ versus $\delta^{18}O_{melt}$ for Prinsen af Wales Bjerge lavas, the Skye main lava series and plutonic rocks from Skye. Data points are olivine $\delta^{18}O$ that have been corrected to melt values ($\Delta_{melt-olivine}$ = -0.4 in Icelandic samples, Eiler et al., 2000b). Mixing trajectories show the expected effects of crustal contamination by Archaean granulite (G), amphibolite (A), Torridonian sandstone (T) and a 60:40 mix of T and A. Percentages shown for amount of crustal contaminant at tick mark. Mixing parameters include mantle that is characterised by $\delta^{18}O$ = 5.18±0.28‰ (Mattey et al., 1994), $^{206}Pb/^{204}Pb$ =17.9, [Pb] = 0.5ppm (Stuart and Ellam, 2000). (G) $\delta^{18}O$ = +5.9‰, $^{206}Pb/^{204}Pb$ =15.96, [Pb] = 11ppm , (A) $\delta^{18}O$ = +0.0‰, $^{206}Pb/^{204}Pb$ =14.93, [Pb] = 12.9ppm, (T) $\delta^{18}O$ = -2.1‰, $^{206}Pb/^{204}Pb$ =18.0, [Pb] = 10ppm. Crustal endmember data derived from Dickin (1981), Gilliam and Valley (1997) and Monani and Valley (2001).

The way in which basaltic melts interact with hydrothermally altered crust or sialic crustal units to change melt $\delta^{18}O$ values can be modelled in two ways. First, assimilation of older lavas in the crust may occur during fractional crystallisation (AFC). Alternatively, basaltic magmatism could introduce sufficient heat to generate rhyolitic crustal melts that could then mix with arriving basaltic magmas. In reality, there is likely to be a spectrum of these two processes but the end member scenarios provide a context for discussing the origin of $\delta^{18}O$ variation in Icelandic and NAIP magmas. Crustal contamination models are also sensitive to the $\delta^{18}O$ value chosen

for the contaminant. In the case of Iceland this is a contentious issue as there is substantial oxygen isotopic heterogeneity recorded in samples of Icelandic crust (Hattori and Muehlenbachs, 1982; Gautason and Muehlenbachs, 1998). Because heterogeneity is likely to be homogenised during crustal melting the $\delta^{18}O$ of Icelandic rhyolites provide an estimate of a generic crustal endmember. For this reason in the section on Icelandic magmatism I adopt the $\delta^{18}O$ of Eiler *et al.* (2000a) of 0‰. This estimate is lower than the value of 2‰ employed by Gautason and Muehlenbachs (1998) or Skovgaard *et al.* (2001) such that modelling here allows greater isotopic leverage for changing melt $\delta^{18}O$ values. For Skye and East Greenland, relationships between $\delta^{18}O$ and $^{206}Pb/^{204}Pb$ (Fig. 2.7) illustrate the role of crustal contamination in this magmatism and, for central Iceland lavas, indices of magmatic differentiation illustrate the role of crustal assimilation processes (Fig. 2.8). In this section I do not discuss the effect of continental lithospheric mantle on these lavas specifically because crustal contamination can explain all the isotopic variations in the dataset.

Evidence for assimilation of crustal lithologies in Skye and limited number of analyses of East Greenland basalts is given by characteristic unradiogenic Pb isotope signatures. CFB lavas in the NAIP show evidence of shallow fractionation and crustal assimilation (Thompson, 1982) and they appear likely to have interacted with Archaean crustal rocks on the basis of their Pb, Sr and Nd isotope systematics (Saunders *et al.*, 1997). Hydrothermal systems associated with the large intrusive centres of Skye are known to have imparted low $\delta^{18}O$ on the crust generating values as low as -5‰ (Taylor and Forrester, 1971; Forrester and Taylor, 1977) suggesting that combined O-Pb isotope systematics of lavas and their phenocrysts may provide useful constraints on crustal contamination processes.

The low $\delta^{18}O$ signatures in NAIP olivines cannot be the result of alteration of the olivines themselves because they are optically fresh in appearance. Archaean granulites and amphibolite crustal rocks tend to have variable $^{18}O/^{16}O$ signatures (Whole rock gneiss $\delta^{18}O$ = +4.9 to +6.9‰; $\delta^{18}O_{zircon}$= +4.79 to +5.32‰; $\delta^{18}O_{quartz}$= +6.85 to +9.67‰, Gilliam and Valley, 1997; Monani and Valley, 2001). Another potential contaminant, Torridonian sandstone, whilst possessing heavy $\delta^{18}O$ (+6.84 to +8.77‰) for quartz also possesses light bulk rock $\delta^{18}O$ (-2.1‰, Monani and Valley, 2001); the reason for this large discrepancy is unclear. Torridonian sandstone

is arkosic, so either (i) a large volume of feldspar is required, or (ii) feldspar with very low $\delta^{18}O$ is required to explain the low $\delta^{18}O$ of the whole rock. In Fig 2.7 a series of bulk mixing trajectories have been generated between a depleted mantle melt and potential crustal assimilates (Amphibolite, granulite gneiss and Torridonian sandstone).

The increasingly unradiogenic $^{206}Pb/^{204}Pb$ with limited variation in $\delta^{18}O$ in some samples can be explained by addition of 0.1 to 0.5% granulite or 10% amphibolite crust. The samples with low $\delta^{18}O$ are best explained by addition of Upper Proterozoic Torridonian sandstone and Archaean amphibolite. These estimates of crustal contamination for mafic rocks concur with studies of Skye granites which show variable contamination by upper crustal (T in Fig 2.7) and Archaean crustal lithologies (A and G, Dickin, 1981). Another explanation for low $\delta^{18}O$ and unradiogenic Pb for some Skye basalts is that assimilation of older Palaeogene intrusive material which has been hydrothermally altered, took place. Assuming magmas interact with this hydrothermally altered basalt material with low $^{206}Pb/^{204}Pb$, a minimum of 5-20% assimilation of hydrothermally altered material is required to explain the Skye main lava series and East Greenland olivine $\delta^{18}O$ data (Fig. 2.7). The key observation remains, regardless of the type of crustal contaminant, that the range of $\delta^{18}O$ measured in NAIP olivines can be most simply explained by crustal assimilation.

Icelandic magmatism erupts through oceanic or 'Icelandic-type' crust and so, unlike NAIP lavas, the young age of the Iceland crust will limit the degree to which Sr, Nd and Pb isotope variation can be generated through *in situ* radiogenic ingrowth. To circumvent this problem $\delta^{18}O$ is plotted versus trace element ratios sensitive to fractional crystallisation and assimilation (Fig. 2.8) providing evidence that crustal contamination plays a major role in the chemical characteristics of central Icelandic lavas. A generally positive correlation between $\delta^{18}O$ and MgO is observed in Fig. 2.8 with Group 3 glasses generally having lower $\delta^{18}O$ and MgO than Group 2 glasses, which in turn have lower $\delta^{18}O$ and MgO than Group 1 glasses. Fractional crystallisation of basaltic magma will cause only a small increase in $\delta^{18}O$ with decreasing MgO (~0.3‰). Therefore the central Iceland data require addition of a low-$\delta^{18}O$ component during differentiation.

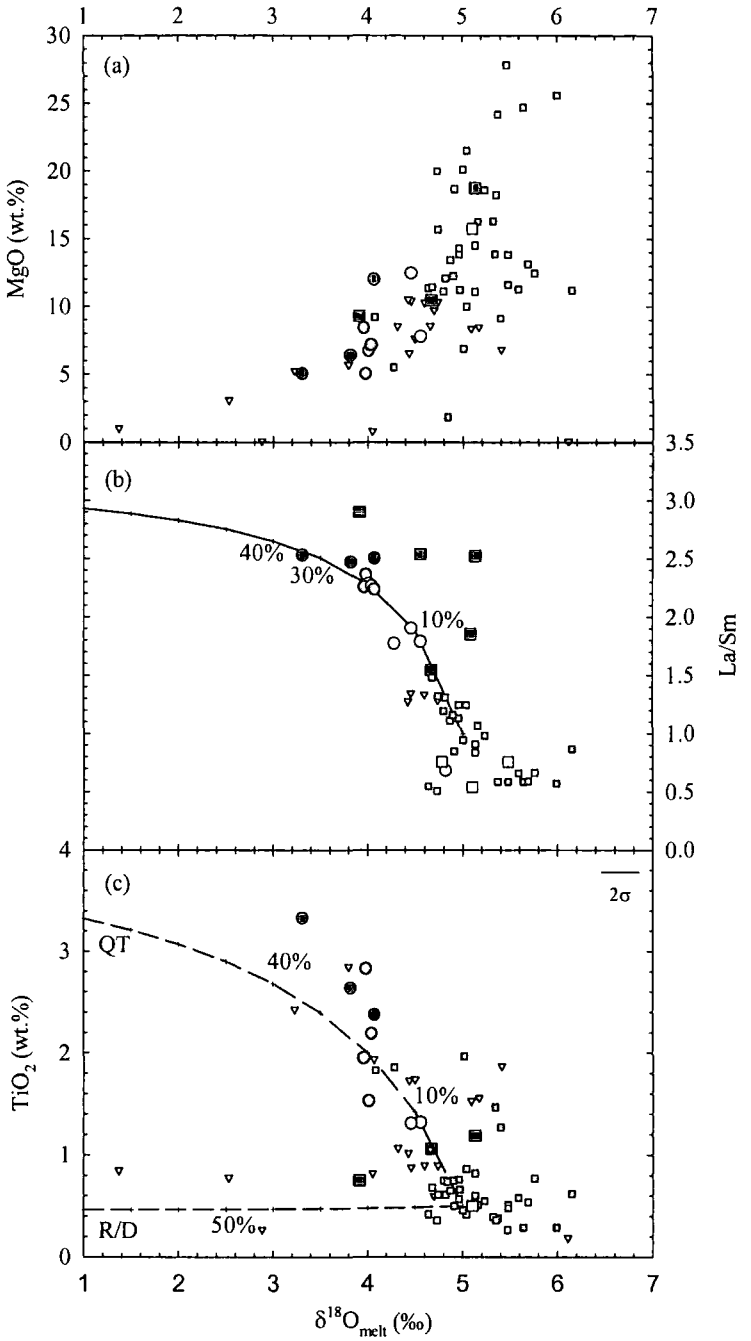

Fig. 2.8: Composite plot of $\delta^{18}O_{melt}$ versus (a) MgO (wt.%), (b) La/Sm and (c) TiO_2 (wt.%) emphasising the presented data set (Table 2.1). Literature values from Condomines et al. (1983); Gee et al. (1998), Eiler et al. (2000), Skovgaard et al. (2001) and Breddam (2002). For modelling in Fig. 2.8b and a crustal endmember was based on the rationale of Eiler et al. (2000c) for an 'average' assimilant with $\delta^{18}O$ of 0‰ because hydrothermally altered rocks in Icelandic crust exhibit extremes in $\delta^{18}O$ (6 to -12‰; Gautason and Muehlenbachs, 1998). A $\Delta_{olivine\text{-}melt}$ -0.4 correction factor is employed for olivine based upon previously derived fractionation factors (Mattey and Macpherson, 1998; Eiler et al., 2000b). A primitive melt composition has been generated to take into consideration the impact of olivine accumulation seen in Fig. 4a ($\delta^{18}O$ =+5.0‰; La/Sm=1, La=0.7ppm). For modelling in Fig 2.8c, binary mixing of a quartz tholeiite (QT) assimilant with 3.5 Wt% TiO_2 and $\delta^{18}O$ of 0‰ and a rhyolite/dacite (R/D) assimilant (based upon crustal rhyolite in Condomines et al. 1983) with 0.46 Wt% TiO_2 and $\delta^{18}O$ of 0‰ was performed for a fractional crystallisation to assimilation ratio of 4:1 (0.25). Symbols same as Fig. 2.4.

A number of parameters for AFC processes have been plotted and a preferred model of $\delta^{18}O$ versus La/Sm is shown in Fig. 2.8. The model parameters of Eiler *et al.* (2000a) who assumed $\delta^{18}O$ = +5.4‰ and La/Sm = 0.5 based on Theistareykir melt estimates have been modified to take account of fractional crystallisation processes and the depleted nature of Thiestareykir melts emphasised in Fig. 2.3 and 2.8: in this case $\delta^{18}O$ = 5.0‰ and La/Sm = 1. Olivine fractional crystallisation alone should not affect trace element ratios but this does not belie the fact that Theistareykir melts tend to have much lower LREE/MREE ratios because of their more depleted nature (Fig. 2.3).

Contamination of a primitive, incompatible trace element-depleted magma (e.g., similar to Th-29) by rhyolite can reproduce the trace element and oxygen isotope characteristics of the central Iceland glasses with 8% to 18% contamination for Group 1, ~ 20% contamination for Group 2 and ~20% to ~35% contamination for Group 3. However, the elevation of SiO_2 and TiO_2 and lowering of FeO that would result from addition of these volumes of rhyolite magma (Eiler et al. 2000a; Skovgaard et al. 2001) are not observed in the central Iceland lavas. Evolved rhyolites and dacites are not suitable crustal contaminants as they typically show low TiO_2 (and FeO) which are not observed in most of the Iceland data plotted in Fig. 2.8.

Trace element ratios may themselves be fractionated during melt – crust interaction. For example, the trace element concentrations and ratios (e.g., La/Sm) of Krafla rhyolites are significantly different from those of the Krafla basalts from which they are derived (Jónasson, 1994). However, such fractionation will also affect the major element composition of the contaminant. The contaminant required to produce the La/Sm variation from a primitive depleted lava through Group 1 to groups 2 and 3 by AFC would possess the trace element composition of a rhyolite (*c.f.*, Skovgaard et al., 2001). The simplest explanation for such a contaminant is that it is a rhyolitic melt, but as discussed above, the major element composition of Group 2 and 3 are inconsistent with addition of a rhyolitic magma component.

An AFC model in which depleted basaltic magma assimilates "median" quartz tholeiite or crustal andesite can produce a closer match to the Group 1 glasses for trace element enrichment and $\delta^{18}O$ (Fig. 2.8). Limited amounts of AFC are also consistent with the mafic character of all of the depleted rocks and similar

conclusions have been reached for depleted lavas in northern and southwestern Iceland (Eiler et al. 2000a). Therefore, the oxygen isotope data for Group 1 support the conclusion that Icelandic mantle which is depleted in incompatible trace elements possesses $\delta^{18}O$ that is within the range of the source of MORB (Eiler et al., 2000a).

A better fit to the Group 2 and 3 data can be achieved for a model in which an invading basalt, with $\delta^{18}O$ resembling Group 1 and the crustal contaminant are both enriched in incompatible trace elements. Between 50% to 75% differentiation by AFC can reproduce the lowering of $\delta^{18}O$ and enrichment of trace elements. While this model does fit the data, it requires that Group 2 melts, erupted at three distinct locations, all experienced very similar amounts of contamination. An alternative interpretation is that the Group 2 lavas retain their primary oxygen isotopic and trace element compositions. In this scenario, Group 3 represents primary Group 2 melts that have experienced relatively limited amounts of crystallisation and contamination. In fact, the extents of differentiation required by this model are very similar to those modelled for incompatible trace element-depleted lavas.

Irrespective whether Group 2 rocks retain their primary oxygen isotopic characteristics or have interacted with the crust, the modelling requires that the initial melts were enriched in incompatible trace elements. Furthermore, since differentiation and hydrothermal alteration by meteoric water will have a negligible influence on radiogenic isotope ratios either model can be reconciled with the Sr and Nd isotopic data (Fig. 2.4). However, the important distinction arises in the implications for $\delta^{18}O$ values in the mantle. If Group 2 lavas have retained their primary $\delta^{18}O$, then all group 2 and 3 melts are derived from low-$\delta^{18}O$ mantle. If, instead, Group 2 have experienced crustal contamination then both groups could be derived from mantle with $\delta^{18}O$ values similar to the rest of upper mantle. This issue can be examined further by using helium isotope data.

2.4.2 Helium-oxygen relationships and magmatic degassing

There are two ways that processes occurring in the shallow crust can affect the He isotope systematics of mantle-derived melts. First, low-pressure magmatic degassing can deplete melts of their intrinsic volatile inventories prior to eruption. Second, the ancient continental crustal terrains of the NAIP and degassed basaltic Iceland crust

of central Iceland are characterised by high (U+Th)/^{3}He values, i.e., radiogenic He with low ^{3}He/^{4}He ratios. Hence magmatic degassing can render He in melts more susceptible to record crustal contamination (Hilton *et al.*, 1993; 1995; 2000b). As AFC processes are also traced by δ^{18}O it should be possible to relate He and O isotope variations as both should respond to processes occurring in either continental or Icelandic crust. Because there is evidence from both δ^{18}O-^{206}Pb/^{204}Pb and δ^{18}O-trace and major element relationships that AFC has had an impact on the isotopic and elemental inventories of NAIP and central Icelandic magmas respectively I examine the effect that this process has had on He isotopes.

2.4.2.1 Icelandic glasses

Fig. 2.9 compares ^{3}He/^{4}He and ^{18}O/^{16}O for all samples in this work together with published values for Iceland (Condomines *et al.*, 1983; Breddam *et al.*, 2000; Breddam, 2002; Skovgaard *et al.*, 2001). Curvature of the binary mixing trajectories can be described by the parameter k (where $k = ([He]/[O]_C)/([He]/[O]_P)$). Assuming that the primitive (P) end member samples a less-degassed mantle source, characterised by both higher ^{3}He/^{4}He and [He] than crust, a crustal contamination trajectory would plot to the left of k=1. However, all Icelandic glasses plot with k-values generally between 5 and 50 (i.e., to the right of k=1) implying that $[^3He]_C$» $[^3He]_P$. It is highly improbable that the degassed igneous Icelandic crust will have more [^{3}He] than mantle-derived melts. Since the helium content of crust can be directly measured (e.g., Hilton *et al.*, 1990) this implies that [He] of melts is lower than expected. This suggests that degassing prior to contamination exerts a strong influence on the susceptibility of melts to crustal contamination.

The abundance of radiogenic He in Icelandic crust depends upon parent element concentration, age of the crust and retentivity of the He produced. Using the figures of Condomines *et al.* (1983) for 1 Ma old altered basalt with U = 0.3ppm, Th/U ~3.5 and assuming 100% He retention, ~6.5×10^{-8} cm^{3}STP^{4}He/g is produced. This value can be reduced or increased proportionally if the crustal assimilant is younger or older. In Fig. 2.9, the k-value of the mixing trajectories that encompass the present

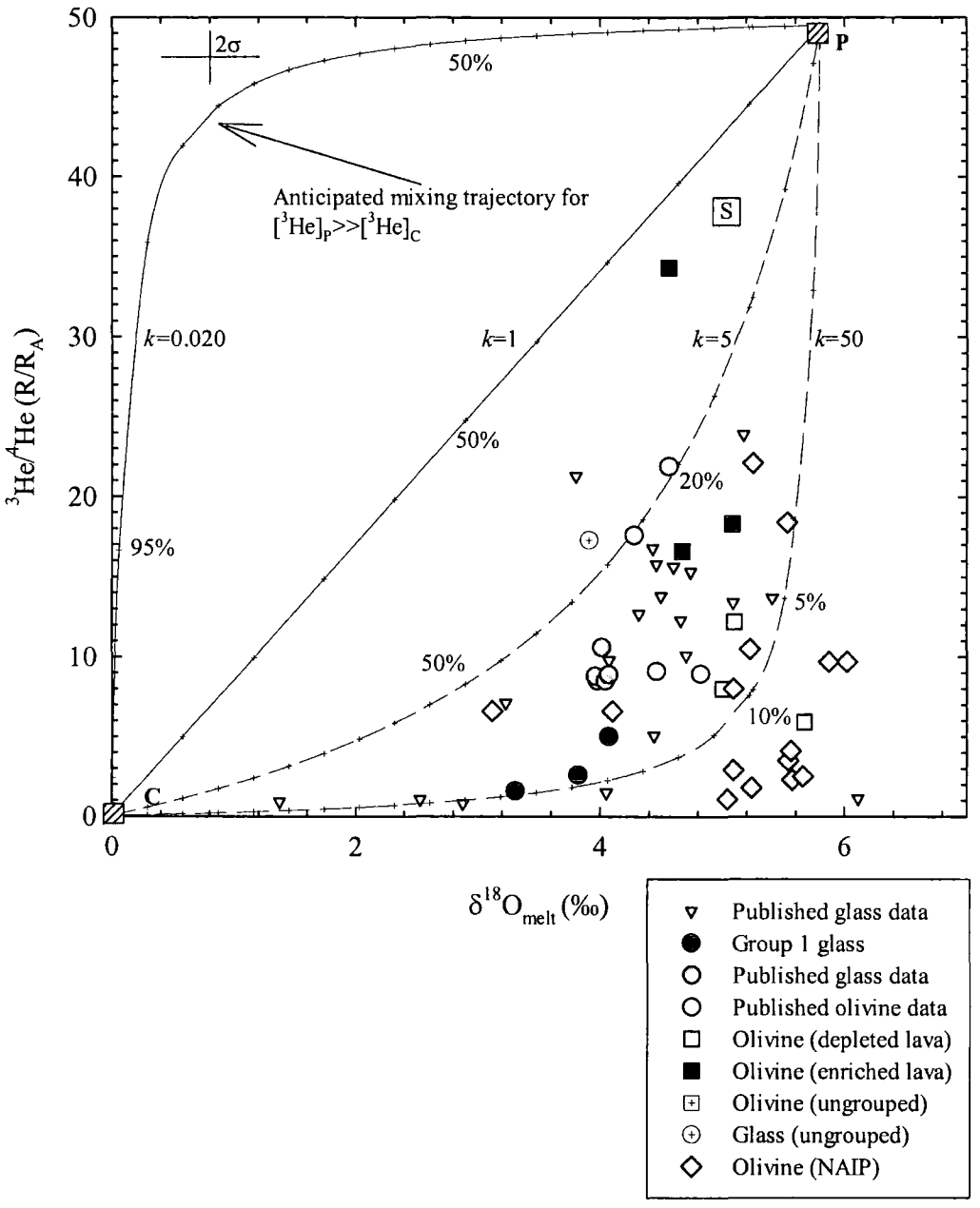

Fig. 2.9: Plot of oxygen and helium isotope ratios (R/R_A notation) for Icelandic glasses and olivines and NAIP olivines. Superimposed on the plot are binary mixing trajectories between a primitive mantle end member P ($49.5R_A$ (Stuart et al., 2003); $\delta^{18}O$ = 5.5‰ (Eiler et al., 2000c)) and a crustal assimilant C ($0.05R_A$ (Andrews, 1985); $\delta^{18}O$ = 0‰ (Eiler et al., 2000a)). Binary mixing trajectories with three different "k-values" are shown ($k = (He/O)_C/(He/O)_P$). Numbers are shown for the % mixtures of C and P to produce the He-O isotope characteristics represented by the tick. If the ^3He content of P is significantly greater than C the mixing curve is concave downward: shown is k=0.02 to illustrate 50×10^3 enrichment in P relative to C (A minimum value suggested by the model of Porcelli and Wasserburg, 1995). All of the Icelandic data plot to the right of k=1 meaning $[^3He]_C >> [^3He]_P$. Degassing of P prior to admixture of C offers an explanation for this observation. Published data from Condomines et al. (1983); Breddam (2002); Breddam et al. (2000); Skovgaard et al. (2001). The square marked 'S' represents the mid Miocene ankaramite SEL 97.

dataset lies between k=5-50: therefore the ^{4}He content of the mantle source (P) endmember would have to fall between 0.36 to 3.6 × 10^{-9} cm^3STP/g. All estimates for mantle [He] are considerably higher than this range. For example, MORB mantle is estimated to have a ^{4}He content of ~1.5 × 10^{-5} cm^3STP/g based on measurements of volatile contents of 'popping-rock' mid-oceanic ridge basalts (Porcelli and Wasserburg, 1995). Theoretical estimates of [^{4}He] in primitive mantle are even higher. Porcelli and Wasserburg (1995) calculated a value of ~6.5×10^{-4} cm^3STP/g based upon a steady-state upper mantle supplied with ^{3}He from a lower mantle reservoir with ~30R_A. On the basis of He-Pb isotope relations in Reykjanes Ridge basalts, Hilton *et al.* (2000b) concluded that primitive mantle should be enriched in ^{3}He over MORB-mantle by a factor of 4 to 140.

To explain the He-O isotope relationships in Fig. 2.9, it is surmised that melts derived from the mantle must have undergone extensive magmatic degassing (leading to a reduction in [He] up to 10^4 times the initial content) prior to contamination processes, introducing radiogenic He and lowering $\delta^{18}O$. Similar degassing processes have been suggested for other Ocean Island settings (Chapter 4; Hilton *et al.*, 1995; 1997a). The enhanced degassing of depleted lavas may be due to higher concentration of intrinsic (source-derived) or extrinsic (crust-derived) water. Icelandic glasses are relatively H_2O-rich (Nichols *et al.*, 2002) and water is known to lower the solubility of CO_2 in basaltic melt (Dixon *et al.*, 1995). CO_2 is the carrier phase for volatile He and so for any confining pressure (e.g., depth to a magma chamber), a water-rich melt will have lost a greater fraction of its intrinsic helium and is, therefore, more likely to record addition of extraneous (crustal) He (Kurz *et al.*, 1996).

2.4.2.2 NAIP and Icelandic olivines

$^{18}O/^{16}O$-$^3He/^4He$ ratio relationships for minerals are more difficult to interpret than glass data because of variable crystallisation histories and non-systematic preservation of volatiles preserved in melt inclusions. However, olivine is an early crystallising phase and is therefore the most likely mineral to retain mantle He and O isotope signatures because of the deeper parts of the magmatic plumbing system they potentially sample. In Fig. 2.9 olivines from Skye and East Greenland are also compared with olivines from the Icelandic rift zones. [He] in crustal materials are

controlled by the concentrations of U and Th and the age of the crust so that a 2Ga gneiss with an initial $^{3}He/^{4}He$ $1R_A$, 1×10^{-10} cm^3STP/g [He], U= 2ppm and Th/U=3.5 will have a maximum of $\sim 9 \times 10^{-04}$ cm^3STP/g [He] and a $^{3}He/^{4}He$ ratio of $\sim 1 \times 10^{-07} R_A$. No direct measurements of $^{3}He/^{4}He$ and [He] are available for Archaean crustal rocks in the NAIP making direct quantitative appraisal of [He] difficult. However, measurements up to $\sim 2 \times 10^{-05}$ cm^3STP/g [He] for Proterozoic granulites with $^{3}He/^{4}He$ >1 on the Kola Peninsula suggest ancient crustal material can have high [He] (Tolstikhin *et al.,* 2002). Even if a large proportion of the helium inventory (>99%) is degassed from the crust during open-system exchange with the atmosphere (e.g., Albarède, 1998), high [He] released from crustal materials during melting and contact of this material with high $^{3}He/^{4}He$ basaltic liquids which have degassed a significant proportion of their [He], might explain the limited variation in $\delta^{18}O$ with large variation in $^{3}He/^{4}He$ for olivines in Fig. 2.9. In this manner, olivine from the NAIP may be retaining $^{3}He/^{4}He$ and $\delta^{18}O$ isotope signatures from interaction with crustal materials that have low $^{3}He/^{4}He$ and mantle-like to elevated $^{18}O/^{16}O$, without necessarily invoking the extensive quantities of shallow-level crustal contamination observed in Icelandic glasses. The obvious differences of mantle-like $\delta^{18}O$ for NAIP olivines and low $\delta^{18}O$ for central Iceland olivines may reflect a source feature and not crustal contamination.

2.4.3 He-O isotope variations in central Iceland and the NAIP

The previous sections have made the case for magmatic degassing prior to crustal contamination as a significant control on the development of $^{3}He/^{4}He$ heterogeneity in central Iceland and NAIP CFB magmatism. In this scenario, the highest $^{3}He/^{4}He$ value of $34.3R_A$ (Vadalda) would represent a binary mixture of He containing the highest proportion of the primitive mantle component. The lowest glass value of Jardfraedingaslod (KVK-168 = $1.6R_A$) would represent a sample largely degassed of its mantle component and having the greatest relative proportion of crustal He. It is important to note here that the entire range of $^{3}He/^{4}He$ ratios and [He] reported here probably reflects variable degrees of both magmatic degassing and addition of radiogenic He. Therefore the absolute mass balance of mantle versus crustal contributions is unique to each sample. In this section two aspects of the binary mixing/degassing model are addressed to better understand details of the He isotope

distribution in Iceland. First the high $^{3}He/^{4}He$ isotope composition of the mantle endmember is examined, and the probability that the high $^{3}He/^{4}He$ ratio measured for Vadalda is the closest approximation to the true high $^{3}He/^{4}He$ mantle component is considered. Secondly, it is assessed whether the sub-Icelandic mantle is characterised by a singular He or O isotope composition or whether heterogeneity in both $\delta^{18}O$ and $^{3}He/^{4}He$ ratios of the mantle endmember(s) can contribute to the range in observed $^{3}He/^{4}He$ values through admixture of different mantle components.

2.4.3.1 The $^{3}He/^{4}He$ endmember in Icelandic and NAIP magmatism

Vadalda has the highest reported $^{3}He/^{4}He$ ratio ($34.3R_A$) of the neovolcanic zones of Iceland. Additionally, Vadalda lies within a proposed mantle 'hotspot' conduit mapped by the regional gravity minimum and seismic low velocity minimum within the upper mantle (Breddam *et al.*, 2000; Foulger and Pearson, 2001). However, there are two reasons to suggest that the $^{3}He/^{4}He$ ratio of Vadalda may not represent the pure high $^{3}He/^{4}He$ mantle endmember composition in Icelandic magmatism. First, although it corresponds well with the predicted $^{3}He/^{4}He$ ratio of $\sim 33R_A$ for a model of k=35 from Hilton *et al.* (2000b), it falls short of the predicted $^{3}He/^{4}He$ ratio of $\sim 55R_A$ based on extrapolation of linear He-Pb mixing relationships observed for the Reykjanes Ridge to a $^{206}Pb/^{204}Pb$ ratio of 19.35. This calculation was made on the assumption that (i) Central Iceland lies at the core of the present-day Icelandic 'hotspot' conduit characterised by an Iceland-Enriched 1 (IE1) component with a $^{206}Pb/^{204}Pb$ ratio of 19.35 (Thirlwall *et al.*, 2004), and (ii) that the Reykjanes Ridge suite also contains IE1 diluted with one or more depleted components characterised by low $^{206}Pb/^{204}Pb$ and $^{3}He/^{4}He$ ratios. Secondly, if the proto-Iceland 'hotspot' at Baffin Island (61Ma) is characterised by a $^{3}He/^{4}He$ ratio of $49.5R_A$ (Stuart *et al.*, 2003) then, for an assumed primitive mantle ^{3}He content of 7.6×10^{10} atoms/g (Porcelli and Ballentine, 2002), closed-system addition of radiogenic He (Bulk Earth U =21ppb and Th/U = 3.8) should produce a present-day Iceland plume $^{3}He/^{4}He$ value of $\sim 48R_A$. This is considerably higher than the observed $^{3}He/^{4}He$ value at Vadalda. Regression of the He-O trajectory for Group 1, 2 and 3 glasses in Fig. 2.9 using a power law, to mantle $\delta^{18}O$ values of 5.5 and 5.8‰ at k=5-50 predicts a primitive mantle end member ratio between $58\text{-}77R_A$; higher still than the most extreme published $^{3}He/^{4}He$ (Stuart *et al.*, 2003) and the extrapolation of Hilton *et al.*

(2000b). These calculations raise the possibility that $^{3}He/^{4}He$ considerably higher than that found at Valdalda await discovery in central Iceland. This assumes that the high $^{3}He/^{4}He$ mantle source that has contributed to NAIP and Icelandic magmatism has not undergone extensive volatile loss and dilution by MORB-like $^{3}He/^{4}He$ since the opening the North Atlantic ~61Ma; a feature that is difficult to discern without further detailed He isotopic work on Iceland and the NAIP.

2.4.3.2 Geographic variation of He-O-Sr-Nd isotopes in Central Iceland

The question of $^{3}He/^{4}He$ and $\delta^{18}O$ isotope heterogeneity in the present-day Icelandic mantle source is raised by numerous studies of trace element and radiogenic isotopes which demand contributions from distinct mantle components characterised by different evolutionary histories (e.g., Schilling *et al.*, 1982; Elliott *et al.*, 1991; Hemond *et al.*, 1993; Chauvel and Hemond, 2000; Skovgaard *et al.*, 2001; Thirlwall *et al.*, 2004). In the most recent iteration, Thirlwall *et al.* (2004) explained Sr-Nd-Pb isotope variations in the Central Iceland region by contributions from (i) an enriched component (IE1; high $^{206}Pb/^{204}Pb$, $^{87}Sr/^{86}Sr$ and low $^{143}Nd/^{144}Nd$) in the southern section of Central Iceland which is taken as the core of the Iceland mantle plume, (ii) a second enriched component (IE2; low $^{206}Pb/^{204}Pb$, high $^{87}Sr/^{86}Sr$ and low $^{143}Nd/^{144}Nd$) increasingly prominent in the NRZ – particularly Theistareykir, and which forms an enriched 'rim' around the hypothetical plume conduit, and (iii) a depleted component (ID1: low $^{206}Pb/^{204}Pb$, $^{87}Sr/^{86}Sr$ and high $^{143}Nd/^{144}Nd$), also observed at Theistareykir and widespread along the Kolbeinsey Ridge. If this broad geographic distribution of hypothesized endmember components is accepted and compared with the distribution of $^{3}He/^{4}He$ ratio in Central Iceland (Fig. 2.2), it is observed that:

- All samples in the Vonarskar region (west of 17°15'W) have high (>>MORB) $^{3}He/^{4}He$ ratios lying between 15.8 and $26R_A$ – high $^{3}He/^{4}He$ extends west of this point all the way down the Reykjanes ridge (e.g., Hilton *et al.*, 2000b).
- The greatest range in $^{3}He/^{4}He$ ratios is found in the region north and east of Dyngjujökull - it is this region, centred on Askja, which has the highest ($34.3R_A$) and lowest ($1.6R_A$) $^{3}He/^{4}He$ ratios (Fig. 2.2). Apart from the Vadalda sample and one literature point of $20.4R_A$, this region is characterised by $^{3}He/^{4}He \leq$MORB. This region also corresponds to the lowest $\delta^{18}O$ of all central Icelandic lavas.

- The Theistareykir sample (Th-29) has a $^{3}He/^{4}He$ value of $12.2R_A$ – considerably higher than the MORB-like range reported previously for Theistareykir (Breddam *et al.*, 2000) and geothermal fluids (Hilton *et al.*, 1990) in the NRZ. This observation means that samples from north of 65°20'N are characterised by high ($>10R_A$) $^{3}He/^{4}He$ that persists northwards up the Kolbeinsey Ridge (e.g., Schilling *et al.*, 1999).

This geographical distribution of helium and oxygen isotopic variation in central Iceland requires explanation in light of the Sr, Nd and trace element variations in the lavas.

2.4.3.3 Models for the origins of He-O isotope variation in Iceland

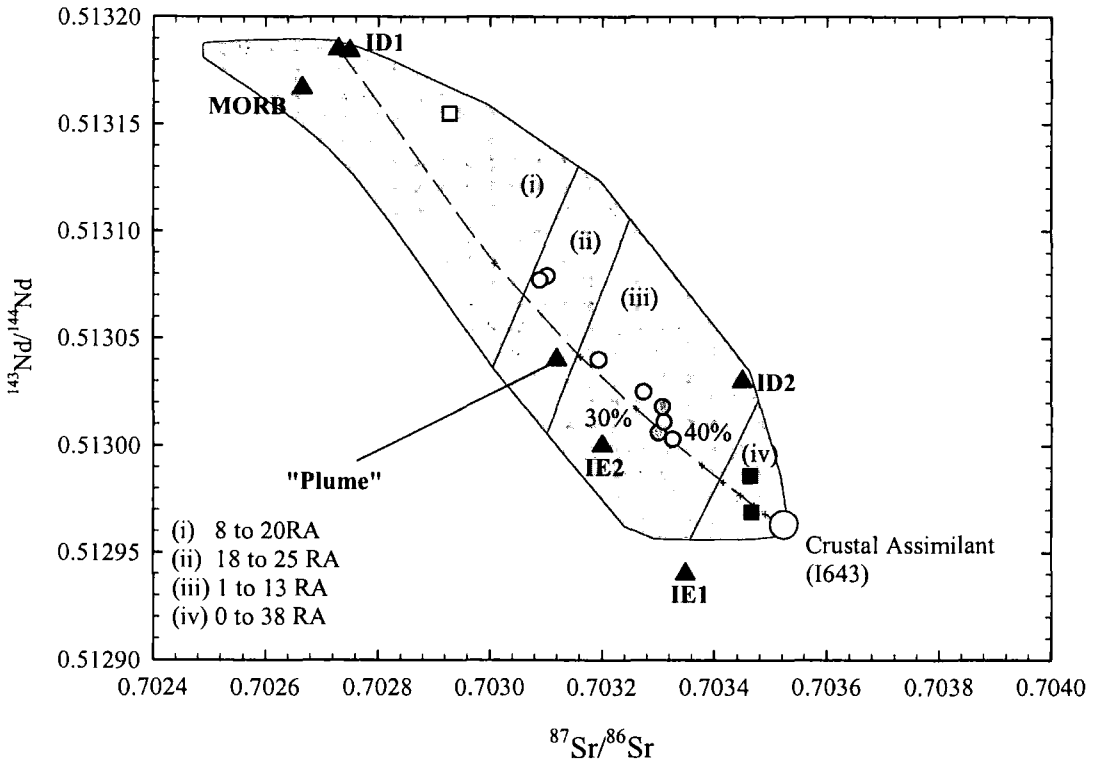

Fig. 2.10: $^{87}Sr/^{86}Sr$-$^{143}Nd/^{144}Nd$ isotope systematics for central Iceland lavas contoured for $^{3}He/^{4}He$ ratios (R/R_A notation). Sr-Nd isotope data from Seth et al. (2004) and He isotope data from this study. Published data from Condomines et al. (1983) and Thirlwall et al. (2004). Sr-Nd bulk mixing models based upon Thirlwall et al. (2004) endmembers with solid crust as sample I643 (MgO 0.0 wt.%, Zr = 1700ppm, 87Sr/86Sr = 0.703507, 143Nd/144Nd = 0.512965 and typical concentrations from fractionated Icelandic lavas [Sr = 250ppm, Nd = 15ppm, from GEOROC compilations]) and ID2/MORB components (Sr = 140ppm, Nd = 2ppm) indicating mixing/assimilation of I643 for Group 2 and 3 lavas in the 30-40% range.

Sr-Nd isotope variations in Icelandic lavas have been contoured in Fig. 2.10 for their He isotope variations. Based on this contouring the relative components of central Iceland samples can be discussed. Depleted lavas, such as Th-29, are characterised by $^{3}He/^{4}He \geq$ MORB and low to MORB-like $\delta^{18}O_{melt}$ values (e.g., Eiler *et al.*, 2000a). Group 1 glasses and glasses from Kistufell, proposed to be primitive melts from the Iceland plume (Breddam, 2002) have "plume"-like Sr and Nd isotope compositions, high $^{3}He/^{4}He$ (18-25R_A) and $\delta^{18}O_{melt}$ = +4.54±0.34‰ (2.S.D, n=8). Group 2 and 3 glasses plot to more radiogenic $^{87}Sr/^{86}Sr$ and less radiogenic $^{143}Nd/^{144}Nd$ and have lower $^{3}He/^{4}He$ (1-13R_A; but mostly ≤MORB) and $\delta^{18}O_{melt}$ = +3.91±0.50‰ (2.S.D, n=8) than Group 1 glasses. Finally the enriched basalts NAL-625 and Th-29 correspond to the most radiogenic Sr, least radiogenic Nd and highest $^{3}He/^{4}He$ (20-38R_A) of all Icelandic samples with $\delta^{18}O_{melt} \leq$5‰. A number of models can be proposed to explain this variation:

- Crustal contamination and concomitant fractional crystallisation – in the previous sections it has been clearly demonstrated that crustal contamination can generate large variations in $^{3}He/^{4}He$ and $\delta^{18}O$. Some of the lavas studied have clearly been contaminated by crust confirming earlier studies (e.g., Condomines *et al.*, 1983 and Eiler *et al.*, 2000a). However, can AFC explain the MORB-like $^{3}He/^{4}He$ and correspondingly high [He] and persistently low $\delta^{18}O$ in all of the lavas?
- Melting dynamics – Elliott *et al.* (1991) proposed that depleted and enriched components in the Iceland mantle plume were the result of enriched plume material being depleted by deeper partial melting. The result of this dynamic melting is that deep-derived enriched melts and shallow-derived depleted picrites can be erupted in close proximity. Central Icelandic samples in this study retain both enriched and depleted characteristics on the basis of their trace elements. Therefore the question raised is can a dynamic melting model generate variations in the $\delta^{18}O$ and $^{3}He/^{4}He$ of central Icelandic magmatism?
- Mantle heterogeneity – Thirlwall *et al.* (2004) have proposed that there are distinct mantle components beneath Iceland on the basis of large variations in Sr, Nd and Pb isotopes. This study has shown that there is a systematic variation of $^{3}He/^{4}He$ and to a lesser or greater degree $\delta^{18}O$ with $^{87}Sr/^{86}Sr$ and $^{143}Nd/^{144}Nd$. In this manner basalts may be recording heterogeneous distributions of variably

radiogenic, MORB-like, or primordial $^{3}He/^{4}He$ and low-$\delta^{18}O$ in the mantle beneath Iceland.

It is notable that central Icelandic lavas with low $^{3}He/^{4}He$ and $\delta^{18}O$ surround the region of Askja. This area is characterised by basaltic to evolved eruptive units and in some cases, highly explosive eruptions that are responsible for a large caldera filled by the Oskjuvatn Lake (Fig. 2.2).

There is a large hydrothermal flux in this area such that several hydrothermal power stations have been built to harness this natural energy. It is hydrothermal active areas such as this where low $^{3}He/^{4}He$ and $\delta^{18}O$ might be expected in lavas. Central Iceland glass Sr-Nd isotope compositions (Fig. 2.10) can be modelled by mixing between MORB/ID1 and highly evolved magmas from central Iceland similarly to estimates of crustal contamination in Fig. 2.8. It is clear that some of the central Icelandic basalts surrounding Askja, most notably the Group 3 glasses, have assimilated crust. However, it is impossible to explain the radiogenic $^{87}Sr/^{86}Sr$ and less radiogenic $^{143}Nd/^{144}Nd$ through crustal assimilation because of the young age of the Icelandic crust. As such the similarity between the enriched-basalt NAL-625 and SEL-97 and the Group 2 and the "crustal assimilation" line in Fig. 2.10 must reflect, to some degree, mixing between discreet mantle components.

A possible method for generating the isotopic and elemental variation in central Icelandic lavas would be for enriched mantle melts to originate from deeper melting due to the less refractory nature of enriched or hydrous phases from an enriched mantle component. Correspondingly depleted melts would originate from shallow adiabatic melting of depleted mantle that has risen through the dynamic melting column. Elliott *et al.* (1991) invoked such a model to explain the differences in elemental and Pb isotope compositions between depleted Thiestareykir picrites and more enriched Reykjanes Ridge basalts. Nichols *et al.* (2002) have also measured high H_2O contents in some Reykjanes Ridge basalts supporting possible notions of enriched, anhydrous, deep melting. A useful guide for assessing depths for magmas is to plot the isotope of interest against a trace element ratio (e.g., Dy/Yb) which is sensitive to the role of garnet, the predominant aluminous phases at depths greater than ~66km in the mantle.

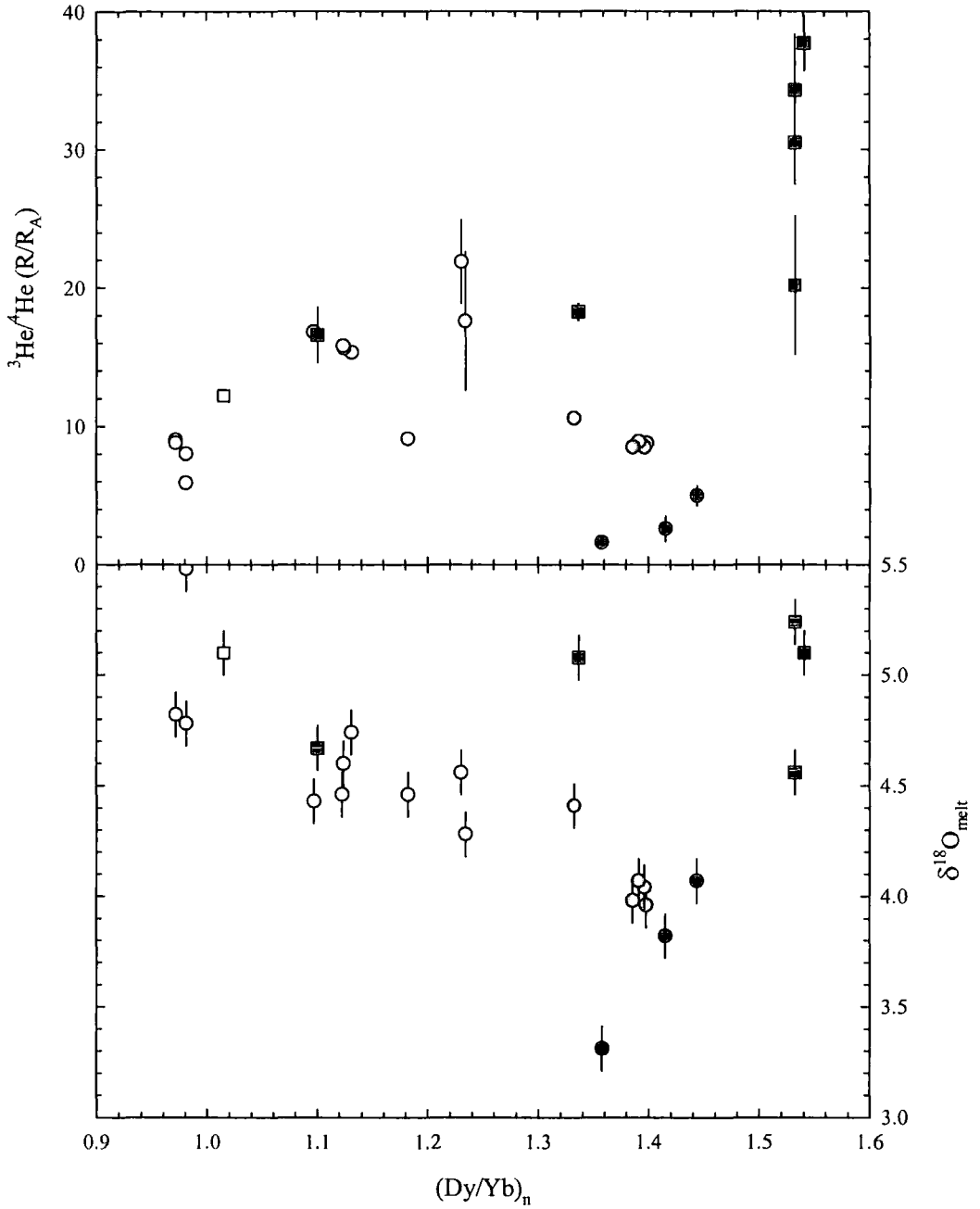

Fig. 2.11: Dy/Yb_n versus $^3He/^4He$ (R/R_A) and $\delta^{18}O$ illustrating the relationship between trace element ratios controlled by melting in spinel- or garnet-melting fields or mantle heterogeneities and He isotope compositions for central Icelandic lavas. Note the generally positive correlation of $^3He/^4He$ with Dy/Yb_n for Group 1 glasses and picrites and the generally negative correlation for $\delta^{18}O$ and Dy/Yb_n for all glasses. Symbols as shown in Fig. 2.5 and errors for $\delta^{18}O$ at 1σ level.

Apart from Group 3 lavas, the positive correlation between $(Dy/Yb)_n$ and $^3He/^4He$ shown in Fig. 2.11 supports the notion of dynamic melting for Icelandic magmatism. $(Dy/Yb)_n$-$^3He/^4He$ relationships suggest that deeper-derived melts are characterised by elevated $^3He/^4He$ whilst shallower melting is characterised by more MORB-like

$^{3}He/^{4}He$. $(Dy/Yb)_n$ versus $\delta^{18}O$ (Fig. 2.11) indicates a generally negative correlation for glasses suggesting that deeper melts have lower-$\delta^{18}O$ and where Group 2 glasses have the lowest $\delta^{18}O$ and deepest melting signatures. There is some evidence that depths of melting have a major influence on the $\delta^{18}O$ and $^{3}He/^{4}He$ measured in Icelandic lavas, however there remains two areas of uncertainty with this model; the Group 2 lavas and the possible controls on trace elements invoked by enriched recycled material required for a low $\delta^{18}O$ mantle component (see section 2.4.3.4).

2.4.3.4 Possible recycled origins for low $\delta^{18}O$, enriched Sr-Nd isotope components in Icelandic magmatism

Previously, the enriched Sr, Nd, Os and Pb isotope compositions and low $\delta^{18}O$ of some Icelandic magmatism has been interpreted in the context of recycled oceanic crustal material of variable age in their source (Thirlwall *et al.*, 1999; Chauvel and Hemond, 2000; Kempton *et al.*, 2000; Skovgaard *et al.*, 2001; Fitton *et al.*, 2003; Thirlwall *et al.*, 2004). Depleted recycled Palaeozoic age crust can explain the Sm-Nd and Lu-Hf isotope systematics and relatively unradiogenic $^{206}Pb/^{204}Pb$ and $^{187}Os/^{188}Os$ isotope compositions of Icelandic basalts (Thirlwall *et al.*, 2004). Mixtures of ambient mantle and Palaeozoic age recycled oceanic crustal material could explain the characteristics seen for Sr, Nd and O isotopes in Icelandic lavas. However, the pervasively low $\delta^{18}O$ in depleted and enriched Icelandic magmas necessarily preclude involvement of the uppermost basaltic and sedimentary portions of oceanic crust which have high $\delta^{18}O$ (e.g., Hansteen and Troll, 2003). Instead these authors suggest that the lower portions of recycled oceanic crust are likely to be involved in Icelandic magmatism. The lower portions of recycled oceanic crustal materials are composed of gabbros and layered harzburgite and dunites.

Gabbros will have elevated $(Dy/Yb)_n$ whilst the layered ultramafic portions will have lower $(Dy/Yb)_n$. In this manner the correlations between $(Dy/Yb)_n$-$\delta^{18}O$-$^{3}He/^{4}He$ in Fig. 2.11 could represent melting of different components of possible recycled oceanic crust. It is unclear why $^{3}He/^{4}He$ should be related to different recycled oceanic crustal components considering the radiogenic nature of $^{3}He/^{4}He$ in oceanic crustal materials (Staudacher and Allégre, 1988). Mixtures of DMM and heterogeneous recycled oceanic crust, whilst providing a logical and elegant answer to Sr, Nd, Pb, Os and O isotope systematics of some Icelandic magmatism are

unable to explain the variations of MORB-like $^{3}He/^{4}He$ and Ne (Dixon, 2002) and high $^{3}He/^{4}He$ routinely measured for Iceland basalts.

The existence of high $^{3}He/^{4}He$ lavas throughout the entire range of $^{87}Sr/^{86}Sr$ and $^{143}Nd/^{144}Nd$ compositions in Iceland could indicate decoupling of $^{3}He/^{4}He$ and enrichment of ^{3}He relative to MORB $^{3}He/^{4}He$ ($8\pm1R_A$) to all of the Icelandic mantle reservoirs. If recycled oceanic crust-ambient mantle melting is responsible for the origin of O, Sr, Nd, Pb, Os isotope variations in Icelandic lavas it cannot be the control on MORB-like or hotspot $^{3}He/^{4}He$ measured consistently in Icelandic lavas because of the radiogenic nature of $^{3}He/^{4}He$ in oceanic crust.

Central Iceland Group 2 glasses possess MORB-like $^{3}He/^{4}He$ ratios and high [He] as well as low $\delta^{18}O$ and enriched Sr and Nd isotope signatures. The slopes of their primitive mantle normalised trace element patterns (Fig. 2.3) are also much steeper in terms of LREE element enrichment than for Group 1 glasses; a feature not easily explained solely by crustal assimilation if the high [He] contents of Group 2 glasses are also considered. These lavas also lie in the physiographic "zone" of low $^{3}He/^{4}He$ observed in central Iceland (Fig. 2.2). The high [He] at relatively constant MORB-like $^{3}He/^{4}He$ indicate that these lavas are unlikely to be the result of degassing of a high $^{3}He/^{4}He$ and incorporation of crust because [He] would be anticipated to be much lower. On the basis of this relationship it would also appear that both a MORB-like $^{3}He/^{4}He$ component and a hotspot $^{3}He/^{4}He$ component characterise Icelandic mantle melts.

The high $^{3}He/^{4}He$ and MORB-like $^{3}He/^{4}He$ components cannot be totally restricted to enriched and depleted domains in the Icelandic mantle because the most trace-element depleted Eggert glasses which have MORB-like $^{3}He/^{4}He$ also have the highest [He]. These observations suggest that the spatial variation in $^{3}He/^{4}He$ is the result of a combination of two major factors, (1) crustal contamination processes at the centre of the Iceland rift zones, an area with the greatest crustal thickness of all of Iceland (Kaban *et al.*, 2002) and has the most intense hydrothermal activity of recent times, and (2) depth and degree of partial melting. Depth and degree of partial melting will itself be a function of crustal and lithospheric thickness (e.g., Ellam, 1992) and the distribution of enriched mantle components available for melting beneath Iceland.

^{3}He-recharging of upper mantle reservoirs by He-rich lower mantle contributions has been suggested previously based upon the He-Nd isotope systematics of proto-Icelandic lavas on Baffin Island (Stuart *et al.*, 2003). Stuart *et al.* (2003) proposed that small volumes of primordial volatile-rich lower mantle material could represent ^{3}He-recharge depleted upper mantle (or HRDM) reservoirs without necessarily affecting Nd (and by inference O, Sr, Pb and Os) isotope systematics. A positive correlation between $(Dy/Yb)_n$ and $^{3}He/^{4}He$ appears to be the most obvious example of deeper fertile partial melts with garnet melting signatures (e.g., NAL-625; Fig. 2.11). This suggests that hotspot $^{3}He/^{4}He$ is added from deep in the Icelandic melting column whilst MORB-like $^{3}He/^{4}He$ is more characteristic of shallower melting. The data presented here from central Iceland modifies the '^{3}He-recharge' theme of Stuart *et al.* (2003) to the complex 'dynamic' melting (Elliott *et al.*, 1991) and the recycled oceanic components observed in Icelandic magmatism.

The focus for the most extreme $^{3}He/^{4}He$ appears to be located over the central Iceland region with mantle domains becoming less affected by HRDM away from the Icelandic main land along the mid-Atlantic ridge (Hilton *et al.*, 2000b). But Central Iceland Group 2 glasses measured in this study possess MORB-like $^{3}He/^{4}He$ ratios and high [He] (Fig. 2.5) which do not appear to conform to a hotspot ^{3}He-charging model in Iceland. This suggests that Group 2 glasses provide evidence for the added variable of depletion of He HRDM by deep partial melting in the 'dynamic' melt column. He is highly incompatible (Brooker *et al.*, 2003) so even small degrees of partial melting will deplete the residuum of [He]. Furthermore, subsequent melting of this high $^{3}He/^{4}He$ residuum would produce melts that are more susceptible to interaction with MORB-like $^{3}He/^{4}He$ melts. Such a circumstance would result in heterogeneous distribution of $^{3}He/^{4}He$ ratios in Iceland. This in turn invokes the possibility of admixture of ^{3}He-charge dominated and DMM $^{3}He/^{4}He$ components taking place in central Iceland.

2.4.3.5 Characterisation of Icelandic mantle and crustal components

$^{3}He/^{4}He$-$^{143}Nd/^{144}Nd$ isotope systematics plotted in Fig. 2.12 offer a visual solution to the observations of (i) ^{3}He-charged mantle components, (ii) enriched recycled oceanic crustal components, (iii) HRDM, (iv) crustal contamination and (v) dynamic melting. Modelling using the approaches in Fig. 2.9 illustrates that multi-component

mixing can describe central Icelandic samples in He-Nd space. Three-component mixing between an enriched $^{143}Nd/^{144}Nd$ reservoir (R) with MORB-like $^{3}He/^{4}He$ and a high $^{3}He/^{4}He$ with enriched $^{143}Nd/^{144}Nd$ (P) and MORB agrees with many of the observations made here and show that crustal contamination of these components yields the samples with variable $^{143}Nd/^{144}Nd$ and low $^{3}He/^{4}He$. From these mixing relationships it is possible to estimate the relative $^{3}He/^{4}He$ and $^{143}Nd/^{144}Nd$ ratios of these potential source components and compare them with the mantle components described by Thirlwall *et al.* (2004):

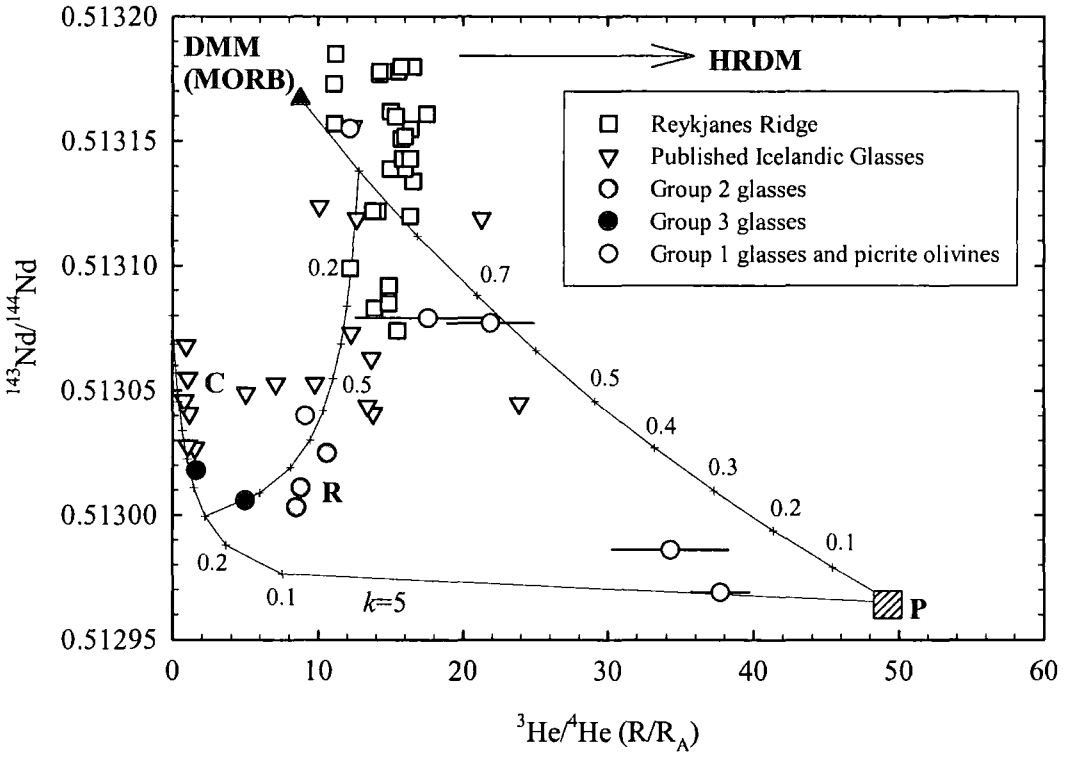

Fig. 2.12: $^{3}He/^{4}He$ (R/R_A notation) versus $^{143}Nd/^{144}Nd$ of Icelandic basalts. Mixing trajectories between a high $^{3}He/^{4}He$, enriched component, P, DMM, Crust (C), and a component defined by Group 2 glasses (R). HRDM = ^{3}He-recharged depleted mantle (Stuart et al., 2003). Modelling using the same method of degassing equation for [He] as in Fig. 2.9, with variable Nd concentrations of respective reservoirs. Data from this study, Condomines et al. (1983), Hilton et al. (2000b), Breddam (2002), Thirlwall et al. (2004). 2σ errors are shown or are smaller than symbols. It should be noted that despite having similar $^{143}Nd/^{144}Nd$ to MORB ($^{3}He/^{4}He$ = 8±2R_A, 2σ), Reykjanes ridge data (white squares) possess systematically higher $^{3}He/^{4}He$.

C – The crustal component has highly variable Sr, Nd and Pb but low $^{3}He/^{4}He$ and $\delta^{18}O$. The low $^{3}He/^{4}He$ and $\delta^{18}O$ in this component can be explained by ingrowth

of radiogenic He and incorporation of meteoric fluid signatures. The Icelandic crust is not sufficiently old to generate large Sr, Nd and Pb isotope variability so variations must reflect mantle signatures. The crust is not a mantle component and was not described by Thirlwall *et al.* (2004).

MORB – The MORB component in Iceland appears to be typical of Atlantic N-MORB but this component represents HRDM resulting in $^{3}He/^{4}He >> 8R_A$. This endmember represents the ID1 and MORB component of Thirlwall *et al.* (2004).

R – A component represented by enriched $^{143}Nd/^{144}Nd$ (~0.51300) as well as MORB-like $^{3}He/^{4}He$. This component likely reflects the IE2 and IE1 components of Thirlwall *et al.* (2004) and is best represented by Group 2 glasses. The explanation for such a component could be Palaeozoic recycled oceanic crustal components (Thirlwall *et al.*, 2004).

P – This represents the enriched plume component with $^{143}Nd/^{144}Nd = 0.51297$ and $^{3}He/^{4}He \geq 50R_A$. This component is not described/identified by Thirlwall *et al.* (2004), and requires high $^{3}He/^{4}He$ in an enriched mantle component, perhaps represented by oceanic crust older than Palaeozoic recycled oceanic crust explaining the slightly more enriched isotopic characteristics of this mantle domain. Such a reservoir might be considered as similar to the FOZO (Focal Zone), C (Common) or PHEM (Primitive He Mantle) invoked to explain the pervasive mantle component in OIB magmatism (Hart *et al.*, 1992; Farley *et al.*, 1992; Hanan and Graham, 1996).

Dynamic melting, different recycled crustal components, HRDM and crustal contamination go some way to solving the riddle of Icelandic magmatism's isotopic characteristics. Melting in a column would generate isotopic and trace element heterogeneity from the constituent mantle domains under Iceland. Dynamic melting would also act to allow heterogeneous distribution of $^{3}He/^{4}He$ (e.g., Fig. 2.11). Crustal contamination lowers $^{3}He/^{4}He$ and $\delta^{18}O$ but does not have a great impact on the other isotopic characteristics.

Central Iceland has been interpreted to represent the centre of the Iceland plume conduit using seismic tomography (Wolfe *et al.*, 1997) and Iceland is also associated with the North Atlantic geoid anomaly. The broad geoid swell and seismic imaging of a low velocity zone in the melting extending to the mantle transition zone (Shen *et*

al., 1998) or deeper (Helmberger *et al.,* 1998; Bijwaard and Spakman, 1999) in conjunction with indiscriminate ^{3}He-charging of mantle domains and identification that the extreme variation of $^{3}He/^{4}He$ is the cause of degassing and subsequent crustal contamination in Iceland provides a strong argument for the involvement of a less-degassed lower mantle component with extreme high $^{3}He/^{4}He$ in the Iceland mantle.

2.4.3.6 Did Palaeogene NAIP magmatism sample the same mantle source regions as present-day central Iceland magmas?

The $^{3}He/^{4}He$ source contribution for Palaeogene NAIP magmatism appears similar to that of modern day central Icelandic magmatism (Fig 2.1). Like the mantle beneath central Iceland, HRDM is likely to have played a significant role in NAIP magmatism (Stuart *et al.,* 2003). Demonstrably crustally uncontaminated NAIP magmas possess Pb isotope systematics (Stuart *et al.,* 2000; Ellam and Stuart, 2000; Peate *et al.,* 2003) that are identical to the enriched and depleted signatures characteristic of lavas from the Reykjanes Ridge and Iceland (Thirlwall *et al.,* 2004). Correlation between $^{143}Nd/^{144}Nd$ and $^{3}He/^{4}He$ also shows that a low $^{143}Nd/^{144}Nd$ component with MORB-like He also exists in NAIP magmatism (Stuart *et al.,* 2003). He-Sr-Nd-Pb isotope evidence points to recycled oceanic crustal material being inherent in NAIP magmas (this study, Thirlwall *et al.,* 2004).

Although low $\delta^{18}O$ in zircons from Skye granites have been suggested as originating from recycled oceanic components in the mantle (Gilliam and Valley, 1997) $\delta^{18}O$ variations in NAIP olivines can be most simply explained by crustal contamination. $\delta^{18}O$ signatures in olivines from magmatic rocks in Prinsen af Wales Bjerge, Skye main lava series and Little Minch sills, approach typical mantle values (e.g., Mattey *et al.,* 1994). In contrast to Iceland, where recycled oceanic crust appears to play a role in generating low $\delta^{18}O$ magmatic signatures, Skye and East Greenland magmatism are better explained by mixtures of DMM, the NAEM and Archaean and upper Proterozoic crust (Ellam and Stuart, 2000).

The Skye and East Greenland olivine data suggest that low $\delta^{18}O$ is not a source feature for NAIP magmatism. Unlike Iceland, NAIP magmatism passed through continental lithosphere and was unlikely to experience the dynamic melting regime operating in the convecting mantle beneath Iceland because of the short periodicity

of the events and the inability of adiabatic melting to account for such voluminous magmatism. One observation is true for both Icelandic and NAIP magmatism: The $^3He/^4He$ data from central Iceland and NAIP CFB strongly suggest that this form of intraplate magmatism is replenished by ^3He from the deep (lower?) mantle. This observation reflects the dichotomy of mantle beneath Iceland and the NAIP, yet the consistently high $^3He/^4He$ measured in volcanic rocks erupted from these regions. This is consistent with conclusions in chapter 3 that no high $^3He/^4He$ shallow reservoir can be identified in the mantle.

2.4.4 Implications for the He-paradox from central Iceland lavas

Lavas with $^3He/^4He$ greater than MORB reflect a higher proportion of primordial volatiles in their source; signatures thought to originate from a less degassed reservoir than DMM, possibly the lower mantle (Graham, 2002 and references therein). However, the helium paradox, an observation that high $^3He/^4He$ lavas from Loihi have lower [He] concentrations than MORB contradicts this paradigm (Graham, 2002). Mechanisms including extensive degassing due to low confining pressures (Hilton *et al.*, 2000b), loss of a CO_2-rich carrier phase at the base of the lithosphere (Hilton *et al.*, 1997a), closed and open system vesiculation processes for MORB and OIB respectively (Moreira and Sarda, 2000), or recharge of DMM by small volumes of primordial volatile-rich material (Stuart *et al.*, 2003) have been proposed to explain the discrepancy between a theoretical He-rich source and He-poor lavas. This study indicates that $^3He/^4He$ and [He] variations measured in central Icelandic basalts are the result of degassing prior to addition of radiogenic, crust-derived He. In central Iceland the He-paradox can be explained by the extensive, complex degassing that takes place in the crust.

2.4.5 Statistical approaches to $^3He/^4He$ examination; lessons from Iceland

The arguments in the preceding discussion have shown that the extreme variation of $^3He/^4He$ from 1.6 to 34.3R_A in central Icelandic lavas can be attributed to variable degassing prior to AFC, and that extreme plume $^3He/^4He$ can be effectively reduced by such processes. It is commonly inferred that two reservoirs exist in the convecting mantle which are sampled by MORB and OIB; these distinctions have been made partly based upon the differences in the different helium isotope ratios of

MORB and OIB lavas. High $^3He/^4He$ in some OIB are generally thought to represent addition of components with a high time integrated $^3He/(U+Th)$ that are less degassed than DMM. The presence of high $^3He/^4He$ isotope ratios in lavas and ground waters in volcanic intra-plate provinces is often a key argument for the existence of deep-seated mantle plumes (e.g., Condomines *et al.*, 1983; Kurz *et al.*, 1983; Hilton *et al.*, 1999; Hilton *et al.*, 2000b; Breddam *et al.*, 2000). $^3He/^4He$ lower than typical MORB have also been measured and have been explained either though sampling of a low time integrated $^3He/(U+Th)$ reservoir (Kurz *et al.*, 1982) or through degassing and crustal assimilation processes (Hilton *et al.*, 1995).

Alternatively, Anderson (1998, 2000, 2001) proposed that statistical analysis of helium datasets indicate that OIB and MORB are actually drawn from the same population. This result has been reached by proportional weighting of helium isotope ratios with helium abundance in the available global helium isotope dataset. The data presented here support observations that lower [^3He] in intraplate volcanism is not the feature of a reservoir with a low total helium concentration but rather the artefact of magmas that have not retained their source volatile inventory due to complex degassing prior to shallow-level mixing processes. The degassing process common to sub-aerially erupted lavas is greatly restricted for deep (>1000m) submarine eruptions. This is because the high pressures generated by the overlying water column prevent volatile expansion and loss. Neglecting the controls of AFC means that the weighting of helium isotopic ratios with helium concentration introduces a low $^3He/^4He$ bias to any dataset. Additionally the standard deviation on any dataset will be increased due to the large contrast that typically exists between magmatic and crustal $^3He/^4He$.

Fig. 2.13 shows the helium dataset of Graham (2002) for MORB, with statistical means calculated by Graham (2002) and Anderson (2001). Also presented are data from Icelandic phenocrysts and glasses, one filtered and the other unfiltered for the effects of shallow-level mixing processes as documented by combined He-O isotope and trace element relationships. Filtering was performed using trace element and O isotope relationships to monitor the effect of AFC processes and using a values between K=5-50. A cut-off value of 20% contamination by oxygen was choosen within the K=50 mixing line in Fig. 2.9 to demonstrate the effect of filtering for the effects of crustal contamination. The unfiltered Iceland dataset (n=53) has a mean

isotopic ratio of 12.54±8.58 (1σ) and includes samples which have clearly had their $^{3}He/^{4}He$ modified through degassing and crustal contamination which may not be evident from their [He]. The large error means that the data overlaps and cannot be discriminated from average MORB (Graham, 2002; unpublished).

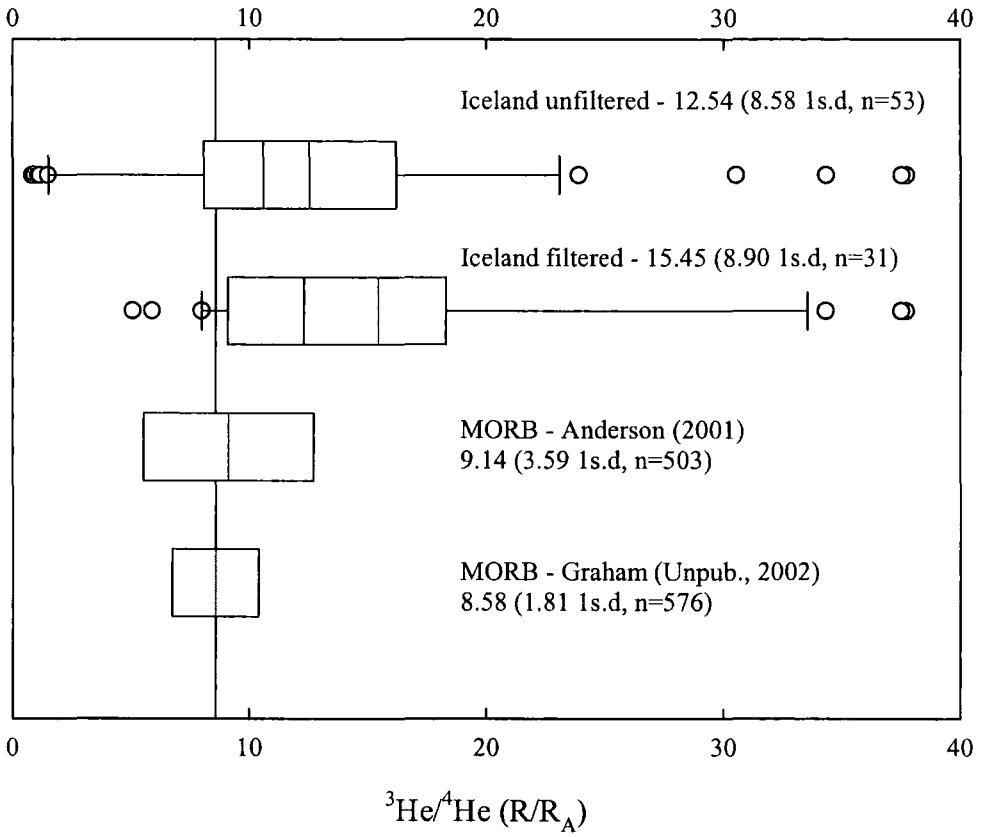

Fig. 2.13: Variability of $^{3}He/^{4}He$ (R/R_A) of MORB from the global spreading ridge system of Graham (2002; unpublished) and unfiltered from Anderson (2001) and for Icelandic lavas. Filtration of the Iceland dataset was performed taking a value of 20% contamination by oxygen for samples between K=5-50 for a primitive mantle source of 49.5R_A. Box plots indicate outliers, mean (grey line), median (black line) and confidence limits for ratios. Data from this study, Condomines et al. (1983); Breddam et al. (2000); Skovgaard et al. (2001) and Breddam (2002)

The Iceland He-O data filtered for the effects of shallow-level mixing processes at a value of 20% contamination by oxygen on binary mixing curves gives a mean $^{3}He/^{4}He$ of 15.85±8.90 (1σ, n=31). The fact that at the 2σ-level, Iceland data overlaps considerably with MORB is for one reason; there is a dearth of available data with O and He isotope systematics on phenocrysts or glasses. With more data or statistical filtration using more common isotopic (e.g., $^{87}Sr/^{86}Sr$) or incompatible element schemes (e.g., Sr/Y) a better statistical appraisal of intraplate $^{3}He/^{4}He$ may be achieved. This simple data manipulation illustrates that not taking magmatic

degassing prior to AFC into account may result in systematic errors in interpretation of these statistics.

2.5 Summary

- The highest modern day $^{3}He/^{4}He$ value measured to date has been identified at Vadalda, a monogenetic volcano in central Iceland ($34.3R_A$). The high $^{3}He/^{4}He$ values are found above locations close to the maximum seismic anomaly in the upper mantle beneath Iceland, which has been interpreted as the main conduit of the plume structure (Wolfe *et al.*, 1997).
- Trace element, oxygen and helium isotope relationships demonstrate that crustal assimilation concomitant with fractional crystallization can significantly affect the helium isotope ratios because of prior degassing of magmas.
- Although coupled He-O isotope signatures show that assimilation of [He] poor, low $^{3}He/^{4}He$, low $\delta^{18}O$ contaminants is a significant process in NAIP magmatism they also indicate that some CFB magmas successfully retain fractions of their original mantle source helium inventory.
- In Iceland, lavas with the most radiogenic $^{87}Sr/^{86}Sr$ and unradiogenic $^{143}Nd/^{144}Nd$, which would classically be considered to have suffered the greatest amount of crustal contamination, have some of the highest $^{3}He/^{4}He$ ratios. This relationship suggests that radiogenic $^{87}Sr/^{86}Sr$ and unradiogenic $^{143}Nd/^{144}Nd$ originate from a component in the Icelandic mantle. Such relationships make identifying crustally contaminated samples on the basis of $^{87}Sr/^{86}Sr$ and $^{143}Nd/^{144}Nd$ difficult.
- Spatial distribution of $^{3}He/^{4}He$, systematic variation between Sr, Nd, $^{3}He/^{4}He$ and systematic variations with depth of melting, indicate that Icelandic magmatism can be explained by admixtures of DMM and recycled oceanic crustal components with low $\delta^{18}O$.
- NAIP magmatism $^{3}He/^{4}He$ and $\delta^{18}O$ cannot be explained in a similar manner to Icelandic magmatism and may suggest that high degrees of partial melting during CFB magmatism could dilute the isotopic and elemental contributions of enriched mantle domains.
- Substantial contribution from a [He]-rich reservoir with high time integrated $^{3}He/(U+Th)$ is common to all Icelandic and Palaeogene NAIP magmatism.

- Observations of crustal contamination (as well as ^{3}He-recharge) indicate that the helium paradox, based on the observation of low [^{3}He] in high $^{3}He/^{4}He$ from Loihi seamount, could result from degassing of magmas which may be exacerbated by high water contents from the addition of hydrated crustal assimilant (Kent *et al.*, 1999). Any crust-mantle interactions would be expected to lower $^{3}He/^{4}He$ ratios. The 'helium paradox' is likely to be the result of extensive degassing of high $^{3}He/^{4}He$ magmas and subsequent crustal modification, processes that are more extreme in sub-aerial ocean islands than on submerged spreading segments.
- These arguments suggest that helium isotope data sets should be thoroughly assessed for the effects of degassing and crustal contamination before detailed statistical analyses of the helium isotope data are performed.

Chapter 3: Does a high time integrated $^3He/(U+Th)$ reservoir exist in the upper mantle? Evidence from continental lithospheric mantle xenoliths and intraplate alkaline volcanics

3.1 Introduction

Radiogenic isotope heterogeneity of the Earth's mantle recorded by variations in ocean island basalts (OIB), is considered to reflect time-integrated effects of (i) variable depletion due to melting and crust extraction, (ii) enrichment through recycling of lithosphere and crust into the convecting mantle and (iii) metasomatism of mantle reservoirs by small degree melts or fluids derived from isotopically heterogeneous reservoirs. The noble gas systematics of OIB, continental flood basalts (CFB) and mid-ocean ridge basalts (MORB) provide important constraints on the evolution and heterogeneity of the mantle (Allégre *et al.*, 1986; Van Keken *et al.*, 2001; Graham, 2002; Allégre and Moriera, 2004). Phenocrysts and glasses from intraplate OIB and CFB lavas can possess higher $^3He/^4He$ ratios than MORB lavas that are derived from the convecting upper mantle (depleted MORB mantle or DMM; $8.8\pm2.1R_A$, 1σ, Graham, 2002; $8\pm1R_A$, 1σ, Farley and Neroda, 1998; Hilton and Porcelli, 2003). This separation of helium isotope compositions between types of magmatism indicates that a high time-integrated $^3He/(U+Th)$ source is common in intraplate magmatism but is lacking, diluted or obscured in MORB petrogenesis (Fig. 3.1). High $^3He/^4He$ values (Clarke *et al.*, 1969), together with solar-like Ne isotope ratios (Honda *et al.*, 1993), have been interpreted to reflect a higher proportion of primordial volatiles in the mantle source region of OIB and CFB relative to that of MORB.

In addition to high $^3He/^4He$, some OIB exhibit consistently low $^3He/^4He$ ratios compared with MORB (e.g., Kurz *et al.*, 1982). Low $^3He/^4He$ OIB cannot exclusively be explained by degassing and $^3He/^4He$ modification by crustal modification which is recognised in some ocean island settings (Hilton *et al.*, 1995). Low $^3He/^4He$ ratios measured in ocean island lavas, such as St. Helena (Graham *et al.*, 1992a) are associated with high $^{238}U/^{204}Pb = \mu$ (HIMU) characteristics

(Thirlwall, 1997) requiring a reservoir with long-term isolation from the convecting mantle. Investigation of Cameroon line magmatism (Barfod *et al.*, 1999) which spans continental and oceanic lithosphere indicated that HIMU characteristics and low $^3He/^4He$ are present even within the lavas erupted on oceanic lithosphere, arguing for negligible lithospheric contribution to noble gas isotopic compositions. Such results also suggest the existence of a low time integrated $^3He/(U+Th)$ reservoir in the sources of OIB.

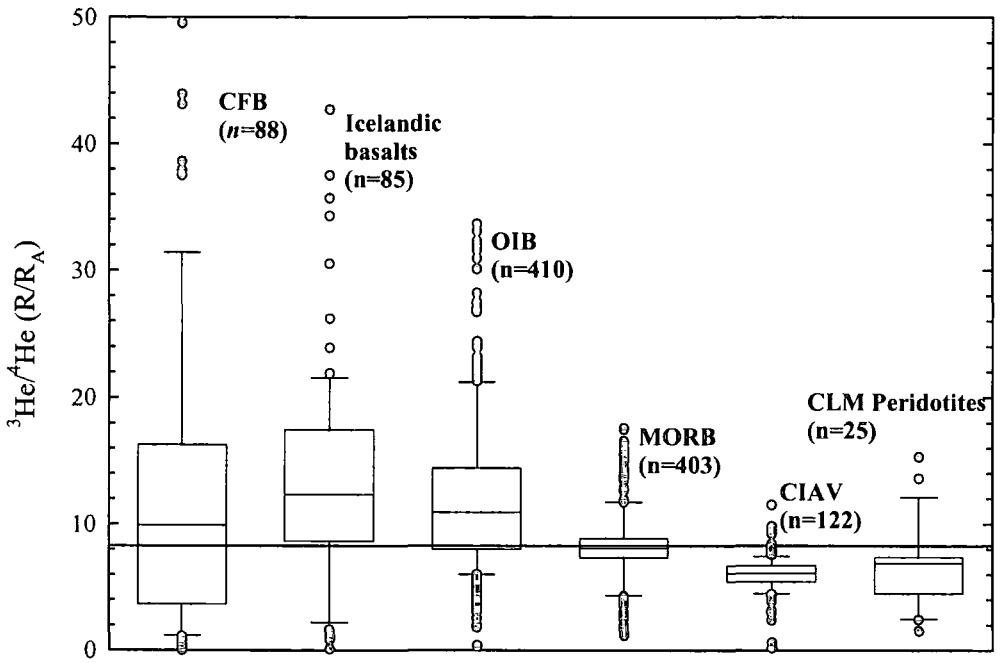

Fig. 3.1: Box and whisker plot for $^3He/^4He$ (R/R_A notation) in olivines from continental flood basalt, ocean island basalt, continental intraplate alkaline volcanics and continental lithospheric mantle peridotite xenoliths, and predominantly glasses from mid-oceanic ridge basalt, helium isotope data. Only samples processed by crushing in vacuo are considered in this plot. Data for CFB from Basu et al., 1995; Marty et al., 1996; Graham et al., 1998; Stuart et al., 2000; Ellam and Stuart, 2000; Peate et al., 2003; Stuart et al., 2003. Data for OIB (excluding Iceland) from Kurz et al., 1982; Kurz et al., 1983, Rison and Craig, 1983; Vance et al., 1989; Graham et al., 1990; Graham et al., 1992a; Poreda and Farley, 1992; Farley et al., 1992; Graham et al., 1993; Hilton et al., 1995; Valbracht et al., 1996; DePaolo et al., 1999; Moriera et al., 1999; Kurz and Geist 1999; Hilton et al., 2000b; Hanyu et al., 2001; Christensen et al., 2001; Revillon et al., 2002. Data for Icelandic basalts from Condomines et al., 1983; Hilton et al., 1999; Breddam et al., 2000; Dixon, 2003; chapter 2. Published data for MORB listed in Graham (2002) and for CIAV and CLM peridotites (Gautheron and Moriera, 2002). Data from this study are included within the CIAV olivine data. CIAV data plot consistently below the MORB mean (8.8±2.1R_A; Graham 2002) and the mean for MORB generated in this compilation (8.3±2.9R_A) whilst OIB and CFB trend toward high $^3He/^4He$ values. Extremely radiogenic $^3He/^4He$ ratios of OIB and CFB are generally ascribed to degassing and subsequent crustal modification processes (Hilton et al., 1995). The box plot illustrates measures of distribution and dispersion of the chosen analyte. Box represents interquartile range (25^{th} to 75^{th} percentiles) and error bars represent 10^{th} and 90^{th} percentiles with outliers plotted as single points. Line within the box represents mean of data.

Two distinct classes of model have been proposed to account for mantle sources with higher time-integrated $^3He/(U+Th)$ than the DMM. The first calls for large-scale stratification of the mantle with preservation of high $^3He/^4He$ in the lower mantle (e.g., Kurz *et al.*, 1983; Porcelli and Wasserburg, 1995; Graham, 2002; Hilton and Porcelli, 2003), or possibly even the core (Macpherson *et al.*, 1998; Porcelli and Halliday, 2001). Coupling of high $^3He/^4He$ values with solar-like Ne isotope ratios (Honda *et al.*, 1993) indicate that this is a primordial volatile component. A lower mantle that has been isolated from the upper mantle is consistent with the noble gas mass balance of the DMM and continental crust (Porcelli and Wasserburg, 1995). Tomographic images of long, narrow, seismically "fast" structures in the lower mantle, which can be mapped to sites of present-day plate convergence at the Earth's surface, also suggest that upper mantle material is transported below the mantle transition zone (van der Hilst *et al.*, 1997). If material is emplaced into the lower mantle, mass balance of these two reservoirs requires that there is return flow from the lower to the upper mantle.

The alternative class of model suggests that the high $^3He/(U+Th)$ reservoir resides in the shallow mantle. In these models, there exists a shallow and volatile-rich mantle characterised by low U and Th relative to DMM, due to ancient melt extraction events (Anderson, 1998). This shallow mantle contains He-rich mineral phases that have captured and preserved high $^3He/^4He$ fluids over extended periods ($>1\times10^9$ years; Natland, 2003; Meibom *et al.*, 2003). The essential pre-requisites for this class of model are that the source maintains: (1) low $^{238}U/^3He$ (NU) for a given U/Th ratio, i.e., the LONU component (Anderson, 1998), resulting in low ^4He production and consequent preservation of high $^3He/^4He$, and (2) residence in the shallow mantle where it would be effectively sampled by low-degree partial melts formed through incipient rifting of continents (e.g., Anderson, 1995; 1998; 2000). LONU mantle can be envisaged as residual and refractory mantle (Anderson, 1998), existing within the 'perisphere', a hypothesised shallow mantle reservoir between the lithosphere and asthenosphere (Anderson, 1995; 2000). Such a model would allow shallow origins for both CFB (e.g., King and Anderson, 1995), and OIB that have high $^3He/^4He$ signatures.

Discriminating between shallow and deep mantle origins for high $^3He/^4He$ measured in volcanic rocks is of fundamental importance to understanding the

evolution and differentiation of the Earth. A deep mantle origin for high $^3He/^4He$ implies some degree of mantle stratification and periodic interaction between shallow and deep mantle reservoirs. A shallow mantle origin for high $^3He/^4He$ ratios would require substantial revision of concepts regarding mantle dynamics (e.g., Porcelli and Ballentine, 2002), models of volatile capture during planetary accretion (e.g., Pepin and Porcelli, 2002) and the partitioning behaviour of helium, uranium and thorium during mantle melting (e.g., Carroll and Draper, 1994).

This chapter tests the hypothesis that a high $^3He/^4He$ component resides in the shallow mantle by following two lines of investigation:

- First, the helium isotope composition and heterogeneity of the CLM is assessed and described to determine if high $^3He/^4He$ can be preserved in this reservoir.
- Second, an appraisal of the helium isotope composition and heterogeneity of continental intraplate alkaline volcanics (CIAV; Fig. 3.2) is conducted. CIAV are terrestrial melts most likely to sample and preserve high $^3He/^4He$ from a high time integrated $^3He/(U+Th)$ source in the upper mantle because they originate close to the boundary layer with the convecting and conducting mantle (Foley, 1992; Wilson *et al.*, 1995; Janney *et al.*, 2002).

The chapter is broken into results and discussion sections in order to present and then discuss the relevant data. Ultimately this chapter assesses the independence of assumptions made regarding the constraints currently placed upon a high time integrated $^3He/(U+Th)$ component existing within the Earth.

3.2 The $^3He/^4He$ characteristics of continental lithospheric mantle; significance as a mantle reservoir

The lithospheric mantle can be defined as the basal part of the Earth's outer rigid mechanical boundary layer where heat loss occurs by conduction. The CLM represents *ca.* 2.5% of the total mantle volume and is a reservoir with great potential for generating and preserving chemical heterogeneity due to its physical isolation from convecting mantle over $>1\times10^9$ year (Ga) time scales (McDonough, 1990; Pearson, 1999; Pearson and Nowell, 2002). Because of the potential to preserve chemically unique components the CLM may retain a wide spectrum of helium

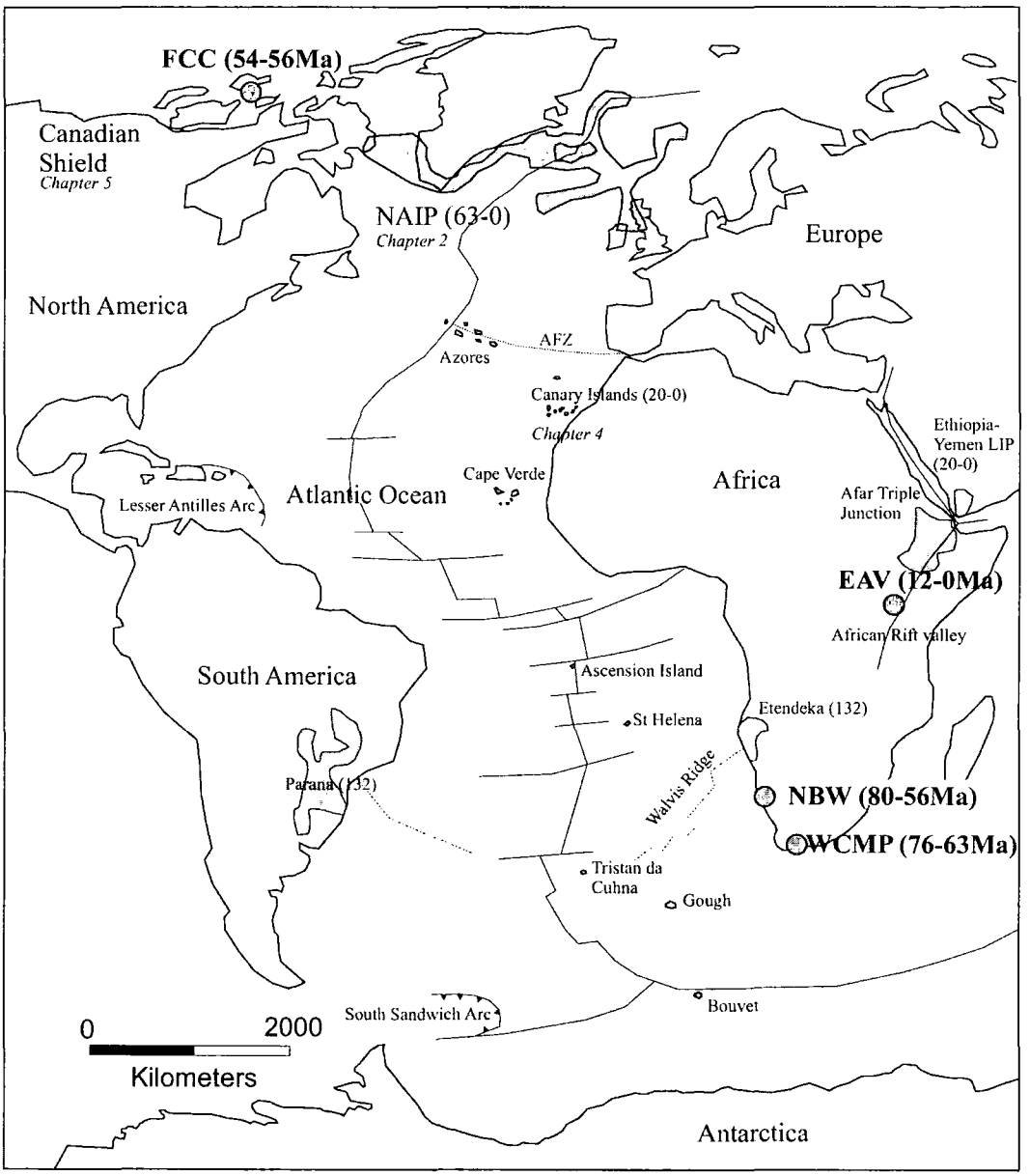

Figure 3.2 Simplified map of the Atlantic Ocean Basin and surrounding continental margins. Selected volcanic and magmatic features are shown including the Mid-Atlantic ridge system, the Afar rift and the South Sandwich and Lesser Antilles intra-oceanic subduction systems. CIAV and Skye and East Greenland lava locations studied here are also shown. Key: FCC, Freemans Cove Complex; NAIP, North Atlantic Igneous Province; EAV, East African Rift Volcanics; NBW, Namaqualand-Bushmanland-Warmbad CIAV lineation; WCMP, Western Cape Melilitite Province. Ages (in Ma) of CIAV and other selected magmatic features are shown in parentheses

compositions and $^3He/^4He$ ratios including the possibility of an end-member with high time integrated $^3He/(U+Th)$.

3.2.1 Physical and chemical attributes of the CLM

Geochemical studies of CLM are limited by the small size and limited spatial distribution of lithospheric mantle material exposed at the Earth's surface. It is unknown whether this available material provides an accurate representation of regional variations in the compositions of CLM. Material from the CLM is accessed either as large tectonically emplaced orogenic peridotite massifs (Menzies and Dupuy, 1991) or as smaller fragments of mantle which are entrained in predominantly alkaline volcanic rocks (i.e., CIAV) during eruption and which are commonly known as mantle xenoliths (Nixon, 1987). Pyroxenite layers within orogenic peridotite massifs and garnet pyroxenite and eclogite xenoliths entrained within CIAV, as well as chemical and textural differences within mantle xenoliths suites indicate that the CLM is heterogeneous at a variety of scales (see Pearson *et al.*, 2003 and references therein).

The diversity of elemental and isotopic signatures revealed in basalts erupted in oceanic and continental intraplate settings generally require input from at least one old radiogenic isotope enriched source region. CLM has been advocated as providing a contribution to oceanic and continental magmatism either by direct melting (Hawkesworth *et al.*, 1983; Turner and Hawkesworth, 1995) or by incorporation of CLM into the convecting mantle (McKenzie and O'Nions, 1983). However, Pearson and Nowell (2002) found that overall CLM is not significantly enriched in incompatible elements and has similar Rb/Sr, Sm/Nd, Lu/Hf and U/Pb ratios to the DMM making it highly unlikely that the CLM is a major source for OIB. Despite this caution, parts of the CLM can generate and retain elemental and isotopic heterogeneity over Ga timescales, especially cratonic peridotites, eclogites and pyroxenites (e.g., Richardson *et al.*, 1984; Walker *et al.*, 1989; Neal *et al.*, 1990; Pearson *et al.*, 1995a,b; Pearson *et al.*, 2003). CLM minerals and peridotite xenoliths also have relatively low U and Th concentrations (see Pearson *et al.*, 2003 and references therein) as well as low U/Pb and Th/Pb; prerequisites for a LONU source (Fig. 3.3).

The most recent estimate of the $^{3}He/^{4}He$ ratio of CLM ($6.1\pm0.9R_A$, n=114; Gautheron and Moriera, 2002) requires a more radiogenic source than that of MORB (8 ± 1; Hilton and Porcelli, 2003; $8.8\pm2.1R_A$; Graham, 2002). This relationship has been attributed to steady-state helium flux into the CLM from the asthenosphere over 0.1Ga timescales (Gautheron and Moriera, 2002). However, in the study of Gautheron and Moriera (2002) a natural sample bias towards Proterozoic circum-cratonic CLM peridotites entrained within young melts is evident. This is because of the lack of published helium isotope data on Archaean CLM peridotites and mafic lithologies such as pyroxenite or eclogite. In order to better characterise the U-Th-He systematics of the CLM and further consider its importance as a reservoir for OIB and CFB magmatism this section will examine two areas of helium isotope geochemistry in the CLM. Firstly, helium isotope results for demonstrably Archaean peridotites and the first measured helium isotopic ratios of Archaean eclogite, that the author is aware of, will be presented. Secondly, a description of helium isotope variation of peridotite xenolith samples from Archaean cratonic and Proterozoic non-cratonic CLM will be provided.

Cosmogenic ^{3}He addition to mantle peridotite samples exposed at the Earths' surface over prolonged periods has caused the elevation of $^{3}He/^{4}He$ in some sample suites (e.g., Porcelli *et al.*, 1987). In this study, samples from recently excavated kimberlite pipes were utilised in order to avoid this complication. Additionally, short crushing times were employed for eclogites to avoid release of lattice-based He (e.g., Hilton *et al.*, 1993; Scarsi, 2000).

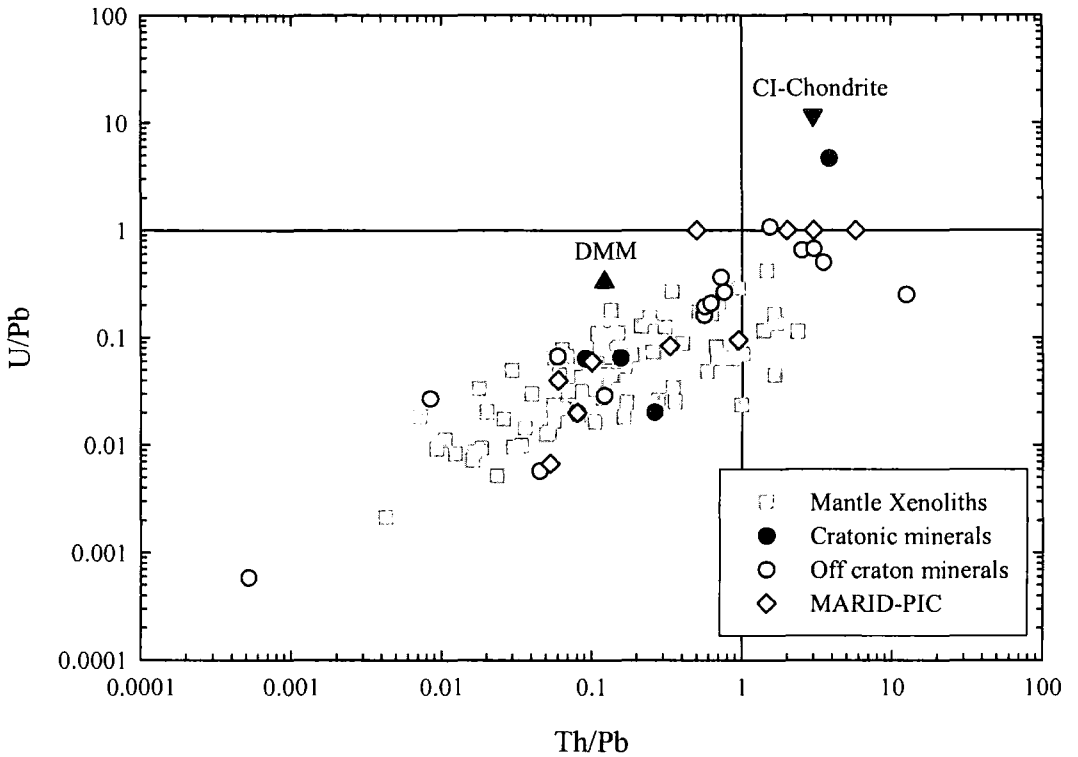

Fig. 3.3: Th/Pb versus U/Pb for CLM materials including whole rock peridotites and minerals from CLM peridotites and mafic xenoliths. Peridotite xenoliths and their minerals are generally characterised by low Th/Pb and U/Pb and low absolute abundances of U and Th. MARID = mica (phlogopite)-amphibole (k-richterite)-rutile-ilmenite-clinopyroxene (diopside) mineral association, PIC = Phlogopite (mica)-ilmenite-clinopyroxene-minor rutile mineral association. Data from Pearson et al. (2003) and references therein.

3.2.2 Eclogite helium results and description of the CLM helium dataset

Garnet and omphacitic pyroxene were separated from an eclogite which was entrained as part of the mantle xenolith suite of the 128 Ma Group 2 Roberts Victor kimberlite pipe, South Africa. Additionally, data from 5 cratonic peridotites including two garnet lherzolites from the 1179Ma Group 1 Premier kimberlite pipe, South Africa and three garnet lherzolites from the 350Ma Group 1 Udachnaya kimberlite pipe, Siberia (Pearson and Burgess, unpublished) are also described to examine their helium isotopic compositions compared to Proterozoic non-cratonic peridotite equivalents. Data are presented in Table 3.1.

Archaean Kaapvaal cratonic peridotite minerals from the Premier kimberlite pipe possess radiogenic helium with $^3He/^4He$ 0.01-0.06R_A whilst olivines from Siberian cratonic peridotites in the Udachnaya kimberlite pipe exhibit slightly less radiogenic $^3He/^4He$ (2.7-3.8R_A; Table 3.1, Fig. 2.5). In the case of the Premier garnet lherzolites

where high and low temperature peridotites have been measured for their $^3He/^4He$ ratios, no obvious difference in $^3He/^4He$ isotope ratios can be differentiated between the suites. $^{18}O/^{16}O$ ratios of garnet and omphacitic pyroxene from the Roberts Victor eclogite indicate that this sample falls into the group II eclogite category of Schulze *et al.* (2000). Both the garnet and pyroxene have highly radiogenic helium isotopic ratios of 0.05 and 0.41R_A respectively (Table 3.1).

Table 3.1 O and He isotope data for mantle xenoliths

Sample /phase	Lithology	$\delta^{18}O$ (‰)[a]	R/R_A (±2σ)[c]	nccSTP/g ^4He (±2σ)
Roberts Victor Kimberlite Pipe, South Africa (128Ma)				
RV2000 (Gt)	Eclogite	3.25	0.05 (0.13)*	140.2 (2.6)*
RV2000 (Px)	Eclogite	3.54	0.41 (0.07)*	115.8 (6.1)*
Premier Kimberlite Pipe, South Africa (1179Ma)				
FRB1350 (Ol)	Low-T garnet lherzolite	5.30[b]	0.04	-
FRB1350 (Cpx)		5.76[b]	0.01	-
FRB1350 (Opx)		5.81[b]	0.01	-
PHN5267 (Opx)	High-T garnet lherzolite	5.63[b]	0.06	-
Udachnaya Kimberlite Pipe, Siberia (350Ma)				
UV84/9 (Ol)		-	2.70	-
UV84/9 (Ol)rpt		-	2.70	-
UV49/76 (Ol)		5.12[b]	3.70	-
UV49/76 (Ol)rpt		-	3.80	-
UV49/76 (Ol)rpt		-	3.80	-
UV417/89 (Ol)	Low-T garnet lherzolite	5.11[b]	2.90	-
UV417/89(Ol) rpt		-	0.06	-

[a] Analysed by laser fluorination (see text for details) – $\delta^{18}O_{samp} = 1000\times(^{18}O/^{16}O_{samp}/^{18}O/^{16}O_{v\text{-}smow}-1)$

[b] Data from Mattey *et al.*, 1994

[c] He and Ar isotopic analyses performed at the University of Manchester and reproduced with permission of Pearson and Burgess (unpublished). Those marked (*) which were analysed at Scripps Institution of Oceanography by JMDD in 2003. Repitition of all samples, except UV417/89 are in excellent agreement. Poor reproducibility of UV417/89 is probably due to release of lattice-based ^4He during crushing of the 2nd aliquot (e.g., Hilton *et al.*, 1993; Scarsi, 2000).

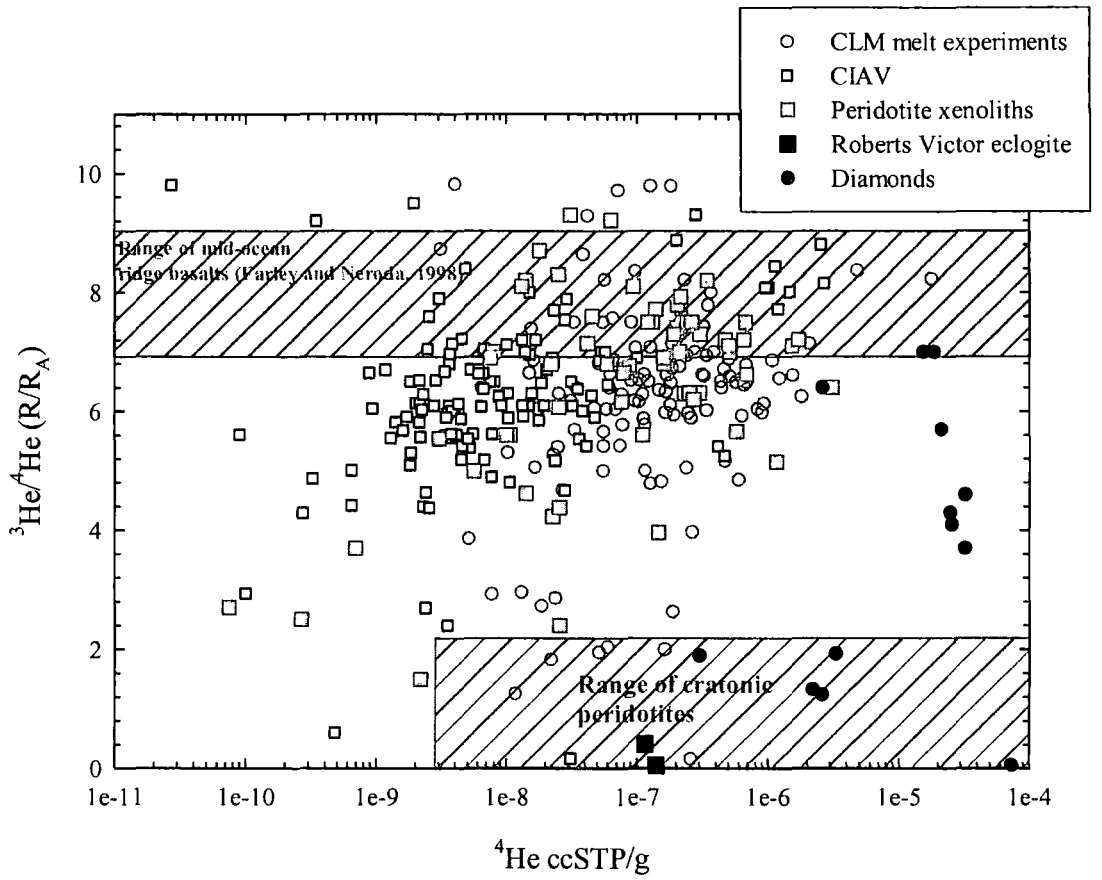

Fig. 3.4: $^3He/^4He$ ratio (R/R_A notation) versus ^4He concentrations for continental lithospheric mantle samples analysed by melting and crushing experiments. Also shown is the mid-ocean ridge basalt mean and standard deviation calculated by Farley and Neroda (1998) and Hilton and Porcelli (2003), ($8\pm1R_A$). The Roberts Victor eclogite data is from this study. Published data from Porcelli et al., 1986; Marty et al., 1994; Dunaï and Baur, 1995; Reid and Graham, 1996; Dodson et al., 1998; Matsumoto et al., 1998; Burgess et al., 1998; Ackert et al., 1999; Matsumoto et al., 2000; Hoke et al., 2000a,b; Matsumoto et al., 2001; Honda et al., 2004. Crushed samples of Porcelli et al. (1986) are the only crush samples of xenoliths with demonstrably higher $^3He/^4He$ than MORB; these samples are garnet lherzolites from the East African rift and have been shown to contain excess cosmogenic ^3He (Porcelli et al., 1987).

Data from the eclogite are compared with published crushing and melting experiment data of minerals from CIAV, mantle xenoliths and fluid inclusions within diamonds in Fig. 3.4. In the discussion section of this chapter, only samples analysed by crushing *in vacuo* will be considered because the technique releases the gas from fluid and melt inclusions that are free of cosmogenic and radiogenic He produced in the matrix (Kurz, 1986; Scarsi, 2000; see Appendix C for analytical techniques and discussion). Melting experiments will be considered briefly in this results section to allow comparison of means between crush and melt experiments. Distinctions have been made between CIAV and Continental Flood Basalts because

of the extreme differences in the degree of partial melting and consideration of tectonic setting between these two types of intraplate magmatism. CIAV associated with CFB provinces both spatially and temporally and those located on ocean islands (technically Oceanic-IAV) are not considered in the compilations. Only volcanic rocks that have previously been ascribed in the literature or are presented here as originating from low degree partial melting and eruption through CLM have been included in the CIAV dataset.

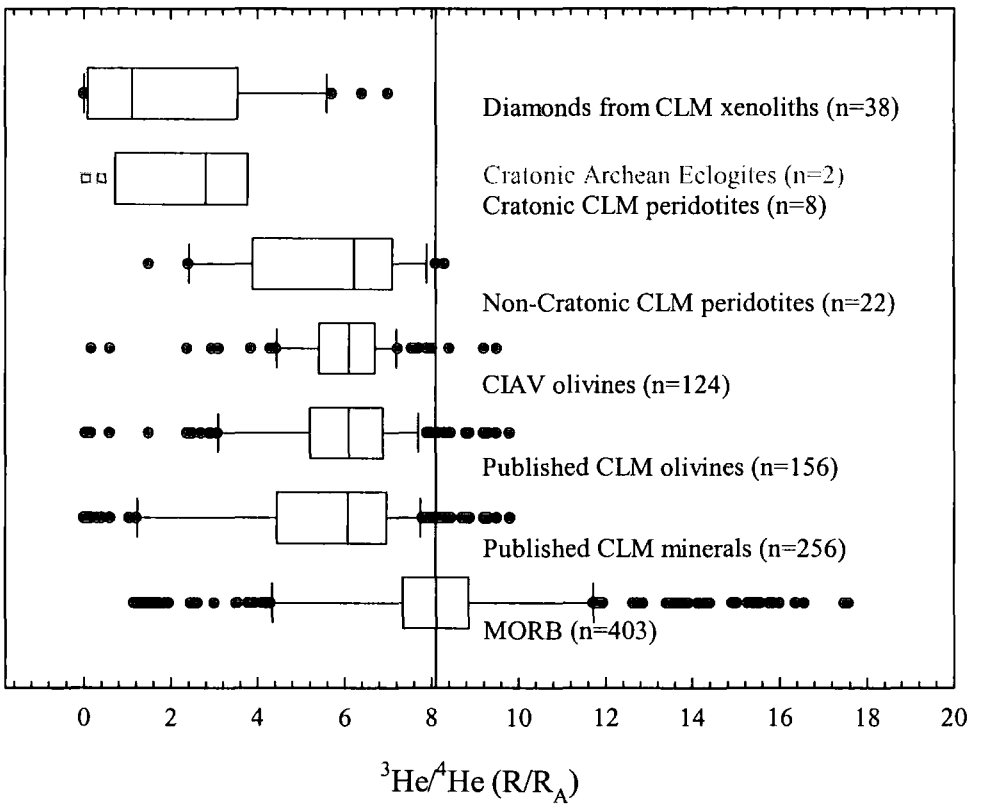

Fig. 3.5: Box and whisker plot for $^3He/^4He$ ratios (R/R_A notation) of MORB and CLM samples analysed by crushing in vacuo including all published CLM minerals, published CLM olivines and olivines from CIAV, Non-cratonic Proterozoic peridotites, Cratonic Archaean peridotites, Cratonic Archaean eclogites and Diamonds entrained in CIAV. Data from this study and references listed in Fig. 3.1 and Fig. 3.4. Information on statistical distribution and dispersion given in Fig 3.1.

The mean melt experiment $^3He/^4He$ ratio is $6.5\pm2.3R_A$ (1.S.D., n=127) versus $5.4\pm2.3R_A$ (1.S.D., n=256) for crush experiments (Fig. 3.4; Fig. 3.5). The less radiogenic $^3He/^4He$ ratio of melting experiments is likely to be due to incorporation of spallation reaction ^3He which is released from mineral lattices during melting but not crushing. If only olivines analysed in crushing experiments are considered a mean $^3He/^4He$ ratio $5.8\pm1.7R_A$ (1.S.D., n=156) is obtained. Olivine phenocrysts from

CIAV, Archaean cratonic peridotites and Proterozoic non-cratonic peridotites give means of 5.9±1.3 (1.S.D., n=124), 2.5±1.6 (1.S.D., n=8) and 5.6±2.0 (1.S.D., n=25) respectively (Fig. 3.5). The mean $^3He/^4He$ ratio of diamond inclusions (1.8±2.2R_A, 1.S.D., n=38) is similar to the mean of olivines from Archaean cratonic peridotites. Diamonds analysed in the two studies quoted here (Burgess *et al.*, 1998; Honda *et al.*, 2004) used a mixture of framesite and carbonado diamonds whose crystallisation ages may not all be Archaean (D.G. Pearson *pers. comm.*).

The individual mean ratios calculated from data presented here and from published samples indicate that all CLM samples exhibit more radiogenic $^3He/^4He$ ratios than MORB (8±1R_A; Hilton and Porcelli, 2003; 8.8±2.1R_A; Graham, 2002). The datasets compiled in this work indicate greater heterogeneity than previously recognised by Gautheron and Moriera (2002) for CLM. Archaean cratonic peridotites and diamond inclusions have more radiogenic $^3He/^4He$ ratios than Proterozoic non-cratonic peridotites and CIAV. The mean $^3He/^4He$ ratio of olivines from the Horoman peridotite in Japan (Matsumoto *et al.*, 2001) provides the only current estimate for orogenic massif peridotite olivines of 7.3±3.9R_A (1.S.D., n=5) and represents the least radiogenic helium isotope ratios of CLM samples. However, the Horoman orogenic massif peridotite probably resided in an arc environment prior to obduction and thus the budget of rare gases is likely to be dominated by arc volatiles which passed through the mantle wedge (Matsumoto *et al.*, 2001).

3.3 $^3He/^4He$ characteristics of CIAV from Canada, South Africa and Uganda

CIAV generated by low degree partial melting form a continuum of chemical transition to increasing silica saturation from group 1 kimberlites, olivine melilitites, nephelinites, basanites through to alkali basalts (Alibert *et al.*, 1983; Janney *et al.*, 2002; 2003). Although CIAV only represent a fraction of a percent of terrestrial volcanism by volume, they provide valuable clues to the origin of mantle source components and because they provide a means to test the presence of a high $^3He/^4He$ reservoir in the shallow mantle. The trace element geochemistry and coupled Sr, Nd, Pb and Os isotope systematics of intraplate alkaline volcanics show similarities with OIB and MORB, and also indicate that CIAV reflect contributions from the following reservoirs: convecting asthenosphere (the source of MORB), continental

lithospheric mantle (CLM) and a HIMU-like mantle component (Brooks *et al.*, 1976; Hawkesworth *et al.*, 1990; Wilson *et al.*, 1995; Janney *et al.*, 2002, 2003). A variety of experimental data on CIAV compositions (Green, 1970; Brey, 1978; Foley, 1992) constrains the depth of generation for these low-degree partial melts to lie near the sub-continental boundary layer - the region separating the convecting and conducting mantle. Consequently, CIAV melts originate from parts of the upper mantle beneath continents that coincide with the envisaged location of the hypothesised LONU source.

Trace element and low silica characteristics of CIAV can be explained by low degree partial melting (<<5%; Rogers *et al.*, 1992) of hydrated carbonate-rich garnet peridotite at mantle potential temperatures between 1000 and 1200°C (Wilson *et al.*, 1995). Kimberlites are likely to be generated at greater pressures (>50kbar) than olivine melilitites (~30-45kbar; Brey 1978), corresponding to thinner lithosphere for the latter (e.g., Ellam, 1992). The variety of sources proposed for CIAV include deep transition zone and core-mantle boundary components (e.g., Ringwood *et al.*, 1992; Collerson *et al.*, 2002) although the majority of studies suggest shallower sources (e.g., Wilson *et al.*, 1995; Janney *et al.*, 2002; 2003, Schersten *et al.*, 2004). In particular, for the rock types studied here (alkali basalt, basanite, nephelinite, melilitite, ugandite), depths of melting <150km are widely accepted, as is a significant contribution to CIAV magmatism from the CLM (e.g., Brey, 1978; Foley *et al.*, 1992).

From this perspective, CIAV offer a means of testing for the presence of a shallow, high time integrated $^{3}He/(U+Th)$ reservoir in the Earth's upper mantle because their origin and sources (Wilson *et al.*, 1995; Janney *et al.*, 2002) are at the inferred site of LONU. CIAV are probes *par excellence* into the upper mantle because:

- CIAV are emplaced onto lithosphere of varying thickness and compositions including cratons, continental rifts and mobile belts (Brey, 1978; Clague and Frey, 1982; Wilson *et al.*, 1995) allowing appraisal of the distribution of a possible high time integrated $^{3}He/(U+Th)$ reservoir within the upper mantle.
- CIAV do not interact directly with shallow asthenospheric melts because after partial melting their parental magmas pass through the CLM.

- Selection of olivine melilitites, nephelinites, basanites and basalts circumvent problems of large volumes of CLM xenocrysts and xenoliths obscuring $^{3}He/^{4}He$ signatures unlike kimberlites which entrain significant quantities of CLM (e.g., Pearson *et al.*, 2003).

3.3.1 Geology of continental intraplate alkaline volcanics (CIAV)

The samples selected for $^{3}He/^{4}He$ isotope analysis for this study are from a larger set of analysed volcanics (Janney *et al.*, 2002; 2003; and unpublished data of J.M.D. Day) and include:

- 23 melilitite, nephelinite, basanite and basaltic volcanics from the Palaeogene Freemans Cove Complex (FCC) in Canada
- A Miocene (12Ma) ugandite from the western branch of the East African rift system
- Two late-Cretaceous to early-Tertiary alkaline magmatic lineaments on the western margin of South Africa

3.3.1.1 Freemans Cove Complex, Nunavut, Canada (FCC)

The FCC is situated at the south-eastern extremity of Bathurst Island in the Canadian Arctic (Fig. 3.2), at the northernmost limit of the Churchill structural province of the Laurentian shield; a Proterozoic mobile belt surrounding the Slave Craton. Volcanic plugs, breccia diatremes, dykes and sills were emplaced into a thick succession of Cambrian to Devonian sedimentary carbonate and calc-silicate strata with subordinate Silurian, Ordovician and Cretaceous marine shales (Harrison and Defreitas, 1999). Diatremes and dykes are closely related to pre-existing fault structures which form a fault-bounded approximately north-south orientated structure. This structure formed prior to eruption of the FCC but which was reactivated synchronously with emplacement of the FCC (Kerr, 1974; Harrison and Defrietas, 1999). Phonolite 'blisters' and absence of water-rock interaction features indicate subaerial eruption.

Previous attempts to date the FCC have employed whole-rock K-Ar and Rb-Sr chronology which provided middle Eocene ages of 47±8Ma and 47.1±4Ma respectively (Kerr, 1974; Mitchell and Platt, 1983). Recent precise Rb-Sr analyses (Barker *et al.*, 2002) have found an absence of isochronous relationships and cast

considerable doubt on the accuracy of previous Rb-Sr derived ages. Newly obtained ^{40}Ar-^{39}Ar age data (Appendix D) give weighted mean plateau ages at the 2σ level of confidence of 56.3±0.5Ma for the basanite, 55.7±0.4Ma for the alkali gabbro and 54.3±0.4Ma for a trachyte indicating measurable apparent age differences between mafic, primitive melts and more evolved equivalents. The new ^{40}Ar-^{39}Ar age data provide excellent plateau with a very high percentage of Ar released and are used in preference to previous Rb-Sr and K-Ar age data for the FCC because of the doubt cast on the accuracy of previously published dates.

The late Palaeocene (Ypresian) is associated with widespread magmatic activity in and around the polar arctic regions and is contemporaneous with kimberlite magmatism in the Lac de Gras region of the Slave Craton (Kjarsgaard, *pers comm.*). Extensive CFB magmatism in East and West Greenland (Hirschmann *et al.*, 1997; Tegner *et al.*, 1998; Storey *et al.*, 1998) coinciding with the onset of sea floor spreading in the North Atlantic east of Greenland (chron 24r) and in the Eurasian basin east of the Lomonosov ridge (Harrison *et al.*, 1999 and references therein) also yield dates within a similar interval to the FCC.

The ^{40}Ar-^{39}Ar ages for the FCC coincide with a shift in the Euler pole of rotation for sea floor spreading in the Labrador Sea and major plate reorganisation related to shifts in the motion of the ancestral Greenland plate with regard to the North American continent (Harrison *pers comm.*). The resultant Eurekan "orogen", which lasted from the late Palaeocene (Selandian) to at least the late Eocene (Priabonian) was due to major shifts in tectonic transport directions resulting in a westward expanding compressional belt generating broad inversion of structures in the arctic (Harrison *et al.*, 1999). Mitchell and Platt (1983) argued that the FCC was due to basin inversion and melting of strongly metasomatised mantle. The sinistral sense of movement between the North American plate and ancestral Greenland plate make the likely melting and emplacement mechanism for FCC volcanism through direct response to transpressional reactivation of pre-existing normal fault structures.

The ^{40}Ar-^{39}Ar age dates suggest a prolonged development of the FCC over a period of 2.0±1.3Ma (2σ). Based upon current estimates of alkaline magmatic differentiation and cooling in crustal environments (e.g., Hawkesworth *et al.*, 2000) and cross-cutting relationships of diatremes and dyke, a single melting and cooling

event to explain the FCC is highly implausible. ^{40}Ar-^{39}Ar ages imply intermittent melting events generating periodic FCC volcanism.

3.3.1.2 Western Cape Melilitite Province, South Africa (WCMP)

The WCMP extends 360km from the Alphard Bank on the continental shelf of South Africa, through the Pan-African Cape Fold Belt and into the early to mid-Proterozoic Namaqua-Natal mobile belt (Doucouré *et al.*, 1996; Fig. 3.2). In this study only olivine melilitites intruded into the Namaqua-Natal mobile belt are considered. Detailed investigation into the morphology and volcanology of WCMP volcanics (Janney *et al.*, 2002 and references therein) suggest common modes of emplacement with pipe-like bodies fed by dykes and sills that tend to intrude along faults and fractures. Melilitites such as those at Salt Petre Kop exhibit prominent ring-structures consisting of potassic trachyte, carbonatite and associated pyroclastics (DeWet, 1975; Verwoerd, 1990).

The WCMP represents one of three late Cretaceous to early Tertiary alkaline magmatic lineations that intersect the south-western margin of South Africa, which are co-linear with older diamondiferous Kimberlite occurrences lying within or at the edges of the Kaapvaal craton. K-Ar age dates for the WCMP range from 75.8 to 62.6Ma for whole rock and phlogopite separates (Duncan *et al.*, 1978) and in combination with the 58.0±2.4Ma sanidine K-Ar age for a Alphard bank trachyte (Dingle and Gentle, 1972, Appendix A) suggests that the WCMP represents an age progressive magmatic lineation with a gross plate motion of 19km/Ma (Janney *et al.*, 2002).

3.3.1.3 Namaqualand-Bushmanland-Warmbad province (NBW)

The NBW is oriented NNE-SSW and extends over 250km from the Namaqualand coast to the Bushmanland plateau (Fig. 3.2). The NBW lies exclusively within Namaqua-Natal mobile belt lithosphere and consists of over 100 pipes, many of which are sediment filled and consist of diatreme facies "parakimberlite", although a significant number of pipes contain fresh olivine melilitite (Moore and Verwoerd, 1985; Janney *et al.*, 2003). The Warmbad kimberlite province (Skinner *et al.*, 1992), lying to the north-east of the Namaqualand-Bushmanland melilitites is considered as a possible extension of this lineament by Janney *et al.* (2003) based upon their

similar ages, chemical and isotopic characteristics and is therefore classed with the melilitites as the NBW. Ages of 56-80Ma for the NBW have been determined by K-Ar, Ar-Ar and U-Pb zircon geochronology (Davis, 1977; Moore and Verwoerd, 1985; G. Kiviets, unpublished data, 2000, Appendix A). NBW pipe ages from the coast to the interior approximately correlate with the African plate motion at this time (e.g., Hartnady and le Roux, 1985).

3.3.1.4 PHN2902A – ugandite from the East African Rift

The western branch of the East African rift system is a classic locality for potassic alkaline magmatism. From north to south the western branch of the East African Rift System consists of carbonatite lavas at Fort Portal, ultrapotassic mafic rocks in the central Katwe-Kirorongo and Bunyaruguru fields and potassic mafic-felsic flows in the Bufumbira volcanic field. Sample PHN2902A is a ugandite from the type locale of Holmes and Harwood (1937) at Bufumbira in southwest Uganda (Fig. 3.2). The Bufumbira field forms the north-eastern most section of the Virunga volcanic field and is made up of basanites and leucitites along with evolved potassic trachytes and phonolites. Geochemical variations in lavas and volcanic products from the volcanic fields have been interpreted as indicating lithospheric erosion or delamination from beneath the western branch of the East African Rift (Furman and Graham, 1999). Magmatism in the western branch of the East African Rift System extends from Miocene (~12Ma) through to recent times (Pasteels *et al.*, 1989).

3.3.2 The geochemistry and petrology of studied CIAV

Published data for WCMP and NBW volcanics (Janney *et al.*, 2002; Janney *et al.*, 2003) are considered with data obtained for the FCC and PHN2902A during the course of this study. These data are explored only briefly here, to maintain focus on the He isotope systematics of CIAV. Tabulated summaries of petrology and geochemical data are provided in the appendices.

3.3.2.1 Petrology

Olivine is the dominant phenocryst phase in WCMP and NBW melilitites and also occurs in the groundmass (Appendix A). Zoned olivine phenocrysts in both provinces reveal complex histories of intermittent recharge and minor differentiation

during petrogenesis (Moore and Erlank, 1979; Boctor and Yoder, 1986). Phenocrysts occur as large, anhedral megacryst grains (1-15mm diameter) exhibiting strain (~10% of total olivine population) especially in melilitites erupted in the Namaqua-Natal mobile belt. Euhedral olivine grains (< 2mm) represent the dominant populations for melilitites erupted in the Cape Fold belt such as Robertson. Strained olivines and olivine aggregates are particularly abundant in "para-kimberlite" volcanics such as Hoedkop. Olivine megacrysts are less forsteritic (Fo_{75-87}, Janney *et al.*, 2002; 2003) than typical mantle olivine from cratonic or circum cratonic Mg-rich peridotites erupted in Kimberlites (Fo_{91-96}; Pearson *et al.*, 2003) but overlap with Fe-rich peridotites (Fo_{83-89}). Janney *et al.* (2002) suggested that the scarcity of mantle-derived xenoliths discovered in the melilitites and the relatively low forsterite contents suggested minimal addition of xenocrystic olivine. However, mantled olivines (McIver and Ferguson, 1979; Boctor and Yoder, 1986; Viljoen, 1988) and the population of strained olivines provide evidence that olivine megacrysts may not be strictly cognate.

The groundmass of the melilitites from the WCMP and NBW includes olivine, melilite, nepheline, clinopyroxene, phlogopite, spinel and perovskite in decreasing order of abundance. Melilitites erupted within the Namaqua-Natal mobile belt contain higher abundances of phlogopite than those from the Cape Fold belt which may indicate a more volatile-rich source for melilitites erupted through the Namaqua-Natal mobile belt (Janney *et al.*, 2002) or greater retention of their initial volatile content. Groundmass olivine is unlikely to comprise a significant fraction of separated olivine from the melilitites because larger, fresh olivines were preferentially hand separated.

Ugandite, PHN2902A, contains phenocrysts of olivine and augite which commonly exhibits zoning with re-adsorbed cores. Groundmass minerals include nepheline, leucite, clinopyroxene, chromite and some interstitial fresh glass. Mixing boundaries recognised by the percentage of glass within parts of the flow along with strong disequilibrium assemblages suggest that PHN2902A may represent a mixture of primitive melt compositions.

The FCC exhibits a continuum of highly alkaline rock types from olivine melilitite through to phonolite. Only melilitites, nephelinites, basanites (will be collectively referred to as nephelinites for the remainder of this chapter) and basalts

are considered in this study because of their primitive nature and ubiquitous presence of olivine (Appendix A). All of the studied volcanic rocks are generally microphenocrystic with macrophenocrysts of olivine, ~10% of which exhibit strain, and augite, many of which are zoned. Olivines range from $Fo_{93.5}$ to Fo_{86}. A large number of FCC basanites also contain small (<1cm^2) polycrystalline aggregates of strained olivine and occasionally glomeroporphyritic rafts of augite.

The groundmass is composed in general order of dominance, clinopyroxene, olivine, Fe-Ti oxides, feldspar (melilitite, nepheline and anorthoclase) and in the case of BI 10G and BI 12, andesine to labradorite plagioclase as well as primary biotite and phlogopite. Rare spinel and chromite are also present in the majority of basanites. Alteration minerals, most prominently after olivine, include calcite, zeolite and clay. The freshest sample, C246149, exhibits large melilite laths and large chromites in a groundmass in-filled by fresh glass, melilite and nepheline. Like the African CIAV studied, groundmass olivine is unlikely to make up a significant proportion of the separated olivine for He and O isotope analysis.

3.3.2.2 Major elements

Fig. 3.6 illustrates the range of compositions of CIAV analysed in this chapter. The new major element data presented for the FCC in this study (Appendix F) follow an alkaline fractionation trend from basanite through to phonolite with a subsidiary trend to more mildly alkaline picrobasalt through to basalt-andesite compositions. The majority of FCC samples analysed for He and O isotopes fall within the basanite field. East African Rift Volcanics show extreme enrichments in alkalis at relatively low silica contents but also exhibit a more transitional alkaline fractionation trend than FCC volcanics (see fields in Fig. 3.6). Highly silica undersaturated olivine melilitites from the WCMP and NBW all plot in the foidite field apart from fractionated samples from the Alphard bank alkali basalts (not analysed in this study) and one Hoedkop sample. IUGS foidite discrimination schemes (Σ(CaO, Na_2O, K_2O) versus $\Sigma(SiO_2, Al_2O_3)$) show that WCMP and NBW volcanics can be classified as true melilitites, PHN2902A can be chemically defined as a nephelinite, whilst the FCC samples studied are all nephelinites apart from C246-149 (melilitite) and KIA-99-BI12 (basalt). The later observation is not reflected in petrographical

descriptions of the majority of FCC nephelinites because of alteration of groundmass nepheline and glass (see Appendix A).

Chemically, the WCMP and NBW melilitites are silica and aluminium-poor (SiO_2 <40%), calcium and magnesian-rich low degree partial melts whose elemental composition is strongly controlled by olivine. A greater degree of olivine control in NBW compared with WCMP melilitites is indicated from elemental compositions (Fig. 3.7). The NBW and WCMP melilitites are more Mg-rich than rift-graben related CIAV of nephelitic/melilititic composition (Rhine Graben and Balcones, Texas) and OIAV (Hawaii and the Canary Islands, Fig. 3.7). Both provinces indicate limited fractionation and predominantly olivine accumulation in conjunction with high compatible element abundances.

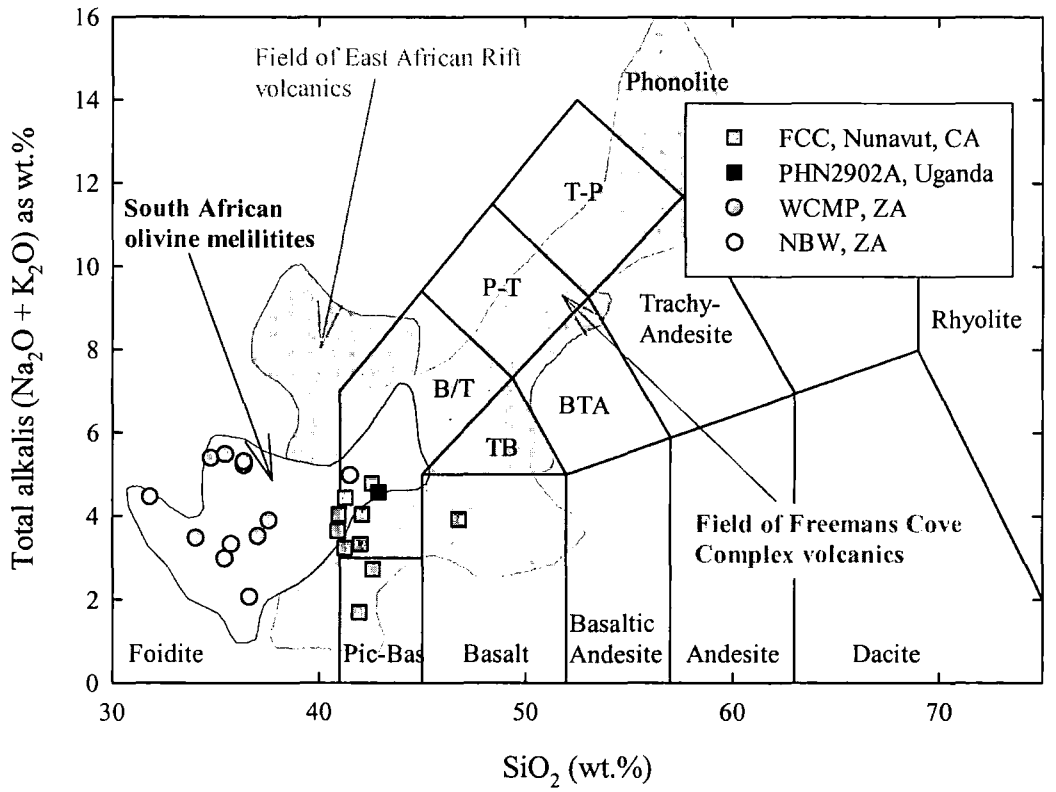

Fig. 3.6: Anhydrous corrected weight percent total alkalis (Na_2O+K_2O) versus SiO_2 diagram for CIAV analysed for O and He isotope ratios in this study. Also shown are compositional fields for the Freemans Cove Complex volcanic rocks (data from Mitchell and Platt, 1984; Day., unpublished), Western branch, East African Rift volcanic rocks (Furman and Graham, 1999 and references therein), Western Cape Melilitite Province (Janney et al., 2002) and the Namaqualand-Bushmanland-Warmbad melilitites (Janney et al., 2003).

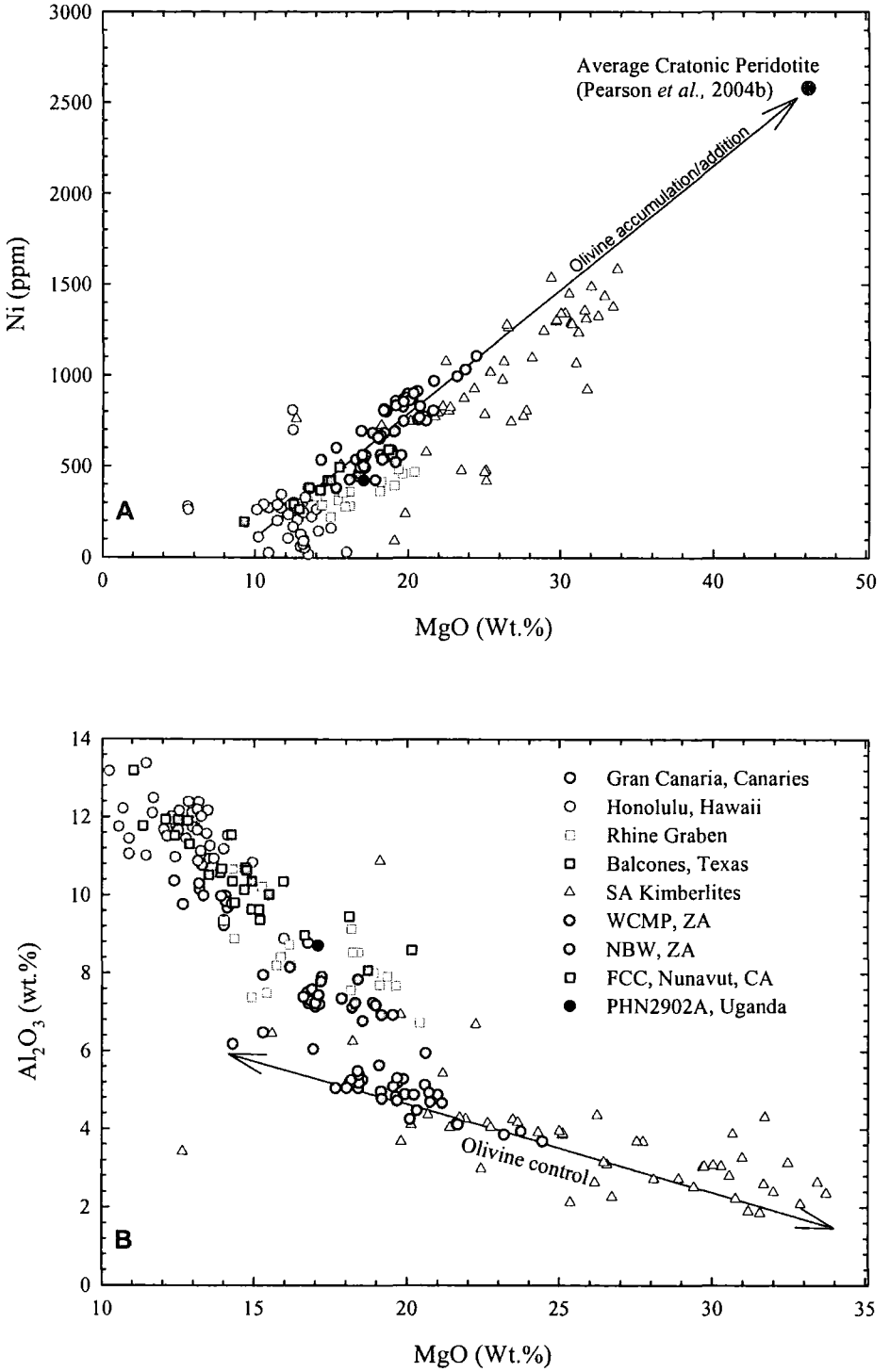

Fig. 3.7: (a) Whole-rock weight percent MgO vs. Ni (ppm) and (b) MgO vs. Al_2O_3 for Continental Intraplate Alkaline Volcanics (CIAV). Additional data in Fig.s (a) and (b) from Spencer, 1969; Clague and Frey, 1982; Spriggs, 1988; Hoernle and Schminke, 1993a; Wilson et al., 1995; Janney et al., 2002; 2003.

FCC volcanics are less Mg-rich than WCMP and NBW melilitites (Fig. 3.7) but show a limited range of SiO_2 (38.70 to 41.84 Wt.%) contents for a large range in

MgO (12.51 to 18.72 Wt.%; excluding KIA-99-BI12) and compatible element concentrations (e.g. Ni), consistent with strong olivine control. Minor olivine addition via mechanical entrainment of CLM peridotite is possible (Petrography Appendix A); indicated from the high MgO contents of NBW melilitites. FCC nephelinites and basanites also exhibit similar trends to other CIAV and OIAV with increasing Al_2O_3 with decreasing MgO (Fig. 3.7). Nephelinites have near-primary *Mg.*-numbers (Mg-no. = 100 × Mg/ (Mg + Fe^{2+})) up to 78.3 and have previously been considered to represent a continuum of melts that have been generated by varying degrees of partial melting (Mitchell and Platt, 1984) and may represent primary, unmodified liquids (Mitchell and Platt, 1983). Comparisons illustrate that FCC volcanics have higher Al_2O_3 but lower $Fe_2O_3^T$ and TiO_2 than WCMP and NBW melilitites and PHN2902A (e.g., Fig. 3.7). The high TiO_2 contents of African CIAV volcanics compared to Canadian CIAV probably represent a fundamental difference in source characteristics. Elevated Ti or V (not plotted) contents are generally due to the quantity and composition of oxides or phases such as amphibole within lava which is correspondingly a function of the composition of oxide or hydroxide phases within the source (e.g., Furman and Graham, 1999).

3.3.2.3 Trace elements

New trace element data for FCC and Ugandite PHN2902A are presented with trace element data from Janney *et al.* (2002; 2003) in Appendix F. CIAV are generally characterised by elevated incompatible element profiles and relative depletions in heavy rare earth elements (HREE) on primitive mantle normalised plots. NBW and WCMP melilitites show significant enrichment in large ion lithophile elements (especially Saltpetre Kop), and have large negative anomalies in K, P, Zr and Hf and in the case of the WCMP, Ti (Fig. 3.8). The difference in incompatible element concentrations and ratios between melilitites from the WCMP has been ascribed to varying amounts of metasomatic enrichment within their sources (Janney *et al.*, 2002). Melilitite diatremes on thinner Cape Fold Belt lithosphere are characterised by incompatible element profiles similar to HIMU-type OIB, with positive Nb and Zr anomalies and low Rb/Nb and Ba/Nb. Craton-wards on Proterozoic Namaqua-Natal mobile belt Nb/Zr and Ba/Nb and Rb/Nb all increase. The WCMP and NBW melilitites overlap with each other and have higher HREE concentrations than

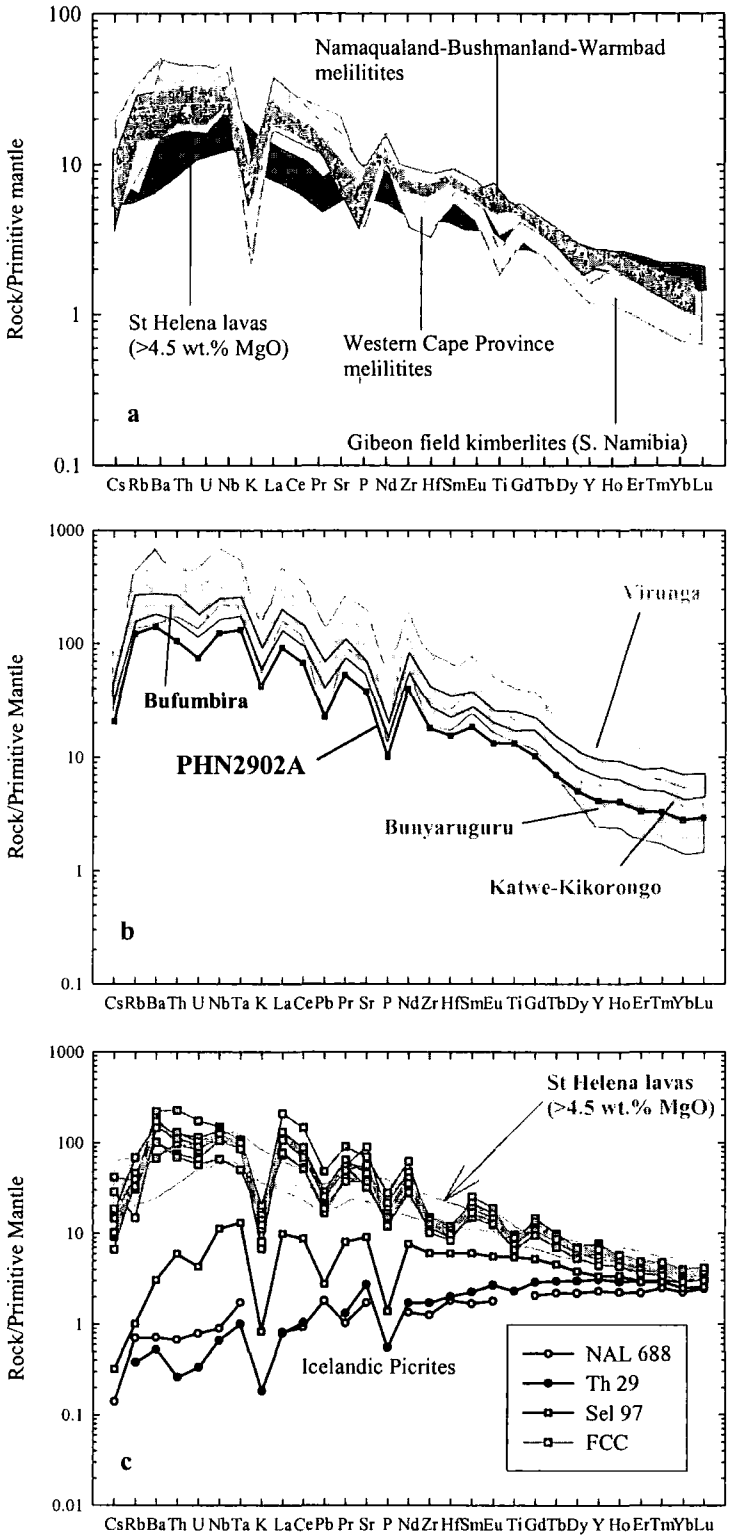

Fig. 3.8: Primitive mantle-normalised (McDonough and Sun, 1995) incompatible element diagrams for CIAV. 3.11(a) WCMP melilitites and NBW melilitites comparison of South African olivine melilitites with South African kimberlites (Spriggs, 1988) and St Helena lavas (Chaffey et al., 1989; Thirlwall, 1997). 3.11(b) Western branch East African Rift valley volcanic fields and PHN2902A, (c) Freemans Cove Complex volcanics compared with St Helena lavas (Chaffey et al., 1989; Thirlwall, 1997) and Icelandic picrites (Chapter 2).

primitive mantle normalised multi-element patterns for Gibeon field kimberlites. This could reflect shallower melting as a result of differences in the thickness of the lithosphere (e.g., Brey, 1978; Ellam, 1992) or different depths of partial melting within the lithospheric mantle itself. The WCMP and NBW have greater enrichment in incompatible elements and lower HREE concentrations than OIB lavas with HIMU affinities from St Helena (Fig. 3.8).

Nephelinites and basanites from the FCC are strongly enriched in moderately to highly incompatible elements, spanning a range of incompatible element concentrations equivalent to that of HIMU-type OIB (Fig. 3.8). FCC volcanics also exhibit significant depletion in HREE relative to middle REE (MREE) and light REE (LREE), indicating generation at least partly in the presence of residual garnet. FCC nephelinites and basanites display similar incompatible element patterns with positive Ba, Nb, Ta and La anomalies and negative Pb, K, P, Zr, Hf and Ti anomalies. These anomalies are more extreme than examples from the East African Rift or HIMU-type OIB, although the overall patterns are similar (Fig. 3.8). Relatively consistent REE patterns from olivine melilitite to basanite suggest similar depths of melting responsible for all FCC volcanics and residual garnet throughout the source. PHN2902A from the Bufumbira field in SW Uganda exhibits a similar incompatible element profile to C246-149, an olivine melilitite from the FCC but smaller negative anomalies in K, Zr and Hf and a positive anomaly for Ti (Fig. 3.8).

Comparison of REE systematics of FCC, EAV, NBW and WCMP volcanics indicate significant differences in their degrees of partial melting, residual garnet components and trace element enrichments within their respective source regions (Fig. 3.9). HREE are strongly compatible in garnet (Green *et al.*, 2000 and references therein.) and garnet-bearing sources will strongly buffer HREE in the residue up to 20% melting. Therefore $(Dy/Yb)_n$ ratios are controlled by the presence of residual garnet in the source and are thus an indication of the depth of partial melting. The parameter $(La/Yb)_n$ is primarily a function of the degree of partial melting. A number of points arise from partial melting models of CIAV trace element abundances in Fig. 3.9:

- FCC magmas were all derived from similar depths but represent different degrees of partial melting (0.1-4%). This is consistent with lithological variation from melilitite to alkali basalt in the FCC.

- Apart from the FCC, none of the other CIAV studied have partial melting features that can be described by an anhydrous primitive mantle source (or, indeed, any type of anhydrous mantle source).
- NBW, WCMP and East African Rift Potassics require a source that has La and Dy >50% enriched relative to Yb at variable degrees of partial melting (0.1-2%).
- The simplest explanation for the features of African CIAV is that variable amounts of amphibole/phlogopite exist in the sources of CIAV and initial quantities and variable exhaustion of these phases in the mantle source during melting can explain the enriched trace element characteristics of this magmatism (e.g., Furman and Graham, 1999). Hydrous phases are unstable in the convecting mantle over extended periods of time providing further evidence that the CLM plays a significant role in CIAV magmatism.

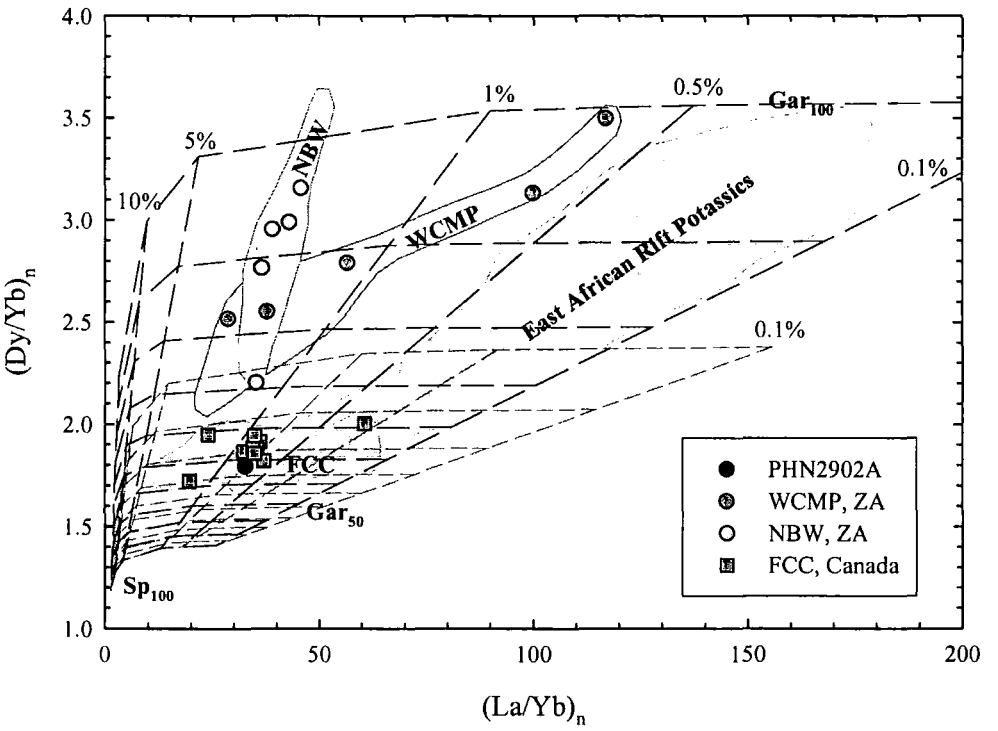

Fig. 3.9: *La/Yb_n versus Dy/Yb_n (chondrite normalised ratios) diagram illustrating point average fractional melting trajectories for anhydrous garnet and spinel lherzolites compared with FCC, WCMP, NBW and East African Volcanic compositions. Melt compositions for batch, non-modal melting with modal proportions and melting proportions for olivine, orthopyroxene, clinopyroxene and garnet+spinel, identical to those quoted in Baker et al., 1994 and Thirlwall et al., 1997. Distribution coefficients are from the compilation of Halliday et al., 1995 and assume a distribution coefficient of 0.01 for spinel based on the arguments of McKenzie and O'Nions (1991). Illustrated is a primitive mantle composition (faint dotted lines; McDonough and Sun, 1995) and an enriched mantle composition with La and Dy 50% enriched relative to PM Yb abundances (bold medium dashed grid). A source with 100% of its aluminium silicate phase as garnet = Gar_{100}, 100% spinel = Sp_{100}.*

Clearly there is evidence for the sources of some of the provinces being volatile rich (e.g., Furman and Graham, 1999) and this is likely to affect both the estimated degree of partial melting and LREE-enrichment of the different CIAV provinces studied here. The large differences in $(La/Yb)_n$ and $(Dy/Yb)_n$ and TiO_2 illustrate that the mantle source regions from which the different African and Canadian CIAV studied here are derived are heterogeneous relative to one another. Different mantle sources and partial melting histories for CIAV provide a robust means for testing the origins of helium isotopic heterogeneity in the inferred LONU source.

3.3.2.4 Sr-Nd isotopes

Detailed isotopic investigation of the WCMP (Janney *et al.*, 2002) and NBW melilitites (Janney *et al.*, 2003) showed evidence for HIMU and metasomatised CLM mixing in their genesis; a relationship that can be applied to CIAV worldwide (Fig. 3.10; Smith, 1983; le Roux, 1986; Wilson *et al.*, 1995). Sr, Nd and Hf isotope data for nephelinitic to evolved FCC volcanics (Barker *et al.*, 2002; Appendix F) indicate a degree of mantle source heterogeneity for the FCC. In Sr-Nd isotope space all nephelinites and basanites analysed by Barker *et al.* (2002) form a diffuse cluster (Fig. 3.10). The FCC cluster falls on or very near a calculated mixing curve between a HIMU end-member represented by 2Ga recycled oceanic crust (Chauvel *et al.*, 1992), and a metasomatised CLM end-member, represented by metasomatised garnet peridotites from the Bulfontein kimberlite at Kimberly, South Africa (Hawkesworth *et al.*, 1990) and extends the array of South African melilitites. FCC can be reproduced by solid-state mixing of 20-80% of a HIMU endmember with CLM; mixtures of melts of CLM and HIMU would fall on similar mixing trajectories but would require 50-80% of a HIMU-recycled oceanic crust component. No Sr-Nd data for East African Rift volcanic rocks are presented here but Furman and Graham (1999) have suggested that the coherent trace element and Sr-Nd isotope variations in them were the result of different quantities of amphibole and phlogopite enriched CLM in their source.

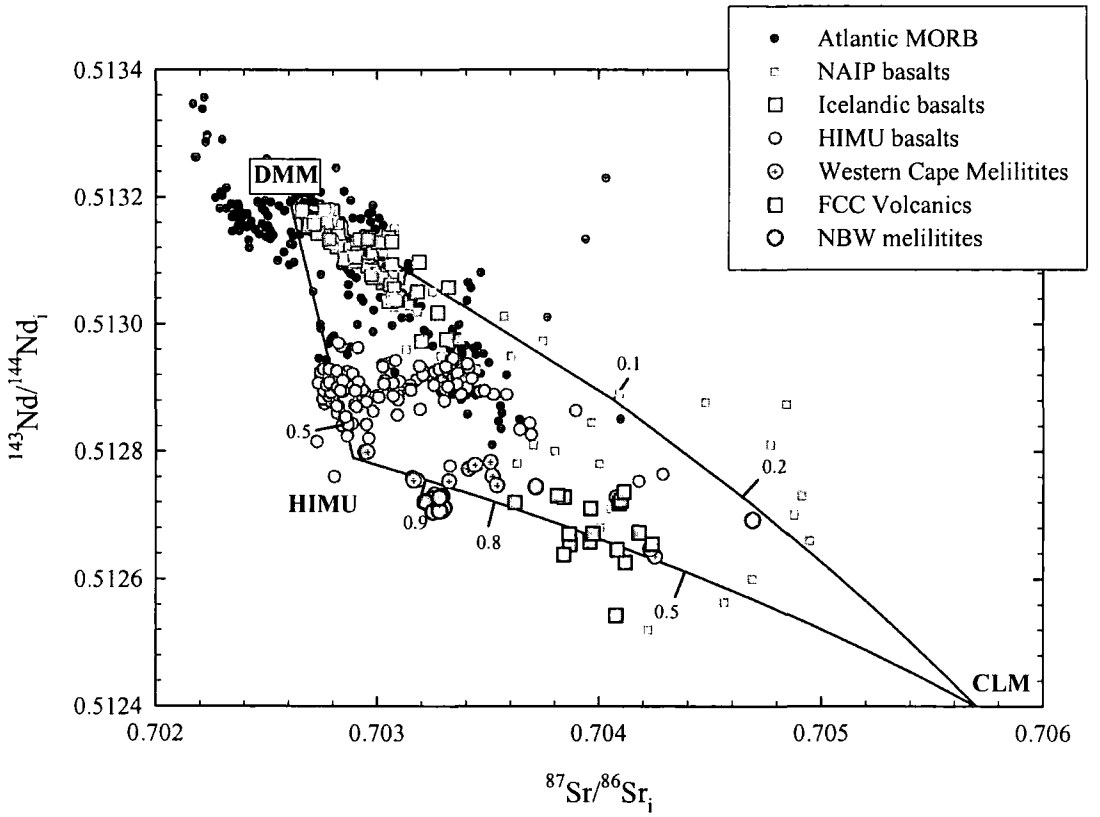

Fig. 3.10: $^{87}Sr/^{86}Sr_i$-$^{143}Nd/^{144}Nd_i$ isotope ratio diagram for WCMP (Janney et al., 2002), NBW (Janney et al., 2003) and the FCC (Barker et al., 2002) with published data for HIMU, North Atlantic Igneous Province, and Icelandic (Data sources Chaffey et al., 1989; Chauvel et al., 1992; Reisberg et al., 1993; Woodhead, 1996; Thirlwall et al., 1997; Salters and White, 1998; Graham et al., 1998; Kempton et al., 2000; Ellam and Stuart, 2000; Geldmacher et al., 2001; Stuart et al., 2003; Peate et al., 2003; Seth et al., 2004). Atlantic MORB data is from between 55°S and 52°N, references found on Pet Database. Endmember modelling compositions and isotopic ratios from Chauvel et al., 1992 (HIMU, DMM) and Hawkesworth et al., 1990 (CLM). Binary melt mixing trajectories are shown.

The Sr and Nd data suggest that all the CIAV studied are, at least in part, derived from the asthenosphere or lithosphere/asthenosphere boundary. Sr-Nd isotopes agree well with other geochemical evidence that all of the CIAV studied originate from within the shallow mantle with some input from the CLM during their genesis. Sr-Nd variations also suggest that whilst the WCMP, NBW and FCC all have HIMU and CLM contributions, there are large differences in mantle source regions for African and Canadian CIAV. These findings provide a robust means for testing the origins of helium isotope heterogeneity at the depths from which CIAV originate.

3.3.3 $^{3}He/^{4}He$ and $^{18}O/^{16}O$ results

New helium and oxygen results are presented for WCMP, NBW, FCC and PHN2902A in order to provide constraints on the He isotope composition of the

mantle sources of CIAV. Description of analytical techniques can be found in Appendix C and data generated by the author can be found in Table 2.2.

3.3.3.1 $^{18}O/^{16}O$ results

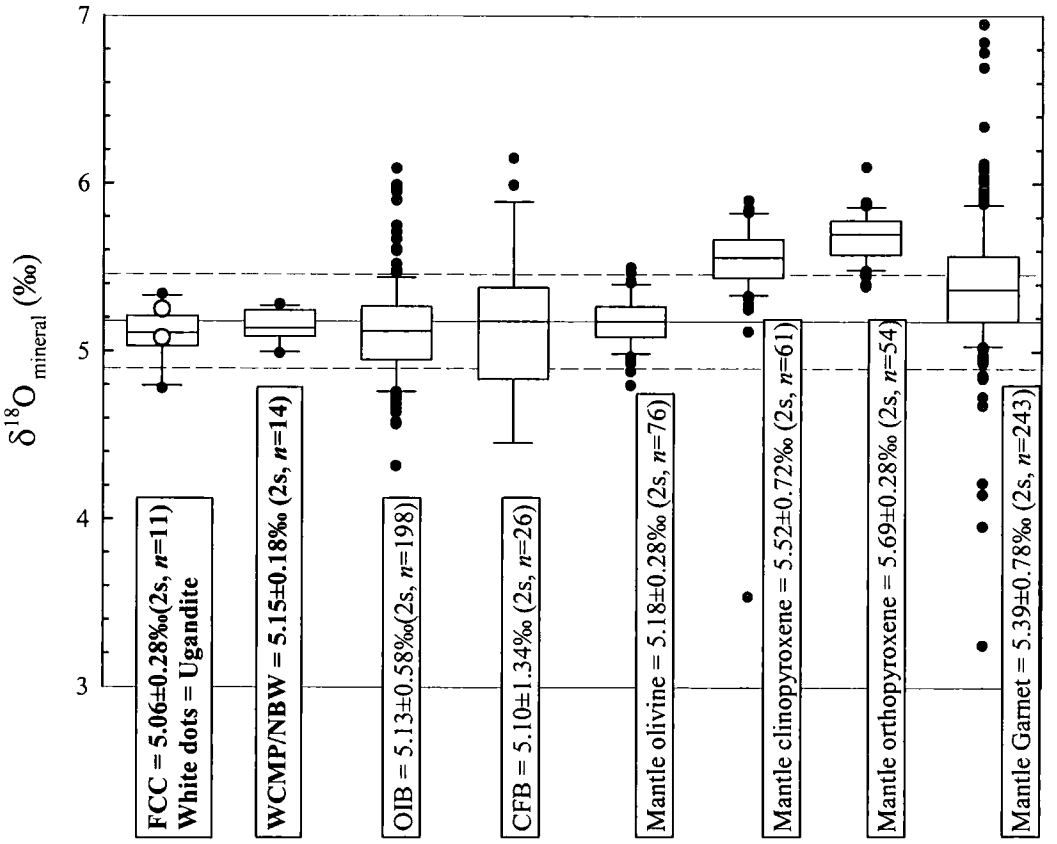

Fig. 3.11: Box plot for compiled, unfiltered CIAV (this study), OIB (Chapter 2 and references therein), CFB (Baker et al., 2000; Chapter 2) and olivine, clinopyroxene, orthopyroxene and garnet from mantle xenoliths (Mattey et al., 1994; Pearson et al., 2003 and references therein). Mean and 2 S.D. variation for Mantle olivine shown as thin dashed and solid lines on the Fig. Details of statistical distribution and dispersion can be found in the caption for Fig. 3.1.

NBW and WCMP melilitite olivines have a restricted range in $\delta^{18}O$ of +5.14‰ to +5.28‰ and +4.99‰ to +5.26‰, respectively (mean = +5.15±0.18‰ 2 S.D., n=14). The $\delta^{18}O_{Ol}$ of the melilitites overlaps the range of olivine from mantle peridotite (+5.18±0.28‰, 2 S.D., n=76; Mattey *et al.*, 1994; Fig. 3.11), MORB (+5.16±0.18‰, 2 S.D., n=6; Eiler *et al.*, 1997), OIB (+5.17±0.49‰, n=62; Eiler *et al.*, 1997) and HIMU-type OIB (+5.03±0.11‰, 2 S.D., n=14; Eiler *et al.*, 1997) analysed by laser

fluorination. In the case of sample HO-5, two visibly different olivine populations could be recognised. Lighter green coloured, strained olivine possessed $\delta^{18}O$ within external error (0.10‰ using the laser fluorination technique, see Appendix C) of darker unstrained equivalents (+5.28‰ versus +5.17‰ respectively). All other oxygen and all helium isotope analyses were performed on darker, unstrained olivine populations.

Table 3.2: Mineral O and He isotope data for CIAV from Canada and Africa

Sample[1]	Phase	MgO (wt.%)	Mg-no. min	$\delta^{18}O$ (‰)[2]	$^3He/^4He^3$	(±2σ)	[He][4]	(±2σ)
Nephelinites and basanites, Freemans Cove Complex, Nunavut, Canada								
C246149	Ol	18.72		5.13	5.6	0.2	152.6	7.3
	Cpx			5.17	5.6	0.2	166.4	5.7
KIA99 BI-5	Ol	13.53	88.1	5.11	3.1	0.1	27.4	0.5
KIA99 BI-10-B	Ol	14.72	86.2	5.03	6.5	0.2	30.3	0.6
KIA99 BI-4-1	Ol	12.51	86.5	5.21	4.7	0.1	13.1	0.2
KIA99 BI-8	Ol	14.26	92.7	5.11 (0.20)	6.2	0.2	11.9	0.2
KIA99 BI-10-C	Ol	14.77	93.5	4.87 (0.11)	6.6	0.2	36.4	0.7
KIA99 BI-10-E	Ol	14.94	89.6	4.78 (0.32)	6.4	0.1	46.3	0.7
KIA99 BI-11-F	Ol	12.88	85.8	5.11	2.4	0.1	3.8	0.1
Alkali Basalts, Freemans Cove Complex, Nunavut, Canada								
KIA99 BI-10-G	Ol	15.50	87.8	5.30	6.7	0.2	43.5	0.9
KIA99 BI-12	Ol	9.30	86.9	5.34 (0.02)	3.1	0.1	5.7	0.1
Ugandite, Uganda								
PHN 2902A	Ol	17.10	90.7	5.25	7.1	0.2	6.9	0.1
	Cpx		87.9	5.48	6.9	0.2	24.2	1.2
Olivine melilitites, Western Cape Melilitite Province, South Africa								
KSV-256	Ol	18.39		5.13	3.1	0.1	33.4	0.9
KSV-266	Ol	19.17		5.12 (0.01)	6.1	0.2	129.8	4.1
SPK-1	Ol	17.18		5.07	5.3	0.1	571.3	58.6
SPK-2	Ol	16.88		5.26	-	-	-	-
SPK-3	Ol	17.10		5.01	5.5	0.2	286.3	17.3
ROB-10	Ol	17.21		4.99	-	-	-	-
ROB-11	Ol	17.00		5.11	-	-	-	-
Olivine melilitites, Namaqualand-Bushmanland-Warmbad, South Africa								
ZW-1	Ol	19.64		5.14	5.3	0.2	205.7	7.8
BKB-10	Ol	18.03		5.24	-	-	-	-
WK-1	Ol	20.76		5.17	5.2	0.2	153.8	11.5
HO-5	Ol	19.10		5.17	5.3	0.2	49.3	1.8
	Ol			5.28	-	-	-	-
SP-4	Ol	20.33		5.25	3.9	0.2	33.4	2.5

1. For location, petrography and age of samples see Appendix A
2. Analysed by laser fluorination. quoted as per mille deviation from SMOW
3. R/RA notation (where RA = 1.39×10-6)
4. He abundance in nccSTP/g

Measured $\delta^{18}O_{Ol}$ values of FCC nephelinites and basanites are generally lower and more variable (+4.78‰ to +5.21‰, mean = +5.06±0.28‰, 2 S.D., n=11) than

WCMP and NBW melilitites, mantle peridotites (Fig. 3.11), and MORB. FCC basalts have slightly higher $\delta^{18}O_{Ol}$ (+5.30‰ and +5.34‰), as does olivine from ugandite PHN2902A (+5.25‰). Clinopyroxene from C246-149 and PHN2902A possesses $\delta^{18}O$ of +5.17‰ and +5.48‰ respectively, giving $\Delta_{cpx\text{-}ol}$ of 0.04‰ and 0.23‰. The $\Delta_{cpx\text{-}ol}$ values are notably lower than values measured in the majority of peridotites or predicted for magmatic temperatures (Mattey *et al.*, 1994; Rosenbaum *et al.*, 1994) and, therefore, may represent disequilibrium between coexisting phenocrysts. The most forsteritic olivines have the lowest $\delta^{18}O_{Ol}$ possibly indicating a xenocrystic origin for the low end of the $\delta^{18}O_{Ol}$ range (Fig. 3.12).

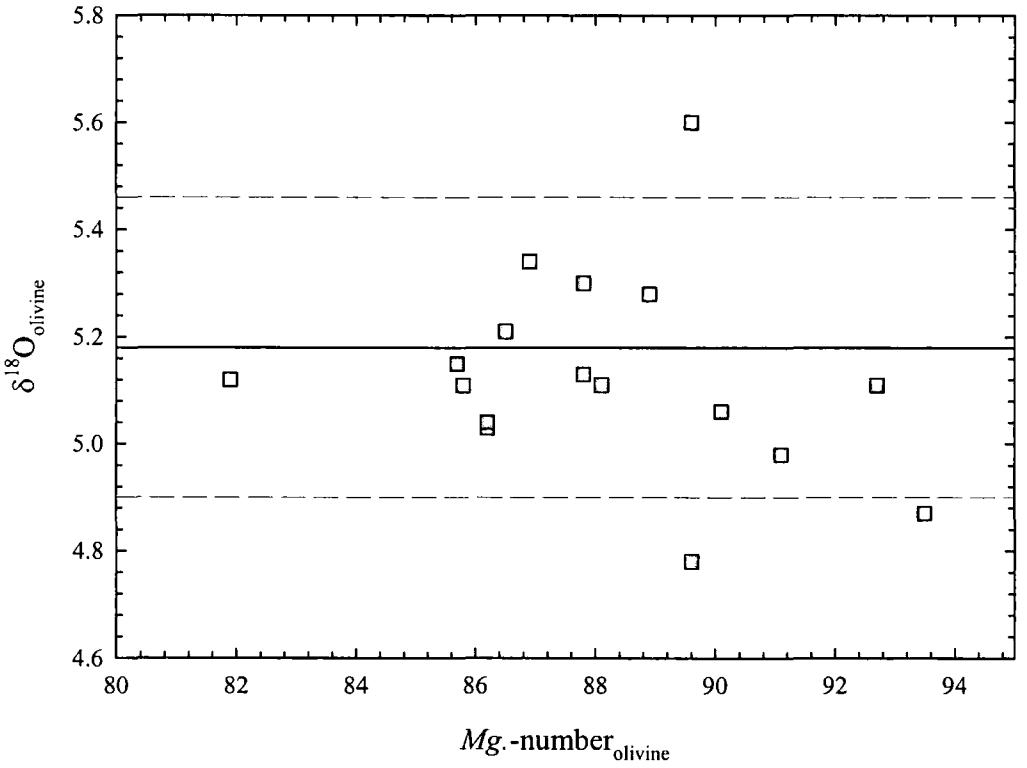

Fig. 3.12: Olivine Mg.-number versus $\delta^{18}O_{Ol}$ (as per mille deviation from SMOW) for Freemans Cove Complex volcanics. Solid and dashed lines represent the average of mantle-derived olivines (+5.18±0.28‰, 2S.D., Mattey et al., 1994). Forsteritic olivines are also characterised by low CaO (<0.2 wt.%).

3.3.3.2 $^3He/^4He$ results

The $^3He/^4He$ isotope ratios of olivines from the WCMP range from $3.07R_A$ to $6.12R_A$, with the entire range exhibited in Sutherland olivine melilitites. $^3He/^4He$ isotopic ratios of the NBW olivine melilitites range from $3.85R_A$ to $5.29R_A$ and combined with WCMP melilitites give a mean of $5.1\pm0.8R_A$ (1.S.D., n=8). [He] and

$^3He/^4He$ ratios of the WCMP and NBW melilitites are similar to or slightly lower than average compositions of published CIAV data ($6.2\pm1.4R_A$) and is significantly lower than average compositions of MORB lavas ($8\pm1R_A$; Hilton and Porcelli, 2003; $8.8\pm2.1R_A$; Graham, 2002).

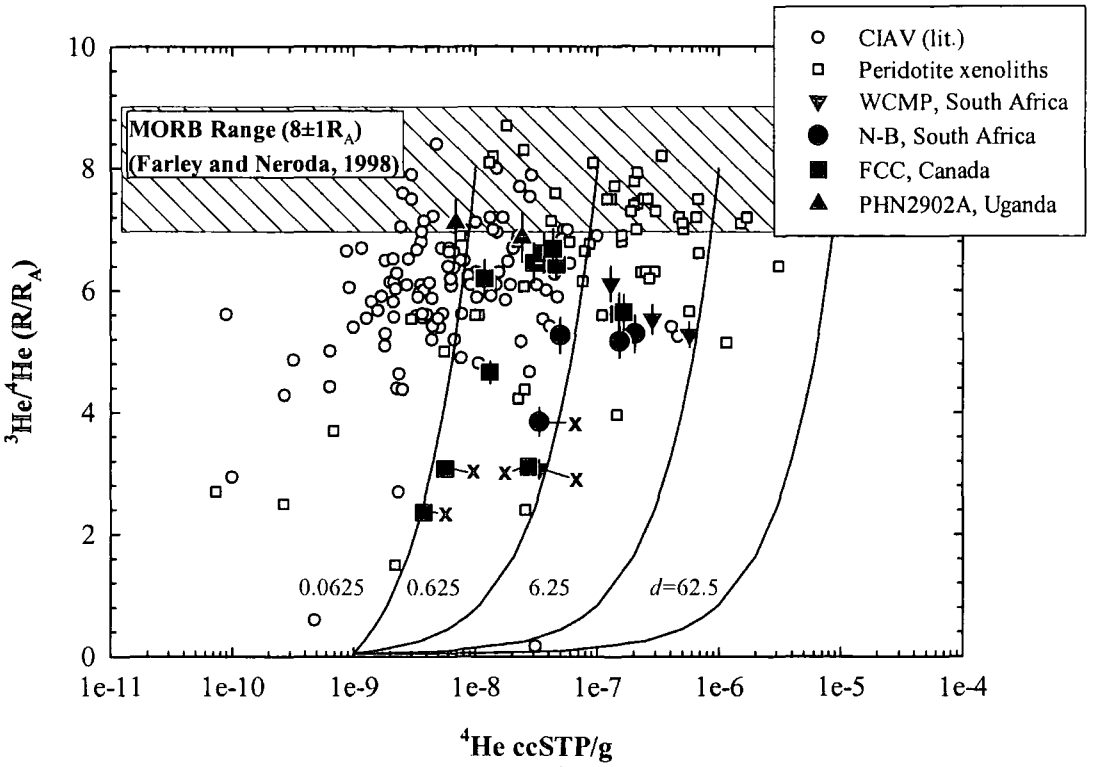

Fig. 3.13: Plot of olivine and clinopyroxene $^3He/^4He$ ratios (R/R_A notation) versus helium concentration ([He]) for continental intraplate alkaline volcanics (CIAV) and continental lithospheric mantle (CLM) peridotite xenoliths. Published data for MORB is cited in Graham (2002) and for CIAV and peridotite xenoliths is cited in Gautheron and Moriera (2002). Only samples processed by crushing in vacuo are plotted. Also shown are trajectories for magma mixing between crustal and depleted MORB mantle reservoirs through pure mixing (d=62.5) and for a melts from depleted MORB mantle that has been extensively degassed (d= 6.25, 0.625 and 0.0625) prior to mixing with crustal helium assuming that phenocrysts crystallised from a primary melt with undegassed, high [He]. d is the degassing values (see section 3.4.4.2) and the orders of magnitude degassing correspond to 10% of original melt gas content (6.25), 1% (0.625) and 0.1% (0.0625) respectively. CIAV and CLM peridotite nodules show significantly more radiogenic helium isotope signatures to MORB even after the effects of crustal contamination on CIAV have been considered. Such radiogenic signatures are readily explained by either CLM contamination of asthenospheric melts or by metasomatism of CLM and ^{3}He-replenishment of the CLM prior to melting to form CIAV. X marks samples thought to be crustally contaminated.

The $^3He/^4He$ isotope ratios of olivines from the FCC range from $3.08R_A$ to $6.69R_A$, whilst ugandite PHN2902A has olivine ($7.11R_A$) and pyroxene ($6.87R_A$) helium isotope compositions within analytical error (Fig. 3.13). Clinopyroxene from FCC olivine melilitite C246-149 gave a $^3He/^4He$ within error of the olivine from the same sample. The unfiltered mean for FCC olivines is $5.1\pm1.7R_A$ (1.S.D., n=10). [He] and

$^3He/^4He$ ratios of the FCC are similar to the range of published CIAV and the WCMP and NBW melilitites. The $^3He/^4He$ ratios of all CIAV analysed are consistently more radiogenic than average MORB ($8\pm1R_A$; Hilton and Porcelli, 2003; $8.8\pm2.1R_A$; Graham, 2002) but are less radiogenic than Archaean cratonic peridotites ($2.5\pm1.6R_A$; section 3.2), inclusions in diamonds (2.1 ± 2.2; Burgess *et al.*, 1998) and Archaean eclogites ($<0.5R_A$; section 3.2).

3.4 Discussion

$^3He/^4He$ data compilations from analyses in this study and from published datasets for CLM peridotites and eclogite show that the CLM is characterised by more radiogenic He than the DMM. This means that the CLM is unable to satisfy the role of a high $^3He/(U+Th)$ source. In the discussion, possible controls on $^3He/^4He$ compositions of the CLM and its significance as a helium isotope reservoir for terrestrial magmatism are considered. Possible controls on CIAV $^3He/^4He$ isotope compositions are also considered in order to determine whether the source of CIAV parental magmas can also be a high time-integrate $^3He/(U+Th)$ source to some OIB and CFB intraplate magmatism.

3.4.1 Modification of $^3He/^4He$ ratios in CLM xenoliths by entrainment in melts and post-eruptive alteration

Mantle xenoliths may be modified by the host magma either via addition of He during eruption or through ^4He ingrowth after emplacement. From Fig. 3.4 it is apparent that [He] in CLM peridotite xenolith and eclogite minerals are the same or greater than phenocrysts from CIAV. For minerals in mantle xenoliths it is highly unlikely that their He compositions will be dominated by the helium inventory of their host alkaline melts at shallow levels because the pressure of the gas phase within inclusions in minerals will be greater than that of the magma volatile pressure and He will be effectively isolated from the magma by the crystal. Dunai and Baur (1995) suggested that this process was important in the melt experiment He-isotope compositions of CLM xenoliths from the European continent. This is confirmed by the fact that olivines and clinopyroxenes from mantle xenoliths have similar $^3He/^4He$ (e.g., FRB 1350, Table 2.1; xenolith data in Barfod *et al.*, 1999) despite the fact that

diffusivity of He in pyroxene at magmatic temperatures is approximately an order of magnitude greater than in olivine (Trull and Kurz, 1993).

Less certainty can be inferred for lithospheric peridotite-magma interaction at depth (>degassing pressure limit). Interaction between partial melts with CLM is an important process which can result in the modification of $^3He/^4He$ ratios in mantle minerals (section 3.4.2). However, this process cannot be pervasive for all CLM peridotite xenolith suites. For example cratonic peridotites, which are the deepest derived of CLM samples, possess lower $^3He/^4He$ ratios than typical CIAV melts in which they are entrained. This suggests the measured $^3He/^4He$ of most analysed peridotites and eclogite are primary since their formation and subsequent depletion events and have $^3He/^4He$ ratios that are more radiogenic than even the MORB source. Post-eruptive in-growth of cosmogenic ^3He is unlikely to be important in mantle xenoliths because short crushing experiments do not tend to release lattice sited He (Kurz, 1986; Hilton *et al.*, 1993; Scarsi, 2000). It is therefore unlikely that eruptive and post-eruptive processes have significantly affected the CLM data obtained by crushing experiments. Post-eruptive ^4He ingrowth through U and Th addition is a very similar process to metasomatism and is therefore considered in the following section.

3.4.2 Impact of metasomatism on CLM $^3He/^4He$ ratios

The incompatible element depleted nature of mantle xenoliths make them highly susceptible to elemental and isotopic enrichment processes either through enrichment by fluids from the asthenosphere, slab fluid and melts obtained from past subduction events and pervasive addition of small degree melts that freeze in CLM (McKenzie, 1989). This process, called metasomatism, can be modelled and addressed as open and steady-state system behaviour in the CLM for noble gases (Gautheron and Moriera, 2002). Considering the highly incompatible nature of helium (Brooker *et al.*, 2003), it is assumed that if metasomatism has taken place, the noble gas inventory of CLM peridotites and their partial melt derivatives will also be dominated by metasomatism. This will either be through ingrowth from U and Th after metasomatism or by direct addition of helium into the CLM from the underlying convecting mantle. For example, arc-related mantle wedge peridotite studies have shown that the He budgets are dominated by pervasive metasomatism

from the wedge and He addition from the convecting mantle (Matsumoto *et al.*, 1998; Dodson and Brandon, 1999).

As previously discussed, CIAV are widely held to be from the boundary between the conducting or convecting mantle or from within the lithosphere (Brooks *et al.*, 1976; Hawkesworth *et al.*, 1990; Wilson *et al.*, 1995; Janney *et al.*, 2002, 2003; Green, 1970; Brey, 1978; Foley, 1992). The He elemental and isotopic compositions of CIAV require that if the CLM is a source for their parental melts, it must have been periodically enriched in He from a source with higher time integrated $^3He/(U+Th)$ than the calculated time evolution of CLM as a closed system (Gautheron and Moriera, 2002). The CIAV data share similarly radiogenic $^3He/^4He$ to that of CLM peridotite xenoliths whose He isotope composition is a function of open-system exchange of He with the asthenosphere (Gautheron and Moriera, 2002; Dunai and Porcelli, 2002). The open-system behaviour of He in the lithospheric mantle means that any magma sourced from within the lithosphere should have a He-isotope signature that is strongly influenced or dominated by the underlying, shallow convecting mantle. Hence, while Sr-Nd-Pb-Os isotopes reflect varying contributions from CLM and asthenosphere in CIAV analysed here (Fig. 3.10), He isotopes more likely reflect the signature of the shallow convecting mantle. So far, wherever $^3He/^4He$ ratios have been measured in CLM peridotite xenoliths, no high $^3He/^4He$ signatures have been found (Dunai and Porcelli, 2002).

The CLM is heterogeneous with respect to $^3He/^4He$ (Fig. 3.5) and steady-state and closed system processes are simultaneously required to generate this observed range (Gautheron and Moriera, 2002). The mechanisms for generating and preserving heterogeneity via radiogenic helium ingrowth processes and replenishment of ^3He are important not only in the context of the evolution of CLM but also during any magmatic events in which the CLM acts as a reservoir. Previous studies have provided strong evidence for CLM exhibiting open system behaviour with respect to their noble gas inventories (Reid and Graham, 1996; Dodson *et al.*, 1998; Gautheron and Moriera, 2002). Indeed, for a closed system model for mean mantle $^3He/^4He$ ratios, an unrealistic ([U]ppm/[^{4}He]ccSTP/g) ratio of 1000-2000 is required (Reid and Graham, 1996; Dodson *et al.*, 1998; Gautheron and Moriera, 2002). For an average [^{4}He] in CLM of 0.1μccSTP/g, U concentrations would be expected to be ~0.1ppb to retain the average $^3He/^4He$ ratio of Proterozoic mantle

xenoliths over 1Ga. The theoretical required U concentration for mantle peridotites is far lower than the content of MORB asthenosphere (5-6ppb) and does not agree with the relative enrichment in U concentrations of some Proterozoic CLM peridotites (Fig. 3.3). In addition, the Archaean cratonic peridotites that do have consistently low U concentrations have radiogenic $^3He/^4He$ ratios suggesting that closed system evolution of the CLM cannot solely explain the $^3He/^4He$ ratios measured in peridotites. Metasomatism and steady-state addition especially to the Proterozoic CLM peridotites therefore represents an important and integral process in CLM helium isotope datasets; ^3He-recharge is a pre-requisite to explain the relatively elevated $^3He/^4He$ measured in Proterozoic peridotites and CIAV.

3.4.3 The significance of CLM as a helium isotope reservoir for terrestrial magmatism

Examination of CLM helium isotope datasets shows that the CLM is (1) heterogeneous with respect to $^3He/^4He$ ratios and (2) CLM $^3He/^4He$ < MORB $^3He/^4He$ (Fig.s 3.4 and 3.5). These observations and the new data presented here provide evidence that the CLM does not possess excess ^3He compared to the asthenospheric mantle. So far, high $^3He/^4He$ measured in CLM xenoliths can be accounted for by addition of cosmogenic ^3He during exposure at the Earth's surface (e.g., Porcelli *et al.*, 1987). The participation of CLM in the source of OIB or continental intraplate magmas is unable to satisfy the role of a high time integrated $^3He/(U+Th)$ mantle reservoir. However, CLM may be able to explain systematically low $^3He/^4He$ ratios and enriched Sr, Nd, Pb (e.g., a HIMU-like and NOT a LONU-like component; Menzies *et al.*, 1987) and variably radiogenic or unradiogenic Os isotope characteristics in some OIB and CFB magmatism (e.g., Graham *et al.*, 1992a; Schaefer *et al.*, 2002; Larsen *et al.*, 2003).

There is clear geodynamic evidence that portions of CLM have been removed beneath some continental areas (Eggler *et al.*, 1988; Molnar *et al.*, 1993; Menzies and Xu, 1998; Lee *et al.*, 2000). Proterozoic non-cratonic CLM is the most probable lithospheric material to be incorporated into the asthenosphere because of its inherent weakness and higher density in contrast to strong, low density cratonic CLM. Proterozoic non-cratonic CLM also retains lower time integrated $^3He/(U+Th)$ variations than Archaean cratonic peridotites ($6.2\pm1.4R_A$ versus $2.5\pm1.6R_A$

respectively). Whilst incorporation of CLM into the asthenosphere could represent an important tectonic process (e.g., McKenzie and O'Nions, 1983) the chemical heterogeneity it would retain as a potential source region for oceanic and continental intraplate magmatism is limited and elemental and isotopic studies of CLM indicate that neither hydrous nor anhydrous CLM makes a singular suitable source for continental or oceanic basalts (Pearson and Nowell, 2002).

Of the components of CLM it is the mafic, metasomatic lithologies such as eclogite, pyroxenites, MARID (mica-amphibole-rutile-ilmentite-diopside) and PIC (phlogopite-ilmenite-clinopyroxene-minor rutile) rather than depleted peridotite that are likely to become involved in intraplate magmatism, because they are more readily fusible. The radiogenic $^{3}He/^{4}He$ signature of eclogite as well as their distinctive Sr-Nd-Hf-Pb isotope characteristics (Pearson *et al.*, 2003 and references therein) make these and other pyroxenites within CLM excellent candidates for generating and preserving noble gas as well as O, Os and lithophile isotope heterogeneity (Chapter 4). Melting of peridotite-pyroxenite sources could release radiogenic He during intraplate oceanic and continental magmatism. Melting of eclogite, pyroxenite or metasomatic veins would also result in isotopically enriched O, Sr, Pb and Os and depleted Nd (and Hf) partial melts (Chapter 4). A test for the overall quantities of these sources is through $^{18}O/^{16}O$ ratios, as large volumes of isotopically distinct pyroxenite or eclogite would be required to affect the isotopic composition of a melt product, because O is the most abundant element in mantle or crustal reservoirs (e.g., Chapter 4). In summary the CLM offers a potential source for a low $^{3}He/^{4}He$ reservoir but not a high $^{3}He/^{4}He$ reservoir in terrestrial magmatism.

A systematic bias regarding CLM mantle xenoliths and CIAV is that their eruptions are the result of melting either directly from the convecting mantle through to the CLM (e.g., Janney *et al.*, 2002) or from the melting of low solidus metasomatic veins originating from the asthenosphere. Because mantle xenoliths are erupted to the surface in alkaline magmas there will be a bias in the available sample suite that have been affected by metasomatic processes and melt interaction. It may be that the vast majority of CLM (Proterozoic and Archaean) has not been subject to metasomatic processes resulting in large swaths of CLM possessing radiogenic $^{3}He/^{4}He$ through closed-system evolution, making it even less likely that the CLM

represents a high $^{3}He/(U+Th)$ reservoir. Metasomatic domination of isotopic signatures of mantle xenoliths is also a valid observation when considering Os, Pb, Sr, Nd and Hf datasets (Pearson *et al.*, 2003). In the next sections the possibility of CIAV sampling a LONU source in the shallow asthenosphere beneath the CLM mantle is considered.

3.4.4 Controls on CIAV $^{3}He/^{4}He$ isotopic compositions: degassing, crustal modification and source mixing processes

Low $^{3}He/^{4}He$ measured in volcanic glasses and phenocrysts can be ascribed to degassing prior to crustal assimilation and concomitant fractional crystallisation processes which have broadly similar signatures to recycled crustal components (e.g., Chapter 2). To assess whether South African, Ugandan or Canadian CIAV helium compositions are the result of such process the following discussion considers the effect of volatile degassing prior to crustal contamination as this can have a profound impact on the helium isotopic characteristics of phenocrysts (e.g., Chapter 2). Secondly, this discussion aims to characterise the sources of studied CIAV and the timing and nature of mixing processes that have played a role in the $^{3}He/^{4}He$ compositions of CIAV. Finally, the $^{3}He/^{4}He$ characteristics of CIAV are used to test the hypothesis that a high $^{3}He/^{4}He$ reservoir exists within the upper mantle.

3.4.4.1 Crustal contamination signatures in CIAV?

Despite the near-primary major element compositions of the CIAV in which $^{3}He/^{4}He$ was measured, they contain either (i) olivine phenocrysts with relatively low forsterite contents or (ii) zoned olivine phenocrysts which are likely to have crystallised from moderately fractionated liquids. This suggests their parental magmas resided in magma chambers at crustal levels where assimilation and melt modification is most likely to occur. Therefore helium isotope heterogeneity observed in studied CIAV could simply represent volatile degassing prior to minor fractional crystallisation and variable degrees of contamination with continental crust rather than variations in age, mineralogy or compositions of their mantle source regions. In order to assess whether crustal contamination has occurred in CIAV I briefly consider the evidence from elemental and O-Sr-Nd isotope data

Incompatible elements show no characteristic correlations or relationships to indicate that crustal assimilation is an important process in WCMP and NBW melilitites (Janney *et al.*, 2002, 2003), FCC nephelinites or the Ugandite PHN2902A (Fig. 3.8). This is despite Hoedkop melilitites or 'para-kimberlites' containing visible crustal fragments (P.E. Janney, pers comm.) and brecciated diatreme in the FCC containing greater than 20% by volume of country rock. For Sr and Nd isotopes relatively small quantities of low concentration Sr and Nd crustal material are unlikely to generate significant isotopic variations because of the high concentration of Sr and Nd in CIAV melts.

$^{18}O/^{16}O$ isotope ratios are powerful tracers of crustal assimilation because of the extreme fractionation that can occur between ^{16}O and ^{18}O in low temperature environments (Chapter 2). Although the FCC nephelinites are hosted by crustal carbonates, nephelinites show only limited ^{18}O-enrichment and in general FCC volcanic rocks extend to low $\delta^{18}O$. Because of their geographical location north of the Arctic Circle at the time of eruption (e.g., Harrison *et al.*, 1999), FCC volcanic rocks could have assimilated altered volcanic edifice rocks with low $\delta^{18}O$ due to interaction with meteoric water similar to relationships observed in Iceland (Chapter 2). Two lines of evidence suggest that this is unlikely. First, unlike Iceland, whose basement is dominated by hydrothermally altered crust, only small diatremes exist in the FCC which do not exhibit signs of reworking by later volcanism (Harrison and DeFrietas, 1999). Second low $\delta^{18}O$ values are measured in olivines with the highest forsterite contents and whose CaO contents are very low (<0.2 Wt.%) suggesting peridotitic origins (Fig. 3.12). In contrast lavas with lower forsterite numbers, including basanites and basalts, have $\delta^{18}O$ similar to mantle values suggesting that crustal contamination has had a limited impact. The range of $\delta^{18}O$ in WCMP, NBW, FCC and PHN2902A is also remarkably limited and lies within the range of predicted mantle values suggesting that crustal contamination played a negligible part in the creation of the geochemical signatures for these CIAV too. Janney *et al.* (2002; 2003) came to a similar conclusion from Os isotope systematics of WCMP and NBW melilitites. It is apparent that elemental, O, Os and Sr-Nd isotope relationships indicate a limited role for crustal modification in the CIAV studied here for their helium isotope compositions.

3.4.4.2 Degassing prior to crustal modification in CIAV

The most prominent feature of the results is that the $^{3}He/^{4}He$ ratios of CIAV are consistently more radiogenic than MORB (Fig. 3.13). Radiogenic $^{3}He/^{4}He$ ratios can be generated through degassing of mantle-derived helium in melts at shallow crustal levels followed by addition of crustal helium (Hilton *et al.*, 1995). There is a relationship of more radiogenic $^{3}He/^{4}He$ ratios with decreasing [He] for CIAV. Fig. 3.13 illustrates possible mixing trajectories for an asthenospheric melt with MORB-characteristics ([He] $>1\times10^{-5}$ ^{4}HeccSTP/g ($8R_A$), Hilton and Porcelli, 2003) whose partial melt interacts with crust that has low [He] ($<1\times10^{-9}$ ^{4}HeccSTP/g) and $^{3}He/^{4}He$ $<0.05R_A$. Mantle melts generally have higher [He] than crustal rocks and will therefore form convex mixing trajectories with crust in the extreme case where no degassing and only mixing takes place or d=62.5. None of the studied CIAV lie near the illustrated undegassed mixing line between crust and an asthenospheric melt. When the effects of degassing prior to crustal modification are considered at different degassing (d-values=$[^{3}He/^{4}He]/[^{4}He]_{Assimilant})/([^{3}He/^{4}He]/[^{4}He]_{Unmodified\ melt})$) mixing trajectories for degassing of volatile phases from the CIAV magmas (up to 99.99% helium loss) of d=0.0625 form mixing trends with crust which more closely explain the low [He] abundance results. Degassing of helium is a well documented process in basaltic melts and occurs through over-saturation of CO_2, the main carrier phase of He in a melt, via low-confining pressures (Hilton *et al,* 1995) or elevated water contents (Hilton *et al.*, 2000b). It is important to note that the entire range of $^{3}He/^{4}He$ and [He] reported here are likely to reflect variable degrees of magmatic degassing and addition of radiogenic He so that the absolute mass balances of mantle versus radiogenic contributions is unique to each sample. This makes quantitative estimation of degassing and radiogenic He addition very difficult. However, it is apparent that crustal contamination cannot explain the $^{3}He/^{4}He$ 'plateaux' of CIAV as well as CLM peridotites at more radiogenic $^{3}He/^{4}He$ than MORB (Fig. 3.13).

Relationships between the oxygen and helium isotope systematics of mineral phases studied for CIAV in this study also confirm that crustal contamination has been limited for these rocks despite obvious degassing of [He]. In Fig. 3.14 CIAV are plotted against MORB and Proterozoic peridotite O and He isotope ranges. Apart from two FCC samples none of the other CIAV lie outside of the oxygen isotope range expected for melts in equilibrium with mantle peridotite. Most of the CIAV lie

below the range of MORB $^3He/^4He$ (Fig. 3.14). These relationships indicate that the $^3He/^4He$ variation is the result of variable degassing and subsequent addition of radiogenic $^3He/^4He$ via crustal contamination which is undetectable using other geochemical approaches. This observation illustrates the extreme sensitivity of melts that have lost a significant fraction of their He inventory through degassing, to crustal contamination. Apart from samples with the lowest [He] and the lowest $^3He/^4He$ (3 from the FCC and 1 each from the WCMP and NBW) the new CIAV He data appear to preserve the primary $^3He/^4He$ of their mantle source regions.

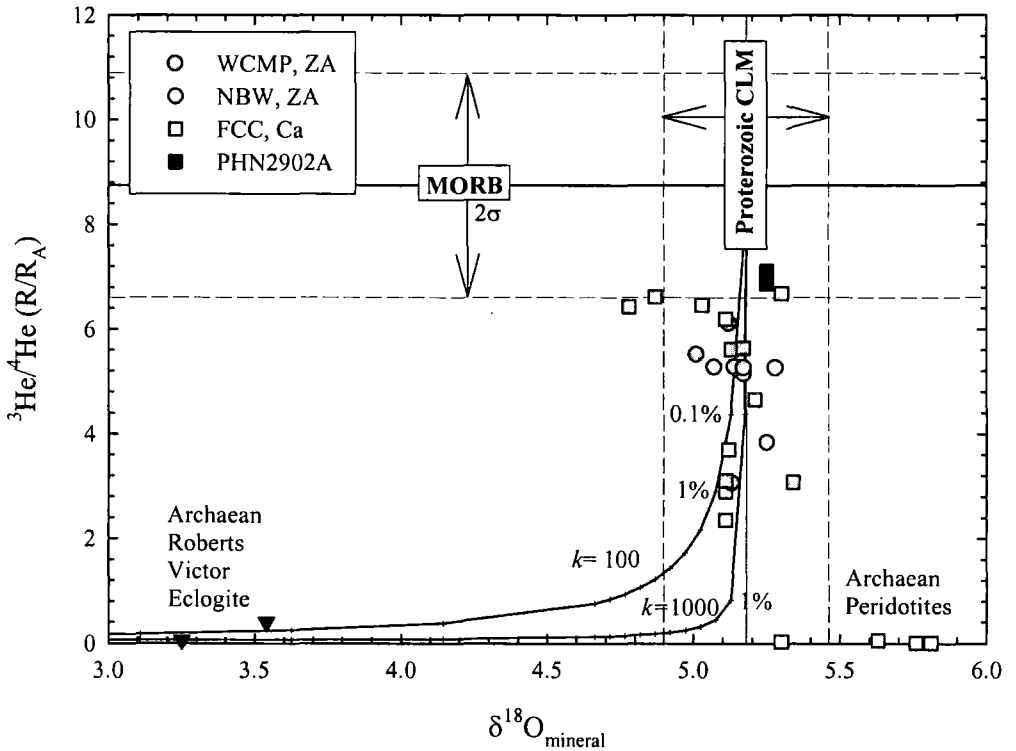

Fig. 3.14: Plot of oxygen versus helium isotope (R/R_A notation) compositions for FCC, WCMP, NBW and ugandite PHN2902A. Also shown are He-O isotope data for eclogite and Archaean peridotites (this study). Means and 2 S.D lines for MORB and Proterozoic have been derived from Ito et al. (1987), Mattey et al. (1994) and Graham (2002). Degassing and crustal contamination models for mixing between a mantle-derived melt and a crustal samples at k=100 and 1000 (See Chapter 2). K=100 is equal to d=0.625 in Fig. 3.13.

If the 5 samples that are interpreted to have been modified by crustal contamination (marked with an 'X' in Fig. 3.13) in the dataset are excluded, the average $^3He/^4He$ ratio for the new CIAV data of 6.0±0.7 (1.S.D., n=15). Canadian and South African CIAV possess $^3He/^4He$ ratios of 6.2±0.4 (1.S.D., n=7) and 5.4±0.4 (1.S.D., n=6), respectively. Crucially, irrespective of location, lithology, or age, all $^3He/^4He$ ratios

for CIAV are less than the canonical average MORB value of $8\pm1R_A$. Melilitites, nephelinites, basanites and basalts from localities in southern Africa, Canada and the western branch of the East African Rift exhibit $^3He/^4He$ lower than is typical of MORB, suggesting derivation from a reservoir with time-integrated $^3He/(U+Th)$ lower than DMM.

3.4.4.3 Limitations on high $^3He/^4He$ and HIMU sources in CIAV

Elemental and isotopic data presented in section 3.3.2 indicate that the WCMP, NBW, FCC and East African Volcanic rocks were derived from a range of sources with coherently varying incompatible element enrichments and isotopic compositions. The chemical and isotopic variations of CIAV are most simply explained as the product of mixtures of three main components.

The first is proposed to be variably metasomatised CLM that is compositionally heterogeneous due to carbonatite or hydrous metasomatism and possesses long-term enriched Sr-Nd isotope characteristics approaching an enriched mantle (EM1; Zindler and Hart, 1986) end-member, has typical mantle $\delta^{18}O$ values (Mattey *et al.*, 1994) and has more radiogenic $^3He/^4He$ ratios than DMM (section 3.2). The CLM component is most apparent in FCC volcanic rocks which are from shallower depths in the mantle (see section 3.3.2.4) compared with South African melilitites generated below the older and thicker lithosphere. The second component is convecting mantle with DMM characteristics with depleted Nd and Sr isotopic compositions, typical mantle $\delta^{18}O$ values and MORB-like $^3He/^4He$ ($8\pm1R_A$). The third component has intermediate Sr-Nd and trace element compositions similar to HIMU-type OIB. The fact that this HIMU signature is best expressed in the WCMP, derived from below the thinnest lithosphere, led Janney *et al.* (2002) to suggest that this component resides either at the base of the lithosphere or within the asthenosphere, an argument similarly advocated for Cameroon line volcanic rocks (Barfod *et al.*, 1999). The HIMU $^3He/^4He$ signature is poorly defined but is likely to be low because of the obvious lack of high $^3He/^4He$ signatures in CIAV.

Mean $^3He/^4He$ for non-cratonic Proterozoic CLM peridotites, Archaean CLM peridotites, Diamonds and CIAV indicates that the CLM and immediately underlying shallow asthenospheric mantle has $^3He/^4He$ less than MORB ($8.75 \pm 2.14R_A$; Graham, 2002). Closed-system evolution of the CLM would result in ratios

far lower than those measured for Proterozoic CLM and CIAV if they are derived solely from the CLM (e.g., Archaean peridotites, This Study; Gautheron and Moriera, 2002). Therefore, the $^3He/^4He$ ratios of NBW and WCMP melilitites, FCC volcanic rocks and PHN2902A must all have been derived in part from convecting upper mantle similar to DMM either by direct melting or through recent metasomatism within the CLM. Such arguments have also been used to explain the marked enrichment in trace elements of CIAV (le Roux, 1986; Wilson *et al.,* 1995; Janney *et al.,* 2002), Although there is some evidence for helium degassing in CIAV magmas (section 3.4.4.2), the similarity of $^3He/^4He$ for He-rich CIAV melilitites and nephelinites and with Proterozoic non-cratonic peridotites (Fig. 3.3) as well as the restricted initial range in $\delta^{18}O$ provides strong evidence for common derivation from a mixed CLM and asthenospheric source.

CIAV $^3He/^4He$ ratios do not indicate that a high time integrated $^3He/(U+Th)$ source is involved in their petrogenesis. In fact the opposite is true. Melilitites, nephelinites, basanites and basalts from localities in Southern Africa, Canada and the western branch of the East African Rift exhibit lower $^3He/^4He$ than typical MORB suggesting derivation from a reservoir with lower time integrated $^3He/(U + Th)$ than DMM. For a high $^3He/^4He$ reservoir to exist in the shallow mantle and not dominate the helium isotope characteristics of CIAV would require it to have lower [He] than MORB melts meaning that its signature should be obliterated by MORB $^3He/^4He$ in every form of terrestrial magmatism. This conclusion is also in conflict to measurements of high $^3He/^4He$ in OIB tholeiitic basalts (Chapter 2) derived from high degrees of partial melting. Similarly the CIAV data suggests that ^3He-recharge models whereby small volumes of volatile-rich material from the lower mantle (Stuart *et al.,* 2003) or from shallow high $^3He/^4He$ do not apply in the genesis of CIAV.

Other models for shallow sources existing within the asthenosphere with extreme $^3He/^4He$ ratios also fail to explain the He isotopic characteristics of CIAV. For example, preservation of extreme $^3He/^4He$ through capture within mantle minerals (Natland, 2003; Meibom *et al.,* 2003) is in direct conflict with [He] in minerals from the CLM (section 3.2) and from oceanic lithosphere (e.g., Vance *et al.,* 1989) which contain between 1×10^{-5} to 1×10^{-10} ccSTP/g [^4He] and $^3He/^4He$ less than $8.8\pm2.1R_A$. Therefore, mantle phases, such as olivine, will not contain high [He] concentrations

compared with the high $^3He/^4He$ and [He] source recognised from degassing relationships (Hilton *et al.*, 1995; Hilton *et al.*, 2000b; chapter 2) and from theoretical calculations (Porcelli and Wasserburg, 1995). Fig. 3.1 summarises the statistical break-down of CFB, OIB, MORB and CIAV magmatism and CLM peridotites for $^3He/^4He$. This plot clearly shows that the shallow mantle, including the CLM and the source of CIAV – a region of the Earth proposed as a LONU mantle source – cannot explain the extreme $^3He/^4He$ in excess of 10-50R_A for CFB and OIB. The CIAV $^3He/^4He$ results presented here indicate that a high time integrated $^3He/(U+Th)$ source is not involved in their petrogenesis and therefore by definition cannot exist in the lithosphere or convecting upper mantle beneath them.

3.5 Summary

A shallow high time integrated $^3He/(U+Th)$ layer or 'perisphere' with LONU characteristics beneath the lithosphere has been proposed to account for the extreme $^3He/^4He$ characteristics of OIB and CFB (Anderson, 1995). This study finds no evidence for such a reservoir:

- The CLM is more heterogeneous than previously assessed by Gautheron and Moriera (2002) and more radiogenic than DMM. Archaean cratonic peridotites possess low time integrated $^3He/(U + Th)$ and low $^3He/^4He$ ratios that are lower than Proterozoic CLM
- The first measured $^3He/^4He$ and [He] measurements for eclogite, a minor but geochemically important constituent of the CLM, indicate that ancient eclogite/pyroxenite lithologies represent a very low time integrated $^3He/(U +Th)$ reservoir in the mantle. Magmas derived from mixed pyroxenite-peridotite sources will be characterised by low $^3He/^4He$. Systematically low $^3He/^4He$ have been measured in a number of HIMU OIB worldwide (Chapter 4, Kurz *et al.*, 1982; Hanyu and Kaneoka, 1997; Hilton *et al.*, 2000a).
- In terms of trace element, Sr, Nd, Pb, Hf, Os and He isotope compositions, the various components of CLM provide both enriched radiogenic and depleted mantle sources for continental and oceanic intraplate magmatism.
- Trace elements, Sr, Nd, He and O isotope signatures for CIAV from Canada, South Africa and Uganda suggest a common mantle source component in their origin that has low $^3He/^4He$.

- There is no evidence of a low $\delta^{18}O$-source in the CIAV analysed in this study.
- CIAV have $^{3}He/^{4}He$ ratios that are more radiogenic than MORB. CIAV do not sample a high-time integrated $^{3}He/(U+Th)$ reservoir in the shallow mantle calling into question arguments for derivation of high $^{3}He/^{4}He$ ratios in OIB and CFB through shallow mantle sources.

Chapter 4: He, O, Sr, Nd, Re-Os and Pb isotope evidence for ancient enriched mantle components in the source of Western Canary Island volcanism

4.1 Introduction of aims

This chapter considers the two westernmost and youngest islands of the Canary Islands that represent the present day peak eruptive centres and hotspot focus of the archipelago, El Hierro and La Palma. Petrographic, elemental and isotopic (He, O, Sr, Nd, Pb, Os) data are presented for high-MgO alkaline basalts from the two islands with a number of aims:

- To assess the relative roles of crust, lithosphere and convecting mantle in the petrogenesis of La Palma and El Hierro lavas.
- To describe the geochemical differences between El Hierro and La Palma and to compare these with the geochemical variations measured in the Canary Islands as a whole.
- To provide further constraints on the mantle source characteristics of these and other Ocean Island Basalts (OIB).

Limited geochemical information is available for El Hierro, but a larger published database is available for La Palma. Lavas from La Palma have been described as highly alkalic basanites and basalts that possess distinctive trace element and isotopic signatures (Marcantonio *et al.*, 1995; Widom *et al.*, 1999; Hilton *et al.*, 2000a). La Palma lavas share elemental chemical characteristics typical of HIMU localities (*c.f.*, Weaver, 1991a,b) but their lead isotope signatures ($^{206}Pb/^{204}Pb$ = 19.2 to 20; Marcantonio *et al.*, 1995) are less radiogenic than typical HIMU islands such as St Helena, Tubuaii or Mangaia ($^{206}Pb/^{204}Pb$ = 20.5 to 22; Graham *et al.*, 1992a; Woodhead, 1996). HIMU is at least one of four commonly recognised geochemical components in OIB (Zindler and Hart, 1986). HIMU mantle is characterised by highly radiogenic Pb ($^{206}Pb/^{204}Pb$ >19.2), usually thought to result from elevated $^{238}U/^{204}Pb$ (μ) ratios over a period in excess of 1.5Ga (Zindler and Hart, 1986; Chauvel *et al.*, 1992), although young HIMU mantle has also been proposed in the source of some OIB (Thirlwall, 1997).

La Palma and El Hierro lavas exhibit some of the most radiogenic $^{187}Os/^{188}Os$ isotope ratios so far measured in OIB (Marcantonio *et al.*, 1995; Widom *et al.*, 1999) as well as $^{3}He/^{4}He$ ratios consistent between mixing of a HIMU (low $^{3}He/^{4}He$) and a high ^{3}He mantle component (Hilton *et al.*, 2000a). The overall geochemical signatures have been interpreted as indicating that La Palma and by inference, El Hierro, are the result of a recycled oceanic crustal or lithospheric component (Marcantonio *et al.*, 1995) and a lower mantle plume (Hilton *et al.*, 2000a). However, the limited geochemical data for El Hierro makes comparison between the source of La Palma and El Hierro magmatism difficult. This study extends the database for both La Palma and El Hierro with the aim of improving constraints on the source components that contribute to Western Canary Island volcanism. This extended database allows their signatures to be placed in the context of models for the generation of intraplate ocean island magmatism.

4.2 Regional geological setting

The Canary Islands consists of a chain of seven main polygenetic volcanic islands and several islets situated ~100km from the northwest Sahara-African continental margin (Fig. 4.1). The islands have had a sub-aerial volcanic history in excess of 20Ma and, with the exceptions of Lanzarote and Fuerteventura, take the form of independent architectural edifices built on increasingly submerged ocean floor that reaches a maximum of ~4km depth under La Palma and El Hierro. The spatial and chronological evolution of the Canary Islands indicates progressively younger magmatism to the west and is strongly symptomatic of a slow-moving mantle 'hotspot' (Morgan, 1981; Carracedo *et al.*, 2001; Fig. 4.1) similar to that recognised for the Hawaii-Emperor seamount chain (Wilson, 1963), but with a much lower buoyancy flux (Sleep, 1990). This interpretation is corroborated by the progressive aging of exposed submarine seamounts on the Islands of Fuerteventura, La Gomera and La Palma (Hoernle and Schminke, 1993b and references therein).

The Canary Islands, with the exception of La Gomera, have all experienced Holocene volcanism, and historic volcanism has occurred on La Palma, Tenerife and Lanzarote and possibly also on El Hierro (Carracedo *et al.*, 2002 and references therein). La Palma and El Hierro are the only islands in the archipelago in the juvenile shield building phase of formation; Tenerife is in a mature shield building

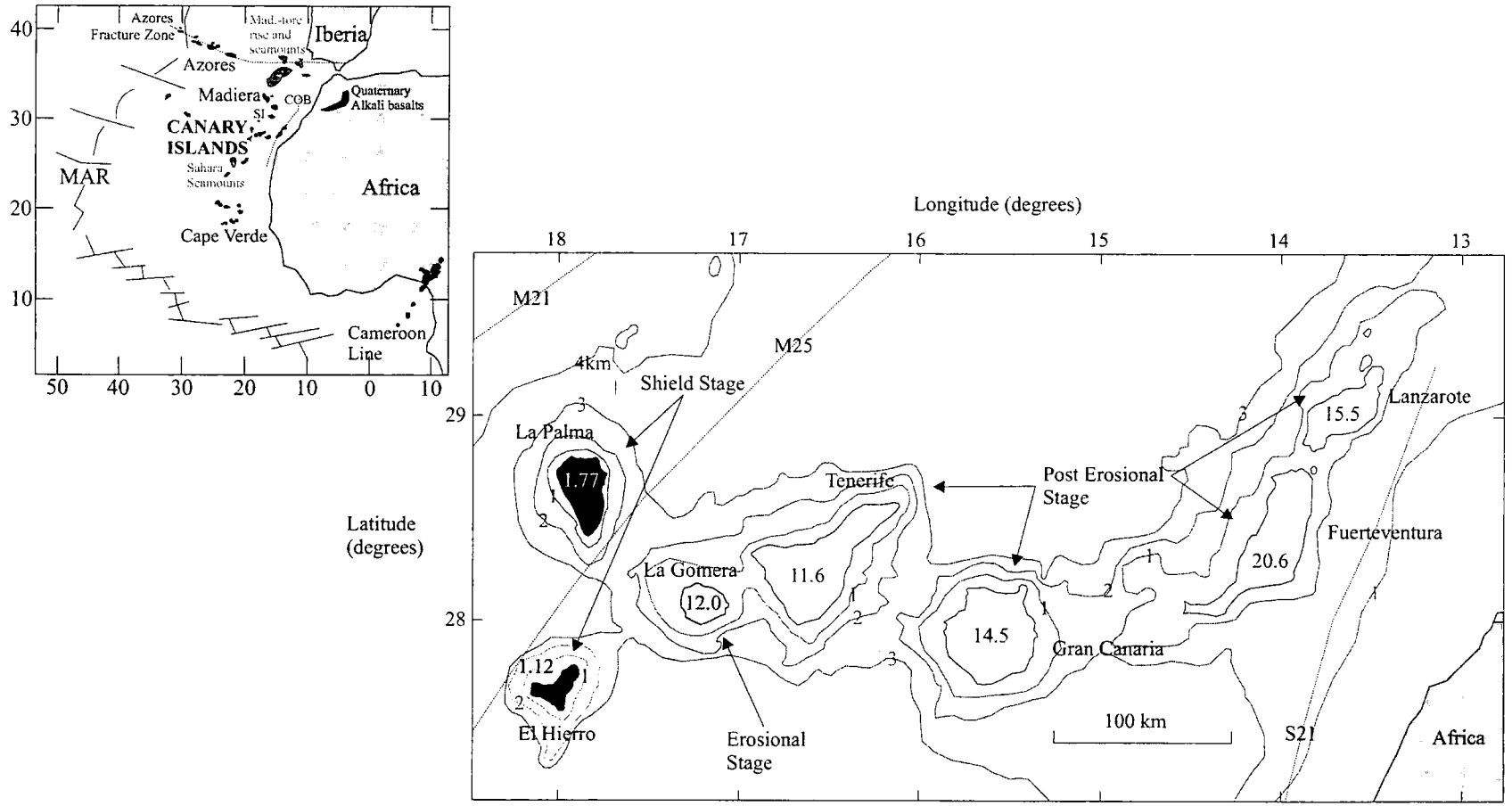

Figure 4.1: Simplified map of the geographic framework of the NW African continental margin volcanic groups and map of the Canary Islands. Shading of islands to represent stages of growth and numbers within islands boundaries represent maximum measured ages of the stratigraphy in Ma. Also shown is the depth of the ocean floor (km) and the palaeomagnetic anomalies M25 and S21. S21 lies close to the continental oceanic boundary (COB).Canarian ages from Abdel-Monem et al. (1971, 1972). McDougall and Schmincke (1996), Carracedo (1979), Ancochea et al. (1990, 1994), Coello et al. (1992), Perez-Torrado et al. (1995), Guillou et al. (1996); Carracedo et al. (2000). Modified from Carracedo et al. (2002)

stage, whilst Gran Canaria, Lanzarote and Fuerteventura are all in the post-erosional stage; La Gomera is in a quiescent erosional phase and volcanism has not occurred on the island during the Quaternary (Fig. 4.1). The majority of volcanism in the Canary Islands is restricted to strongly alkalic compositions with all islands possessing basanites and alkali basalt with SiO_2 □46 wt. % and MgO >8 wt. % within their stratigraphies.

The magmatic processes that generated the Canary Islands are generally attributed to either a hotspot beneath the slowly eastward progressing African plate (Carracedo 1999; Hoernle and Schmincke 1993b; Carracedo *et al.,* 1998), to propagating westward trending fracture (Anguita and Hernán, 1975), or to a mix of both models (Anguita and Hernán, 2000). Some studies have also related the magmatism on the Canary Islands to a large-scale mantle up-welling extending from the Cape Verde Islands to eastern Europe (Hoernle *et al.,* 1995; Oyarzun *et al.,* 1997) or a relic Triassic-Jurassic 'mantle enrichment' event (Anguita and Hernán, 2000) perhaps associated with the Central Atlantic Magmatic Province. Geochronological and chemical studies of volcanic seamounts and islands in the Atlantic basin from the Azore-Gibralter fracture zone south of the Iberian peninsula to the Sahara seamounts >100km south of El Hierro, indicate that there are at least two age-progressive hotspot tracks currently terminating at the islands of Madeira and El Hierro (Geldmacher *et al.,* 2000; 2001). The age-progressive tracks, persisting since the Tertiary, are consistent with the slow opening of the Atlantic Ocean (*c.* 9mm/yr) and are parallel and congruent with the rotation of the African plate (e.g., Morgan 1983). There are a number of Tertiary aged alkaline volcanics in the Atlas Mountains adjacent to the Canary Islands volcanic chain (e.g., Rachdi *et al.,* 1997) that may represent the continental expression of the younger ocean basin volcanism (Anguita and Hernán, 2000).

The nature of the lithospheric mantle beneath the Canary Islands has been a long-standing controversy, however, the presence of tholeiitic MORB gabbro xenoliths which occur on Lanzarote, Gran Canaria and La Palma (Hoernle, 1998; Schmincke *et al.,* 1998), as well as seismic refraction studies (e.g., Bossard and Macfarlane, 1970; Banda *et al.,* 1981), argue for the presence of oceanic crust beneath all of the Canary Islands. Indeed the nearest continental basement rocks are 515Ma old and have been discovered to the north in deep water (4000m) at the base of the Mazagan

escarpment ~100km west of Casablanca, Morocco (DSDP leg 79, Hole 544A; Kreuzer *et al.*, 1984). The age of underlying oceanic crust indicates that it is some of the oldest in the Atlantic Ocean basin or in any ocean basin globally and is bracketed by palaeo-magnetic anomalies S1 (175Ma) to the east of Fuerteventura and Lanzarote and M25 (156Ma) between La Palma and El Hierro, which are the westernmost and youngest Islands (Fig. 4.1; Roeser, 1982; Klitgord and Schousten, 1986; Verhoef *et al.*, 1991; Roest *et al.*, 1992).

4.3 Geology, stratigraphy and evolution of La Palma

La Palma has been the most volcanically active of the Canary Islands in historic times with eruptions recorded in ~1440, 1585, 1646, 1677, 1712, 1949 and 1971 (Hernandez-Pacheco and Valls, 1982; Fig. 4.2). La Palma has been the focus of intense geological study since the early 19th century when the large central depression in the island became the type locale for a 'caldera' (Von Buch, 1825; Lyell, 1855; Reiss, 1861). This feature has now been recognised as the surface expression of a debris avalanche collapse scar and not the result of a massive evacuating eruption(s) causing central edifice subsidence, as the term now implies. La Palma lies to the west of the M25 palaeo-magnetic anomaly on the youngest oceanic lithosphere of all the Canary Islands and rises ~6500m above the seafloor to a maximum elevation of 2426m above present-day sea level. The island has the approximate shape of a tear-drop, oriented north-south with a surface area of 706km^2. La Palma is made up of two poly-genetic volcanic edifices, the Northern Shield and the Cumbre Vieja Ridge (Fig. 4.2). The overall volume of the edifice can be estimated to be in excess of 14000 km^3 based upon the basal area and height of the edifice.

El Hierro is the smallest (287km^2) and youngest island in the Canary Island archipelago. Unlike La Palma, El Hierro is geologically speaking, relatively unstudied. There is a paucity of historical eruptions on the island with a questionable record of eruption at Lomo Negro volcano in 1793 (Hernández Pacheco, 1982). El Hierro lies to the east of the M25 palaeo-magnetic anomaly and is in the form of a tri-lobate rift structure due to three-branched rift zone development (Carracedo, 1994, 1996). El Hierro rises ~5500m above the seafloor to a maximum elevation of 1501m a.s.l. (Fig. 4.3) making it one of the steepest oceanic shield volcanoes in the

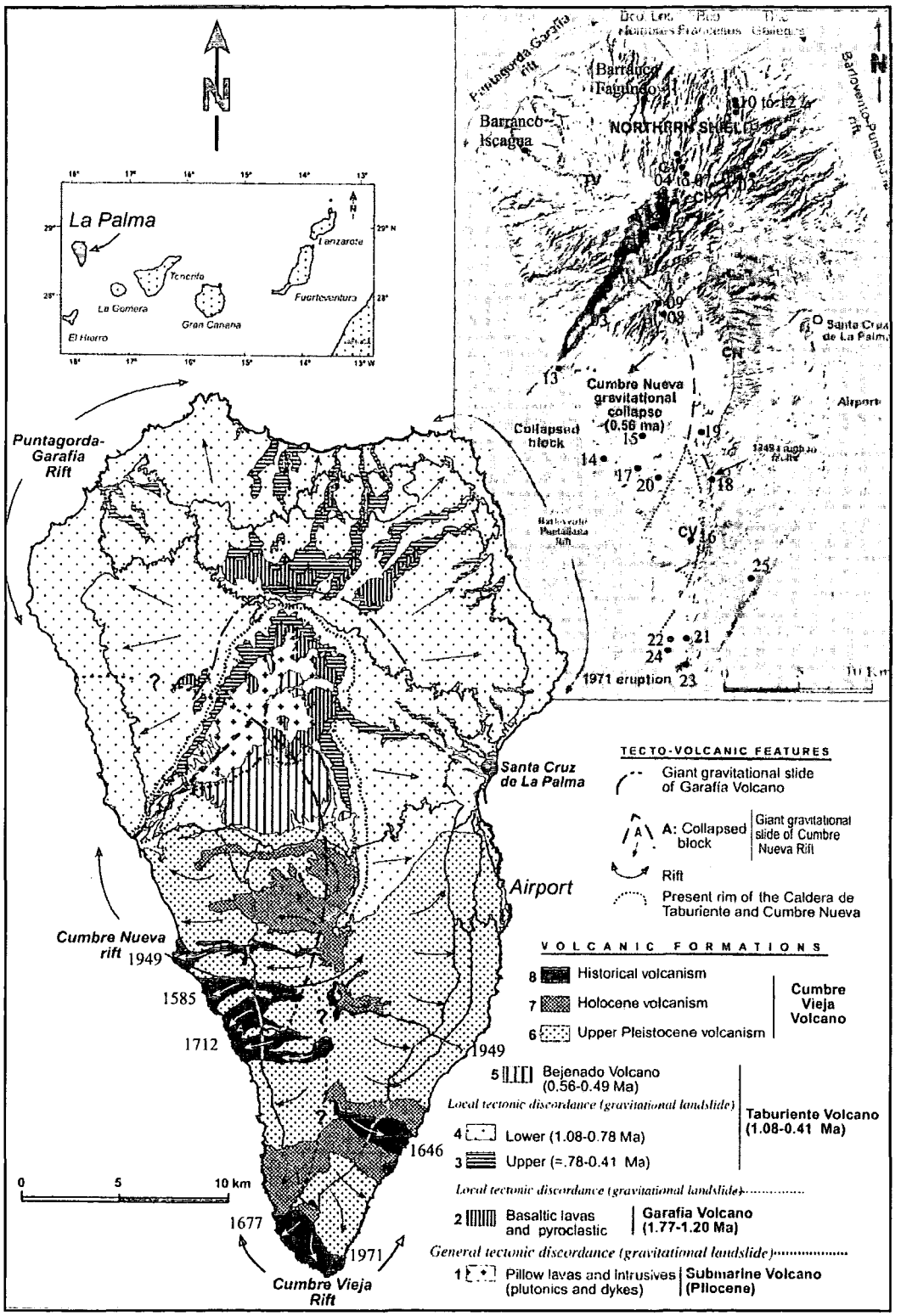

Figure 4.2 Simplified geological map of La Palma (modified from Carracedo et al. 2002) and Grafcan image with locations of JMDD LP samples inset. Key: BV, Benajado Volcano; CP, Central Plateau (lavas filling Garafía collapse); CT, Caldera de Taburiente; CN, Cumbre Nueva; CV, Cumbre Vieja; GV, Garafía Volcano; TV, Taburiente Volcano

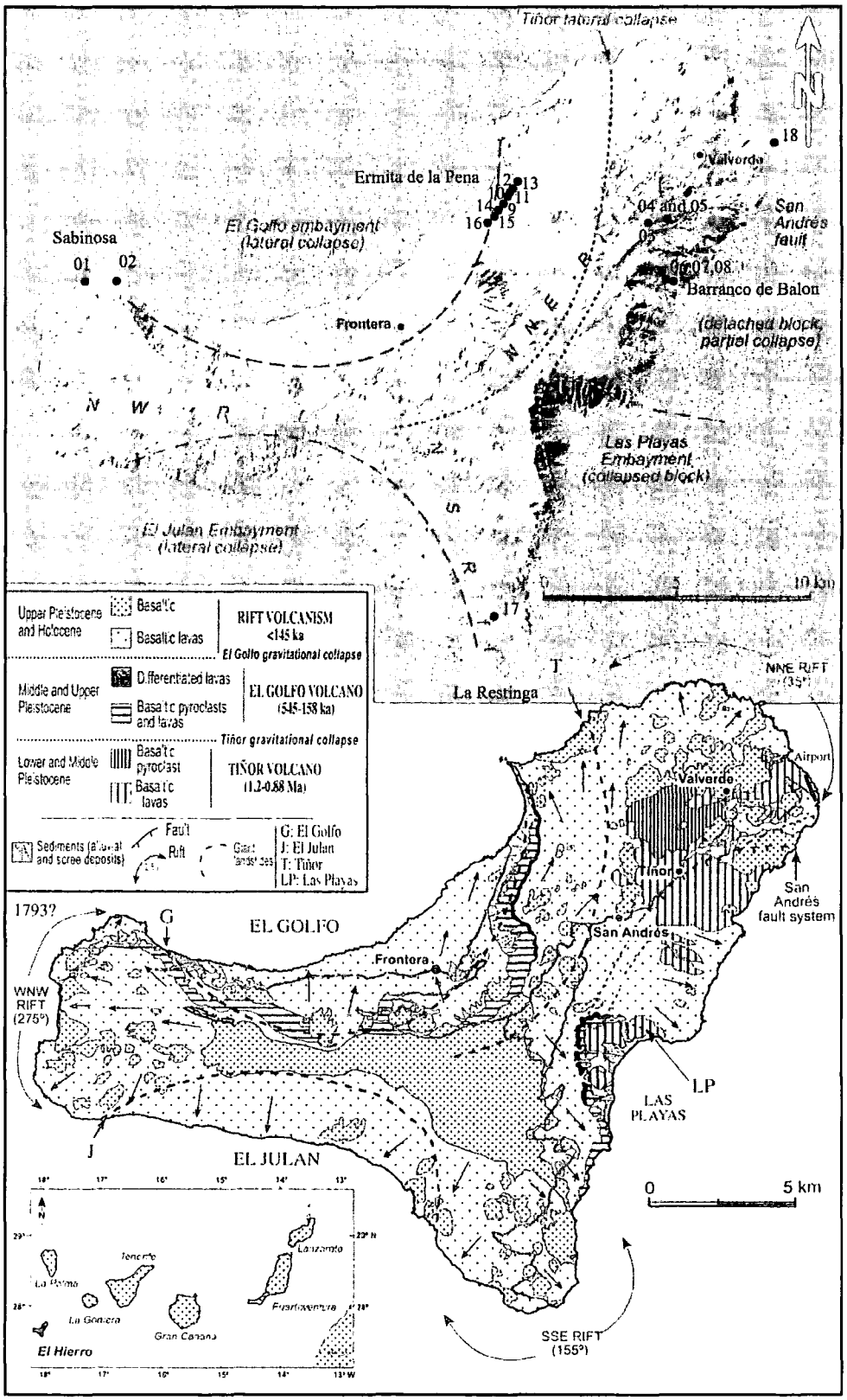

Fig. 4.3: Simplified geological map of El Hierro (modified from Carracedo et al.2002) and Grafcan image with locations of JMDD EH samples inset.

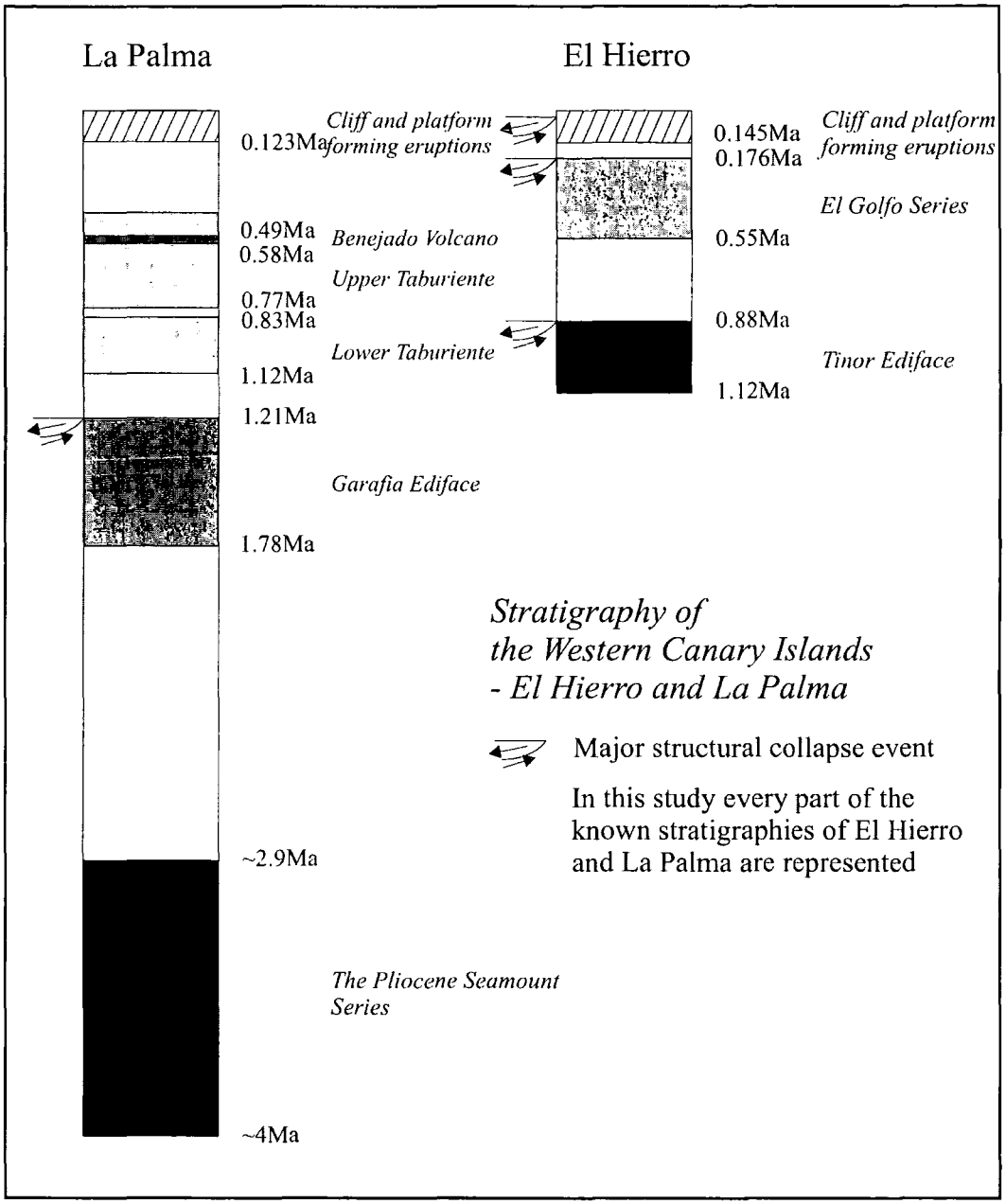

Fig. 4.4: Summary of the stratigraphies of La Palma and El Hierro including maximum and minimum age constraints on the main stratigraphic units. Age data and stratigraphic subdivisions summarised in Appendix G. Information on major collapse events can be found in Carracedo et al. (2001).

world (Carracedo *et al.*, 2001). The volume of the El Hierro edifice is estimated at 5500 km^3 based upon the basal area and height of the edifice.

Combined sub-aerial volumes and age constraints of the Northern Garafia and Taburiente Volcanoes and Cumbre Vieja suggest eruptive rates in the region of 0.2 and 0.9km^3/Ka, respectively (Carracedo *et al.*, 2002); by comparison average magma supply rates for the island of Hawaii are estimated in the order of 20km^3/Ka (Moore and Clague, 1992). Combined sub-aerial volume and age constraints on the island of El Hierro suggests a magma supply rate of ~0.1km^3/Ka, however debris avalanche deposits account for large volumes (>1000km^3 sub-aerial and submarine) of the edifice and magma supply rates are therefore likely to be higher than estimated and more akin to those on La Palma. Like La Palma, El Hierro has a well constrained stratigraphy based upon K-Ar, ^{40}Ar-^{39}Ar ages and palaeomagnetic data. The stratigraphy of both islands is described in detail in Appendix G with a stratigraphic summary in Fig 4.4.

4.4 Petrology of La Palma and El Hierro lavas

Samples were collected by the author from La Palma and El Hierro in April 2002 to expand the La Palma sample suite made available for geochemical analysis by T. Elliott and which have previously been described in Marcantonio *et al.* (1995), Hilton *et al.* (2000a) and Nikogosian *et al.* (2002). The Elliott sample suite are highly alkalic basanitic and basaltic lavas, typical of La Palma shield basalts, and 93LP134 which is a gabbroic sill from the Pliocene Seamount (see Marcantonio *et al.*, 1995; Hilton *et al.*, 2000; Nikogosian *et al.*, 2002). The locations and petrography of the 2002 sample suite are described in detail in Appendix A.

4.4.1 La Palma lavas

Lavas analysed in this study range over the entire known stratigraphy of La Palma (Fig. 4.4). JMDDLP03 is a picritic pillow-basalt sampled in the Pliocene seamount series. Despite alteration, this sample still possesses fresh olivine cores. The intrusive formation of the Pliocene seamount series is represented by 93LP134 which has been has been described by Marcantonio *et al.* (1995) and Hilton *et al.* (2000a). Sub-aerially erupted ankaramite, basanite and alkali basalt lavas were collected from the Garafia, Lower Taburiente, Upper Taburiente and Benejado series

of the northern shield of La Palma including hornblende-phyric basalt from Benejado volcano. All collected sub-aerial lavas were optically fresh, showing no signs of secondary mineral addition. Basanitic flows and some more evolved volcanics including phonolite plugs were also collected from the Cumbre Vieja. Ankaramites are generally porphyritic and highly vesiculated, with fresh large olivines and zoned clinopyroxene and rare phenocrystal (titano)-magnetite. Groundmass consists of olivine, clinopyroxene, minor plagioclase, magnetite, chromite and glass. Basanites and alkali basalts are not porphyritic but have similar mineralogy and vesicularities to the ankaramites with fresh olivines and clinopyroxene – many of the Cumbre Vieja basanites contain amphibole and rare phlogopite as well as xenoliths which are often apatite- or amphibole-rich. The phonolite plugs of Roques De Jedey and Roques de Teneguia were also sampled and contain abundant haüyne.

4.4.2 El Hierro lavas

Collected lavas range over the entire known stratigraphy of El Hierro. The ankaramites, basanites and alkali basalts from El Hierro are very similar to lavas from the Northern Taburiente and Garafia lavas from La Palma and only differ significantly from those from Benejado and Cumbre Vieja by the fact that they do not contain amphibole. All collected sub-aerial lavas were optically fresh, showing no signs of secondary mineral addition. Mantle xenoliths are only present in lava samples JMDD EH04 and JMDD EH05 which are from the Ventejís volcano group of the Tiñor volcanic series. One trachyte was collected, JMDD EH09, which lies at the top of the UEGS (Fig. 4.4). The general petrology of units within El Hierro is described more fully elsewhere (Appendix A and G; Carracedo *et al.*, 2001).

4.5 Geochemistry of La Palma and El Hierro lavas

Samples are discussed according to stratigraphic position in their respective edifices such that La Palma lavas are discussed as Seamount, Garafia, Taburiente (lower and upper) and CFE/PFE units (includes historical La Palma eruptions). El Hierro lavas are discussed in terms of Tiñor, El Golfo (Lower and Upper) and CFE/PFE units (including all pre-historic and historic eruptions). Fig.s 4.2 and 4.3 illustrate the geographical locations of JMDD LP and JMDD EH samples respectively. Analytical

techniques for major and trace elements are documented in Appendix B. Analytical techniques for Sr-Nd-Pb and Re-Os isotope analyses were performed at AHIGL by the author and are documented in Appendix C. O and He isotope analyses were performed by the author at Royal Holloway, University of London and Scripps Institution of Oceanography respectively and techniques for this are documented in Appendix C. Major and trace element data for lavas considered in this chapter can be found in Appendix G.

4.5.1 Whole rock major element variations

The Canary Islands as a whole are composed mainly of alkaline to highly alkaline lavas, with La Palma possessing the most alkaline differentiation trend for its volcanic rocks (Carracedo *et al.*, 2002). Tholeiitic basalts are only recognised in the oldest units of Gran Canaria and the youngest units of Lanzarote. Highly alkaline olivine melitites and nephelinites are minor constituents of Gran Canaria and Lanzarote volcanism, whilst intrusive carbonatite bodies have been recognised on Fuerteventura (Barrera *et al.*, 1981; Demény *et al.*, 1998). The majority of lavas analysed in this study lie in the field of highly alkaline picro-basalts or basanite with few evolved compositions (Appendix G; Fig. 4.5). The sampling methodology for this study was to search for primitive mafic and phenocryst-rich lavas. This resulted in deliberate bias toward mafic and ultramafic high MgO (> 8 wt. %) lavas. Nevertheless, the few evolved samples collected from La Palma show a trend toward highly alkaline phonolite compositions whereas the evolved lava from El Hierro is more transitional-alkaline in character. The evolution to highly alkalic compositions is seen in all parts of the La Palma stratigraphy apart from the seamount series that follow the transitional alkaline fractionation trend that is common to all El Hierro lavas (see data presented in Carracedo *et al.*, 2001 and references therein).

A large fraction (12 El Hierro lavas and 16 La Palma lavas) of the lavas analysed in this study have MgO >10 wt. %, are porphyritic and are probably accumulative, with excess olivine and clinopyroxene. *Mg*-numbers for El Hierro basalts, basanites and ankaramites range from 59 to 70, similar to La Palma mafic lavas (*Mg*-number = 46-71) with the notable exception of picrite JMDD LP03 (*Mg*.-number = 80). Major element variation is largely controlled by fractionation or accumulation of olivine and clinopyroxene. Since clinopyroxene (augite) contains ~50% SiO_2 the

fractionation vector is steep on plots such as Fig. 4.5. Deep (sub-Moho, 12-40km) clinopyroxene fractionation has been previously been proposed as a major factor in the generation of the highly alkaline characteristics of La Palma lavas (Nikogosian *et al.*, 2002). Marked major element differences exist between El Hierro and La Palma basalts and basanites with El Hierro lavas exhibiting more elevated TiO_2, Fe_2O_3 and P_2O_5 at similar MgO (Fig. 4.6). This difference may be partly explained by the presence of Ti-rich clinopyroxene (Titano-augite) in El Hierro ankaramites. Decreases in TiO_2, Fe_2O_3 and P_2O_5 for evolved lavas in El Hierro and La Palma is taken to indicate fractional crystallisation of Titano-augite, Fe-Ti oxides, amphibole (Klugel *et al.*, 2000) and apatite which are common in samples with MgO <6 wt. % MgO.

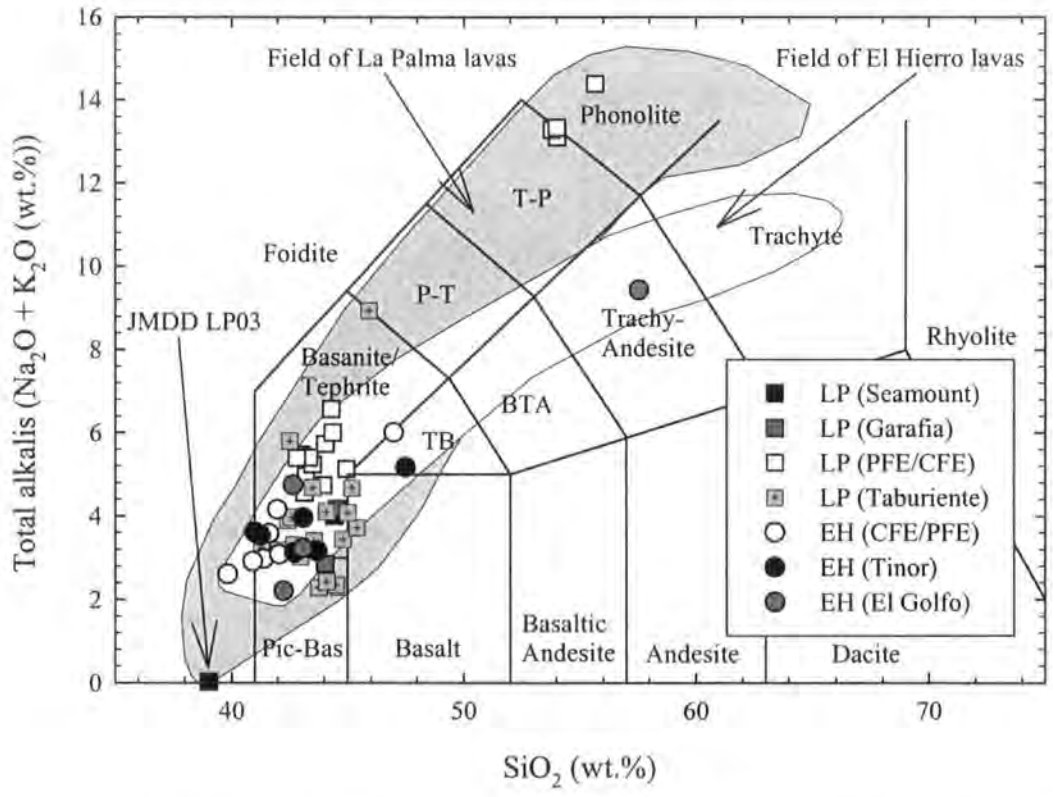

Fig. 4.5: Silica versus total alkalis (K_2O+Na_2O) as weight percentages of lavas from El Hierro and La Palma. Field and terms from LeMaitre et al. (1989). The annotated sample JMDD LP03 is a picrite pillow from the Seamount series of La Palma which has been hydrothermally altered explaining its low total alkali content. Fields for La Palma (grey) and El Hierro (white) from data compiled in Carracedo et al. (2002).

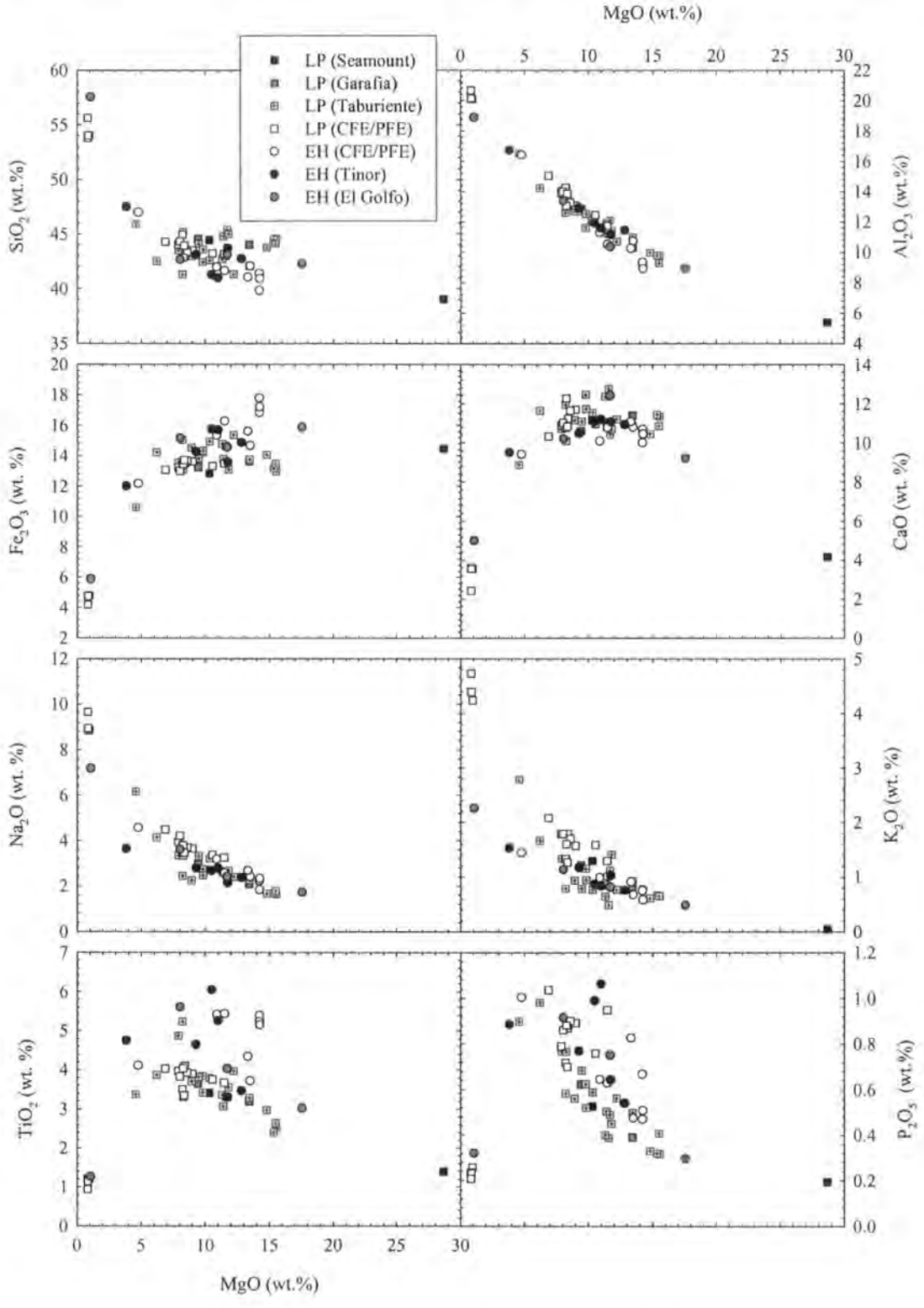

Fig. 4.6: MgO (wt. %) versus major element oxides (wt.%) for La Palma and El Hierro lavas.

SiO_2, K_2O and Na_2O all increase with decreasing MgO, illustrating that these elements behave incompatibly until advances stages of differentiation. The large

variation in Fe and Ti in the more primitive lavas from El Hierro and La Palma to some degree, reflect the variable contents of clinopyroxene in samples. However, the variations in Ti, Fe and P must also reflect fundamental differences in melt compositions between La Palma and El Hierro lavas. This is because ankaramites from both islands contain similar quantities of clinopyroxene and olivine (Appendix A) yet El Hierro ankaramites have systematically elevated abundances of Fe, Ti and P. Although magnetite fractionation is evident from Fe and Ti inflections at ~6 wt.% MgO, there is abundant petrological evidence for magnetite fractionation from more primitive lava compositions especially for El Hierro ankaramites that often contain chromite and magnetite as phenocryst phases. Fractionation of magnetite over a wide range of MgO implies relatively high fO_2 for El Hierro and La Palma magmas. The high oxygen activities can explain the failure of basanitic magmas to evolve to phonolite compositions for El Hierro and the Garafia and Taburiente edifices on La Palma.

4.5.2 Whole rock trace element variations

Compatible trace element variations are strongly controlled by olivine accumulation in La Palma and El Hierro lavas (Fig 4.7). The variable Sc contents at >10 wt. % MgO also indicate that clinopyroxene accumulation plays an important role in the compatible and major element concentrations of Western Canary Island lavas (Fig 4.7). The generally negative loss on ignition measured for El Hierro and La Palma lavas suggests that the majority of samples analysed in this study are fresh and have not suffered alteration mobilisation of elements after emplacement of the lavas. This statement is corroborated by their petrographic freshness. The only exception to this is JMDD LP03 which has suffered up to hornfels facies metamorphism in the seamount and which is visibly altered (Appendix A) with a LOI >6 wt. %; despite this JMDD LP03 still retains fresh olivine cores. Na loss and variation in $FeO–Fe_2O_3$ in this sample has resulted in its exceptionally depleted total alkalis content in Fig. 4.5.

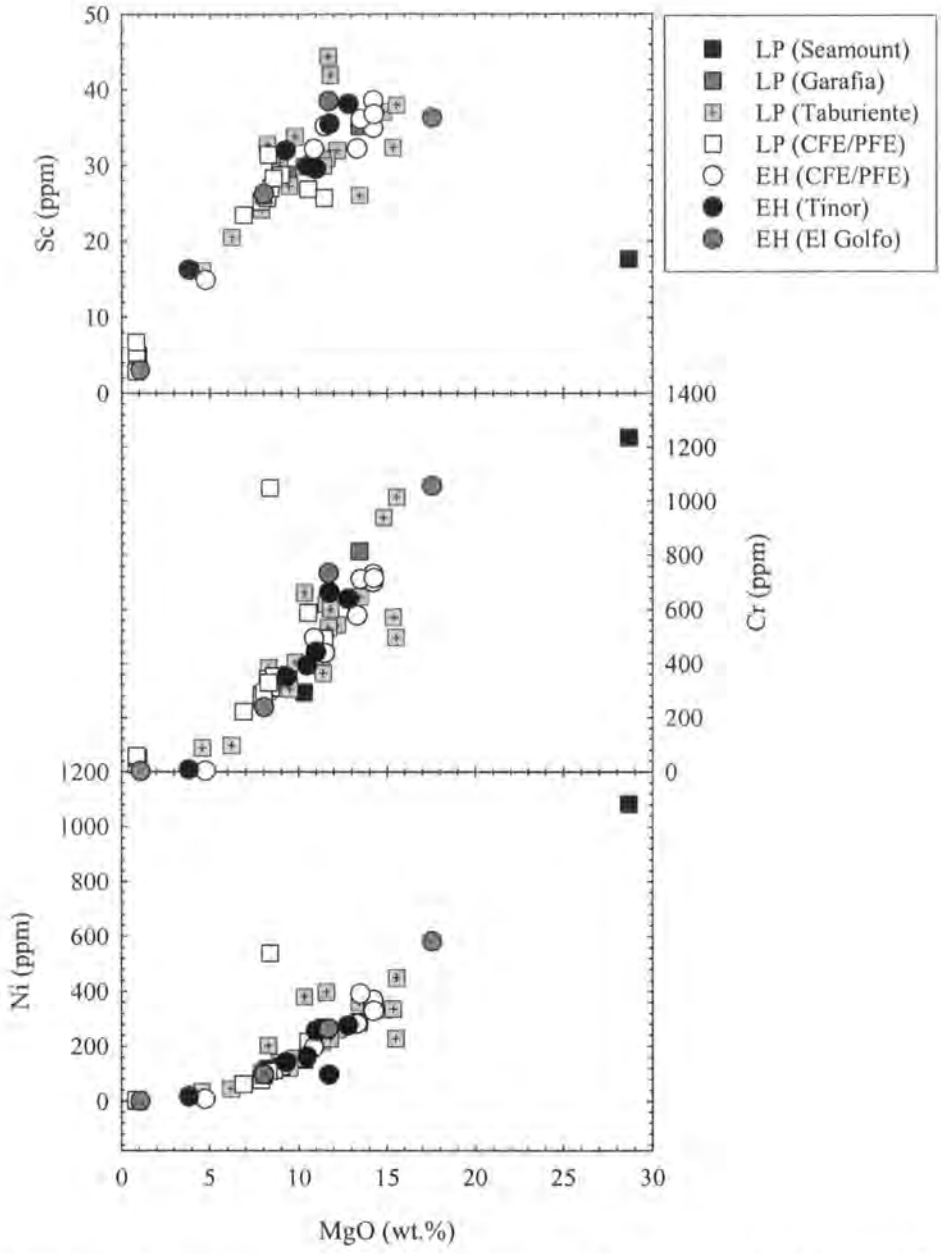

Fig. 4.7: MgO (wt. %) versus compatible elements Sc, Cr and Ni (ppm) in La Palma and El Hierro lavas. Positive correlations between MgO and compatible trace elements indicate the role of olivine and clinopyroxene accumulation in Western Canary Island lavas.

Primitive mantle multi-element variation diagrams for El Hierro and La Palma reveal that the trace element inventories of basanites and alkali basalts from the two islands are very similar both temporally and spatially (Fig. 4.8). Substantial crystallisation (≥20%; Appendix A) of olivine, clinopyroxene and Fe-Ti oxides, whilst resulting in large compatible element depletions, will only have a modest effect on incompatible element concentrations. Primitive lavas from El Hierro and

La Palma show features characteristic of HIMU ocean islands such as St Helena in terms of their primitive mantle normalised trace element patterns (Fig. 4.8). These features include enrichment in Nb and Ta and relative depletion in Pb (and K) as well as high Ce/Pb and Th/U and low Zr/Nb (Table 4.1). $(La/Yb)_n$ and $(Sm/Yb)_n$ vary from 10.1-30.2, 4.9-7.1 and 12.1-28.0, 4.3-7.1 for El Hierro and La Palma lavas. The majority of El Hierro and La Palma lavas have positive Ti anomalies.

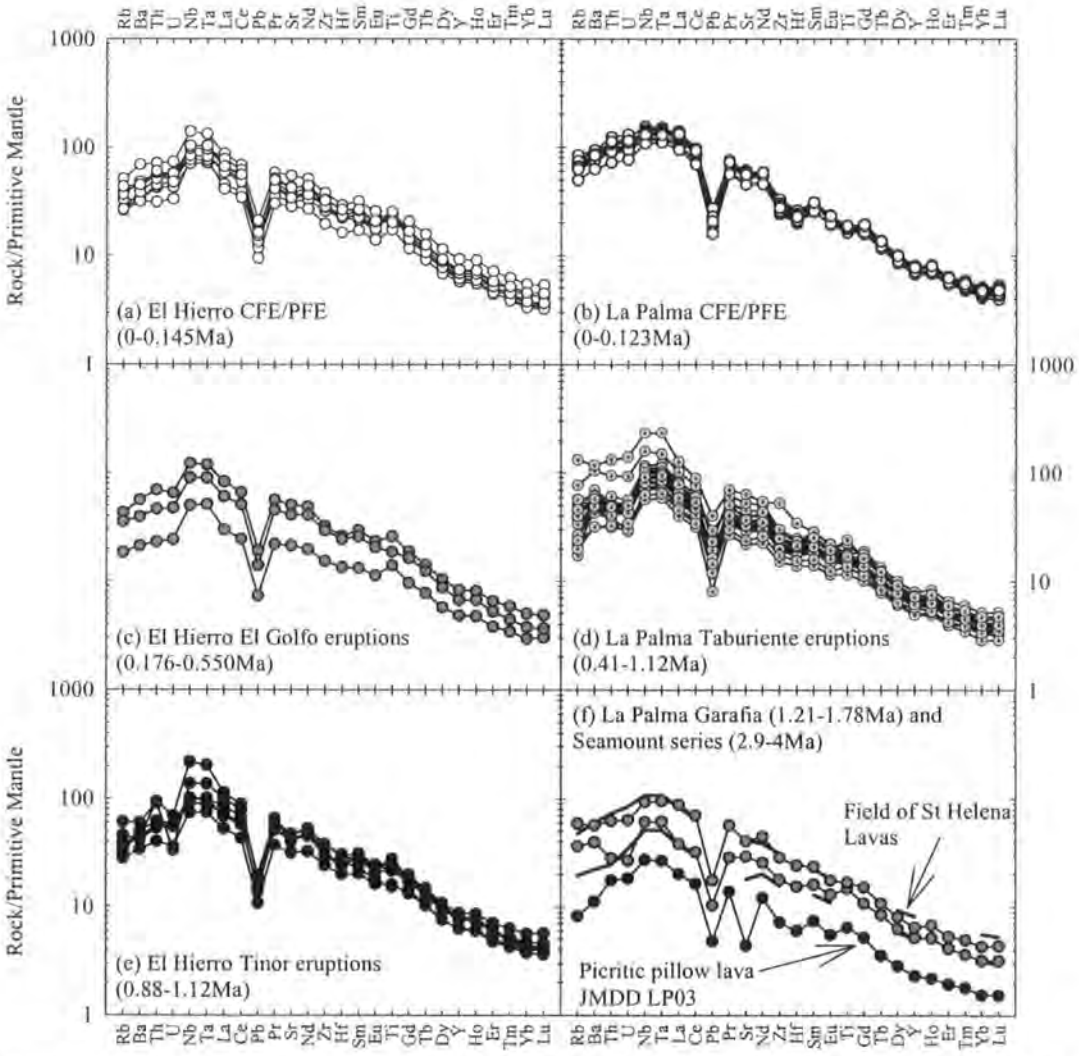

Fig. 4.8: Primitive mantle normalised multi-element variations for El Hierro and La Palma ankaramites, basanites and basalts as a function of their stratigraphic position and age.

The older Tiñor and Garafia series on both islands and the La Palma CFE and PFE which were all erupted on the Cumbre Vieja appear to be geochemically distinct. In the case of the Tiñor series some lavas possess variable abundances of Th and one lava (JMDDEH07) has a very large positive Nb and Ta anomaly. For the two Garafia lavas one (JMDDLP02) is characterised by a small positive Nb and Ta

Table 4.1: Trace element ratios for El Hierro, La Palma, other OIB and terresrial reservoirs

	Age (Ma)	Zr/Nb	Nb/Ta	Ce/Pb	Th/Nb	La/Nb	Th/U
El Hierro							
Tinor	0.88-1.12	4.55	17.8	41.2	0.07	0.69	5.54
El Golfo	0.176-0.55	4.68	17.5	33.3	0.06	0.62	4.04
PFE-CFE	0-0.145	4.90	17.7	34.3	0.07	0.64	4.10
	Island Av.	***4.7***	***17.6***	***36.3***	***0.06***	***0.65***	***4.6***
		±0.2	***±0.1***	***±4.3***	***±0***	***±0.03***	***±0.8***
La Palma							
Seamount	2.9-4	4.15	17.7	32.5	0.08	0.71	3.88
Garafia	1.21-1.78	4.70	17.2	34.1	0.07	0.76	4.12
Taburiente	0.41-1.12	4.01	17.1	29.5	0.06	0.67	4.20
PFE-CFE	0-0.123	3.34	17.5	39.0	0.09	0.89	3.85
		4.1	***17.4***	***33.8***	***0.07***	***0.76***	***4.0***
	Island Av.	***±0.6***	***±0.3***	***±4.0***	***±0.01***	***±0.10***	***±0.2***
Other Canary Island averages							
Marcantonio La Palma (av.)[a]		-	-	41.0	0.08	0.78	-
Gran Canaria[b]	0-14.5	7.20	-	45.4	0.07	-	3.85
Tenerife[b]	0-11.6	3.90	-	39.6	0.07	-	4.59
Fuerteventura[b]	0-20.6	4.20	-	43.5	0.06	-	4.29
Extreme HIMU OIB							
Saint Helena[c]		4.5	-	34.9	0.08	0.69	3.45
Mangaia[c]		3.8	-	31.9	0.10	0.77	3.68
Tubuaii[c]		3.2	-	37.6	0.09	0.72	4.07
Iceland[b]		8.3	-	29.9	-	-	-
Other terrestrial and extraterrestrial reservoirs							
CI-Chondrite[d]		15.9	17.7	0.25	0.12	0.99	3.92
Bulk C.Crust[e]		10.3	10.9	3.30	0.47	1.50	3.90
DMM[f]		55.4	17.8	29.9	0.05	0.72	2.69
Pyroxenite[g]		3.25	9.03	91.7	0.04	0.84	4.95
Peridotite[g]		12.0	9.48	5.01	0.30	1.49	7.96

[a]Marcantonio data from Marcantonio *et al.* (1995) [b]Data from Thirlwall (1997)
[c]Data from Weaver (1991a,b) and Thirlwall (1997) [d]Data from McDonough and Sun (1995)
[e]Data from Rudnick (1995) [f]Data from GERM database
[g]Data from authors own compilation of CLM peridotites and pyroxenite xenoliths

anomaly whilst the other (JMDDLP01) is characterised by LILE enrichment (Ba and Rb) and a large positive Nb and Ta anomaly. Cumbre Vieja PFE and CFE lavas have limited positive Nb and Ta anomalies because of their relative enrichment of Rb, Ba, U and Th and slightly negative Ti anomalies; Cumbre Vieja mafic lavas also have pronounced negative Zr and Hf anomalies and are slightly more incompatible trace element enriched than El Hierro CFE and PFE, El Golfo or Tińor lavas, or older Taburiente, Garafia or Seamount series lavas on La Palma. Salient features of the more evolved lavas (omitted from Figs. for clarity), especially the phonolites, are the positive U, Th, Zr and Hf anomalies which they possess.

Table 4.2: He and O isotope results for El Hierro and La Palma lavas

Sample	Series	Age (Ka)	MgO[1]	Phase	Mass (g)	$^3He/^4He$[2]	(±2σ)	[He][3]	(±2σ)	$\delta^{18}O$[4]
El Hierro, Western Canary Islands, Spain										
JMDD EH01	PFE	<1	14.22	Ol	1.2	11.8	0.6	4.9	0.1	5.26
				Cpx	0.5	8.1	0.5	4.5	0.2	5.59
JMDD EH03	Tinõr	1030	12.82	Ol	1.0	8.2	0.2	36.2	0.7	5.12
JMDD EH07	Tinõr	1030	11.74	Ol	0.8	7.6	0.3	17.7	0.5	5.34
				Cpx	0.5	7.0	0.4	7.3	0.3	5.48
JMDD EH10	CFE	160	14.22	Ol	1.0	7.5	0.4	3.6	0.1	5.04
				Cpx	0.4	6.5	0.3	10.1	0.5	5.41
JMDD EH11	CFE	160	11.49	Ol	1.0	7.8	0.3	9.8	0.2	5.22
				Cpx	0.5	5.0	0.2	17.2	0.7	5.41
JMDD EH12	CFE	135	13.49	Ol	-	-	-	-	-	5.23
JMDD EH13	CFE	135	14.24	Ol	1.1	7.7	0.2	15.9	0.3	5.15
				Ol	-	8.2	0.3	13.3	0.3	-
				Cpx	0.6	4.2	0.1	18.2	0.6	5.37
JMDD EH14	UEG	265	8.03	Ol	0.8	7.2	0.3	8.7	0.2	5.13
JMDD EH15	UEG	335	17.57	Ol	0.9	7.8	0.3	10.5	0.2	5.08
				Cpx	0.5	7.0	0.2	31.4	1.3	5.44
JMDD EH16	LEG	540	11.70	Ol	0.9	7.8	0.2	13.3	0.3	5.08
				Cpx	0.7	7.8	0.3	22.3	0.7	5.27
JMDD EH17	PFE	<10	13.31	Ol	0.9	7.5	0.2	31.0	0.7	5.13
JMDD EH18	PFE	<1	10.88	Ol	0.9	7.6	0.3	13.2	0.3	5.26
				Cpx	0.8	7.1	0.2	38.3	1.0	5.40
La Palma, Western Canary Islands, Spain										
JMDD LP01	Garafia	1440	13.43	Ol	1.1	7.2	0.4	4.6	0.1	4.88
				Cpx	0.7	7.1	0.3	24.9	0.7	5.12
JMDD LP02	Garafia	1440	9.43	Ol	1.1	7.5	0.2	38.4	0.7	4.73
				Cpx	0.6	5.2	0.3	11.3	0.4	5.01
JMDD LP03	Seamount	3000	28.66	Ol	1.3	9.7	0.3	1.9	0.0	5.00
JMDD LP04	L. Tab.	1020	7.90	Ol	1.1	7.9	0.4	7.3	0.1	4.74
				Cpx	0.6	4.3	0.2	8.1	0.2	5.05
JMDD LP05	L. Tab.	1020	12.20	Ol	0.9	7.8	0.3	10.8	0.2	4.86
				Cpx	0.8	6.8	0.2	37.1	0.9	4.99
JMDD LP07	L. Tab.	1020	9.79	Ol	0.9	7.1	0.2	32.4	0.8	4.72
JMDD LP09	Benejado	490	13.45	Ol	0.9	8.8	0.3	7.2	0.2	4.93
				Cpx	0.8	8.1	0.3	44.1	1.1	5.02
JMDD LP10	U. Tab.	900	14.80	Ol	1.1	7.2	0.3	1.4	0.0	4.90
JMDD LP11	U. Tab.	570	8.92	Ol	1.3	6.6	0.3	6.0	0.1	4.71
JMDD LP14	CFE	120	11.46	Ol	0.7	7.3	0.2	28.2	0.8	4.90
LP96-66	U. Tab.	850	15.54	Ol	0.9	7.9	0.3	15.8	0.35	4.83
151LP69E[a]	1949 SJ	0	8.35	Ol	*0.8*	*7.8*	*0.2*	*30.2*	-	5.01
				Cpx	*0.9*	*7.6*	*0.2*	*57.3*	-	5.17
96LP46[a]	Tab.	700	11.40	Ol	*0.9*	*8.0*	*0.3*	*16.5*	-	4.90
				Cpx	*0.8*	*7.7*	*0.5*	*8.5*	-	5.42
93LP106[a]	Tab.	700	-	Ol	*0.9*	*8.9*	*0.7*	*2.7*	-	4.84
				Cpx	*0.9*	*7.9*	*4.7*	*0.7*	-	5.75
93LP107[a]	Tab.	700	15.50	Ol	*0.9*	*7.1*	*1.5*	*0.9*	-	5.35
				Cpx	*0.9*	*7.4*	*0.8*	*0.9*	-	5.49
93LP110[a]	Tab.	700	9.81	Ol	*0.9*	*6.8*	*0.5*	*11.6*	-	5.01
				Cpx	*0.5*	*7.2*	*1.5*	*3.1*	-	5.23
93LP113[a]	Tab.	700	8.27	Ol	*0.9*	*8.0*	*0.3*	*11.3*	-	4.76
				Cpx	*0.9*	*6.4*	*1.0*	*3.0*	-	5.16
93LP134[a]	Seamount	3000	10.30	Ol	*0.9*	*8.3*	*0.2*	*44.7*	-	4.89
				Cpx	*0.9*	*8.4*	*0.3*	*28.6*	-	5.39

1. as whole rock weight percentage
2. Measured $^3He/^4He$ (R/R_A) notation
3. He abundance in nccSTP/g
4. as per mille devation from SMOW

[a]- He abundance and isotope data from Hilton *et al.* (2000a)

4.5.3 $^{3}He/^{4}He$ isotope variations of phenocrysts

New analyses of He isotope ratio and [He] variations in phenocrysts of olivine and clinopyroxene from lavas from El Hierro and La Palma collected in 2002 are combined with published data for La Palma lavas (Hilton *et al.*, 2000a). New oxygen isotope analyses are presented for phenocrysts analysed for helium from the 2002 sample suite and for some lavas presented in Hilton *et al.* (2000a; Table 4.2).

4.5.3.1 He isotope ratio variation for La Palma and El Hierro

A $^{3}He/^{4}He$ ratio of $11.8R_A$ for olivine phenocrysts from recently erupted El Hierro lava JMDDEH01 is the highest measured $^{3}He/^{4}He$ ratio of any sample analysed in the Canary Islands (Table 4.2). Olivine phenocrysts from a seamount picrite have the highest measured $^{3}He/^{4}He$ ratio for a La Palma lava of $9.7R_A$. The measurement of $^{3}He/^{4}He$ $>8R_A$ in mafic phenocrysts confirms reports of elevated $^{3}He/^{4}He$ in geothermal fluid samples from the Taburiente caldera structure by Perez *et al.* (1996; $^{3}He/^{4}He = 9.7R_A$) and Hilton *et al.* (2000a; $^{3}He/^{4}He = 9.5R_A$). The highest $^{3}He/^{4}He$ phenocryst values for both islands and geothermal fluid values for La Palma lie just within to outside of the nominal adjacent Atlantic-MORB ratio of $8.1\pm1.4R_A$ (2σ, n=79 (Data from Graham *et al.* 1992b; Moreira and Allègre, 1999) and indicate that La Palma and El Hierro both sample a source with excess ^{3}He with respect to the DMM.

Previously, the highest reported $^{3}He/^{4}He$ for olivine phenocrysts from the Taburiente series were $8.7R_A$ (Graham *et al.*, 1996) and $8.9R_A$ (Hilton *et al.*, 2000a) and these values are similar to the $^{3}He/^{4}He$ ratio measured for olivines from the Benejado volcano ($8.8R_A$). Excluding the sample with the most elevated $^{3}He/^{4}He$ ratio (JMDDEH01), olivines from El Hierro possess a restricted range of $^{3}He/^{4}He$ ratios ($7.2\text{-}8.2R_A$; Figs. 4.9 and 4.10). This range exceeds the previous range quoted for El Hierro in Graham (2002) of $7.5\text{-}7.9R_A$. Excluding the most extreme $^{3}He/^{4}He$ ratio ($11.8R_A$), these olivine values lie within the MORB range with a tightly defined average of $7.7\pm0.5R_A$ (2σ, n=10). $^{3}He/^{4}He$ ratios for clinopyroxene from El Hierro possess more radiogenic values than their co-genetic olivines and range from $4.2\text{-}8.1R_A$ with an average of $6.6\pm2.7R_A$ (2σ, n=8). Including mafic phenocrysts reported in Hilton *et al.* (2000a), $^{3}He/^{4}He$ ratio ranges and averages for olivine and

clinopyroxene from La Palma are 6.6-9.7R_A; 7.7±1.4 (2σ, n=22) and 4.3-8.8R_A; 7.1±2.1 (2σ, n=16), respectively. The ranges and values reported here exceed ranges quoted for olivine and clinopyroxene in Hilton *et al.* (2000a) as well as variations quoted in Graham *et al.* (1996) and Graham (2002) for the islands of La Palma or El Hierro. A summary of $^3He/^4He$ variations in phenocrysts from La Palma and El Hierro lavas is provided in Table 4.3.

4.5.3.2 He isotope ratio and [He] between co-magmatic mineral pairs

Hilton *et al.* (2000a) showed that the majority (10 out of 11) of their co-magmatic olivine-clinopyroxene mineral pairs were, within error, in equilibrium with each other. New data for El Hierro and La Palma co-magmatic olivine-clinopyroxene mineral pairs shows that while in some lavas mineral pairs show isotopic equilibrium a large number (n=13) show $^3He/^4He$ ratio disequilibrium (Fig. 4.9). The observed $^3He/^4He$ relationships between mineral pairs from La Palma and El Hierro occur over a wide range of [He]. For co-genetic pairs in isotopic equilibrium this normally means $[He]_{clinopyroxene}>[He]_{olivine}$. For samples in disequilibrium, $[He]_{olivine} \geq [He]_{clinopyroxene}$ (Fig. 4.9; Fig. 4.10). The disequilibrium between mineral phases is highly unlikely to be the result of modification of mineral phases since crystallisation (Hilton *et al.*, 1993; Marty *et al.*, 1994; Hilton *et al.*, 1995) and lava eruption because of the young ages and 'freshness' of minerals within lavas exhibiting He-isotope disequilibrium. Instead, the lower measured $^3He/^4He$ ratio in clinopyroxene is more likely to reflect the different crystallisation order of the olivine (crystallised early) and clinopyroxene (crystallises later than olivine).

Variation of $^3He/^4He$ and [He] according to assigned formations reveals that the El Hierro PFE-CFE lavas possess mafic phenocrysts spanning the entire observed range of $^3He/^4He$ and [He] of all El Hierro lavas. For La Palma, Taburiente series lavas generally have the lowest [He] and most variable $^3He/^4He$ ratios whilst the most [He]-rich phenocrysts are preserved in the Cumbre Vieja PFE-CFE lavas (Fig. 4.9; 4.10). A summary of [He] variations in phenocrysts from La Palma and El Hierro lavas is provided in Table 4.3.

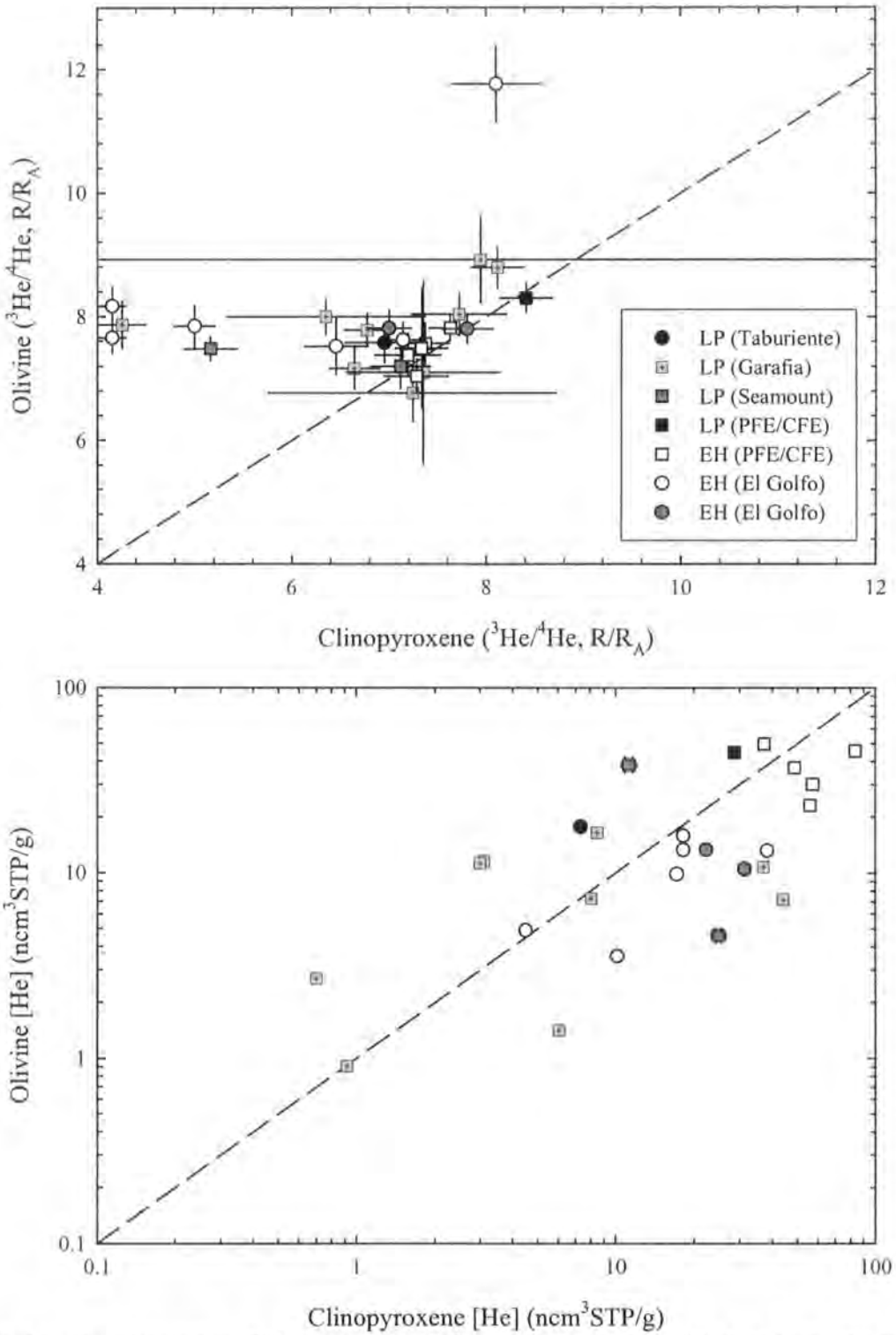

Fig. 4.9: He isotope ratios (R/R_A notation) as well as He concentrations ([He]) of co-genetic olivine and clinopyroxene for La Palma and El Hierro lavas (Table 4.2). The dashed diagonal lines represent He isotopic and concentration equilibrium in the compared mineral phases. In contrast to the study of Hilton et al. (2000a) 13 of the measured olivine-clinopyroxene pairs lie off the He isotope ratio equiline (within 2σ analytical error). Highest [He] are found in the La Palma Cumbre Vieja PFE/CFE lavas and the lowest [He] are found in Taburiente lavas. Data from this study and Hilton et al. (2000a).

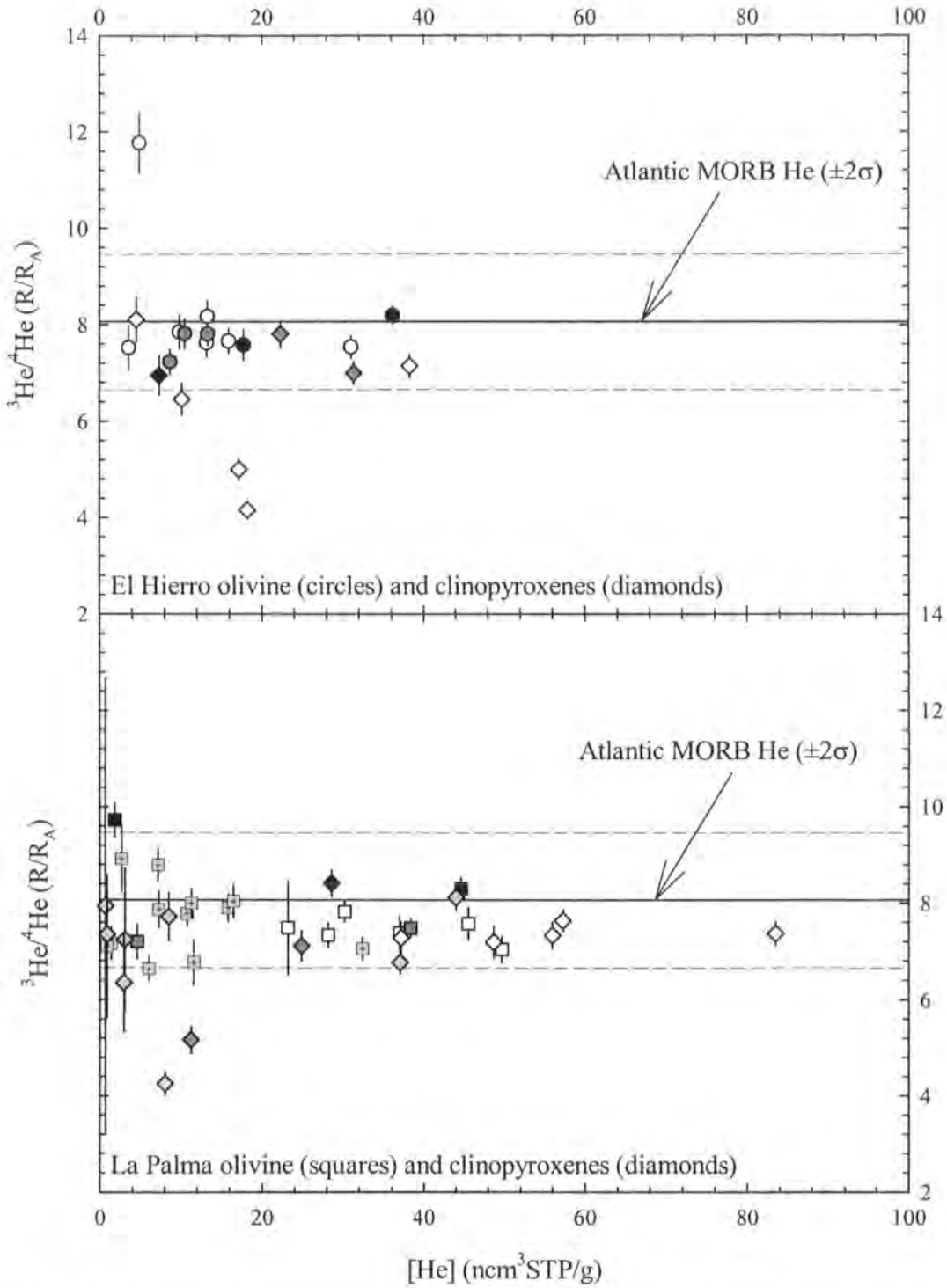

Fig. 4.10: Plot of He isotope ratios (R/R_A notation) versus He concentrations ([He]) for olivine and clinopyroxene for El Hierro (top panel) and La Palma lavas (Table 4.2). The average MORB $^3He/^4He$ ratio ($8.1\pm1.4R_A$ n=79, 2σ; Graham et al., 1992b; Moriera and Allègre, 1999 and is similar to the global MORB average of 8±2 (2σ) from Hilton and Porcelli (2003). Symbol colours and data sources are the same as Fig. 4.9 except that pyroxenes are shown as diamonds and olivines as squares.

4.5.3.3 Island-wide and Atlantic related He isotope variation

The combined He isotope database for La Palma (4.3-9.7R_A; this work, Vance *et al.*, 1989; Perez *et al.*, 1994; Graham *et al.*, 1996; Hilton *et al.*, 2000a) and El Hierro (4.2-11.8R_A; this work) straddles the range nominally associated with MORB mantle (8±1R_A). The more elevated $^3He/^4He$ ratios of La Palma and El Hierro lie above depleted MORB mantle estimates which are located distant from intraplate and arc-related magmatism (see Hilton *et al.*, 2000a and references therein; Hilton and Porcelli, 2003). The values of 9.7R_A and 11.8R_A from olivine phenocrysts from La Palma and El Hierro respectively, fall beyond the 95% confidence limit from the most recent estimates of the MORB mean (Allègre *et al.*, 1995; Hilton and Porcelli, 2003) meaning these samples are statistically outside of the population believed to represent DMM.

Plots of $^3He/^4He$ ratio variation for the Canary Islands (Fig. 4.11) and versus OIB located in the northern hemisphere Atlantic Ocean (see Hilton *et al.*, 2000a; Fig. 5) illustrate the variation with respect to MORB. Ignoring the obvious Icelandic magmatism influences north of 50°N (e.g., Chapter 2), the $^3He/^4He$ ratio for the MORB segments in this area is 8.1±1.4R_A (2σ, *n*=79). The maximum $^3He/^4He$ ratios for El Hierro and La Palma along with the Azores (11.3R_A; Moriera *et al.*, 1999) and the Cape Verde Islands (13.8R_A; Christensen *et al.*, 2001) lie conspicuously above the uppermost limit of the MORB range. It is also noteworthy that both the Azores (3.8-11.3R_A; Moriera *et al.*, 1999) and the Cape Verde Islands (3.2-13.8R_A; Christensen *et al.*, 2001) exhibit large variations in $^3He/^4He$ ratios similar to both El Hierro and La Palma.

Comparison with the five other main islands of the Canary Archipelago (Fig. 4.11) reveals an increase in the maximum $^3He/^4He$ ratio for each island from east to west, coincident with the formation ages of the islands. Following similarities between the Canaries and the Azores, as well as similar patterns of $^3He/^4He$ ratio variations for the Galapagos (Graham *et al.*, 1993; Kurz and Geist, 1999; Goff *et al.*, 2000) it seems logical to suggest that the western most Canary Islands sample a ^3He-enriched mantle source relative to DMM. For the more continent-ward islands this high $^3He/^4He$ source has either been obscured by degassing and contamination processes or these islands sample a mantle source with lower $^3He/^4He$; possibly the continental lithospheric mantle.

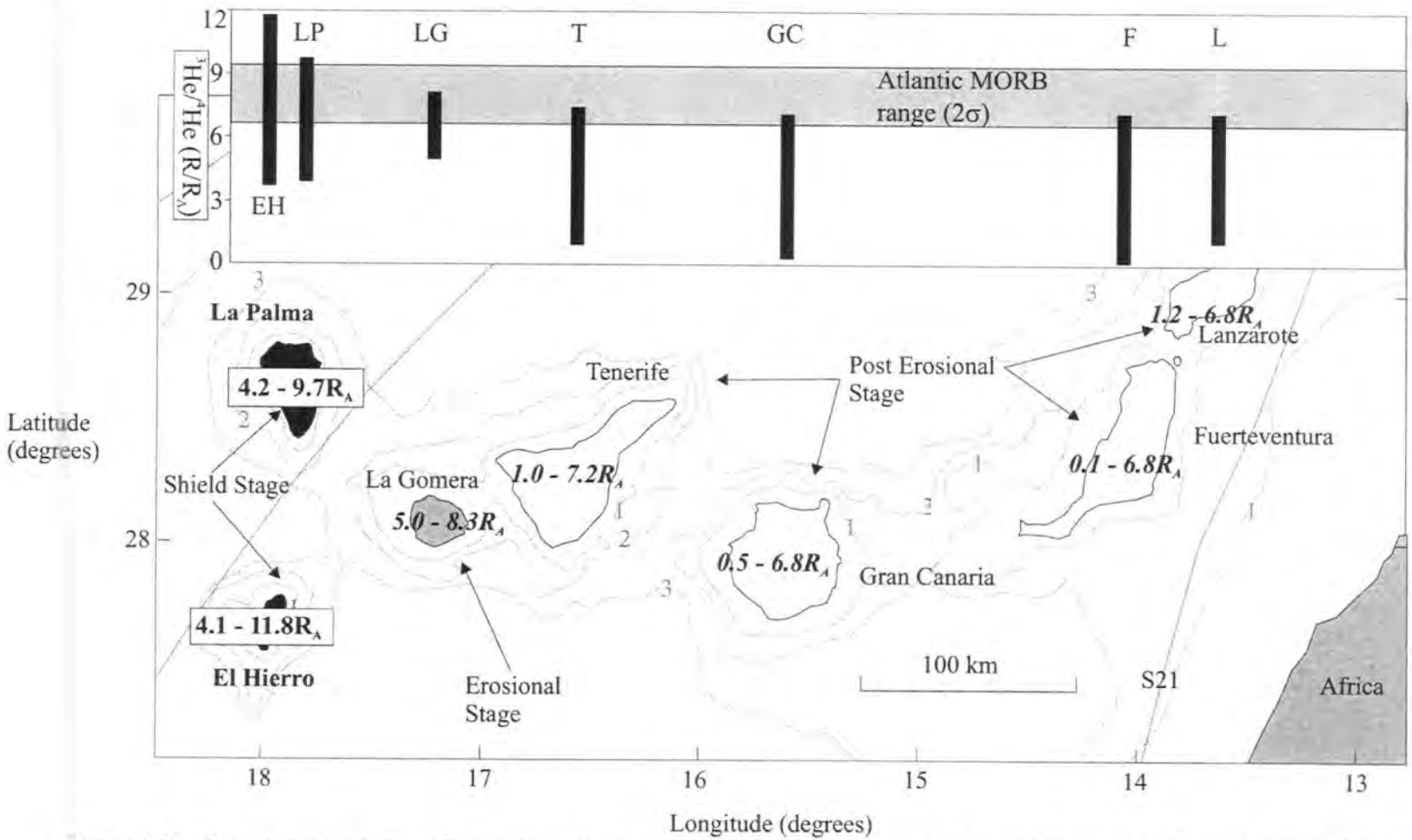

Figure 4.11: He isotopic variation (R/R_A notation) for the Canary Islands. Variation from El Hierro and La Palma from this study. Data for eastern Canary Islands from Vance et al. (1989); Perez-Torrado et al. (1994; 1996); Graham (1996; 2002). Data for phenocrysts and geothermal fluids used in compilations.

Table 4.3: Summary of O and He isotope variations in Western Canary Island lavas

		$\delta^{18}O_{Ol}$ (‰)	$\delta^{18}O_{Cpx}$ (‰)	$^{3}He/^{4}He_{Ol}$ [a]	$[He]_{Ol}$ [b]	$^{3}He/^{4}He_{Cpx}$ [a]	$[He]_{Cpx}$ [b]
La Palma	Range	4.71-5.35	4.99-5.75	9.7-6.6	1.4-44.7	8.8-4.3	0.7-57.3
	Av.[c]	4.89±0.15	5.22±0.27	7.8±0.8	15.1±13.7	6.9±1.2	18.1±19.7
	n	22	12	22	22	12	12
El Hierro	Range	5.04-5.34	5.27-5.59	11.8-7.2	3.6-36.2	8.1-4.2	4.5-38.3
	Av.[c]	5.16±0.09	5.42±0.09	8.1±1.2	14.8±9.7	6.6±1.4	18.7±11.7
	n	11	8	11	11	8	8

[a] - (R/R_A notation) [b] - ncm^3/g [c] - ±1SD

4.5.4 $^{18}O/^{16}O$ isotope variations of phenocrysts

Oxygen isotope ratios for olivine and clinopyroxene phenocrysts from El Hierro lavas range from +5.04‰ to +5.34‰ and +5.27‰ to +5.59‰ respectively (Table 4.2). El Hierro olivine and clinopyroxene averages are within analytical uncertainty of each other using the technique employed in this study at +5.16±0.18‰ (2σ, *n*=11) and +5.42±0.18‰ (2σ, *n*=8) respectively. Oxygen isotope ratios for olivine and clinopyroxene phenocrysts from La Palma range from +4.71‰ to +5.35‰ and +4.99‰ to +5.75‰ respectively (Table 4.2). The averages of olivine and clinopyroxene from La Palma lavas are outside analytical uncertainty of each other using the technique and are on average 0.20-0.25‰ lower than the averages of mafic phenocrysts from El Hierro at +4.89±0.30‰ (2σ, *n*=20) and +5.23±0.46‰ (1σ, *n*=12) respectively. A summary of $\delta^{18}O$ for phenocrysts from El Hierro and La Palma is provided in Table 4.3.

The oxygen isotope ratios of phenocrysts are controlled by the $\delta^{18}O_{melt}$ and the temperature of equilibration between the melt and crystal. The most rigorous method for testing whether minerals were in isotopic equilibrium with their melt is to examine co-magmatic mineral phase relationships (Macpherson, 1995), therefore olivine-clinopyroxene pairs have been plotted for El Hierro and La Palma lavas in Fig. 4.12. Considering that the bulk of mantle peridotite xenolith olivines and pyroxene pairs are likely to be in isotopic equilibrium with one another at high temperature (Mattey *et al.*, 1994), they can be considered proxies for the variation seen for mafic phenocryst pairs that have crystallised from melts at basaltic magma temperatures. This is because, despite recently recognised $^{87}Sr/^{86}Sr$ and $^{143}Nd/^{144}Nd$

disequilibrium between mantle peridotite mineral phases (D.G. Pearson pers. comm.) the oxygen isotope systematics of these pairs are likely to be in equilibrium in these high temperature peridotites. Evidence for isotope equilibrium for mantle peridotite mineral pairs is corroborated by theoretical data of Zheng (1990, Fig 4.12). Nearly all of the El Hierro and La Palma olivine-clinopyroxene pairs lie within the extrapolated field for isotopic equilibrium deduced from peridotite olivine-clinopyroxene mineral pairs (Fig. 4.12). The only exception to this is Taburiente series lava 93LP106 whose clinopyroxene (+5.75‰) is more ^{18}O-enriched than expected if in equilibrium with its olivine pairing (+4.82‰).

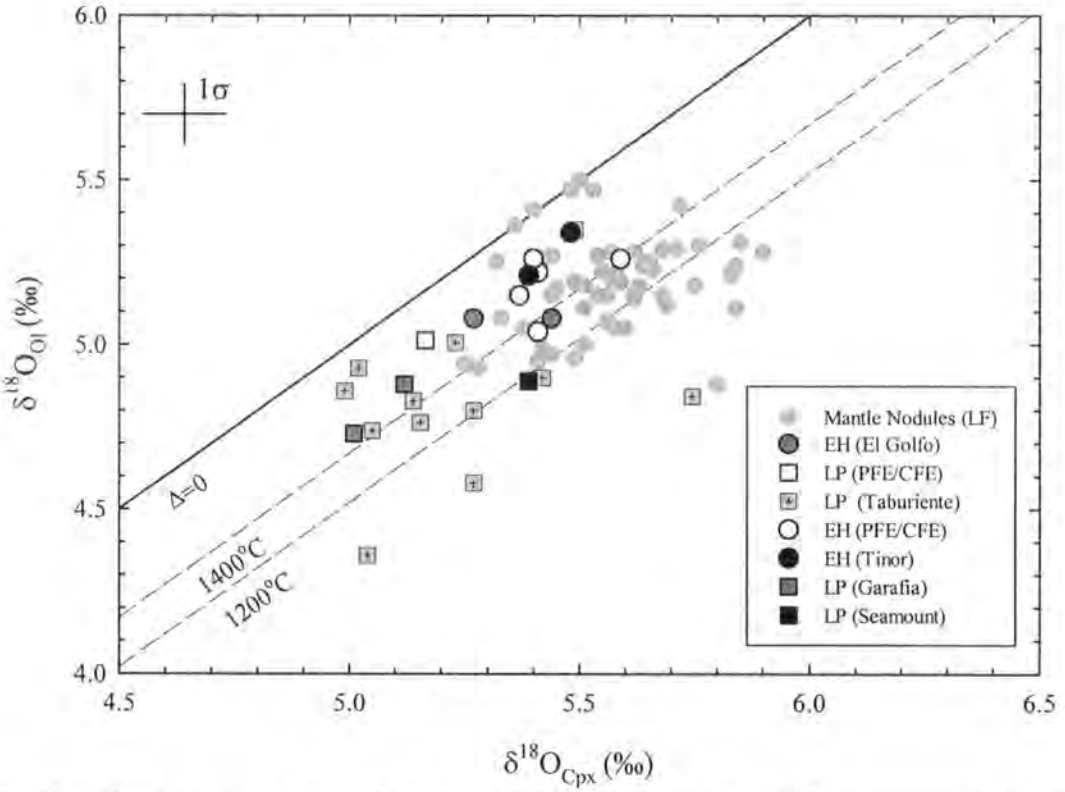

Fig. 4.12: $\delta^{18}O_{Cpx}$ versus $\delta^{18}O_{Ol}$ in La Palma and El Hierro lavas. Dashed lines represent $\Delta_{Cpx\text{-}Ol} = 0$ and isotherms are from Zheng (1990). Mantle nodules analysed by laser fluorination are from Mattey et al. (1994).

Comparison with other OIB lavas analysed for the $\delta^{18}O$ of their phenocrysts (Fig 4.13) reveals that whilst El Hierro samples lie within the field of mantle $\delta^{18}O$, La Palma lavas trend to more ^{18}O-depleted signatures. However, the relationship between MgO and $\delta^{18}O$ is not as extreme as in some Icelandic basalts (e.g., Chapter 2). Widom and Farquhar (2003) explained the low $\delta^{18}O$ of Sao Miguel in terms of

10% recycled oceanic crustal component in their source. Trends to low $\delta^{18}O$ for Hawaiian, Icelandic and Tristan lavas have been interpreted in terms of crustal contamination (Garcia *et al.*, 1998; Chapter 2; Harris *et al.*, 2000); however, some Icelandic lavas may also contain a small contribution of recycled oceanic material within their sources (Chapter 2). High $\delta^{18}O$ has been interpreted as addition of sediment to Hawaiian, Society Island and Gran Canaria magmatism (Eiler *et al.*, 1997; Thirlwall *et al.*, 1997) and also to different recycled oceanic components in the source of Icelandic lavas (Skovgaard *et al.*, 2001).

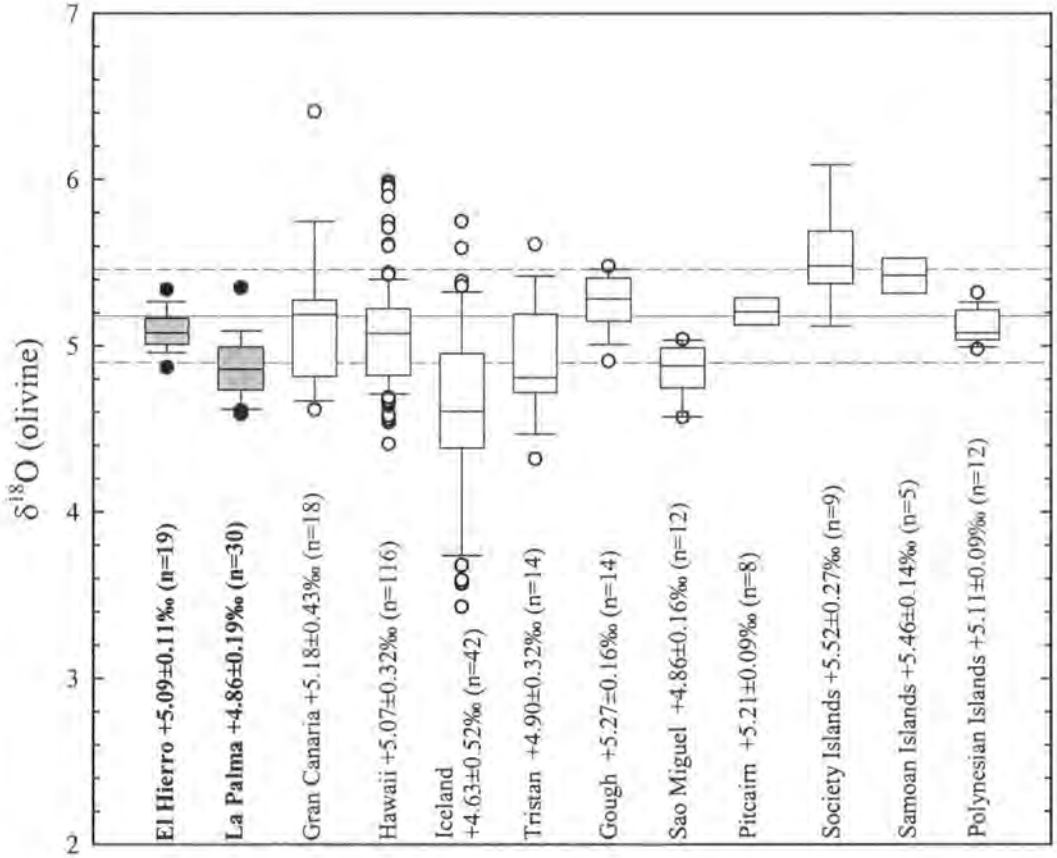

Fig. 4.13: Box plots for $\delta^{18}O$ (as olivine or equivalent) for OIB. El Hierro and La Palma $\delta^{18}O$ data from this study. Iceland data from Chapter 2. Published data from Thirlwall et al. (1997), Garcia et al. (1998), Eiler et al. (1995; 1996; 1997; 2000), Harris et al. (2000), Widom and Farquhar (2003). 1 standard deviation quoted. The box plot illustrates measures of distribution and dispersion of the chosen analyte. Box represents interquartile range (25^{th} to 75^{th} percentiles) and error bars represent 10^{th} and 90^{th} percentiles with outliers plotted as single points. Line within the box represents means of data.

4.5.5 Whole rock Sr, Nd and Pb isotope variations

Table 4.4: Sr, Nd and Pb isotope data for El Hierro and La Palma lavas

Sample	Age (Ka)	$^{87}Sr/^{86}Sr$	2σ	$^{143}Nd/^{144}Nd$	2σ	$^{206}Pb/^{204}Pb$	2σ	$^{207}Pb/^{204}Pb$	2σ	$^{208}Pb/^{204}Pb$	2σ
JMDD EH01	1	0.702960	4	0.512981	6	19.358	2	15.596	2	39.014	5
JMDD EH03	1030	0.702944	6	0.512965	3	19.392	4	15.571	3	39.023	8
JMDD EH07	1030	0.703205	4	0.512904	3	20.141	1	15.657	1	40.014	3
JMDD EH10	160	0.702974	5	0.512941	3	19.597	7	15.584	6	39.244	14
JMDD EH11	160	0.703004	4	0.512929	3	19.634	1	15.610	1	39.334	2
JMDD EH12	135	0.703024	5	0.512958	4	19.291	8	15.531	6	38.933	17
JMDD EH13	135	0.702997	5	0.512940	2	19.532	2	15.596	2	39.209	4
JMDD EH14	265	0.702968	5	0.512967	3	19.332	5	15.562	4	39.018	9
JMDD EH15	335	0.703028	5	0.512972	4	19.462	2	15.593	2	39.167	5
JMDD EH16	540	0.702856	5	0.513002	3	19.109	2	15.561	2	38.727	5
JMDD EH17	10	0.702974	4	0.512955	3	19.409	9	15.570	7	39.089	18
JMDD EH18	1	0.703128	5	0.512951	5	19.666	1	15.617	1	39.348	3
JMDD LP01	1440	0.703041	5	0.512914	4	19.759	1	15.627	1	39.704	2
JMDD LP02	1440	0.703134	5	0.512929	4	20.152	1	15.659	1	39.882	2
JMDD LP03	3000	0.703948	4	0.512965	17	19.698	7	15.596	6	39.292	14
JMDD LP04	1020	0.703075	4	0.512896	3	19.909	1	15.627	1	39.695	3
JMDD LP05	1020	0.703046	5	0.512920	3	19.720	1	15.619	1	39.468	3
JMDD LP07	1020	0.703047	6	0.512895	3	19.842	1	15.626	1	39.721	2
JMDD LP09	490	0.703026	4	0.512992	4	19.134	2	15.567	2	38.878	5
JMDD LP14	120	0.703101	4	0.512922	2	19.527	3	15.592	2	39.277	6
LP69A[a,b]	700	0.70311	-	0.51292	-	19.580	-	15.630	-	39.450	-
LP 113[b]	700	-	-	-	-	19.877	-	15.669	-	39.774	-
LP 107[b]	700	-	-	-	-	20.010	-	15.671	-	39.738	-
LP 110[b]	700	-	-	-	-	19.812	-	15.651	-	39.633	-
LP 134[b]	3000	-	-	-	-	19.942	-	15.671	-	39.808	-
LP 106[b]	700	-	-	-	-	19.938	-	15.653	-	39.764	-

[a] Data from Elliott (1991)

[b] Data from Marcantonio *et al.* (1995)

External reproducibility for Sr based on 17 runs of NBS987 during the analytical session in which samples were run is equal to 15ppm (2σ). All internal precision for samples are better than this (typically ≤5ppm). Samples were normalised to a value for NBS987 = 0.710250. External reproducibility of Nd based on 13 runs of J&M std was 27ppm (2σ). All internal precision on samples are better than this (typically <6ppm). Samples are normalised to a value = 0.511111. External reproducibility for NBS981 is quoted in Appendix C. Internal precisions for samples are generally equal to the external reproducibility.

Sr, Nd and Pb isotope data for El Hierro and La Palma samples are presented in Table 4.4. Unleached $^{87}Sr/^{86}Sr$ for El Hierro lavas ranges from 0.70286 to 0.70321 and for La Palma lavas range from 0.70303 to 0.70395. Sample JMDDLP03 has the most radiogenic $^{87}Sr/^{86}Sr$ of all lavas analysed (0.70395) and also possesses a negative Sr anomaly (Fig. 4.8). The Sr isotope value of this picrite is similar to a gabbro xenolith from the 1949 eruption on La Palma (Hoernle, 1998) whose $^{87}Sr/^{86}Sr$ signature is the result of significant seawater interaction. $^{143}Nd/^{144}Nd$ for El Hierro lavas ranges from 0.51290-0.51300 (εNd = +5.2 to +7.1) and for La Palma lavas ranges from 0.51290-0.51299 (εNd = +5.0 to +6.9). In $^{87}Sr/^{86}Sr$-$^{143}Nd/^{144}Nd$

space (Fig. 4.14) El Hierro lavas form a negative array with the majority (n=10) of lavas plotting within the field for mantle xenoliths from El Hierro (Whitehouse and Neumann, 1995). La Palma lavas have a more restricted range of $^{87}Sr/^{86}Sr$ that is generally more radiogenic than El Hierro lavas and apart from JMDDLP03, plot within the range of published Sr-Nd isotope data for La Palma.

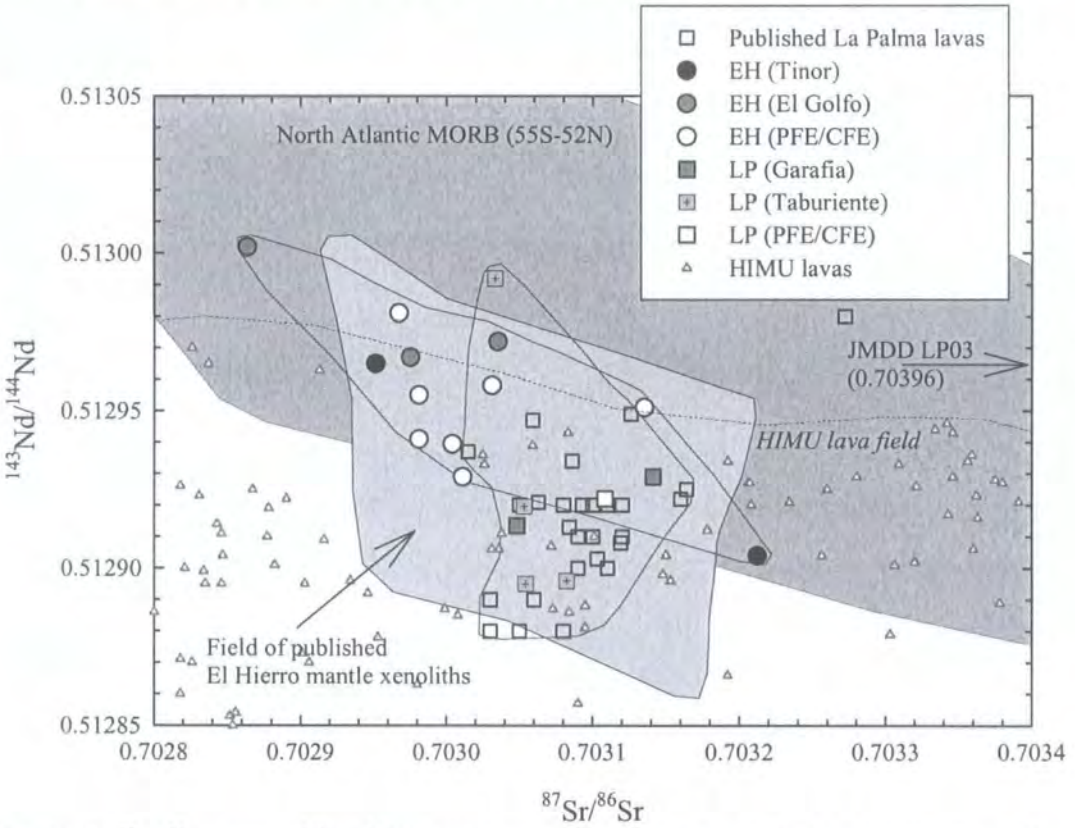

Fig. 4.14: $^{87}Sr/^{86}Sr$ versus $^{143}Nd/^{144}Nd$ isotope ratio diagram for La Palma and El Hierro lavas. Published data for El Hierro mantle xenoliths and La Palma from Whitehouse and Neumann (1995) and Ovchinnikova et al. (1995). Data for HIMU and North Atlantic MORB listed in Fig. 3.9.

Pb isotope data for La Palma and El Hierro lavas are plotted in Fig. 4.15. Data fall along the NHRL (Hart, 1984) with $\Delta^{7/4}$ = +0.6 to -5.2 and +0.2 to -3.0 and $\Delta^{8/4}$ = +1.8 to -7.6 and +18.8 to -15.0 for El Hierro and La Palma lavas, respectively. El Hierro and La Palma lavas have similar extremes of radiogenic and unradiogenic Pb. The least radiogenic Pb within each island are defined by JMDDLP09 and JMDDEH16 ($^{206}Pb/^{204}Pb$ =19.134 and 19.109 respectively). The most radiogenic Pb within each island are possessed by JMDDLP02 and JMDDEH07 ($^{206}Pb/^{204}Pb$ =20.152 to 20.141 respectively). These extremes span almost the entire range of measured Pb isotope ratios in the Canary Islands ($^{206}Pb/^{204}Pb$=18.8 to 20.2: Sun, 1980; Hoernle *et al.,* 1991; Marcantonio *et al.,* 1995; Thirlwall *et al.,* 1997). Despite similar extreme values, the overall characteristics in Pb isotope space for the two

islands are that El Hierro lavas generally have less radiogenic Pb isotope compositions than La Palma lavas. The range and means of Sr, Nd and Pb isotopic compositions for La Palma and El Hierro lavas analysed in this study are summarised in Table 4.6.

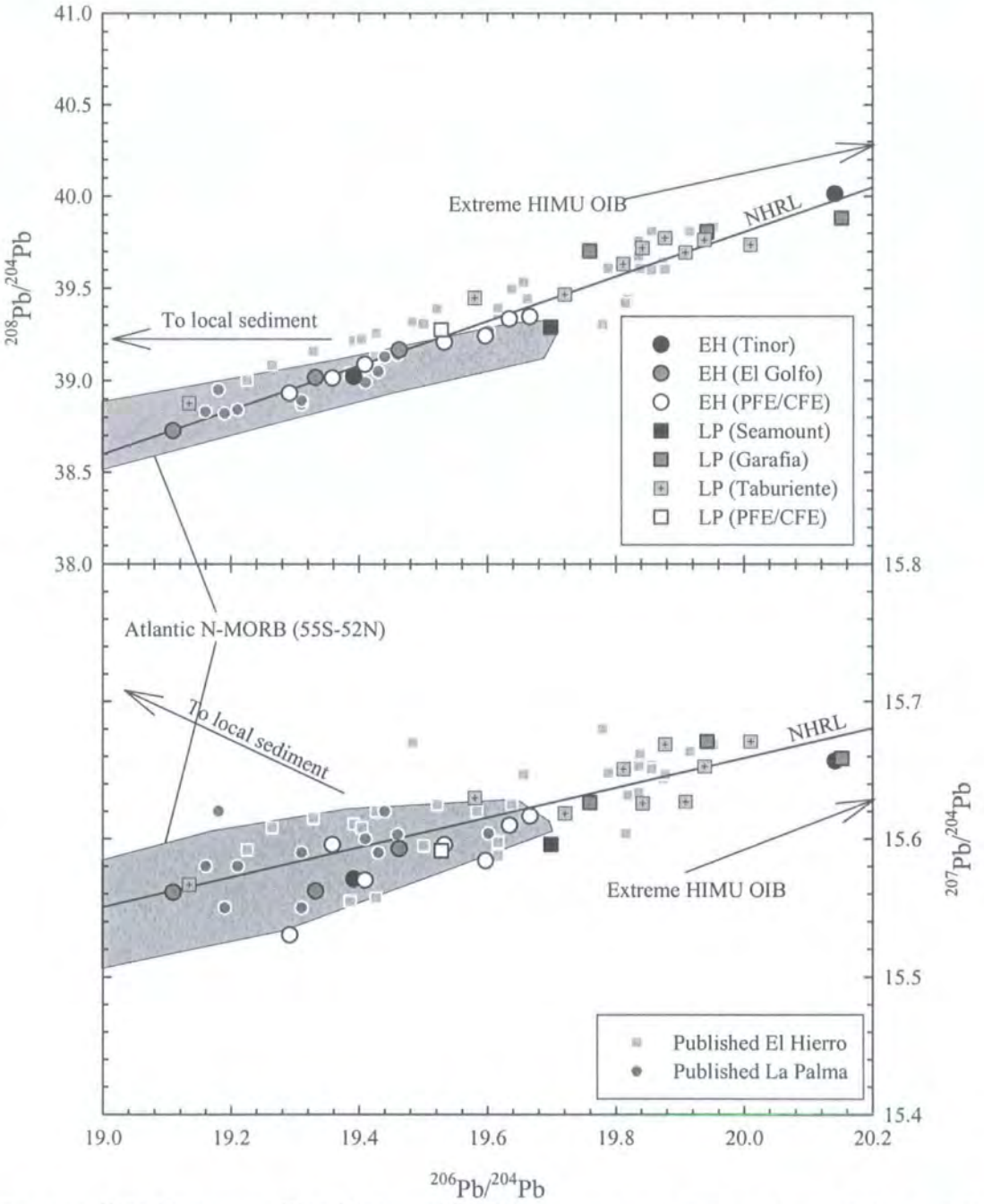

Fig. 4.15: $^{206}Pb/^{204}Pb$ versus $^{208}Pb/^{204}Pb$ and $^{207}Pb/^{204}Pb$ isotope ratio diagrams for La Palma and El Hierro lavas. NHRL = Northern Hemisphere Reference Line after Hart (1984). Published La Palma and El Hierro data are from Sun (1980), Elliott (1991), Whitehouse and Neumann (1995) and Marcantonio et al. (1995). Data for Atlantic MORB is from the Pet Database. Vector to sediment based upon data from Sun (1980) and Hoernle et al. (1991). 2σ errors are smaller than errors.

4.5.6 Whole rock Re-Os isotope variations

Table 4.5: Re and Os concentrations and Os isotope results for El Hierro and La Palma lavas

Sample	Series	Age (Ka)	Re (ppb)	Os (ppb)	$^{187}Re/^{188}Os$[a]	$^{187}Os/^{188}Os_m$[b]	±	1σ	$\gamma Os_{(t)}$[c]
El Hierro, Western Canary Islands, Spain									
JMDD EH01	PFE	<1	0.473	0.065	35.37	0.14579	±	15	14.3
	Duplicate		0.486	0.073	31.97	0.14640	±	5	14.8
JMDD EH03	Tiñor	1030	0.287	0.133	10.43	0.16760	±	48	31.4
JMDD EH07	Tiñor	1030	0.274	0.095	14.02	0.16700	±	10	30.9
JMDD EH10	CFE	160	0.188	0.184	4.93	0.14811	±	5	16.1
JMDD EH11	CFE	160	0.337	0.055	29.58	0.15202	±	7	19.2
JMDD EH12	CFE	135	0.105	0.141	3.63	0.17502	±	6	37.2
	Duplicate		0.089	0.088	4.93	0.15702	±	5	23.1
JMDD EH13	CFE	135	0.251	0.058	20.92	0.16434	±	7	28.8
JMDD EH14	UEG	265	0.462	0.024	94.30	0.15396	±	7	20.7
JMDD EH15	UEG	335	0.121	0.158	3.69	0.15895	±	4	24.6
	Duplicate		0.138	0.176	3.79	0.15662	±	25	22.8
JMDD EH16	LEG	540	0.226	0.089	12.32	0.15693	±	5	23.0
	Duplicate		0.185	0.097	9.24	0.15621	±	6	22.5
JMDD EH17	PFE	<10	0.505	0.041	59.84	0.14715	±	71	15.3
	Duplicate		0.159	0.039	19.81	0.13914	±	25	9.1
JMDD EH18	PFE	<1	0.482	0.099	23.49	0.15301	±	5	19.9
La Palma, Western Canary Islands, Spain									
JMDD LP01	Garafia	1440	0.188	0.143	6.37	0.14327	±	8	12.3
	Duplicate		0.185	0.103	8.65	0.14456	±	6	13.3
JMDD LP02	Garafia	1440	0.478	0.060	38.39	0.14875	±	7	16.6
JMDD LP03	Seamount	3000	0.272	0.285	4.61	0.14405	±	3	12.9
JMDD LP04	L. Tab	1020	0.455	0.032	67.67	0.14788	±	17	15.9
JMDD LP05	L. Tab	1020	0.461	0.023	96.55	0.13783	±	57	8.0
JMDD LP07	L. Tab	1020	0.377	0.052	35.24	0.14898	±	8	16.8
JMDD LP09	Benejado	490	0.067	0.157	2.05	0.14582	±	6	14.3
JMDD LP14	CFE	120	0.473	0.066	34.36	0.14162	±	24	11.0
LP 96-14	U. Tab	550	0.291	0.070	20.12	0.15480	±	17	21.3
LP 96-22	U. Tab	550	0.416	0.070	28.80	0.14486	±	13	13.6
LP 96-83	U. Tab	550	0.495	0.096	24.84	0.14172	±	49	11.1
LP 96-41	L. Tab	850	0.368	0.308	5.77	0.14387	±	9	12.8
LP 96-46	L. Tab	850	0.267	0.083	15.51	0.14423	±	94	13.1
LP 96-48	L. Tab	850	0.263	0.053	24.07	0.14834	±	17	16.3
LP 96-63	L. Tab	850	0.489	0.207	11.39	0.14601	±	10	14.5
LP 96-66	L. Tab	850	0.231	0.209	5.35	0.14380	±	31	12.7
	Duplicate		0.216	0.209	4.99	0.14214	±	15	11.4

[a]The 2σ error in this ratio is 0.37% (Re) and 0.125% (Os) and is a function of spike uncertainty however this does not account for non-stoichiometry of the Os spike calibration (Appendix C)

[b] 1σ error of the internal precision of measurement generally better than 2σ of UMCP std data at similar run intensities (Appendix C).

[c]Age corrected γOs values. γOs is the percentage difference between the age corrected $^{187}Os/^{188}Os$ ratio and the 187Os/188Os ratio of a chondritic mantle where the present-day chondritic mantle has $^{187}Os/^{188}Os$=0.12757 and $^{187}Re/^{188}Os$=0.3972 (Walker *et al.*, 1989)

New Re-Os isotope data for El Hierro and La Palma are presented in Table 4.5. Re concentrations range from 0.089-0.505ppb and 0.044-0.719ppb for 14 El Hierro and 23 La Palma lavas respectively. Re generally correlates positively with TiO_2 and

negatively with MgO for both islands although El Hierro lavas have generally have higher TiO_2 for a given Re abundance (Fig. 4.16).

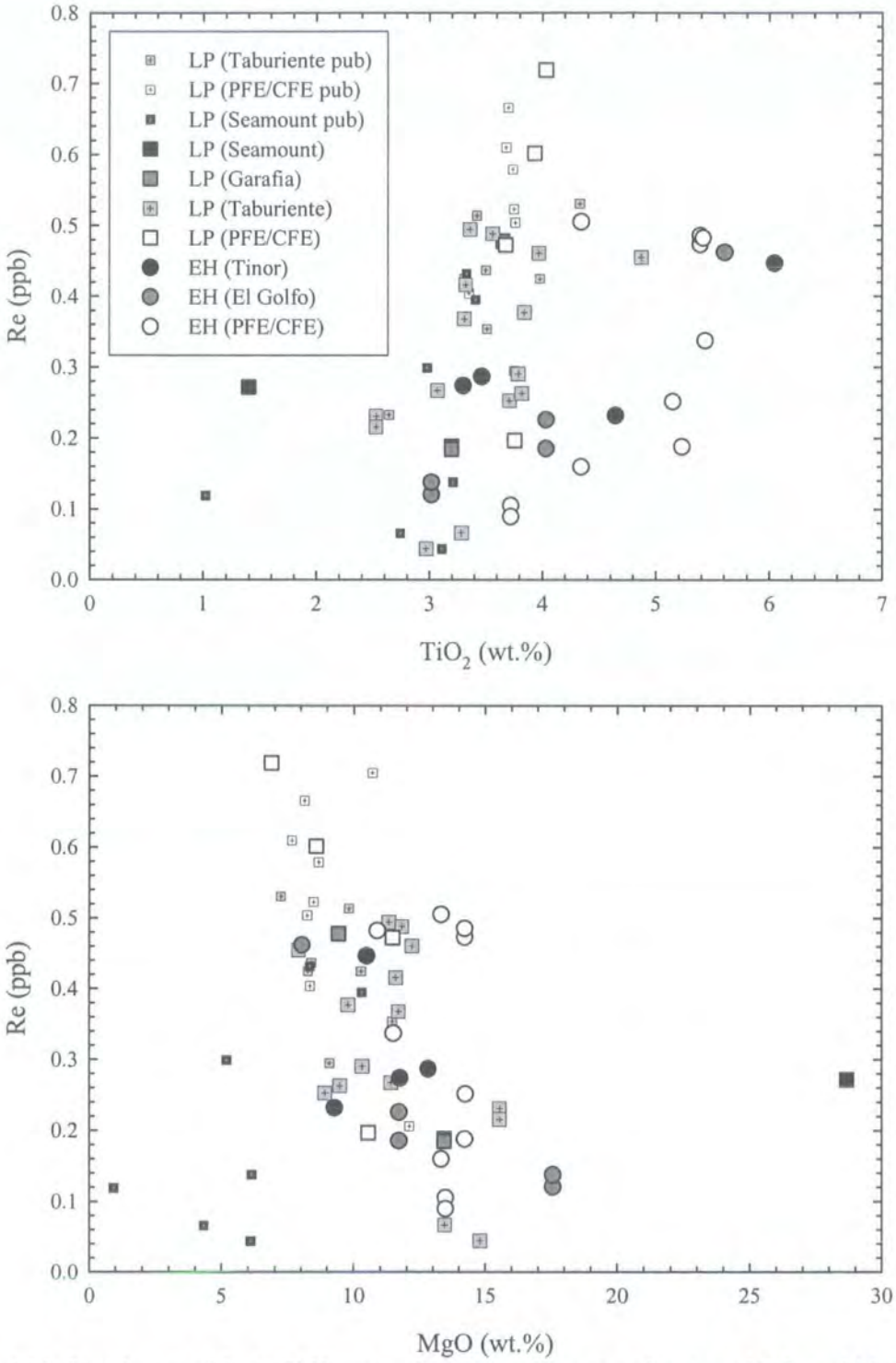

Fig. 4.16: Distribution of Re in El Hierro and La Palma lavas as a function of TiO_2 and MgO. Data from table 4.3 and 4.4, Marcantonio et al. (1995) and Widom et al. (1999). Note different correlations for La Palma and El Hierro lavas in Re vs. TiO_2 with El Hierro lavas trending to lower Re and higher TiO_2 concentrations.

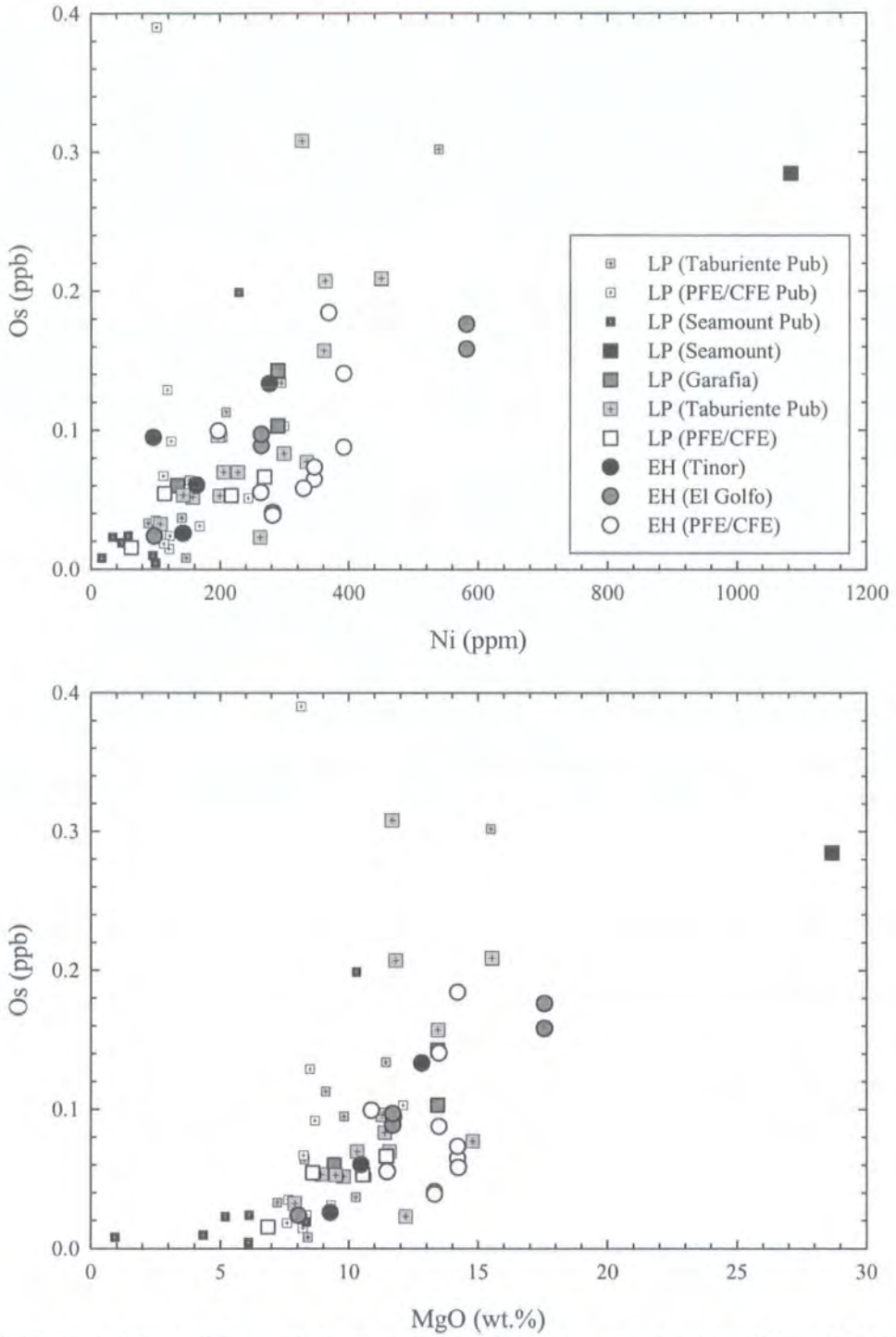

Fig. 4.17: Distribution of Os in El Hierro and La Palma lavas as a function of Ni and MgO. Data from table 4.3 and 4.4, Marcantonio et al. (1995) and Widom et al. (1999).

Os abundances range from 0.024-0.176ppb and 0.016 to 0.308ppb for studied El Hierro and La Palma lavas respectively. The western Canary Island lavas exhibit strong positive correlations between MgO, Ni and Os contents (Fig 4.17). The

highest Os concentrations were measured in the Seamount picrite and a Taburiente series lava from Barranco de Fagundo. Published values for La Palma lava Os concentrations by Marcantonio *et al.* (1995) are generally higher for a given MgO than La Palma lavas analysed in this study. The new data presented here also defines tighter trends than previously published Os abundance data.

El Hierro and La Palma lavas are compared for Re/Os* and Os* with continental intraplate magmatism (CFB, Komatiites, CIAV) and lavas erupted at plate boundaries (MORB) in Fig. 4.18. El Hierro and La Palma lavas lie within the lower range of CFB and CIAV lava Re/Os*-Os* fields with Re/Os* consistently in excess of chondritic.

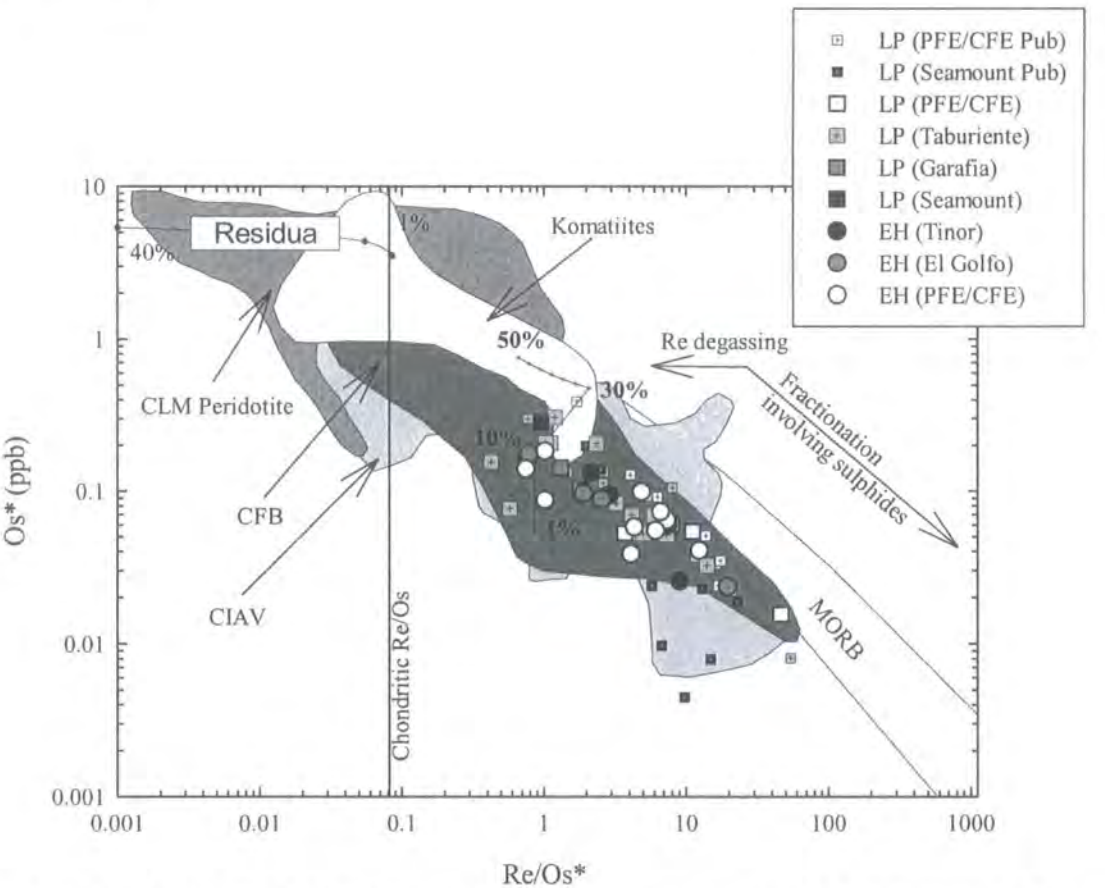

Fig. 4.18: Re/Os vs. Os* for El Hierro and La Palma lavas compared with CFB, Komatiites, MORB, CLM peridotites and CIAV (Data compiled from Shirey and Walker, 1998 and references therein). *Os = common Os. The partial melting trend (up to 50% melt interval) is for mantle with CI-chondrite Re/Os ratios and containing 3.5ppb Os. The model assumes that residual sulphides control the Re and Os concentrations up to their exhaustion point at 30% melting (after Roy-Barman and Allègre, 1995). Complementary depletion trends for CLM peridotites are also shown as are vectors for sulphide fractionation and Re volatility during shallow volcanic degassing. HIMU component is estimated from Hauri and Hart, 1993.*

Six samples were analysed in duplicate to investigate the effects of 'nuggeting' in La Palma and El Hierro lavas. OIB lavas have been shown to be affected by nuggeting,

possibly through micro-sulphides that are heterogeneously distributed during powdering (e.g., Reisberg *et al.*, 1993; Widom *et al.*, 1999). Most duplicates are in close agreement for both Re and Os concentrations and Os isotope analyses and agree within 10% for abundance measurements and <5% for isotopic measurements (Table 4.5). In some circumstances isotopic and abundance reproducibility for Os between replicates was up to 11% and 60% respectively. For example JMDDEH12, for which the most radiogenic $^{187}Os/^{188}Os$ was measured, reproduced lower $^{187}Os/^{188}Os$ with lower Os concentrations. In light of the fact that blank contributions were systematically low for both filament material and total procedures (Appendix C), this is considered to reflect the 'nugget effect'. Such variations reflect the effect of micro-inclusions within the whole rock which are ineffectively homogenised during powdering of the sample and result in heterogeneous distribution of siderophile elements and radiogenic and unradiogenic $^{187}Os/^{188}Os$. A good example of this effect can be seen in the Rhode Island MORB standard EN026 10D-3 (Appendix C) for which a sub-chondritic initial is derived. In the case of La Palma and El Hierro lavas, aliquots with higher Os tend to have more radiogenic $^{187}Os/^{188}Os$.

$^{187}Os/^{188}Os$ ratios of La Palma lavas range from 0.1378 to 0.1548 with an average $^{187}Os/^{188}Os$ for all studied lavas of 0.1449±0.0072 (2σ, n=23). The two extreme compositions were measured in basanite lavas with >50ppt Os; the highest Os samples (>120ppt) yield $^{187}Os/^{188}Os$ = 0.14214 to 0.14601. These results are similar to values previously published using NiS fire-assay for mafic (>8% MgO and excluding samples with Os <50ppt) lavas by Marcantonio *et al.* (1995; 0.139-0.151) but do not extend to the extremely radiogenic $^{187}Os/^{188}Os$ ratio of 0.175 for sample LP-4 using Carius tube-ID methods by Widom *et al.* (1999). It should be noted that sample LP-4 of Widom *et al.* (1999; 51ppt) only just lies within the 50ppt Os cut-off value for lavas thought to be resistant to crustal assimilation effects. $^{187}Os/^{188}Os$ ratios of El Hierro lavas show a large range from 0.1458 to 0.1750, extending the limited range of $^{187}Os/^{188}Os$ measured for 3 El Hierro lavas by Widom *et al.* (1999; 0.144-0.148), and yielding an average $^{187}Os/^{188}Os$ of 0.1559±0.0168 (1σ, n=17). The highest Os samples (>120ppt) yield some of the most radiogenic $^{187}Os/^{188}Os$ measured in El Hierro (0.14811-0.17502). All of the samples analysed in this study have supra-chondritic γOs (La Palma γOs = +8.0 to +21.3; El Hierro γOs = +14.3 to

+37.2) and have high Os (>50ppt) abundance basalts with radiogenic $^{187}Os/^{188}Os$. The range and means of $^{187}Os/^{188}Os$ isotope ratios for La Palma and El Hierro lavas analysed in this study are summarised in Table 4.6.

Table 4.6: Summary of Sr, Nd, Pb and Os isotope variations in Western Canary Island lavas

		$^{87}Sr/^{86}Sr$	$^{143}Nd/^{144}Nd$	$^{206}Pb/^{204}Pb$	$^{207}Pb/^{204}Pb$	$^{208}Pb/^{204}Pb$	$^{187}Os/^{188}Os$
La Palma	Range	0.70304-0.70314	0.51299-0.51290	19.134-20.152	15.567-15.671	38.878-39.882	0.1378-0.1548
	Av.[a]	0.70307±4	0.51293±3	19.78±25	15.63±3	39.58±28	0.1451±37
	n	6	7	14	14	14	18
El Hierro	Range	0.70287-0.70322	0.51300-0.51290	19.109-20.141	15.531-15.657	38.727-40.014	0.1391-0.1750
	Av.[a]	0.70301±9	0.51296±3	19.49±26	15.59±3	39.17±32	0.1556±91
	n	12	12	12	12	12	17

[a] - ±1SD

This study provides the first comprehensive Re-Os data for the entire lava stratigraphies of La Palma and El Hierro and includes new data on a picrite from the La Palma Seamount Series, two ankaramites from the Garafia series, upper and lower Taburiente series lavas and for El Hierro, Tiñor, El Golfo and CFE/PFE lavas. Age constraints provided by island-wide and detailed stratigraphic ^{14}C, K/Ar and $^{40}Ar/^{39}Ar$ methodologies (Guillou *et al.*, 1996; 1998; 2001, Szérémata *et al.*, 1999; Carracedo *et al.*, 2001) allow tight temporal constraints on the spatially well-constrained samples collected in April 2002. In Fig. 4.19 $^{187}Os/^{188}Os$ of La Palma and El Hierro samples are plotted against their relative position in the island's stratigraphies. There is no systematic variation in $^{187}Os/^{188}Os$ with age for La Palma lavas. However younger Cumbre Vieja and Upper Taburiente lavas both have greater ranges in $^{187}Os/^{188}Os$ than the Lower Taburiente, Garafia or Seamount series lavas (discounting obviously contaminated low Os pillow lavas measured by Marcantonio *et al.* 1995). The most elevated $^{187}Os/^{188}Os$ measured for Cumbre Vieja and Upper Taburiente series lavas were reported for low Os lavas in Widom *et al.*, 1999 ($^{187}Os/^{188}Os$ = 0.174) and Marcantonio *et al.*, 1995 ($^{187}Os/^{188}Os$ = 0.168) respectively.

A striking feature of the El Hierro $^{187}Os/^{188}Os$ variation is the systematic decrease in $^{187}Os/^{188}Os$ with time. So far as the author is aware, this is the first time that such systematic variation with time for Os has been observed for any ocean island. There

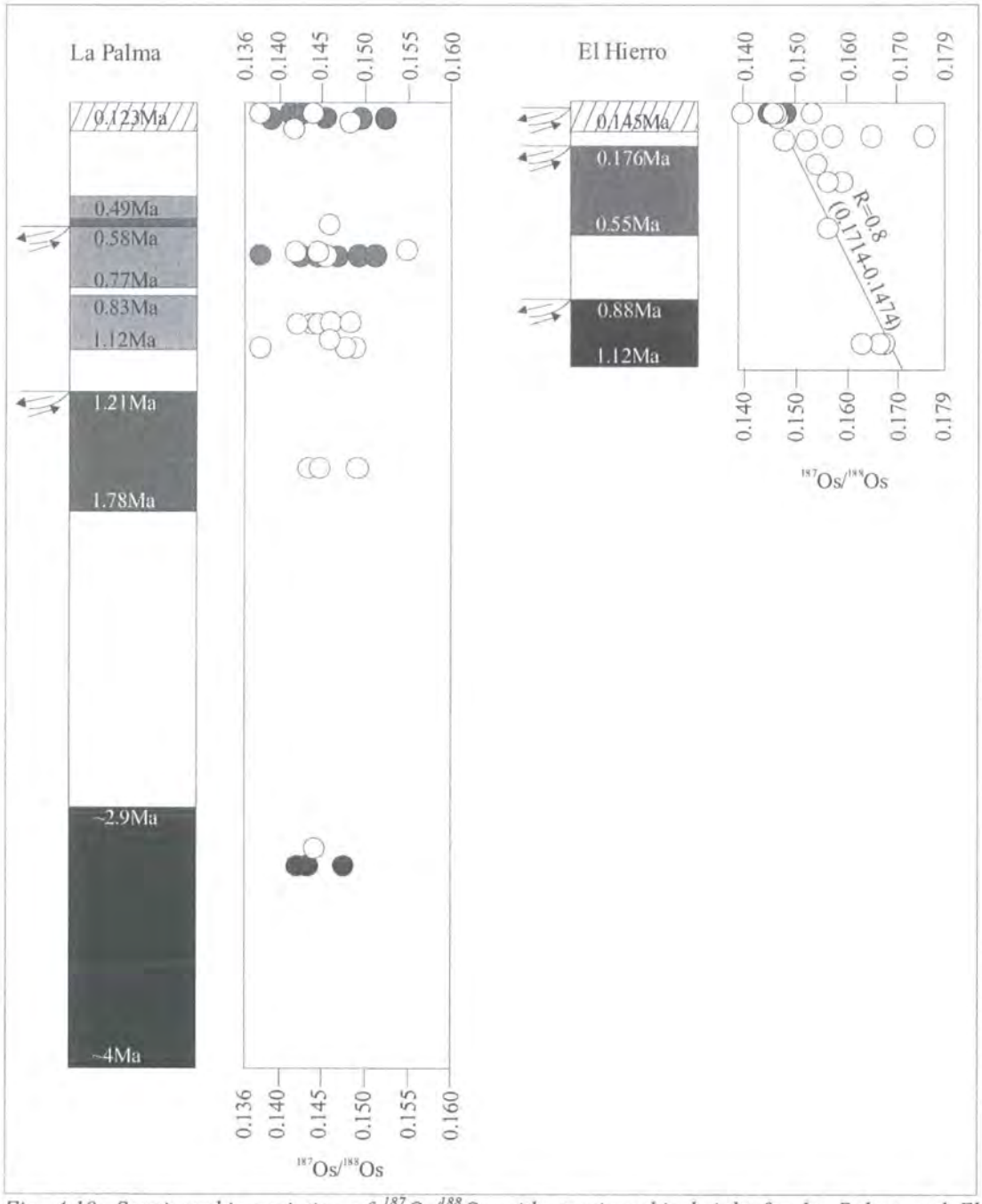

Fig. 4.19: Stratigraphic variation of $^{187}Os/^{188}Os$ with stratigraphic height for La Palma and El Hierro. Grey and black circles from Marcantonio et al. (1995) and Widom et al. (1999). White circles from this study.

is a trend from more to less radiogenic $^{187}Os/^{188}Os$ for El Hierro lavas with relative stratigraphic position and time, a deviation equal to ~15% reduction in radiogenic Os in the space of ~1Ma (Fig. 4.19). This trend is only disrupted by CFE lavas JMDD EH12 and EH13 which lie close to the age of the massive El Golfo collapse event. This observation indicates for the first time in a single ocean island that $^{187}Os/^{188}Os$ can vary greatly (15% relative to chondrite) in an ocean island building interval. El

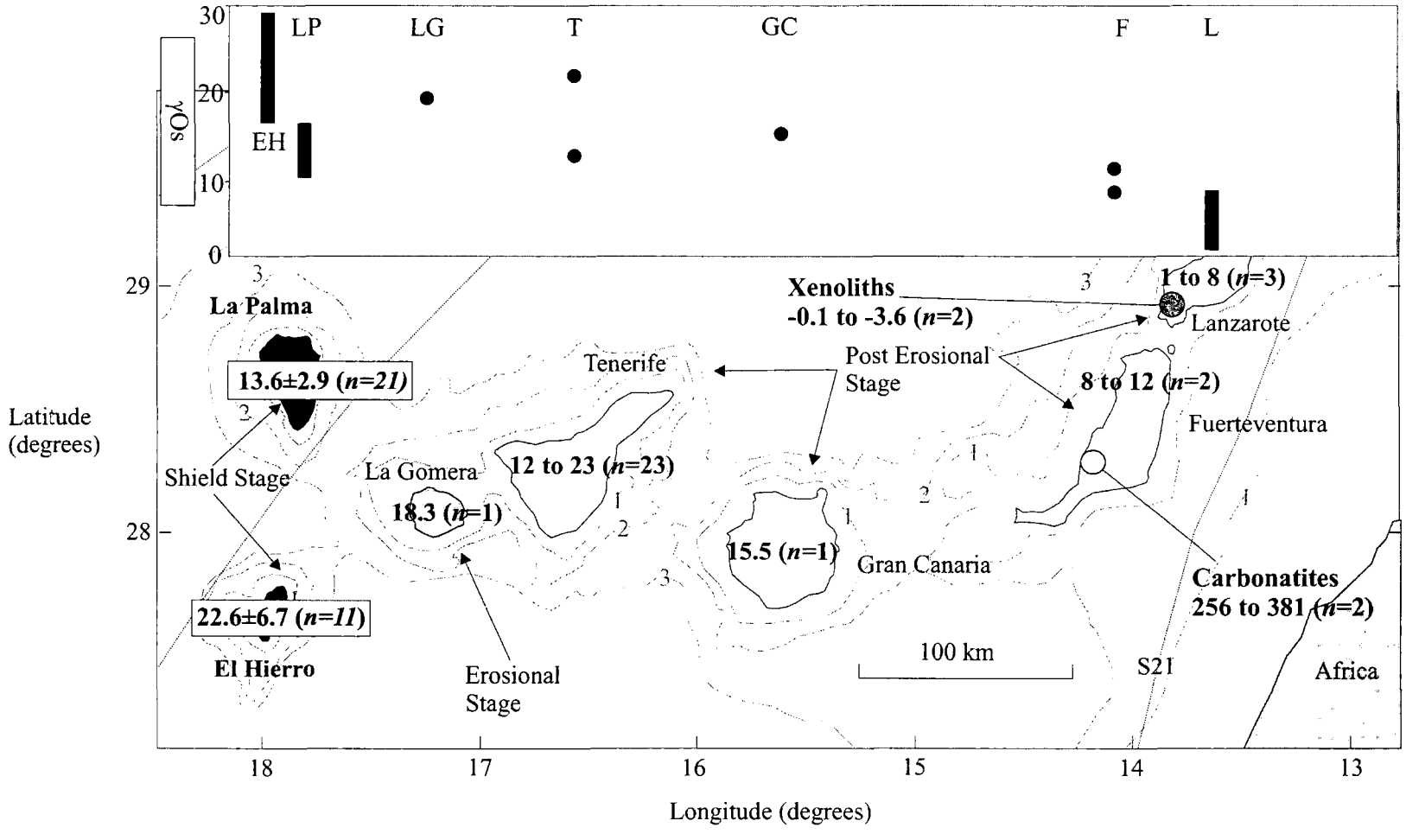

Figure 4.20: Os isotopic variation (γOs notation) for the Canary Islands. Variation from El Hierro and La Palma from this study. Data for eastern Canary Islands from Widom et al. (1999). One standard deviation quoted for El Hierro and La Palma variations.

Hierro also possess the most radiogenic $^{187}Os/^{188}Os$ for mafic lavas (>8 Wt% MgO, >50ppt Os) of all the Canary Islands (Fig. 4.20) and currently of all OIB globally (Fig. 4.21). El Hierro has an average $^{187}Os/^{188}Os$ greatly in excess of all Atlantic OIB and is also greatly in excess of EM-type Islands (Savaii, Pitcairn), HIMU Islands (Mangaia, Tubuaii) or Hawaiian volcanoes. It is also apparent from Fig. 4.20 that, like $^{3}He/^{4}He$, a systematic variation from relatively unradiogenic $^{187}Os/^{188}Os$ to $^{187}Os/^{188}Os$ greatly in excess of chondritic is measured from east to west in the Canary Islands.

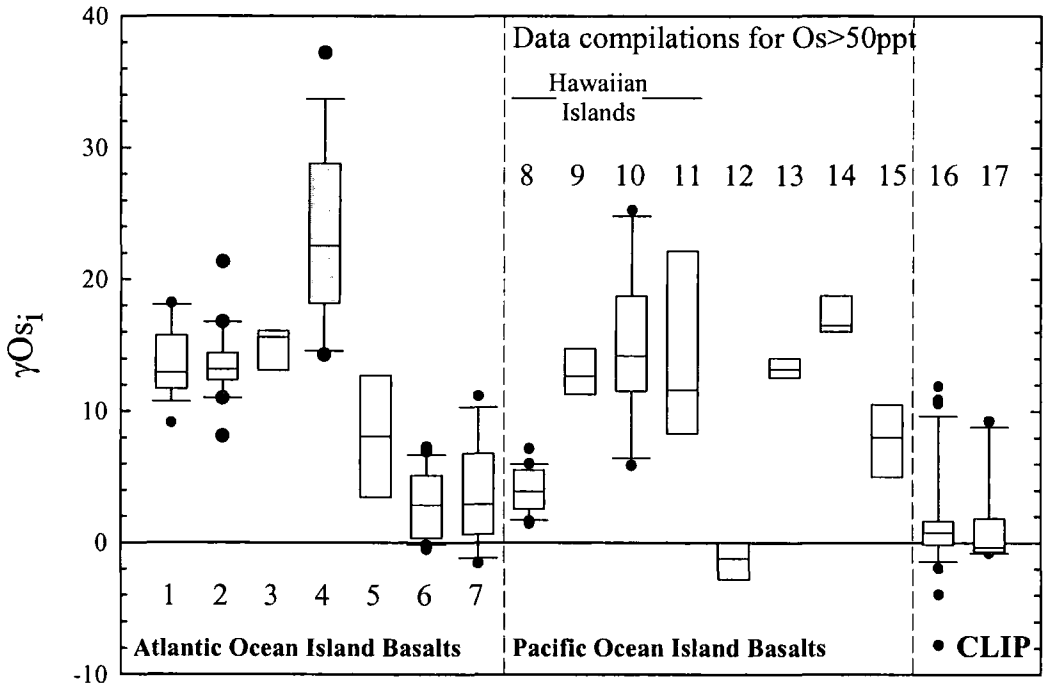

Fig. 4.21: Box plots for $^{187}Os/^{188}Os$ for OIB. There is no correlation with underlying oceanic lithospheric age. El Hierro and La Palma data from this study, Marcantonio et al. (1995) and Widom et al. (1999). Published data from Walker et al. (2001), Schaefer et al. (2002), Widom and Shirey (1996), Smit (2001), Eisele et al. (2002), Hauri and Hart (1993), Hauri et al. (1996), Lassiter et al. (1998; 2000). 1 - La Palma (published - 13.6±2.6, 17) 2 - La Palma (this study - 13.6±2.7, 20) 3 - El Hierro (published - 14.9±1.6, 3) 4 - El Hierro (this study - 23.1±6.6, 15) 5 - Eastern Canary Islands (9.1±5.9, 7) 6 - Iceland (2.9±2.5, 39) 7 - Azores (3.9±3.8, 12) 8 - Mauna Kea (4.0±1.7, 20) 9 - Koolau (12.8±1.9, 8) 10 - Oahu (15.1±5.5, 10) 11 - Kauai (14.1±6.9, 8) 12 - Savaii (-1.3±1.5, 4) 13 - Mangaia (13.2±0.9, 6) 14 - Tubuaii (17.1±1.7, 7) 15 - Pitcairn (8.2±4.6, 6) 16 - Gorgona (1.6±4.0, 34) 17 - Curacao (1.1±3). Box represents interquartile range (25^{th} to 75^{th} percentile) and error bars represent 10^{th} and 90^{th} percentiles with outliers as single points. Line within the box represents means of data.

4.6 Discussion

A number of features would appear to make ocean islands ideal places to sample and understand isotopic heterogeneity in the mantle. First the limited age of the oceanic plates (<200Ma) and plate subsidence (e.g., Sclater *et al.*, 1981) resulting in the submergence of seamounts and ocean islands means that OIB lavas tend to be geologically young (0-15Ma). This means that the post-emplacement alteration of ocean island lavas is not likely to be as serious as that for CFB lavas erupted onto continents (e.g., Chapter 5). Second, the fact that ocean islands form on oceanic plate and are in general intraplate, means they are not subject to the effects of continental crustal contamination and tend to remain structurally undeformed.

By the same token there are restrictions to what ocean islands can reveal about mantle structure and dynamics. The young age of OIB means that they only cover a small fraction of geological time (0.3 to 0.5%). Also because OIB are erupted through oceanic lithosphere and crust, the effects of high level crustal contamination and lithospheric modification can be very difficult to quantify. In this discussion the elemental and He-O-Sr-Nd-Os-Pb isotope systematics of Western Canary Island lavas outlined in previous sections will be considered in the context of:

- Lava eruption and post-emplacement processes
- Fractional crystallisation and radiogenic He-ingrowth of melts
- Volcanic edifice and underlying oceanic crust contamination
- Variation due to partial melting

Ultimately the fact that El Hierro and La Palma lavas retain the isotopic characteristics of their mantle source regions allows discussion of:

- The types of, and relative contributions from mantle sources
- Comparison with Eastern Canary Island magmatism and other OIB

4.7 Lava eruption and post-emplacement processes

4.7.1 Element mobility – JMDD LP03

Despite sub-aerial oceanic island lavas being young and generally unaltered, older parts of the OIB volcanic edifice can suffer post-emplacement alteration. Post-emplacement alteration of lavas is most commonly the result of hydrothermal processes acting in response to the intrusion of dykes or magmatic bodies into the

growing lava pile. These hydrothermal processes can either occur by fluxing of meteoric fluids or saline marine fluids. Such high temperature hydrothermal alteration of lavas can lead to low $\delta^{18}O$ which is subsequently superimposed on magmas that assimilate this material (e.g., Chapter 2). This process has been documented in a number of ocean islands (e.g., Hawaii, Garcia *et al.*, 1998; Tristan da Cuhna, Harris *et al.*, 2000).

Picritic pillow lava, JMDD LP03 that is from the uppermost section of the submarine lavas, shows signs of hydrothermal alteration, although it retains fresh olivine cores. The bulk rock has anomalously low abundances of Rb, Ba and Sr and possesses radiogenic $^{87}Sr/^{86}Sr$ (0.70396). LILE such as Rb, Ba and Sr (+ Cs) are easily mobile and indicate that this sample has been affected by interaction with seawater that has radiogenic $^{87}Sr/^{86}Sr$ (0.709). Mobilisation of trace elements has resulted in ~66% loss of initial Sr abundance from the pillow basalts based on relationships between Pr and Nd (Fig. 4.8). Otherwise, JMDD LP03 has very similar $^{143}Nd/^{144}Nd$, $^{187}Os/^{188}Os$ and Pb isotope ratios to fresh subaerial La Palma lavas, as well as mantle-like $\delta^{18}O$ (5.0‰) and $^{3}He/^{4}He$ systematics ($9.7R_A$) for its olivine phenocrysts. Therefore, apart from $^{87}Sr/^{86}Sr$ and LILE, original elemental and isotopic signatures can be obtained from at least a portion of the sample.

4.7.2 Volatile element degassing during sub-aerial eruption

Chalcophile elements can exhibit volatile behaviour in magmatic systems, especially in oxidising, H_2O-rich environments (e.g., Bernard *et al.*, 1990). Previous studies have shown that low Re contents in some sub-aerially erupted lavas are due to magmatic degassing rather than source characteristics (Chapter 5; Bennett *et al.*, 2000; Sun *et al.*, 2003a,b,c; Lassiter, 2003; Norman *et al.*, submitted). These studies were performed on CFB, arc, MORB, back-arc basin or Hawaiian tholeiitic basalts. Alkali basalts tend to have much higher concentrations of H_2O and CO_2 (e.g., Hilton *et al.*, 1997b) which will promote degassing and loss of volatile elements (Dixon *et al.*, 1995). Consequently, it is important to assess the effect of degassing during sub-aerial eruption of highly alkaline basalts and basanites from La Palma and El Hierro on Re abundances.

Re and Cu are considered to be similarly incompatible although Cu is not considered to be as volatile (Hinkley *et al.*, 1999; Bennett *et al.*, 2000; Sun *et al.*,

2003a,b,c) making comparison between Re and Cu a useful indicator of degassing. Fig. 4.22 shows Re/Yb versus Cu/Re for Western Canary Island lavas.

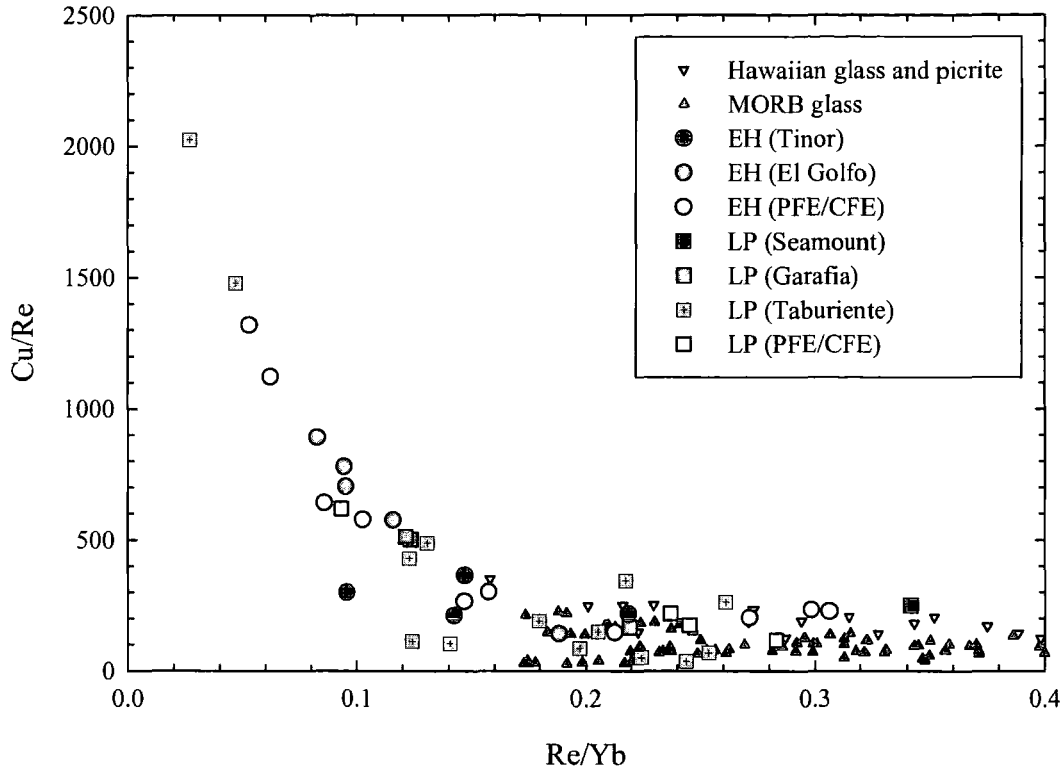

Fig. 4.22: Variation of Re/Yb versus Cu/Yb for El Hierro and La Palma lavas compared with tholeiitic MORB and Hawaiian glasses and lavas (Bennett et al., 2000; Norman et al., submitted) and MORB glasses (Sun et al., 2003a). Alkaline El Hierro and La Palma lavas trend to more extreme Cu/Re and Re/Yb than tholeiitic magmas which indicates degassing processes occurred during eruption.

Western Canary Island lavas trend to very low Re/Yb and high Cu/Re ratios (>2000). Because Cu contents in tholeiites are only slightly less than alkali basalts, the high Cu/Re ratios (up to 5 times greater than tholeiites from Hawaii) of alkaline lavas from the Canary Islands are due to the low Re contents in these lavas. Lavas most heavily affected by eruptive degassing are those from the Taburiente series of La Palma and the El Golfo and PFE/CFE eruptions of El Hierro; the PFE/CFE eruptions on the Cumbre Vieja ridge appear relatively undegassed compared to these series. Taken at face values the difference in Cu/Re ratios between alkali and tholeiitic basalts suggest that alkali lavas are 20-80% more volatile depleted than tholeiites assuming similar initial Cu/Re ratios for starting melts.

The Re contents of alkali basalts are typically similar to, or lower than, tholeiites despite the larger degrees of partial melting of the latter. This relationship indicates

that some process other than partial melting must explain this variation. There is very clear evidence of Re degassing from Western Canary Island lavas presented in this study. This observation means that the Re/Os ratio cannot be used as a reliable indicator of partial melting in sub-aerially erupted lavas. Re degassing demonstrated in this study also explains why Re contents in OIB, whose products are commonly samples as subaerial erupted lavas, are lower than Re contents in MORB lavas.

4.8 Relative roles of crustal contamination and fractional crystallisation in Western Canary Island lavas

The ^{3}He-elevated (>1R_A or atmospheric) isotope signatures and basaltic nature of Western Canary Island lavas clearly indicate their derivation, at least in part, from the mantle. Mantle-derived magmas undergo a variety of processes prior to eruption in oceanic Islands which can potentially alter their primary chemical compositions and thereby obscure the nature of their sources. In this section I examine the possible effects that shallow-level pre-eruptive volatile degassing, fractional crystallisation, crustal assimilation and oceanic lithosphere interaction may have on the primary mantle compositions of Western Canary Island magmatism.

4.8.1 Fractional crystallisation

Fractional crystallisation plays a major role in the compatible/incompatible element abundances of lavas. In keeping with the phenocryst phases present in these rocks, systematic variations of major elements with MgO (Fig. 4.6) suggest fractional crystallisation of olivine, clinopyroxene, Fe-Ti oxide and apatite in the differentiation of La Palma and El Hierro lavas. Fractional crystallisation is likely to occur at a range of depths within both the edifice and the underlying mantle. For example Nikogosian *et al.* (2002) have proposed that the low SiO_2 and high incompatible element concentrations of basanite lavas in the Canary Islands are the result of deep (12-40km) clinopyroxene fractionation from alkali basaltic magmas (transitional to silica-undersaturated). Whilst substantial amounts of crystallisation of anhydrous minerals affect compatible element abundances it cannot:

- Explain the variations seen in the incompatible trace element patterns of the lavas between the different stratigraphic units (Fig. 4.8; Table 4.1).

- Explain the He, O, Sr, Nd, Os, Pb isotope variation observed for Western Canary Island lavas.

Within the sample suite analysed for isotopic variations there is no observable evidence for extreme variations in the degree of fractional crystallisation; all samples analysed have MgO >8 wt.%. The fractional crystallisation trends in Fig. 4.6 are defined by the small number of evolved samples on these plots. In assessing incompatible element variations in these rocks, fractional crystallisation is insignificant (e.g., Fig 4.8).

For compatible elements such as Os fractional crystallisation is likely to be important because it results in lower Os abundances in more evolved magmas compared with primitive melts. In Fig. 4.17 there are clearly positive correlations between Os, Ni and MgO indicating that lower Os abundance lavas are the result of fractional crystallisation. While correlating with indices normally associated with increasing olivine addition, Os is incompatible in olivines (D_{ol}=0.4-0.6; Puchtel *et al.*, 2004) and so Os abundances are more likely to be controlled by sulphide/PGE-alloys retained within chromite inclusions or olivine; similar relationships have been documented in CFB (Schaefer *et al.*, 2000; Chapter 5) as well as other OIB suites (Hauri and Hart, 1993; Martin *et al.*, 1994; Hauri *et al.*, 1996; Widom *et al.*, 1999).

Re correlates positively with TiO_2 and negatively with MgO indicating that fractional crystallisation may also be important in the distribution of this element. The El Hierro and La Palma lavas show different correlations between TiO_2 and Re (Fig. 4.16). These relationships could reflect the incompatible nature of Re and the influence of olivine, clinopyroxene and Fe-Ti oxide mineral fractionation. However, this relationship cannot represent variation in TiO_2 in the source of the two islands because of the similar Re/Ti ratios for the most primitive (highest MgO) lavas from both islands. Another notable feature of the Re dataset is the generally more elevated Re for La Palma PFE/CFE lavas (this study, Marcantonio *et al.*, 1995; Widom *et al.*, 1999) erupted on the Cumbre Vieja compared with lavas from other stratigraphic units of the two islands. Observation of more elevated [He] for these lavas has also been made in section 4.5.4.2. and these relationships will be discussed in later sections. The trend to low Re with less evolved lavas in Fig 4.16 could also reflect processes other than fractional crystallisation and indicate that more primitive (higher temperature, lower viscosity) melts lose more Re during eruptive degassing.

Therefore the Os and Re abundance relationships can be explained by melting and fractional crystallisation in the presence of sulphides and in the case of sub-aerial lavas, Re-degassing.

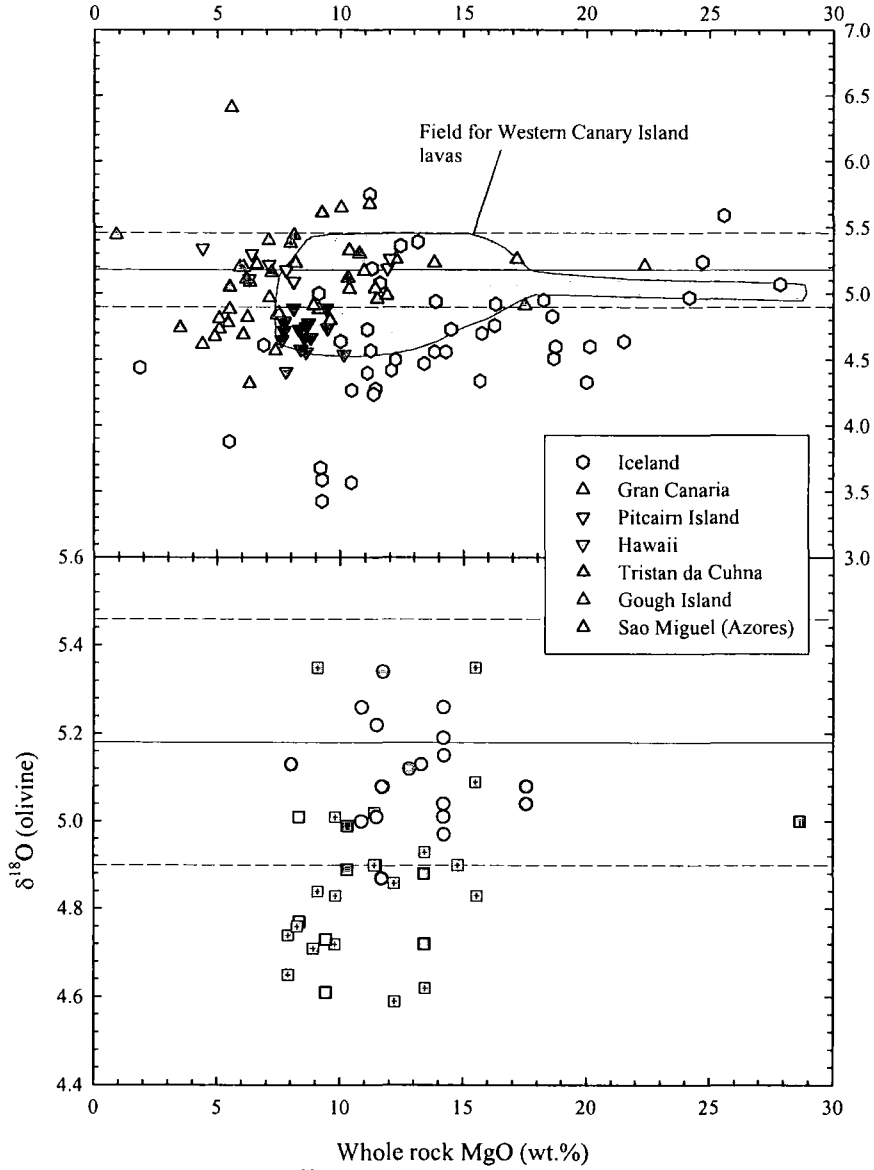

Fig. 4.23: Whole rock MgO versus $\delta^{18}O$ (or "olivine equivalent") for La Palma, El Hierro and other OIB lavas. All $\delta^{18}O$ values were measured on olivines apart from the Gran Canaria data, for which clinopyroxene data have been converted to olivine equivalents assuming $\Delta_{Cpx\text{-}Ol} = 0.30$ (Mattey et al., 1994). Literature data from Harris et al. (2000), Eiler et al. (1995), Gee et al. (1998), Thirlwall et al. (1997), Garcia et al. (1998), Eiler et al. (2000) and Chapter 2. Symbols as for Fig. 4.17.

For He small-scale diffusive fractionation of $^3He/^4He$ can occur during partial melting (Burnard, 2004), but there is no recognised method for fractional crystallisation of anhydrous or hydrous mineral phases to generate large-scale variations in [He] or variation in $^3He/^4He$. For O, there is evidence that fractional crystallisation of mineral phases can generate ~0.3‰ increases in □^{18}O due to

removal of isotopically light Fe-Ti oxides (e.g., Harris *et al.*, 2000). However, when $\delta^{18}O$ is plotted against indices of differentiation such as MgO no discernable increase in $\delta^{18}O$ with decreasing MgO is observed (Fig. 4.23). It is, however, apparent that La Palma lavas have systematically lower $\delta^{18}O$ for a given MgO than El Hierro lavas. Therefore, despite being an important petrogenetic process, the effect of fractional crystallisation alone, cannot be used to explain the large isotope variations of Western Canary Island lavas.

4.8.2 Insitu radiogenic ingrowth of ^{4}He in melts

The impact of *in situ* radiogenic ingrowth of ^{4}He in melts or 'magma aging' was discussed in detail by Hilton *et al.* (2000a) for La Palma lavas. These authors found that for uranium contents of La Palma basaltic lavas (≤1.6ppm) and the U/Th ratio (3.5 to 3.8) crustal residence times in excess of 10Ma would be required for a magma to generate enough radiogenic He to considerably affect ^{3}He/^{4}He ratios. This calculated estimate is obviously at odds with (i) the age of the Western Canary Island volcanoes, (ii) U-Series disequilibrium in La Palma lavas (Elliott, 1991), (iii) the fast ascent rates (1.1×10^{-8} Ma) of magmas and (iv) magma residence times in crustal magma chambers based upon xenolith eruption mechanics and fluid barometry (Klugel *et al.*, 1997; Klugel, 1998). The negligible effect of magma aging on He isotopes in La Palma phenocrysts (as well as magma aging for other isotopic systems) can be extrapolated to El Hierro magmas because the El Hierro lavas have similar to lower U contents and the Island of El Hierro is significantly younger than La Palma.

4.8.3 Crustal contamination

Crustal contamination of magmas in ocean islands is restricted to assimilation of the iland edifice and to the components of oceanic crust upon which the island rests. The type and depth of crustal assimilation can be tracked by different chemical signatures which are outlined below.

4.8.3.1 Volcanic edifice based crustal contamination

Uniquely traceable edifice contaminants include:

- Highly fractionated lithologies with distinct incompatible element compositions such as phonolites.
- Degassed hydrothermally altered basalts with radiogenic He. Helium in mantle melts only degasses at low (shallow crust) pressures so $^{3}He/^{4}He$ ratios will only be susceptible to shallow-level contamination processes in the volcanic edifice.

Evolved trachytes and phonolites are easily distinguished because of their elevated trace element concentrations relative to basanites and alkali basalts, and because they generally possess positive U and Th anomalies, Pb, Zr and Hf enrichment and negative Ti anomalies (e.g., Carracedo *et al.,* 2001). The excess U, Th, Pb, Zr and Hf are due to the presence of accessory phases such as apatite, zircon and haüyne in these rocks. The small volume and extent of evolved lavas on El Hierro and La Palma restricts the likelihood of evolved volcanics acting as contaminants. In La Palma, phonolite plugs are only located on the Cumbre Vieja and for El Hierro a single, thick trachyte flow caps the top of the El Golfo series. For lavas erupted close to, or synchronously with phonolites spines, such as the 1585AD eruption on La Palma (Johansen *et al.,* 2003) there is no obvious trace element evidence that contamination of basanite by phonolite has occurred. For example, the strongly negative Ti and positive Zr, Hf and Pb anomalies symptomatic of phonolite and trachyte are not observed in basanites and alkali basalts from PFE/CFE Cumbre Vieja that have similar negative Zr and Hf anomalies to other La Palma and El Hierro lavas (Fig. 4.6). Furthermore, the relatively young ages of these lavas mean that it would be impossible to generate the significant $^{87}Sr/^{86}Sr$, $^{143}Nd/^{144}Nd$ or Pb isotope variations seen in the Western Canary Island lavas by aging alone (Figs. 4.14, 4.15).

The submerged section of volcanic edifice can potentially be assimilated to alter the isotope compositions of OIB magmas. For example, JMDD LP03 has radiogenic $^{87}Sr/^{86}Sr$ as a result of seawater interaction. However, none of the subaerial lavas studied exhibit this feature and the Pb, Nd and Os isotope systematics of the lavas are unlikely to be affected by assimilation of volcanic edifice material because the material is not sufficiently old enough to generate radiogenic isotopic heterogeneity (e.g., Hoernle, 1998).

A significant process in the volcanic edifice that can substantially alter the isotopic systematics of magmas is degassing of He, exacerbating the effects of

radiogenic He addition (Chapter 2). The wide range in La Palma and El Hierro $^3He/^4He$ ratios, especially for clinopyroxene, raises the possibility that the He isotope signature of the mantle source has been modified. He can be an exceptionally sensitive indicator of crustal contamination because degassed basaltic and evolved material can generate radiogenic $^3He/^4He$ in a short space of time (e.g., Condomines *et al.,* 1983). The abundance of radiogenic He in La Palma or El Hierro edifice lithologies depends upon parent element concentration, age of the rock and retentivity of produced He. For 1Ma old buried altered basalt with U = 0.3ppm, Th/U ~3.5 and assuming 100% He retention, ~6.5×10^{-8} cm^3STP^4He/g is produced. This value can be reduced or increased proportionally if the crustal assimilant is younger or older.

To some extent, crustal contamination can be assessed through a comparison of measured $^3He/^4He$ in co-genetic olivine and clinopyroxene (Hilton *et al.,* 1995; Hilton *et al.,* 2000). Diffusivity of He in clinopyroxene is approximately an order of magnitude greater than olivine (Trull and Kurz, 1993) so clinopyroxene with low [He] will be more susceptible to crustal (radiogenic) He incorporated en route to the surface (Chapter 2, Hilton *et al.,* 1993; Hilton *et al.,* 1995). Whilst $^3He/^4He$ isotope equilibrium has been recognised between some clinopyroxene-olivine pairs, a significant number of pairs analysed in this study and by Hilton *et al.* (2000a) (14/26) show isotopic disequilibrium (Fig. 4.9). This indicates that some crustal He contamination occurred during storage of La Palma magmas. Generally, the clinopyroxenes with low $^3He/^4He$ also have relatively low [He] abundances (Fig. 4.10) suggesting that crustal contamination has indeed been exacerbated by shallow-level degassing within the volcanic edifice where radiogenic He addition must have occurred.

A simple method to test if addition of crust has altered $^3He/^4He$ isotope ratios of clinopyroxene is to investigate the O-He isotope systematics of magmatic mineral or glass phases (e.g., chapter 2). In La Palma, the submarine edifice possesses hydrated submarine erupted lavas and intrusive rocks that have low $\square^{18}O$ (-1.2‰ Javoy *et al.,* 1986). The Seamount series is > 3Ma, so could generate significant quantities of radiogenic He (in excess of 1×10^{-7} cm^3STP^4He/g). Additionally there is evidence that some of the seamount series was erupted at shallow water depths (large hyaloclastite deposits). Thus, [He] may have been lost during hydrothermal

alteration, meaning that some of the submerged volcanic edifice is characterised by low $^{3}He/^{4}He$ and low $\delta^{18}O$. He-O isotope systematics for La Palma and El Hierro minerals are plotted in Fig. 4.24 with NAIP and Iceland olivines and the *k*-parameter (where $k = ([He]/[O]_{Crust})/([He]/[O]_{Mantle})$). Clearly the *starting* $^{3}He/^{4}He$ ratios pertaining to Icelandic glasses are too extreme to place meaningful constraints on the isotope systematics of Western Canary Island pyroxenes so instead, for illustrative purposes, modelling of MORB-like ($8\pm1R_A$) and mantle $\delta^{18}O$ has been employed to El Hierro and La Palma lavas.

In the lowermost panel of Fig. 4.24 a series of *k*-parameter mixing lines have been produced between a mantle-derived melt with MORB $^{3}He/^{4}He$ ($8\pm1R_A$; Hilton and Porcelli, 2003) and mantle $\delta^{18}O_{olivine}$ (5.18±0.28‰, 2σ, Mattey *et al.*, 1994) and volcanic edifice material with low $\delta^{18}O$ (0‰) and radiogenic $^{3}He/^{4}He$ ($0.05R_A$). The *k*-parameter mixing lines correspond to a mantle-derived mantle source which has 25 and 50 times less [He] than the assimilant: i.e. it has significantly degassed. For El Hierro pyroxenes ~1% assimilation of volcanic edifice at $k = 50$ can explain their $^{3}He/^{4}He$. La Palma pyroxenes conform to different *k*-parameters (5-25) and require more assimilation (6-8%) if the initial starting $\delta^{18}O$ of El Hierro and La Palma melts are considered to be similar. There is no obvious reason why the islands should conform to different degassing and assimilation processes. Both islands have formed from similar depths of ocean floor and should therefore both have an altered submarine volcanic edifice. In Fig. 4.23 it was noted that for a given MgO, $\delta^{18}O$ was systematically lower for La Palma lavas compared to El Hierro lavas. Therefore *k*-models equal to 25 and 50 are also shown to reflect a 0.25‰ difference between the averages of mafic phenocrysts from the two islands (Table 4.3) in Fig. 4.24. The estimates of crustal contamination at these degassing values and at modified $\delta^{18}O$ starting compositions means that La Palma and El Hierro clinopyroxene values can be explained by between 1 and 2% crustal addition at *k*-values = 25-50.

On this basis it can be concluded that whilst $^{3}He/^{4}He$ ratios measured in clinopyroxene reflect to some extent, shallow-level degassing and subsequent assimilation of crust prior to crystallisation, the original $\delta^{18}O$ compositions of La Palma and El Hierro appear to have been different. Equally, whilst low $^{3}He/^{4}He$ in some Western Canary Island phenocrysts can be explained by crustal contamination and edifice assimilation, the variation of $^{3}He/^{4}He$ in olivines ($6.6\text{-}11.8R_A$) lies within

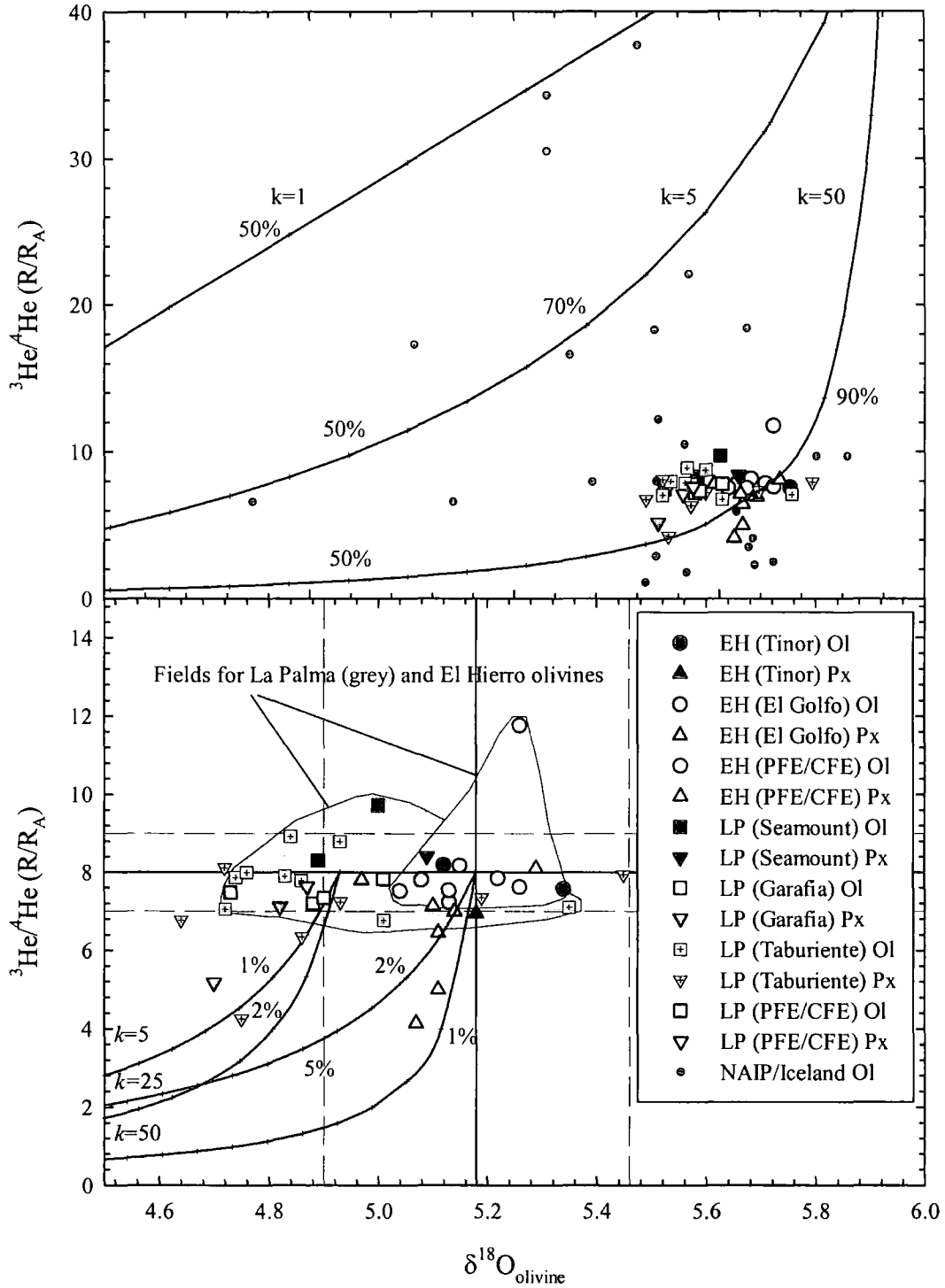

Fig. 4.24: $\delta^{18}O$ (or "olivine equivalent") versus $^3He/^4He$ (R/R_A notation) for La Palma, El Hierro and Skye and Island lavas (top panel only) from Chapter 2. Clearly El Hierro and La Palma lavas do not conform well to the modelled parameters of Chapter 2 and the degassing and subsequent radiogenic He addition to Western Canary island lavas is better explained using a lower $^3He/^4He$ (MORB; Farley and Neroda, 1998; Hilton and Porcelli, 2003) and mantle-like $\delta^{18}O$ (Mattey et al., 1994). Modelling methods same as for Fig 2.9 of chapter 2. Fields drawn around La Palma and El Hierro olivines. $\Delta_{Cpx\text{-}Ol} = 0.30$ in accordance with majority of equilibrium information in Fig. 4.9.

or above the bounds of MORB $^{3}He/^{4}He$ and more closely reflects mantle source characteristics as there is no obvious evidence of radiogenic addition of He especially in samples with high [He] (Fig. 4.10).

4.8.3.2 Oceanic crust contamination – O, Sr, Nd, Pb isotopes

The oceanic crust beneath the Canary Islands is some of the oldest in the ocean basins (150-180Ma; Hoernle, 1998) and possesses distinct isotopic compositions. The oceanic crust beneath Gran Canaria consists of two major units: an igneous unit (4.5km thick, layers 2 and 3) overlain by a thick sedimentary apron (up to 6km thick, layer 1). These layers have distinct isotopic compositions (Table 4.7) including radiogenic $^{87}Sr/^{86}Sr$, unradiogenic $^{143}Nd/^{144}Nd$ and high $^{208}Pb/^{204}Pb$ and $^{207}Pb/^{204}Pb$ for a given $^{206}Pb/^{204}Pb$ (Hoernle, 1998). Additionally, these layers are characterised by very different average $\delta^{18}O$ (Hansteen and Troll, 2003). The oceanic crustal samples analysed by Hoernle (1998) and Hansteen and Troll (2003) cover 50% of the $^{87}Sr/^{86}Sr$ observed in OIB, 60% of the range in $^{206}Pb/^{204}Pb$ and 100% of the $\delta^{18}O$. Contamination by oceanic crustal components has been documented in some Canary Island volcanic suites. For example shield basalts from Gran Canaria which have elevated $\delta^{18}O$, $^{87}Sr/^{86}Sr$, low $^{143}Nd/^{144}Nd$ and lie off the Northern Hemisphere Reference Line (NHRL, Hart, 1986) for Pb isotopes, have been suggested to contain substantial (8%) passive margin sediment (e.g. Layer 1) (Thirlwall *et al.*, 1997). Samples from El Hierro and La Palma are correlated in Pb-isotope space and lie along or are parallel with the NHRL (Fig. 4.15). They are also correlated in terms of their Sr-, Nd- and O-Pb isotope systematics (Fig. 4.26). Linearity in multi-isotopic space suggests two component mixing. This could reflect contamination by a crustal component but cannot be the result of sediment which would force Western Canary island lavas above the NHRL.

Bulk mixing between solid crust and mantle-derived magmas is not an efficient process since the assimilation processes in general causes fractional crystallisation of the magma (AFC, DePaolo, 1981). AFC typically results in more crust-like isotopic compositions in more evolved magmas but no such relationship is seen for El Hierro or La Palma lavas (section 4.9.1; Fig. 4.23; 4.25). Fractional crystallisation is likely to have occurred at a range of depths in the crust and oceanic lithosphere but there is no observable systematic variation between indices of differentiation and isotopic

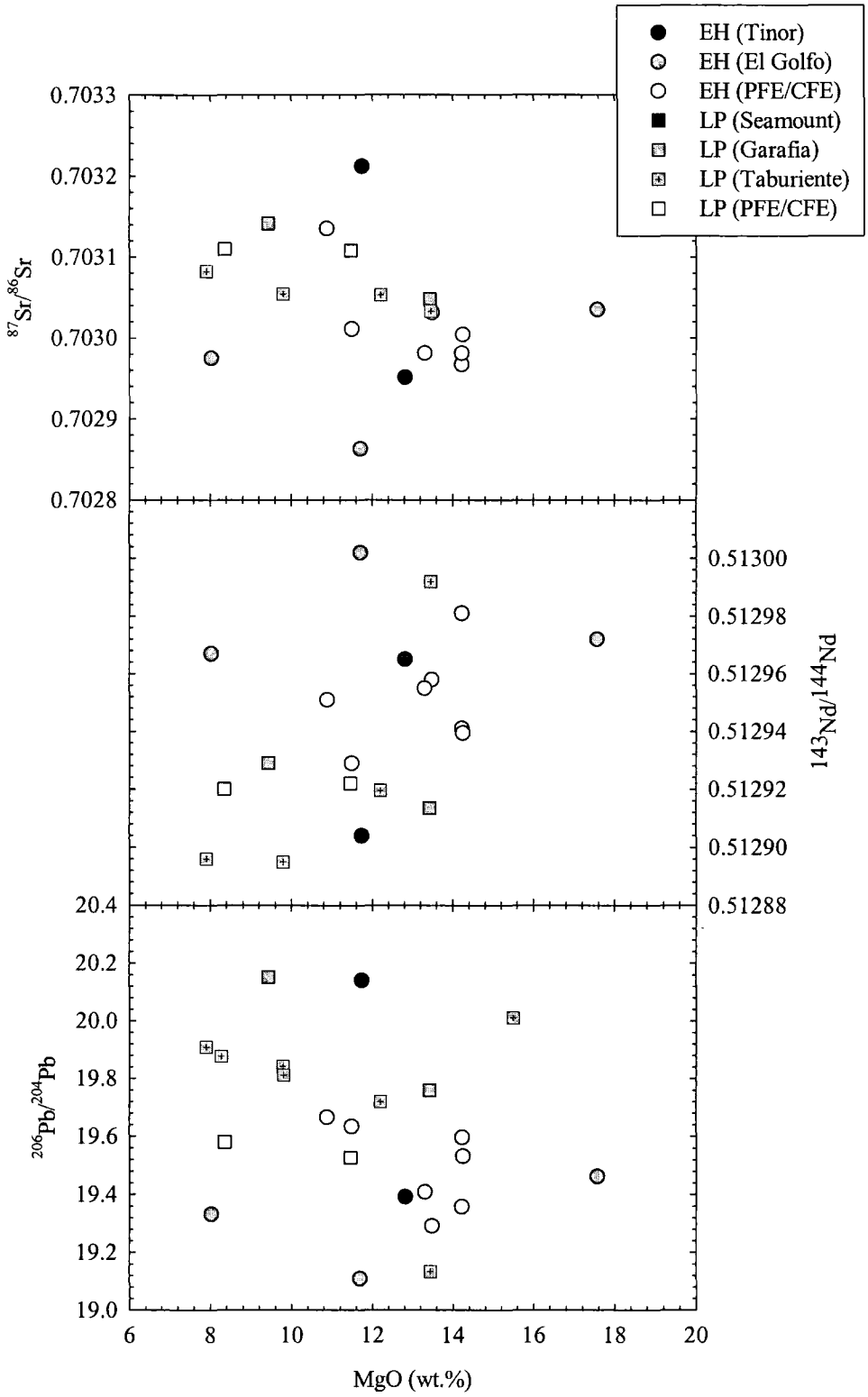

Fig. 4.25: MgO (wt. %) versus $^{206}Pb/^{204}Pb$, $^{143}Nd/^{144}Nd$, and $^{87}Sr/^{86}Sr$ for La Palma and El Hierro lavas (this study).

composition in the La Palma and El Hierro O, Sr, Nd and Pb isotope datasets. Therefore in this section the approach followed is that of Thirlwall *et al.* (1997) who

modelled bulk mixing processes for Gran Canaria lavas based upon similar arguments for lack of obvious fractional crystallisation effects to those made here.

Table 4.7: Summary of crustal contaminants and mantle components

Type	Age (Ma)	$^{3}He/^{4}He$	[He]	$\delta^{18}O$	$^{87}Sr/^{86}Sr$	[Sr]	$^{143}Nd/^{144}Nd$	[Nd]	$^{206}Pb/^{204}Pb$	[Pb]	$^{187}Os/^{188}Os$	[Os]	Ref.
Crustal Assimilants													
Edifice													
Seamount	3	0.05	1.0E-08	-1.2	0.70400	100	0.51298	4	18.99	0.5	-	-	a,b
Oceanic Crust													
Layer 1	150-180	-	-	14.0	0.71368	612	0.51198	16.9	18.97	12.1	1.00	0.02	a,c,d
Layer 2	150-180	-	-	8.0	0.70362	106	0.51298	7.3	18.62	1	0.26	0.05	a,c,d
Layer 3	150-180	-	-	4.0	0.70362	106	0.51298	7.3	18.62	1	0.26	0.05	a,c,d
Fe-Mn Crust	-	-	-	-	0.70900	-	0.51201	-	18.93	-	1.07	1.83	e,f
Mantle sources													
Met. OL -Car	150	-	-	5.2	0.70362	106	0.51298	7.3	18.62	0.01	0.6000	0.05	a,c,d
CLM	1200	6±2	1.0E-06	5.2	0.70397	80	0.51266	5	19.37	0.01	0.1130	3.3	g
ROC	1200	<1	-	4.0-14.0	-	-	-	-	-	-	-	0.05	c,d
	1800	<1	-	4.0-14.0	-	-	-	-	21.00	0.25	1.6100	0.05	c,d
	2000	<1	-	4.0-14.0	0.70289	94	0.51279	9.3	22.67	0.23	1.7800	0.05	c,d
ROL	1200	<1	-	5.2	-	-	-	-	-	-	0.1100	3.3	h
Core-mantle	-	?	-	-	-	-	-	-	9.31	400	0.1499	2800	i,j,k
DMM	-	8±2	1.0E-05	5.2	0.70260	14	0.51320	1.3	18.24	0.06	0.1246	3.3	l, m, n
HRDM	-	>49.5	variable	5.2	0.70260	14	0.51320	1.3	18.24	0.06	0.1246	3.3	l, n, o

Met. OL –Car = Carbonatite metasomatised oceanic lithosphere, CLM = Continental lithospheric mantle, ROC = Recycled oceanic crust, ROL = Recycled oceanic lithosphere, DMM = Depleted MORB mantle, HRDM = Helium recharged depleted MORB mantle. Data sources are a – Hoernle (1998), b – Javoy (1986), c – Hansteen and Troll (2003), d – Widom *et al.* (1999), e – Claude-Ivanaj *et al.* (2001), f – Burton *et al.* (1999a,b), g – Gautheron and Moriera (2002), h – Schaefer *et al.* (2002), i – Brandon *et al.* (2003), j – Widom and Shirey (1996), k – GERM, l – Chauvel *et al.* (1992), m – Hilton and Porcelli (2003), n – Snow and Reisberg (1995), o – Stuart *et al.* (2003). [He] as nccSTP/g, [Sr], [Nd], [Pb] = ppm, [Os] ppb

In Fig. 4.26 the $^{206}Pb/^{204}Pb$, $\delta^{18}O$, $^{87}Sr/^{86}Sr$ and $^{143}Nd/^{144}Nd$ isotope systematics of El Hierro and La Palma lavas are compared with bulk mixing models for oceanic crustal components listed in Table 4.7. This modelling indicates that oceanic crust provides poor fits for the observed isotope systematics of Western Canary Island lavas:

- Bulk mixing between layer 1 sediments and a FOZO-like mantle is orthogonal to the trends observed for the lavas and is unable to account for the observed isotopic systematics of Western Canary Island lavas.
- Minor addition of layer 1 sediments would result in Pb isotope ratios diverging above the NHRL. In contrast all La Palma and El Hierro lavas lie along the NHRL (Fig. 4.15).
- Layer 2 pillow basalts and dykes have too high $\delta^{18}O$ to explain the systematics of the La Palma and El Hierro lavas, however layer 3 gabbros possess low $\delta^{18}O$ and so, on this basis, may be a possible contaminant.

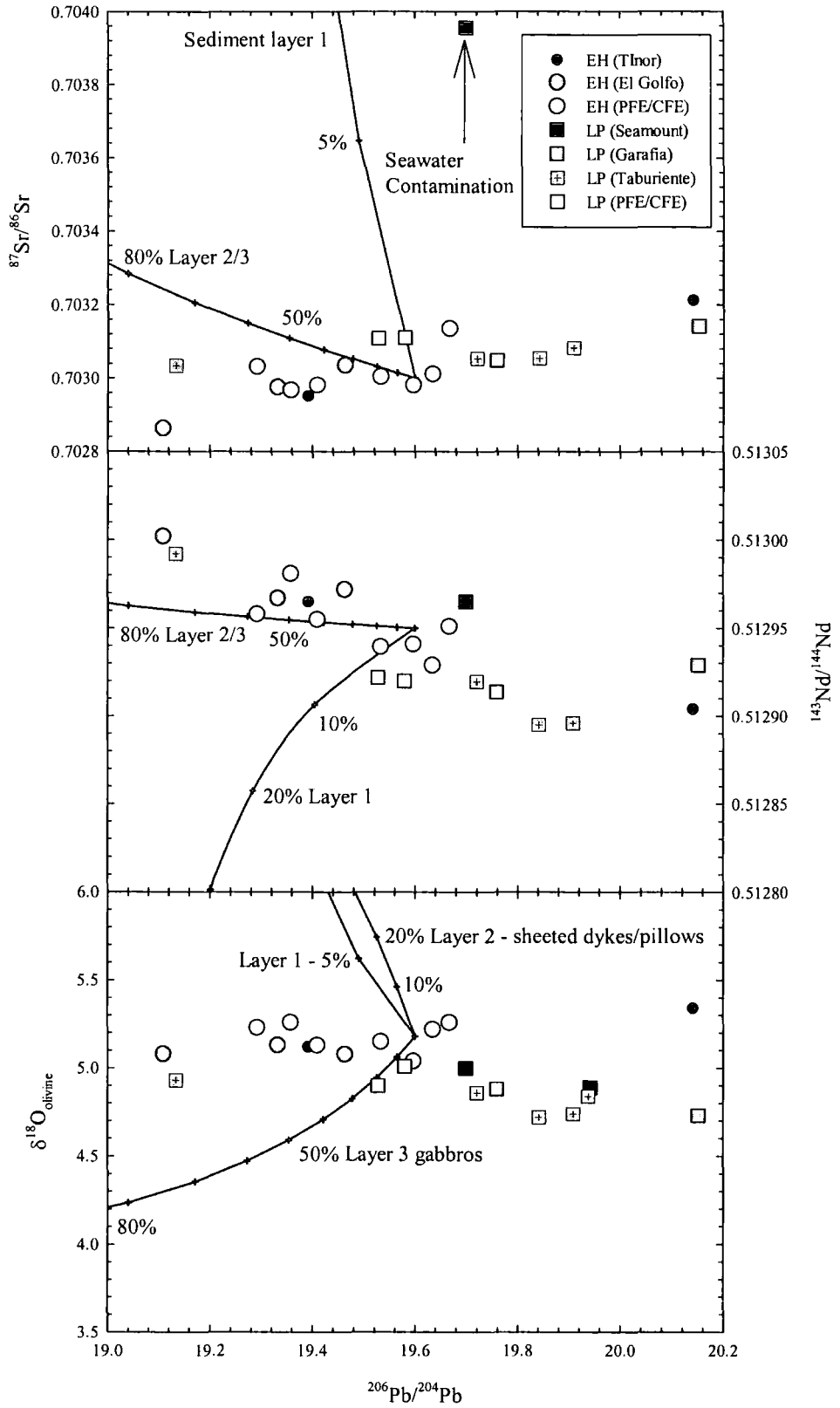

Fig. 4.26: $^{206}Pb/^{204}Pb$ versus $\delta^{18}O_{olivine}$, $^{143}Nd/^{144}Nd$, and $^{87}Sr/^{86}Sr$ for La Palma and El Hierro lavas (this study). Models assume bulk-mixing between a FOZO-like component (see mantle components discussion) and Layer 1, 2 and 3 Jurassic Oceanic crust (for modelling parameters see Table 4.7).

- Mixtures of mantle components, even with higher $^{206}Pb/^{204}Pb$, and layer 3 gabbros cannot explain the correlation seen in the Western Canary Island lavas of lower $\delta^{18}O$, $^{143}Nd/^{144}Nd$ and more radiogenic $^{87}Sr/^{86}Sr$ with high $^{206}Pb/^{204}Pb$.

From these observations it appears that for isotopic systems whose elements behave incompatibly during melting and fractional crystallisation (Rb-Sr, Sm-Nd, U-Pb) as well as stable isotope systems (O) the effects of traversing the oceanic crust has been negligible.

4.8.3.3 Oceanic crust and lithospheric mantle contamination – Os isotopes

4.8.3.3.1 Oceanic crust

Os isotopes can be more sensitive to the impact of crustal contamination than O, Sr, Nd and Pb isotopes because of the very low concentrations of Os in some basalts due to its compatible nature.

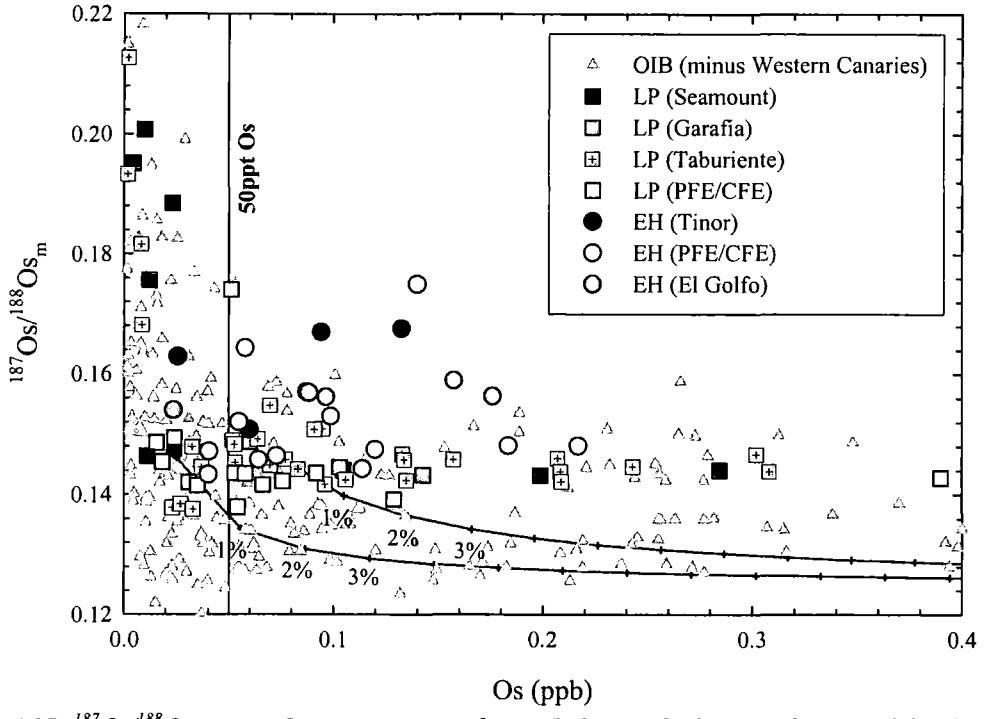

Fig. 4.27: $^{187}Os/^{188}Os$ versus Os concentration for La Palma and El Hierro lavas and for the global OIB dataset. Mixing curves illustrate the effect of bulk assimilation of oceanic lithospheric mantle using the modelling parameters of Widom et al. (1999) –Melt $^{187}Os/^{188}Os$=0.146, Os = 25 and 75ppt, Oceanic lithosphere $^{187}Os/^{188}Os$ = 0.125, Os =3100ppt. Few of the samples in this study show evidence for bulk assimilation of oceanic lithosphere.

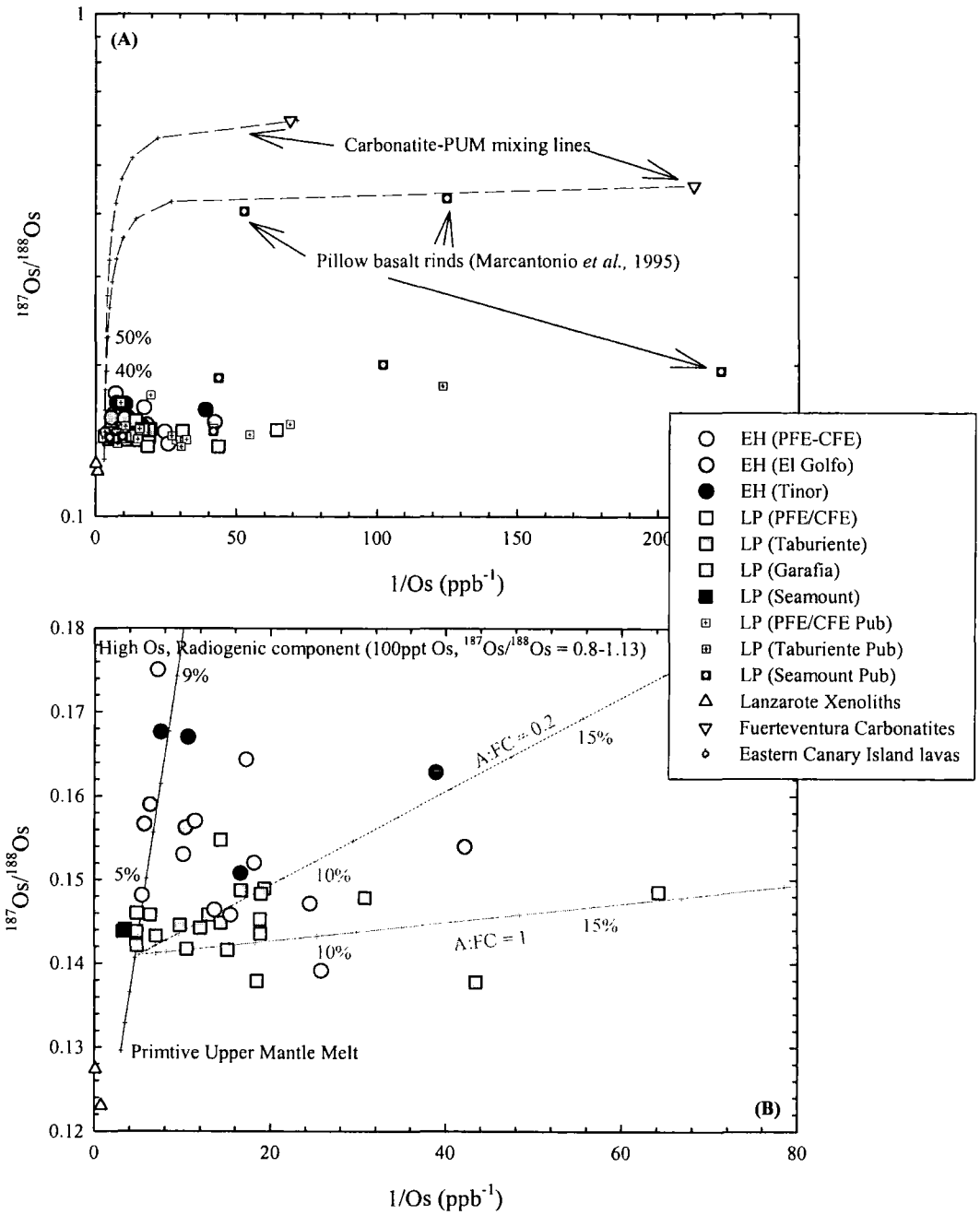

Fig. 4.28: Reciprocal Os versus $^{187}Os/^{188}Os$ for La Palma and El Hierro lavas. Data also included from Marcantonio et al. (1995) and Widom et al. (1999). Assimilation and Fractional Crystallisation models based upon range of oceanic crustal values in table 4.7. A maximum of 16% crust is required to explain the variations in La Palma lavas although correlations are poor. High Os, radiogenic $^{187}Os/^{188}Os$ samples cannot be described by mixing with carbonatite but instead require a proportion of a high Os source with radiogenic Os, in this case 100ppt, with $^{187}Os/^{188}Os$ =0.8 (shown in B). In (A) primary magmas mix with Fuerteventura carbonatites (Widom et al., 1999) in (B) AFC mixing between oceanic crust (Table 4.7) and a non-crustal high Os radiogenic component.

The $^{187}Os/^{188}Os$ ratios of OIB found in low Os concentration basalts are generally indicative of crustal contamination (Reisberg *et al.*, 1993; Marcantonio *et al.*, 1995;

Widom *et al.*, 1999). Contaminated basalts are generally recognised by correlation of Os abundance with $^{187}Os/^{188}Os$ ratio (Fig 4.27). In Fig. 4.28 $^{187}Os/^{188}Os$ ratios of lavas from La Palma and El Hierro are plotted against their reciprocal Os concentrations. AFC mixing models have been generated to take into account the compatible nature of Os (section 4.9.1) and are for AFC ratios of 0.2 and 1. Some of the Canary Island lavas with radiogenic $^{187}Os/^{188}Os$ and low Os abundance can be explained by ~10-15% AFC. Whilst some La Palma lavas correlate with AFC =>0.2, there is considerable scatter for a reciprocal Os plot. El Hierro lavas which lie at radiogenic $^{187}Os/^{188}Os$ for relatively high concentrations of Os cannot be explained by AFC processes.

Only crustal contaminants with high Re/Os ratios and low Os concentrations would be able to generate large enough isotopic heterogeneity to explain the $^{187}Os/^{188}Os$ of some high Os concentration El Hierro lavas. An extreme example would be carbonatite. Widom *et al.* (1999) analysed two carbonatites from the basement complex of Fuerteventura which had extremely radiogenic $^{187}Os/^{188}Os$ (0.614 and 0.455) but very low Os concentrations (<10ppt). 20-30% carbonatite addition would be required to explain the $^{187}Os/^{188}Os$ of El Hierro and La Palma lavas. Addition of this much carbonatite would drastically affect the CaO, Sr and LREE concentrations of the basalts, which is not observed.

High Os abundance sedimentary materials are also a possible contaminant to explain the radiogenic $^{187}Os/^{188}Os$ provided that they conform to restrictions placed by Sr, Nd, O and Pb correlations. As high Os concentration lavas converge at ~250ppt and $^{187}Os/^{188}Os = 0.141$ (Fig. 4.28) this value is selected as the endmember composition for mixing in Fig. 4.29. Because of the failure of AFC to explain all the Os isotope variation or Sr and Nd isotope compositional variability, the models in Fig. 4.29 represent only bulk mixing trajectories between a mantle-derived magma and potential crustal contaminants. These models show that both sedimentary material or Jurassic aged oceanic crust are unable to explain the Os isotope heterogeneity of La Palma and El Hierro lavas for the following reasons:

- Assimilation of Jurassic oceanic crust cannot explain the unradiogenic $^{87}Sr/^{86}Sr$ and radiogenic $^{187}Os/^{188}Os$ observed in the majority of El Hierro lavas.

- Assimilation of Jurassic oceanic crust cannot explain the $^{143}Nd/^{144}Nd$ variations over wide ranges of $^{187}Os/^{188}Os$ and requires unreasonably high amounts of bulk assimilation (70%).

Possible sedimentary contaminants (both in the volcanic edifice and oceanic crust) are Fe-Mn oxide coatings and nodules which could contribute significant radiogenic $^{187}Os/^{188}Os$ because of their high Os contents (Luck and Turekian, 1983; Palmer and Turekian, 1986; Esser and Turekian, 1988; Palmer *et al.*, 1988; Reisberg *et al.*, 1993; Burton *et al.*, 1999a; McDaniel *et al.*, 2004). However there are a number of reasons why this material is unlikely to generate the Os isotope signatures seen in El Hierro and La Palma lavas.

- Up to 0.5% Fe-Mn oxide assimilation is required by bulk mixing models to reproduce the $^{187}Os/^{188}Os$ values seen in El Hierro lavas, and 0.1% for La Palma lavas, assuming the starting composition of lavas is 0.141. Such amounts of assimilation would cause large differences in MnO, Co and other metal contents between El Hierro and La Palma lavas. In addition there would be a correlation between $^{187}Os/^{188}Os$ and MnO assuming that fractional crystallisation does not modify the concentrations of these elements. These relationships are not observed in the La Palma and El Hierro lava suite.
- Study of low Os abundance pillow rinds from the Pliocene seamount series by Marcantonio *et al.* (1995) (Fig. 4.24) reveals that Fe-Mn oxide precipitation has not affected higher Os concentration lavas or pillow interiors, suggesting that this form of contamination is superficial.
- Contamination of mantle-derived melts by Fe-Mn crusts would imply that the melts interact with the oceanic sediment layer where large Fe-Mn nodules form. There is no evidence from Pb-Pb isotope arrays that La Palma or El Hierro lavas have interacted with sediment (Fig 4.15).
- Fe-Mn crusts have seawater Sr, Nd and Pb isotope compositions. These compositions cannot explain the large range in $^{187}Os/^{188}Os$, $^{206}Pb/^{204}Pb$, $^{143}Nd/^{144}Nd$ and $^{87}Sr/^{86}Sr$ between La Palma and El Hierro (Fig.4.29).
- There is no obvious reason why the islands of La Palma and El Hierro should show different contributions from Fe-Mn nodules. El Hierro does lie on slightly older Oceanic crust (Fig 4.1) but the very low Re/Os of Fe-Mn nodules (Table 4.7) would not permit significant isotope variation in this space of time. There is

evidence for variations in seawater chemistry over time and potentially nodules on older oceanic crust could have more elevated $^{187}Os/^{188}Os$.

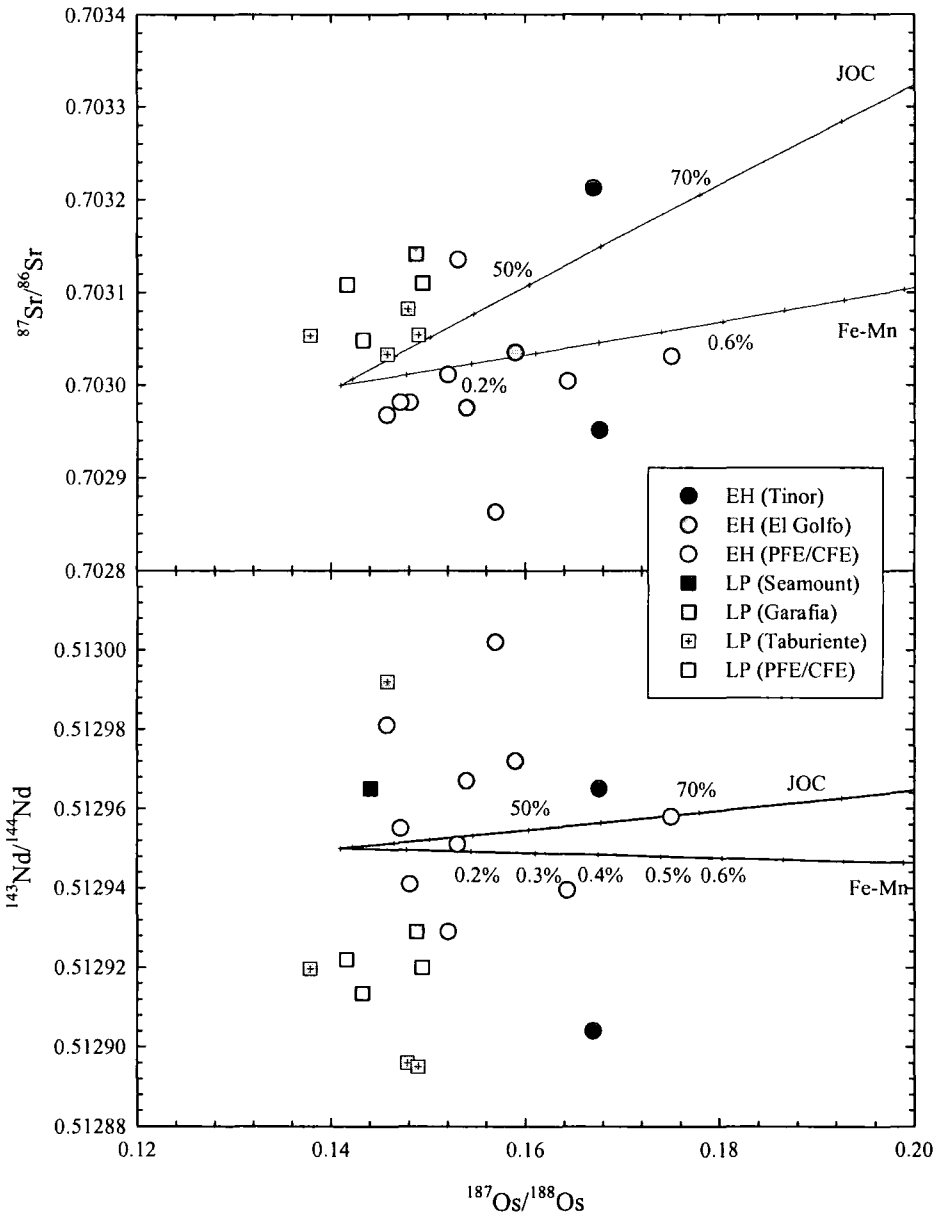

Fig. 4.29: $^{187}Os/^{188}Os$ versus $^{143}Nd/^{144}Nd$, and $^{87}Sr/^{86}Sr$ for La Palma and El Hierro lavas. JOC = Jurassic Oceanic Crust. Fe-Mn = Ferromagnesian nodules. Bulk mixing models are assumed and indicate unrealistically large quantities of both Fe-Mn crust and Jurassic Oceanic crustal components are required to explain the large isotopic variations of La Palma and El Hierro lavas. See table 4.7 for modelling parameters.

- In absence of high Re/Os ratios the difference in Fe-Mn crusts the difference in $^{187}Os/^{188}Os$ would have to be due to the Os isotope composition of seawater over period of Jurassic oceanic crust formation. The seawater $^{187}Os/^{188}Os$ would have to be 5 times greater for older Jurassic seawater to account for the variation in Fe-

Mn nodule ages imparting signatures to La Palma and El Hierro lavas. Jurassic seawater at this time was actually less radiogenic than it is today (Cohen and Coe, 2002).

4.8.3.3.2 Oceanic lithospheric mantle

Carbonatite metasomatism of lithospheric mantle suggested by melt infiltration of La Palma and El Hierro xenoliths (Hansteen *et al.*, 1991; Wulff-Pedersen *et al.*, 1996) would result in abnormal CaO, Sr and LREE concentrations in Western Canary Island xenoliths. Despite their uncertain provenance, entrained cumulates or lithospheric mantle (Klugel, 2001a) are unlikely to be able to produce the large isotopic variations observed between or within the Western Canary Island lavas. Assimilation of oceanic lithospheric material can severely affect the $^{187}Os/^{188}Os$ of OIB. As little as 1% addition of this high Os material can dominate the Os isotopic compositions of some lavas (Reisberg *et al.*, 1993; Widom *et al.*, 1999), resulting in unradiogenic $^{187}Os/^{188}Os$. However, few of the lavas analysed in this study contain xenolith material and few show systematics affected by mixtures with Fuerteventura lithospheric mantle (Fig. 4.27 and 4.28**).** An interesting feature of the El Hierro and La Palma lavas is that despite some containing dunite and harzburgite xenoliths which contain high Os (e.g., Widom *et al.*, 1999, Lanzarote xenoliths) these lavas show no evidence of excess assimilation of their xenolith cargo from Os or Re abundances (e.g., JMDDEH04). Furthermore, lavas converge to radiogenic $^{187}Os/^{188}Os$ (0.141) at high concentrations (250ppt) in contrast to the unradiogenic $^{187}Os/^{188}Os$ of abyssal peridotites (0.122-0.127; Luck and Allègre 1992, Snow and Reisberg, 1995) indicating insignificant input of lithospheric mantle to Western Canary Island lavas.

In summary, assimilation of volcanic edifice, layer 1 sediment or igneous oceanic crust and lithosphere is unable to explain the large variation in O, Sr, Nd, Os and Pb isotope systematics within and between El Hierro and La Palma. Low Os concentration samples may record some radiogenic $^{187}Os/^{188}Os$ addition, however these samples also lie within the $^{187}Os/^{188}Os$ ranges of El Hierro lavas with relatively high Os contents (>50ppt, Fig 4.27). On this basis, the correlations in multi-isotopic space and differences in isotopic compositions (e.g., O and Os) within and between

La Palma and El Hierro samples analysed here are ascribed to be dominated by mantle and not crustal contributions.

4.9 Elemental constraints on the source of Western Canary Island magmatism

4.9.1 Major element constraints

La Palma and El Hierro lavas can be effectively considered as uncontaminated, mantle-derived rocks. This means that partial melting estimates and consideration of the isotopic systematics of these lavas in the context of their mantle sources may be made. The alkaline nature of the El Hierro and La Palma lavas in conjunction with available olivine microprobe data from La Palma (Nikogosian *et al.,* 2002) and elemental and olivine microprobe from some of the other Canary Islands (Thirlwall *et al.,* 1997; Thirlwall *et al.,* 2000) suggests that there is little evidence for unusually hot mantle beneath any of the Canary Islands. Therefore, the ambient temperature for ordinary upper mantle must always be considered to avoid invoking unreasonable petrogenetic models for the origin of the Canary Islands.

The high total iron contents of La Palma and El Hierro primitive magmas, like those for Tenerife (Thirlwall *et al.,* 2000), hinders the use of major element compositional data for inferring partial melting, temperatures and pressures since the oceanic source may be Fe-rich (e.g., Takahashi *et al.,* 1993; Francis, 1995). Basanites and alkali basalts with >6 wt. % MgO are plotted in Fig. 4.30 with melt inclusion data from La Palma and experimental melt products from dry melting of peridotites KLB-1 and HK-66 (Hirose *et al.,* 1993) as well as more recent experimental data on pyroxenite melt products (Hirschmann *et al.,* 2003; Kosigo *et al.,* 2003; Keshav *et al.,* 2004). The El Hierro and La Palma bulk compositions extend to higher Fe_2O_3 and much lower SiO_2 than experimental melting of peridotites. They more closely approximate to the lower temperature and pressure pyroxenite melt products. The extension away from the pyroxenite and peridotite melt field for bulk lavas can be explained through olivine and clinopyroxene accumulation. However, primary melt inclusions from Taburiente series lavas in the Barranco de Fagundo (Nikogosian *et al.,* 2002) also lie away from typical low-Fe peridotite melting (KLB-1). Bulk composition data indicate that, like the basaltic

shield-building phase of Tenerife (Thirlwall *et al.*, 2000), El Hierro and La Palma magmas are derived from a significantly more Fe-rich mantle source than MORB; a characteristic also common to Hawaiian magmatism (Takahashi *et al.*, 1993; Hauri, 1996). The higher observed Fe_2O_3 in some El Hierro lavas might also indicate a larger portion of Fe-enriched mantle involved in their petrogenesis compared with La Palma lava. The overall conclusion from the Western Canaries agrees with results from empirical partial melting experiments suggesting that the source of OIB could be the result of mixed peridotite-pyroxenite sources in the generation of OIB (Hauri, 1996; Hirschmann *et al.*, 2003; Kosigo *et al.*, 2003).

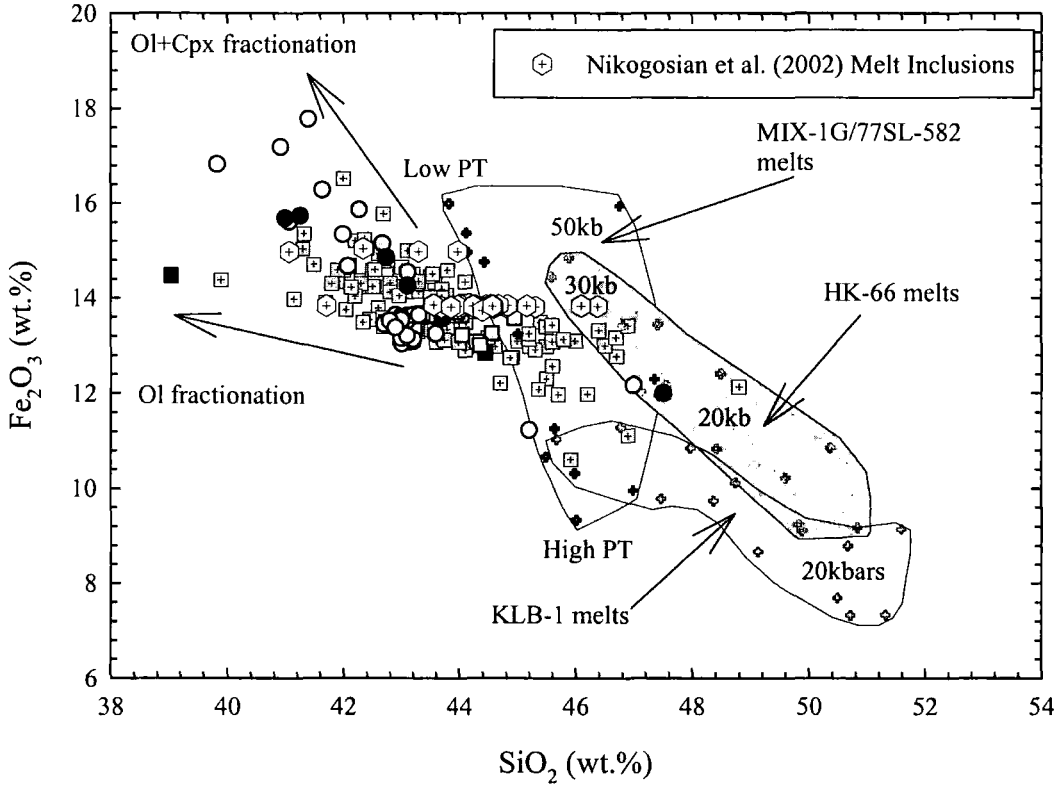

Fig. 4.30: SiO_2 versus Fe_2O_3 (total) as wt.% for La Palma and El Hierro lavas and La Palma melt inclusions (Nikogosian et al. 2002) versus partial melting experiments for peridotite KLB-1 and Fe-rich peridotite HK-66 (from Hirose and Kushiro, 1993) and pyroxenites MIX-1G and 77SL-582 (Kosigo et al., 2003; Keshav et al., 2004). Major element data from this study and Elliott (1991). Symbols as for Fig 4.21. Lavas with less than 6 wt.% MgO not plotted and lavas not fractionation corrected.

4.9.2 Trace element constraints

Some of the more primitive Cumbre Vieja, La Palma lavas studied here contain amphibole as a crystallising phase (Appendix A) indicating the presence of elevated water in the source of La Palma lavas relative to El Hierro lavas. Class and

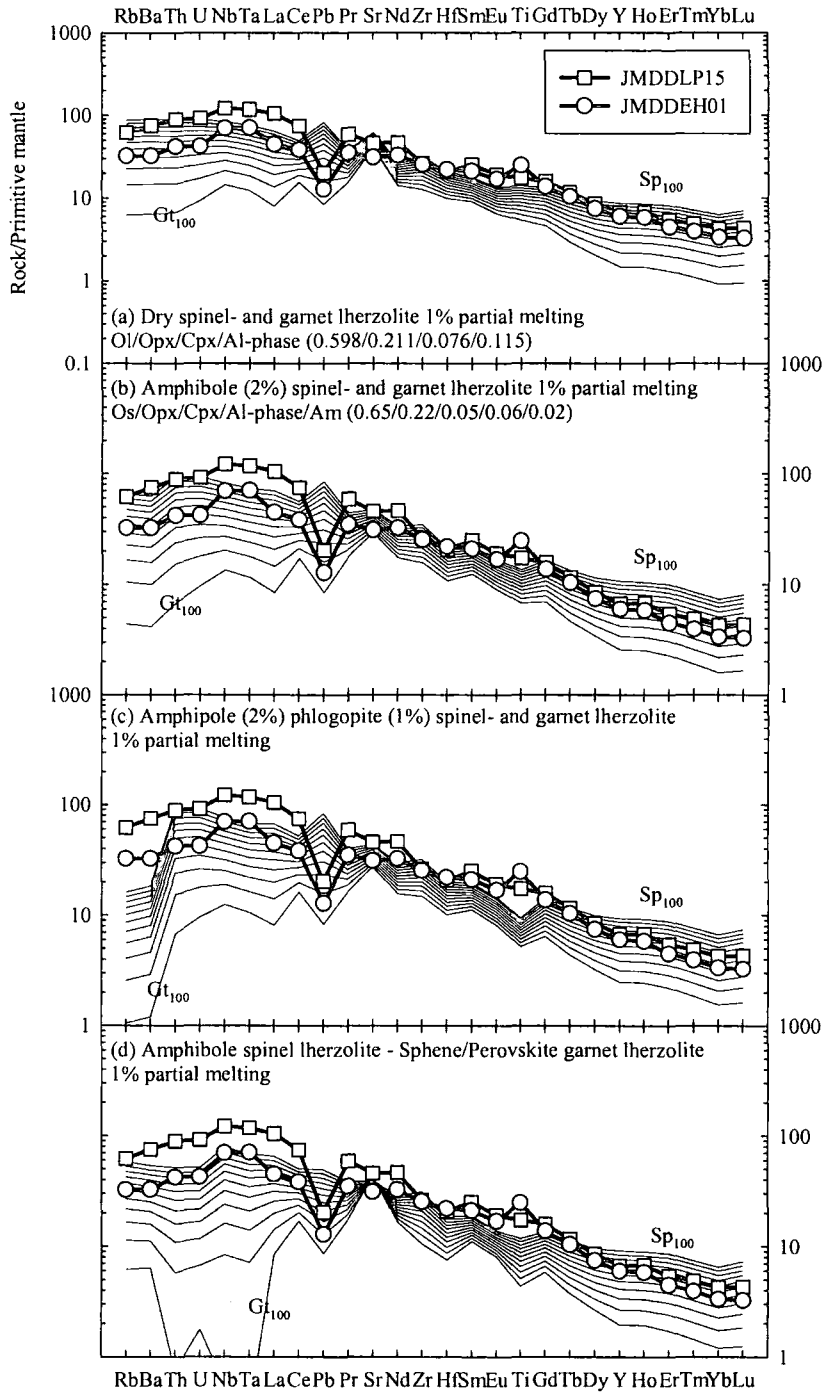

Fig. 4.31: Primitive mantle normalised multi-element plots indicating garnet to spinel source partial melting models at 1% partial melting. Panel (a) anhydrous melting of peridotite, (b) hydrous lherzolite source, (c) two component hydrous lherzolite source and (d) hydrous spinel lherzolite, garnet sphene perovskite melting to illustrate effect of sphene phases on Nb, Nb, U and Th. Partial melting requires complete exhaustion of some hydrous mineral phases to explain elevated Nb, Ta, Ti, U and Th in El Hierro and La Palma lavas. More of a hydrous component is required for Cumbre Vieja lavas than any other stratigraphic group in Western Canary islands. No single model fits the El Hierro or La Palma trace element abundance patterns reflecting the restrictions of current partition coefficient data as well as knowledge of initial source mineralogy. Partition coefficient data from McKenzie and O'Nions (1991), Halliday et al. (1995), Williams et al. (2004).

Goldstein (1997) defined a model that allowed estimation of the magma source mineralogy of OIB using a best-fit model of measured trace element patterns. These models are strongly dependant on experimentally or quantitatively defined mineral-melt partition coefficients and the proportions on minerals (e.g. starting composition) in the mantle source and this might account for some of the model uncertainties observed in some elements. Partial melting models show that HIMU-type OIB trace element patterns cannot be replicated by simple spinel or garnet lherzolite partial melting (Class and Goldstein, 1997) or by addition of hydrous phases (Fig 4.31). La Palma sample JMDDLP15 (1949 Eruption) and El Hierro lava sample JMDDEH01 (recent <1Ka eruption) are compared with different mineralogical source compositions for 1% partial melting in Fig. 4.31. Key features in the trace element patterns of Western Canary Island primitive lavas are the relative U and Th anomalies and Pb depletions as well as Ti enrichment which cannot be explained by current estimates for amphibole or phlogopite partition coefficients. Although melting studies have indicated that amphibole breaks down at the solidus (Wallace and Green, 1991), in which case its trace element control might not be expected, these melting experiments do not resolve phase relationships of low degree partial melts.

Despite evidence for increased H_2O contents in the source of some Western Canary Island lavas, none of the hydrous phase partial melting models fit any better than the anhydrous melting model (Fig 4.31a). Therefore to estimate partial melting, an anhydrous source is assumed for two reasons: (1) to be able to compare the results of melting between other partial melting estimates provided for the Canary Islands (e.g., Thirlwall *et al.,* 2000; Carracedo *et al.,* 2001); and (2) because of the greater uncertainty in partition coefficients for REE into hydrous phases compared with anhydrous phases for which a great deal of data are available (Williams *et al.,* 2004).

Relative concentrations of REE in lavas are very useful for providing depth constraints on magma generation because of their radically different partitioning into spinel and garnet (e.g., McKenzie and O'Nions, 1991). Additionally, trace element patterns as a whole are also useful for inferring mineralogical processes acting to control the compositions of magmas in OIB (Class and Goldstein, 1997). Comparison plots of primitive mantle-normalised La/Yb versus Dy/Yb provide

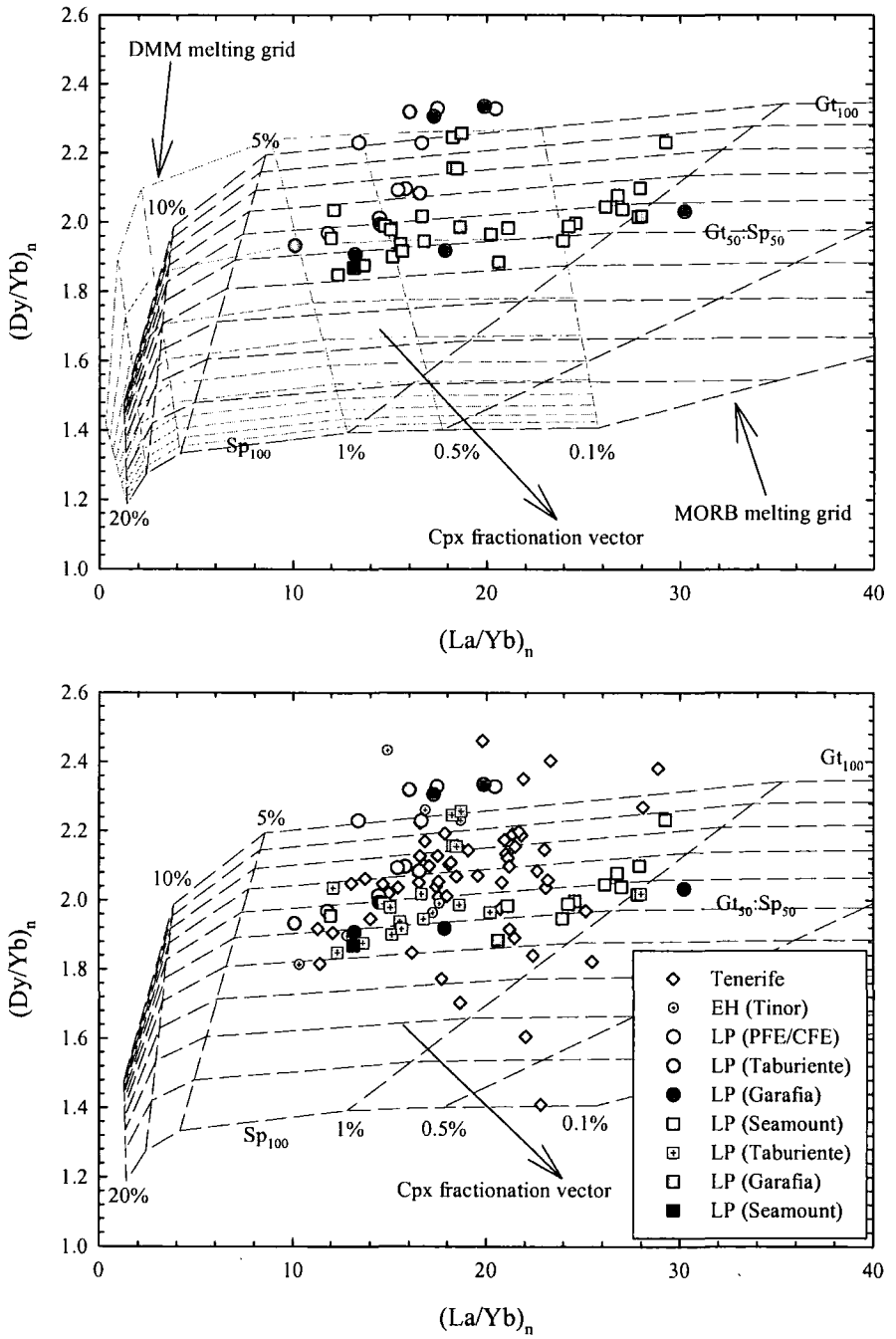

Fig. 4.32: Primitive mantle normalised La/Yb vs. Dy/Yb for La Palma, El Hierro and selected Tenerife lavas (from Thirlwall et al., 2000). Lavas with less than 6 wt.% MgO not plotted and samples are uncorrected for fractionation/accumulation. Also shown is a grid of melt compositions produced by 0.1, 0.5, 1, 5, 10 and 20% of incremental batch partial melting of a MORB source and a DMM source (light grey) with 0-100% of this melting occurring in the presence of residual garnet with the relative percentage of aluminium silicate phases (100% Garnet = Gt_{100}; 100% spinel = Sp_{100}). The melting model assumes the modes and proportions for olivine, orthopyroxene, clinopyroxene and spinel/garnet respectively noted in Thirlwall et al. (2000).

approximate constraints on melting conditions because of the different relative partitioning of these elements into high-pressure mantle mineral phases (e.g., Thirlwall *et al.*, 1994; Baker *et al.*, 1997; Thirlwall *et al.*, 2000). Fig. 4.32 shows fractional melting for DMM and MORB source compositions for La Palma and El Hierro lavas with MgO >6 wt. %. Samples greater than 6 wt. % MgO were selected to avoid samples that have suffered apatite or haüyne fractionation. Clinopyroxene fractionation may also affect this plot, reducing Dy/Yb and increasing La/Yb and a fractionation trajectory is plotted for clinopyroxene in Fig. 4.32.

El Hierro samples plot close to, or in the pure garnet lherzolite melting field but show a positive correlation to lower normalised La/Yb and Dy/Yb ratios indicating some melting in the spinel lherzolite field occurred for both El Hierro and La Palma lavas. Secular variation in the islands is seen from melting characteristics. Older northern shield lavas of La Palma are derived from similar degrees of melting as El Hierro lavas. The younger PFE-CFE eruptions of the Cumbre Vieja have a steep positive correlation in normalised La/Yb-Dy/Yb space, consistent with lower degrees of partial melting at similar depths in the garnet and spinel melting fields. When compared with lavas from Tenerife, similar depths of melting are estimated. On the basis of trace element inversion modelling, Carracedo *et al.* (2001) suggested depths of melting in the region of 80-110km at ~1.2-2.2% partial melting after removing the effects of 25% fractionation of olivine and clinopyroxene phenocryst phases. These values are broadly consistent with the estimates of depth and partial melting presented in Fig. 4.32 indicating that the effect of fractionation is not significant on lavas with >6wt% MgO. Discrepancies in the partial melting model still exist, however, as El Hierro lavas and the La Palma PFE/CFE plot at high $(Dy/Yb)_n$ in the opposite sense to clinopyroxene fractionation.

4.10 Mantle source contributions to La Palma and El Hierro lavas

The calculated melting and buoyancy fluxes for different OIB vary widely (Sleep, 1990). The ocean islands with the highest buoyancy flux are the Hawaiian Island chain but most other ocean island are estimated to have lower fluxes. Partial melting in the source of low buoyancy flux ocean islands is likely to preserve information on the local nature and scale of chemical variation. Previous work has confirmed the presence of mantle compositional heterogeneity for the Canary Islands (Hoernle *et*

al., 1991, 1993b; Marcantonio *et al.*, 1995; Widom *et al.*, 1999) and a number of source components have been identified:

- A long-term incompatible element depleted mantle signature reflected in SiO_2 undersaturated lavas from Gran Canaria (Hoernle *et al.*, 1991).
- A HIMU component, especially prominent in the radiogenic $^{187}Os/^{188}Os$ and $^{206}Pb/^{204}Pb$ of La Palma lavas (Marcantonio *et al.*, 1995).
- Enriched mantle components (EM I, EM II), seen in SiO_2-saturated Gran Canaria basalts and attributed to enriched continental lithospheric mantle (Hoernle *et al.*, 1991).

Mafic magmatism on the islands of La Palma and El Hierro have very similar HIMU-like trace element abundances, probably derived from small (1-2.5%) degree partial melts of their mantle source. The Western Canary Island lavas show strong positive correlations in $^{206}Pb/^{204}Pb$-$^{207}/^{204}Pb$, $^{206}Pb/^{204}Pb$-$^{208}Pb/^{204}Pb$ (being co-linear with the NHRL), and $^{87}Sr/^{86}Sr$-$^{206}Pb/^{204}Pb$ space. They show negative correlations in $^{206}Pb/^{204}Pb$-$^{143}Nd/^{144}Nd$ and $^{206}Pb/^{204}Pb$-$\delta^{18}O$ space indicating a lack of EM I or EMII like components in their mantle sources. Generally, La Palma lavas lie at one end of the Western Canary Island correlation with radiogenic $^{87}Sr/^{86}Sr$ and $^{206}Pb/^{204}Pb$, unradiogenic $^{143}Nd/^{144}Nd$ and low $\delta^{18}O$ (+4.86±0.38‰, 2S.D, n=30), whilst El Hierro lavas possess relatively less radiogenic $^{87}Sr/^{86}Sr$ and $^{206}Pb/^{204}Pb$, radiogenic $^{143}Nd/^{144}Nd$ and higher $\delta^{18}O$ (+5.09±0.18‰, 2S.D, n=30). Such correlations appear to be consistent with a larger component of a 'young' HIMU component in La Palma lavas, with relatively high time integrated Rb/Sr, U/Pb and lower Sm/Nd and lower $\delta^{18}O$, than the mantle components responsible for El Hierro magmatism. In contrast El Hierro lavas possess much more elevated γOs (23.1±6.6, n=16) than La Palma lavas (13.6±2.9, n=23) indicating a mantle source with higher time integrated Re/Os ratios for El Hierro. Both El Hierro and La Palma possess similar $^{3}He/^{4}He$ for their olivine and clinopyroxene phenocrysts (4.1 to 11.8R_A versus 4.2 to 9.7R_A, respectively).

The similarities and the large isotopic variation between the two islands require explanation. A number of source components have been proposed to account for the large isotopic variations measured in OIB suites:

- Metasomatised oceanic lithosphere
- Recycled oceanic crust

- Recycled oceanic lithospheric mantle
- Metasomatised continental lithospheric mantle
- Core-mantle interaction

The possible contributions of these components in the source of Western Canary Island magmatism will now be assessed and compared with the global OIB database.

4.10.1 Nature of mantle components beneath La Palma and El Hierro

Certain trace element ratios in OIB have been considered as characteristic of mantle source derivation (e.g., Weaver, 1991a, b; Chauvel *et al.,* 1992). For instance, HIMU basalts (Canaries, St Helena, Mangaia), which have radiogenic Pb isotope compositions, have significantly different trace element enrichments to EMI- and EMII-type OIB such as Tristan da Cuhna (EMI) and Tahaa (Society, EMII). Zr/Nb, Nb/Ta, Ce/Pb, Th/Nb, La/Nb and Th/U ratios for El Hierro and La Palma lavas are compared with averages from other Canary Islands and OIB in Table 4.1. The La Palma Ce/Pb ratio average from this study is significantly lower than the estimate of Marcantonio *et al.* (1995); possibly reflecting the more accurate analysis of samples using ICP-MS in this study. Otherwise El Hierro has higher Zr/Nb, Ce/Pb and Th/U relative to La Palma lavas, with both islands exhibiting trace element ratio characteristics comparable to extreme HIMU OIB.

In terms of their trace elements, there appears to be little secular variation within the islands of La Palma and El Hierro. The only significant variation is that the PFE-CFE lavas of La Palma exhibit the most extreme Ce/Pb for that island whereas the older Ti□or edifice has the most extreme Ce/Pb and Th/U for El Hierro. Thirlwall (1997) stated that is was still unclear how much can be read into trace element ratios of OIB because of the inherent problem of inter-laboratory differences and the fact that some of the ratios correlate with indices of increasing partial melting. Furthermore, Thirlwall (1997) has suggested that while useful for comparison, trace element ratio variations in OIB and MORB offer little to models for OIB origins based on isotopic systematics. The data obtained for this thesis by ICP-MS only correlate loosely with indices of partial melting (Fig 4.33) and reveal similar groupings and clusters with partial melting models in Fig 4.32.

Despite the caveats regarding trace elements, their ratios do indicate that the Western Canary Islands originate from melting of mantle sources with similar

incompatible trace element ratios to extreme HIMU OIB from the Pacific and the Atlantic. On the basis of Sr, Nd and Pb isotopes there is little doubt of the involvement of a HIMU mantle domain in the origin of Western Canary Island lavas (Figs. 4.14 and 4.15). Radiogenic Pb isotope signatures of endmember HIMU OIB are commonly attributed to a component of recycled oceanic crust in the mantle source (Hofmann and White, 1982; Zindler and Hart, 1986). Radiogenic $^{187}Os/^{188}Os$ of HIMU OIB have been explained in a similar manner (Pegram and Allègre, 1992; Hauri and Hart, 1993; Reisberg *et al.*, 1993; Roy-Barman and Allègre, 1995; Marcantonio *et al.*, 1995). Marcantonio *et al.* (1995) observed correlations of Os and Pb isotopes in La Palma lavas consistent with mixing between a HIMU component and another isotopically enriched (relative to DMM) element in their mantle source. Widom *et al.* (1999) modified this theme to incorporate a LVC (the so-called Low Velocity Composition component) recognised by Hoernle *et al.* (1995) which is essentially a hybrid mixture of 1.2Ga recycled oceanic crust and depleted mantle.

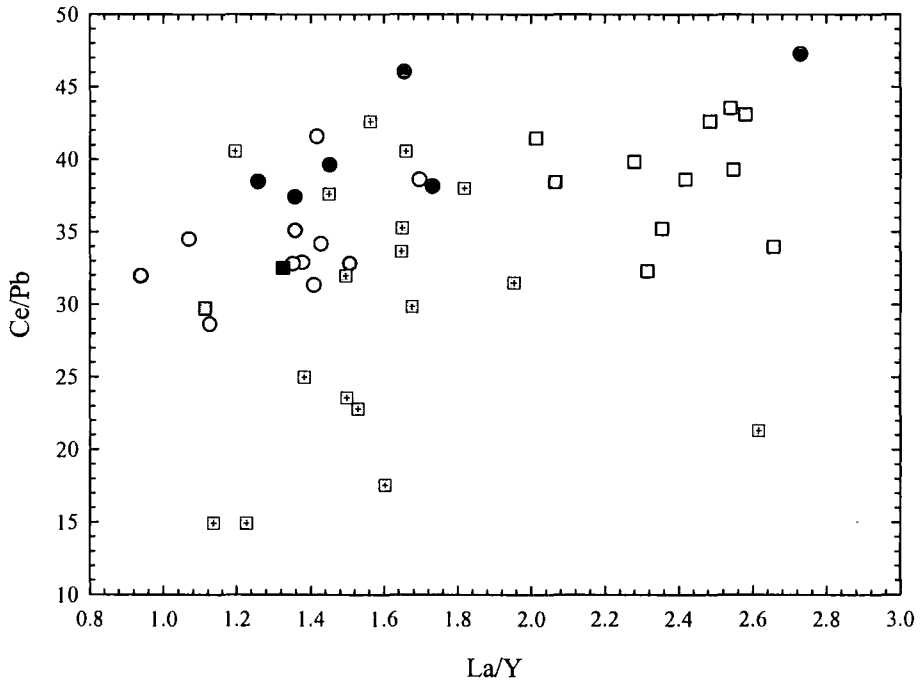

Fig. 4.33: La/Y versus Ce/Pb variations for El Hierro and La Palma lavas. Thirlwall (1997) noted systematic increase with partial melting of Ce/Pb. In La Palma and El Hierro this scenario is complicated by accumulation of mineral phases but generally positive correlations can be seen between Taburiente and LP (PFE/CFE) lavas. LP (PFE/CFE) lavas are generated from lower degrees of partial melting according to Fig. 4.32. Data symbols same as for Fig. 4.32.

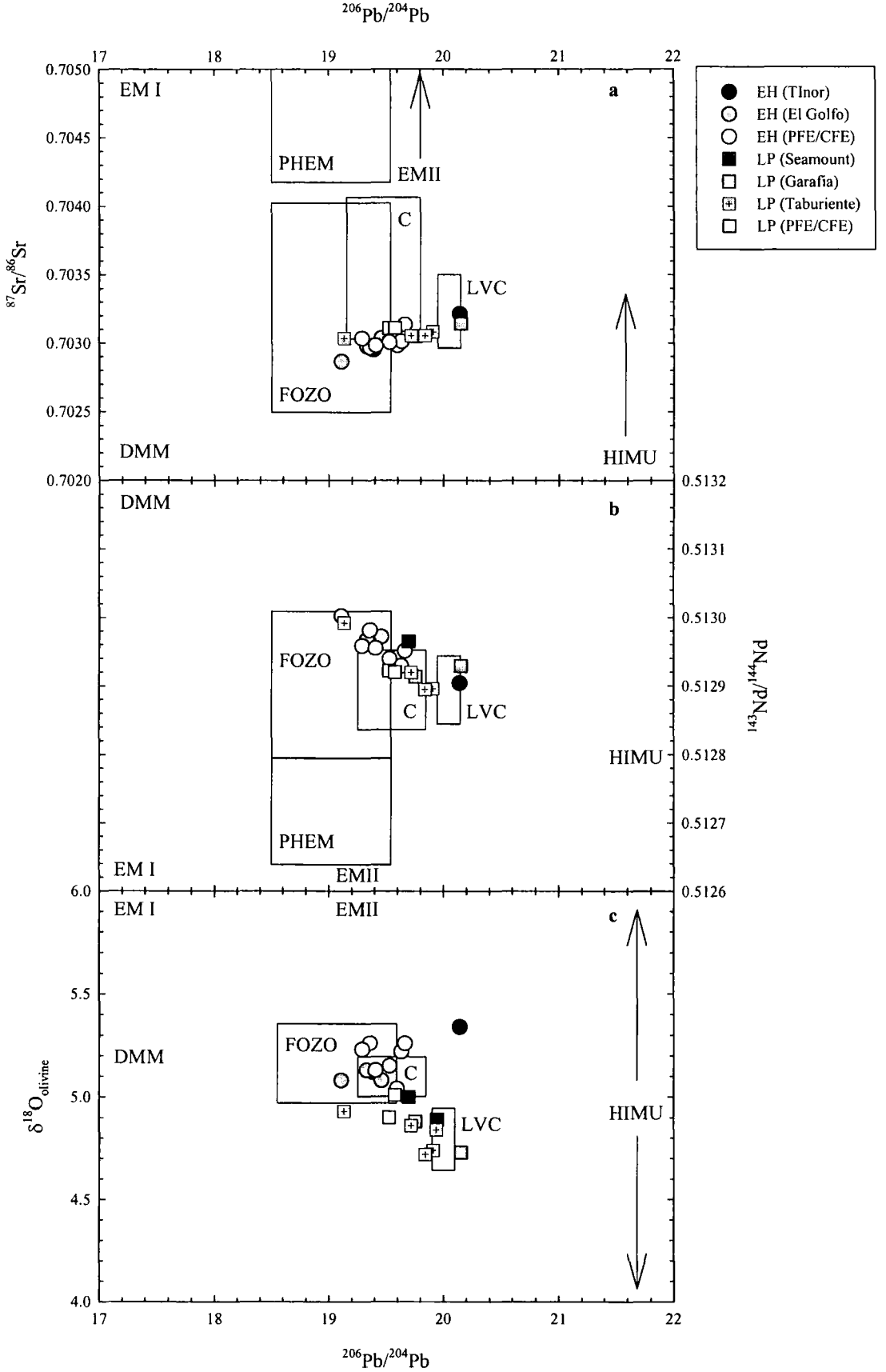

Fig. 4.34: $^{206}Pb/^{204}Pb$ versus (a) $^{87}Sr/^{86}Sr$, (b) $^{143}Nd/^{144}Nd$, (c) $\delta^{18}O_{olivine}$, and for La Palma and El Hierro lavas. Also shown are mantle components which are tabulated in table 4.8.

The LVC of Hoernle *et al.* (1995) is one of a number of commonly recognised components to OIB world-wide. Hart *et al.* (1992) demonstrated that in Sr-Nd-Pb isotope space OIB lavas, whilst showing component mixing with MORB, HIMU and EMI/EMII, did not show convergence towards depleted MORB mantle or toward bulk silicate Earth. OIB in fact mix towards a common depleted component distinct from MORB. This component, known as FOZO (Focus Zone) is related to other estimates of universal components such as PHEM (Primitive He Mantle; Farley *et al.*, 1992) or 'C' (Common; Hanan and Graham, 1996) and also to the LVC of Hoernle *et al.* (1995). Table 4.8 outlines proposed $^{3}He/^{4}He$, $^{87}Sr/^{86}Sr$, $^{143}Nd/^{144}Nd$, $^{187}Os/^{188}Os$ and $^{206}Pb/^{204}Pb$ compositions for these components. In Fig 4.34 the positions of El Hierro and La Palma lavas with respect to this FOZO, PHEM, C or LVC component are shown. El Hierro and La Palma lie within the fields of the proposed mantle components. The positive correlations in $^{206}Pb/^{204}Pb$-$^{87}Sr/^{86}Sr$ and negative correlation in $^{206}Pb/^{204}Pb$- $^{143}Nd/^{144}Nd$ infer that El Hierro correspond to addition of FOZO whilst La Palma require more of a HIMU component and lie in the LVC field in Fig. 4.34. These relationships indicate that El Hierro and La Palma lavas conform to mixtures of FOZO and HIMU.

Table 4.8 - The Focal Zone, Common, PHEM or LVC mantle components

Type	$^{3}He/^{4}He$ (R/RA)	$^{87}Sr/^{86}Sr$	$^{143}Nd/^{144}Nd$	$^{206}Pb/^{204}Pb$	$^{187}Os/^{188}Os$	Ref.
FOZO	>37.7	0.7025-0.7040	0.51300-0.51280	18.5-19.5	-	1, 2, 3
PHEM	>24	0.7042-0.7052	0.51265-0.51280	18.5-19.0	-	4
C	>37.7	0.7030-0.7040	0.51295-0.51284	19.2-19.8	-	5
LVC	-	0.7030-0.7034	0.51282-0.51294	19.9-20.1	0.146	6, 7

Data for the proposed fifth mantle components derived from 1 – Hart et al. (1992), 2 – Hauri et al. (1994), 3 – Hilton et al. (1999), 4 – Farley et al. (1992), 5 – Hanan and Graham (1996), 6 – Hoernle et al. (1995), 7 – Widom et al. (1999).

On the basis of the correlations between La Palma and El Hierro lavas in Fig. 4.34 possible endmember $\delta^{18}O$ compositions for FOZO, C and LVC have been tentatively suggested. The positive $^{206}Pb/^{204}Pb$-$^{87}Sr/^{86}Sr$ and negative $^{206}Pb/^{204}Pb$- $^{143}Nd/^{144}Nd$ correlations for El Hierro and La Palma lavas require a HIMU component. This endmember appears to have low $\delta^{18}O$. For El Hierro samples with higher $\delta^{18}O$ than La Palma samples the lavas require contributions from a FOZO-like component. To

investigate these relationships further the Os-Pb isotope systematics of El Hierro and La Palma lavas can be compared to OIB globally.

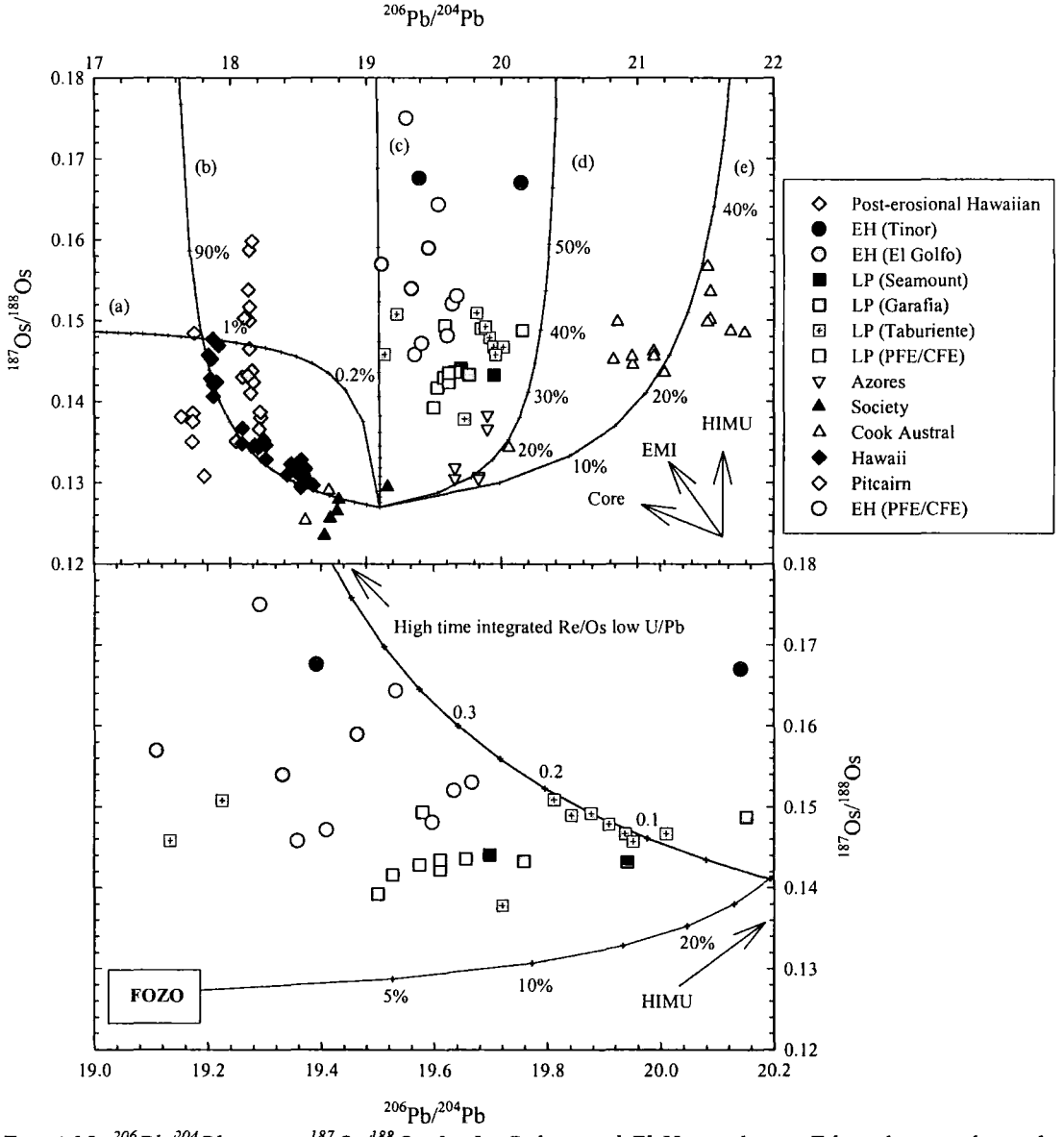

Fig. 4.35: $^{206}Pb/^{204}Pb$ versus $^{187}Os/^{188}Os$ for La Palma and El Hierro lavas. Filtered to employ only lavas with Os >50ppt from the Western Canary Island and global OIB dataset. Also shown are mantle components tabulated in table 4.7 and 4.8. In upper panel bulk mixing between endmember is shown (a) Core-FOZO, (b) EMI-FOZO, (c) Beni Bousera Pyroxenite-FOZO, (d) 1.2Ga HIMU-FOZO, (e) 2Ga HIMU-FOZO. In lower panel bulk mixing model (d) is shown with, for illustrative purposes, mixtures from a low time integrated U/Pb ($^{206}Pb/^{204}Pb$ =19, 100ppm Pb) high time integrated Re/Os ($^{187}Os/^{188}Os$ = 0.6, 0.1ppb Os) composition. Other modelling parameters in Table 4.7. Published data from Hauri and Hart (1993), Marcantonio et al. (1995),Widom et al. (1996), Hauri et al. (1996), Lassiter et al. (1998; 2000), Eisele et al. (2002). Post-erosional Hawaiian lavas thought to be derived from pyroxenite-peridotite mixing (Lassiter et al., 2000) shown as grey diamonds.

OIB with >50ppt Os have consistently more radiogenic $^{187}Os/^{188}Os$ than bulk silicate Earth and abyssal peridotites (Hauri and Hart, 1997). The only exception in the OIB dataset are some Azores lavas which possess unradiogenic $^{187}Os/^{188}Os$ suggesting a possible depleted lithospheric mantle provenance, but these lavas have <50ppt Os (Schaefer *et al.*, 2002). In Fig. 4.35 El Hierro and La Palma samples are plotted versus other ocean islands which possess lavas with Os concentrations greater than 50ppt. This cut-off value has been selected to avoid OIB samples contaminated by crust, sediment or lithosphere (Fig 4.27). Lavas from El Hierro have the most radiogenic $^{187}Os/^{188}Os$ of any OIB measured so far (Fig 4.35).

La Palma samples have lower $^{187}Os/^{188}Os$ but more radiogenic $^{206}Pb/^{204}Pb$ compared to El Hierro lavas. The radiogenic $^{187}Os/^{188}Os$ and $^{206}Pb/^{204}Pb$ of HIMU ocean islands such as the Cook-Austral chain can be reproduced by incorporation of 20-35% of 1.8 to 2Ga recycled oceanic crust into their sources using a 'universal' enriched mantle composition ($^{206}Pb/^{204}Pb$ = 19.1 (Widom *et al.*, 1999)) with a near-chondritic $^{187}Os/^{188}Os$ compositions (0.1270). The more radiogenic $^{187}Os/^{188}Os$ of Western Canary Island lavas and HIMU islands such as the Cook-Austral might suggest that Western Canary Island magmas might incorporate a component of recycled oceanic crust, which despite the less radiogenic $^{206}Pb/^{204}Pb$ signature (Marcantonio *et al.*, 1995) could be of a different age.

Another method for generating variable Pb isotope signatures would be to add pelagic sediment to 2Ga subducted oceanic crust (Roy-Barman and Allègre, 1995). Addition of even small amounts of sediment directly into the source of OIB would result in large deviations from the NHRL in Pb-Pb isotope space. This is not seen in either El Hierro or La Palma lavas (Fig. 4.15). This relationship shows that the addition of sedimentary components must be exceedingly small for La Palma and El Hierro. Alternative models to generate this variation using recycled oceanic crustal components could invoke the involvement of high Re/Os, high □^{18}O sheeted dyke and upper layered gabbro sequence of oceanic crust; a source which would probably be co-linear with the NHRL. However, for sheeted dykes the relative Os/Pb ratio would be exceedingly low requiring excessive amounts of such material in the source of El Hierro lavas.

Considering Os isotopes alone in Fig. 4.35, a model invoking 1.2Ga recycled oceanic crust implies 20-35% of this material (curve d) can explain the Pb-Os

isotope systematics of La Palma lavas. In contrast between 30 and 50% of this material is required to explain the El Hierro $^{187}Os/^{188}Os$. This observation is at odds with the much lower $^{206}Pb/^{204}Pb$ of El Hierro compared with La Palma because an increased quantity of 1.2Ga recycled oceanic crust in the source of El Hierro lavas should drive $^{206}Pb/^{204}Pb$ to more radiogenic compositions. When both Pb and Os isotopes are considered, another component with lower $^{206}Pb/^{204}Pb$ but more radiogenic $^{187}Os/^{188}Os$ is required to explain the systematics of all Western Canary Island lavas. Younger recycled oceanic crust will plot to increasingly unradiogenic $^{206}Pb/^{204}Pb$ and $^{187}Os/^{188}Os$ on Fig. 4.35. On this basis, recycled oceanic crust and lithosphere of different ages or with variable Re/Os and U/Pb ratios can thus account for the entire variation of $^{206}Pb/^{204}Pb$ and $^{187}Os/^{188}Os$ for HIMU OIB in Fig 4.35. Therefore the observed isotopic difference between El Hierro and La Palma lavas could be due to the involvement of recycled oceanic crust with different ages and time-integrated P/D ratios.

The convergence of OIB to a location defined by $^{206}Pb/^{204}Pb$ = 19.1 and $^{187}Os/^{188}Os$ = ~0.1270 is a similar observation to the correlations between Sr, Nd and Pb in OIB (Hart *et al.*, 1992; Farley *et al.*, 1992; Hauri *et al.*, 1994; Hoernle *et al.*, 1995; Hanan and Graham, 1996) and suggests that a mantle component with chondritic to supra-chondritic □Os is common to all OIB. Along with Sr, Nd, Pb and Os these correlations strongly infer that FOZO, C or PHEM represent mixtures of depleted peridotite and enriched components (HIMU, e.g., Hauri, 2002). A noticeable attribute of the $^{206}Pb/^{204}Pb$-$^{187}Os/^{188}Os$ correlations is that despite a wide variation of $^{206}Pb/^{204}Pb$ all OIB tend to have radiogenic $^{187}Os/^{188}Os$. This means that OIB tap either variably aged reservoirs with variable but high Re/Os ratios or a single reservoir with high Re/Os.

If a single component is preferred instead of variably aged oceanic crust, an outer core contribution may be possible (Walker *et al.*, 1995; Widom and Shirey, 1996; Brandon *et al.*, 1998; 1999; 2003). Around 99% of the Earth's Re and Os inventory is likely to reside in the core with the bulk of the core retaining Re/Os and $^{187}Os/^{188}Os$ ratios similar to bulk Earth estimates. Solidification of the inner core could fractionate Re/Os and Pt/Os resulting in growth of radiogenic $^{187}Os/^{188}Os$ and $^{186}Os/^{188}Os$ in outer core material, which could potentially be transferred in small quantities, to intraplate magmatism in the guise of a deep mantle plume (Walker *et*

al., 1995; Walker *et a.*, 1997; Brandon *et al.*, 1998; Brandon *et al.*, 1999; Brandon *et al.*, 2003).

With correspondingly elevated $^{187}Os/^{188}Os$, outer core material should also be characterised by very unradiogenic $^{206}Pb/^{204}Pb$ (Widom and Shirey, 1996). Using the point of convergence for Hawaii and Gorgona lavas and Noril'sk ore estimated by Brandon *et al.* (2003) on the basis of $^{187}Os/^{188}Os$-$^{186}Os/^{188}Os$ correlations, the core should have a present day □Os = 17.5. In Fig. 4.35 a mixing trajectory between outer core material (2800ppb Os) and the FOZO/C/PHEM component is shown. This mixing trajectory, while potentially offering an explanation for Hawaiian OIB in terms of $^{187}Os/^{188}Os$-$^{186}Os/^{188}Os$ systematics, is curved in the opposite sense of HIMU OIB and does not replicate the Pb-Os systematics of Hawaii lavas well either. The Hawaiian correlation in Fig. 4.35 is much better explained by mixture of the FOZO/C/PHEM component and EMI. For Hawaii, SiO_2, Sr and Os relations are also better explained by this correlation (e.g., Hauri *et al.*, 1996). In the case of La Palma and El Hierro, further problems are encountered with an outer core model to explain either FOZO/C/PHEM or the high $^{187}Os/^{188}Os$ component(s). These include (i) the low buoyancy flux of the Canary Island hotspot, (ii) low Os concentrations of Canary Island lavas (addition of even 0.01% core material would result in addition of 28ppb Os to the OIB source) and (iii) lack of very unradiogenic $^{206}Pb/^{204}Pb$ isotope compositions. Hauri (2002) has outlined further problems with an outer core incorporation model such as the specific set of circumstances to drive outer core addition models (siderophile element fractionation, formation of the inner core early in Earth history, isotopic disequilibrium between the inner and outer core persisting for the age of the Earth, and a specific flux of Os from the core to the mantle). Interestingly, if El Hierro and La Palma lavas had radiogenic $^{187}Os/^{188}Os$ because of core material, $^{186}Os/^{188}Os$ ratios up to 0.119882 would be predicted for these lavas, 12ppm higher than the point of convergence estimate for outer core made by Brandon *et al.* (2003).

4.10.2 Documenting temporal and spatial geochemical variations between and within El Hierro and La Palma lava suites

Nikogosian *et al.* (2002) on the basis of melt inclusion relationships, offered an explanation for the variation in lava types from highly alkalic, basanitic lavas (the

Izcagua suite) and silica-rich, "transitional" lavas (the Fagundo suite) which have similar ranges of elemental abundances such as MgO. Nikogosian *et al.* (2002) explained this variation by the deep (12-40km) fractionation of a clinopyroxene-rich assemblage generating an Izcagua-like melt from a Fagundo-like parental magma. Isotopic variations between SiO_2 undersaturated and saturated lavas in Gran Canaria, have been explained in terms of contamination by sub-Canarian lithosphere of the latter by Hoernle *et al.* (1991). Nikogosian *et al.* (2002) pointed out that this 'direction of change' is opposite to that inferred from their study and as such any isotopic changes between Fagundo and Izcagua lavas should be documented to see if similar variations are seen between La Palma suites compared to Gran Canaria lavas.

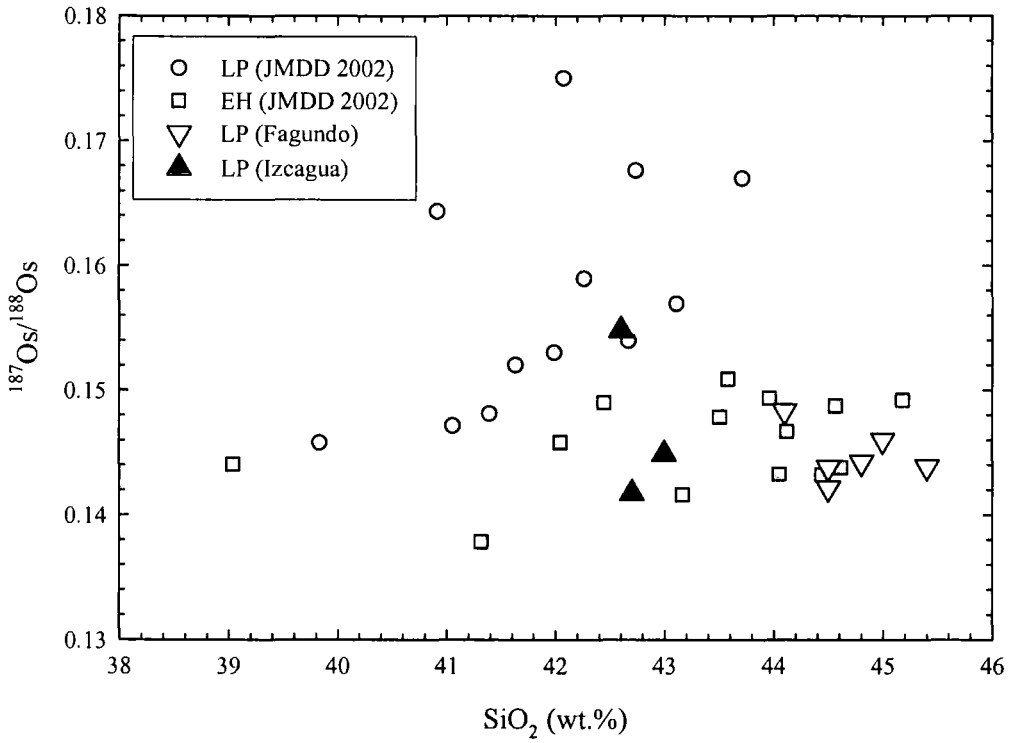

Fig 4.36: $^{187}Os/^{188}Os$ versus SiO2 for La Palma Barranco de Izcagua and Fagundo lavas. Also shown are the La Palma and El Hierro lavas collected in 2002 which form the major part of this study.

Whole rock Re-Os isotope data are presented for lavas analysed by Nikogosian *et al.* (2002) from Barranco de Fagundo and Izcagua. Izcagua and Fagundo samples are plotted versus their SiO_2 abundances in Fig 4.36. Izcagua and Fagundo lava flows mostly lie within the SiO_2-$^{187}Os/^{188}Os$ defined by the 2002 La Palma sample suite. The only exception in LP96-14, which was the only sample analysed from Izcagua

in this study that was not presented in Nikogosian *et al.* (2002). This sample lies within the SiO_2-$^{187}Os/^{188}Os$ defined by El Hierro lavas. In short there are no significant $^{187}Os/^{188}Os$ isotope differences between the Izcagua and Fagundo lavas suites. In terms of Re and Os concentrations, the only differences between the samples are that Fagundo samples trend to higher Re concentrations with increasing SiO_2 (not shown). There are apparent differences between the Iscagua and Fagundo suites in terms of age, however. The mapping and age dating studies of Carracedo *et al.* (2001) indicate that the lavas of Barranco de Fagundo form part of the Lower Taburiente series whereas Barranco de Izcagua are from the Upper Taburiente series. These series are defined by (i) different ages and (ii) different eruptive styles (Carracedo *et al.* 2001).

In Fig. 4.35 there are 'within stratigraphy' correlations in $^{187}Os/^{188}Os$ and $^{206}Pb/^{204}Pb$. For example there are positive correlations for PFE/CFE lavas from both islands as well as a negative correlation in Pb and Os isotopes for La Palma Taburiente lavas. In addition to these variations other stratigraphically constrained variations are apparent for La Palma and El Hierro. For example $^{187}Os/^{188}Os$ ratios decrease up the El Hierro stratigraphy (Fig 4.19). CFE/PFE Cumbre Vieja lava from La Palma have the highest $(La/Yb)_n$ and possess phenocrysts with the highest [He] of all Western Canary Island lavas (Fig 4.9). Variability in [He] between different lava series has been reported for the Juan-Fernandez archipelago (Farley *et al.*, 1993) and ascribed to variations in He abundances in the mantle source. The Cumbre Vieja ridge is propagating southward away from the main focus of La Palma volcanism, the Northern Shield (Seamount, Garafia, Taburiente, Benejado). The Cumbre Vieja ridge possesses primitive lavas that contain abundant amphibole, form generally positive correlations in Os-Pb isotope space (Fig 4.35) and were formed by different degrees of partial melting (Fig 4.32) compared with Northern Shield lavas. These variations need to be explained in the context of a mantle source model.

La Palma and El Hierro histories have been punctuated by rare but catastrophic debris avalanches. Lavas from the Benejado volcano, believed to have formed after the 'Caldera de Taburiente' collapse (Carracedo *et al.*, 2001, e.g., JMDD LP09) and from the uppermost CFE of El Hierro (JMDDEH12, JMDDEH13) related to the major El Golfo collapse possess anomalous isotopic compositions. For example JMDDLP09 has the most unradiogenic Pb and $^{87}Sr/^{86}Sr$ and highest $^{143}Nd/^{144}Nd$ of

La Palma lavas analysed in this study. Similarly El Hierro lavas JMDDEH12 and JMDDEH13 have the most radiogenic $^{187}Os/^{188}Os$ of the younger (<0.5Ma) lavas on that island. A possibility for this isotopic variation might be similar to that proposed for Pb isotope variations in glacial and post-glacially erupted lavas from Iceland (Gee *et al.,* 1998b). Removal of dense material (in excess of $1000km^3$ in a single event) would result in load loss from the volcanic edifice and could result in decompression melting. This hypothesis requires further testing, but whatever the cause, there is obvious variation in isotopic composition that correlates in Pb-Os isotope space (Fig 4.35). This relationship implies that components in the mantle sources of the Canary Islands with different $^{187}Os/^{188}Os$ and $^{206}Pb/^{204}Pb$ have been melting to generate these variations.

The close proximity, both spatially and temporally, of isotopic variation measured within and between La Palma and El Hierro lavas requires explanation at (i) the length scales invoked for such variation (i.e., less than 1×10^2km or less than 0.1Ma) and (ii) in the context of the overall isotopic variation seen in Western Canary Island lavas.

4.10.3 Pyroxenite-peridotite mixtures – banded or veined mantle

A significant problem with invoking recycled oceanic crust in the source of OIB is the impact it would have on major element characteristics of lavas. For example melting of recycled oceanic crust would result in silica-rich, low magnesium melts (Niu and O'Hara, 2003). This makes melting of large proportions of oceanic crust that are required for some oceanic islands based on isotopic compositions, highly unlikely. Hauri (2002) observed that the difference in $^{187}Os/^{188}Os$ ratios between OIB and abyssal peridotites, both of which are from the convecting mantle, are strikingly similar to the difference in $^{187}Os/^{188}Os$ isotope ratios of peridotites and eclogites from the continental lithosphere. There is evidence from peridotite massifs that precursor recycled oceanic crust is responsible for the generation of pyroxenites through high pressure melting (Pearson *et al.,* 1993). These mafic lithologies are characterised by a large variation of $^{187}Os/^{188}Os$ (0.134 to 0.833), $^{206}Pb/^{204}Pb$ (18.21-19.90), $^{87}Sr/^{86}Sr$ (0.7025-0.7110), $^{143}Nd/^{144}Nd$ (0.51223 to 0.51390) and $\delta^{18}O$ (+4.5 to +8.7‰; conventional fluorination, Pearson *et al.,* 1991; Pearson *et al.,* 1993;

Pearson and Nowell, 2004). This variation exceeds the range of all the Western Canary Island lavas.

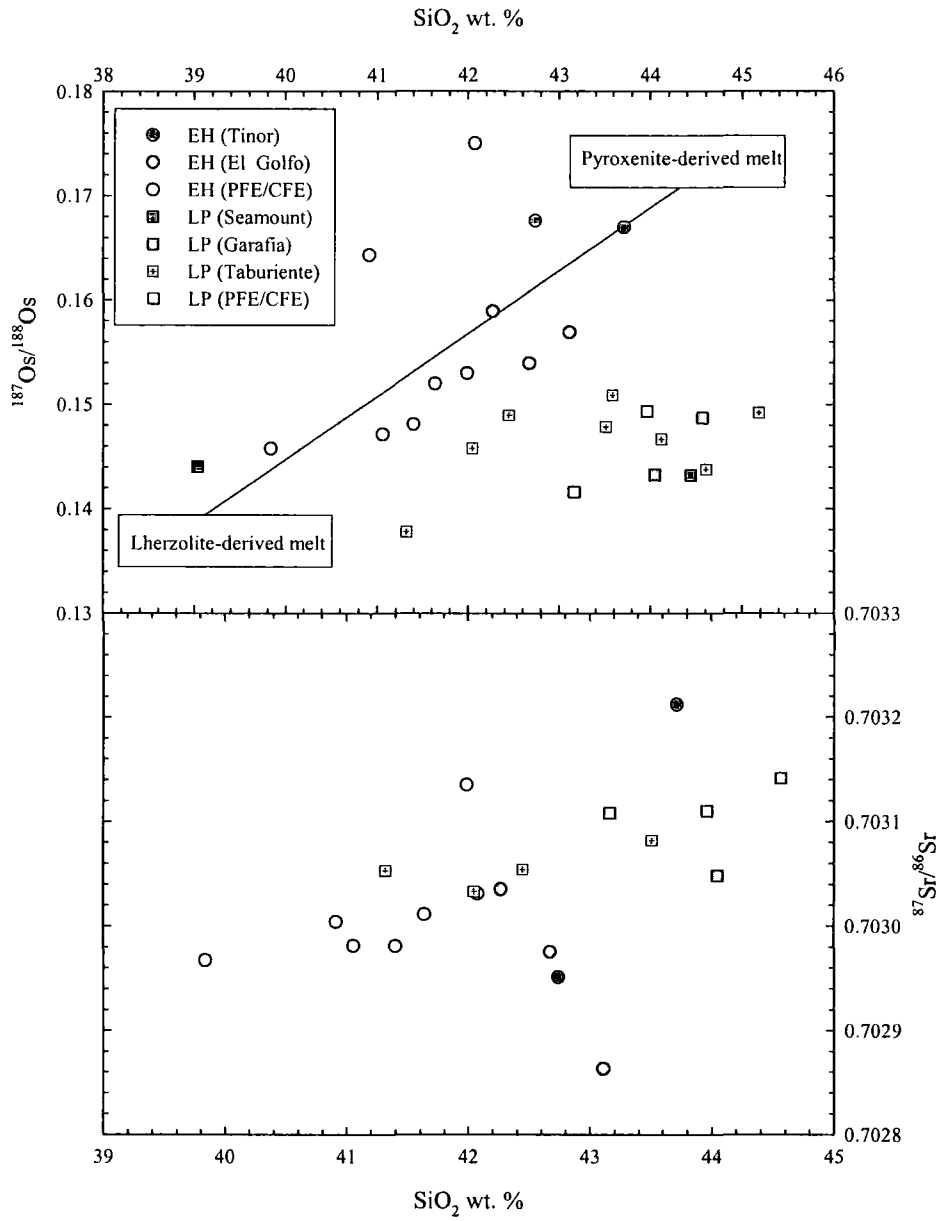

Fig. 4.37: SiO_2 (wt.%) versus $^{87}Sr/^{86}Sr$ and $^{187}Os/^{188}Os$ for La Palma and El Hierro lavas. Interpretation of Hawaiian post-erosional melts (Lassiter et al., 2000) shown with La Palma and El Hierro lavas in upper panel (see discussion).

Melting of pyroxenite lithologies produces silica-undersaturated, iron-rich melts with high MgO (Hirschmann *et al.*, 2003; Kosigo *et al.*, 2003) and so correlations between Os isotopes and major elements are unlikely to trend to extreme SiO_2 enrichment. However, positive correlations might be observed in some instances (e.g., Lassiter *et al.*, 2000). For example, in Fig. 4.37 El Hierro samples appear to

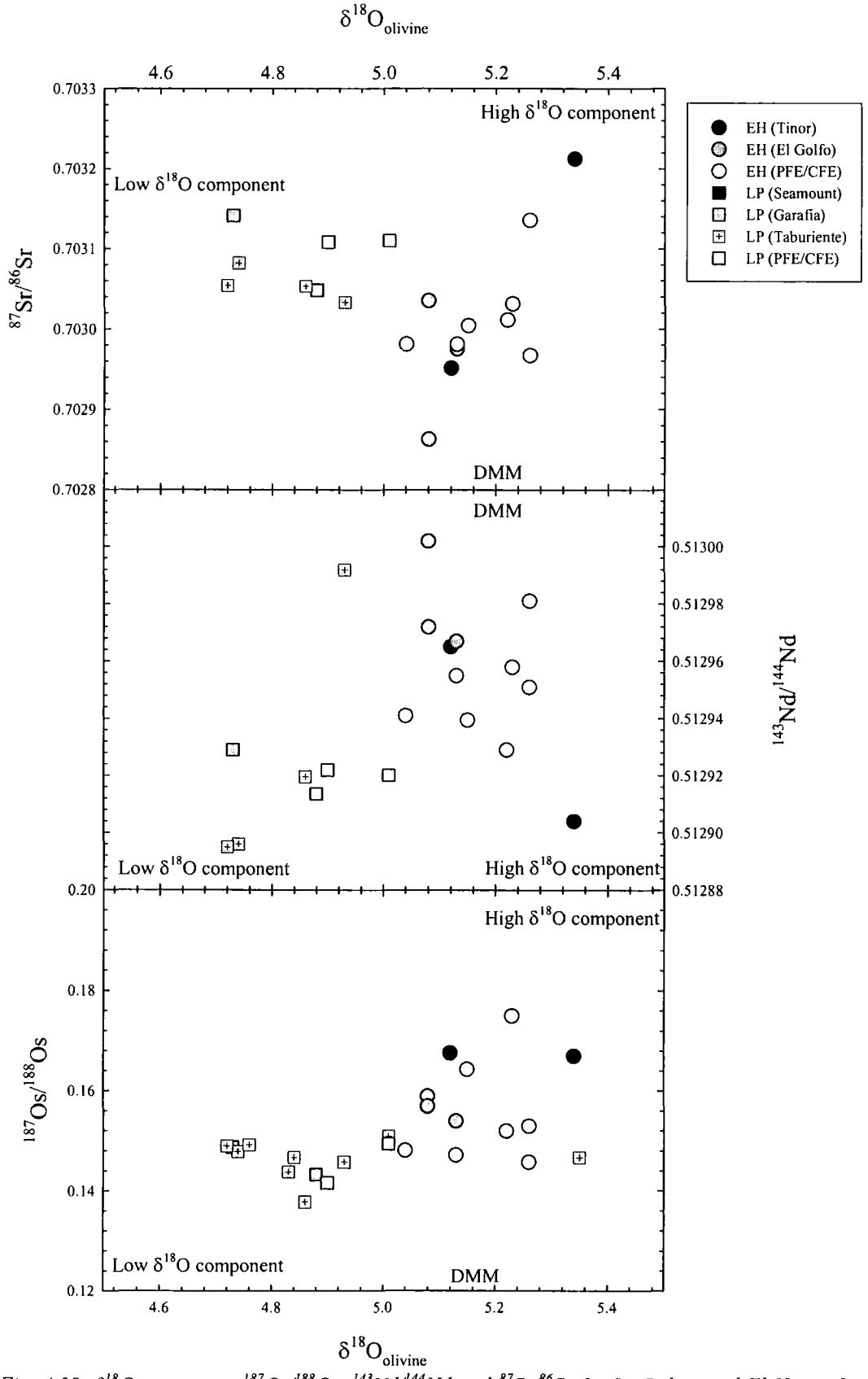

Fig. 4.38: $\delta^{18}O_{olivine}$ versus $^{187}Os/^{188}Os$, $^{143}Nd/^{144}Nd$ and $^{87}Sr/^{86}Sr$ for La Palma and El Hierro lavas. Note the near-perfect separation of La Palma and El Hierro lavas on the basis of $\delta^{18}O_{olivine}$

plot to more radiogenic $^{187}Os/^{188}Os$ with slightly increasing SiO_2 whilst La Palma lavas have higher SiO_2 contents and more radiogenic $^{87}Sr/^{86}Sr$ than El Hierro lavas. This relationship appears to be consistent with the trends shown for post-erosional lavas from Hawaii (Lassiter *et al.*, 2000). It also suggests that the more HIMU-like source of La Palma lavas is more SiO_2 enriched compared with El Hierro lavas. In Fig. 4.37 the trend predicted by Lassiter *et al.* (2000) for lavas resulting from mixed peridotite-pyroxenite sources is indicated. Obviously such correlations are complicated by shallow and deep-level fractionation and addition of clinopyroxene during petrogenesis of lavas (e.g., Nikogosian *et al.*, 2002) but they illustrate that mixed peridotite-pyroxenite sources cannot be discounted.

In Fig. 4.35 a potential pyroxenite melt mixing line has been modelled with unradiogenic $^{206}Pb/^{204}Pb$ (18.6) and radiogenic $^{187}Os/^{188}Os$ (0.6). Clearly the large isotopic variations of pyroxenites coupled with their melting characteristics make them strong candidates for generating the large isotopic variations seen in OIB. This statement is supported by the fact that pyroxenite veins are observed in many massif peridotites, ophiolites and xenolith suites worldwide (e.g., Reisberg *et al.*, 1991; Pearson *et al.*, 1993; Roy-Barman *et al.*, 1996) and pyroxenites maybe an intrinsic part of the mantle. Despite the small volume of the uppermost mantle that pyroxenites are likely to make up (2-5%; Hirschmann and Stolper, 1996; Pearson and Nowell, 2004), they may contribute to melt generation in OIB disproportionately because of their lower solidi and greater melt productivity relative to peridotites (Hirschmann *et al.*, 2003). Assuming that the large isotopic variations of pyroxenites are not restricted to the massif peridotites, it can be suggested that mixed peridotite-pyroxenite sources, generated from pre-cursor recycled oceanic crust, can explain the large variation of Sr, Nd, Os and Pb isotope systematics of Western Canary Island lavas. Because of the large variations in O-isotopes measured in pyroxenites (Pearson *et al.*, 1993), melting of pyroxenites might also be able to explain the O-isotope variations measured between El Hierro and La Palma lavas.

From Os-Pb isotope systematics it appears that variably aged recycled oceanic can contribute to the sources of HIMU ocean islands (Fig. 4.35). As such there is likely to be a great deal of isotopic heterogeneity preserved in the source of these islands resulting in considerable variations in Os-Pb isotope space. Similarly the

large variation in $^{187}Os/^{188}Os$ and $\delta^{18}O$ in peridotite-pyroxenite sources would also generate considerable variation in plots of Nd, Sr and Os versus $\delta^{18}O$ (Fig. 4.38).

Orogenic-massif pyroxenites and eclogite lithologies have highly variable $\delta^{18}O$ (Pearson *et al.*, 1993; Pearson *et al.*, 2003). Melting of pyroxenite-peridotite mixtures to generate parental Western Canary Island lavas can explain the large variation of $\delta^{18}O$ with $^{87}Sr/^{86}Sr$, $^{187}Os/^{188}Os$ and $^{206}Pb/^{204}Pb$ seen in Fig. 4.38. For example mixtures of a source with mantle-like to high $\delta^{18}O$, radiogenic $^{87}Sr/^{86}Sr$, $^{187}Os/^{188}Os$ and low $^{143}Nd/^{144}Nd$ (FOZO/PHEM/C) with components with $\delta^{18}O$ = ~5.1‰, unradiogenic $^{87}Sr/^{86}Sr$, $^{187}Os/^{188}Os$, high $^{143}Nd/^{144}Nd$ and low $\delta^{18}O$ = ~<4.7‰, unradiogenic $^{87}Sr/^{86}Sr$, $^{187}Os/^{188}Os$, and low $^{143}Nd/^{144}Nd$ can explain the variations for El Hierro and La Palma lavas, respectively, in Fig. 4.38. Along with variations between other isotopic schemes (e.g., Pb-Os, Fig. 4.35) these variations indicate that the mantle sources that are responsible for such variable isotopic compositions within and between the Western Canary Islands must be separated by short length scales ($<1\times10^3$ km) as well as in the 4th dimension, temporal scales (see section 4.10.2).

Mixed pyroxenite-peridotite sources are capable of explaining the O, Sr, Nd, Os and Pb isotope heterogeneity of OIB. In addition, they explain the Fe-rich and SiO_2-undersaturated nature of some OIB (e.g., Allègre and Turcott, 1986). Mixed pyroxenite-peridotite sources might also explain:

- The disparities observed for La Palma and El Hierro lavas for trace element modelling (section 4.10)
- The spatial and temporal variations in isotopic and elemental compositions measured within and between the Western Canary Islands
- Possible correlations between composition of lavas after major volcanic edifice collapses and through south-ward propagation of the Cumbre Vieja ridge through preferential melting of low solidi pyroxenite in the mantle source.

Furthermore, pyroxenites could potentially generate large variations in $^{186}Os/^{188}Os$. For example, some pyroxenites contain high Pt/Os and Re/Os ratios (Bay of Islands ophiolite, Edwards, 1990) that, over time, will translate to correlated $^{187}Os/^{188}Os$-$^{186}Os/^{188}Os$ variations (Smith, 2003). Pyroxenite-peridotite sources will have highly variable Re/Os (possibly Pt/Os), U/Pb, Rb-Sr, Sm-Nd and $\delta^{18}O$ at very short length scales (1×10^{-1} to 1×10^4 km) that may survive for billions of years. In summary,

variably aged recycled oceanic crust derived pyroxenite-peridotite sources provide a simple solution to the isotope variability and isotope-isotope and isotope-elemental compositions measured within and between the islands of El Hierro and La Palma.

4.10.4 Mantle mixing hypotheses for He-Nd-Os-Pb

Olivine phenocrysts from both the Islands of El Hierro and La Palma are characterised by a range of $^{3}He/^{4}He$ (7.2 to 11.8R_A and 6.6 to 9.7R_A respectively). Hilton *et al.* (2000a) concluded that the high $^{3}He/^{4}He$ ratios measured in La Palma geothermal fluids and phenocrysts rules out the 'open-system' model of Hanyu and Kaneoka (1998) in which diffusive exchange of He from the ambient depleted MORB mantle into recycled oceanic crustal components explaining the origin of HIMU-OIB. The model of Hanyu and Kaneoka (1998) is similar to the open-system models invoked to explain the less radiogenic $^{3}He/^{4}He$ ratios measured in Proterozoic CLM (Gautheron and Morieira, 2002). Instead Hilton *et al.* (2000a) proposed possible mixing hypotheses involving two, three or four component mixtures of a high $^{3}He/^{4}He$ component, HIMU with radiogenic He, Os and Pb, a 'frozen' plume component with radiogenic $^{3}He/^{4}He$ and a DMM component.

On the basis of coupled He, O, Sr, Nd, Os, Pb isotope evidence presented here, a number of restrictions can be placed upon mantle mixing hypotheses for He. Firstly, there is little evidence for the direct involvement of DMM in the generation of the Western Canary Islands (Section 4.10.2). Instead Western Canary Island lavas correspond to a mixture of an ancient HIMU-like component that has interacted with a source more like FOZO/C/PHEM and other young HIMU sources. Secondly, the large variation in possible mixing scenarios to explain Os-Pb isotope systematics suggests that mixing scenarios are not well constrained in terms of mass-balance. Thirdly, on the basis of Os-Pb isotope systematics, mixing is likely to occur through solid-state mixing and not melt-solid interaction. This is because of the expected impact melt-solid interaction would have on lowering $^{187}Os/^{188}Os$ and that this infers He mixing occurs before He degassing; this inference is identical to that of Hilton *et al.* (2000a).

In the first of their mantle mixing hypothesis, Hilton *et al.* (2000a) modelled mixing between a 'plume' endmember with high $^{3}He/^{4}He$ and 'intermediate' $^{206}Pb/^{204}Pb$ and a HIMU-source with both radiogenic $^{206}Pb/^{204}Pb$ and $^{3}He/^{4}He$. This

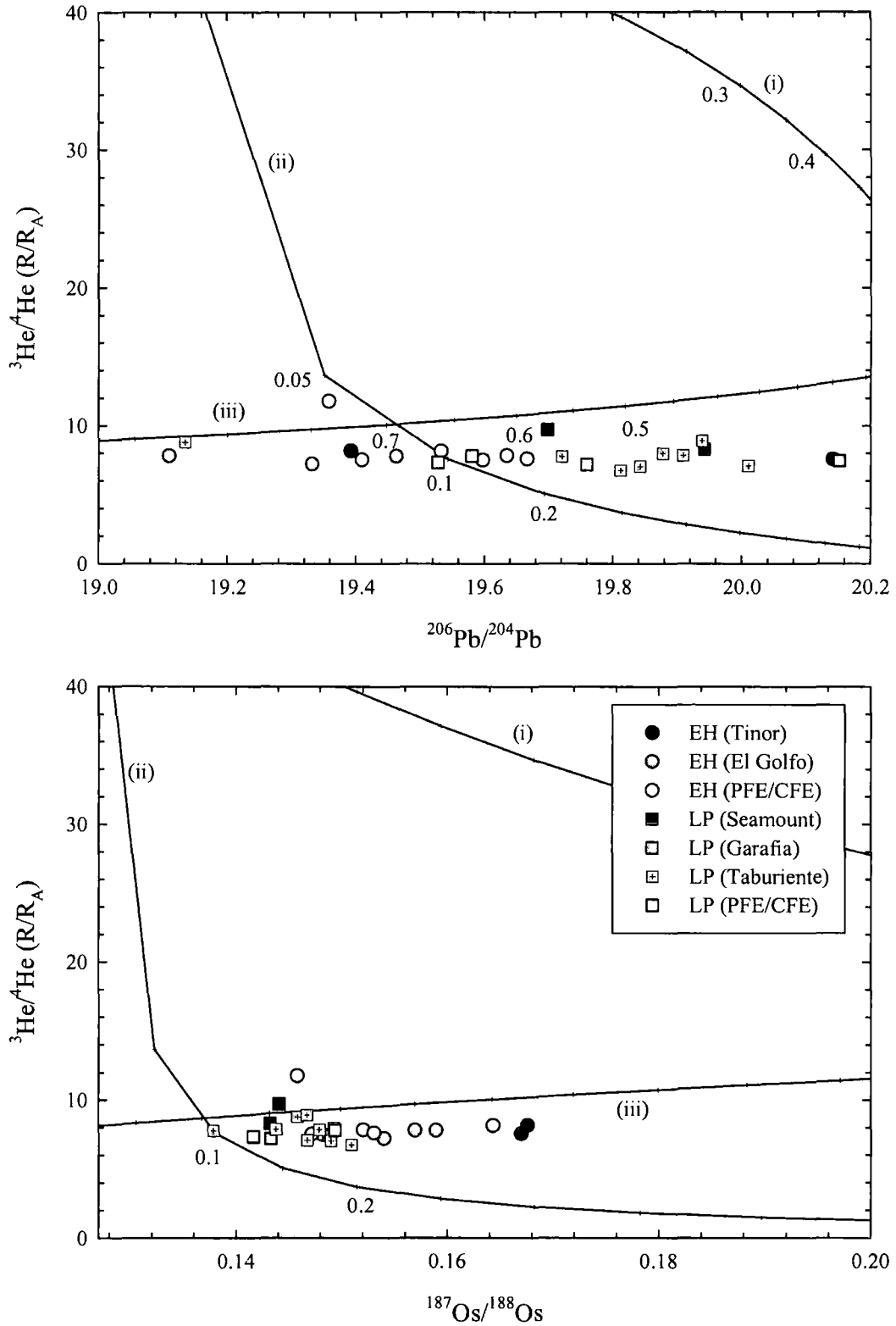

Fig. 4.39: $^{187}Os/^{188}Os$ and $^{206}Pb/^{204}Pb$ versus $^3He/^4He$ for La Palma and El Hierro lavas analysed in this study. Solid binary mixing trajectories (described in text) are for (i) high $^3He/^4He$ with equal [He] to a HIMU component, (ii) 50× depleted high $^3He/^4He$ relative to HIMU and (iii) combined High $^3He/^4He$-HIMU source and DMM mixing trajectory (models after Hilton et al. 2000a). In all cases the fraction of the low $^3He/^4He$ involved in binary mixing is placed next to tick marks.

mixing requires a 'plume' endmember substantially depleted in He and no singular depleted He plume source can uniquely explain the La Palma He-Pb correlations. Hilton *et al.* (2000a) concluded that the only plausible explanation for this mixing would be for the HIMU component to reside in the oceanic lithosphere or slightly deeper mantle. In their second model Hilton *et al.* (2000a) proposed involvement of the DMM in the origin of $^{3}He/^{4}He$ ratios of La Palma lavas. In this favoured mixing scenario Hilton *et al.* (2000a) modelled the plume as a composite body with a high $^{3}He/^{4}He$ component and a HIMU component that displays both high $^{3}He/^{4}He$ and radiogenic Pb (and by inference Os) that mixed with DMM. They also considered a scenario where melts were frozen into the lithosphere and subsequently re-melted to explain the variation in He abundances and isotopic ratios for La Palma lavas.

Fig. 4.39 shows the $^{3}He/^{4}He$, $^{187}Os/^{188}Os$ and $^{206}Pb/^{204}Pb$ isotope data for La Palma and El Hierro. Binary mixing trajectories have been constructed for the two models invoked by Hilton *et al.* (2000a) with a high $^{3}He/^{4}He$ component represented by the extreme $^{3}He/^{4}He$ measured for Baffin Island picrites by Stuart *et al.* (2003) with FOZO $^{206}Pb/^{204}Pb$ and $^{187}Os/^{188}Os$ of 19.1 and 0.1270 respectively (Pb = 24ppm, Os = 1.6 ppb (calculation based on FOZO mixture)). The HIMU component (1.2Ga recycled crust) is represented by $^{187}Os/^{188}Os$ = 1.13, Os = 0.1ppb, $^{206}Pb/^{204}Pb$ = 20.5, Pb = 100ppm and $^{3}He/^{4}He = 0.05R_A$ (inferred from eclogite, Chapter 3). The DMM component is characterised by $^{187}Os/^{188}Os$ = 0.1246, Os = 3.3ppb, $^{206}Pb/^{204}Pb$ = 18.5, Pb = 250ppm and $^{3}He/^{4}He = 8R_A$. These model parameters are based on the FOZO-like component and a HIMU-like component in Western Canary Island lavas identified in the previous sections. In both Os-He and Pb-He isotope space mixtures between a low $^{3}He/^{4}He$ HIMU component and a high $^{3}He/^{4}He$ component poorly describe the pre-existing and new La Palma and El Hierro data (Fig. 4.39). In agreement with the findings of Hilton *et al.* (2000a), no singular degassed high $^{3}He/^{4}He$ component can adequately describe the He-Pb or He-Os relationships. This is even more extremely emphasised for El Hierro samples which possess lower $^{206}Pb/^{204}Pb$ than La Palma lavas.

Using a component that is formed of a high $^{3}He/^{4}He$ component and HIMU $^{206}Pb/^{204}Pb$ component, that is mixed with DMM provides a better fitted model to describe the La Palma and El Hierro data. In this model a high $^{3}He/^{4}He$ component that has been diluted heavily (70%) with a young HIMU component has been used.

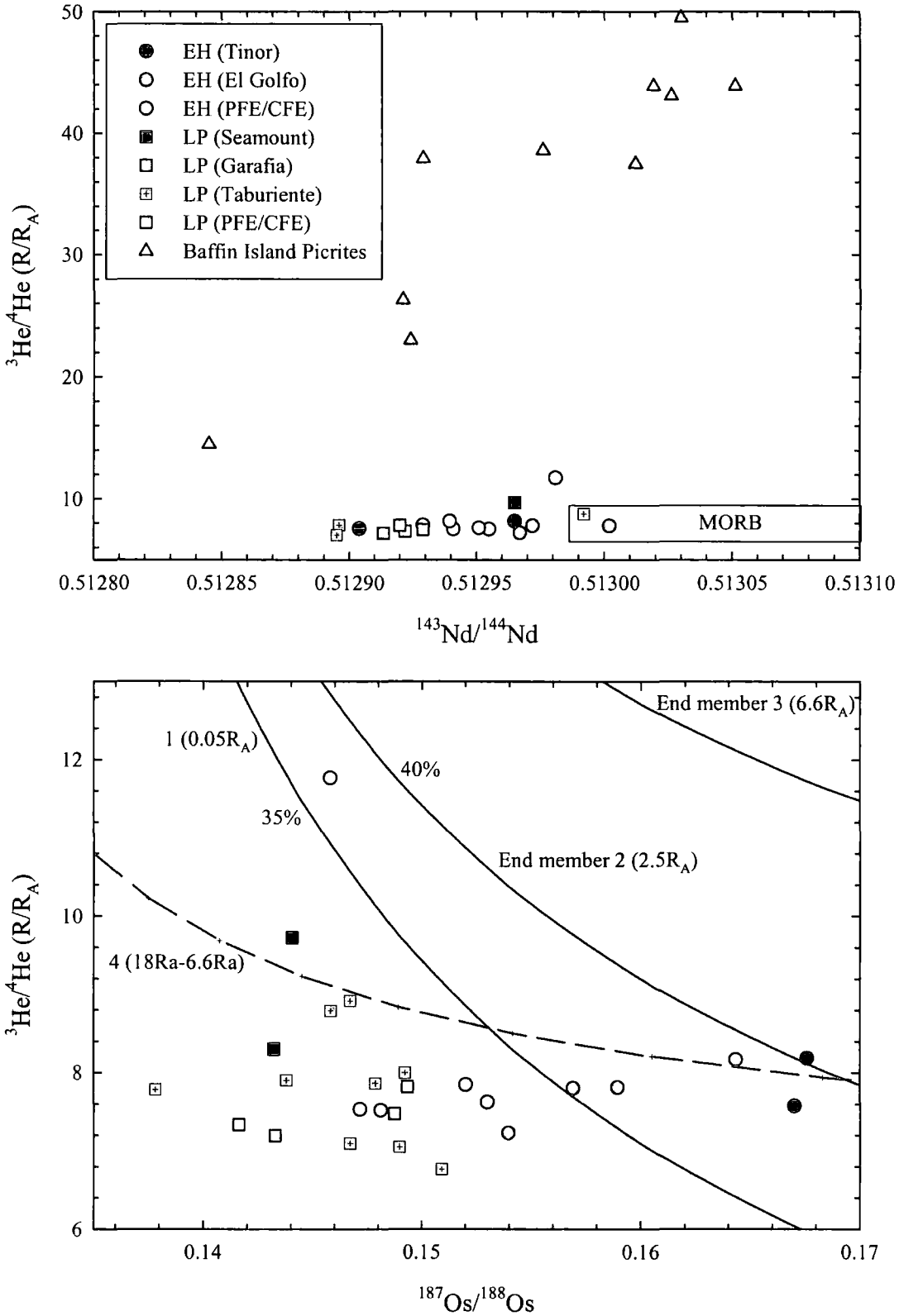

Fig. 4.40: $^{187}Os/^{188}Os$ and $^{143}Nd/^{144}Nd$ versus $^3He/^4He$ for La Palma and El Hierro lavas analysed in this study. Solid and dashed binary mixing trajectories (described in text) are for mixing between HRDM (Stuart et al., 2003) and HIMU components that experienced both closed and open system histories for He (Hanyu and Kaneoka, 1998). Baffin Island picrite data from Stuart et al. (2003).

The mixing relationships indicate increasing contribution of DMM from La Palma to El Hierro lavas consistent with O, Sr, Nd, Pb, Os isotope observations. Modelling in both He-Os and He-Pb isotope space indicates between 10-33% and 15-70% of a HIMU component, respectively, with the He-Os estimates in close agreement with calculations of HIMU components from Os-Pb mixing (15-40%; Fig 4.35). Hilton *et al.* (2000a) suggested that the modelling was more compatible with a more radiogenic $^{206}Pb/^{204}Pb$, high $^{3}He/^{4}He$ component (12-19% HIMU). The variations of La Palma and El Hierro lavas in Os-Pb space do not suggest ancient HIMU with more radiogenic $^{206}Pb/^{204}Pb$ recycled oceanic components in their mantle sources, discounting this possibility.

Stuart *et al.* (2003) have suggested that ^{3}He-recharge may explain the coupling of MORB-like Sr and Nd isotope compositions and high $^{3}He/^{4}He$ in Baffin Island picrites. A similar mechanism has been invoked for lavas analysed in Chapter 2 of this thesis. The possibility therefore remains that mixing between HIMU, DMM and a high $^{3}He/^{4}He$ component lie in the opposite sense to the model invoked by Hilton *et al.* (2000a) and that either a FOZO/C/PHEM component or a DMM is ^{3}He-recharged (Helium recharged depleted mantle: HRDM, Stuart *et al.*, 2003 versus Helium recharged FOZO: HRFOZO. For the purposes of this discussion a helium recharged reservoir is referred to as HRDM in order to provide consistency with the original model of Stuart *et al.* (2003)). A He-recharge model would explain why, relative to HIMU or DMM, the high $^{3}He/^{4}He$ component has a lower helium content than predicted for a two-layer, steady state model of mantle structure (Stuart *et al.*, 2003).

In Fig. 4.40 La Palma and El Hierro samples are plotted with Baffin Island samples in He-Nd isotope space and the few high $^{3}He/^{4}He$ Western Canary Island samples plot with more MORB-like $^{143}Nd/^{144}Nd$ ratios. Fig 4.40 shows models of HRDM–endmember 1 (based on eclogite, Chapter 3) and endmembers 2 and 3 (2.5 and $6.6R_A$ respectively based upon different CLM components listed in Chapter 3). Although CLM is clearly unable to generate the observed O, Sr, Nd, Os and Pb isotope signatures the open and closed-system addition of He invoked by Gautheron and Moriera (2002) make them proxies for recycled oceanic components. This concept is a hybrid of the approaches to interpret HIMU $^{3}He/^{4}He$ by Hanyu and Kaneoka (1998).

Modelling indicates that for the La Palma and El Hierro lavas a HRDM with around 5-10 times less [He] than endmembers 1, 2 or 3 can account for the variations of He-Os isotope compositions in the lower panel of Fig. 4.40. Solid state mixing between HRDM and HIMU with endmember 2 and 3 compositions could provide an adequate model for the origin of the high $^{3}He/^{4}He$ component in La Palma and El Hierro lavas with calculated amounts of recycled components equal to between 35 and 40%; similar to the estimates from Os-Pb relationships in Fig. 4.35. The steepness of the trajectory to Baffin Island extreme $^{3}He/^{4}He$ in both He-Os and He-Nd isotope space indicate a much lower $^{3}He/^{4}He$ ratio for the He-recharged mantle reservoir beneath the Western Canaries than beneath the source of NAIP or Icelandic magmatism. However, even the fit for mixing for the endmember 4 line representing binary mixing between HIMU ($6.6R_A$) and HRDM ($18R_A$) is poor. Instead it appears that in contrast to Baffin Island rocks, there is poor correlation for La Palma and El Hierro lavas because high ^{3}He-recharge has not been pervasive beneath the Canary Islands. Hence MORB-like $^{3}He/^{4}He$ ratios are symptomatic of Western Canary Island lavas.

The NAIP, Iceland as well as other high $^{3}He/^{4}He$ provinces are associated with a high buoyancy flux (Davies, 1988; Sleep, 1990) and much higher degrees of partial melting than Western Canary Island lavas (e.g., tholeiitic magmas). Graham (2002) found poor correlation with plate speed, buoyancy flux, or oceanic lithosphere age for OIB making variation with $^{3}He/^{4}He$ and different buoyancy and melting fluxes on this basis, unlikely. Lack of correlation between $^{3}He/^{4}He$ and $^{143}Nd/^{144}Nd$, $^{206}Pb/^{204}Pb$ or $^{187}Os/^{188}Os$ for Western Canary Islands might imply that in this circumstance $^{3}He/^{4}He$ ratios are decoupled from other chemical variations.

Although a mixed high $^{3}He/^{4}He$ component and HIMU cannot be discounted the HRDM-HIMU model is favoured here based upon the increasing recognition of similar source characteristics in mantle environments elsewhere (Stuart *et al.*, 2003; Chapter 3). The suggestion that a higher proportion of HIMU may act to obscure the high ^{3}He component (Hilton *et al.*, 2000a) appears to be an unlikely possibility for Western Canary Island lavas, especially in light of the less radiogenic $^{206}Pb/^{204}Pb$ and MORB-like $^{3}He/^{4}He$ values for most El Hierro lavas. First order observations for the $^{3}He/^{4}He$ ratio of Western Canary Island lavas are:

- Contributions from reservoirs with MORB-like $^{3}He/^{4}He$ ($8\pm1R_A$) and a high $^{3}He/^{4}He$ ($>12R_A$) are required to explain the $^{3}He/^{4}He$ of La Palma and El Hierro lavas.
- $^{3}He/^{4}He$ ratios show no measurable variation spatially or temporally within or between the islands of La Palma and El Hierro. As such He is probably decoupled from O, Sr, Nd, Os and Pb isotopes and does not track the large compositional variations of these isotopic schemes.

4.11 Summary

A stratigraphically well-constrained, large isotopic (He, O, Sr, Nd, Pb, Os) and elemental dataset has been presented for lavas from the Western Canary Islands of El Hierro and La Palma from which it can be concluded that:

- Alkaline lavas from the islands of La Palma and El Hierro are derived from low degrees of partial melting of a mantle source that cannot be replicated using anhydrous mantle melting models.
- Sub-aerially erupted alkaline lavas from the Western Canary Islands of La Palma and El Hierro trend to exceptionally high Cu/Re ratios in Re/Yb-Cu/Re space – a result predicted from degassing of Re. Compared with tholeiitic lavas and glasses from Hawaii (Bennett *et al.*, 2000; Norman *et al.*, submitted) the Western Canary alkaline lavas indicate more extensive degassing because of the elevated Cu/Re ratios.
- Re loss during degassing prevents use of Re/Os ratios in sub-aerially erupted lavas to infer degrees of partial melting. Re and Os can also be substantially fractionated by crystallisation of melts. The coupled variation of Re and TiO_2 in La Palma and El Hierro lavas indicates that Re is closely associated with titano-augite and Fe-Ti oxides.
- Os is a compatible element and correlates positively with Ni and Cr. This could suggest that it is retained most effectively in early crystallised chromite and olivine phases during fractional crystallisation. However, Os has a low bulk partition coefficient in olivine (0.4 to 0.6; Puchtel *et al.*, 2004) but experimental data shows that Os strongly partitions into sulphide phases ($D_{Sulf\text{-}Sil}$ = 0.6 to 3 $\times10^4$; e.g., Fleet *et al.*, 1991a,b; 1996; 1999a,b). Positive correlations between Os and compatible elements in Western Canary Island lavas Os is likely to be

controlled by sulphide. Therefore the results of this study support previous examination of magmatic systems and the compatibility of Os in sulphides (e.g., Ravizza and Hart, 1996; Schaefer *et al.*, 2000; Puchtel *et al.*, 2004).

- Low $\delta^{18}O$ in La Palma lavas and $^{87}Sr/^{86}Sr$, $^{143}Nd/^{144}Nd$, and Pb isotopes in the Western Canary Islands as a whole do not correlate with indices of crustal contamination or fractional crystallisation and indicate that correlations between these isotopes reflect mantle melt extraction.
- $^{187}Os/^{188}Os$ in lavas from El Hierro correlate poorly with assimilation and fractional crystallisation models. These lavas possess $^{187}Os/^{188}Os$ and high Os abundances retaining the isotopic compositions of their mantle source.
- El Hierro and La Palma lavas generally lie at either end of the isotopic arrays for Western Canary Islands lavas and their phenocrysts have very different $\delta^{18}O$ signatures. The radiogenic $^{187}Os/^{188}Os$ and mantle-like $\delta^{18}O$ of El Hierro lavas and the low $\delta^{18}O$ and more radiogenic $^{87}Sr/^{86}Sr$, $^{143}Nd/^{144}Nd$ and $^{206}Pb/^{204}Pb$ isotopic composition of La Palma lavas indicates that the mantle sources of the two islands are quite different. El Hierro is derived from a mantle source with higher time integrated Re/Os. La Palma lavas sample a mantle source with higher time integrated U/Pb, Rb/Sr, Sm/Nd and lower $\delta^{18}O$ than El Hierro.
- La Palma and El Hierro lavas do not correlate as well as EMI OIB like Hawaii in $^{206}Pb/^{204}Pb$-$^{187}Os/^{188}Os$ isotope space and indicate an isotopically variable mantle source is present beneath the Western Canary Islands.
- The isotopic differences between El Hierro and La Palma can be explained by different mixtures of recycled oceanic crustal material into the mantle source of Western Canary Island volcanism. The more silica-undersaturated nature of El Hierro lavas also suggests that pyroxenite-peridotite mantle sources can best explain the isotopic and elemental variations seen within and between El Hierro and La Palma lavas. The pre-cursor of peridotite-pyroxenite sources is likely to be a mixture of young (<1.2Ga) recycled oceanic crust and the mantle which contains a FOZO/PHEM/C component.
- Olivine phenocrysts in lavas from El Hierro and La Palma that have not experienced crustal contamination possess $^{3}He/^{4}He$ ratios that lie within the 95% confidence limits of MORB $^{3}He/^{4}He$ ratios. However the most extreme $^{3}He/^{4}He$ values for phenocrysts from La Palma ($9.7R_A$) and El Hierro ($11.8R_A$) that are

presented in this study lie outside the 95% confidence limits of MORB $^{3}He/^{4}He$ ratios. He appears to be decoupled from O, Sr, Nd, Os and Pb isotope systematics and supports the notion of ^{3}He-recharge to mantle source regions beneath intraplate magmas (e.g., Stuart *et al.*, 2003).

- Study of Western Canary Island lavas in conjunction with the global OIB dataset allow some new constraints to be placed on the isotopic compositions of the universal mantle component (C/PHEM/FOZO). □^{18}O for this mantle component appears to be similar to mantle-derived peridotites (e.g., Mattey *et al.*, 1994) whilst the $^{187}Os/^{188}Os$ ratio of the universal component is similar to that estimated from the Os mantle evolution curve for Archaean and Proterozoic mafic magmatism (e.g., Chapter 5). Lack of He-coupling for OIB (especially the Western Canary Islands) indicates that this component is not characterised solely by high $^{3}He/^{4}He$.

Chapter 5: Re-Os isotope constraints on mantle and crustal contributions to the 1.27Ga Mackenzie magmatic event, NWT, Canada

5.1 Introduction and aims

The mid-Proterozoic intraplate Mackenzie magmatic event comprises three major components (Fig. 5.1):

- The Mackenzie dyke swarm which covers an area of 2.7×10^6 km^2 and is the largest preserved terrestrial dyke swarm (Ernst *et al.*, 1995) with a focal point on northern Victoria Island (Baragar *et al.*, 1996).
- The Coppermine Continental Flood Basalt (CMV) and Ekalulia basalt outliers preserved 400km to the south of the focal point.
- The Muskox layered mafic-ultramafic intrusion located beneath the southernmost exposure of the Coppermine CFB.

Combined volumes estimated for the structural components of the Mackenzie large igneous province (LIP) indicate that the event is comparable to other LIP examples worldwide (see Fig 1.2) and may even represent the largest LIP in the geological record. Despite these facts the Mackenzie LIP has received little attention, with only a limited number of published geochemical datasets relating to the event (Griselin *et al.*, 1997 and references therein).

In this chapter the first Re-Os isotope data for the Mackenzie LIP are presented with new trace element data from the Coppermine CFB and a large trace element dataset for the Muskox layered intrusion. The preliminary objectives of the study are to examine the age relationships of the CMV and Muskox intrusion and to place constraints on crustal modification processes on CFB and layered intrusions using Os isotopes. The ultimate objective is to recognise the mantle sources responsible for Mackenzie LIP magmatism and to provide constraints on the Os isotope evolution of Earth's mantle during the mid-Proterozoic. To achieve these goals the Coppermine CFB and Muskox Intrusions are considered individually to document their elemental and Re-Os isotope characteristics with respect to post-crystallisation element mobility, upper and lower crustal contamination, fractional crystallisation and partial

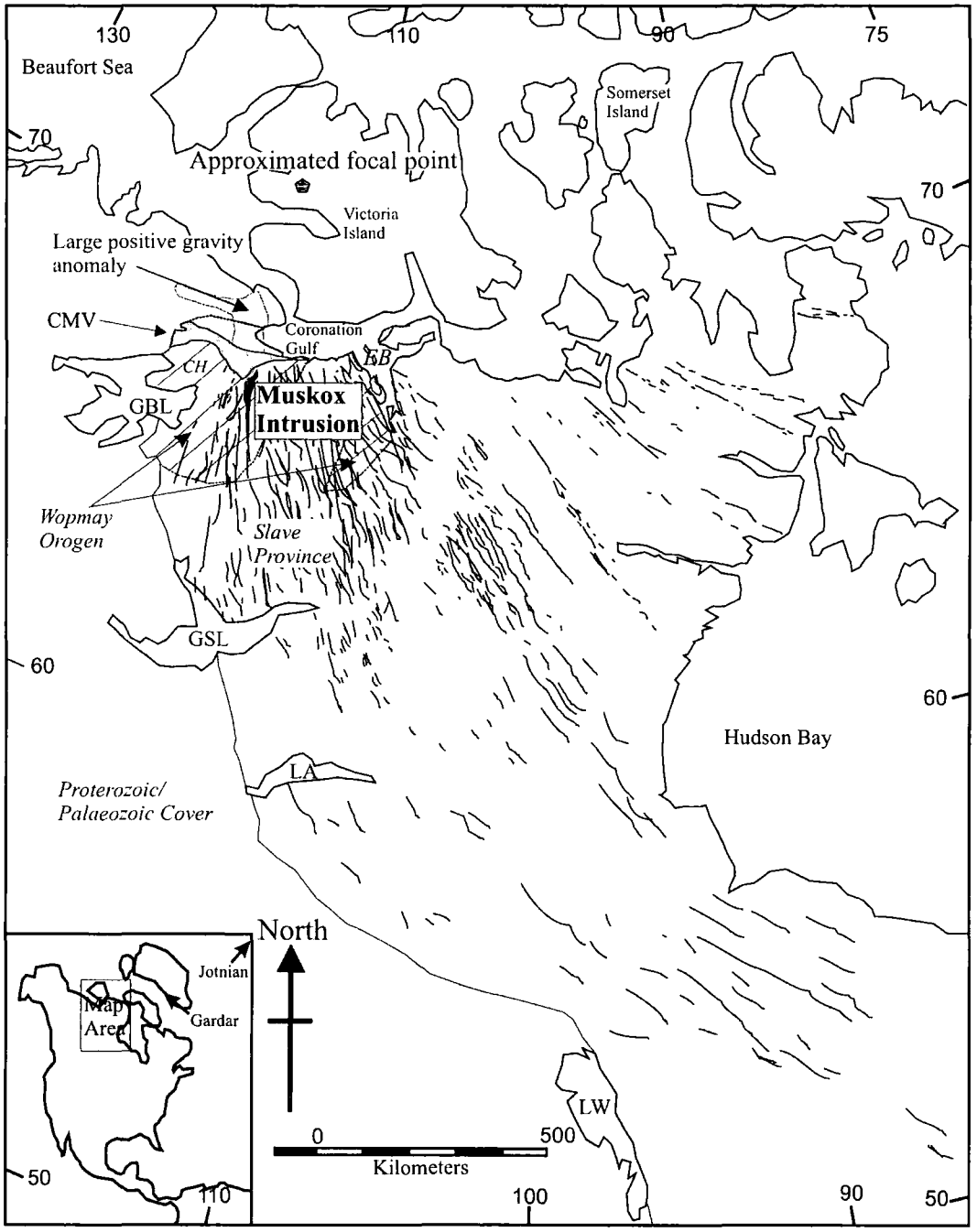

Fig. 5.1: Map of the Mackenzie Large Igneous Province. Modified from Le Cheminant and Heaman, (1989) with approximate focal point from Baragar et al. (1996). Abbreviations are as follows: EB - Ekalulia basalts, CMV - Coppermine River Volcanics, CH - Coppermine homocline, GBL - Great Bear Lake, GSL - Great Slave Lake, LA - Lake Athabasca, LW - Lake Winnepeg.

melting effects.The CFB-layered intrusion relationships are subsequently considered to assess the temporal evolution and the range of possible mantle sources responsible for the Mackenzie LIP.

5.2 Geology and age constraints for the Mackenzie LIP

The exposed stratigraphy of the Muskox intrusion and Coppermine CFB are tilted 3-5° to the north in a broad homocline (the Coppermine Homocline; Kerans *et al.*, 1981). It comprises the largely siliclastic Hornby Bay and dolomitic Dismal Lakes sedimentary formations which unconformably overlie >1.8Ga Wopmay Orogen rocks (Hoffman, 1980), collectively termed the Helikian Sequence (Fig. 5.2). The Hornby Bay and Dismal Lake groups comprise two successions of fluvial to shallow marine sedimentary rocks (Kerans *et al.*, 1981). A zircon U-Pb age from a capping rhyolite porphyry of the Hornby Bay group defines a minimum depositional age of 1663±8Ma (Bowring and Ross, 1985). Overlying strata of the Dismal Lakes group exhibit evidence of subaerial exposure prior to Coppermine CFB volcanism in the form of a regional extensive palaeokarst horizon (Kerans, 1983) succeeded by a thin dolomite unit suggesting short-lived marine transgression (LeCheminant and Heaman, 1989). In the homocline, the Coppermine CFB reach a maximum thickness of 4.5km and to the south the Mackenzie Dykes are heavily concentrated and show greater diversity in thickness and compositions than elsewhere in the dyke swarm (Baragar *et al.*, 1996).

The Coppermine River group, a sequence of basaltic lavas and sills, represents the uppermost unit within the Coppermine homocline and comprises the Copper Creek and Husky Creek formations of the Coppermine CFB. The Coppermine CFB extends in an east-west orientation for almost 300km and has an estimated volume of 1.4×10^5 km^3 (Irvine and Baragar, 1972 in LeCheminant and Heaman, 1989), although this estimate does not include the volume of basalt covered by late Proterozoic and early Phanerozoic strata. K-Ar and Rb-Sr errorchron ages for the Coppermine CFB (Fahrig, 1987) suggest that the CFB are similar in age to the Mackenzie dyke swarm and Muskox. Unpublished U-Pb Concordia ages for zircons from a Lower Copper Creek Flow gives an age of 1270Ma (M.A. Hamilton, pers. comm.).

Emplacement of the Muskox intrusion occurred early in Mackenzie magmatism (LeCheminant and Heaman, 1989). The intrusion has been precisely dated using U-Pb on baddeleyite and zircon fractions (1270±4Ma; LeCheminant and Heaman, 1989) and subsequently by reassessment of the baddeleyite fraction data by French *et al.* (2002) to give an age of 1269±1Ma. This highly precise age suggests the Muskox intrusion is slightly older than Mackenzie diabase dykes (1267±2Ma; LeCheminant and Heaman, 1989). This is supported by field observations that Mackenzie diabase dykes cross-cut parts of the Muskox intrusion (Findlay and Smith, 1965) (Fig. 5.2).

The Mackenzie dykes fan out in a radial array (~100° of arc) that extends more than 2400km along strike and has a maximum width of 1800km before being buried under younger cover. The Mackenzie dykes are generally tholeiitic, although more alkalic compositions do occur in the easterly stream of the dykes. The dykes become increasingly evolved with distance from the focal point, possibly due to crystal settling in transport (Baragar *et al.*, 1996). The Mackenzie dykes generally lack olivine apart from dykes in the Lake Athabasca region (1500km from the focal point) that comprise both olivine-bearing and olivine-free dolerites (Hulbert *et al.*, 1993). Although the dykes average 30m in thickness, many are up to 150m thick and are characterised by coarse-grained gabbroic centres and well-defined chilled margins.

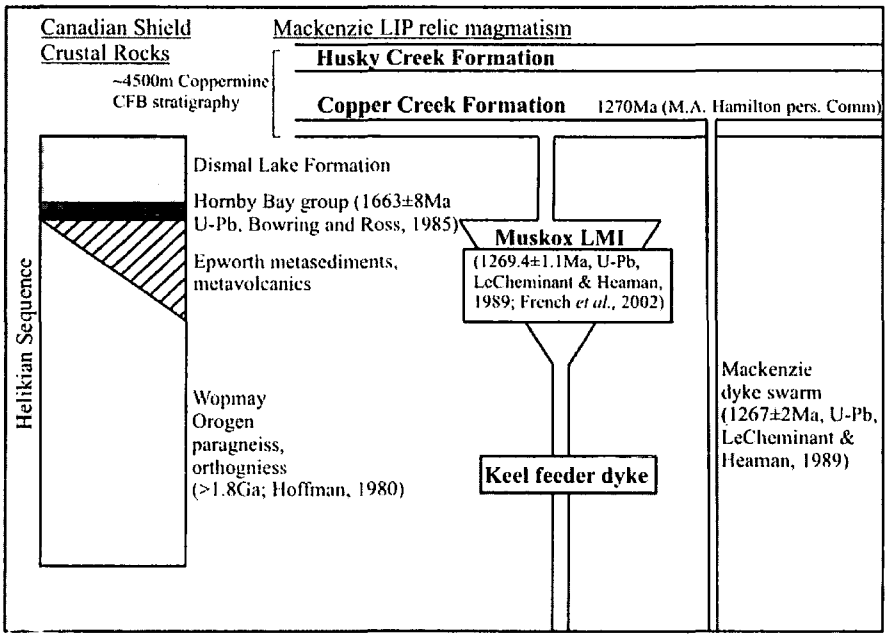

Fig. 5.2: Schematic illustration of the known age relationships compiled from published and unpublished data pertaining to the Mackenzie LIP. References cited in figure.

Conservative estimation of the total volume of the Mackenzie dyke swarm, assuming a total length of 6×10^4km, an average width of 30m and a downward extent of 50km is about 9×10^4 km^3.

The northernmost dykes of the swarm terminate within the lower flows of the Coppermine CFB indicating that some of the dykes acted as feeders to some of the flows. Anisotropy of magnetic susceptibility (AMS) data for the Mackenzie dykes indicate near-vertical flow at sites 400-500km from the focal point at northern Victoria island and horizontal flow at >600km (Ernst and Baragar, 1992) indicating common derivation for the Mackenzie dykes within a 1000km radius of the focal point. U-Pb baddeleyite dating of selected Mackenzie dykes from an array of distances from the assigned focal point give a composite Concordia age of 1267±2Ma (LeCheminant and Heaman, 1989) establishing that although younger than the Muskox intrusion, the entire Mackenzie magmatic event was essentially contemporaneous throughout its enormous geographical extent (Fig. 5.2).

The Mackenzie magmatic event is at the very least comparable in volume with other Proterozoic and Palaeozoic LIP. With a conservative estimate of 1.4×10^5 km^3 for the Coppermine CFB, 9×10^4 km^3 for the Mackenzie dykes and an unknown but substantial volume for the Muskox intrusion the total volume is comparable with that of the North Atlantic Igneous Province ((6-10) $\times10^6$ km^3), Columbia River (0.3×10^6 km^3), Parana-Etendeka (0.93×10^6 km^3), Karoo (>1.0×10^6 km^3) and Keweenawan (1.3×10^6 km^3) LIP (Hutchinson *et al.*, 1990; Saunders *et al.*, 1997). Combined geophysical evidence that substantial volumes of the Coppermine CFB and Muskox intrusion are covered by Palaeozoic strata, and the possibility that the Gardar province in Greenland (1284 to 1144Ma, U-Pb radiometric dates compiled in Upton *et al.*, 2003) and 1265Ma Jotnian sills and dykes of the Central Scandinavian Dolerite Complex on the Baltic Shield (Buchan *et al.*, 2001) are part of the same event imply that the Mackenzie magmatic event may represent one of the largest continental LIP in the geological record.

5.3 The Coppermine River CFB

The Coppermine River CFB (henceforth abbreviated to the Coppermine CFB) are best exposed to the south of the Coronation Gulf (Fig. 5.1), where they outcrop without interruption over a >250km east-west striking distance (Baragar, 1969; Le

Cheminant and Heaman, 1989). The Coppermine CFB have also been intersected in boreholes 250km to the west of the main outcrops and are manifested as the Elukia basalts 200km to the east. Samples analysed for their Re-Os isotope systematics in this study were selected from a larger sample suite from the Geological Survey of Canada (GSC) collections. Samples analysed and described in this study are all from the centre of lava flows or flow horizons.

5.3.1 Structure and stratigraphy of the Coppermine CFB

The Coppermine CFB is composed of the early Copper Creek and later Husky Creek Formations and this succession measures ~4500m in thickness (Fig. 5.3). The Copper Creek Formation consists of ~150 flows ranging from 8 to 25m in thickness with massive bases, amygloidal tops (Dostal *et al.,* 1983), and contains isolated pillow lavas (Griselin *et al.,* 1997). The lower flows lie directly on top of one another with no intervening sediment horizons whilst the upper Copper Creek flows are intermittently packaged with red fluvial sandstones that become even more common to the Husky Creek Formation. The Copper Creek Formation can be subdivided into the lower, middle and upper Copper Creek Formations (Fig. 5.3). The most important addition to the Coppermine CFB stratigraphy is the new discovery of picrite flows in the lower Copper Creek Formation during the 1999 summer field season led by L.J. Hulbert of the GSC.

The picrite flows cover a limited stratigraphic thickness (~200m) and are also associated with a single, thick (~60m) andesite lava flow with a ~1m glass horizon at its top (Fig. 5.3). This newly recognised picrite zone in the Coppermine CFB shows petrographical and geochemical similarities to those found in Phanerozoic equivalents of Disko and Baffin Island of the NAIP LIP, the Tafelkop picrites of the Etendeka, the picrites of the Lebombo monocline area of the Karoo CFB (e.g., Cox, 1980) and the Gudchikhinsky Formation of the Siberian CFB (Wooden *et al.,* 1993). The picrite zone of the lower Copper Creek Formation differs only from Phanerozoic equivalents in the fact that it is associated with a major andesite eruptive flow.

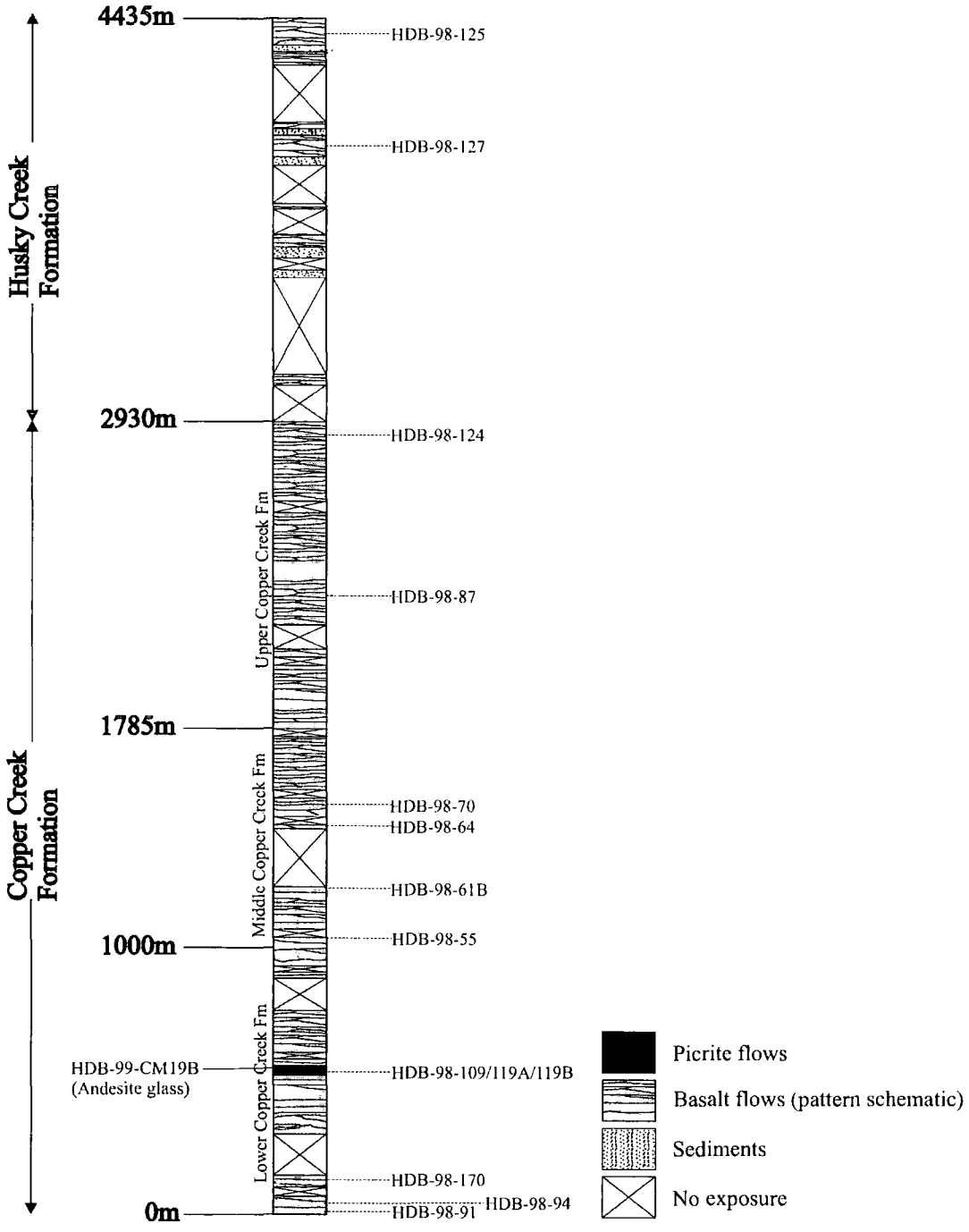

Fig 5.3: Graphic representation of the known stratigraphy of the Coppermine CFB, Canadian Shield with location of samples analysed for Re-Os isotopes in this study. Modified after Griselin et al. (1997) with the hitherto unrecognised picrite zone identified in 1999 marked.

5.3.2 Petrology of the Coppermine CFB

The *ca.* 4500m exposed Coppermine CFB lava pile is dominated by tholeiitic basaltic flows. These flows are generally composed of augite, plagioclase and magnetite with rare phenocrystic olivine (Appendix A) in a cryptocrystalline, ophitic or intersertal-textured matrix. The basalts are generally fresh with only minor quantities of alteration minerals, including serpentine, calcite, chlorite, iron hydroxide and zeolite. Dostal *et al.* (1983) noted important systematic petrographic variations in the Coppermine CFB which are summarised in Fig. 5.4; Copper Creek and Husky Creek basalts analysed in this study conform to previously published petrographical observations (see Appendix A). The lower Copper Creek Formation picrites contain up to 15% olivine as both phenocrysts and micro-phenocrysts forming an almost 'sugary' texture, and have fresh, heavily fractured cores and altered rims. The groundmass is composed of ophitic augite, olivine, plagioclase, chromite, magnetite, and orthopyroxene (hypersthene). Minor alteration of primary magmatic minerals is common for the picrites but limited secondary chlorite, calcite, zeolite and iron hydroxides are present.

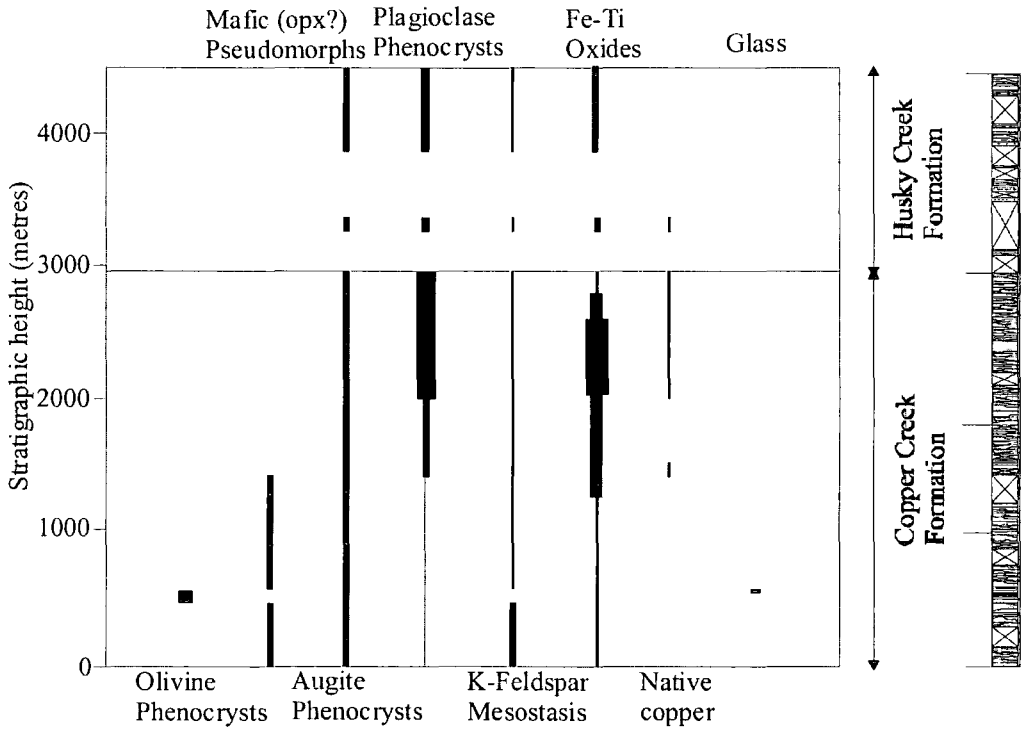

Fig. 5.4: Summary of petrographic relationships through the Coppermine CFB. Bars indicate relative and not absolute proportions; diagram modified after Baragar et al. (1996).

The andesite glass flow represents perhaps the most distinctive flow-type so far recognised in any LIP. Despite its mid-Proterozoic antiquity the glass still remains

optically fresh, with only minor perlitic cracks developed (Appendix A). Mineralogically, the glass contains small (<0.5mm) chromite, orthopyroxene, olivine, plagioclase and magnetite. The silicate minerals exhibit skeletal- or acicular-type textures (e.g., Wager *et al.*, 1960), typical of fast quenching and develop helix-type matrices throughout the 2D representation of the thin sections suggesting the possibility of an early developed crystal framework; plagioclases form spherulitic patches within the glass and a few of the orthopyroxene crystals appear to be unquenched on the basis of their euhedral crystal habits.

5.3.3 Major element variations in Coppermine CFB

The Coppermine CFB lavas are generally quartz-normative tholeiitic basalts with <50 wt. % SiO_2 evolving to andesite compositions (Fig. 5.5).

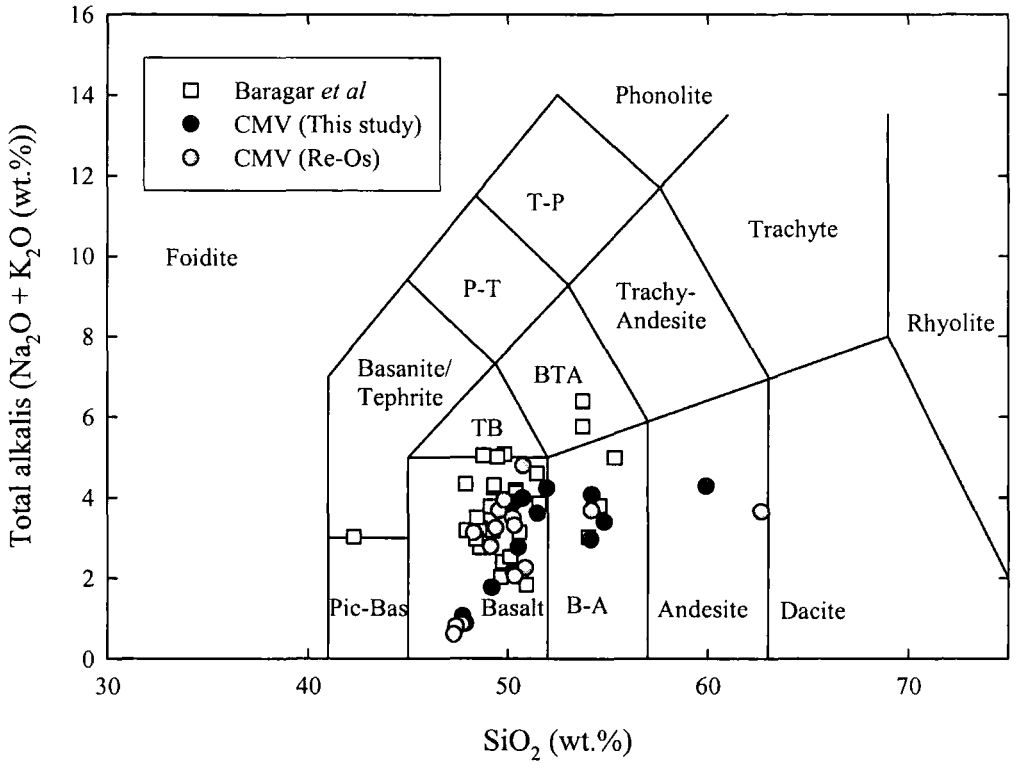

Fig. 5.5: Total alkalis versus silica (as anhydrous corrected weight percentages) plot for Coppermine CFB lavas. White squares are from Baragar (1969), Dostal et al. (1983) and Baragar et al. (1996). Sample analyses of Baragar and co-workers were performed using a rapid, wet chemistry method which may yield more imprecise Na_2O and K_2O data than XRF data presented for this study. Samples analysed for Re-Os isotopes are shown as filled grey dots.

New major element data (reported in Appendix H) for Copper Creek Formation and Husky Creek Formation lavas indicate the same broad characteristics described previously for the Coppermine CFB (Dostal *et al.*, 1983; Baragar *et al.*, 1996). Recently discovered picrites and an andesite glass flow expand the range of tholeiitic compositions seen in Fig. 5.5. The glass flow possesses an anomalously high *Mg.*-number of 56.5 (relative to its SiO_2 content).

The picritic-basalt lavas all have *Mg.*-numbers greater than 75 and MgO between 12 and 21.5wt. %. IUGS classification places these picrites in the range of komatiites (e.g., Le Bas 2000, 2001) but they do not contain spinifex textured olivines disqualifying classification as komatiites (e.g., Kerr and Arndt, 2001). Instead the picrites contain accumulative olivine with Fo_{75-78} (Hulbert pers. comm. 2004). The picrites also contain >45wt. % SiO_2 resulting in their classification on a TAS plot as 'basalts' (Fig. 5.5). Removal of 15% olivine, in keeping with petrographical observations (Appendix A), with Fo_{77} results in a magmatic liquid MgO composition of between 12-15wt. % as an estimate of the initial liquid composition of melts feeding the picrites and basalts of the Coppermine CFB.

5.3.4 Trace element variations in the Coppermine CFB

New trace element data for Coppermine lavas (Appendix H) show post-crystallisation element mobility for Ba, Rb, Sr and Pb similar to observations of other Coppermine CFB lavas (Griselin *et al.*, 1997). U, Th, Zn, Cu, high field strength elements (HFSE – e.g., Nb, Ta, Hf) and rare earth elements (REE – e.g., La, Sm, Yb) are all considered immobile (Griselin *et al.*, 1997). Examples of mobile and immobile elements are shown in Fig. 5.6 where incompatible LILE, Sr, and a HFSE, Hf are plotted against Zr which is considered to be highly incompatible and immobile (Griselin *et al.*, 1997). The large variation in Sr concentrations for a given Zr abundance in some of the Copper Creek Formation and Husky Creek Formation lavas illustrate the possible impact element mobility processes have had on LILE in the uppermost sections of the lava pile. None of the picrites or the glass show Rb, Sr, Ba or Pb loss or gain and represent lava flows least affected by element mobility. The andesite glass flow possesses high abundances of Pb, Th and Ce which are considered to be primary magmatic features because these elements, with the exception of Pb are relatively immobile. With stratigraphic height, trace elements

indicate decreases in Light REE (LREE; La) and Middle REE (MREE; Sm) relative to Heavy REE (HREE). With stratigraphic height compatible trace elements such as Cr decrease in a manner similar to the Mg/Fe ratio (e.g., Fig. 5.12). However, Cr for the Husky Creek Formation lavas never reaches the concentrations seen in the Lower Copper Creek Formation despite similar Mg/Fe ratios. The andesite glass flow has extreme Th/Nb (>1), Ce/Pb (<4), La/Nb (>2) and Nb/Ta (<12) (Table 5.1).

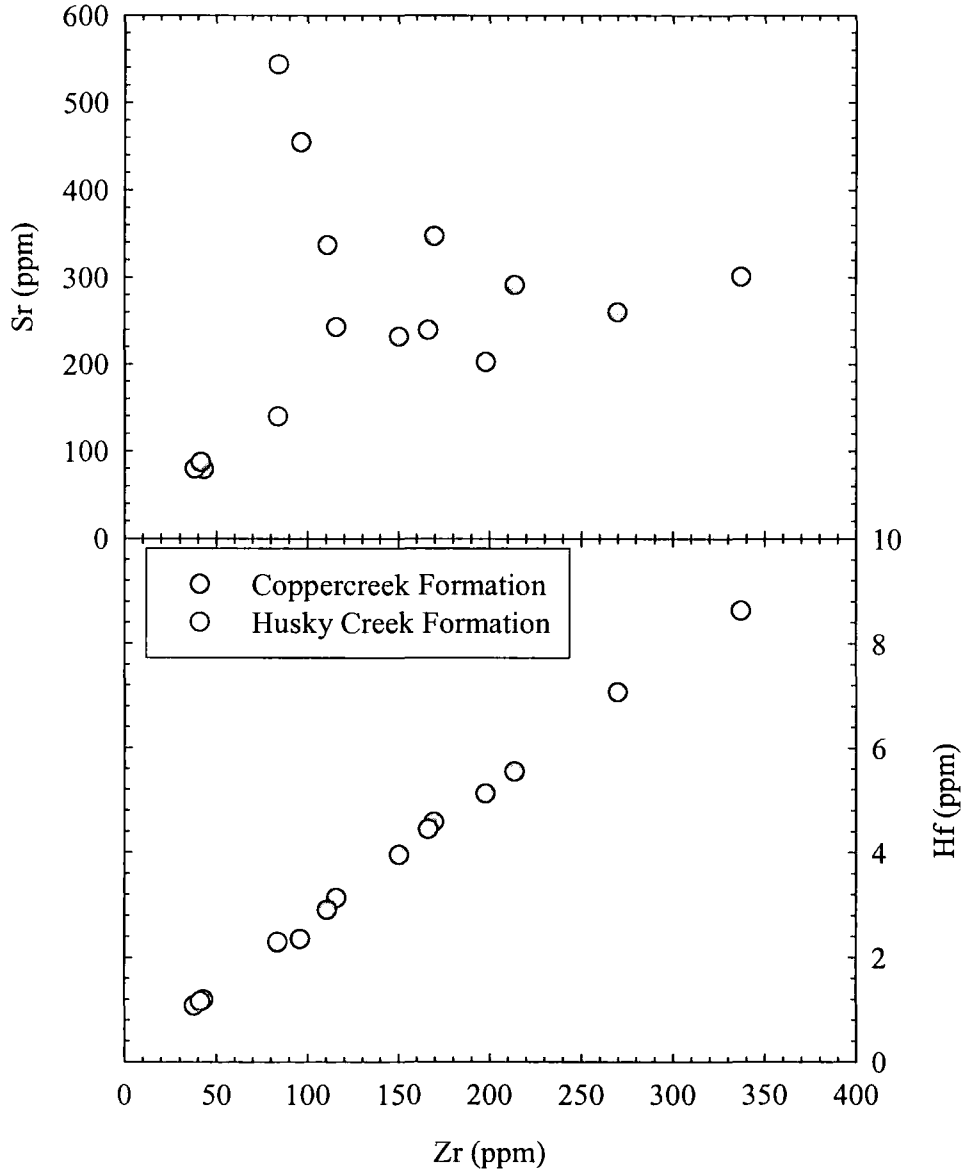

Fig. 5.6: Plots of Zr versus Sr and Hf to illustrate mobile and immobile behaviour subsequent to eruption and emplacement of the Coppermine CFB. Zr is an incompatible element during magmatic differentiation that is highly immobile. Lack of correlation between elements such as Ba, Rb, Sr and Pb with Zr suggest that their abundances in some of the lavas have been modified by post-emplacement hydrous reworking. Correlations between elements such as Nb, Ta, Hf, U and Th suggest that their abundances have not been modified in the lavas and these elements are therefore considered immobile.

Table 5.1: Trace element ratios of Coppermine CFB lavas

Sample	Nb/Ta	Ce/Pb	Th/Nb	La/Nb
HDB-98-91	15.1	5.33	0.26	1.53
HDB-98-94	14.9	5.81	0.25	1.50
HDB-98-170	14.9	5.89	0.31	1.61
HDB-98-119A	12.4	7.37	0.26	1.52
HDB-98-119B	14.9	8.11	0.30	1.65
HDB-98-109	14.9	8.72	0.28	1.58
HDB99-CM19-B (Glass)	11.6	2.13	1.10	2.84
HDB-98-55	15.3	5.23	0.12	1.02
HDB-98-61B	15.7	6.97	0.10	0.96
HDB-98-64	15.5	10.98	0.10	0.96
HDB-98-70	15.3	17.27	0.11	0.99
HDB-98-87	15.4	8.75	0.10	0.94
HDB-98-124	15.4	12.71	0.11	0.95
HDB-98-127	15.9	17.35	0.07	0.77
HDB-98-125	15.7	10.47	0.08	0.91
Average CCF (ex. Glass)	14.9	8.60	0.19	1.27
1 St Dev	0.9	3.56	0.09	0.31
CI-Chondrite[a]	17.7	0.25	0.12	0.99
Wopmay Gneiss	10.6	1.84	1.03	2.27
Hornby Bay Sst	12.4	6.27	2.92	14.04
Upper crust[b]	12.5	4	0.99	2.69
Bulk Crust[c]	10.9	3.3	0.47	1.50
DMM[d]	17.8	29.87	0.05	0.72
CLM[e]	9.5	5.01	0.30	1.49

[a]Data from McDonough and Sun (1995)

[b]Data from Barth et al. (2000) and Marcantonio et al. (1995)

[c]Data from Rudnick (1995)

[d]Data from GERM database

[e]Data from authors own compilation of CLM peridotite xenoliths

The picrites and lower Copper Creek Formation basalts exhibit high Th/Nb, La/Nb and low Ce/Pb as well as negative Nb anomalies (Fig. 5.7) whilst the upper Copper Creek and Husky Creek formation possess lower Th/Nb, La/Nb and higher Nb/Ta and Ce/Pb ratios. Fig. 5.7 compares crustal rocks surrounding the Muskox intrusion with the tholeiitic basalts, picrites and the andesite glass flow from the Copper and Husky Creek formations. Negative Nb, Ta and Ti anomalies and positive Th and LREE, including steep abundance profiles for LREE/MREE, characterise the Wopmay gneiss and Hornby Bay sandstone crustal samples. Copper Creek Formation and Husky Creek Formation basalts show only minor inflections at Ti on primitive mantle normalised diagrams (Fig. 5.7) and the Husky Creek Formation

lavas have LILE enrichments and depletions. The incompatible element abundances of the Copper Creek formation basalts increase with increasing magmatic differentiation (see Hf versus Zr in Fig. 5.6) in Fig. 5.7.

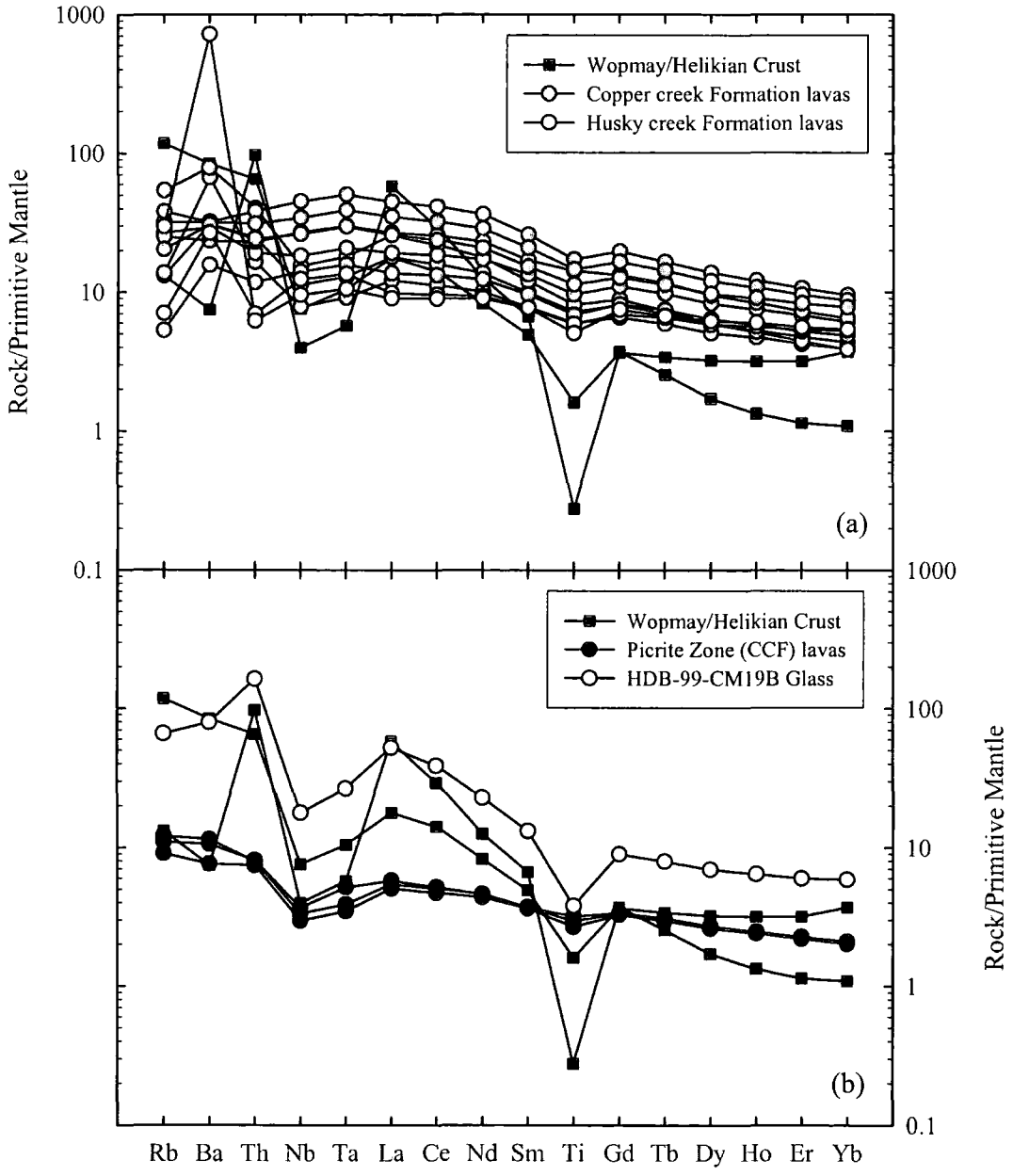

Fig. 5.7: Primitive mantle normalised multi-element plot for (a) Crustal Wopmay and Helikian rocks, Copper Creek Formation and Husky Creek Formation tholeiitic basalts and (b) crustal rocks and picrite zone lavas from the Lower Copper Creek Formation. Husky Creek Formation lavas are characterised by extreme large ion lithophile element variations. Crustal data from DDH-MX-N1 and DDH-MX-S195 from this study (see Muskox section). Despite the fact that the crustal country rocks lie within the thermal aureole of the Muskox intrusion, the relative immobility of Nb, Ta, Ti, Th and REE makes it likely that the measured signatures represent Wopmay and Helikian crust; at any rate these crustal units are likely to be highly heterogeneous at the outcrop scale.

The picrites exhibit significant negative Nb and Ta and lesser Ti anomalies, indicating that relatively hot, low concentration ultramafic lavas are more susceptible to HFSE and incompatible element contamination by crust than more evolved basalts. The primitive mantle normalised andesite glass pattern shows similarities to the crustal samples with elevated Th and LREE, steep LREE/MREE concentration trajectories as well as depletions in Nb, Ta and Ti consistent with the low Ce/Pb, Nb/Ta and high Th/Nb and La/Nb ratios.

Fig. 5.8 illustrates the evolution of REE up the stratigraphic succession for the Coppermine CFB. The early Lower Copper Creek Formation lavas are the most HREE-depleted lavas in the entire succession, especially the picrites, and have steep REE patterns. The middle and upper Copper Creek Formations are less HREE-depleted and have higher total abundances of REE than the lower Copper Creek Formation. The Husky Creek Formation has the lowest concentrations of LREE and MREE as well as the flattest REE patterns of all the succession.

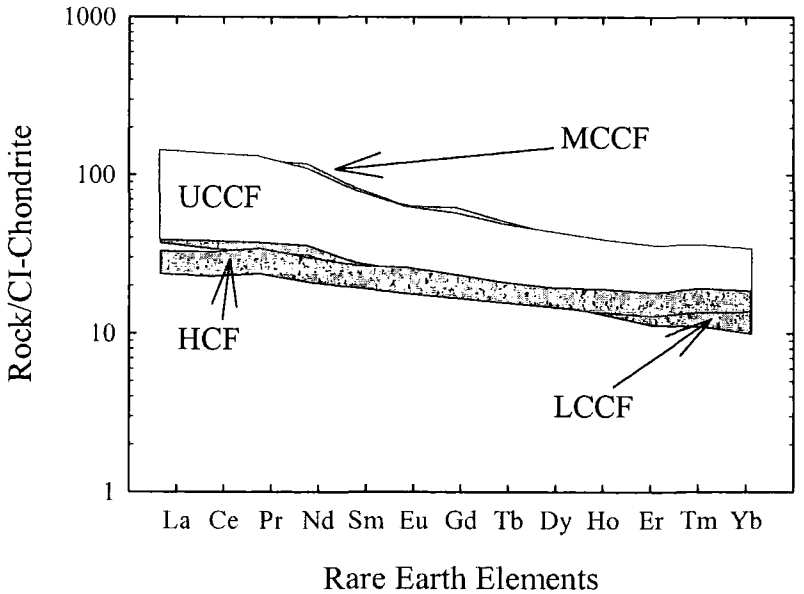

Fig. 5.8: Evolution of Coppermine CFB from REE patterns. LCCF = Lower Copper Creek Formation, MCCF = Middle Copper Creek Formation, UCCF = Upper Copper Creek Formation, HCF = Husky Creek Formation. A change in abundance and REE patterns (increased shallowing) is observed with increasing height from the base of the Coppermine CFB stratigraphy.

5.3.5 Re-Os isotope results for the Coppermine CFB

This study presents the first Re-Os isotope results for the Coppermine CFB (Table 5.2). 15 lavas, including the andesite glass flow and three picritic flows were analysed using the methods outlined in Appendix C. These samples range across the entire stratigraphy of the Coppermine CFB and include Husky Creek Formation as well as Copper Creek Formation lavas. Os concentrations (uncorrected for ^{187}Re in-growth) in Copper Creek and Husky Creek Formation lavas range from 0.027 to 3.843ppb, with Re concentrations from 0.036 to 0.948ppb. The broad positive and negative correlations of Re with TiO_2 and MgO, respectively, indicate control of Re abundances during fractionational crystallisation of olivine and Fe-Ti oxides (Fig. 5.9); some of the scatter may also be generated by volatile degassing or hydrothermal reworking (see discussion). Similar correlations are also observed in picrites from Proterozoic (Keweenawan; Shirey, 1997) and Phanerozoic CFB (West Greenland Picrites; Schaefer *et al.*, 2000).

Table 5.2: Re and Os concentration and Os isotopic data for the Coppermine CFB

Sample	Re (ppb)	Os (ppb)	$^{187}Re/^{188}Os$[a]	$^{187}Os/^{188}Os_m$[b]	±	1σ	$\gamma Os_{(t)}$[c]
Husky Creek Formation - Coppermine Volcanics							
HDB-98-125	0.600	0.039	88.6	1.7495	±	0.0016	-202.2 (±23)
HDB-98-127	0.898	0.034	194.3	3.9896	±	0.0016	-193.6 (±51)
Copper Creek Formation - Coppermine Volcanics							
HDB-98-124	0.626	0.027	162.2	3.6626	±	0.0021	69.3 (±43)
HDB-98-87	0.314	0.046	35.9	0.8561	±	0.0005	-24.9 (±10)
HDB-98-70	0.732	0.041	109.9	2.3602	±	0.0019	-86.0 (±26)
HDB-98-64	0.864	0.032	203.2	4.4954	±	0.0017	34.5 (±54)
HDB-98-61B	0.619	0.150	21.0	0.5326	±	0.0002	-29.0 (±5)
HDB-98-55	0.289	0.082	17.7	0.4848	±	0.0004	-10.4 (±5)
HDB99-CM19-B	0.342	3.843	0.4	0.1307	±	0.0000	2.1 (±0.1)
HDB-98-109	0.046	0.630	0.3	0.1275	±	0.0001	0.8 (±0.1)
HDB-98-119B	0.036	0.777	0.2	0.1264	±	0.0001	2.2 (±0.1)
HDB-98-119A	0.126	0.652	0.9	0.1360	±	0.0001	-2.5 (±0.3)
HDB-98-170	0.204	0.131	7.7	0.3079	±	0.0001	20.7 (±2.0)
HDB-98-94	0.948	0.722	6.4	0.2542	±	0.0001	-1.7 (±1.7)
HDB-98-91	0.720	0.228	15.8	0.4169	±	0.0001	-32.7 (±4.2)

[a] *The 2σ error in this ratio is 0.37% (Re) and 0.125% (Os) and is a function of spike uncertainty however this does not account for non-stoichiometry of the Os spike calibration (Appendix C)*

[b] *1σ error of the internal precision of measurement generally better than 2σ of UMCP std data at similar run intensities (Appendix C).*

[c] *Age corrected γOs values. γOs is the percentage difference between the age corrected $^{187}Os/^{188}Os$ ratio and the 187Os/188Os ratio of a chondritic mantle where the present-day chondritic mantle has $^{187}Os/^{188}Os=0.12757$ and $^{187}Re/^{188}Os=0.3972$ (Walker et al., 1989)*

High Os concentrations (0.63 to 0.77ppb) are found in the picrites and high-MgO basalt HDB-98-170. However, with 3.843ppb Os, glass HDB99-CM19-B is the highest Os concentration lava in the Coppermine CFB. The observation that a low-MgO andesite has the highest Os abundances of any lava, including picrites, in a CFB stratigraphy is highly unusual. The andesite glass lies off the otherwise well-defined positive correlations observed between MgO, Ni and Os abundances (Fig. 5.10) for other Coppermine CFB lavas. The positive correlations between Os, MgO and Ni indicate that Os is fractionated by phases prior to or during olivine fractionation.

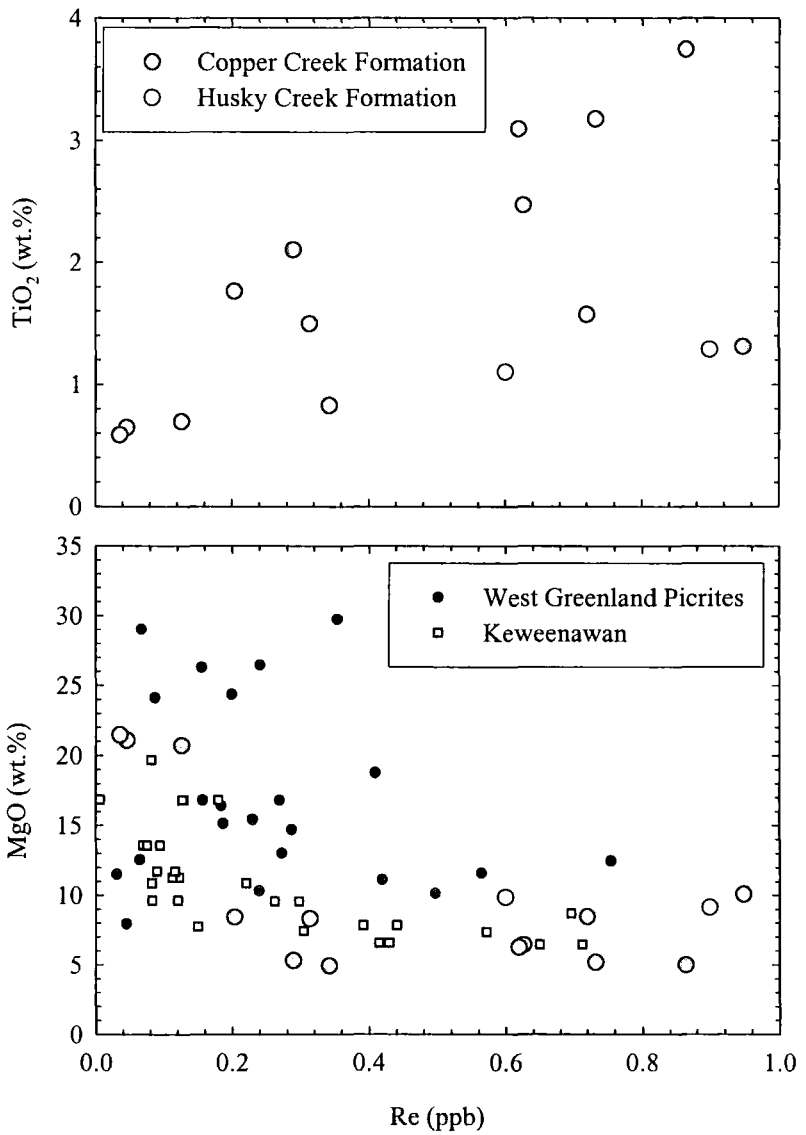

Fig. 5.9: Distribution of Re in Coppermine CFB as a function of TiO_2 and MgO. West Greenland picrite data from Schaefer et al. (2000) and Keweenawan CFB lavas from Shirey (1997).

Empirical estimates of partition coefficients of Os into olivine are low (bulk $D_{olivine-liquid}$ = 0.4-0.6; Puchtel *et al.*, 2004) and so these correlations are consistent with Os abundances having been controlled by sulphide or osmiridium inclusions trapped within the olivine crystal lattice (Hart and Ravizza, 1996; Schaefer *et al.*, 2000). The high Os content observed in glass HDB99-CM19-B also strongly suggests that Os is decoupled from silicate phase control. Instead the major control on Os seems to be sulphide and precious metal alloys trapped within early crystallising phases such as chromite that is present in the glass (Cr =2500ppm) at greater abundances than in the picrites (Cr = 1700 to 1990ppm).

Coppermine CFB are compared for Re/Os* and Os* with other continental intraplate lavas (Komatiites, CIAV), mid-Ocean ridge basalts (MORB), continental lithospheric mantle (CLM) peridotites and Keweenawan and Western Greenland picrites in Fig. 5.11. Like Keweenawan and Western Greenland picrites, the Coppermine CFB lavas form an array from near-chondritic Re/Os* high Os* lavas to more fractionated, high Re/Os*, low Os* lavas. Some of the Coppermine CFB lavas also have Re/Os* ratios lower than chondritic mantle, probably as a result of Os-rich mineral accumulation in these flows. Similar relationships for Re/Os and Os are also observed for CIAV, Komatiites, MORB, OIB (Chapter 4) and arc lavas (Alves *et al.*, 2002) and can be partially explained by melting and fractional crystallisation in the presence of sulphides, as well as Re-volatility through eruptive degassing (see discussion). Some of the Coppermine CFB picrites have similar Os* and Re/Os* to Komatiites; an observation also true for Keweenawan, Siberian, Karoo and Western Greenland picrite equivalents. It seems that all CFB sequences that contain picrite lavas share similar Os contents that are as high as Komatiites and higher than most OIB.

Fig. 5.12 is a plot of *Mg.*-number, Cr, Re, Os* and γOs_i (corrected to 1270Ma) through the Coppermine CFB succession to examine stratigraphic variation. Os behaves compatibly like Cr and MgO and is most elevated in the lower Copper Creek formation. It was noted previously that whilst Mg/Fe ratios are comparable between lower Copper Creek and Husky Creek formations the Cr concentrations are far lower for the Husky Creek formation. This relationship is also true for Os*. Re increases slightly in abundance through the succession apart from lower Re abundances measured in the picrite zone.

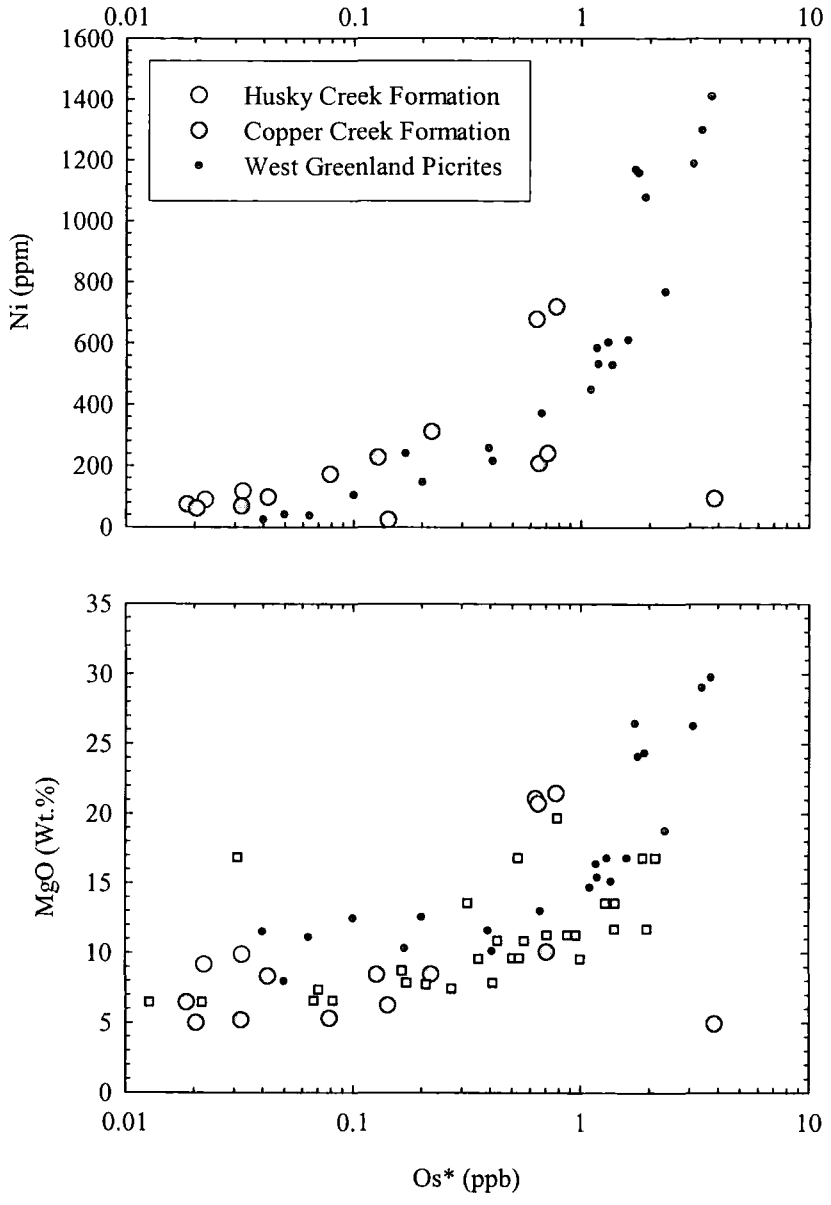

Fig. 5.10: Distribution of common Os in Coppermine CFB as a function of Ni and MgO. Data sources and symbols are the same as for Fig. 5.9.

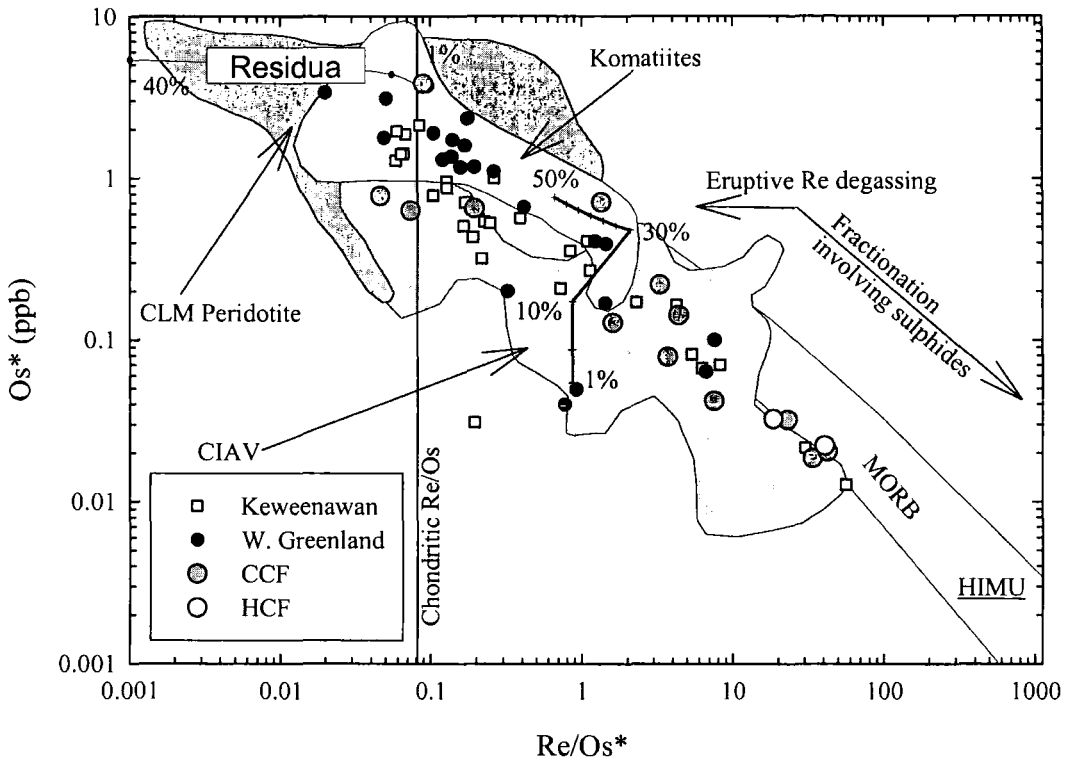

Fig. 5.11: Re/Os vs. Os* for Coppermine CFB compared with Komatiites, MORB, CLM peridotites and CIAV (Data compiled from Shirey and Walker, 1998 and references therein). *Os = common Os. The partial melting trend (up to 50% melt interval) is for mantle with CI-chondrite Re/Os ratios and containing 3.5ppb Os. The model assumes that residual sulphides control the Re and Os concentrations up to their exhaustion point at 30% melting (after Roy-Barman and Allègre, 1995). Complementary depletion trends for CLM peridotites are also shown as are vectors for sulphide fractionation and Re volatility during shallow volcanic degassing. HIMU component is estimated from Hauri and Hart, 1993. CCF = Copper Creek Formation, HCF = Husky Creek Formation.*

Measured $^{187}Os/^{188}Os$ ratios for Coppermine CFB range from 0.1264 to 3.98. The andesite glass flow and picrite lavas have the least radiogenic measured $^{187}Os/^{188}Os$ of 0.1264 to 0.1360. $^{187}Os/^{188}Os$ corrected for ^{187}Re ingrowth over 1270Ma and expressed as γOs (γOs = percentage deviation from CI-chondrite $^{187}Os/^{188}Os$ at time, *i* or initial, in this case 1270Ma ago) are presented in table 5.2 and Fig. 5.12. γOs_i ranges from +69.3 to -202.2 for the entire stratigraphy with γOs_i in the picrite zone and andesite glass ranging from +2.2 to -2.5. γOs_i varies systematically from near-chondritic in the lowermost portions of the stratigraphy to increasingly negative γOs_i (apart from two samples) for the top ~3.5km of the flood basalt pile (Fig. 5.12).

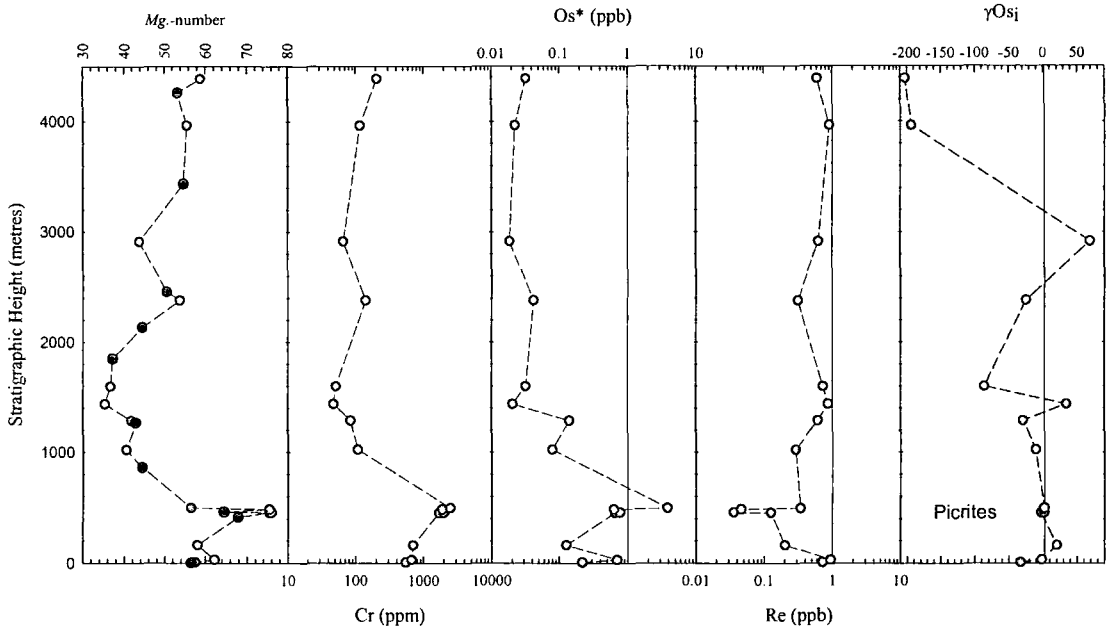

Fig. 5.12: Variation in MgO, Cr, Re, Os and γOs_i with stratigraphy for Coppermine CFB lavas analysed in this study. Black circles represent major element data for samples from this study not analysed for Re-Os isotope systematics.*

5.4 The Muskox Intrusion

The Muskox ultramafic-mafic layered intrusion is situated in the Bear structural province on the northwestern edge of the Canadian Shield, north of the Arctic Circle (Fig. 5.2). The Muskox intrusion is emplaced into Aphebian basement complex of Wopmay paragneiss and orthogniess, metavolcanics and metasediments, just at the base of the 3-5° north-ward dipping Helikian sequence (Fig. 5.2). The intrusion was discovered by H. Vuori of the Canadian Nickel Company in 1956 and has been a long-term target for precious mineral and metal exploration. 36 samples were carefully selected for Re-Os isotope analysis from a large (~600), well characterised, sample suite from the Muskox north and Muskox south drill holes. These drill holes dissect the entire, known 1800m stratigraphy of the intrusion and were drilled as part of the International Upper Mantle Project in the summer of 1963 (Findlay and Smith, 1965). A further 3 keel dyke specimens and 3 main reefal chromitite horizons collected during field seasons by L.J. Hulbert (GSC) were also analysed for Re-Os isotopes to complement the data collected from the diamond drill hole cores.

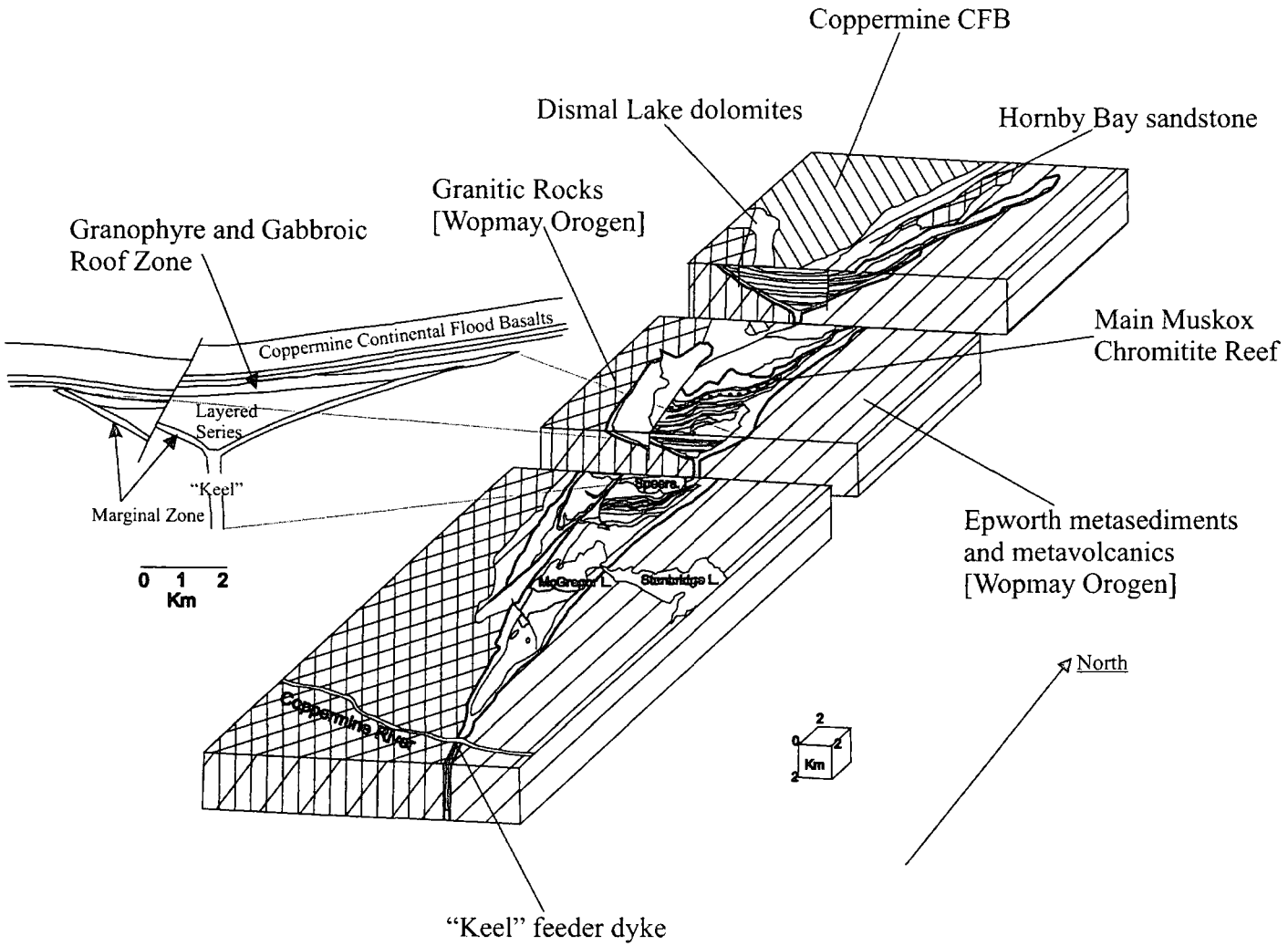

Fig 5.13: Exploded block diagram of the Muskox Intrusion, showing its structural relations. Also shown is a restored cross-section of the exposed parts of the intrusion (Modified from Irvine and Smith, 1967 and Irvine, 1980)

5.4.1 Structure and stratigraphy of the Muskox intrusion

The geology and structure of the Muskox intrusion has been described in detail by Findlay and Smith (1965) and their findings are summarised in Fig. 5.13. Exposed, the intrusion is 125km long, 11km wide in the north and 0.1km wide in the south forming a wedge-shaped body that trends NNW-SSE (Fig. 5.13). In the overall structure of the intrusion a thin southern tail takes the form of a vertical en-echelon 'keel-like' dyke whilst the main body of the Muskox can be considered as a giant funnel-shaped dyke. The Muskox intrusion is outstanding among mafic-ultramafic intrusions in that: (a) it is exceptionally well developed and structurally undeformed; (b) it features a complete rock differentiation series from high-temperature dunitic cumulates, peridotites, pyroxenites, gabbros through to relatively low-temperature granophyres; (c) it is the most ultramafic large layered intrusion so far recognised on Earth with an ultramafic/mafic ratio of ~9:1 (compared with a ratio of ~1:9 for the Bushveld Intrusion) and (d) it has been considered to be related in space and time to the extensive Coppermine CFB (Baragar, 1969; Francis, 1994; Baragar *et al.*, 1996). Aeromagnetic and gravity anomaly studies show that the intrusion extends for at least another 250km under younger cover where it becomes wider (Fig. 5.2). The present exposure probably only represents a thin, oblique slice through a much larger intrusion with an estimated volume in excess of 20,000km^3. Detailed summaries of the stratigraphy shown in Fig. 5.14 is given in Appendix H with petrographical data given in Appendix A.

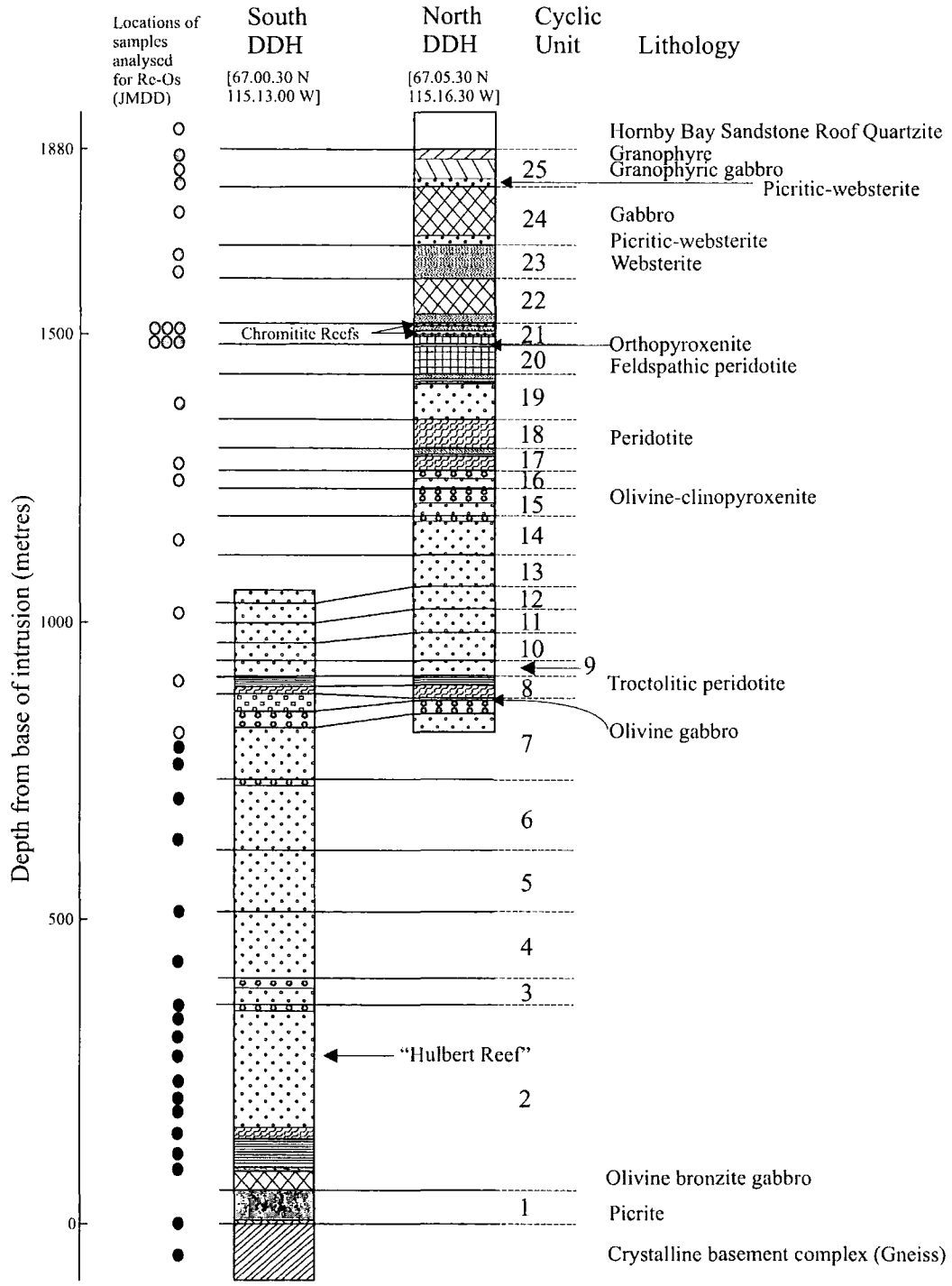

Fig 5.14: Drill-core sections of the Muskox Intrusion with positions of samples analysed for Re-Os from them (black dots = south diamond drill hole (DDH), grey dots = north DDH). Diabase dykes have been omitted for clarity. A more detailed description of the drill cores is given in Findlay and Smith (1965).

5.4.2 Major element variations in the Muskox Intrusion layered series

The layered series are cumulate rocks and as such the minerals they accumulate define their major and trace element concentrations (Appendix H) (Fig. 5.15). The selected data from a much larger major element data base (n=~600; Hulbert, unpublished), shows that the Muskox intrusion layered series is characterised by inflections in MgO and SiO_2 from pyroxenite layers (in this case cyclic units 8 and 16) which are sandwiched between dominantly dunite and peridotite units which have relatively invariant SiO_2 <50 wt. % and MgO >35 wt. % (Fig. 5.15). Diagnostic chemical features of the cyclic units themselves are upward trends of decreasing *Mg.*-number and compatible element contents but an overall increasing trend through the intrusion up to the main chromite horizon. These represent fractional crystallisation trends for the cumulate minerals and are a form of cryptic layering (*c.f.* Wager and Brown, 1968). For the major element data presented here this cryptic layering is best displayed by cyclic unit 2 (Fig. 5.15), however it is also well developed in cyclic units 4 to 7 (Irvine, 1975). The marginal zone at the base of the intrusion shows increases in MgO and FeO but shows little variability in SiO_2. There is no evidence of systematic SiO_2 enrichment in the intrusion and this is illustrated by the Dunites which contain as little 38 wt. % SiO_2. After the appearance of the main chromitites reef at ~1550m, MgO decreases and SiO_2 increases to ~50 wt. % in the roof rocks. There is no trend toward silica-enrichment in the roof zone but there is a slight increase in FeO* suggesting crystallisation of magnetite and high fO_2 (e.g., Kennedy, 1948; Osborn, 1959).

All the layered series cumulate rocks have low alkalis (Na_2O + K_2O) contents; however, the more differentiated rocks of the marginal zones have total alkali contents up to 5.5 wt. % (anhydrous) and define a tholeiitic fractionation path consistent with FeO* enrichment at elevated fO_2 in the roof zone. Dunite *Mg.*-numbers range from 80 to 87 with up to 45 wt. % MgO measured in some of the most serpentinised cyclic units. Pyroxenite units have similar *Mg.*-numbers to the dunites but have lower MgO and FeO* contents. The chromitite horizons have low *Mg.*-numbers due to the abundance of chromite which contains iron; dunite rocks contain 1-2% chromite, however the content of chromite does not correlate well with FeO* abundances in these cyclic units. Despite the Mg-rich nature of the dunite

units, their olivines are not as forsteritic as those for large layered mafic/ultramafic intrusions elsewhere. Occasionally cyclic units contain olivines with Fo_{88}, however the majority of the dunite cyclic units have Fo_{84-86} (Hulbert, pers. comm. 2004). Keel dyke samples analysed in this study have restricted *Mg.*-numbers of ~79 and SiO_2 (45.6 to 46.5) and have similar MgO and Mg/Fe compositions to Lower Copper Creek picrite lava flows.

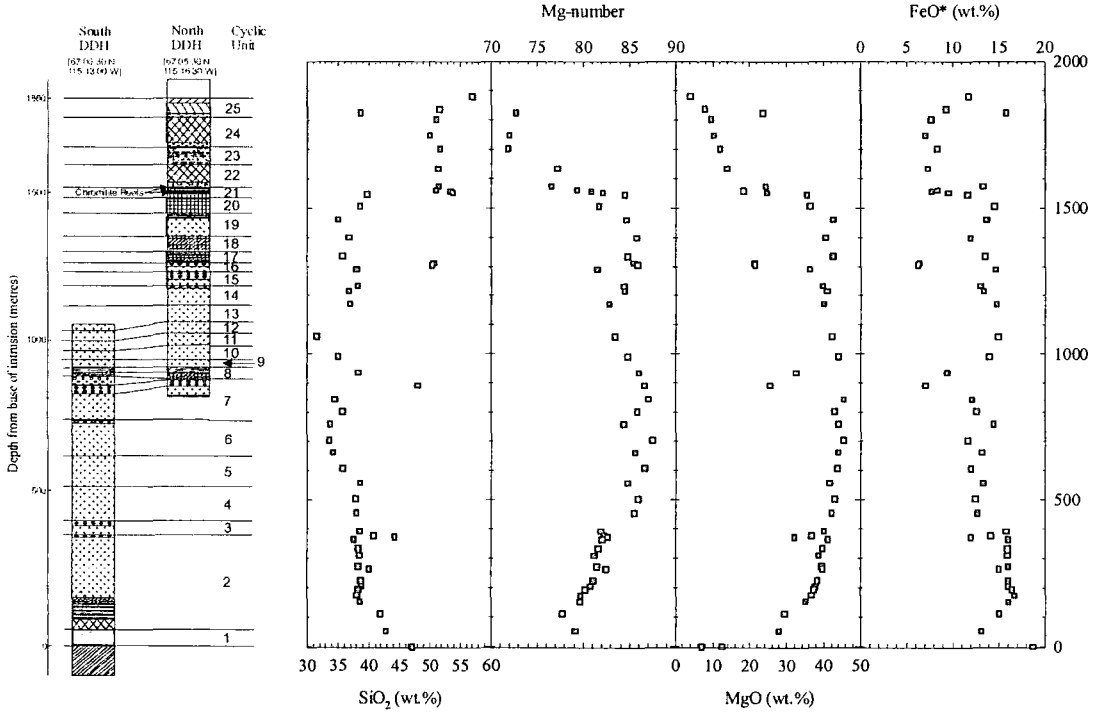

Fig. 5.15: Variation in major elements with stratigraphy of the Muskox Intrusion vs. SiO_2, Mg.-number (noted expanded scale to remove fractionated samples), MgO and total FeO. Data are from this study and are anhydrous corrected– country rocks DDH-MX-N1 and DDH-MX-S195 not shown.

5.4.3 Trace element variations in the Muskox Intrusion layered series

In this section new ICP-MS trace element data are presented as well as S analyses (L.J Hulbert, unpublished; Appendix H). Mafic-ultramafic layers have low absolute incompatible trace element abundances. Incompatible element depletion combined with compatible element variation reflects the role of olivine and chromite accumulation. Compatible trace elements correlate with *Mg.*-number such that the variations with stratigraphic height of Cr and Ni are very similar to the MgO and FeO* major element variations (Fig. 5.16). Variable S contents of 5000 to 50000 ppm occur in marginal zone rocks (DDH-MX-S192, DDH-MX-S195). S abundances are low in the dunites, especially those that are serpentinised (Fig. 5.16). From ~1000m in the intrusive stratigraphy, S increases progressively to the concentrations

measured in the lower marginal zone rocks (1000's ppm). Francis (1994) has shown with a much larger marginal zone dataset that S is preferentially concentrated along the contacts of the intrusion. Cu (Fig. 5.16) exhibits similar trends in concentration to S reflecting its chalcophile tendencies.

V content is exceptional for the transition metals in that it decreases from the marginal zone, into the layered series and then increases into the roof zone forming a bow shape (Fig. 5.16). Apart from clinopyroxene (K_D= >1.8; Hauri *et al.,* 1994), V is negligibly partitioned into anhydrous silicate phases but has great affinity for oxide minerals, especially magnetite ($D_v \geq 25$; Dostal *et al.,* 1983b). However, unlike layered mafic-ultramafic intrusions elsewhere (e.g., Skaergaard), the V content of Muskox cyclic units appears unrelated to magnetite or chromite fractionation in the layered series. Instead the V concentration decrease appears to be controlled by clinopyroxene fractionation. This is confirmed by the high V contents in clinopyroxenites compared with dunite units and suggests that in addition to olivine control, elemental abundances are also dependant upon the modal proportions of clinopyroxene.

Low abundances of LILE (e.g., Sr), REE (e.g., Nd) and HFSE are found in the intrusive rocks and show similar stratigraphic trends to V (Figs. 5.16) suggesting that the predominant control on these trends are clinopyroxene fractionation and because of the incompatibility of these elements into olivine compared with the melt. Initial concentrations for Sr and Nd in Muskox layered series rocks prior to post-solidus alteration processes can be estimated from the un-serpentinised cyclic 2 units which have ~50ppm Sr and 2-3ppm Nd. The low concentrations of Sr and Nd make the Rb-Sr and Sm-Nd isotope systematics of these rocks highly susceptible to crustal contamination (*cf.,* Stewart and DePaolo, 1992). Pb concentrations only vary significantly at the base of the marginal zone and top of the roof zone, and appear to follow cryptic layering trends similar to those seen in the major element profiles (Fig. 5.16). Pb forms prominent positive anomalies on the primitive mantle normalised plots (Fig. 5.17). For the marginal and roof zones Pb anomalies are in excess of 10 to 100 times primitive mantle values whilst the layered series have Pb anomalies 5 to 30 times primitive mantle.

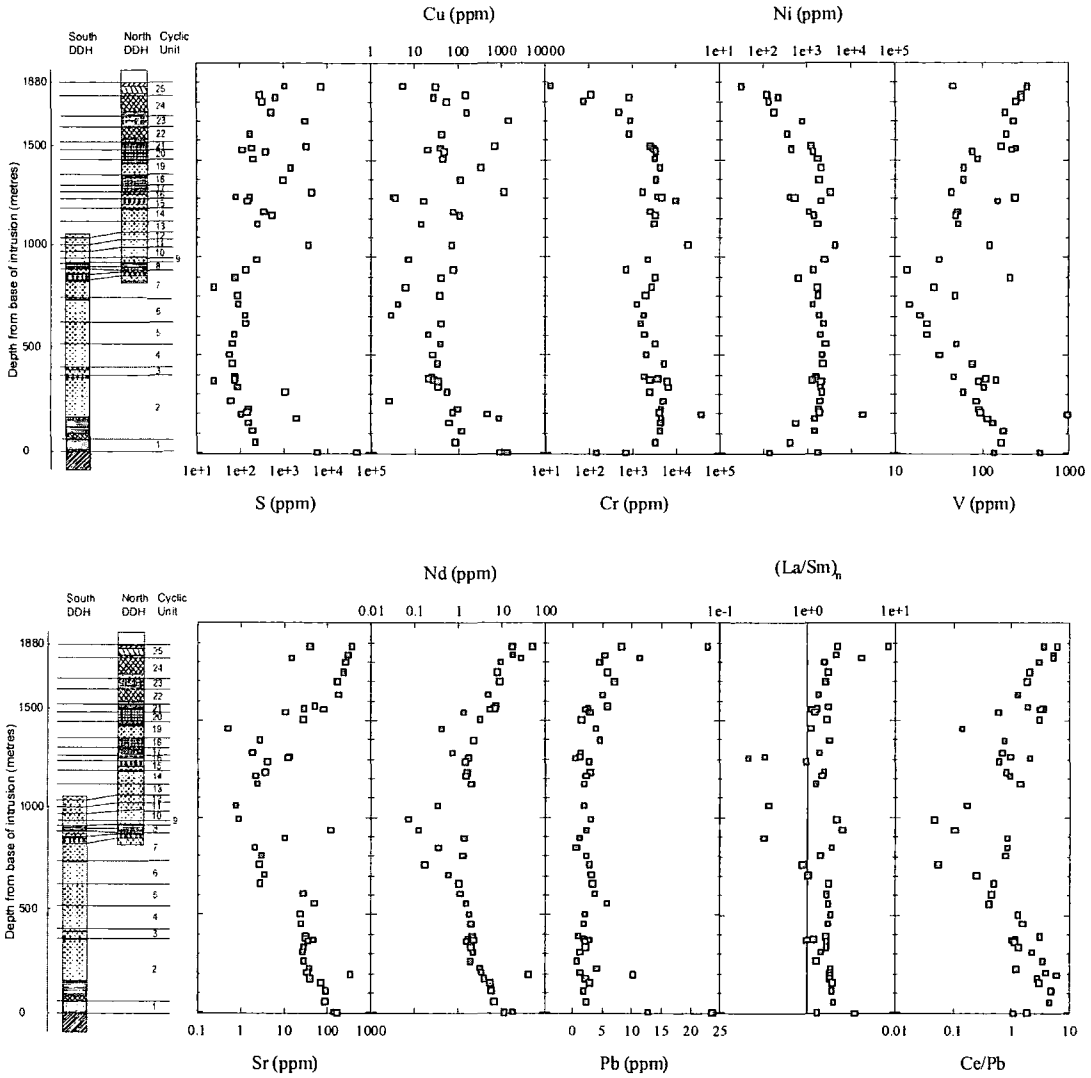

Fig. 5.16: Variation in trace element chemistry with stratigraphy of the Muskox Intrusion versus S, Cu, Cr, Ni, V, Sr, Nd and Pb, primitive mantle normalised La/Sm and Ce/Pb. Normalisation values after Sun and McDonough (1989).

REE are immobile but are at low abundances (Fig. 5.17). $(La/Sm)_n$ are supra-chondritic (Fig. 5.16) whilst the Ce/Pb ratios vary with stratigraphy as seen for V, Sr and Nd (Fig. 5.16). Ce/Pb ratios for the serpentinised layered series rocks fall to abnormally low ratios of ~0.08 whilst the less altered cyclic unit 2 dunites also have relatively low Ce/Pb ratios of ~1-8 (DMM Ce/Pb = 30, bulk crust Ce/Pb = 3.3, table 5.1). Primitive mantle normalised multi element plots of Muskox Keel, marginal zone, roof zone and layered series rocks reveal similar profiles for cyclic unit 2 dunites and the Muskox keel feeder dyke (Fig. 5.17). The plots in Fig. 5.17 also illustrate the large variations for LILE (Rb, Ba), the generally negative anomalies for Ti and Nb, positive anomalies for Pb and Th and the extreme variability of Ta seen in Muskox Intrusion rocks. Elevated Rb, Ba and Th and negative Nb, Ta and Ti

anomalies are characteristic of the Wopmay orogen gneiss and these same features are prominent in the Keel dyke and cyclic layer 2. Th excess in the Hornby Bay sandstone roof rock (DDH-MX-N1) is also obvious in DDH-MX-N3 and DDH-MX-N14 but not, surprisingly, in other roof rocks (Fig. 5.17). Other samples with notable element geochemistry include the main chromitite layer samples which all exhibit positive Ti anomalies, probably from Ti-rich chromite, and distinct Nb, Ta and Pb anomalies (Fig. 5.17).

The effects of plagioclase fractionation are obvious in the trace element abundances of the ultramafic layered series. There are dramatic variations in Eu anomalies, from negligible in Muskox Keel dyke samples (Eu/Eu*=0.92 to 1.06) through to large positive and negative anomalies in cyclic units 7 to 21 (Eu/Eu* = 0.67 to 3.09). A feldspathic olivine troctolite (DDH-MX-N151) has the most positive Eu anomaly of all the layered series rocks whilst the main chromite layer also has positive Eu anomalies. These lines of evidence suggest that Eu was predominantly charged as Eu^{3+} during crystallisation of much of the layered series and oxygen activities were high whereas Eu was charged as Eu^{2+} (Drake and Weill, 1975) during chromite formation and oxygen activities were low. Plagioclase fractionation and accumulation is the dominant control in this process. Cyclic unit 2 dunites have lower overall REE concentrations but similar REE patterns to the Keel dyke samples. Elsewhere, the marginal zone cyclic units DDH-MX-S182 and DDH-MX-S171 have similar REE patterns to cyclic unit 2 layers; however DDH-MX-S192 – a bronzite gabbro - has a similar REE pattern to the Wopmay Gneiss (DDH-MX-S195). REE pattern profiles are relatively consistent for the layered series cyclic units 2-7 apart from the notable exceptions of DDH-MX-S44, DDH-MX-S60 which are comparatively depleted in LREE and MREE. Cyclic units 21-25 constitute the roof zone.

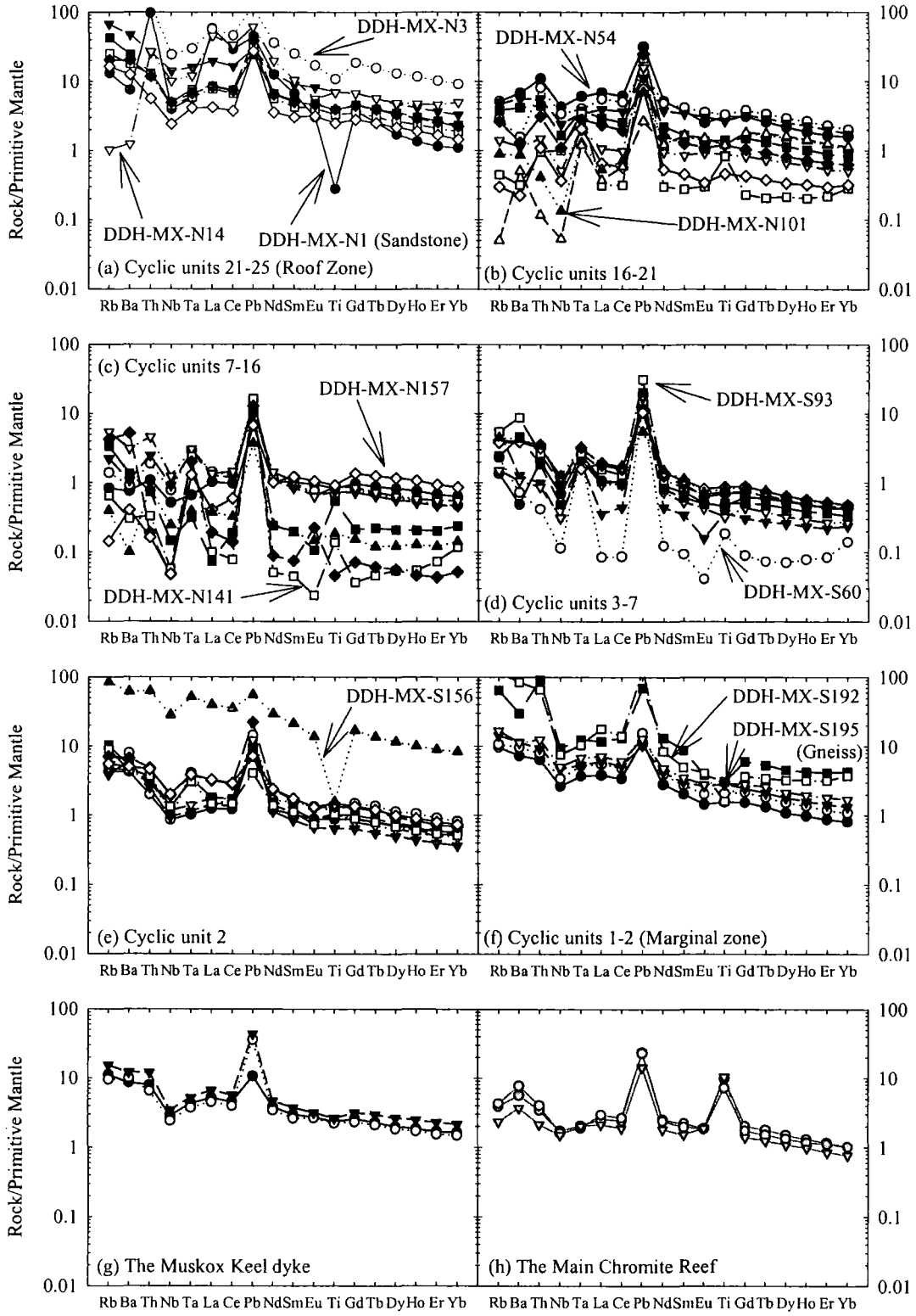

Fig. 5.17a-h: Primitive mantle normalised multi-element variation diagrams for Muskox intrusion cyclic units, chromitites and the Keel dyke. Hornby Bay sandstone and Wopmay Gneiss country rocks are indicated otherwise all other samples represent magmatic rocks of the Muskox layered intrusion. Normalisation after Sun and McDonough (1989).

5.4.4 Re-Os isotope results for the Muskox Intrusion layered series

The first Re-Os isotope data for the Muskox layered mafic-ultramafic intrusion and keel feeder dyke are presented in Table 5.3. Layered series peridotites and pyroxenites, roof zone and marginal differentiates and crustal rocks from the Muskox Intrusion have Re concentrations that vary widely from 0.018ppb in serpentinised dunite units and clinopyroxenites to 105ppb in a marginal zone bronzite gabbro. Re concentrations tend to be higher for samples with elevated TiO_2 and low MgO (Fig. 5.18) reflecting, similar to the Coppermine CFB trends, that Re behaves incompatibly and is controlled by crystal fractionation of olivine, Fe-Ti oxide as well as Ti-rich chromitite.

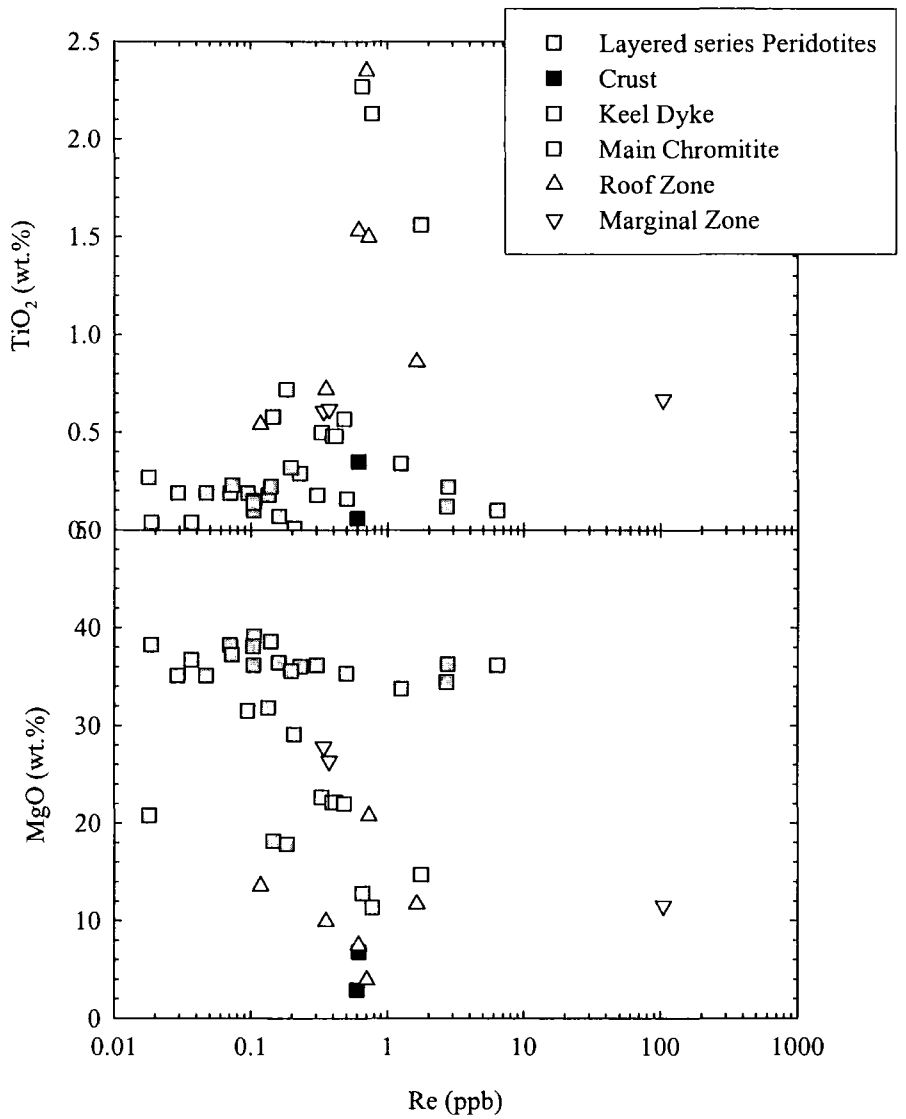

Fig. 5.18: Distribution of Re in Muskox Intrusion rocks as a function of TiO_2 and MgO.

Table 5.3: Re and Os concentration and Os isotopic data for the Muskox Intrusion (Canada)

Sample	Re (ppb)	Os (ppb)	$^{187}Re/^{188}Os$[a]	$^{187}Os/^{188}Os_m$[b]	±1σ	γOs_i[c]
DDH-MX-N-1 *Cr*	0.595	0.018	210	2.4180	0.0056	1853.1
DDH-MX-N-3	0.703	0.040	105	2.0082	0.0010	-307.0
DDH-MX-N-11	0.613	0.037	96.1	1.7779	0.0011	-332.5
DDH-MX-N-14	0.725	0.875	4.0	0.1857	0.0000	-16.2
DDH-MX-N-27	0.355	0.197	8.8	0.2866	0.0001	-18.4
DDH-MX-N-35	1.642	1.824	4.4	0.2817	0.0000	57.2
DDH-MX-N-46	0.118	2.917	0.2	0.1396	0.0001	13.8
HDB-2000-MX-04a	0.771	39.91	0.09	0.1502	0.0001	24.5
HDB-2000-MX-26a	1.754	56.74	0.15	0.1444	0.0000	18.6
HDB-2000-MX-40a	0.654	201.4	0.02	0.1338	0.0000	12.0
DDH-MX-N-55	0.184	1.570	0.6	0.1443	0.0000	11.1
DDH-MX-N-56	0.146	1.468	0.5	0.1497	0.0001	17.0
DDH-MX-N-59	0.095	0.693	0.7	0.1491	0.0001	13.4
DDH-MX-N-75	0.304	70.32	0.02	0.1243	0.0000	4.0
DDH-MX-N-97	6.329	14.43	2.1	0.1841	0.0001	16.4
DDH-MX-N-100	0.018	0.597	0.15	0.1281	0.0001	5.0
DDH-MX-N-104	0.135	4.249	0.15	0.1287	0.0000	5.3
DDH-MX-N-115	0.498	1.620	1.4	0.1622	0.0001	9.6
DDH-MX-N-129	2.707	19.30	0.7	0.1487	0.0000	12.7
DDH-MX-N-151	0.208	4.515	0.2	0.1316	0.0000	6.5
DDH-MX-S-44	0.019	7.741	0.01	0.1228	0.0000	2.9
DDH-MX-S-51	0.105	5.706	0.1	0.1262	0.0000	4.4
DDH-MX-S-60	0.037	0.956	0.2	0.1407	0.0001	14.9
DDH-MX-S-76	0.160	14.51	0.05	0.1271	0.0000	5.8
DDH-MX-S-102	0.106	2.044	0.3	0.1417	0.0000	14.5
DDH-MX-S-110	0.070	3.887	0.09	0.1255	0.0000	3.9
DDH-MX-S-123	0.029	1.846	0.08	0.1327	0.0006	10.1
DDH-MX-S-123(II)	0.047	0.917	0.3	0.1288	0.0001	3.7
DDH-MX-S-128	0.104	6.247	0.08	0.1244	0.0000	3.1
DDH-MX-S-133	0.073	5.350	0.07	0.1235	0.0000	2.6
DDH-MX-S-137	2.761	9.092	1.5	0.2539	0.0001	86.5
DDH-MX-S-144	0.140	6.554	0.10	0.1261	0.0000	4.1
DDH-MX-S-151	0.230	5.993	0.2	0.1302	0.0000	6.0
DDH-MX-S-154	0.198	6.549	0.15	0.1320	0.0000	8.2
DDH-MX-S-160	1.262	5.291	1.2	0.1916	0.0000	40.1
DDH-MX-S-171	0.341	3.101	0.5	0.1381	0.0000	6.5
DDH-MX-S-182	0.376	2.471	0.7	0.1363	0.0000	1.3
DDH-MX-S-192	105.4	3.342	207	2.9301	0.0005	1365.6
DDH-MX-S-195 *Cr*	0.615	0.205	15.6	0.7345	0.0004	237.0
Keel Feeder Dyke Samples						
MU 033.241.21	0.330	2.203	0.7	0.1366	0.0000	1.7
MU 033.252.76	0.398	1.928	1.0	0.1480	0.0023	6.4
MU 033.252.76(II)	0.416	1.881	1.1	0.1424	0.0000	0.4
HDB-2001-MX5	0.482	1.611	1.5	0.1540	0.0000	3.4

[a] *The 2σ error in this ratio is 0.37% (Re) and 0.125% (Os) and is a function of spike uncertainty however this does not account for non-stoichiometry of the Os spike calibration (Appendix C)*

[b] *1σ error of the internal precision of measurement generally better than 2σ of UMCP std data at similar run intensities (Appendix C).*

[c] *Age corrected γOs values. γOs is the percentage difference between the age corrected $^{187}Os/^{188}Os$ ratio and the 187Os/188Os ratio of a chondritic mantle where the present-day chondritic mantle has $^{187}Os/^{188}Os=0.12757$ and $^{187}Re/^{188}Os=0.3972$ (Walker et al., 1989)*

Cr = Country rock samples

Os concentrations are also highly variable (total range = 0.018-3.34ppb) for marginal and roof country rocks. Os in layered series peridotites and Main chromitites range between (0.597 to 70.3ppb) and are generally lower than Os in the main chromitite horizons (39.9-201.4ppb). Os* concentrations form a positive correlation with Ni (Fig. 5.19) apart from the Main Chromitites that do not lie on the positive correlation of the other samples. In general, a positive correlation between Os* and MgO is also observed, but more scatter is evident if only the layered series peridotites are considered. This is because of heterogeneous distribution of Os* in the layered series dunites (Fig. 5.19). These correlations are consistent with Os being fractionated by early crystallising phases captured within olivine.

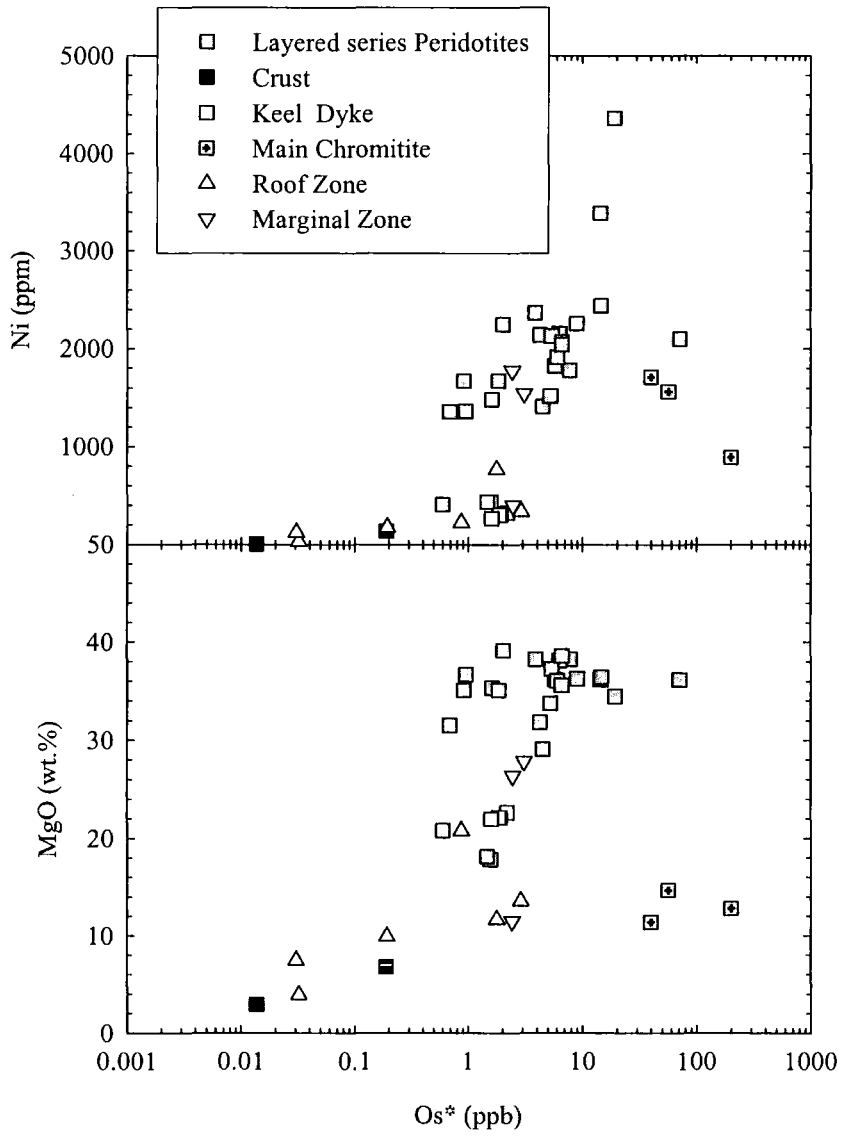

Fig. 5.19: Distribution of common Os in Muskox Intrusion rocks as a function of Ni and MgO.

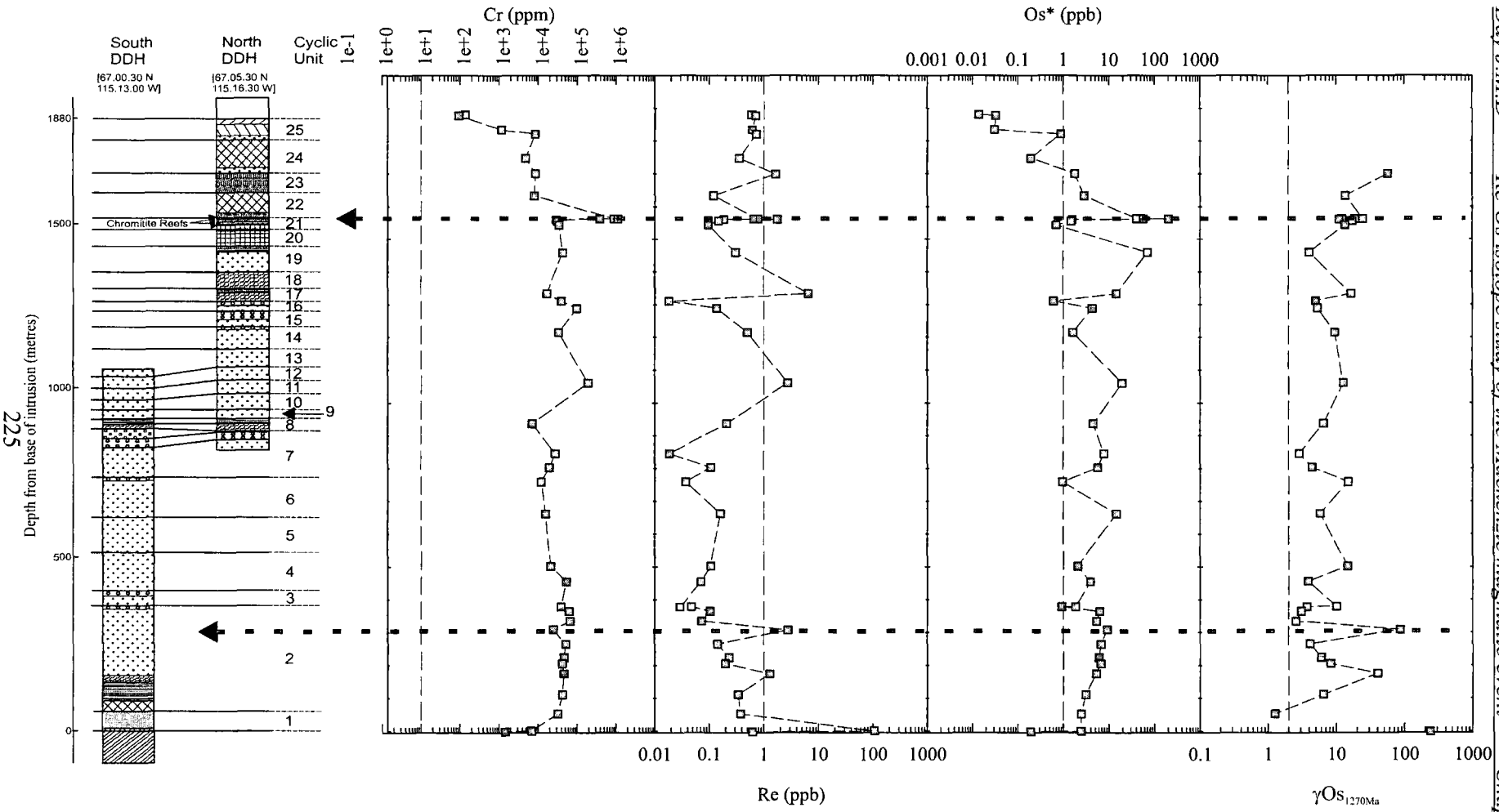

Fig 5.20: Variation in Cr, Re, Os and γOs_i with depth from base in the Muskox Intrusion. Marked are the Main and 'Hulbert' Chromitite reefs.*

Re, Os* and γOs_i are plotted against depth from the base of the intrusion to the roof contact in Fig. 5.20. Like the relationships seen in the Coppermine CFB (Fig. 5.12), Os* acts compatibly, like Cr, whilst Re acts incompatibly and is depleted in the layered series peridotites and pyroxenites. In detail, Re generally decreases in the lowermost cyclic units (unit 2) with increasing depth from base and remains consistently low throughout the serpentinised zone of the layered series up to ~1000m. Re then increases up to the roof zone. Both Re and Os are highly variable in the chromitite reef where Os* variation tracks Cr. All layered series rocks have >0.9ppb Os* up to 1300m. After the main chromitite horizon, Os* steadily decreases in the roof zone to abundances of less than 50ppt.

Measured $^{187}Os/^{188}Os$ for the entire intrusion range from 0.1228 to 2.93. Layered series units and the chromite reef have $^{187}Os/^{188}Os$ ranging from 0.1228 to 0.2539 and 0.1338 to 0.1502, respectively. Rocks in the roof zone range from less radiogenic ($^{187}Os/^{188}Os$ = 0.1396) to more radiogenic ($^{187}Os/^{188}Os$ =2.01) as they approach the Hornby Bay sandstone ($^{187}Os/^{188}Os$ = 2.42). The most radiogenic $^{187}Os/^{188}Os$ is possessed by the bronzite gabbro in the marginal zone ($^{187}Os/^{188}Os$ = 2.93) and is more radiogenic than the single measurement for the crustal Wopmay gneiss ($^{187}Os/^{188}Os$ = 0.7345). Keel dyke samples have $^{187}Os/^{188}Os$ samples ranging from 0.1366 to 0.1540. γOs_i is variable and in excess of 1 for all layered series peridotites and increases up the layered series succession. Cyclic unit 2 shows great variation in γOs_i and includes layers with high Os* abundances (0.917-9.09ppb) but highly variable γOs_i (+2.6 to +86.5) with the highest γOs_i measured in a dunite with the highest Os* concentration. This sample (DDH-MX-S137) is the cryptic representation of what has been interpreted as a chromitite horizon, the 'Hulbert Reef' in Cyclic Unit 2. γOs_i is >10 for all of the chromitite horizon rocks. Some of the rocks have Re-excess such that their γOs_i are negative; this is best typified in DDH-MX-S192 which has a γOs_i of -1366.

Re-Os isotope systematics of smaller scale layered mafic sills and flows and individual horizons have been investigated previously (Marcantonio *et al.*, 1993; Walker *et al.*, 1997; Schoenberg *et al.*, 1999; Horan *et al.*, 2001; Hanski *et al.*, 2001; Marques *et al.*, 2003) and all possess variable Os* and Re abundances and γOs_i. However, the Muskox intrusion represents the largest, and most ultramafic intrusion so far examined with well defined Re-Os isotope variations.

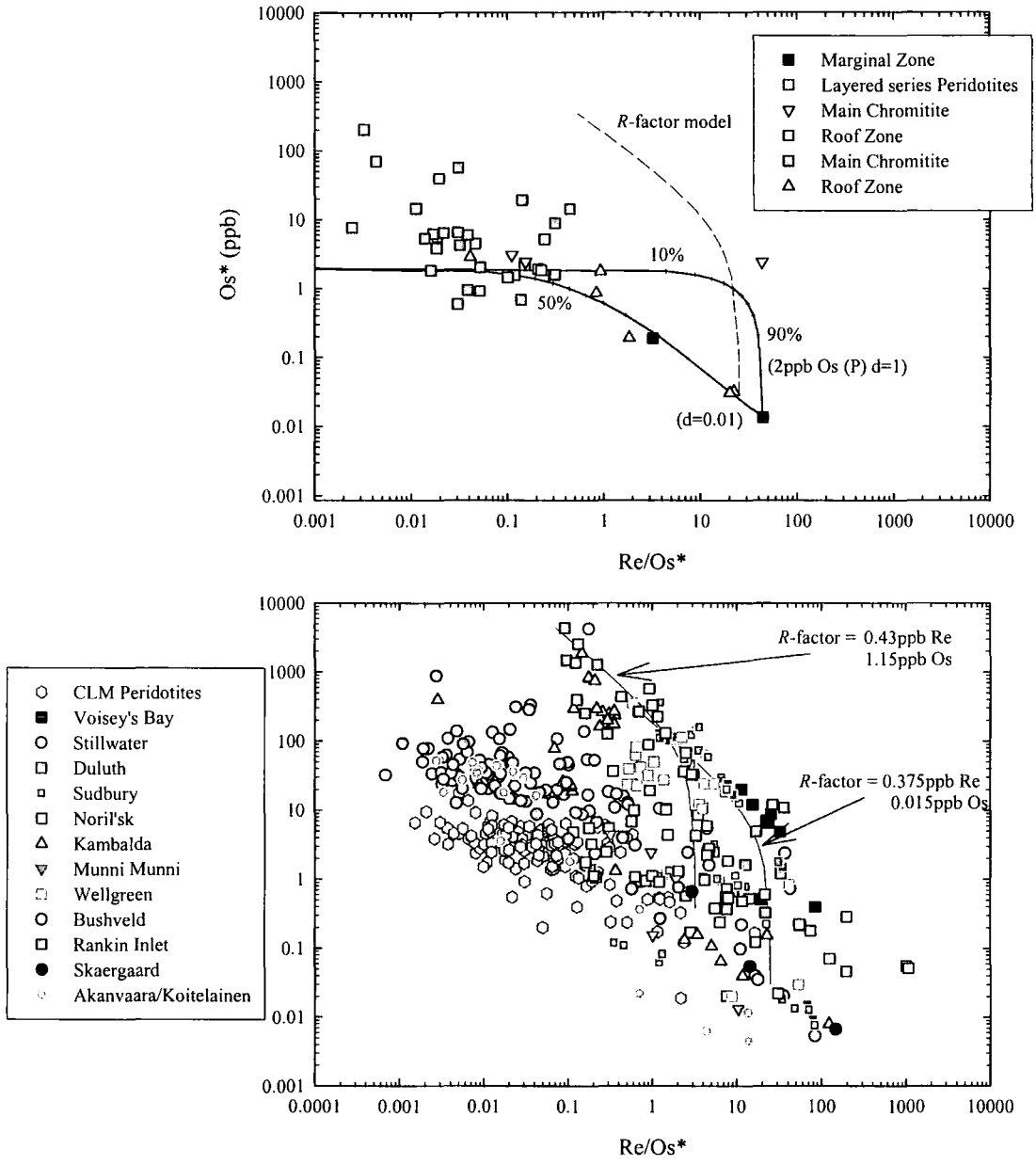

Fig. 5.21: Re/Os vs. Os* abundance data for Muskox Intrusion rocks and for LMIs globally. Mixing models in upper Fig. generated by mixing at extremes of AFC 1:1 and 1:10 (bulk D_{Os} = 15). Modelled R-factor pathways derived using the equation of Campbell and Naldrett (1979) and assuming D_{Re}=500 and D_{Os}=30000 (After Lambert et al., 1999). Data sources for CLM are from Pearson et al. (2003) and references therein. Data for LMIs from Martin (1989), Lambert et al. (1998), Ripley et al. (1999), McCandless and Ruiz (1991), Lambert et al. (1989), Dickin et al. (1992), Marcantonio et al. (1993), Hulbert and Gregoire (1993), Marcantonio et al. (1994), Walker et al. (1994), Foster et al. (1996), Walker er al. (1997), Puchtel et al. (1999), McCandless et al. (1999), Schoenberg et al. (1999), Lambert et al. (1999), Brooks et al. (1999), Cohen et al. (2000), Horan et al. (2001), Hanski et al. (2001), Morgan et al. (2002) , Marques et al. (2003), Arndt et al. (2003)*

Os* abundance data and Re/Os* ratios from the Muskox Intrusion (Fig. 5.21) can be compared with age corrected Os* and Re/Os* ratios from other layered intrusions

and CLM peridotites. Muskox peridotites, marginal zone, roof zone, Keel dyke and chromitites generally have low Re/Os* ratios. Muskox chromitites are comparable to Bushveld or Stillwater chromitites in terms of their Os* and Re/Os*.

5.5 Discussion

This discussion compares the geochemical evidence gathered for the origin of the Coppermine CFB and Muskox layered intrusion in this chapter. Employing the two components of the Mackenzie LIP, a number of issues that are important for Re-Os geochemistry and the evolution of the LIP are addressed. Namely these are:

- Element mobility
- Crustal contamination and fractional crystallisation
- Partial melting regimes
- Re-Os geochronology and the temporal linkages between the Coppermine CFB and Muskox layered intrusion
- Source compositions of the Mackenzie LIP

The findings from this work lead me to address two important areas in Os isotope geochemistry:

- The $^{187}Os/^{188}Os$ isotope evolution of the terrestrial mantle
- Contributions of high time-integrated $^{190}Pt/^{188}Os$ and $^{187}Re/^{188}Os$ reservoirs to intraplate magmatism

5.6 Element mobility in Mackenzie LIP rocks

The effect of post-crystallisation hydrothermal alteration or serpentinisation on the mobility of Re and Os in mafic-ultramafic systems is still poorly understood. Recent studies of peridotites at convergent margins have suggested that high concentrations of Os can be transferred in fluids (e.g., McInnes *et al.*, 1999). Additionally, Re-Os element exchange is becoming an increasingly recognised process in ancient magmatic rocks (e.g., Burton *et al.*, 2000). If these processes occurred in the Coppermine CFB and Muskox layered intrusion they could account for the calculated negative γOs_i and high $^{187}Os/^{188}Os$ ratios in high and low Os abundance lavas, peridotites and chromitites. Another significant process for sub-aerial

eruptions is the volatility of Re (Sun *et al.*, 2003a,b,c). This section assesses whether this process can be tracked in ancient volcanic rocks.

5.6.1 Element mobility in the Coppermine CFB

Element mobility of Ba, Rb, Sr and Pb has already been illustrated for Coppermine CFB lavas (Fig. 5.6). This indicates that some post-eruptive mobility of mobile elements occurred in the Coppermine CFB lava pile. Os is compatible in early crystallising sulphide phases (e.g., Puchtel *et al.* 2004) and should therefore show positive correlations with immobile elements such as MgO and Ni (Fig. 5.10). Os* is plotted against incompatible Zr in Fig. 5.22 and shows a generally negative correlation consistent with compatible element fractionation and Os immobility. The two Husky Creek formation lavas lie below the general correlation defined by Copper Creek lavas but this could be due to their slightly different petrogenetic histories (e.g., Fig. 5.8). On this basis Os can be deemed as compatible and immobile for the Coppermine CFB.

Re does not show compatible element behaviour and so should increase proportionally to other indices of differentiation. Fig. 5.22 illustrates the concentrations of Re versus Zr (immobile) in the Coppermine CFB versus Zr/Re ratios; these results are similar to that of TiO_2 (Fig. 5.9). From the relationships between Re, Zr and TiO_2 at least four of the Coppermine CFB can be distinguished as suffering significant addition of Re. These samples (HDB-98-91, -94, -125, -127), which lie close to a Zr/Re = 100000 reference line, all have variably negative γOs_i with the two lower Copper Creek lavas possessing γOs_i that are less negative than the two Husky Creek lavas. The two lower Copper Creek lavas have an order of magnitude more Os than the Husky Creek lavas indicating that the effect of Re addition is also proportional to the Re/Os ratio. Mobility of Re at some stage after the crystallisation of the Coppermine lavas has resulted in significant Re addition to some of the lavas resulting in calculated γOs_i being strongly negative. The eleven other samples, for which Re mobility is not obvious, form a positive correlation with Zr and TiO_2 with a great deal of scatter between the Zr/Re <400000:1 to 800000:1 reference lines. Some of these samples are optically fresh and suggest no Re loss or addition through hydrothermal processes. Another mechanism may be required to explain their low Re/Os ratios.

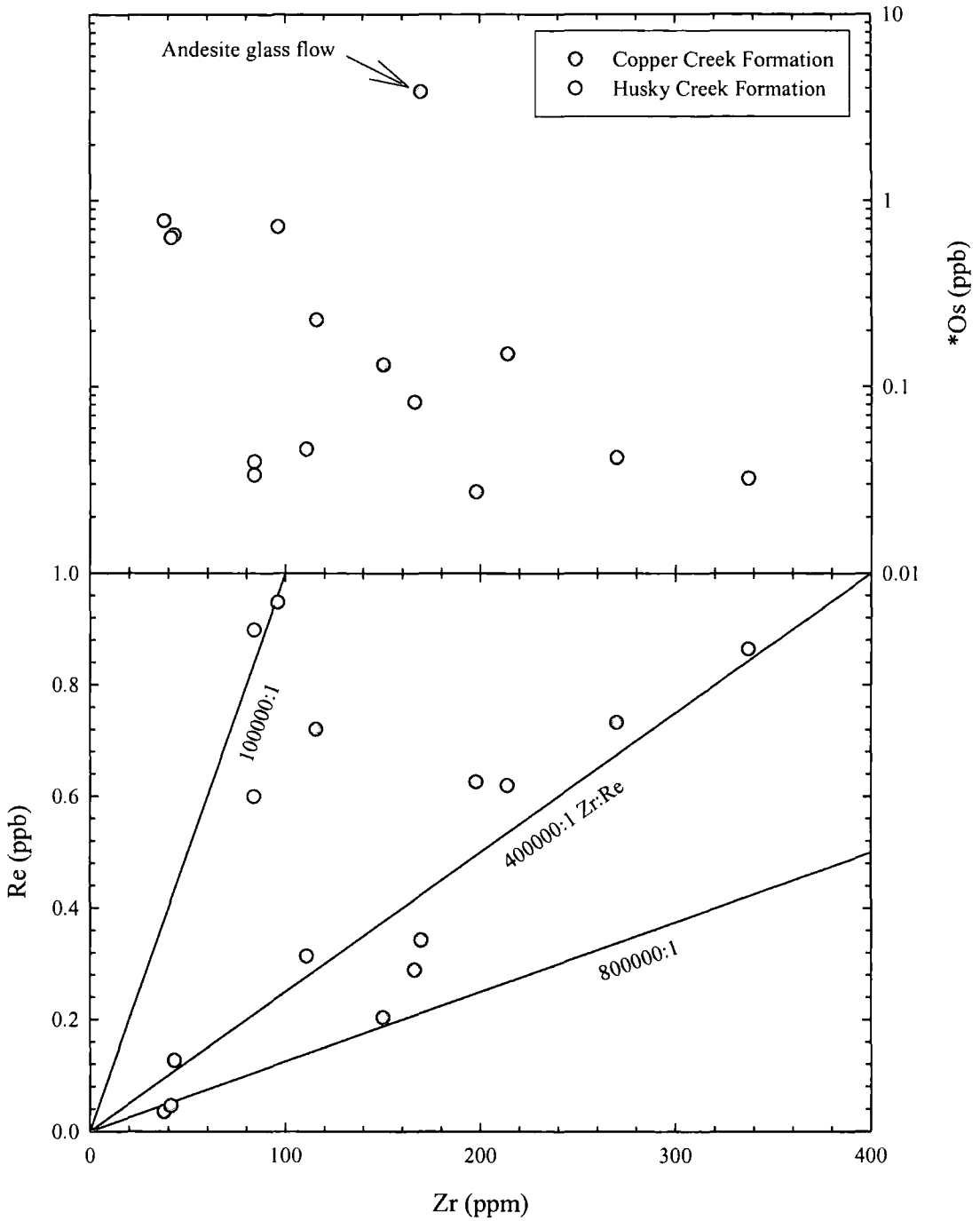

*Fig. 5.22: Zr versus *Os and Re for the Coppermine CFB. Re and Zr are both incompatible elements so magmatic rocks that have been undisturbed by post-magmatic alteration should lie on a straight, positive correlation. Os is an incompatible element so will form broadly negative correlations with indices of differentiation. Coppermine CFB deviate greatly from Zr/Re ratios making assessment of the magmatic Zr/Re ratio difficult and suggesting Re addition after emplacement of the lava flows.*

An increasingly recognised feature of Re behaviour is volatility during sub-aerial eruption. The observation that Re concentrations in MORB were ~2.6 times greater than those of OIB (Hauri and Hart, 1997) and the apparent correlation of Re with Yb

has led to the assumption that Re is compatible in garnet (e.g., Schaefer *et al.*, 2000; Woodland *et al.*, 2002) and that missing Re must reside in a mantle reservoir not sampled by OIB magmatism (Hauri and Hart, 1997). Several lines of evidence indicate that Re is likely to be highly volatile during magmatic degassing. These include:

- High aerosol metal fluxes from fumaroles and volcanic eruptions (Hinkley *et al.*, 1999)
- Systematically high Re concentrations in Hawaiian submarine lavas compared with subaerial lava Re concentrations (Bennett *et al.*, 2000) and submarine glasses in different melting environments (Sun *et al.*,2003a,b,c; Norman *et al.*, submitted).
- Extreme variation in Cu/Re ratios for Western Canary Island lavas (Chapter 4)

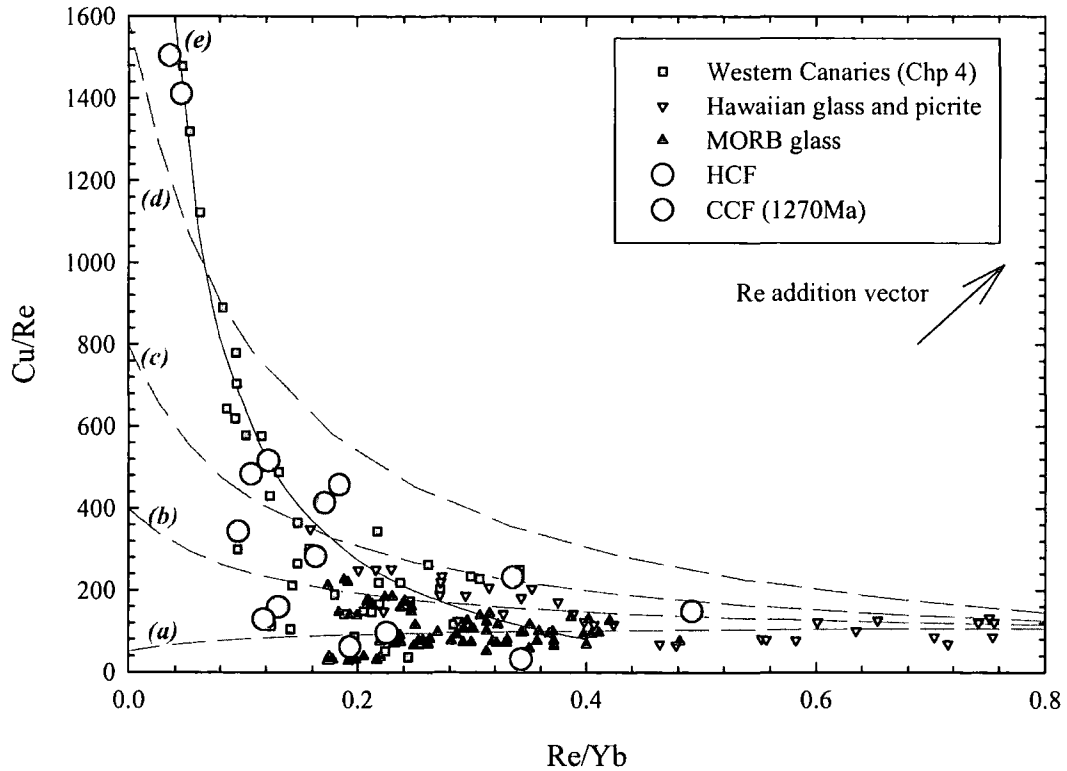

Fig. 5.23: Variation of Re/Yb and Cu/Yb for Coppermine CFB lavas compared with Western Canary Island lava data (Chapter 4), Hawaiian glass and picrites (Bennett et al., 2000; Norman et al. in press) and MORB glasses (Sun et al. 2003a). Modelled degassing lines calculated using k-values where $k=([Cu/Re]/[Re/Yb]_{Degassed}/[Cu/Re]/[Re/Yb]_{Undegassed})$. *The k-trajectories therefore represent relative differences and not absolute values. For k using a Depleted upper mantle source (Re/Yb =1.4, Cu/Yb =108) (a)* 8×10^{-5}, *(b)* 2×10^{-5}, *(c)* 1×10^{-5}, *(d)* 0.5×10^{-5}, *and for k using a bulk silicate earth source (Re/Yb = 0.4, Cu/Yb = 80) (e)* 0.2×10^{-5}. *These trajectories indicate a greater degree of Re degassing for Coppermine tholeiites compared to modern day Hawaiian and MORB tholeiites.*

Re and Cu are considered to be similarly incompatible in melts, although Cu is not considered to be as volatile (Hinkley *et al.*, 1999; Bennett *et al.*, 2000; Sun *et al.*, 2003a,b,c) making comparison with Re and Cu a useful indicator of degassing. Fig. 5.23 shows Re/Yb versus Cu/Re for Coppermine CFB lavas compared with modern day Hawaiian lavas and MORB glasses. Samples that have been shown to have Re added to them plot at elevated Re/Yb ratios. The 11 remaining Coppermine CFB lavas trend to extremely high Cu/Re and low Re/Yb ratios relative to the trend of Hawaiian or MORB lavas ascribed to degassing by Bennett *et al.* (2000) and Sun *et al.* (2003). The reason for the more elevated Cu/Re trend in the Coppermine CFB could be accounted for by addition of Cu (e.g., Fig. 5.4) but this solution alone does not satisfy the low Re/Yb ratios of Coppermine CFB lavas. Addition of Cu would be expected to cause considerable scatter on the Re/Yb-Cu/Re plot (Fig. 5.23) which is not observed. Hydrothermal fluid fluxing did affect the upper part of the Coppermine stratigraphy, where Cu-precipitation took place and serpentinisation of mafic minerals also occurred. The Coppermine data more closely approximate to the correlation of Re/Yb-Cu/Re seen in alkali basalts from the Western Canaries. These relationships indicate that despite some potential Re addition and Cu-precipitation, Re-degassing of Coppermine CFB lavas can still be recognised. Degassing of lavas and resultant Re volatility will not affect the calculated γOs_i of the lavas but suggests that volcanic processes acting upon Re during eruption of the mid-Proterozoic tholeiites must have been similar to the processes seen in sub-aerially erupted alkaline lavas from the Canary Islands today.

5.6.2 Element mobility in the Muskox Intrusion

There is copious petrographic evidence for hydrothermal processes altering the layered cyclic units in the Muskox intrusion. Heavy serpentinisation, Mg-rich chlorite and zonation of native metals (Chamberlain *et al.*, 1965) all attest to highly reducing fluid fluxing through the intrusion. Using the methods employed to address element mobility in Coppermine CFB lavas, Zr (incompatible-immobile) versus Sr (LILE) and Hf (HFSE) are plotted for the Muskox Intrusion. The relationships between Zr, Sr and Hf indicate that post crystallisation element mobility has occurred for the Muskox intrusion for some elements (Fig. 5.24). Immobile elements such as REE, Hf, Nb and Th form straight correlations between indices of

differentiation like the trends seen for Coppermine CFB (Fig. 5.6). However, significant scatter between Sr and Zr in Fig. 5.24 shows that LILE elements in the Muskox intrusion have been affected by plagioclase removal/addition, and possibly have suffered post-crystallisation element mobility resulting in loss or gain of certain elements to different rock units. Plotting Os* and Re versus Zr for Muskox intrusion rocks shows significant scatter in both elements. For Os* this could be considered as mobility, however, broad positive correlations between Os* and Ni and MgO suggest that Os* has not suffered post-crystallisation re-mobilisation (Fig. 5.19).

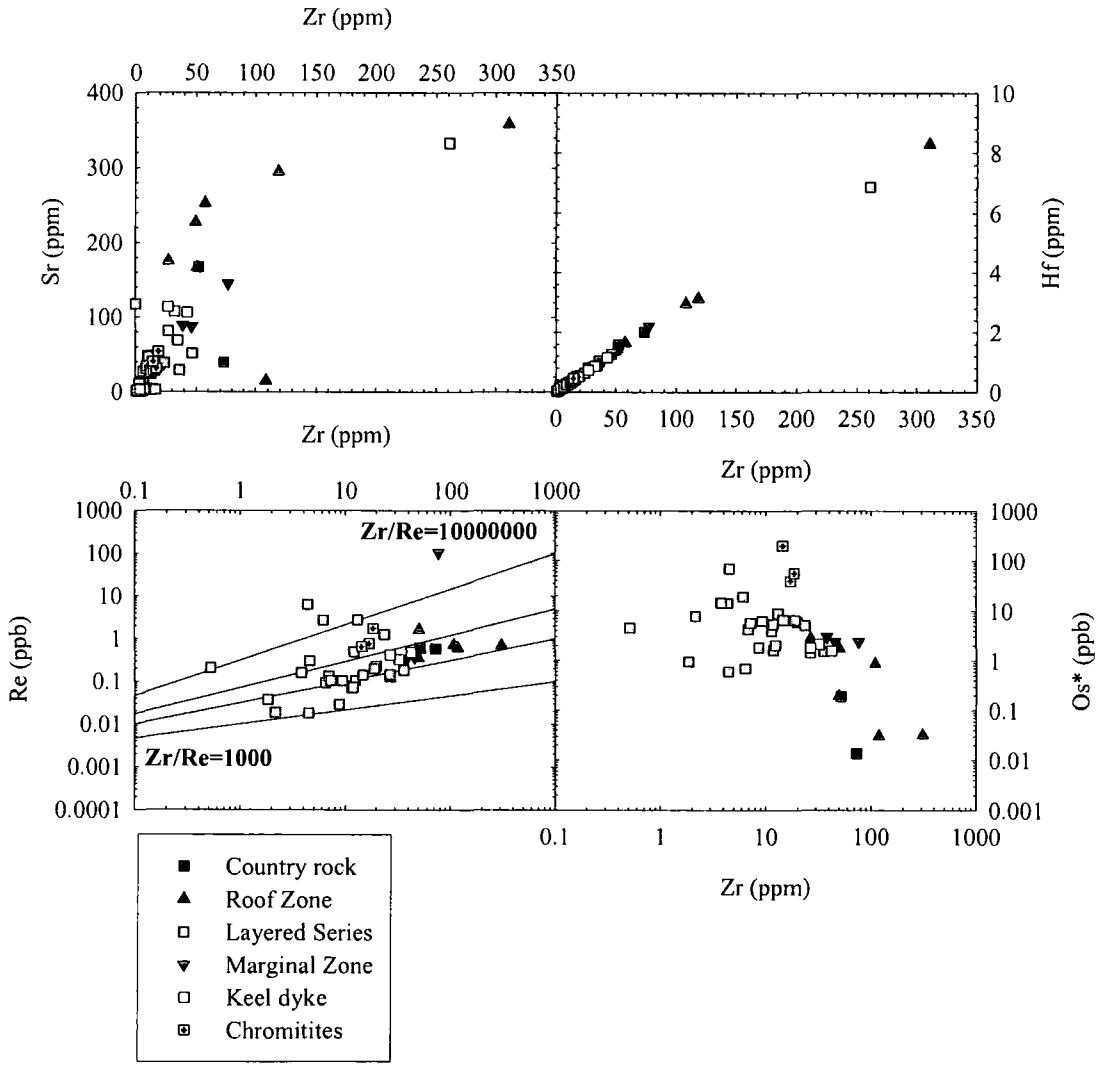

Fig. 5.24: Zr versus Sr, Hf, Os and Re for the Muskox layered intrusion. Re and Zr are both incompatible elements so magmatic rocks that have been undisturbed by post-magmatic alteration should lie on a straight, positive correlation. Muskox intrusion rocks deviate greatly from Zr/Re ratios making assessment of the magmatic Zr/Re ratio difficult. The majority of samples lie between Zr/Re ≈ 10000 and 100000. This plot suggests Re addition and loss after crystallisation of the intrusion. Os is a compatible element so correlation with Zr in the layered series peridotites would be unexpected.

The range in Os*, especially for the layered series units could also reflect new influx of Os*-rich magmas into the intrusion or heterogeneous distribution of Os-rich phases during accumulation of the layered series (e.g., Puchtel *et al.*, 2004). The evidence for Os mobility will be discussed in greater detail further on.

There is a broad positive correlation between Re and Zr indicating Re incompatible nature (Fig. 5.24). However, some of the units appear to have suffered excessive Re loss or gain with samples lying on Zr/Re lines = 1000:1 to 10000000:1. Model ages and Re-Os systematics are relatively insensitive to initial $^{187}Os/^{188}Os$ in mantle-derived systems, so these features are indicative of open-system behaviour subsequent to magmatic crystallisation in the Muskox. There is considerable scatter on a Re-Os isochron plot away from the 1270Ma reference isochron (Fig. 5.25) giving a much younger mean age than the age of crystallisation of the intrusion from U-Pb Concordia (LeCheminant and Heaman, 1989).

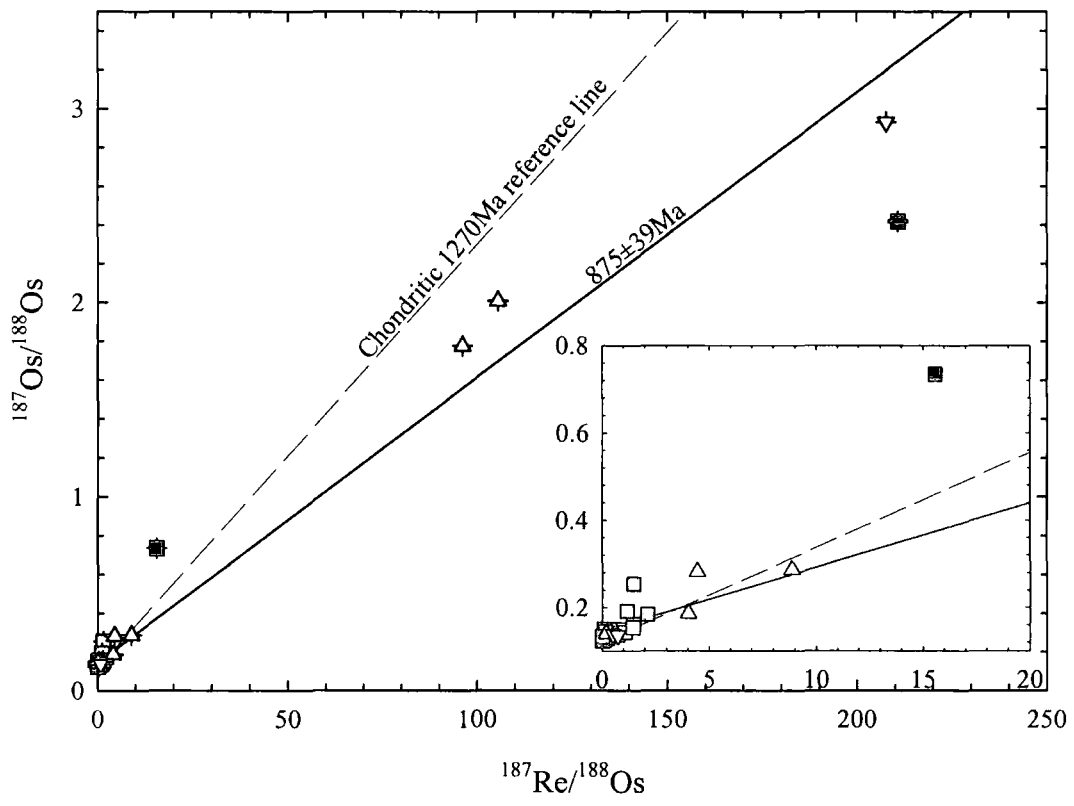

Fig. 5.25: $^{187}Re/^{188}Os$-$^{187}Os/^{188}Os$ data for all Muskox intrusion samples. Regression of all data yields 875±39Ma and an initial $^{187}Os/^{188}Os$ = 0.145±0.026 (γOs = +22.2±4.0)

The Hornby Bay sandstone has also suffered open system behaviour of Re-Os in the thermal aureole of the intrusion. Re variation with stratigraphic height shows a slight 'bow' shape through the intrusion (Fig. 5.20) and correlates positively with S (not shown), suggesting that reducing and oxidising fluids transported interstitial sulphide phases from the base to the tops and sides of the intrusion. Similar distribution of LILE in the intrusion also supports this notion. Rocks with the greatest Re addition are close to the margins and roof of the intrusion suggesting that the younger ages are due to hydrothermal removal and addition of Re and that Re addition has to some extent altered Re/Os ratios for some of the samples.

Despite the whole layered series giving an error-chron age close to that of the U-Pb Concordia age (Fig. 5.26), post-crystallisation open system behaviour of the Re-Os isotope system has also affected layered series peridotites which derive an ancient Archaean error-chron age (Fig. 5.26). The fact that the U-Pb age of the Muskox intrusion is well defined (LeCheminant and Heaman, 1989) and that host country rocks are significantly younger than this Archean error-chron 'age' indicate that this has no significance and that the layered series peridotites have suffered Re loss or Os gain. Re/Os ratios higher (younger model ages) and lower (older model ages) than the original Re/Os ratio directly after crystallisation of cyclic units attest to significant disturbance and element mobility in the Muskox Intrusion.

Post-crystallisation hydrothermal alteration of either Re or radiogenic Os has been well documented for large layered mafic intrusions (Hart and Kinloch, 1989; McCandless and Ruiz, 1991; Marcantonio *et al.,* 1993; 1994). Previous studies have found a relationship of low Os and radiogenic $^{187}Os/^{188}Os$ in layered peridotites from the Wellgreen (Marcantonio *et al.,* 1994) and accounted for this variation by radiogenic Os mobilisation. In Fig. 5.27 Os isotope compositions and Os abundances of Muskox intrusion rocks are compared and show a trend of lower Os abundances and radiogenic $^{187}Os/^{188}Os$. In the Muskox intrusion the majority of this relationship can be attributed to higher Re/Os ratios in samples with low Os. For samples with high Os concentrations and radiogenic $^{187}Os/^{188}Os$ less certainty can be inferred for hydrothermal radiogenic Os mobilisation. Indeed distinguishing between crustal contamination of hydrothermal fluid processes for these samples can become somewhat of a 'vicious circle'. Petrographical data suggests that the majority of samples with high Os abundance and radiogenic $^{187}Os/^{188}Os$ are optically fresh.

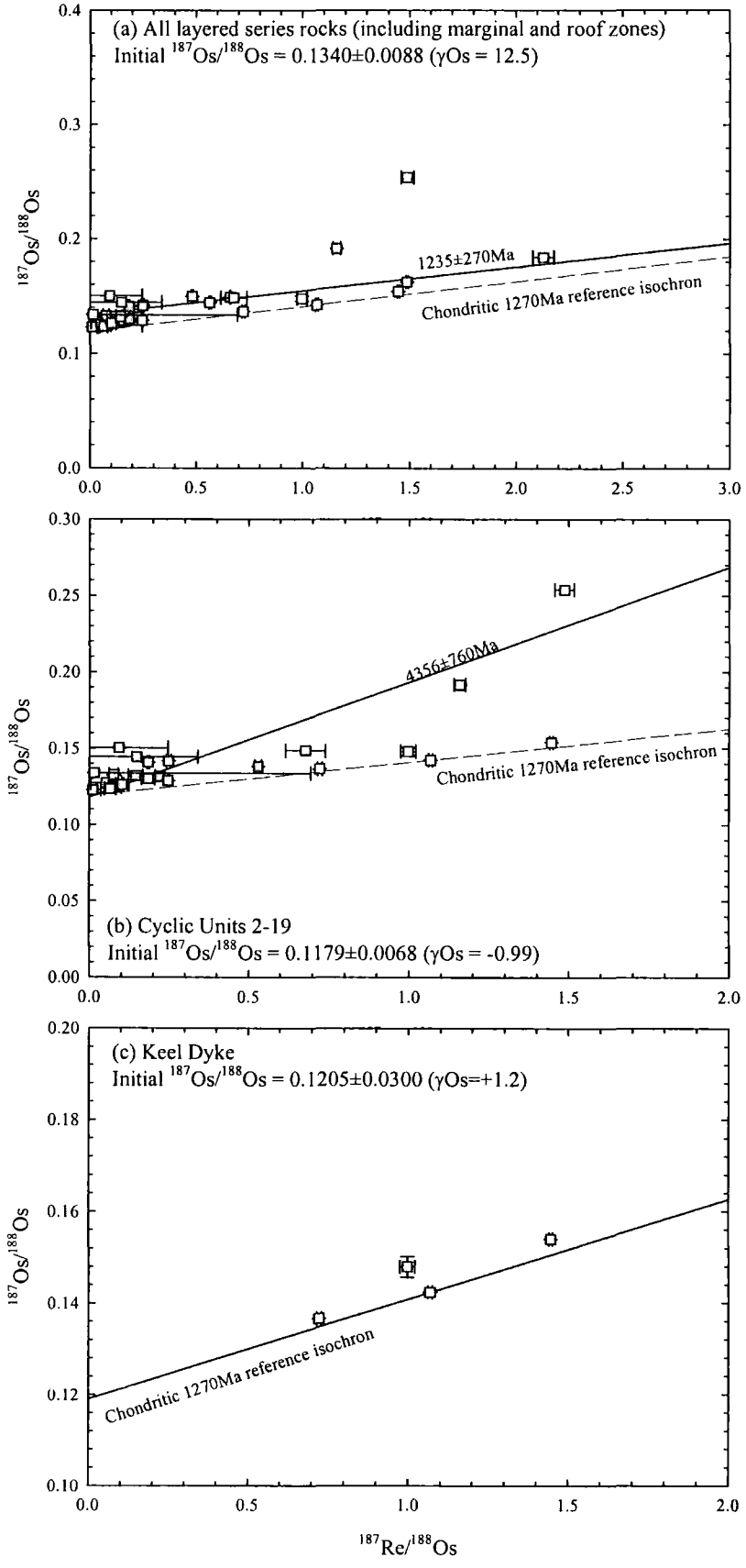

Fig. 5.26a-c: Re-Os isochron plots for Muskox layered series peridotites and Keel dyke samples

Although circumstantial, this evidence appears to suggest that for samples such as the main Chromitite reef, Os is immobile.

The Keel dyke provides relative constraints on the timing and distribution of hydrothermal fluid events because the Keel is demonstrably older and underlies the rest of the intrusion. Relationships of more radiogenic $^{187}Os/^{188}Os$ with lower Os contents for Keel dyke samples which are petrographically fresh and have unaltered incompatible element profiles (Fig. 5.17) suggests that hydrothermal mobilisation was the direct result of the thermal gradients generated by the intrusion itself and that this process must have occurred relatively soon after the whole intrusion crystallised. This conclusion is further substantiated by the zonation of native metal alloys, awaruite, wairauite and native copper within the intrusion (e.g., Chamberlain *et al.*, 1965) suggesting that temperature gradients in the intrusion drove hydrothermal circulation.

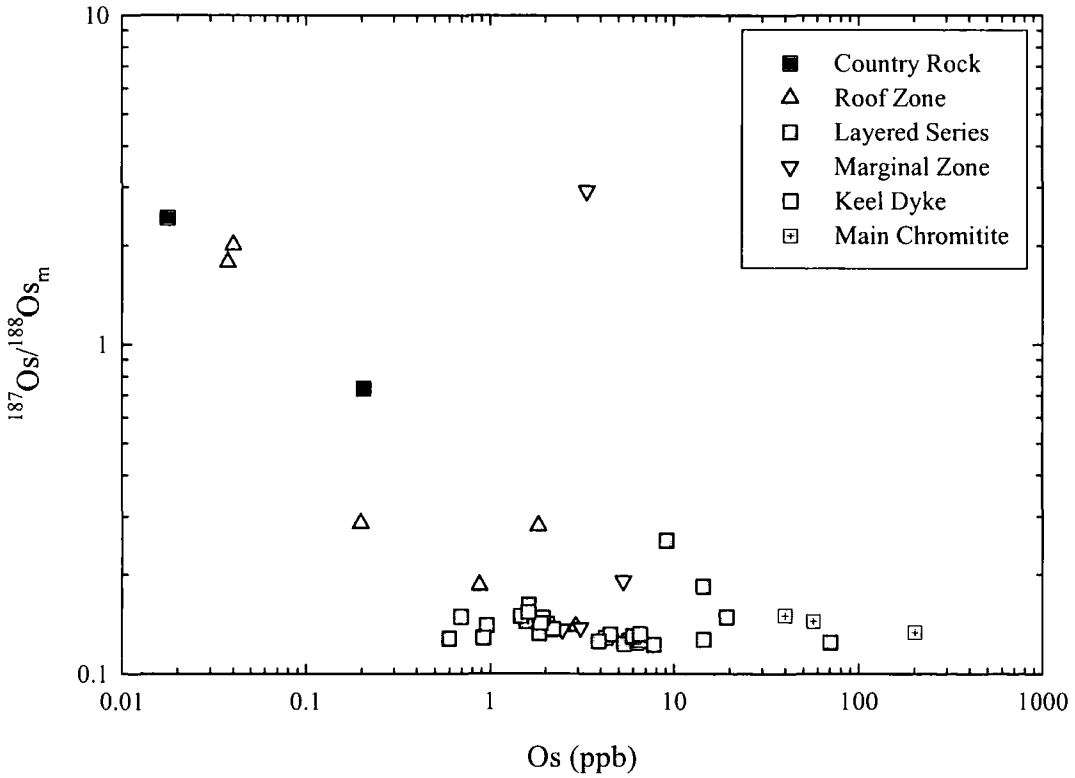

Fig. 5.27: Initial $^{187}Os/^{188}Os$ versus Os concentration data for all Muskox intrusion samples.

Relationships of more radiogenic $^{187}Os/^{188}Os$ with lower Os contents for Keel dyke samples also indicate that correlations between Os and $^{187}Os/^{188}Os$ cannot be uniquely described by hydrothermal alteration of samples but are equally the result of other igneous processes. In the next section crustal contamination of the Coppermine CFB and Muskox Intrusion is considered in detail in order to recognise the mantle Os contributions to the Muskox intrusion.

5.7 Crustal contamination and fractional crystallisation

5.7.1 Crustal contamination and fractional crystallisation in the Coppermine CFB

Two contrasting styles of crustal contamination have been documented in elemental and isotopic studies of CFB. One is AFC (DePaolo, 1981) where the degree of contamination increases in more fractionated lavas (e.g., Parana CFB, Hawkesworth *et al.,* 1988). In the other, more magnesian, less fractionated lavas show the greatest degree of crustal contamination (e.g., Deccan CFB, Devey and Cox, 1987). Low incompatible trace element abundances and higher liquidus temperatures render mafic-ultramafic magmas more susceptible to modification by crustal contamination. A key feature of the Coppermine CFB trace element data is that from trace element ratios (table 5.1) the andesite glass has a strong crustal signature. The glass has extreme Th/Nb (>1), Ce/Pb (<4), La/Nb (>2) and Nb/Ta (<12) that can only be explained by extensive upper continental crustal additions to mantle-derived melts (e.g., Weaver, 1991a,b; Marcantonio *et al.* 1995). The picrites and lower Copper Creek Formation basalts show less extreme, but obvious crustal signatures as the glass, with high Th/Nb, La/Nb and low Ce/Pb as well as negative Nb anomalies. Husky Creek and upper Copper Creek Formations resemble more primitive, less crustal contaminated melts on the basis of Nb/Ta, Th/Nb and La/Nb ratios, however these basalts still posses low Ce/Pb compared with MORB-derived lavas. This may, in part, be due to hydrothermal alteration of the lava pile and mobilisation of Pb and Ce. The most crust-like Nb/Ta, Ce/Pb, Th/Nb and La/Nb ratios are possessed by the picrites and the glass.

In Fig. 5.28 immobile elements Nb/Ta versus La/Nb are plotted for the Coppermine CFB to track crustal contamination for the lavas. Mixing between PM and DMM (La/Nb = 0.24) and Wopmay crust indicate that between 1-10% crustal

contamination can account for the variation in these elements for the basalts and two of the picrites. The glass and a picrite (HDB-98-119A) have anomalously low Nb/Ta ratios and indicate greater than 10% crustal contamination can be inferred for these lavas. It is noteworthy that the lavas show a trend from enriched source (PM) to depleted source (DMM) with stratigraphic height consistent with a temporal evolution in REE abundances and LREE/HREE of the lavas.

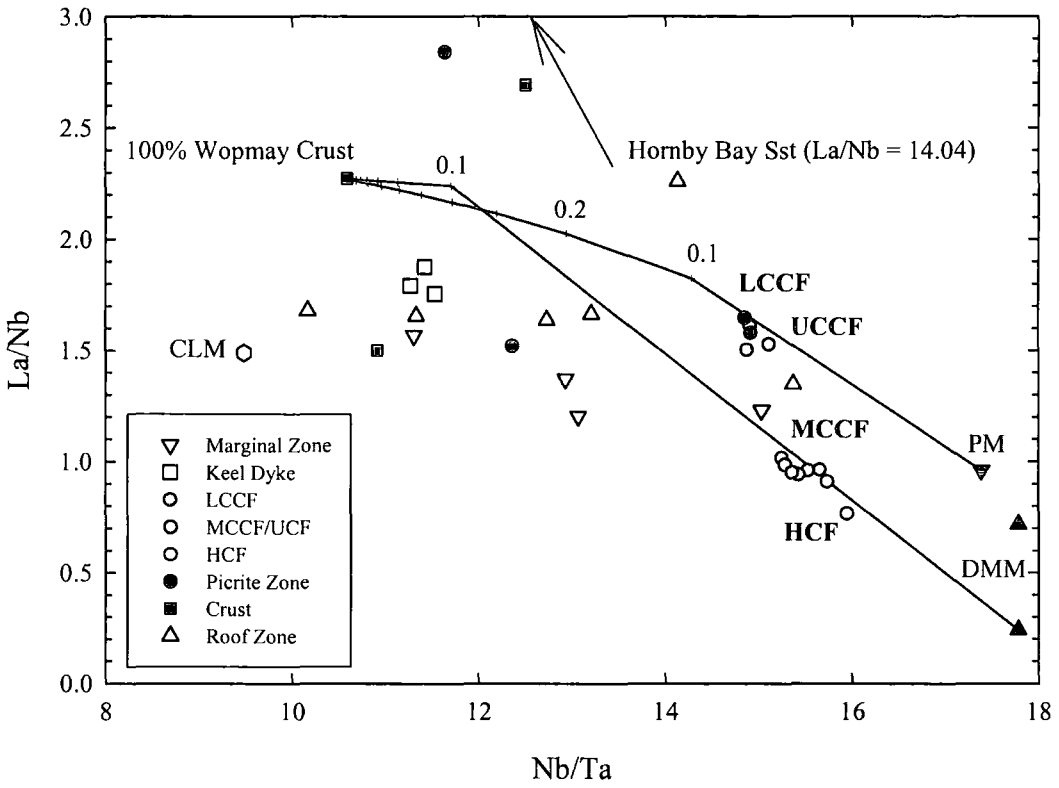

Fig. 5.28: Nb/Ta vs. La/Nb for Coppermine CFB lavas and selected Muskox Intrusion rocks showing bulk mixing between primitive mantle (PM) and the depleted MORB mantle (DMM) and Wopmay crustal lithologies. Also shown is the average for CLM peridotites (data from Table 5.1); abbreviations as in Fig. 5.8.

The values derived for crustal contamination from trace element modelling are similar to those calculated by Dupuy *et al.* (1992) for Pb-Nd isotope compositions and Griselin *et al.* (1997) for Nd isotopes on suites of rocks from the Coppermine CFB. The exception for the dataset presented here is that the glass shows in excess of 20% crustal contamination. However, the absolute crustal contamination proportions are difficult to gauge for this rock because its trace elements characteristics are dissimilar to either the Wopmay gneiss or the Hornby Bay sandstone (anomalously high La/Nb ratio) used for crustal mixing calculations. Four

lower Husky Creek Formation basalts analysed by Griselin *et al.* (1997) have negative εNd values (-1.1 to -3.7) indicating as much as 40% crustal contamination to those lavas. On that basis ≥50% crustal contamination for the glass is probably a reasonable estimate.

To constrain the effects of crustal contamination on Re-Os isotope systematics Fig. 5.29 shows Re/Os* versus initial γOs in which an upper crustal end member from the Canadian Shield (Wopmay Gneiss) is plotted and mixing and assimilation and fractional crystallisation trajectories are shown for an initial Coppermine CFB melt (Re/Os* = ~0.1, γOs = 2). Samples which have clearly been affected by post-crystallisation alteration of Re and Os and which have anomalous negative γOs_i are not plotted on this diagram. The Re-Os isotope systematics of the more evolved Coppermine CFB lavas are more variable than for the picrites which are effectively uncontaminated in terms of their Os isotope characteristics. Of the low Re/Os* samples only basalt HDB-98-170 plots to high γOs compositions and the majority of Coppermine CFB lie at chondritic to sub-chondritic γOs. These features are not characteristic of crustal contamination.

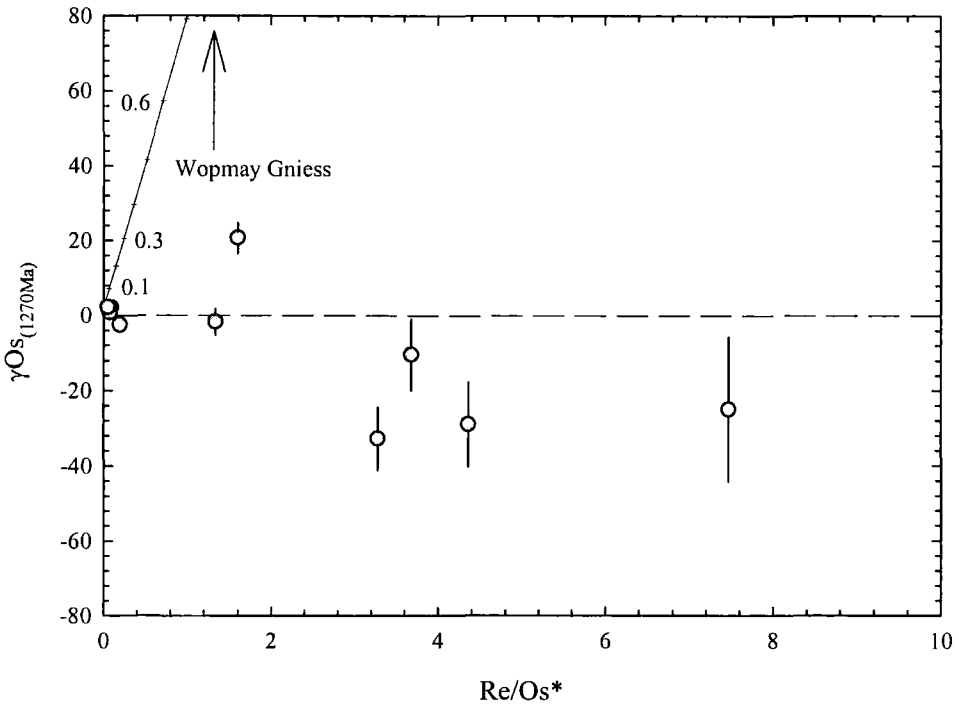

Fig. 5.29: Calculated initial γOs vs. Re/Os for Coppermine CFB lavas. AFC mixing trajectory between Canadian shield crustal samples made using atomic mass correction models with an initial γOs of +2 and a Re/Os* equal to the low Re/Os Lower Copper Creek Formation picrites. 2σ Errors shown.*

Limited upper crustal contributions to the Re-Os isotope systematics of Coppermine CFB picrites and basalts parental melts is at odds with trace element, Rb-Sr, Sm-Nd and Pb isotope evidence for ~5-40% crustal contribution to Coppermine basalt lavas (this study; Dupuy *et al.*, 1992; Griselin *et al.*, 1997). Trace element and Os isotope assessment of crustal contamination are antithetic because of the compatible nature of Os and incompatibility of trace elements employed to track crustal contamination. This is most extremely shown by the fact that the andesite glass lacks Os isotope evidence for significant amounts of crustal contamination yet incompatible trace element profiles indicate a dominantly crustal signature persists. This means that the upper lavas of the Coppermine stratigraphy were more susceptible to high Re/Os crustal contaminants and this is reflected in the isotopic differences measured between the different stratigraphic levels (Fig. 5.12).

5.7.2 Crustal contamination and fractional crystallisation in the Muskox Intrusion

A meaningful evaluation of the role of crustal contamination in the genesis of continental intraplate magmatism requires an understanding of the chemical interaction between mafic magmas and continental crust. Both upper and lower crustal material can contaminate primitive mantle melts. Saal *et al.* (1998) found that lower-crustal xenoliths from North Queensland, Australia, have 1-2 times as much Os and half as much Re as modern day upper crust (Esser and Turekian, 1993). As a result Saal *et al.* (1998) have suggested the Continental intraplate magmas may have their initial mantle Os isotope signatures dramatically changed by ponding and fractionating within the lower continental crust.

Crustal contamination is clearly a significant process in generating the trace element signatures observed in the Muskox layered series. Negative Nb, Ta and Ti anomalies and positive Pb, Th, Rb and Ba anomalies present in the majority of layered series rocks as well as the Keel dyke suggest that all of the Muskox intrusion rocks have experienced some degree of crustal contamination. Trace element evidence for substantial crustal contamination at the margins of the intrusion and more limited contamination in the layered series and Keel dyke is substantiated by the following features:

- Similar sulphur isotope compositions between country rocks ($\delta^{34}S$ -6 to +13‰) and marginal rocks (+2 to +17‰), roof rocks (+3 to +26‰), layered series peridotites (+1 to +11‰) and the Keel dyke (+6 to +15‰; Sasaki, 1969).
- The radiogenic $^{87}Sr/^{87}Sr$ and negative εNd_i that characterise the roof rocks (Stewart and DePaolo, 1992).
- The enhanced LILE, HFS and orthopyroxene along the intrusive contacts (Francis, 1994).
- Locally some of the roof zone rocks possess similar trace element patterns to the country rocks suggesting active sidewall and roof assimilation took place during intrusive emplacement.
- The presence of xenolith country rock material. Areas of country rock have melted to form marble textured migmatite and plagioclase porphyry diorites
- Increasing orthopyroxene contents in crystallised magmas at the intrusive margins (Francis, 1994).

There are negative Nb, Ta and Ti and positive Pb anomalies in the Keel feeder dyke and all the layered series peridotites. Pearson and Nowell (2002) have shown that enriched CLM does not have negative Nb and Ta or positive Pb anomalies and so these features are unlikely to be derived from the mantle source. If these signatures are not the result of CLM addition they therefore also require crustal contributions to initial Muskox magmas. Using the same approach as for the Coppermine CFB Nb/Ta and La/Nb ratios for the Muskox keel dyke, roof and marginal zones are plotted in Fig. 5.28. These samples lie well away from the contamination trends for Coppermine CFB lavas to lower Nb/Ta ratios and suggest that whilst crustal contamination has occurred, the absolute concentrations between reservoirs has been different. Extensive contamination of marginal zone and roof zone rocks in the Muskox Intrusion has been well documented by Stewart and DePaolo (1992) and Francis (1994) and is indicated by trace element data presented here. However this contamination is not ubiquitous. This is demonstrated by the roof contact zone where less contaminated units lie sandwiched between the roof zone and more contaminated units; surprisingly it seems that the cyclic unit most extensively contaminated by the Hornby Bay roof rock is not a layer lying close to the contact but is DDH-MX-N14 ~60m from the roof contact. This could imply (i) late stage magma replenishment at the roof margins, (ii) heterogeneous distribution of roof

xenoliths in the drill core materials, (iii) magma overturn in the chamber during crystallisation.

Fractional crystallisation has clearly played a fundamental role in the distribution of chemical variations in the Muskox intrusion. The ultramafic and mafic cumulates were derived from fractional crystallisation of a high-Mg magma (Smith and Kapp, 1963; Irvine, 1980). The corresponding evolved liquids must have either (i) been erupted to the surface as lava flows or (ii) are preserved northward along strike under younger cover forming an evolved fractional crystallisation trend. The accumulation of silicate crystals with low bulk D for Re has resulted in a layered series that has generally low Re/Os* and Roof and Marginal zones that exhibit a large variation in Re/Os* (Fig. 5.18 and 5.19). The variations in Re/Os* may also be in part due to concomitant assimilation of crustal material with high Re/Os* in the marginal and roof zone rocks.

Accumulation of Os in early crystallising sulphide and precious metal alloy phases means that it is very difficult to model crustal contamination in these rocks by direct comparison with crustal assimilates. To overcome this problem theoretical assimilation and fractional crystallisation models (AFC) of initial Muskox melts with between 0.1 and 1 ppb Os and chondritic initial $^{187}Os/^{188}Os$ (Re/Os* = ~0.1, $\gamma Os = 0$) have been plotted in Fig. 5.30. The model shows mixing curves for an AFC ratio ($M_{Assimilant}/M_{Magma}$) of 0.8 and an Os bulk D of 15 indicate between 2 and 4% contamination by upper crustal gneisses or lower crustal granulites can explain the entire Os isotope variation observed in the Muskox layered series. For lower ratios of 0.2 and unity AFC would be equal to 16-26% and 22-74% respectively. The two scenarios of AFC at unity or 0.2 are geologically speaking, unrealistic and greatly at odds with the ultramafic nature of the Intrusion and the much smaller crustal contamination estimates from trace elements. The observation of crustal contamination by country rock explains the elevated γOs derived from the entire Muskox dataset ($\gamma Os_i = +34.8$; Fig. 5.25) and from the combined layered series peridotite and pyroxenite data ($\gamma Os_i = +12.5$; Fig. 5.26).

The large range in Os (this study) and S isotope compositions (Sasaki *et al.*, 1969) measured for marginal and roof zone rocks supports the notion that crustal contamination in these zones was excessive (Francis, 1994), generating both hypersthene-normative and high-Al andesite contaminated magma types. Francis

(1994) concluded that contamination of the layered series was effectively buffered by sealing of the margins of crystal cumulates and that large scale contamination was infrequent and/or episodic. However, variation in initial $^{187}Os/^{188}Os$ can explained by <4% crustal contamination, indicating that the layered series was not totally spared from crustal assimilation. In the following section the origin of the radiogenic $^{187}Os/^{188}Os$, high Os chromitites and chromite-rich dunites will be considered in the context of crustal contamination and post-crystallisation Os mobility.

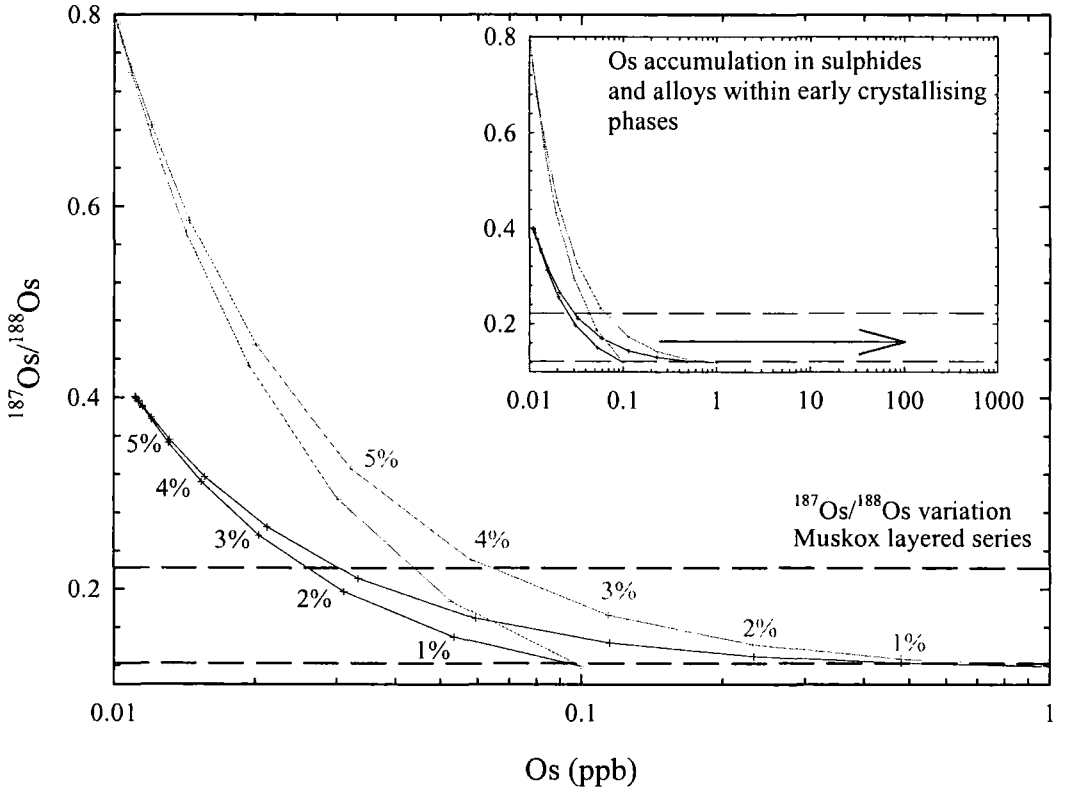

Fig. 5.30: Calculated initial $^{187}Os/^{188}Os$ vs. Os. Model to show the effect of crustal assimilation and concomitant fractional crystallisation on Muskox melts. This model indicates that a fractional crystallisation to assimilation ratio of 0.8, ~2.5% crustal addition of Wopmay gneiss and 4% crustal addition of LCC can explain the entire Os variation in the Muskox intrusion layered series units. Subsequent accumulation of Os would result in the high Os concentrations seen in layered series rocks. If the ratio of fractional crystallisation to assimilation decreases the amount of contamination proportionally increases and if the ratio increases less contamination is required. Variation of $^{187}Os/^{188}Os$ measured in Layered Series peridotites shown as dashed lines.

5.7.3 Crustal contamination versus post-crystallisation Os mobility in the generation of Os-rich, radiogenic $^{187}Os/^{188}Os$ stratiform layers

Ni-Cu-PGE ores from layered intrusions such as Noril'sk, Voisey's Bay or Sudbury have most commonly been interpreted as forming through sulphide saturation and immiscible sulphide ore formation processes; the so called *R*-factor (Fig. 5.21). This *R*-factor can be defined as the effective mass of silicate magma with which a given mass of sulphide magma has equilibrated (Campbell and Naldrett, 1979). Sulphide saturation is most commonly considered a consequence of assimilation of crust or crustally derived sulphur into sulphide-undersaturated basaltic, picritic or komatiitic magmas (Foster *et al.*, 1996; Lambert *et al.*, 1998, 1999). Apart from one marginal zone rock (DDH-MX-S-192), Muskox Intrusion rocks do not conform to an *R*-factor model and appear more like residual CLM peridotites because of their low Re/Os* ratios and high Os* abundances (Fig. 5.21). The majority of stratiform chromitite deposits in other layer mafic intrusions do not conform to *R*-factor models either (Fig. 5.21).

In layered mafic intrusions the precious metal deposits that do conform to *R*-factor models tend to lie in marginal zones at the contacts between the intrusion and their country rocks. These deposits are generally Ni-Cu-PGE rich sulphides with highly supra-chondritic γOs consistent with high *R*-factors (Fig. 5.31). Examples of marginal zone sulphide ores with high Re/Os* and γOs include Voisey's Bay (Lambert *et al.*, 1999), Duluth (Ripley *et al.*, 1999) and the Sudbury Igneous Complex (e.g., Morgan *et al.*, 2002). No stratiform chromitite deposits possess Re/Os* and supra-chondritic γOs anywhere near as high as the values seen in side-wall sulphide deposits. Chromitite ores possessing low Re/Os* generally have supra-chondritic and occasionally sub-chondritic γOs in the region of -10 to +100 (Fig. 5.31). Examples of these forms of stratiform deposit can be found in various sized mafic-ultramafic layered intrusions including Bushveld (γOs = +10 to +55; e.g., Schoenberg *et al.*, 1999), Stillwater (γOs = +12 to +34; e.g. Lambert *et al.*, 1994) and the Ipueira-Medrado sill (γOs = -4.6 to +3.3; Marques *et al.*, 2003). Chromitites and Os-rich dunites from the Muskox intrusion also yield low Re/Os* and high γOs (+12 to +87).

The fact that Muskox intrusion layered series rocks and chromitite horizons in other mafic-ultramafic intrusions do not follow an *R*-factor enrichment model suggests that limited crustal sulphide addition took place in the layered series of the intrusions and sulphide addition from the country rocks was only significant for magmas which interacted in the marginal and roof zones. Magmas that eventually crystallised to form the layered series were relatively sulphide under saturated. An *R*-factor mixing model for crustal assimilation of Wopmay Paragneiss to mantle-derived magmas is shown in Fig. 5.31. This model is controlled by the sulphide melt: silicate melt which is given in as a ratio against tick marks in Fig. 5.31. From the diagram a number of observations can be made relating to the Wopmay paragneiss *R*-factor model:

- Very low sulphide melt: silicate melt ratios are predicted for the Muskox layered series rocks as well as low Re/Os* chromitites in layered intrusions globally.
- Keel dyke samples do not conform at all to an *R*-factor model suggesting that these and the low γOs_i dunites probably offer the best $^{187}Os/^{188}Os$ for the Muskox primary melt.
- Paragneiss and by virtue of their similar Os concentrations and $^{187}Os/^{188}Os$ compositions, lower crustal rocks (Saal *et al.*, 1998) are unable to explain the trends to sulphide enrichment seen in Ni-Cu-PGE side wall deposits. This observation suggests that some intrusions will trend to greater Os (and therefore precious metal enrichment) if sulphide-rich, high Re/Os lithologies are present in the country rock formations that they intrude. For example sulphide over-saturation in the Noril'sk intrusion which has generated PGE-rich sulphide ores is primarily attributed to assimilation of sulphide-rich annhydrite into the primary magmas (Arndt *et al.*, 2003).

If sulphide over-saturation is not the cause of Os enrichment in chromitites and high Os concentration dunites then what is? Two possible models can be invoked to explain Os (+PGE) enriched horizons in layered mafic intrusions. The first was proposed in 1975 and subsequently modified in 1977 by T.N. Irvine and was based on the Muskox Intrusion. This model proposes that mixing between a mafic magma with silica-enriched, crustally contaminated magmas forces pure chromite crystallisation which is immediately followed by pyroxene crystallisation. This model fits well with the Muskox intrusion main chromitite reefs which are enclosed

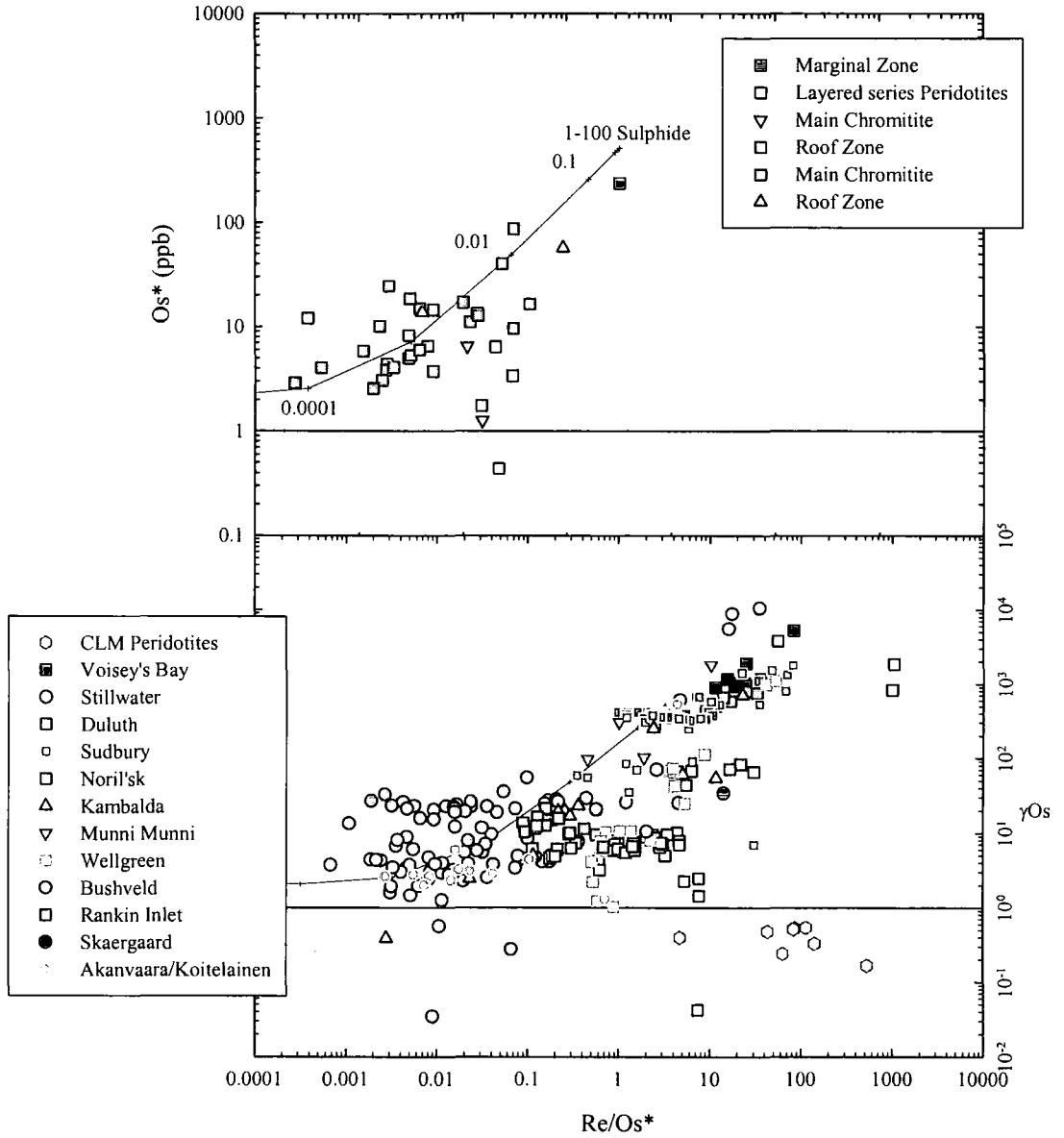

Fig. 5.31: Re/Os vs. *Os and γOs data for Muskox Intrusion rocks and for LMIs globally. Modelled R-factor pathways derived using the equation of Campbell and Naldrett (1979) and assuming D_{Re}=500 and D_{Os}=30000 (After Lambert et al., 1999). Values in upper figure equate to sulphide melt:silicate melt ratio (the R-factor) and indicate that a very small sulphide:silicate ratio is required to explain mixing between Wopmay paragneiss crustal contaminant and a primary melt liquid to account for the variation in Re/Os* in the Muskox Intrusion Layered Series. Data sources for CLM are from Pearson et al. (2003) and references therein. Data for LMIs from Martin (1989), Lambert et al. (1998), Ripley et al. (1999), McCandless and Ruiz (1989), Lambert et al. (1989), Dickin et al. (1992), Marcantonio et al. (1993), Hulbert and Gregoire (1993), Marcantonio et al. (1994), Walker et al. (1994), Foster et al. (1996), Walker er al. (1997), Puchtel et al. (1999), McCandless et al. (1999), Schoenberg et al. (1999), Lambert et al. (1999), Brooks et al. (1999), Cohen et al. (2000), Horan et al. (2001), Hanski et al. (2001), Morgan et al. (2002) , Marques et al. (2003), Arndt et al. (2003)*

by pyroxenite (Appendix A). The chromites also contain small (<50μm) silicate inclusions (>60 wt. % SiO_2; Irvine, 1977) with sulphides minerals such as pyrrhotite

and chalcopyrite (as well as rutile explaining the high TiO_2 of these chromitites) within them that indicate (1) a silica-rich magma was involved in chromite genesis and (2) that what little sulphide existed in the magmatic systems effectively scavenged and hosts the Os in the chromitites. Irvine (1975) also proposed that the sulphides themselves crystallised as a function of mafic melt: silicic melt interaction perhaps indicating why high-silica melts are trapped as inclusions within chromite. The model of Irvine (1975; 1977) when applied to highly siderophile element chemistry also explains the radiogenic $^{187}Os/^{188}Os$ of chromitites and Os rich dunitic horizons in the Muskox Intrusion.

Another model for the generation of Os and PGE rich horizons is post-crystallisation mobilisation of radiogenic Os. This process has been discussed in previous sections. For dunites such as DDH-MX-S137 and DDH-MX-N129 which have supra-chondritic γOs_i (+12.7 to +85.6), have no petrographical relationship with silica-enriched minerals such as orthopyroxene and which are not associated with large changes in chemistry (for example at the boundary between the Main Muskox chromitites a jump of >10% SiO_2 is observed (Fig. 5.15)) the model of Irvine (1975; 1977) breaks-down. Instead for these dunite/peridotite cyclic units their silicate minerals are heavily serpentinised and some of the chromitites form an interstitial framework with secondary magnetite around the olivine-pseudomorphs (Appendix A). Distinguishing between Os mobilisation and crustal contamination as the cause of this Os enrichment is difficult and a future aim is to analyse Nd isotopes on these samples as Nd is immobile and is likely to allow recognition between crustal contamination and element mobility processes.

5.8 Depth and degree of partial melting estimates for the Mackenzie LIP

The Coppermine CFB contains picrites with Os contents that are higher than modern day OIB lavas (chapter 4) and that are comparable with Proterozoic and Phanerozoic picrites from other CFB (e.g., Shirey, 1997; Schaefer *et al.*, 2000) and Archaean and Phanerozoic Komatiites (e.g., Walker *et al.*, 1999; Wilson *et al.*, 2003). The high concentrations of Os in some Coppermine CFB lavas could be primary-melt concentrations or as a result of accumulation of an Os-rich mineral in melts that originally had much lower Os inventories. Horan *et al.* (1995) discussed scenarios to

explain the extremely high Os contents of Noril'sk picrites which may also be applied to other CFB formations. These explanations included (i) that the Os abundances are true melt concentrations, (ii) that there is preferential removal of sulphides during melt segregation, (iii) that melting occurred under sulphur-undersaturated conditions rendering Os less compatible during melting (Morgan *et al.*, 1983; Brügmann *et al.*, 1993), or (vi) that an Os-rich phase accumulated in a crustal magma chamber (Brügmann *et al.*, 1993).

High densities of sulphides in the mantle argue against preferential removal of sulphides during melt segregation (Fleet *et al.*, 1991a). On the basis of positive correlations with Ni, MgO and Os* it seems more probable that physical accumulation of an Os-rich phase took place during fractionation of magmas in the crust (Fig. 5.10). The observation of high Os* abundances in an andesite composition glass that also contains abundant early crystallising chromite also strongly advocates a crustal magma chamber origin for Os concentrations in CFB lavas and suggests that high measured Os* abundances in lavas cannot always be used to infer that they have been impervious to crustal contamination or have resulted from large degrees of partial melting. In searching for a more robust means for gauging the degree and depth of partial melting responsible for the various components of the Mackenzie LIP trace element methods that have been applied successfully to CFB in the past (e.g., Thirlwall *et al.*, 1994; Baker *et al.*, 1997) are briefly explored.

5.8.1 Depth, degrees of partial melting for the Coppermine CFB

The Coppermine CFB lavas display highly variable REE concentrations with a marked change in REE patterns with stratigraphic position (Fig. 5.8). Variable depletion in HREE indicates generation of the Copper Creek Formation lavas, at least partly, in the presence of residual garnet. A relatively fertile peridotite source for the Coppermine CFB is required for models of REE concentrations and ratios (Fig. 5.8). For the Husky Creek formation lavas flatter REE patterns suggest an increase in the contribution from spinel peridotite in the melt column. This temporal evolution cannot be explained by exhaustion and depletion of garnet through time during tholeiitic magmatism as this would result in HREE-enriched patterns as seen

in komatiites formed by high degrees of partial melting of their mantle source (e.g., Wilson *et al.*, 2003).

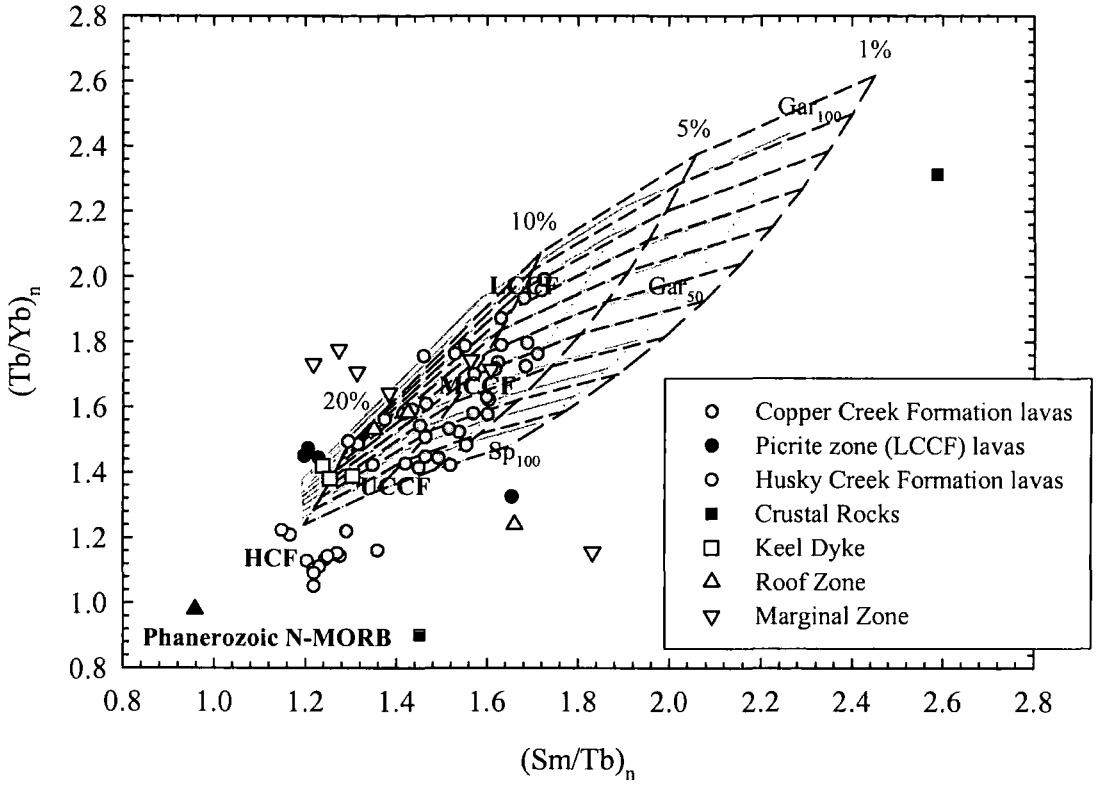

Fig. 5.32: Primitive mantle normalised Sm/Tb vs. Tb/Yb for Coppermine CFB lavas and selected Muskox Intrusion rocks. Also shown is a grid of melt compositions produced by 1, 5, 10 and 20% of incremental batch partial melting of a primitive mantle source and a DMM source (light grey) with 0-100% of this melting occurring in the presence of residual garnet. The melting model assumes the following modes and proportions for olivine, orthopyroxene, clinopyroxene and spinel/garnet respectively: 0.4/0.3/0.1/0.1 and 0.25/0.25/0.25/0.25. Hypothetical sources are from Sun and McDonough (1989) and the GERM database. Abbreviations as in Fig. 5.8.

The stratigraphic progression in REE patterns implies that Lower Copper Creek Formation lavas representing the lowest melt fractions (≥ 5%) with 40-90% of the total melt fraction occurring in the garnet stability field (Fig. 5.32). The picrite zone of the Lower Copper Creek Formation marks a change to higher degrees of partial melting (≥20%) at greater than 30% melting in the garnet stability field. Middle and Upper Copper Creek Formation lavas show ever greater degrees of melting with variable garnet-spinel sources; this variability may in part be due to source depletion as seen by the difference in depleted source and primitive mantle composition models in Fig. 5.28. The Husky Creek Formation lavas, although not as depleted as modern day N-MORB for MREE and HREE, show characteristics that can be

explained solely as melting in the presence of a spinel sources at high degrees of partial melting.

The observations of possible high mantle potential temperatures, a fertile mantle source, temporal change from deep, low degree partial melting to deep high degree partial melting and then ever increasing partial melting of an increasingly more depleted and shallow source support a model of rifting and significant thinning of the lithosphere during the formation of the Mackenzie LIP, possibly related to the opening of the Poseidon Ocean at that time (Fahrig, 1987; Griselin *et al.*, 1997).

5.8.2 Depth, degrees of partial melting for the Muskox intrusion

The accumulative nature of layered series rocks such as those in the Muskox layered series results in few of the samples conforming to partial melting models. For this reason only roof rock, keel dyke and marginal zone rocks have been plotted in Fig. 5.32. The steep REE profiles and apparent position of Keel and layered series peridotites in Fig. 5.17 suggest initial Muskox melts came from the garnet stability field. U-Pb ages show that the Muskox intrusion is one of the oldest components in the Mackenzie LIP (LeCheminant and Heaman, 1989) so a garnet stability field origin for the Muskox melts agrees with initial melting in the garnet stability field early in the evolution of the younger Coppermine CFB. If Keel dyke samples are taken as a proxy for melting then in excess of 20% partial melting of a mantle source with residual garnet is required to explain the trace element characteristics of Muskox layered series rocks.

5.9 Re-Os geochronology – Mackenzie temporal and chemical links

5.9.1 Spatial – temporal linkage

In this section the possible relationships between the Coppermine CFB and the Muskox intrusion are addressed. Previous studies have inferred a chemical or temporal link with parts of the Coppermine CFB stratigraphy and the Muskox layered intrusion (Irvine, 1970; Francis, 1994; Baragar *et al.*, 1996; Griselin *et al.*, 1997). There is need to further investigate the similarities in the sources of magmatism to the Muskox intrusion and Coppermine volcanics because of the

implications it may have for the Re-Os systematics of the mantle source(s). As well as obvious spatial linkages outlined at the beginning of the chapter, U-Pb Concordia dating of the Muskox intrusion (1269±1Ma, French *et al.*, 2002), the Mackenzie dykes (1267±2Ma, Lecheminant and Heaman, 1989) and the Coppermine Volcanics (1270Ma; M.A. Hamilton pers. comm.) indicate the formation of the Mackenzie LIP over a relatively short duration and generation of the structural components in a similar time span. U-Pb age data for the lowermost flows of the Coppermine CFB are supplemented by the new Re-Os isochron ages for the Coppermine CFB presented here. Robust regression of all 15 samples together gives a Re-Os isochron age of 1213+65/-39Ma and an initial $^{187}Os/^{188}Os$ of 0.1215±0.0031 (Fig. 5.33a).

Copper Creek formation lavas (n=13) define an apparent age of 1222+62/-12Ma and an initial $^{187}Os/^{188}Os$ of 0.1210±0.0027 (Fig. 5.33b) whilst Copper Creek formation lavas selected on the basis that they yield reasonable γOs_i (n=7) define a model 3 isochron age of 1284±13Ma and an initial $^{187}Os/^{188}Os$ of 0.1215±0.0020 (Fig. 5.33c). All three separate regressions give ages within error of U-Pb Concordia ages of Coppermine CFB, Mackenzie dyke and Muskox intrusion magmatism (1267-1270Ma; LeCheminant and Heaman, 1989; French *et al.*, 2002; M.A. Hamilton pers. comm.) and demonstrate the general closure of the Re-Os system in Coppermine CFB lavas at that time. It is notable that older ages are defined for the Copper Creek formation than if Husky Creek formation lavas are included and also that selected Copper Creek lavas (Fig. 5.33c) define an older age than for the entire Copper Creek formation dataset. The majority of lavas plotted in Fig. 5.33c are from close to or within the newly defined picrite zone implying that there may be measurable age differences in the Coppermine CFB up succession. It should also be noted that despite Re mobility in four of the Coppermine samples (see section on element mobility) these samples still lie close to or on an error-chron regression suggesting that Re-gain occurred relatively soon after formation of the Coppermine CFB. Coppermine CFB picrite lavas and also the glass have slightly greater initial $^{187}Os/^{188}Os$ than for chondrites at 1270Ma ($^{187}Os/^{188}Os$ = 0.1191). It is important to note that the individual regressions of all data, Copper Creek formation lavas and Picrite zone lavas alone show slight differences in initial Os isotope ratio (0.1215±0.031, 0.1210±0.0027, 0.1215±0.0020, respectively).

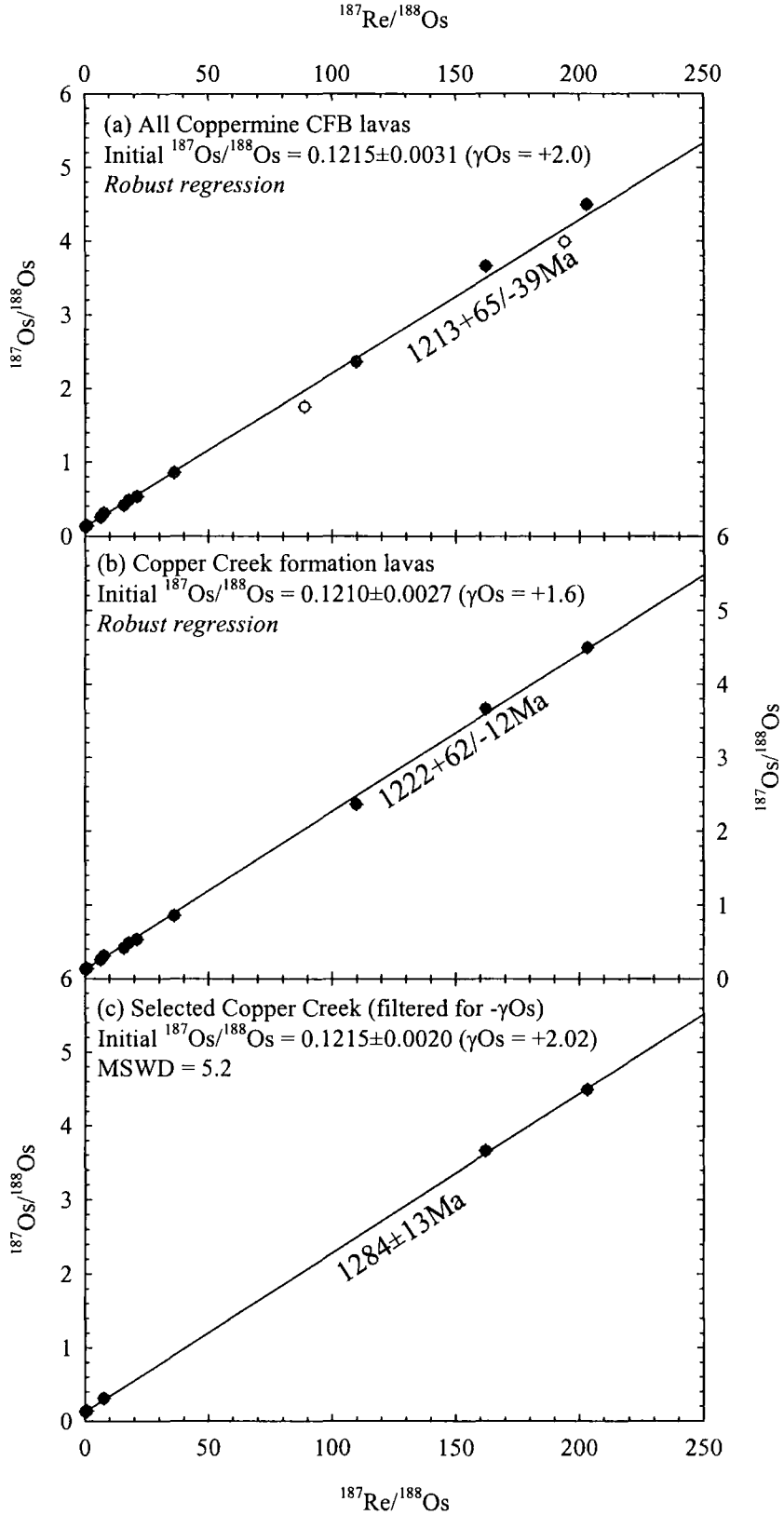

Fig. 5.33a-c: Re-Os isochron plots for Coppermine CFB lavas. White circles = Husky Creek Formation, Black Circles = Copper Creek Formation. Robust regressions and Model 3 isochrons with 2σ absolute errors made using Isoplot 3.0 (Ludwig, 2003).

All of these initial Os isotopic compositions (γOs values of +2.02±0.03, +1.60±0.04 and +2.02±0.03, respectively) are elevated relative to the estimated Os composition for the chondritic mantle at 1270Ma (γOs = 0).

Re-Os age information for the Muskox intrusion has already been detailed in the element mobility discussion (Fig. 5.25 and 5.26) and indicates a large amount of scatter about a 1270Ma reference isochron. Nearly all of the rocks in the intrusion have been affected by post-crystallisation element mobility resulting in older (Re-loss, Os-addition) or young ages (Re-addition, Os-loss) for cyclic units 2-19 layered series peridotites and roof and marginal zone rocks respectively. Combined, all the layered series data define an errorchron age of 1235±270Ma, within error of the precise U-Pb Concordia ages for the intrusion (LeCheminant and Heaman, 1989; French *et al.*, 2002). Equally the Keel dyke samples lie along a 1270Ma reference line. The Re-Os geochronology for the Coppermine CFB and to some extent the Muskox intrusion support the ages for the Mackenzie LIP based on highly precise U-Pb Concordia. However, the variability from the 1270Ma reference isochron for the Muskox intrusion illustrate the importance of post-crystallisation hydrothermal alteration on the layered series of large mafic intrusions. More accurate Re-Os geochronology has been presented on sulphide ores from the Noril'sk intrusion (Walker *et al.*, 1994) and Voisey's Bay (Lambert *et al.*, 1999) and pure chromitite separates from Stillwater (Lambert *et al.*, 1994) and Ipueira-Medrado sill (Marques *et al.*, 2003). Future lines of work on the Muskox intrusion should consider analysis of pure chromitites as well as sulphide ores from the marginal zones in order to understand if Os and Re mobility is restricted to the layered series from Re-Os isochron relationships.

5.9.2 Chemical linkage

As well as being spatially and contemporaneously linked this study also shows that there is chemical linkage between the Coppermine CFB and Muskox layered intrusion. Firstly the Copper Creek formation and Muskox intrusion were both fed by magmas generated by peridotite melting in the garnet stability field (see previous sections). In general, the Copper Creek picrites and Muskox Keel dyke samples require $\geq$ 20% partial melting. Husky Creek lavas as well as lavas from the upper and middle Copper Creek formations are less likely to be directly associated with the

intrusion. Unlike the lower Copper Creek lavas which have high Mg/Fe ratios as well as high Cr and Os contents, the Husky creek and Middle and Lower Copper Creek formations do not. The transition from garnet to spinel facies melting suggest that

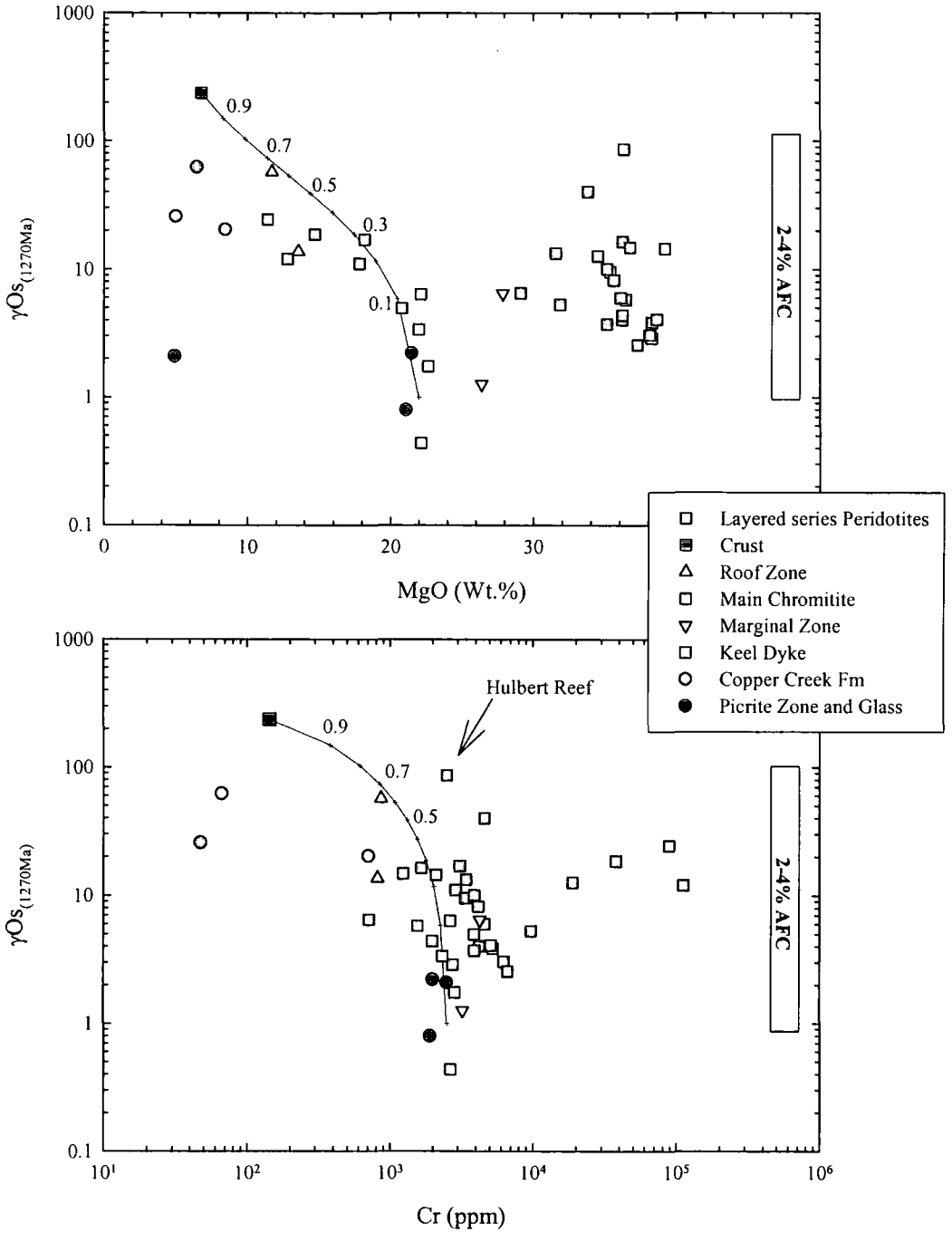

Fig. 5.34: γOs_i vs. Cr and MgO for Muskox intrusion and Coppermine Volcanics. Binary solid mixing models between Keel and Coppermine picrite average with Wopmay Paragniess for evolved marginal zone and roof rocks. Bar illustrates range of γOs generated by 2-4% AFC of melt modelled in Fig. 5.30 illustrating that small amounts of crustal contamination can generate the large ranges in γOs measured in Muskox layered series and main chromitites.

the upper stratigraphy of the Coppermines is more likely to be sourced from younger Mackenzie dykes which share similar chemical characteristics to the upper portions of the Coppermine CFB stratigraphy (Baragar *et al.*, 1996) and are slightly younger than the Muskox intrusion on the basis of U-Pb dating (LeCheminant and Heaman, 1989).

A strong line of evidence for the involvement of a magma chamber in the origin of the Coppermine CFB comes from the unusual observation of high Os abundance in the andesite glass flow from the Coppermine CFB and is best explained by Os-rich phase accumulation in a crustal magma chamber (Brügmann *et al.*, 1993).The glass is enriched in Os from chromite possibly by the silicate melt:mafic melt mechanism invoked by Irvine (1975; 1977) for chromite generation in the Muskox intrusion main chromitite reef. The event must also have coincided with significant crustal contamination which, although having a limited impact on early crystallising Os-rich phases, greatly affected the trace element characteristics of the glass and suggest over 99% of the Os was mantle-derived. Main chromitites also have fractionated trace element characteristics and it may be that the glass horizon, which is located with a thick andesite flow, is the surface expression of an extensive crustal assimilation event that triggered the crystallisation of chromitite whilst simultaneously generating a large volume silicic eruption in the form of the 60m thick andesitic flow capped by the glass. On this basis, Os isotopes support the hypothesis that stratiform chromitite deposits are formed through silica-over saturation (Irvine, 1977). The differences in chromite formation in normal layered series peridotites (e.g., Hulbert Reef; early crystallising phases after Os-alloys) and chromitites (e.g., Main chromitites; forced crystallisation through SiO_2 over-saturation) represent fundamental differences in chromitite type and explain why the Os isotope systematics of chromitites and chromite-rich dunites are so different (Fig. 5.34).

5.10 Initial γOs for the Coppermine CFB and Muskox Intrusion

The observations that Re and Os elemental mobility, upper crustal assimilation and fractional crystallisation have been relatively insignificant in modifying the Re-Os isotope systematics of picrite lavas from the Coppermine CFB suggest that the initial

$^{187}Os/^{188}Os$ generated from isochronous relationships between measured $^{187}Re/^{188}Os$ and $^{187}Os/^{188}Os$ is the true initial composition of magmas feeding the Coppermine CFB. This initial γOs for the Coppermines is +2. Lack of isochronous relationships does not allow as accurate an assessment of initial γOs of the melts feeding the Muskox Intrusion. However, Keel dyke samples, which have been unaffected by element mobility yield an errorchron initial γOs = +1.2. This initial γOs appears to be an appropriate estimate for the melts feeding the intrusion on the basis of the Keel dyke samples having similar γOs to the picrites (Fig. 5.34).

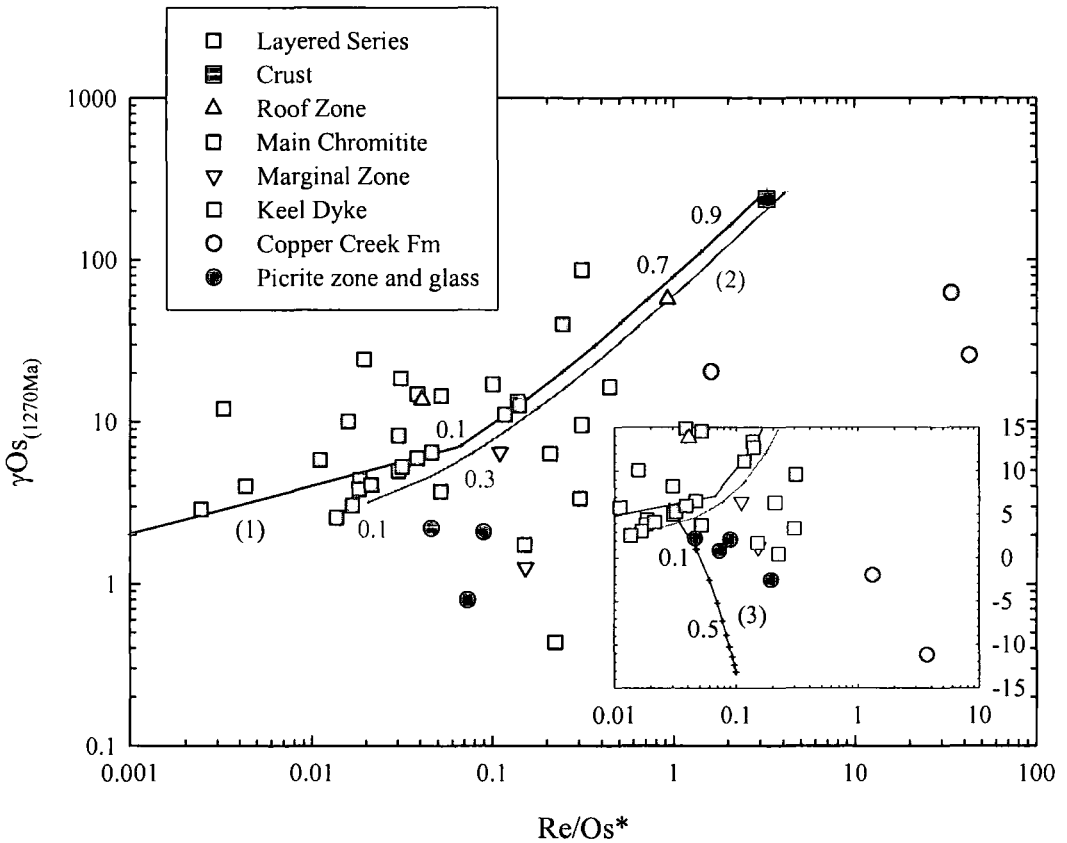

Fig. 5.35: Initial γOs for Muskox Intrusion units and Coppermine CFB lavas against Re/Os. Models in lower panel correspond to atomic mass correction models for mixing between a typical Mackenzie LIP magma (γOs =+2, Os = 1ppb, Re = 1ppb) and (1) Wopmay paragneiss, (2) Lower Continental Crust (Saal et al., 1998) and (3) Slave and Churchill province continental lithospheric mantle peridotite (Irvine et al. 2003). See text for details.*

Individual γOs_i for layered series peridotites and the Keel dykes range from = +0.4 to +86.5. This range has been explained through crustal contamination (Fig. 5.30 and Fig. 5.35). These lines of evidence indicate that whilst the lowest estimates of initial γOs for both the Coppermines and the Muskox intrusion appear to be slightly supra-chondritic, the large range in γOs could be explained by variable degrees of upper and lower crustal contamination. Melts that fed the Muskox intrusion and

Coppermine CFB were likely to have already experienced some crustal contamination. In the absence of other supporting isotopic datasets (e.g. Nd) and evidence for totally uncontaminated melts in the Coppermine CFB or Muskox Intrusion it can be concluded that the initial melt composition of the Coppermine CFB and Muskox Intrusion was slightly supra-chondritic γOs at that time. The initial γOs of the Coppermine CFB (+2.0) and Keel dyke (+1.2) are taken for the purposes of the next discussion.

5.11 The Mackenzie LIP and mantle Os isotope evolution

Isotopic and chemical studies of intraplate magmatism have generally considered layered intrusions and CFB separately despite their obvious genetic link. In the majority of cases Re-Os isotopic studies of layered intrusions have illustrated the important role that crustal assimilation has played in the generation of elevated $^{187}Os/^{188}Os$ as well as $^{186}Os/^{188}Os$ ratios (Lambert *et al.*, 1989; Martin, 1989; McCandless *et al.*, 1991; Dickin *et al.*, 1992; Foster *et al.*, 1996; Lambert *et al.*, 1998; Ripley *et al.*, 1999; McCandless *et al.*, 1999; Lambert *et al.*, 1999a, b; Horan *et al.*, 2001; Hanski *et al.*, 2001; Morgan *et al.*, 2002; Arndt *et al.*, 2003). Some studies of layered intrusions have also highlighted the possible roles of post-crystallisation hydrothermal fluids (Marcantonio *et al.*, 1993; 1994) and a few studies have considered the Os isotopic compositions of layered intrusions from the perspective of derivation from an enriched asthenospheric mantle source (Walker *et al.*, 1994; Puchtel *et al.*, 1999). In the case of CFB, constraining the source characteristics of continental LIPs has proved difficult because interaction with continental crust and CLM typically overprint most primary isotope and trace element systematics (e.g., Carlson, 1991). Re-Os studies have revealed cases where significant crustal contamination has been involved in the petrogenesis of basalts (Molzahn *et al.*, 1996; Hart *et al.*, 1997; Chesley *et al.*, 1998). Radiogenic Os isotope compositions of some CFB are also considered to be due to a convecting mantle source variably mixed with CLM (Ellam *et al.*, 1992; Horan *et al.*, 1995; Shirey, 1997). In others, relatively unradiogenic $^{187}Os/^{188}Os$ is thought to be implicitly related to be dominated by the composition of a mantle plume with little or no evidence of CLM (Schaefer *et al.*, 2000).

Picrites and basalts from the Copper Creek formation have γOs initials that are slightly supra-chondritic similar to lavas from younger Proterozoic and Phanerozoic CFB (Horan *et al.*, 1995; Shirey, 1997). Estimates for a Muskox γOs initial, which samples deeper parts of the Mackenzie magmatic plumbing system, lie close to chondritic $^{187}Os/^{188}Os$ more akin to Archaean ultramafic rocks, Komatiites, and some Phanerozoic CFB (Allègre *et al.*, 1999; Schaefer *et al.*, 2000; Puchtel *et al.*, 2001; Bennett *et al.*, 2002; Wilson *et al.*, 2003; Gangopadhyay and Walker, 2003; Puchtel *et al.*, 2004).

A possible mantle reservoir involved in the formation of the Mackenzie LIP could be the CLM. Irvine *et al.* (2003) observed that some kimberlite-borne peridotites showed evidence of disturbance at around the time of the Mackenzie LIP inception perhaps suggesting that interaction between asthenospheric melts and lithosphere had taken place at that time. In Fig. 5.35 an average γOs for ~0.1133, Os = 3.5ppb and Re=0.35ppb has been taken from the averages of Somerset Island peridotites (Irvine *et al.*, 2003) to model the effects of CLM peridotite contamination to Mackenzie age asthenospheric magmas with a γOs initial = 0. The model allows that some CLM addition may be responsible for the Lower Copper Creek lavas as Re mobility was not observed for these rocks. However, for samples with high Re/Os the sub-chondritic γOs initials are due to Re-addition. For the Muskox there is no evidence of CLM melting to source magmatism suggesting that the Mackenzie LIP was almost exclusively sourced from the asthenospheric mantle.

5.11.1 Implications for the $^{187}Os/^{188}Os$ evolution of the terrestrial mantle

The initial near-chondritic γOs of Mackenzie LIP magmatism represents an important tie-point in the Os isotopic evolution of the Earth's mantle. This is because few mafic-ultramafic lavas and related rocks have been studied extensively or are well preserved in the mid-Proterozoic. Estimates of initial Os isotopic compositions of the Earth can be inferred from meteorite investigations. High precision isotope investigations of meteorites have revealed fine-scale differences in initial Re/Os ratios and $^{187}Os/^{188}Os$ in iron meteorites and less precise compositions for rocky meteorites (Smoliar *et al.*, 1996; Shen *et al.*, 1996). Primitive upper mantle (PUM) estimates also define the present-day isotopic composition of portions of the mantle revealed by lithospheric mantle peridotites (Meisel *et al.*, 1996; 2001).

Combined with Re-Os isotope systematics for mantle xenoliths (Pearson, 1999), ophiolites (Walker *et al.*, 2002), abyssal peridotites (Snow and Reisberg, 1995; Brandon *et al.*, 2000) and orogenic lherzolite massifs (Reisberg and Lorand, 1995; Pearson *et al.*, 2004) Archaean to Proterozoic rock complexes have demonstrated that the mantle on average has evolved with Re/Os ratio within 10% of that in chondrites.

In Fig. 5.36 the initial $^{187}Os/^{188}Os$ compositions of Coppermine CFB and selected Muskox intrusion rocks and Keel dykes together with the averages of ophiolite chromitites, abyssal peridotites, Komatiites, carbonaceous, enstatite and ordinary chondrite estimates for PUM from global studies of mantle xenoliths, and the solar system initial (SSI) are plotted against time. A regression line through SSI and the Mackenzie LIP source intersects the present-day at $^{187}Os/^{188}Os = 0.1296\pm0.0071$ in agreement with PUM estimates (0.1296 ± 0.0008; Meisel *et al.*, 2001). A PUM of 0.1296 requires that the source of the Mackenzie LIP evolved with a $^{187}Re/^{188}Os$ similar to that of PUM (0.4308) which is ~7% higher than the chondritic reference line (0.4019; Shirey and Walker, 1998) and ~9% higher than the $^{187}Re/^{188}Os$ in Carbonaceous chondrite. The $^{187}Re/^{188}Os$ of the Muskox mantle source is only marginally higher than estimates of ordinary (0.4148) and enstatite (0.4226) chondrites.

An examination of the high precision Re-Os isotope database available reveals a bimodal distribution of $^{187}Os/^{188}Os$ isotope compositions with the majority of data scattering along the chondritic reference line of Shirey and Walker (1998) indicating derivation from sources that evolved with time-integrated chondritic Re/Os ratios. A growing body of evidence indicates that these reference parameters may not accurately represent terrestrial mantle evolution (this study, Meisel *et al.*, 1996; 2001; Bennett *et al.*, 2002; Puchtel *et al.*, 2004) which is better reflected by $^{187}Os/^{188}Os = 0.1296\pm0.0008$. In this study the method of presenting data as % deviation from carbonaceous chondrite (Shirey and Walker, 1998) has been retained. Explicitly stated, the supra-chondritic initials of the Muskox Intrusion and Coppermine Volcanics are the result of the initial $^{187}Os/^{188}Os$ better resembling enstatite and ordinary chondrites rather than carbonaceous chondrite.

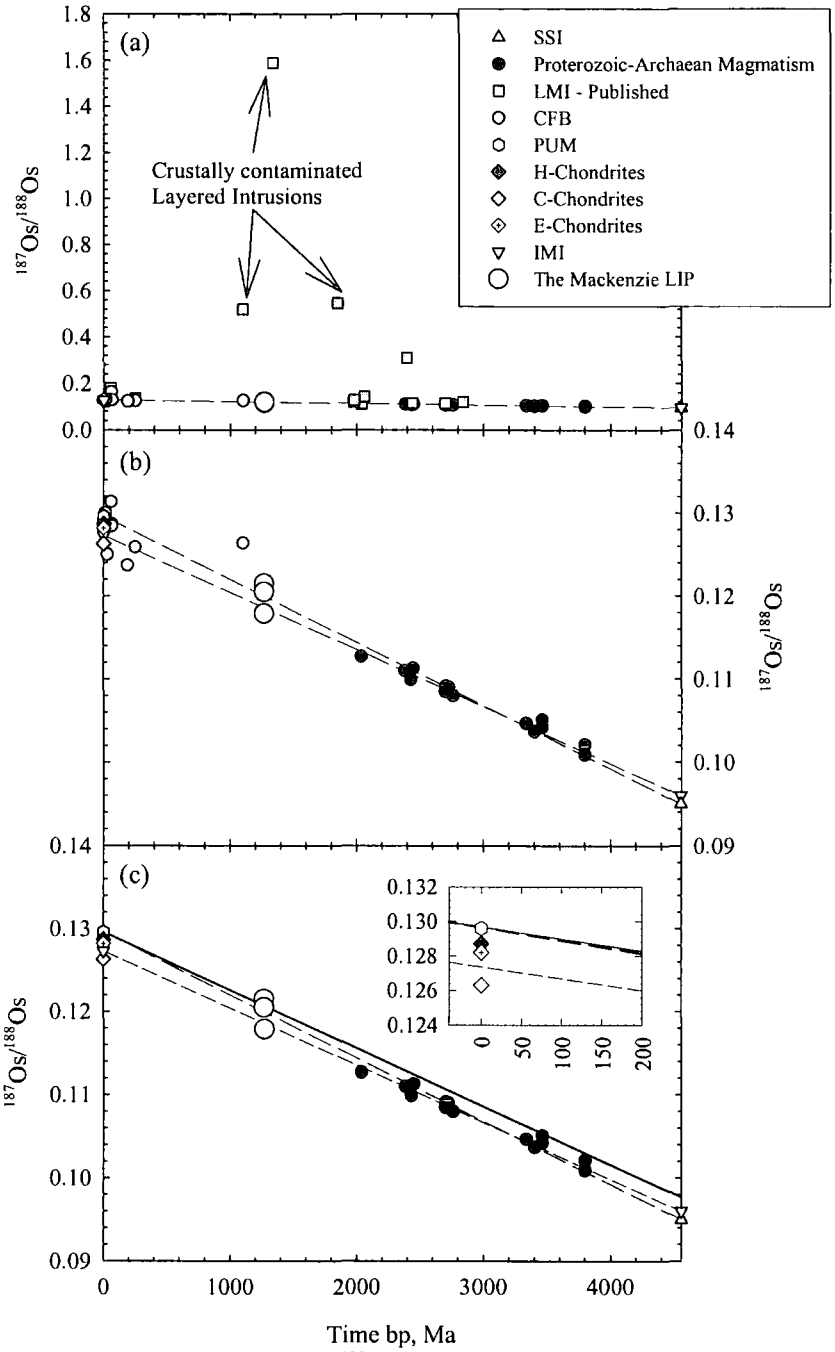

Fig. 5.36: Evolution diagram of $^{187}Os/^{188}Os$ vs. time for selected mantle-derived materials, chondrites, solar system initial (SSI) and iron meteorite initial (IMI). (a) Dashed line represents regression line through SSI (Shirey and Walker, 1998) and that of the Mackenzie LIP source. (b) Crustally contaminated LMI and CFB removed from plot, dashed line is IMI composition regression and second dashed line is SSI composition regression. (c) Archaean and Proterozoic mantle compositions with regressions for SSI and IMI as in (b) with solid line representing SSI regression through Mackenzie LIP source compositions. Mackenzie event show Coppermine (+2.02), Keel (+1.2) and Layered Series (-0.99) initial γOs. These models indicate that chondritic $^{187}Os/^{188}Os$ compositions have been a feature of the mantle source for intraplate magmatism and mantle-derived melts for 3.8Ga (Bennett et al., 2002) until at least the mid-Proterozoic. Keweenawan samples appear anomalous and are associated with the demonstrably crustally contaminated Duluth intrusion so they have been excluded in the lower plot. Data sources found in Shirey and Walker (1998) and Puchtel et al. (2004).

There are some notable excursions from the overall trend in Fig. 5.34. A large number of layered intrusions and LIPs deviate from the chondritic evolution line to more radiogenic $^{187}Os/^{188}Os$ suggesting a supra-chondritic Re/Os source. However, most of these layered intrusions (and associated CFB) are demonstrably crustally contaminated and therefore the cause of such supra-chondritic $^{187}Os/^{188}Os$ is likely to be crustal contamination that has not been accounted for. In other cases an outer core (Walker *et al.*, 1995) or recycled oceanic crust contribution (Shirey, 1997) has been proposed to explain these deviations. Similarly, sub-chondritic $^{187}Os/^{188}Os$ are inferred to come from complementary low Re/Os reservoirs such as the CLM (Ellam *et al.*, 1992).

In order to trace the $^{187}Os/^{188}Os$ isotopic evolution of the mantle over geological time, the available database for mafic-ultramafic lavas and related rocks has been filtered in two steps:

- An initial γOs has been regressed for data from individual provinces using isochron or errorchron initials.
- If evidence for crustal contamination in lavas is cited they have been removed. In the case of highly crustally contaminated systems cited in the literature these have been removed from regressions altogether.

Using this filtering method accurate Os isotopic compositions unambiguously shown to reflect that of contemporary mantle have been determined. On the $^{187}Os/^{188}Os$ isotopic evolution diagram (Fig. 5.35) data plot along a well defined trend (r=0.98) which gives intercepts at $^{187}Os/^{188}Os$= 0.0969±0.0009 (4550Ma) and 0.1289±0.0012 (0Ma). When only Proterozoic (including Mackenzie LIP) or older examples are plotted and regressed then they plot along a well defined trend (r=0.99) which gives intercepts at $^{187}Os/^{188}Os$= 0.0950±0.0014 (4550Ma) and 0.1270±0.0019 (0Ma). The lower intercept of Proterozoic and Archaean examples is identical within uncertainty to the SSI or 0.09531±0.00011 (Shirey and Walker, 1998) and to the present day chondritic reference of 0.1270 (Shirey and Walker, 1998). These data indicate that the mantle over Earth history evolved from SSI $^{187}Os/^{188}Os$ ratios with $^{187}Re/^{188}Os$ = 0.390. It was therefore 9% depleted relative to PUM. If it is considered that spinel peridotites have been chosen to represent PUM (Meisel *et al.*, 1996; 2001), whereas Komatiites and OIB (Hawaii, Gorgona) have been argued to originate from deep mantle reservoirs then regions of the lower mantle must have evolved similar Os

isotopic compositions, and thus Re/Os ratios as the upper mantle. Overall Os isotopic evolution of the mantle points towards SSI values but there remain significant examples of OIB and CFB which possess supra- or sub-chondritic γOs (chapter 4 and references therein; this chapter). These examples must be considered in any overall appraisal of Os isotopic signatures in intraplate magmatism (chapter 4).

5.11.2 Implications for coupled ^{186}Os-^{187}Os enrichment and long-term Os isotope heterogeneity

As well as ^{187}Re decay to ^{187}Os ($t_{½}$ = 41.6Ga), the ^{190}Pt-^{186}Os decay scheme is becoming increasingly utilised in geochemical interpretation of crustal, mantle and extraterrestrial-derived rocks due to improvements in analytical chemistry. ^{190}Pt decays to ^{186}Os with a half life of *c.* 450Ga (Cook *et al.*, 2004). Despite the low atomic abundance of ^{190}Pt (0.01292%; Morgan *et al.*, 2002) measurable differences in $^{186}Os/^{188}Os$ have been documented between the present-day $^{186}Os/^{188}Os$ ratio for DMM (0.119835±1; Walker *et al.*, 1997; Brandon *et al.*, 2000) and intraplate magmas. For example, taking into account post-crystallisation in-growth, radiogenic $^{186}Os/^{188}Os$ have been measured in Noril'sk intrusion ores (up to 0.119849±5; Walker *et al.*, 1997), Hawaiian picrites (up to 0.119848±3; Brandon *et al.*, 1999), Gorgona Komatiites (up to 0.119847±4; Brandon *et al.*, 2003) and in low Pt/Os iridosmine grains thought to be derived from Klamath Mountain peridotites (up to 0.119856±1; Bird *et al.*, 1999; Meibom and Frei, 2002). Additionally these radiogenic $^{186}Os/^{188}Os$ ratios have been consistently measured on samples that have coupled supra-chondritic γOs. Positive correlations between $^{186}Os/^{188}Os$ and $^{187}Os/^{188}Os$ indicate that a common theme is applicable to all magmas with radiogenic Os signatures; their mantle sources contain high time-integrated $^{190}Pt/^{188}Os$ and $^{187}Re/^{188}Os$.

In contrast to the 1.27Ga Mackenzie LIP, modern OIB are enriched in ^{187}Os by >20% relative to chondrites (e.g., Hauri and Hart, 1993; chapter 4). These enrichments, if coupled with radiogenic $^{186}Os/^{188}Os$ have to be produced by a geologically feasible process. A number of terrestrial reservoirs possess high Re/Os and Pt/Os ratios which may be able to generate the large variations in $^{186}Os/^{188}Os$

and $^{187}Os/^{188}Os$ through time. Going from the surface to the interior of the Earth, these reservoirs include:

- Continental crustal material
- Hydrogenous ferro-magnesian nodules and crusts in the ocean basins
- Sulphide-rich lithologies (sulphide ore horizons, anhydrite, recycled sulphide-rich sediments)
- Mafic veins in the lithosphere, and possibly material preserved in the asthenosphere, as (garnetiferous-) pyroxenites and eclogites
- Outer core contributions to the lower mantle that are subsequently transferred to the surface

A model for radiogenic ^{187}Os-^{186}Os through core-mantle interaction and incorporation into mantle plumes has been outlined in detail elsewhere (Walker *et al.,* 1995; Widom and Shirey, 1996; Brandon *et al.,* 1999; Puchtel *et al.,* 2001) and has been invoked for the Siberian Traps (Walker *et al.,* 1997), Hawaiian lavas (Brandon *et al.,* 1999), iridosmine grains (Bird *et al.,* 1999) and Gorgona Island Komatiites (Brandon *et al.,* 2003). Core-mantle interaction models to explain radiogenic $^{186}Os/^{188}Os$ in these rocks have met with problems because of the lack of measurable W isotope anomalies in 'plume' samples (Schersten *et al.,* 2004). However, ^{182}W isotopic anomalies are critically dependant upon timing of core formation because of the short half life of the parental ^{182}Hf radionuclide. Also, there is doubt whether incorporation of ferromagnesian crustal materials directly, or mobilisation of high Re/Os and Pt/Os fluids into the mantle wedge could equally generate such enriched signatures given sufficient time (Baker and Krogh Jensen, 2004). Young ferro-magnesian crusts have highly elevated $^{187}Os/^{188}Os$ (0.52-1.06; Burton *et al.,* 1999b), Pt/Os (~150), variably radiogenic to unradiogenic $^{186}Os/^{188}Os$ (0.119829±1 to 0.119848±1; McDaniel *et al.,* 2004), but they also have low Re/Os (0.01). This means that in some circumstances, mixtures of this material with typical mantle peridotite could generate the observed, coupled ^{187}Os-^{186}Os enrichments in some OIB (Baker and Krogh Jensen, 2004).

A significant problem with interpreting coupled ^{187}Os-^{186}Os in CFB or layered mafic intrusions such as Noril'sk is the contribution from continental crust. Morgan *et al.* (2002) found that Sudbury igneous complex ores had highly radiogenic $^{186}Os/^{188}Os$ (up to 0.119867±2 (measured in dynamic mode)) and that this could be

explained by melting of country rock with radiogenic Os. Some continental crustal rocks have very high Re/Os and correspondingly radiogenic $^{187}Os/^{188}Os$ (>0.8 for lower continental crust; Saal *et al.*, 1998; 1.2-1.3 for upper crustal sediments; Esser and Turekian, 1993) and some crustal rocks also have high Pt/Os. For example a black shale analysed by Horan *et al.* (1994) from the Yukon, had an average Pt/Os ratio >22 corresponding to a $^{190}Pt/^{188}Os = 0.02$.

Evidence from the Muskox Intrusion suggests that the supra-chondritic γOs measured in some of the Os-rich horizons is the result of contamination by small amounts of upper Wopmay crust. In Fig. 5.37 the ^{187}Os-^{186}Os isotope systematics of Noril'sk ores, Sudbury ores, and abyssal peridotites are plotted with the range of Muskox Intrusion layered peridotite γOs.

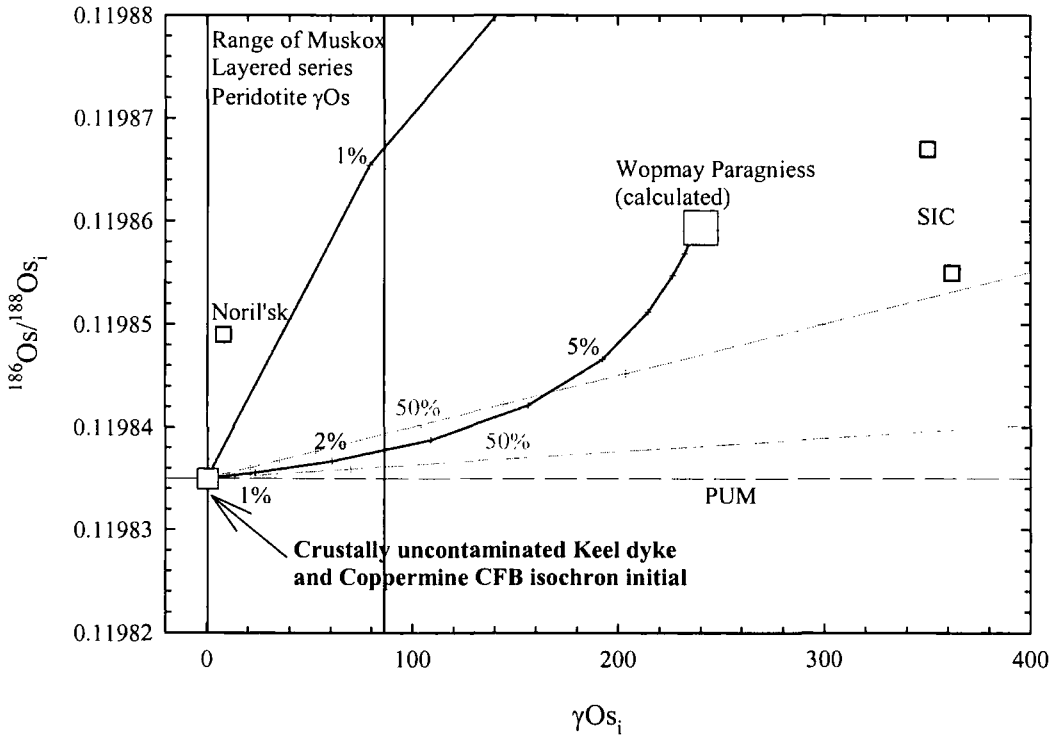

Fig. 5.37: γOs-$^{186}Os/^{188}Os$ relationships for large mafic intrusions including the Muskox intrusion, Noril'sk and the Sudbury Igneous Complex (SIC). The AFC modelling agrees with the melt mixing model in Fig 5.30. Noril'sk and Sudbury data from Walker *et al.* (1997) and Morgan *et al.* (2002). See text for details.

Solid-state mixing (dark grey) and melt A:FC (black, R=0.8, D_{Os} =15) models for 1270Ma melt mixtures of primitive mantle (1ppb Os, $^{187}Re/^{188}Os = 0.390$, $\gamma Os = 0$; $^{190}Pt/^{188}Os = 0.00174$; $^{186}Os/^{188}Os = 0.119832$), 1.8Ga Wopmay continental crust (0.2ppb Os, $^{187}Re/^{188}Os = 15.6$, $\gamma Os_{1270} = 237$, $^{190}Pt/^{188}Os$ ratio of 0.01, Calculated

initial $^{186}Os/^{188}Os$ = 0.119859) and 400Ma sulphide rich anhydrite sediments estimated from Ripley *et al.* (1999) and Horan *et al.* (1994) (0.4ppb Os, $^{187}Re/^{188}Os$ = 300, γOs = 3400, $^{190}Pt/^{188}Os$ ratio of 0.05, Calculated initial $^{186}Os/^{188}Os$ = 0.119933) are plotted in Fig. 5.37. Solid-state mixing models require unfeasibly large amounts of crust to explain coupled ^{187}Os-^{186}Os of layered intrusion. However, AFC models for crustal contamination suggest that:

- Only minor addition of old (>0.4Ga), relatively high Os (0.1-0.4ppb) abundance, high Re/Os, Pt/Os crustal rocks to mantle-derived magmas with PUM or DMM characteristics can explain the radiogenic $^{187}Os/^{188}Os$ and $^{186}Os/^{188}Os$ measured in layered mafic intrusions.
- Muskox samples have been modelled to show that as little as 2.5% crustal contamination (A:FC = 0.8) by local country rock can explain the elevated γOs of layered series peridotites. This degree of crustal contamination is predicted to generate difference in $^{186}Os/^{188}Os$ for high γOs dunites and chromites of only 9ppm (i.e., 0.119835 to 0.119844). Future work will be to analyse samples from the Muskox intrusion with supra-chondritic γOs for $^{186}Os/^{188}Os$ to assess whether these estimates, due solely to crustal contamination, are valid.

5.12 Summary

A number of features of the Mackenzie LIP suggest that it is the result of mantle upwelling when compared with typical ocean basin-forming or arc-related magmatism. The large volume of magma produced - the relatively short period of time measured for the entire magmatic event (Le Cheminant and Heaman, 1989; this study) - the presence of high MgO and Mg/Fe lavas in early phase of magmatism and subsequent tholeiitic basaltic magmatism - the uplift/subsidence history and topographic drainage and gravity structure of the region (e.g., Baragar *et al.*, 1996) which coincides with the focal point of Mackenzie dyke propagation (Ernst and Baragar, 1992) - all point toward a plume-impact and failed rifting origin for the Mackenzie LIP. However, the Os isotope systematics of the Mackenzie LIP have near-chondritic γOs_i for the event. There is no reason to invoke recycled oceanic crust and lithosphere in the source of Continental intraplate magmas subsequent to initiation of Archaean subduction (Shirey, 1997). Persistence of primordial stratification of Re and Os in the mantle (Walker *et al.*, 1994) or the possibility of

core-mantle interaction (Walker *et al.*, 1994, 1995; Brandon *et al.*, 1998) can also be rejected on the base of Re-Os isotope systematics of the Mackenzie LIP alone. In summary the intraplate magmatism in the Canadian Shield during the mid-Proterozoic was sourced by asthenospheric mantle domains characterised by near-chondritic Re/Os ratios and $^{187}Os/^{188}Os$.

- The Coppermine CFB is composed of a thick succession of lavas which evolve from picrites, basalts and andesites of the lower Copper Creek ultimately derived from melting in the garnet stability field to Husky Creek formation lavas generated almost exclusively by shallower spinel facies melting. This temporal evolution is consistent with plume-induced rifting during the formation of the Mackenzie LIP (e.g., Griselin *et al.*, 1997) and is possibly related to the opening of the Poseidon Ocean (Fahrig, 1987).
- Major- and trace-element and Re-Os isotope systematics of newly recognised picrites in the Copper Creek Formation of the Coppermine CFB are similar to younger Proterozoic and Phanerozoic equivalents (e.g., Shirey, 1997; Schaefer *et al.*, 2000) and trace elements suggest that in general the lavas have suffered <10% crustal assimilation.
- Re-Os isochron regressions for the whole suite of Coppermine CFB give an age of 1213+65/-39Ma. Samples that have been undisturbed by post crystallisation element mobility give a more precise age of 1284±13Ma. These ages are within error of unpublished U-Pb Concordia and give γOs initials representative of pre-crustal contamination that are slightly supra-chondritic ($\gamma Os = +2$).
- Major and trace element data for the Muskox intrusion indicate the controls of mineral fractionation (chromite + olivine + pyroxene ± plagioclase) of this major intrusive body.
- Trace element data in conjunction with petrographical observations indicate that post-solidification hydrothermal alteration was a significant factor in the compositional variation in layered series peridotites. Trace elements also indicate crustal contamination, although affecting the layered series units, was most prominent in the marginal and roof zones of the intrusion.
- Re-Os error-chron ages for the Muskox intrusion are younger than the U-Pb age for the intrusion (LeCheminant and Heaman, 1989). This disturbance reflects the

post-crystallisation hydrothermal alteration noted from trace element characteristics. Best estimate γOs for the Muskox intrusion come from the undisturbed Keel samples (+1.2).

- This study has strengthened the link between the Coppermine CFB and Muskox layered intrusion spatially, temporally and chemically and illustrates the important role crustal contamination plays in LIPs for modifying Re-Os isotope systematics of asthenospheric melts. Combined, the data from the Coppermine CFB and Muskox layered intrusion suggest an initial melt composition with 15-20% MgO from the garnet stability field indicating ~20% partial melting.
- CLM has had little impact in changing the asthenospheric mantle Re-Os compositions of these Mg-rich melts.
- Melting appears to have initiated quickly at ~1270Ma with the eruption of the lower Copper Creek Formation and emplacement of the Muskox intrusion. Subsequently emplacement of the Mackenzie dyke swarm ~1267Ma and eruption of the middle and upper Copper Creek formations ensued prior to more protracted eruption for the Coppermine CFB. Further lithospheric thinning may have produced Husky Creek formation melts in the spinel facies field. Although conjectural, the Mackenzie LIP may have been succeeded by anomalous magmatism in the form of a hotspot tail under the Greenland and Baltic shields generating the Gardar province and Jotnian sills which have similar to slightly older apparent ages (e.g., Buchan *et al.*, 2001; Upton *et al.*, 2003).
- The slightly supra-chondritic to chondritic initial ratios derived from the Coppermine CFB and Muskox layered intrusion indicate derivation from a mantle source which closely resembled enstatite or ordinary chondrite $^{187}Os/^{188}Os$ at 1270Ma.
- This finding is similar to Archaean and Proterozoic continental intraplate magmatism worldwide and suggests that the source responsible for these events has had chondritic proportions of highly siderophile elements since the early Archaean (e.g., Bennett *et al.*, 2002); on the basis of Re-Os isotope systematics alone it is difficult to advocate anything other than a primitive upper mantle source for the derivation of the Mackenzie LIP. This signature may be typical of continental LIPs that show evidence of large scale melting over broad areas in

short spaces of time and show that the input from recycled oceanic crustal material, CLM or interaction with the core-mantle boundary is limited.

- These results imply that the Re-Os isotope compositions of LIP provide valuable information on the evolution of the mantle and its constituent parts as a whole whilst OIB provide a more localised understanding of components residing within the mantle.

Chapter 6: Conclusions

6.1 Intraplate magmatism

Four case studies of intraplate magmatism have been presented in this thesis to investigate modification of intraplate magmas during transport and eruption, their mantle sources and to establish what intraplate magmatism can offer in understanding stratification and evolution of the Earth's mantle. They show that whilst modification of magmas during transport and eruption can dramatically alter the chemical signatures of mantle-derived magmas the recognition of these effects allow constraints on the mantle sources of intraplate magmatism. In turn, each of the case studies has allowed a number of new insights to be made into the nature of the mantle beneath them. In conjunction with earlier case studies of intraplate magmatism these new observations allow some comment on mantle stratification and evolution. In the following sections major observations arising from this thesis are summarised and areas of future work suggested.

6.2 Crustal processes acting on intraplate magmas

Interaction between magmas and crust can result in significant modification of the initial chemical inventory of mantle-derived magmas by assimilation or entrainment of this material. Different types of intraplate magma intersect different types of crust (e.g., oceanic or continental) that may result in very different geochemical effects during magmatic modification. Two other significant processes that can occur and may be important when performing geochemical studies on volcanic rocks are syn-eruptive processes and post-emplacement modification.

6.2.1 Post-emplacement modification

- Re-Os error-chron ages for the Muskox intrusion are imprecise but within error of the U-Pb age for the intrusion (LeCheminant and Heaman, 1989). Re or Os loss and gain after emplacement and crystallisation of the intrusion can explain the variable error-chron initials. Several studies have advocated post-emplacement mobilisation of Os to explain radiogenic $^{187}Os/^{188}Os$, high Os abundance layered

rocks in mafic layered intrusions (Marcantonio *et al.*, 1993; 1994). This work has been unable to conclusively confirm or reject this process for the Muskox Intrusion, but does illustrate that small amounts of crustal contamination can equally explain the trend to high Os abundance radiogenic $^{187}Os/^{188}Os$ layered series cyclic units.

- Highly negative initial γOs values are calculated for Coppermine CFB and Muskox Intrusion rocks presented in this study. These signatures are the result of post-emplacement element mobility of Re. Post-emplacement hydrothermal alteration is also tracked by variation in large ion lithophile element abundances.

6.2.2 Syn-eruptive Re degassing

- A key observation from this thesis is that clear evidence exists for the degassing of Re which supports recent suggestions that this may be an important process from Re abundances of MORB glasses (e.g., Sun *et al.*, 2003a). Sub-aerially erupted alkaline lavas from the Western Canary Islands of La Palma and El Hierro trend to exceptionally high Cu/Re ratios in Re/Yb-Cu/Re space – a result predicted from degassing of Re. Compared with tholeiitic lavas and glasses from Hawaii (Bennett *et al.*, 2000; Norman *et al.*, submitted) the Western Canary alkaline lavas indicate more extensive degassing because of their elevated Cu/Re ratios.
- Mid-Proterozoic Coppermine CFB tholeiitic lavas show evidence for degassing that can be resolved from post-emplacement alteration. The fact that Coppermine tholeiites lie on the Western Canary Island lava Re-degassing trajectory suggests that degassing processes similar to those acting on El Hierro and La Palma lavas rather than modern-day tholeiitic equivalents (Hawaii, Mid-Ocean Ridge Basalts) are responsible for the Re-variations in Coppermine CFB lavas.

6.2.3 Fractional crystallisation processes – Re and Os

- Findings from this study indicate that Re loss during degassing prevents use of Re/Os ratios in sub-aerially erupted lavas to infer degrees of partial melting. Re and Os can also be substantially fractionated by crystallisation of melts. The coupled variation of Re and TiO_2 in La Palma and El Hierro lavas indicates that

Re is closely associated with titano-augite and Fe-Ti oxides. In Coppermine CFB lavas higher Re concentrations are also measured in lavas with high TiO_2 concentrations. Rocks with higher TiO_2 have generally higher Re contents: this might suggest that the Re inventory of these rocks is not as heavily depleted as other sub-aerially erupted rocks because Re is trapped within TiO_2 rich mineral phases that crystallised prior to eruption.

- Os is a compatible element and correlates positively with Ni and Cr. This could suggest that it is retained most effectively in early crystallised chromite and olivine phases during fractional crystallisation. However Os has a low bulk partition coefficient in olivine (0.4 to 0.6; Puchtel *et al.*, 2004) but experimental data shows that Os strongly partitions into sulphide phases ($D_{Sulf\text{-}Sil}$ = 0.6 to 3 $\times 10^4$; e.g. Fleet *et al.*, 1996; 1999a; 1999b). High Os abundances are found in an andesite glass from the Coppermine CFB and in the Muskox Intrusion main chromitite reef. In the case of the Muskox Intrusion chromitite reef there is clear evidence that chromitites contain sulphide micro-inclusions (Irvine, 1977). On the basis of this evidence, as well as positive correlations between Os and compatible elements in Western Canary Island lavas, Os is likely to be controlled by sulphide. Therefore the results of this study support previous examination of magmatic systems and the compatibility of Os in sulphides (e.g., Hart and Ravizza, 1996; Schaefer *et al.*, 2000; Puchtel *et al.*, 2004). The retention of Os and other siderophile elements in sulphides explains the 'nugget' effect, especially in low Os concentration lavas.

6.2.4 He degassing and crustal contamination

- It has previously been demonstrated that significant degassing of He from mantle-derived magmas renders them more susceptible to crustal contamination (Hilton *et al.*, 1995). This finding is corroborated by trace element, oxygen isotope and helium isotope relationships in central Icelandic lavas, and demonstrates that crustal assimilation can significantly affect helium isotope ratios because of prior degassing of magmas.
- A similar result is found in La Palma and El Hierro clinopyroxene phenocrysts which, in some cases, are in $^3He/^4He$ disequilibrium with olivines within the same

lava flow. Relationships between $\delta^{18}O$ and $^{3}He/^{4}He$ for these clinopyroxene require less than 1% addition of radiogenic crustal-derived He to explain their lower $^{3}He/^{4}He$.

- Lower $^{3}He/^{4}He$ with low [He] is also an inherent feature of olivines from continental intraplate alkaline volcanics (CIAV) which were mostly emplaced as hypabyssal plugs and sills and so are unlikely to be the result of degassing and subsequent crustal contamination.
- These observations show that He is a highly sensitive tracer of crustal contamination in He-degassed mantle derived magmas. The evidence of He-degassing in sub-aerially and sub-glacially erupted lavas presented in this thesis supports previous studies that have indicated that the pressure of the overlying water column is the primary control on He and Re degassing (Hilton *et al.*, 2000b; Sun *et al.*, 2003a,b,c).
- He degassing of mantle-derived magmas and subsequent addition of crustal-derived radiogenic He can obscure the primary mantle source $^{3}He/^{4}He$ signatures. In some cases, degassing lowers [He] (e.g., Chapter 2, Chapter 4, Hilton *et al.*, 1995). The highest $^{3}He/^{4}He$ ($>30R_A$) have been measured in olivine phenocrysts from sub-aerially erupted OIB and CFB lavas. Degassing of He from parental melts of sub-aerially erupted lavas without addition of crustally derived radiogenic He explains why they have high $^{3}He/^{4}He$ and lower absolute [He] compared with submarine eruptions of MORB. The olivines with high $^{3}He/^{4}He$ in OIB or CFB may be related to He loss in the parental melt during simultaneous fractional crystallisation of these phases.
- These arguments suggest that helium isotope data sets should be thoroughly assessed for the effects of degassing and crustal contamination before detailed statistical analyses of the helium isotope data are performed.

6.2.5 Evidence of crustal contamination from $\delta^{18}O$ and $^{187}Os/^{188}Os$

- In central Iceland and the North Atlantic igneous province (NAIP) the low $\delta^{18}O$ measured in some phenocrysts and glasses reflects crustal contamination. However, in the case of central Icelandic samples, those with the most radiogenic $^{87}Sr/^{86}Sr$ and unradiogenic $^{143}Nd/^{144}Nd$ have some of the highest $^{3}He/^{4}He$ ratios.

This relationship suggests that radiogenic $^{87}Sr/^{86}Sr$ and unradiogenic $^{143}Nd/^{144}Nd$ originate from a component in the Icelandic mantle. Such relationships make identifying crustally contaminated samples on the basis of $^{87}Sr/^{86}Sr$ and $^{143}Nd/^{144}Nd$ difficult and allow the possibility that some low $\delta^{18}O$ measured in some central Icelandic lavas may be mantle-derived.

- The effect of crustal contamination in CFB and LIP is traceable because of the large contrasts between ancient crustal materials and mantle-derived magmas. Layered series peridotites from the Muskox Intrusion possess a wide range of initial γOs which can be explained by between 2.5-4% crustal contamination by lower or upper crustal gneiss with concomitant fractional crystallisation. Crustal contamination is corroborated by trace element variations in Muskox Intrusion cyclic units, S isotope variations (Sasaki, 1969) and evidence of extensive interaction around the marginal zones of the intrusion (Francis, 1995). This suggests that only small amounts of fractional crystallisation and crustal contamination are required to generate large variations in γOs and by inference $^{186}Os/^{188}Os$ ratios. Crustal materials, especially sulphide-rich sediments, can contain elevated Pt/Os ratios which would generate radiogenic $^{186}Os/^{188}Os$ ratios through time. This suggests that some high $^{186}Os/^{188}Os$ signatures in LIP (e.g., Noril'sk, Walker *et al.*, 1997) could result from crustal contamination.

6.3 Mantle sources of intraplate magmatism

6.3.1 Continental lithospheric mantle as a $^{3}He/^{4}He$ reservoir (Chapter 3)

- Previous studies have evaluated the role of continental lithospheric mantle (CLM) in the sources of intraplate magmas and indicate that this reservoir is not likely to be a significant source of intraplate magmas (e.g., Pearson and Nowell, 2002). Gautheron and Moriera (2002) have also summarised the $^{3}He/^{4}He$ composition of Proterozoic circum-cratonic CLM. This thesis addresses the lack of Archaean cratonic peridotites in the CLM $^{3}He/^{4}He$ dataset. The large $^{3}He/^{4}He$ variations between Archaean cratonic and Proterozoic circum-cratonic peridotites indicate that the CLM maybe more heterogeneous than previously thought. Archaean cratonic peridotites possess low time integrated $^{3}He/(U + Th)$ and low $^{3}He/^{4}He$

ratios which are lower than Proterozoic CLM and provides substantive evidence that the CLM has more radiogenic $^3He/^4He$ than DMM.

- This study also presents the first $^3He/^4He$ and [He] measurements for eclogite, a minor but geochemically important constituent of the CLM. The low $^3He/^4He$ ratios of eclogite minerals indicates that ancient eclogite/pyroxenite lithologies represent a very low time integrated $^3He/(U+Th)$ reservoir in the mantle. Magmas derived from mixed CLM pyroxenite-peridotite sources will be characterised by low $^3He/^4He$. Systematically low $^3He/^4He$ have been measured in a number of HIMU OIB worldwide (e.g., Kurz *et al.*, 1982; Hanyu and Kaneoka, 1997; Hilton *et al.*, 2000).

6.3.2 Continental intraplate alkaline volcanics (CIAV; Chapter 3)

- Trace elements, Sr, Nd, He and O isotope signatures for CIAV from Canada, South Africa and Uganda indicate the involvement of CLM and a common asthenospheric mantle source component in their origin with low $^3He/^4He$. CIAV have $^3He/^4He$ ratios that are systematically more radiogenic than MORB. The CIAV studied here do not sample a high-time integrated $^3He/(U+Th)$ reservoir in the shallow mantle. No evidence has been found to support a shallow-derived LONU reservoir suggested by Anderson (1994; 1995; 2001).
- There is no evidence for a low $\delta^{18}O$-mantle for any of the CIAV analysed in this study despite evidence of a HIMU source in these types of intraplate magmatism (Janney *et al.*, 2002).

6.3.3 Iceland and the North Atlantic Igneous Province (Chapter 2)

- Spatial distribution of $^3He/^4He$, systematic variation between Sr, Nd and $^3He/^4He$ and depth of melting indicate that Icelandic magmatism can be explained by admixtures of DMM and recycled oceanic crustal components with low $\delta^{18}O$.
- For NAIP magmatism, high $^3He/^4He$ and mantle-like $\delta^{18}O$ signatures cannot be explained in a similar manner to Icelandic magmatism. This could indicate that either (i) high degrees of partial melting during CFB magmatism dilute the isotopic and elemental contributions of enriched mantle domains recognised in Iceland or (ii) that these domains were not sampled by NAIP magmas.

- Substantial contribution from a [He]-rich reservoir with high time integrated $^{3}He/(U+Th)$ is common to all Icelandic and Palaeogene NAIP magmatism despite their Sr, Nd, Pb and O isotopic compositions supporting ^{3}He-recharge models to mantle reservoirs (e.g., Stuart *et al.* 2003).

6.3.4 The Western Canary Islands (Chapter 4)

- Alkaline lavas from the islands of La Palma and El Hierro are derived from low degrees of partial melting of a mantle source which cannot be replicated using anhydrous mantle melting models.
- Low $\delta^{18}O$ in La Palma lavas and $^{87}Sr/^{86}Sr$, $^{143}Nd/^{144}Nd$, and Pb isotopes in the Western Canary Islands as a whole do not correlate with indices of crustal contamination or fractional crystallisation and indicate that correlations between these isotopes reflect mantle source mixing.
- $^{187}Os/^{188}Os$ in lavas from El Hierro correlate poorly with assimilation and fractional crystallisation models. These lavas possess $^{187}Os/^{188}Os$ and high Os abundances retaining the isotopic compositions of their mantle source.
- El Hierro and La Palma lavas generally lie at either end of the isotopic arrays for Western Canary Islands lavas and their phenocrysts have very different $\delta^{18}O$ signatures. The radiogenic $^{187}Os/^{188}Os$ and mantle-like $\delta^{18}O$ of El Hierro lavas and the low $\delta^{18}O$ and more radiogenic $^{87}Sr/^{86}Sr$, $^{143}Nd/^{144}Nd$ and $^{206}Pb/^{204}Pb$ isotopic composition of La Palma lavas indicates that the mantle sources of the two islands are quite different. El Hierro is derived from a mantle source with higher time integrated Re/Os. La Palma lavas sample a mantle source with higher time integrated U/Pb, Rb/Sr, Sm/Nd and lower $\delta^{18}O$ than El Hierro.
- La Palma and El Hierro lavas do not correlate as well as EMI OIB like Hawaii in $^{206}Pb/^{204}Pb$-$^{187}Os/^{188}Os$ isotope space and indicate an isotopically variable mantle source is present beneath the Western Canary Islands.
- The isotopic differences between El Hierro and La Palma can be explained by different mixtures of recycled oceanic crustal material into the mantle source of Western Canary Island volcanism. The more silica-undersaturated nature of El Hierro lavas also suggests that pyroxenite-peridotite mantle sources can best

explain the isotopic and elemental variations seen within and between El Hierro and La Palma lavas. The precursor of peridotite-pyroxenite sources is likely to be a mixture of young (<1.2Ga) recycled oceanic crust and the mantle which contains a FOZO/PHEM/C-like component.

- Olivine phenocrysts in lavas from El Hierro and La Palma that have not experienced crustal contamination possess $^{3}He/^{4}He$ ratios that lie within the 95% confidence limits of MORB $^{3}He/^{4}He$ ratios. However the most extreme $^{3}He/^{4}He$ values for phenocrysts from La Palma ($9.7R_A$) and El Hierro ($11.8R_A$) that are presented in this study lie outside the 95% confidence limits of MORB $^{3}He/^{4}He$ ratios. He appears to be decoupled from O, Sr, Nd, Os and Pb isotope systematics and supports the notion of ^{3}He-recharge to mantle source regions beneath intraplate magmas (e.g., Stuart *et al.*, 2003).

6.3.5 The Mackenzie LIP (Chapter 5)

- A Re-Os isochron regression for the whole suite of Coppermine CFB gives an error-chron age of 1213+65/-39Ma. When the dataset is filtered for samples which have suffered post-emplacement element mobility a regression age (1284±13Ma) within error of the U-Pb age for the Muskox Intrusion is obtained (1270±4Ma; LeCheminant and Heaman, 1989). The Re-Os isochron regressions yield γOs initials representative of pre-crustal contamination that are slightly supra-chondritic ($\gamma Os = +2.0\pm0.1$) and similar to the initial γOs of the Muskox keel dyke ($\gamma Os = +1.2\pm0.3$).
- This study has strengthened the link between the Coppermine CFB and Muskox layered intrusion temporally and chemically and illustrates the important role crustal contamination plays in LIPs for modifying Re-Os isotope systematics of asthenospheric melts. Combined, the data from the Coppermine CFB and Muskox layered intrusion suggest an initial melt composition with 15-20% MgO from the garnet stability field and corresponds to ~20% partial melting.
- CLM has had little impact in changing the asthenospheric mantle Re-Os compositions of these Mg-rich melts.
- Melting appears to have initiated quickly at ~1270Ma with the eruption of the lower Copper Creek Formation and emplacement of the Muskox intrusion.

Subsequently emplacement of the Mackenzie dyke swarm ~1267Ma and eruption of the middle and upper Copper Creek formations ensued prior to more protracted eruption for the Coppermine CFB possibly with lithospheric thinning producing Husky Creek formation melts in the spinel facies.

- Large $^{187}Os/^{188}Os$ isotope variations measured in the Muskox layered series can be explained by assimilation of upper and/or lower crust. In conjunction with near-chondritic γOs initials it seems that despite being one of the largest LIP events on record, there is no evidence for involvement of material derived from the core-mantle boundary or recycled oceanic crustal contributions.

6.4 Intraplate magmatism – mantle stratification and evolution

From the case studies presented in this thesis some first-order observations may be made regarding the Earth's mantle, its stratification and evolution.

- A shallow high time integrated $^{3}He/(U+Th)$ layer or 'perisphere' with LONU characteristics beneath the lithosphere has been proposed to account for the extreme $^{3}He/^{4}He$ characteristics of OIB and CFB (Anderson, 1995). CIAV originate from the boundary between the CLM and the asthenosphere (e.g., Foley *et al.*, 1992; Wilson *et al.*, 1995; Janney *et al.*, 2002) – the proposed site of LONU. Because the CLM is ruled out as a high $^{3}He/^{4}He$ source, the asthenosphere could be the only place where LONU might exist. However there is no evidence for a LONU source in this study. CIAV have $^{3}He/^{4}He$ ratios that are more radiogenic than MORB. The CIAV studied here do not sample a high-time integrated $^{3}He/(U+Th)$ reservoir in the shallow mantle.
- The He, O, Sr and Nd isotope compositions of lavas from central Iceland indicate that these mantle-derived magmas sample a heterogeneous mantle source. The mantle source beneath Iceland is characterised by helium recharged depleted mantle (HRDM) and enriched mantle components with variable $^{3}He/^{4}He$ ($\geq$MORB) and low $\delta^{18}O$. These lines of evidence support arguments by Stuart *et al.* (2003) of minor contributions from the lower mantle in the guise of ^{3}He addition as well as contributions from young (Palaeozoic; Thirlwall *et al.*, 2004) recycled oceanic crust. There is no evidence of recycled crustal contributions to

NAIP magmatism from $\delta^{18}O$ of olivines but these lavas also adhere to a HRDM model (e.g., Stuart *et al.*, 2003).

- The Western Canary Island lavas also appear to fit a ^{3}He-replenishment model to explain their high and MORB-like $^{3}He/^{4}He$. However, unlike Iceland or NAIP lavas, the $^{3}He/^{4}He$ ratios of Western Canary Island lavas are only slightly elevated with respect to MORB $^{3}He/^{4}He$. This difference might correlate with the estimated buoyancy flux beneath different OIB.
- The variations in $^{3}He/^{4}He$, $\delta^{18}O$, $^{87}Sr/^{86}Sr$, $^{143}Nd/^{144}Nd$, $^{187}Os/^{188}Os$ and $^{206}Pb/^{204}Pb$ isotope compositions of Western Canary Island lavas provide convincing evidence for similar but older mantle sources to Icelandic lavas. There is evidence for recycled oceanic crust of variable age ($\leq$1.2Ga) with variable $\delta^{18}O$ and Rb/Sr, Sm/Nd, U/Pb and Re/Os ratios in the sources of the Western Canary Islands. In addition, there is a component in Western Canary Island lavas that is also common to OIB world-wide; the so-called FOZO, PHEM, or C component (Hart *et al.*, 1992; Farley *et al.*, 1992; Hauri *et al.*, 1994; Hanan and Graham, 1996).
- The variations measured within and between El Hierro and La Palma are best explained by a highly heterogeneous mantle source beneath the Western Canaries. In this thesis the concept of a pyroxenite-peridotite source is preferred to explain this variation.
- The slightly supra-chondritic to chondritic γOs initials derived from the Coppermine CFB and Muskox layered intrusion indicate derivation from a mantle source which closely resembled enstatite or ordinary chondrite $^{187}Os/^{188}Os$ at 1270Ma.

6.5 Isotopic taxonomy of OIB, universal relations in intraplate magmatism?

6.5.1 Background to the 'fifth mantle component'

Four mantle components with variable chemical characteristics have been recognised in OIB (White, 1985; Allegre and Turcotte, 1985) which were named by Zindler and Hart (1986) as DMM, HIMU, EMI and EMII. The four components can be plotted so that they define a tetrahedron in which multi-component mixing can be

tracked. Original distinction of these mantle components was made on the basis of Sr, Nd and Pb isotope characteristics and subsequently enhanced through recognition of trace element ratio variations (e.g., Weaver, 1991a,b). To assess whether four-endmember mantle components were sufficient to explain the OIB Sr-Nd-Pb isotope dataset, Hart *et al.* (1992) performed principle component analysis on a subset of OIB Sr-Nd-Pb data and discovered that many islands did not conform to addition of a DMM component and instead converged to a focal zone (FOZO) within the tetrahedron defined by the four main components. Hart *et al.* (1992) explained this variation in one of two ways. First that the FOZO component represents a mix of DMM and HIMU. Second that FOZO represents a discrete mantle component; they even suggest that the depth of origin for FOZO was beneath the upper mantle (>670km).

Hart *et al.* (1992) further suggested that high $^{3}He/^{4}He$ was implicitly associated with FOZO and as such ruled out mixtures of DMM and HIMU (their model 1) because neither DMM- or HIMU-derived melts (e.g., MORB and extreme HIMU OIB) are characterised by high $^{3}He/^{4}He$. Following from this and related work (Hauri *et al.,* 1994), Farley *et al.* (1992, primitive helium mantle or PHEM) and Hanan and Graham (1996; common component or C) also proposed a fifth discrete mantle component in the mantle tetrahedron. Farley *et al.* (1992) and Farley and Craig (1992) showed that islands with low $^{3}He/^{4}He$ appeared to plot towards the FOZO component, whilst the proposed PHEM component, lying in the centre of the tetrahedron, provided better fits to the high $^{3}He/^{4}He$ islands, suggesting that a PHEM and not a FOZO component was required to explain OIB compositions; a claim hotly contested by Hart *et al.* (1992b) in their reply. Hanan and Graham (1996) defined the component 'C' solely on the basis of MORB data and considered this component to be the same as PHEM and FOZO and reside in the lower mantle. The same observation is true to all of these models; that the C, PHEM or FOZO component reflect a lower mantle contribution implicitly associated with high $^{3}He/^{4}He$ whilst EMI, EMI, HIMU and DMM components reside in the uppermost mantle.

6.5.2 Western Canary Islands and Iceland in the context of isotopic taxonomy

Hilton *et al.* (1999) found that SEL97, a mid-Miocene lava from Iceland with high $^3He/^4He$ ($37.7R_A$) lay within the range of the fifth mantle component (C/PHEM and/or FOZO) and proposed that this sample best approximated this common mantle component. The similarities between SEL 97 and NAL-625 (Chapter 2) suggests that some central Icelandic lavas might also approximate to this mantle component. The finding in Chapter 2 that Icelandic lavas show similar ^3He-recharge to Baffin Island picrites (Stuart *et al.* 2003), resulting in lavas with *both* DMM and C/PHEM/FOZO characteristics having elevated $^3He/^4He$, casts some degree of doubt on the concept that high $^3He/^4He$ and the fifth mantle component are intrinsically linked. Furthermore, glasses with low $\delta^{18}O$ in central Iceland (group 2 glass, Chapter 2), which lie close to SEL 97 in Sr-Nd isotope space have MORB-like $^3He/^4He$ suggesting that the FOZO/PHEM/C component is an artefact of ^3He-recharge of variable mantle compositions beneath Iceland.

Lavas from El Hierro and La Palma plot within the range of the proposed FOZO and C components in Sr-Nd-Pb isotope space (Fig 4.34). The majority of El Hierro and La Palma lavas possess phenocrysts which retain MORB-like $^3He/^4He$ signatures. Mantle sources for these lavas can still be interpreted in terms of a ^3He-recharge model because some have elevated $^3He/^4He$ (up to $11.8R_A$). A recharge model is also required for HIMU sources because of the low $^3He/^4He$ anticipated from radiogenic ^4He and because HIMU sources are thought to represent subducted oceanic crust which possesses low $^3He/^4He$ even prior to entrainment within the mantle (Staudacher and Allègre, 1988). On this basis it is very difficult to link the $^3He/^4He$ ratios of any OIB source a universal fifth mantle component. Instead it would seem that high $^3He/^4He$ is better correlated to ocean islands with high buoyancy flux or growth rates (i.e. those melt regions receiving large ^3He recharge fluxes). ^3He-recharge, whilst implying high $^3He/^4He$ for the lower mantle contribution (e.g., Stuart *et al.*, 2003), may also occur via diffusion of MORB-like $^3He/^4He$ into mafic mantle sources that has initially low $^3He/^4He$, over time. Very low $^3He/^4He$ mafic mantle components do exist in the mantle (e.g., eclogite, Chapter 3). He diffusivity in the mantle would explain the paucity of mantle-derived very

low $^{3}He/^{4}He$ that would be expected with HIMU or EM mantle signatures in OIB providing yet more evidence for He-decoupling in the mantle.

In addition to the constraints offered by He-Sr-Nd-Pb isotope systematics in deciphering the mantle contributions to OIB, the Western Canary Island suite offers an opportunity to use Os and O isotopes to investigate the origin of the proposed fifth mantle component. The low $\delta^{18}O$ in La Palma lavas and the positions they occupy in Sr-Nd isotope space are similar to group 2 glasses from central Iceland that also possess low $\delta^{18}O$. Both central Icelandic glasses and La Palma lavas possess MORB-like $^{3}He/^{4}He$. El Hierro lavas that lie within the field of FOZO in Sr, Nd and Pb isotope space have mantle-like $\delta^{18}O$ and generally MORB-like $^{3}He/^{4}He$. The MORB-like $^{3}He/^{4}He$ can be explained by MORB-like He recharge to mantle components beneath both Iceland and the Western Canary Islands. The low $\delta^{18}O$ in La Palma and group 2 Icelandic glasses appears to correspond to a HIMU-like component (i.e. recycled hydrothermally altered oceanic crust). If related to FOZO/PHEM/C this component must be heterogeneously distributed otherwise low $\delta^{18}O$ would be expected in all FOZO-like components. Group 2 glasses and most Icelandic lavas lie to the left of the FOZO component in Fig 4.34 because they have unradiogenic $^{206}Pb/^{204}Pb$ (<18.5; Seth *et al.*, 2004). This means that the low $\delta^{18}O$ component, if HIMU, must be much younger beneath Iceland than the HIMU component beneath La Palma (e.g., young HIMU of Thirlwall, 1997) or must have a very low U/Pb ratio. Like El Hierro lavas, Icelandic samples SEL-97 and NAI-625 which lie in the field of FOZO or C, do not possess low $\delta^{18}O$. On this basis it appears that FOZO/PHEM or C possess mantle-like $\delta^{18}O$. To explain La Palma lavas and central Iceland group 2 glasses, this component must variably mix with low $\delta^{18}O$ components which lie heterogeneously within the mantle. Discounting OIB whose $\delta^{18}O$ is generally explained in terms of crustal contamination (e.g., Iceland, Gran Canaria, Tristan Da Cuhna, Hawaii) there is exceptionally limited variation in $\delta^{18}O$ for OIB globally (Fig. 4.13). This limited variation further suggests that the proposed fifth mantle component, which is common in all these OIB, does not possess inherently low $\delta^{18}O$.

It is difficult to define the exact $^{187}Os/^{188}Os$ composition of the end-member component in OIB unlike for ancient rocks because precise initials cannot generally

be generated from isochrons and because of the low Os concentrations of most OIB. However, the global OIB Pb-Os isotope systematics reveals a common mixing component to which all data converge (Fig 4.35). This component has $^{206}Pb/^{204}Pb$ very similar to the proposed FOZO, C or PHEM component and is best represented by carbonaceous chondrite to slightly supra-chondritic primitive upper mantle, enstatite or ordinary chondrite like $^{187}Os/^{188}Os$ compositions (0.1270 to 0.1296; Meisel *et al.*, 1996; 2001; Walker *et al.*, 2001). The universal component for OIB in Pb-Os isotope space cannot be explained by DMM. This suggests that the universal (C/PHEM/FOZO) component in OIB has a $^{187}Os/^{188}Os$ similar to that predicted from Os isotope evolution curves of Proterozoic and Archaean mantle-derived magmatism (see Chapter 5). In the absence of a contribution from the outer core (see section 4.10), this observation suggests that a component common to modern-day OIB and Proterozoic to Archaean CFB has existed in the mantle since at least the geological record began.

6.5.3 $^{186}Os/^{188}Os$-$^{187}Os/^{188}Os$ and a universal mantle component

Some studies have suggested that radiogenic $^{186}Os/^{188}Os$ might be coupled with radiogenic $^{187}Os/^{188}Os$ and with high $^{3}He/^{4}He$ (Brandon *et al.*, 1999). Furthermore it has been proposed that $^{186}Os/^{188}Os$ ratios measured in OIB record interaction of the lower mantle and outer core resulting in a 'zone of convergence' in $^{186}Os/^{188}Os$-$^{187}Os/^{188}Os$ space (Brandon *et al.*, 2003). It has already been illustrated that outer core addition to the lower mantle, and subsequently intraplate magmatism, does not fit well with Os-Pb isotope systematics of OIB (Fig 4.35). It is also apparent that, like Sr, Nd, Pb and possibly O isotopes, the universal (C/PHEM/FOZO) Os isotope component is not always coupled with He isotopes (Fig 4.40).

Apart from possible correlations between $^{3}He/^{4}He$ and $^{186}Os/^{188}Os$ in Hawaiian lavas (Brandon *et al.*, 1999), studies of coupled $^{186}Os/^{188}Os$-$^{187}Os/^{188}Os$ in West Greenland Picrites and Icelandic lavas with high $^{3}He/^{4}He$ do not reveal (i) radiogenic $^{186}Os/^{188}Os$ for these lavas or (ii) correlation between $^{186}Os/^{188}Os$, $^{187}Os/^{188}Os$ or $^{3}He/^{4}He$ (Pearson *et al.*, 1999; Brandon, 2002). These studies indicate that the $^{186}Os/^{188}Os$ of the proposed fifth mantle component, like that of $^{187}Os/^{188}Os$, is near-chondritic. The lack of radiogenic $^{186}Os/^{188}Os$ (Pearson *et al.*, 1999; Brandon, 2002)

in extreme $^{3}He/^{4}He$ magmas (e.g., Stuart *et al.*, 2003) and the existence of $^{186}Os/^{188}Os$ anomalies in Hawaiian lavas with high $^{3}He/^{4}He$ could be related to decoupling of He from other isotopic schemes. Hawaiian lavas conform to mixtures with an EMI component in Os-Pb isotope space and it maybe that this component has elevated $^{186}Os/^{188}Os$ whilst the common component has chondritic $^{186}Os/^{188}Os$. Furthermore, the fact that this component is common to all OIB with Os >50ppt but with wildly different buoyancy fluxes suggests it is distributed throughout the Earth's mantle and is not solely derived from the lower mantle or the core-mantle boundary region.

6.5.4 Relationships of OIB and LIP

Distribution of a universal component throughout the mantle that feeds OIB and possibly some anomalous mid-oceanic ridge sections (e.g., Hanan and Graham, 1996) could indicate that the correlations in multi-isotopic space are best explained by banded or veined mantle where pyroxenite-peridotite mixing takes place and where variable ^{3}He-recharge also occurs; a modified version of the marble-cake mantle of Allègre and Turcotte (1986). In the absence of shallow mantle sources (Chapter 3), high $^{3}He/^{4}He$ compositions are likely to be related to lower mantle with high time integrated $^{3}He/(U+Th)$. Therefore the observation of high $^{3}He/^{4}He$ and FOZO-like compositions, without substantiated geophysical models, provides weak argument to invoke any particular mechanism (e.g., a mantle plume). On the other hand, pyroxenite-peridotite sources whose precursors are recycled lithospheric and crustal components and the mantle, which appear to contain a universal mantle component, will retain isotopic heterogeneity (O, Rb/Sr, Sm/Nd, Re/Os, Pt/Os, U/Pb) over variable length-scales. During melt extraction, the degree of partial melting will define the overall homogenisation of the pyroxenite-peridotite mixture.

At low degrees of partial melting pyroxenite signatures will become more obvious (e.g., OIB), whereas at high degrees of partial melting of a mixed pyroxenite-peridotite source, the pyroxenite signature is likely to become obscured (e.g., CFB/LIP). In addition to understanding OIB, such a model might explain the Fe-rich nature of early erupted picritic-basalts prior to the major onset of CFB volcanism. Furthermore such a model provides a working mechanism for

decompression melting through glacial isostasy or structural collapse of an Ocean island edifice. This type of sudden melting may be sampling variable pyroxenite-peridotite mixtures with variable melting solidi as opposed to melting of solely peridotite. This feature might explain the different chemical characteristics of melts thought to be generated by sudden decompression melting on Iceland and in the Western Canary Islands. Heterogeneous mantle (pyroxenite-peridotite) generated through passive mantle convection driven by plate tectonics could potentially provide a 'unified model' with which to place intraplate magmatism in context with the overwhelmingly simple plate tectonic theory.

There is clear evidence from the highly siderophile elements of LIP (e.g., Re and the platinum group elements) that mantle evolution best corresponds to an enstatite or ordinary chondrite accretionary source (Chapter 5). OIB provide evidence that a common component exists in the Earth's mantle and shows a common linkage between intraplate magmatism. These observations suggest that whilst plate tectonics generates mantle heterogeneity over different length scales, many forms of intraplate magmatism show chemical evidence for a universal component (C/PHEM/FOZO) in their sources. Oceanic crust is shown to subduct through the mantle transition zone (e.g., van der Hilst *et al.* 1997) indicating that the overall mass-balance requires flow from the lower to the upper mantle. As such, the universal (C/PHEM/FOZO) component may well reside partially in the lower mantle as suggested by Hart and others (Hart *et al.,* 1992; Hauri *et al.,* 1994; Farley *et al.,* 1992; Hanan and Graham, 1996). However, the chondritic $^{187}Os/^{188}Os$ ratio of this universal component provides further evidence, in conjunction with Proterozoic-Archaean Os mantle evolution curve, that overall, the Earth's mantle has a predominantly chondritic Re/Os ratio. The chondritic Os composition of the Earth's mantle could be the result of:

- Inefficient sequestration of siderophile elements during the Terrestrial core forming event
- Late-accretion of chondritic material to the Earth after core formation (e.g., Chou, 1978)

These hypotheses still require testing. However, it requires special pleading to account for chondritic siderophile element signatures from material transfer from the

outer core into the lower mantle. This is because of the effect such mixing is likely to have on Pb isotopic compositions of magmas and because this mixing cannot account for the most radiogenic $^{187}Os/^{188}Os$ measured in some OIB. As such it appears unlikely that the universal (C/PHEM/FOZO) component can be the result of core-mantle interaction.

In summary, evidence from CIAV and CLM is that it is highly unlikely for a high $^{3}He/^{4}He$ component to reside in the shallow mantle. Recharge of ^{3}He to OIB and CFB mantle reservoirs (e.g., Stuart et al., 2003), especially those with high buoyancy fluxes from a reservoir located in the mantle but that is decoupled from other isotopic tracing schemes provides the most logical solution to high $^{3}He/^{4}He$ in OIB and CFB and could suggest He-replenishment from the lower mantle. Radiogenic $^{186}Os/^{188}Os$ ratios measured in OIB and LIP may not necessarily be the result of core-mantle interaction. Other potential methods for generating correlated $^{187}Os/^{188}Os$-$^{186}Os/^{188}Os$ would be through addition of ancient continental crust with high Re/Os and Pt/Os in the case of continental intraplate magmas or addition of pyroxenite with high Re/Os and Pt/Os to oceanic intraplate magmatism (e.g., Smith, 2003). These results imply that the Re-Os isotope compositions of LIP provide valuable information on the evolution of the mantle and its constituent parts as a whole whilst OIB show that this universal component also exists in their mantle sources but is partially obscured by mixing with other heterogeneous mantle components at lower degrees of partial melting. The trend to extreme $^{87}Sr/^{86}Sr$, $^{143}Nd/^{144}Nd$, $^{187}Os/^{188}Os$ and $^{206}Pb/^{204}Pb$ in OIB suggest that they preserve evidence of localised components residing within the mantle whereas LIP do not because of the effect of sum upon melting and averaging (e.g., Meibom *et al.*, 2003). These observations provide further evidence for banded or veined mantle and the possible consequence of pyroxenite-peridotite sources (e.g., Allègre and Turcotte, 1986; Lassiter *et al.*, 1998).

6.6 Future work

The case studies in this thesis touch on a wide-range of issues in the ongoing research into intraplate magmatism. The issues relating directly to work in this thesis that require resolution and that can be realistically met are:

- Distribution and degassing of platinum group elements (PGE) - It has been demonstrated in this study that Re degasses during sub-aerial eruption in Western Canary Island lavas. The Western Canary Island suite provide an ideal opportunity to further constrain the impact of degassing on Re as well as the PGE (e.g., Ir, Pt, Pd). PGE studies of the ancient Coppermine CFB and Muskox Intrusion may also reveal information on the processes of degassing and element mobility on ancient continental magmatism.
- Pyroxenite-peridotite sources - PGE analyses of pyroxenites could reveal if these mafic mantle lithologies have high enough Pt/Os ratios to generate correlated radiogenic $^{187}Os/^{188}Os$ - $^{186}Os/^{188}Os$ over geological time-scales.
- Contamination by continental crust - There are two avenues of research which can between them, constrain crustal contamination in continentally derived intraplate magmas. First, analysis of $^{143}Nd/^{144}Nd$ isotope variations in Muskox Intrusion layered series rocks would be able to help distinguish crustal contamination vs. radiogenic Os mobility processes in the generation of high Os abundance radiogenic chromitites. This is because both Sm and Nd are immobile whilst continental crust has distinct $^{143}Nd/^{144}Nd$ isotopic compositions relative to mantle-derived melts. These attributes mean that combined Os-Nd isotope variations will allow estimation of post-emplacement mobility processes on Os. Second, as well as tracing correlated radiogenic $^{187}Os/^{188}Os$ - $^{186}Os/^{188}Os$ in oceanic intraplate magmas it is desirable to understand the origin of correlated radiogenic $^{187}Os/^{188}Os$ - $^{186}Os/^{188}Os$ measured in some continental intraplate environments (e.g., Walker *et al.*, 1997; Morgan *et al.*, 2002). Analysis of key samples from the Muskox intrusion will provide a simple test to the predicted variations in correlated radiogenic $^{187}Os/^{188}Os$-$^{186}Os/^{188}Os$ from crustal contamination made here.

References

Ackert R.P., Barclay D.J., Borns H.W., Calkin P.E., Kurz M.D., Fastook J.L. and Steig E.J. (1999) Measurements of past ice sheet elevations in interior west Antarctica. *Science*, **286**, 276-280

Albarède F. (1998) Time-dependant models of U-Th-He and K-Ar evolution and the layering of mantle convection. *Chemical Geology*, **145**, 413-429

Albarède F.F. Van Der Hilst R.D. (2002) Zoned mantle convection. *Philosophical Transactions of the Royal Society of London.* A **360**, 2569-2592

Alibert C., Michard A., Albarede F. (1983) The transition from alkali basalts to kimberlites: isotope and trace element evidence from melilitites. *Contributions to mineralogy and petrology*, **82**, 176-186

Allègre C.J., Turcotte D.L. (1986) Implications of a two component marble-cake mantle. *Nature*, **323**, 123-127

Allègre C.J., Moreira M. (2004) Rare gas systematics and the origin of oceanic islands: the key role of entrainment at the 670 km boundary layer. *Earth and Planetary Science Letters*, **228**, 85-92

Allègre C.J., Staudacher T., Sarda P. (1986/1987) Rare gas systematics, formation of the atmosphere, evolution and structure of the Earth's mantle. *Earth and Planetary Science Letters*, **81**, 127-150

Allègre C.J., Moriera M., Staudacher T. (1995) $^{4}He/^{3}He$ dispersion and mantle convection. *Geophysical Research Letters*, **22**, 2325-2328

Allègre C.J., Birck J.L., Capmas F., Courtillot V. (1999) Age of the Deccan traps using ^{187}Re-^{187}Os systematics. *Earth and Planetary Science Letters*, **170**, 197-204

Alves S., Schiano P., Capmas F., Allègre C.J. (2002) Osmium isotope binary mixing arrays in arc volcanism. *Earth and Planetary Science Letters*, **198**, 355-369

Ancochea E., Hernan F., Cendrado A., Cantagrel J.M., Fuster J.M., Ibarrola E., Coello J. (1994) Constructive and destructive episodes in the building of a young oceanic island, La Palma, Canary Islands, and genesis of the Caldera de Taburiente. *Journal of Volcanology and Geothermal research*, **60**, 243-262

Anderson A.T., Clayton R.N., Mayeda T.K. (1971) Oxygen isotope thermometry of mafic igneous rocks. *Journal of Geology*, **79**, 715-729

Anderson D.L. (1994) The sublithospheric mantle as the source of continental flood basalts; the case against the continental lithosphere and plume head reservoirs. *Earth and Planetary Science Letters*, **123**, 269-280

Anderson D.L. (1995) Lithosphere, asthenosphere and perisphere. *Reviews in Geophysics.* **33**, 125-149

Anderson D.L. (1998) A model to explain the various paradoxes associated with mantle noble gas geochemistry. *Proceeds of the National Academy of Science*, **95**, 9087-9092

Anderson D.L. (2000) The statistics and distribution of helium in the mantle. *International Geology Reviews.* **42**, 289-311

Anderson D.L. (2001) A statistical test of the two reservoir model for helium isotopes. *Earth and Planetary Science Letters*, **193**, 77-82

Andrews J.N (1985) The isotopic composition of radiogenic helium and its use to study groundwater movement in confined aquifers. *Chemical Geology*, **49**, 339-351

Anguita F., Hernan F. (1975) A propagating fracture model versus a hotspot origin for the Canary Islands. *Earth and Planetary Science Letters*, **27**, 11-19

Anguita F., Hernan F. (2000) The Canary Islands origin: a unifying model. *Journal of Volcanology and Geothermal Research*, **103**, 1-26

Ardnt N.T., Czamanske G.K., Walker R.J., Chauvel C., Fedorenko V.A. (2003) Geochemistry and origin of the intrusive hosts of the Noril'sk-Talnakh Cu-Ni-PGE sulphide deposits. *Economic Geology*, **98**, 494-515

Baker J.A., Menzies M.A., Thirlwall M.F., Macpherson C.G. (1997) Petrogenesis of Quaternary intraplate volcanism, Sana'a, Yemen: implications for plume-lithosphere interaction and polybaric melt hybridisation. *Journal of Petrology,* **38**, 1359-1390

Baker J.A., Macpherson C.G., Menzies M.A., Thirlwall M.F., Al-Kadasi M., Mattey D.P. (2000) Resolving crustal and mantle contributions to Continental Flood volcanism, Yemen; Constraints from mineral oxygen isotope data. *Journal of Petrology,* **41**, 1805-1820

Baker J.A., Krogh-Jensen K. (2004) Coupled ^{186}Os-^{187}Os enrichments in the Earth's mantle – core-mantle interaction or recycling of ferromanganese crusts and nodules? *Earth and Planetary Science Letters,* **220**, 277-286

Ballentine C.J. (1997) Resolving the mantle He/Ne and crustal $^{21}Ne/^{22}Ne$ in well gases. *Earth and Planetary Science Letters,* **152**, 233-250

Ballentine C.J., Lee. D.-C., Halliday A.N. (1997) Hafnium isotopic studies of the Cameroon line and new HIMU paradoxes. *Chemical Geology,* **157**, 111-124

Banda E., Dañobeitia J.J., Surinach E., Ansorge J. (1981) Features of crustal structure under the Canary Islands. *Earth and Planetary Science Letters,* **55**, 11-24

Baragar W.R.A. (1969) The geochemistry of the Coppermine River basalts. *Geological Survey of Canada Paper,* **69-44**, 43pp.

Baragar W.R.A., Ernst R.E., Hulbert L., Peterson T. (1996) Longitudinal petrochemical variation in the Mackenzie dyke swarm, Northwestern Canadian Shield. *Journal of Petrology,* **37**, 317-359

Barfod D.N., Ballentine C.J., Halliday A.N. and Fitton J.G. (1999) Noble gases in the Cameroon line and the He, Ne and Ar isotopic compositions of high υ (HIMU) mantle. *Journal of Geophysical Research,* **104**, 29509-29527

Barling J., Goldstein S.L., Nicholls I.A. (1994) Geochemistry of Heard Island (Southern Indian Ocean): characterisation of an enriched mantle component and implications for enrichment of the sub-Indian ocean mantle. *Journal of Petrology,* **35**, 1017-1053

Barker A., Day J.M.D., Pearson D.G., Kjarsgaard B.A., Harrison J.C., Nowell G.M., Macpherson C.G. (2002) Age and petrogenesis of the Freemans Cove Igneous Complex, Bathurst Island, Nunavut. *Volcano and Magmatic Studies Group 2002 (Part II) Conference abstracts, University of Edinburgh, UK*

Barnes S.-J., Francis D. (1995) The distribution of platinum-group elements, nickel, copper , and gold in the Muskox layered intrusion, Northwest Territories, Canada. *Economic Geology,* **90**, 135-154

Barrera J.L., Fernandez Santin S., Fúster J.M., Ibarrola E. (1981) Ijolitas-Sienitas-Carbonititas de los Macizos del Norte del Complejo Plutónico Basal de Fueteventura (Islas Canarias). *Boletín Geológico y Minero,* **92**, 309-321

Barth M.G., McDonough W.F., Rudnick R.L. (2000) Tracking the budget of Nb and Ta in the continental crust. *Chemical Geology,* **165**, 197-213

Barth M.G., Rudnick R.L., Horn I., McDonough W.F., Spicuzza M.J., Valley J.W., Haggerty S.E. (2002) Geochemistry of xenolithic eclogites from west Africa: Part II. Origins of the high MgO eclogites. *Geochimica et Cosmochimica Acta,* **66**, 4325-4345

Basu A.R., Renne P.R., DasGupta F., Teichmann Y.R., Poreda RJ. (1993) Early and late alkali igneous pulses and a high-^{3}He plume origin for the Deccan flood basalts. *Science,* **261**, 902-906

Basu A.R., Poreda R.J., Renne P.R., Teichmann F., Vasiliev Y.R., Sobolev N.V., Turrin B.D. (1995) High ^{3}He plume origin and temporal-spatial evolution of the Siberian flood basalts. *Science,* **269**, 822-825

Bennett V.C., Esat T.M., Norman M.D. (1996) Two mantle-plume components in Hawaiian picrites inferred from correlated Os-Pb isotopes. *Nature,* **381**, 221-224

Bennett V.C., Norman M.D., Garcia M.O. (2000) Rhenium and platinum group element abundances correlated with mantle source components in Hawaiian picrites: sulphides in the plume. *Earth and Planetary Science Letters,* **183**, 513-526

Bennett V.C., Nutman A.P., Esat T.M. (2002) Constraints on mantle evolution from $^{187}Os/^{188}Os$ isotopic compositions of Archaean ultramafic rocks from southern West Greenland (3.8Ga) and Western Australia (3.46Ga). *Geochimica et Cosmochimica Acta,* **66**, 2615-2630

Bernard A., Symonds R.B., Rose W.I., Jr. (1990) Volatile transportation and deposition of Mo, W, and Re in high temperature magmatic fluids. *Applied Geochemistry,* **5**, 317-326

Bhattacharji S., Smith C.H. (1964) Flowage differentiation. *Science,* **145**, 150-153

Bijwaard H., Spakman W. (1999) Tomographic evidence for a narrow whole mantle plume below Iceland. *Earth and Planetary Science Letters,* **166**, 121-126

Birck J.-L., Roy-Barman M., Capmas F. (1997) Re-Os isotopic measurements at the femtomole level in natural samples. *Geostandards Newsletter.* **21**, 21-28

Bird J.M., Meibom A., Frei R., Nagler Th.F. (1999) Osmium and lead isotopes of rare OsIrRu minerals: derivation from the core-mantle boundary region? *Earth and Planetary Science Letters,* **170**, 83-92

Bizimis M., Sen G., Salters V.J.M. (2003) Hf-Nd isotope decoupling in the oceanic lithosphere: constraints from spinel peridotites from Oahu, Hawaii. *Earth and Planetary Science Letters,* **217**, 43-58

Blichert-Toft J., Frey F.A., Albarède F. (1999) Hf isotope evidence for pelagic sediments in the source of Hawaiian basalts. *Science,* **285**, 879-882

Boctor N.Z., Yoder H.S. (1986) Petrology of some melilitite-bearing rocks from Cape Province, Republic of South Africa: relationship to kimberlites. *American Journal of Science,* **286**, 513-539

Bossard H. Macfarlane D.J. (1970) Crustal structure of the western Canary Islands from seismic refraction and gravity data. *Journal of Geophysical Research,* **75**, 4901-4918

Bowring S.A., Ross G.M. (1985) Geochronology of the Narakay Volcanic Complex: implications for the age of the Coppermine Homocline and Mackenzie Igneous events. *Canadian Journal of Earth Sciences,* **22**, 774-781

Brandon A.D. (2002) ^{186}Os-^{187}Os systematics of Gorgona Komatiites and Iceland picrites. *Geochimica et Cosmochimica Acta,* **A66**, 100

Brandon A.D., Walker R.J., Morgan J.W., Norman M.D., Prichard H.M. (1998) Coupled ^{186}Os and ^{187}Os evidence for Core-Mantle interaction. *Science,* **280**, 1570-1573

Brandon A.D., Norman M.D., Walker R.J., Morgan J.W. (1999) ^{186}Os-^{187}Os systematics of Hawaiian picrites. *Earth and Planetary Science Letters,* **174**, 25-42

Brandon A.D., Snow J.E., Walker R.J., Morgan J.W., Mock T.D. (2000) ^{190}Pt-^{186}Os and ^{187}Re-^{187}Os systematics of abyssal peridotites. *Earth and Planetary Science Letters,* **177**, 319-355

Brandon A.D., Walker R.J., Puchtel I.S., Becker H., Humayun M., Revillon S. (2003) ^{186}Os-^{187}Os systematics of Gorgona Island Komatiites: implications for early growth of the inner core. *Earth and Planetary Science Letters,* **206**, 411-426

Breddam K. (2002) Kistufell: Primitive Melt from the Iceland Mantle Plume. *Journal of Petrology,* **43**, 345-373

Breddam K., Kurz M.D. and Storey M. (2000) Mapping out the conduit of the Iceland mantle plume with helium isotope. *Earth and Planetary Science Letters,* **176**, 45-55

Brey G. (1978) Origin of olivine melilitites – chemical and experimental constraints. *Journal of Volcanology and Geothermal Research,* **3**, 61-88

Brooks C., James D.E., Hart S.R. (1976), Ancient lithosphere: its role in young continental volcanism. *Science,* **193**, 1086-1094

Brooks C.K., Keays. R.R., Lambert D.D., Frick L.R., Nielsen T.F.D. (1999) Re-Os isotope geochemistry of the Tertiary picritic and basaltic magmatism of East Greenland: constraints on plume-lithosphere interactions and the genesis of the Platinova reef, Skaergaard intrusion. *Lithos,* **47**, 107-126

Brooker R.A., Du Z., Blundy J.D., Kelley S.P., Allan N.L., Wood B.J., Chamorro E.M., Wartho J.-A., Purton J.A. (2003) The 'zero-charge' partitioning behaviour of noble gases during mantle melting. *Nature,* **423**, 738-741

Brown P.E., Evans I.B., Becker S.M. (1996) The Prince of Wales Formation – post-flood basalt alkali volcanism in the Tertiary of East Greenland. *Contributions to mineralogy and petrology,* **123**, 424-434

Brügmann G.E., Arndt N.T., Hofmann A.W., Tobschall H.J. (1987) Noble metal abundances in komatiite suites from Alexo, Ontario, and Gorgona Island, Colombia. *Geochimica et Cosmochimica Acta.* **51**, 2159-2169

Brügmann G.E., Naldrett A.J., Asif M., Lightfoot P.C., Gorbachev N.S., Fedorenko V.A (1993) Siderophile and chalcophile metals as tracers of the evolution of the Siberian Trap and Noril'sk regions, Russia. *Geochimica et Cosmochimica Acta,* **57**, 2001-2018

Buchan K.L., Ernst R.E., Hamilton M.A., Mertanen S., Pesonen L.J., Elming S.-A. (2001) Rodinia: the evidence from integrated palaeomagnetism and U-Pb geochronology. *Precambrian Research,* **110**, 9-32

Burgess R., Johnson L.H., Mattey D.P., Harris J.W., Turner G. (1998) He, Ar and C isotopes in coated and polycrystalline diamonds. *Chemical Geology*, **146**, 205-217

Burnard P. (2004) Diffusive fractionation of noble gases and helium isotopes during mantle melting. *Earth and Planetary Science Letters,* **220**, 287-295

Burton K.W., Lee D.-C., Christensen J.N., Halliday A.N., Hein J.R. (1999a) Actual timing of neodymium isotopic variations recorded by Fe-Mn crusts in the western North Atlantic. *Earth and Planetary Science Letters,* **171**, 149-156

Burton K.W., Bourdon B., Birck J.-L., Allègre C.J., Hein J.R. (1999b) Osmium isotope variations in the oceans recorded by Fe-Mn crusts. *Earth and Planetary Science Letters,* **171**, 185-197

Burton K.W., Capmas F., Birck J.-L. Allègre C.J., Cohen A.S. (2000a) Resolving crystallisation ages of Archean mafic-ultramafic rocks using the Re-Os isotope system. *Earth and Planetary Science Letters,* **179**, 453-467

Burton K.W., Schiano P., Birck J-L., Allegre C.J., Rehkamper M., Halliday A.N., Dawson J.B. (2000b) The distribution and behaviour of rhenium and osmium amongst mantle minerals and the age of the lithospheric mantle beneath Tanzania. *Earth and Planetary Science Letters*, **183**, 93-106

Campbell I.H., Naldrett A.J. (1979) The influence of silicate/sulphide ratios on the geochemistry of magmatic sulphides. *Economic Geology,* **74**, 1503-1505

Campbell I.H., Griffiths R,W. (1990) Implications if mantle plume structure for the evolution of flood basalts. *Earth and Planetary Science Letters,* **99**, 79-93

Caporuscio F.A., Smyth J.R. (1990) Trace element crystal chemistry of mantle eclogites. *Contributions to mineralogy and petrology,* **105**, 550-561

Carius L. (1865) *Justus Liebegs Ann. Chem.*, **136**, 129

Carlson R.W., Lugmair G.W., Macdougall J.D. (1981a) Crustal influence in the generation of continental flood basalts. *Nature,* **289**, 160-162

Carlson R.W., Lugmair G.W., Macdougall J.D. (1981b) Columbia River volcanism: the question of mantle heterogeneity or crustal contamination. *Geochimica et Cosmochimica Acta,* **45**, 2483-2499

Carlson R.W. (1991) Physical and chemical evidence on the cause and source characteristics of flood basalt volcanism. *Australian Journal of Earth Sciences,* **38**, 525-544

Carlson R.W., Irving A.J. (1994) Depletion and enrichment history of subcontinental lithospheric mantle: an Os, Sr, Nd and Pb isotopic study of ultramafic xenoliths from the north-western Wyoming craton. *Earth and Planetary Science Letters,* **126**, 457-472

Carracedo J.C. (1994) The Canary Islands: an example of structural control on the growth of large oceanic-island volcanoes. *Journal of Geothermal Research,* **60**, 225-241

Carracedo J.C. (1996) Morphological and structural evolution of the western Canary islands: Hotspot-induced three-armed rifts or regional tectonic trends? *Journal of Volcanology and Geothermal Research,* **72**, 151-162

Carracedo J.C. (1999) Growth, structure, instability and collapse of Canarian volcanoes and comparison with Hawaiian volcanoes. *Journal of Volcanology and Geothermal Research,* **94**, 1-19

Carracedo J.C., Day S., Guillou H., Badiola E.R., Canas J.A., Pérez-Torrado F.J. (1998) Hotspot volcanism close to a passive continental margin: the Canary Islands. *Geological Magazine,* **135**, 591-604

Carracedo J.C., Day S.J., Guillou H., Gravestock P. (1999) Later stages of volcanic evolution of La Palma, Canary Islands: Rift evolution, giant landslides, and the genesis of the Caldera de Taburiente. *Geological Society of America Bulletin,* **111**, 755-768

Carracedo J.C., Badiola E.R., Guillou H., de la Nuez J., Pérez-Torrado F.J. (2001) Geology and volcanology of La Palma and El Hierro, Western Canaries. *Estudios Geologicos,* **57**, 175-273

Carracedo J.C., Pérez-Torrado F. J., Ancochea E., Meco J., Hernán F., Cubas C. R., Casillas R., Badiola E. R., Ahijado A. (2002) Cenozoic volcanism II: the Canary Islands. ***In:*** Gibbons W., Moreno T. (Eds.) *The Geology of Spain.* Geological Society, London, Pp. 439-472

Carroll M.R., Draper D.S. (1994), Noble gases as trace elements in magmatic processes. *Chemical Geology,* **117**, 37-56

Chaffey D.J., Cliff R.A., Wilson B.M. (1989) Characterisation of the St. Helena magma source. ***In:*** Saunders A.D., Norry M.J. (eds.) *Magmatism in the Ocean basins. Geological Society of London, Special Publication.* **42**, 257-276

Chamberlain J.A., McLeod C.R., Traill R.J., Lachance G.R. (1965) Native metals in the Muskox intrusion. *Canadian Journal of Earth Sciences,* **2**, 188-215

Chamberlain J.A. (1967) Sulfides in the Muskox Intrusion. *Canadian Journal of Earth Sciences,* **4**, 105-154

Chauvel C., Hofmann A.W., Vidal P. (1992) HIMU-EM: the French Polynesian connection. *Earth and Planetary Science Letters,* **110**, 99-109

Chauvel C., Hémond C. (2000) Melting of a complete section of recycled oceanic crust: Trace element and Pb isotope evidence from Iceland. *Geochemistry, Geophysics, Geosystems,* **1**, Paper number 1999GC000002

Chesley J.T., Ruiz J. (1998) Crust-mantle interaction in large igneous provinces: Implications from the Re-Os isotope systematics of the Columbia River Flood basalts. *Earth and Planetary Science Letters,* **154**, 1-11

Christensen B.P., Holm P.M., Jambon A., Wilson J.R. (2001) Helium, argon and lead isotopic composition of volcanics from Santo Antao and Fogo, Cape Verde Islands. *Chemical Geology,* **178**, 127-142

Chou C.-L. (1978) Fractionation of siderophile elements in the Earth's mantle. *Proceeds of the Lunar and Planetary Science Conference,* **IX**, 219-230

Clague D.A., Frey F.A. (1982) Petrology and trace element geochemistry of the Honolulu volcanics, Oahu: implications for the oceanic mantle below Hawaii. *Journal of Petrology,* **23**, 447-504

Clarke W.B., Beg M.A., Craig H. (1969) Excess He-3 in the sea: evidence for terrestrial primordial helium. *Earth and Planetary Science Letters,* **6**, 213-220

Class C., Goldstein S.L. (1997) Plume-lithosphere interactions in the ocean basins: constraints from the source mineralogy. *Earth and Planetary Science Letters,* **150**, 245-260

Claude-Ivanaj C., Hofmann A.W., Vlastélic I., Koschinsky A. (2001) Recording changes in ENADW composition over the last 340ka using high-precision lead isotopes in a Fe-Mn crust. *Earth and Planetary Science Letters,* **188**, 73-89

Coffin M.F., Elderholm O. (1993) Large igneous provinces. *Scientific American,* **269**, 42-49

Cohen A.S., Waters F.G. (1996) Separation of osmium from geological materials by solvent extraction for analysis by thermal ionisation mass spectrometry. *Analytica Chimica Acta,* **332**, 269-275

Cohen A.S., Burnham O.M., Hawkesworth C.J., Lightfoot P.C. (2000) Pre-emplacement Re-Os ages from ultramafic inclusions in the sublayer of the Sudbury Igneous complex, Ontario. *Chemical Geology,* **165**, 37-46

Cohen A.S., Coe A.L. (2002) New geochemical evidence for the onset of volcanism in the Central Atlantic magmatic province and environmental change at the Triassic-Jurassic boundary. *Geology,* **30**, 267-270

Collerson K.D., Schoenberg R., Kamber B.S. (2002) Unradiogenic W in kimberlites: direct evidence for core-mantle interaction. *Geochimica et Cosmochimica Acta,* **A66**, 148

Condomines M., Grönvold K., Hooker P.J., Muehlenbachs K., O'Nions R.K., Óskarsson N. and Oxburgh E.R. (1983) Helium, oxygen, strontium and neodymium isotope relationships in Icelandic volcanoes. *Earth and Planetary Science Letters,* 66, 125-136

Cook D.L., Walker R.J., Horan M.F., Wasson J.T., Morgan J.W. (2004) Pt-Re-Os systematics of group IIAB and IIIAB iron meteorites. *Geochimica et Cosmochimica Acta,* **68**, 1413-1431

Cooper K.M., Eiler J.M., Asimow P.D., Langmuir C.H. (2004) Oxygen isotope evidence for the origin of enriched mantle beneath the mid-Atlantic ridge. *Earth and Planetary Science Letters,* **220**, 297-316

Cox K.G. (1980) A model for flood basalt volcanism. *Journal of Petrology,* **21**, 629-650

Craig H., Clarke W.B., Beg M.A. (1975) Excess ^{3}He in deep water on the east Pacific rise. *Earth and Planetary Science Letters,* **26**, 125-132

Craig H., Lupton J.E. (1976) Primordial neon, helium and hydrogen in oceanic basalts. *Earth and Planetary Science Letters,* **31**, 369-385

Creaser R.A., Papanastassiou D.A., Wasserburg G.J. (1991) Negative thermal ion mass spectrometry of osmium, rhenium and iridium. *Geochimica et Cosmochimica Acta,* **55**, 397-401

Darbyshire F.A., White R.S. and Priestly K.F.(2000) Structure of the crust and uppermost mantle of Iceland from combined seismic and gravity study. *Earth and Planetary Science Letters,* **181**, 409-428

Davies G.F. (1988) Ocean bathymetry and mantle convection. *Journal of Geophysical Research,* **93**, 10467-10480

Davies G.F. (1999) Geophysically constrained mantle mass flows and the ^{40}Ar budget: a degassed lower mantle? *Earth and Planetary Science Letters,* **166**, 149-162

Day J.M.D. (2001) Testing for the sources of high $^{3}He/^{4}He$ in failed rift and "plume" related Large Igneous Provinces. *American Association of Petroleum Geologists Bulletin,* **85-11**, 2048

Day J.M.D., Hilton D.R., Macpherson C.G., Grönvold K. (2002) Oxygen and trace element evidence for the role of crustal interaction in moderating extreme $^{3}He/^{4}He$ in recent central Icelandic lavas. *Volcano and Magmatic Studies Group 2002 (Part II) Conference abstracts, University of Edinburgh, UK*

Day J.M.D., Pearson D.G., Nowell G.M. (2003) High precision rhenium and platinum isotope dilution analyses by plasma ionisation multi-collector mass spectrometry ***In:*** Holland J.G and Tanner S.D. (eds.) *Plasma Source Mass Spectrometry, Applications and Emerging Technologies.* Royal Society of Chemistry Special Publication, 374-390

Day J.M.D., Hulbert L.J., Pearson D.G., Nowell G.M. (2003) Re-Os isotopic study of the Muskox Intrusion, NWT, Canada. *Geophysical Research Abstracts,* 5, 06848

Day J.M.D., Hulbert L.J., Pearson D.G. (2004) Os isotopic constraints on the mantle sources of the mid-Proterozoic Mackenzie magmatic event, Canadian Shield. *IAVCEI general assembly, Pucón, Chile*

Demény A., Ahijado A., Casillas R., Vennemann T.W (1998) Crustal contamination and fluid/rock interaction in the Carbonatites of Fuerteventura (Canary Islands, Spain): a C, O, H isotope study. *Lithos,* **44**, 101-115

DePaolo D.J. (1981) Trace element and isotopic effects of combined wallrock assimilation and fractional crystallisation. *Earth and Planetary Science Letters,* **53**, 189-202

DePaolo D.J., Bryce J.G., Dodson A., Shuster D.L., Kennedy B.M. (2001) Isotopic evolution of Mouna Loa and the chemical structure of the Hawaiian plume. *Geochemistry, Geophysics, Geodynamics,* paper #2000GC000139

DeWet J.J. (1975) Carbonatites and related rocks at Saltpetre Kop, Sutherland, Cape Province. *Annals, University of Stellenbosch (Series A1),* **1**, 193-232

Devey C.W., Cox K.G. (1987) Relationships between crustal contamination and crystallisation in continental flood basalt magmas with special reference to the Deccan Traps of the Western Ghats, India. *Earth and Planetary Science Letters,* **84**, 59-68

Dickin A.P. (1981) Isotope geochemistry of Tertiary igneous rocks from the Isle of Skye, N.W. Scotland. *Journal of Petrology,* **22**, 155-190

Dickin A.P., Richardson J.M., Crocket J.H., McNutt R.H., Peredery W.V. (1992) Osmium isotope evidence for a crustal origin of platinum group metals in the Sudbury nickel ore, Ontario, Canada. *Geochimica et Cosmochimica Acta,* **56**, 3531-3537

Dingle R.V., Gentle R.I (1972) Early Tertiary volcanic rocks on the Agulhas bank, South African continental shelf. *Geological magazine,* **109**, 137-146

Dixon E.T. (2003) Interpretation of helium and neon isotopic heterogeneity in Icelandic basalts. *Earth and Planetary Science Letters,* **206**, 83-99

Dixon E.T., Hondo M., McDougall I., Campbell I.H., Sigurdsson I. (2000) Preservation of near-solar neon isotopic ratios in Icelandic basalts. *Earth and Planetary Science Letters,* **180**, 309-324

Dixon J.E., Stolper E.M., Holloway J.R. (1995) An experimental study of water and carbon dioxide solubilities in mid-ocean ridge basaltic liquids. Part I: Calibration and solubility models. *Journal of Petrology,* **36**, 1607-1631

Dixon J.E., Clague D.A. (2001) Volatiles in basaltic glasses from Loihi seamount, Hawaii: Evidence for a relatively dry plume component. *Journal of Petrology,* **42**, 627-654

Dodson A., DePaolo D.J. and Kennedy B.M. (1998) Helium isotopes in lithospheric mantle: Evidence from Tertiary basalts of the western USA. *Geochimica et Cosmochimica Acta,* **62**, 3775-3787

Dodson A., Brandon A.D. (1999) Radiogenic helium in xenoliths from Simcoe, Washington, USA: implications for metasomatic processes in the mantle wedge above subduction zones. *Chemical Geology,* **160**, 371-385

Dostal J., Baragar W.R.A., Dupuy C. (1983) Geochemistry and petrogenesis of basaltic rocks from Coppermine River area, Northwest Territories. *Canadian Journal of Earth Sciences,* **20**, 684-698

Dostal J., Dupuy C., Carron J.P., Kerneizon M., Maury R.C. (1983b) Partition coeffiecients for trace elements: applications to volcanic rocks from St. Vincent, West Indies. *Geochimica et Cosmochimica Acta,* **47**, 525-533

Doucouré M., De Wit M.J., Mushayandebvu M.F. (1996) Effective elastic thickness of the continental lithosphere in South Africa, *Journal of Geophysical Research,* **101**, 11291-11304

Dowall D.P., Nowell G.M., Pearson D.G. (2003) Chemical pre-concentration procedures for high-precision analyses of Hf-Nd-Sr isotopes in geological materials by plasma ionisation multi-collector mass spectrometry (PIMMS) techniques ***In:*** Holland J.G and Tanner S.D. (eds.) *Plasma Source Mass Spectrometry, Applications and Emerging Technologies.* Royal Society of Chemistry Special Publication, 321-337

Drake M.J., Weill D.F. (1975) Partitioning of Sr, Ba, Ca, Y, Eu^{2+} ,Eu^{3}+ and other REE between plagioclase feldspar and magmatic liquid – an experimental study. *Geochimica et Cosmochimica Acta,* **39**, 689-712

Dunai T.J and Baur H. (1995) Helium, neon, and argon systematics of the European subcontinental mantle: Implications for its geochemical evolution. *Geochmica et Cosmochimica Acta,* **59**, 2767-2783

Dunai T.J., and Porcelli D. (2002) The storage and transport of noble gases in the subcontinental lithosphere *Reviews in Mineralogy and Geochemistry,* **47**, 371-409

Duncan R.A., Hargraves R.B., Brey G.P. (1978) Age, palaeomagnetism and chemistry of melilitite basalts in the Southern Cape, South Africa. *Geological Magazine,* **115**, 317-327

Dupuy C., Michard A., Dostal J., Dautel D., Baragar W.R.A. (1992) Proterozoic flood basalts from the Coppermine River area, Northwest Territories: isotope and trace element geochemistry. *Canadian Journal of Earth Sciences,* **29**, 1937-1943

Edwards S.J. (1990) Harzburgites and refractory melts in the Lewis Hills massif, Bay of Islands ophiolite complex: base metals and precious metals story. *Canadian Mineralogist,* **28**, 537-552

Eggins S.M., Rudnick R.L., McDonough W.F. (1998) The composition of peridotites and their minerals: a laser ablation ICP-MS study. *Earth and Planetary Science Letters,* **154**, 53-71

Eggler D.H., Meen J.K., Welt R., Dudas F.O., Furlong K.P., Macallum M.E., Carlson R.W. (1988) Tectonomagmatism of the Wyoming province. *Colorado schools of mines quarterly,* **83**, 25-40

Eiler J.M. (2001) Oxygen isotope variations of basaltic lavas and upper mantle rocks. *Reviews in Mineralogy and Geochemistry,* **43**, 319-364

Eiler J.M., Farley K.A., Valley J.W., Stolper E.M., Hauri E., Craig H. (1995) Oxygen isotope evidence against bulk recycled sediment in the source of Pitcairn Island lavas. *Nature,* **377**, 138-141

Eiler J.M., Farley K.A., Valley J.W., Hoffman A.W. and Stolper E.M. (1996) Oxygen isotope constraints on the sources of Hawaiian volcanism. *Earth and Planetary Science Letters,* **144,** 453-468

Eiler J.M., Farley K.A., Valley J.W., Hauri E., Craig H., Hart S.R. and Stolper E.M. (1997) Oxygen Isotope variations in ocean island basalt phenocrysts. *Geochimica et Cosmochimica Acta,* **61** (11), 2281-2293

Eiler J.M., Farley K.A., Stolper E.M. (1998) Correlated helium and lead isotope variations in Hawaiian lavas. *Geochimica et Cosmochimica Acta,* **62**, 1977-1984

Eiler J.M., Grönvold K. and Kitchen N. (2000a) Oxygen isotope evidence for the origin of chemical variations in lavas from Theistareykir volcano in Iceland's northern volcanic zone. *Earth and Planetary Science Letters,* **184**, 269-286

Eiler J.M., Crawford A., Elliott T., Farley K.A., Valley J.W. and Stolper E. (2000b) Oxygen isotope geochemistry of oceanic arc lavas. *Journal of Petrology,* **41**, 229-256

Eiler J.M., Schiano P., Kitchen N. and Stolper E.M. (2000c) Oxygen-isotope evidence for recycled crust in the sources of mid-ocean-ridge basalts. *Nature,* **403,** 530-534

Eisele J., Sharma M., Galer J.G., Blichert-Toft J., Devey C.W., Hofmann A.W. (2002) The role of sediment recycling in EM-1 inferred from Os, Pb, Hf, Nd, Sr isotope and trace element systematics of the Pitcairn hotspot. *Earth and Planetary Science Letters,* **196**, 197-212

Ellam R.M., Cox K.G. (1991) An interpretation of Karoo picrite basalts in terms of interaction between asthenospheric magmas and the mantle lithosphere. *Earth and Planetary Science Letters,* **105**, 330-342

Ellam R.M. (1992) Lithospheric thickness as a control on basalt geochemistry. *Geology,* **20**, 153-156

Ellam R.M., Carlson R.W., Shirey S.B. (1992) Evidence from Re-Os isotopes for plume-lithosphere mixing in Karoo flood basalt genesis. *Nature,* **359**, 718-721

Ellam R.M., Stuart F.M. (2000) the sub-lithospheric source of north Atlantic basalts: Evidence for, and significance of, a common end-member. *Journal of Petrology,* **41**, 919-932

Elliott T.R. (1991) Element fractionation in the petrogenesis of ocean island basalts. *Unpublished PhD thesis, The Open University.*

Elliott T.R., Hawkesworth C.J., Grönvold K., (1991) Dynamic melting of the Iceland plume. *Nature,* **351**, 201-206

Ernst R.E., Baragar W.R.A. (1992) Evidence form magnetic fabric for the flow pattern of magma in the Mackenzie giant radiating dyke swarm. *Nature,* **356**, 511-513

Ernst R.E., Head J.W., Parfitt E., Grosfils E., Wilson L. (1995) Giant radiating dyke swarms on Earth and Venus. *Earth Science Reviews,* **39**, 1-58

Esperanca S., Carlson R.W., Shirey S., Smith D. (1997) Dating crust-mantle separation: Re-Os isotopic study of mafic xenoliths from central Arizona. *Geology,* **25**, 651-654

Esser B.K., Turekian K.K. (1988) Accretion rate of extraterrestrial particles determined from osmium isotope systematics of Pacific pelagic clay and manganese nodules. *Geochimica et Cosmochimica Acta,* **52**, 1383-1388

Esser B.K., Turekian K.K. (1993) The osmium isotopic composition of the continental crust. *Geochimica et Cosmochimica Acta,* **57**, 3093-3104

Evans N.J., Davis J.J., Byrne J.P. and French D. (2000) Contamination-free preparation of geological samples for ultra-trace platinum group element and gold analysis. *Unpublished manuscript*

Fahrig W.F. (1987) The tectonic settings of continental mafic dyke swarms: failed arm and early passive margin. **In**: Halls H.C., Fahrig W.F. (Eds.) *Mafic Dyke Swarms.* Geological Association of Canada Special Paper, **34**, 331-348

Farley K.A., Craig H. (1992) Mantle plumes and mantle sources. *Science,* **258**, 821

Farley K.A., Natland J.H., Craig H. (1992) Binary mixing of enriched and undegassed (primitive?) mantle components (He, Sr, Nd, Pb) in Samoan lavas. *Earth and Planetary Science Letters,* **111**, 183-199

Farley K.A., Basu A.R., Craig H. (1993) He, Sr and Nd isotopic variations in lavas from the Juan-Fernandez archipelago, SE Pacific. *Contributions to Mineralogy and Petrology,* **115**, 75-87

Farley K.A., Neroda E. (1998) Noble gases in the Earths mantle. *Annual Reviews of Earth and Planetary Sciences,* **26**, 189-218

Fitton J.G., Gill R.C.O (1970) The oxidation of ferrous iron in rocks and minerals during mechanical grinding. *Geochimica et Cosmochimica acta,* **34**, 518-524

Fitton J.G., Saunders A.D., Norry., Hardarson B.S., Taylor R.N. (1997) Thermal and chemical structure of the Iceland plume. *Earth and Planetary Science Letters,* **153**, 197-208

Fitton J.G., Saunders A.D., Kempton P.D., Hardarson B.S. (2003) Does depleted mantle form an intrinsic part of the Iceland plume? *Geochemistry, Geophysics, Geosystems,* **4**, 2002.GC000424

Findlay D.C., Smith C.H. (1965) The Muskox Drilling Project. *Geological Survey of Canada paper,* **64-44**, 170pp.

Fleet M.E., Stone W.E., Crocket J.H. (1991a) Partitioning of palladium, iridium and platinum between sulphide liquid and basaltic melt: Effects of melt composition, concentration and oxygen fugacity. *Geochimica et Cosmochimica Acta,* **55**, 2545-2554

Fleet M.E., Crocket J.H., Stone W.E. (1991b) Partitioning of platinum group elements (Os, Ir, Ru, Pt, Pd) and gold between sulphide liquid and basalt melt. *Geochimica et Cosmochimica Acta,* **60**, 2397-2412

Fleet M.E., Crocket J.H., Liu M., Stone W.E. (1999a) Laboratory partitioning of platinum-group elements (PGE) and gold with application to magmatic sulphide-PGE deposits. *Lithos,* **47**, 127-142

Fleet M.E., Liu M., Crocket J.H. (1999b) Partitioning of trace amounts of highly-siderophile elements in th Fe-Ni-S system and their fractionation in nature. *Geochimica et Cosmochimica Acta,* **63**, 2611-2622

Foley S. (1992) Petrological characterisation of the source components of potassic magmas: geochemical and experimental constraints. *Lithos,* **28**, 187-204

Forester R.W., Taylor Jr. H.P. (1977) $^{18}O/^{16}O$, D/H, and $^{13}C/^{12}C$ studies of the Tertiary igneous complex of Skye, Scotland. *American Journal of Science.* **277**, 136-177

Foster J.G., Lambert D.D., Frick L.R., Maas R. (1996) Re-Os isotopic evidence for genesis of Archaean nickel ores from uncontaminated Komatiites. *Nature,* **382**, 703-706

Foulger G.R., Pearson D.G. (2001) Is Iceland underlain by a plume in the lower mantle? Seismology and helium isotopes *Geophysical Journal International,* **145**, F1-F5

Francis D. (1994) Chemical interaction between picritic magmas and upper crust along the margins of the Muskox Intrusion, Northwest Territories. *Geological Survey of Canada Paper,* **92-12**, 94pp

Francis D. (1995) Implications of picritic lavas for the mantle sources of terrestrial volcanism. *Lithos,* **34**, 89-105

French J.E., Heaman L.M., Chacko T. (2002) Feasibility of chemical U-Th-total Pb baddeleyite dating by electron microprobe. *Chemical Geology,* **188**, 85-104

Freydier C., Ruiz J., Chesley J., McCandless T., Munizaga F. (1997) Re-Os isotope systematics of sulfides from felsic igneous rocks: Application to base metal porphyry mineralization in Chile. *Geology,* **25**, 775-778

Furman T., Graham D. (1999) Erosion of lithospheric mantle beneath the East African rift system. Geochemical evidence from the Kivi volcanic province. *Lithos,* **48**, 237-262

Fuster J.M., Hernan F., Cendrero A., Coello J., Canatagrel J.M., Ancocha E., Ibarrola E. (1993) Geochronalogica de la Isla de El Hierro (Islas Canarias). *Bol. R. Soc. Esp. Hist. Nat (Sec. Geol),* **88**, 85-97

Gallagher K., Hawkesworth C.J. (1992) Dehydration melting and the generation of continental flood basalts. *Nature,* **358**, 57-59

Gangopadhyay A., Walker R.J. (2003) Re-Os systematics of the ca. 2.7-Ga Komatiites from Alexo, Ontario, Canada. *Chemical Geology,* **196**, 147-162

Gannoun A., Tessalina S., Bourdon B., Orgeval J.-J., Birck J.-L., Allègre C.J. (2003) Re-Os isotopic constraints on the genesis and evolution of the Dergamish and Ivanovka Cu (Co, Au) massive sulphide deposits, south Urals, Russia. *Chemical Geology,* **196**, 193-207

Garcia M.O., Ito E., Eiler J.M., Pietruszka A.J. (1998) Crustal contamination of Kilauea volcano magmas revealed by oxygen isotope analyses of glass and olivine from Puu Oo eruption lavas. *Journal of Petrology,* **39**, 803-818

Garlick G.D., MacGregor I.D., Vogel D.E. (1971) Oxygen isotope ratios in eclogites from kimberlites. *Science,* **172**, 1025-1027

Gautason B. and Muehlenbachs K. (1998) Oxygen isotopic fluxes associated with high temperature processes in the rift zones of Iceland. *Chemical Geology,* **145**, 275-286

Gautheron C., Moriera M. (2002) Helium signature of the subcontinental lithospheric mantle. *Earth and Planetary Science Letters,* **199**, 39-47

Gee M.A.M., Thirlwall M.F., Taylor R.N., Lowry D. and Murton B.J. (1998) Crustal processes: major controls on Reykjanes peninsula lava chemistry, SW Iceland. *Journal of Petrology,* **39**, 819-839

Gee M.A.M., Taylor R.N. Thirlwall M.F., Murton B.J. (1998b) Glacioisostacy controls chemical and isotopic characteristics of tholeiites from the Reykjanes peninsula, SW Iceland. *Earth and Planetary Science Letters,* **164**, 1-5

Geldmacher J., Hoernle K. (2000) The 72Ma geochemical evolution of the Madeira hotspot (eastern North Atlantic): recycling of Palaeozoic (≤500Ma) oceanic lithosphere. *Earth and Planetary Science Letters,* **183**, 73-92

Geldmacher J., Hoernle K., van den Bogaard P., Zankl G., Garbe-Schönberg D. (2001) Earlier history of the ≥70Ma-old Canary hotspot based on the temporal and geochemical evolution of the Selvagen Archipelago and neighbouring seamounts in the eastern North Atlantic. *Journal of Volcanology and Geothermal Research,* **111**, 55-87

Gill R.C.O., Pedersen A.K., Larsen J.G. (1992) Tertiary picrites in West Greenland: melting at the periphery of a plume? ***In:*** Storey B.C., Alabaster T., Pankhurst R.J. (eds) *Magmatism and the causes of Continental break-up. Geological Society special publication* **68**, 335-348

Gilliam C.E., Valley J.W. (1997) Low $\delta^{18}O$ magma, Isle of Skye, Scotland: Evidence from zircons. *Geochimica et Cosmochimica Acta,* **61**, 4975-4981

Goff F., McMurtry G.M., Counce D., Simac J.A., Roldan-Manzo A.R., Hilton D.R. (2000) Contrasting hydrothermal activity at Sierra Negra and Alcedo volcanoes, Galapagos Archipelago, Ecuador. *Bulletin of Volcanology,* **62**, 34-52

Graham D.W. (2002) Noble gas geochemistry of mid-ocean ridge and ocean island basalts: Charecterisation of mantle source reservoirs. ***In:*** Porcelli D., Ballentine C.J., Wieler R. (Eds.) Noble gases in geochemistry and cosmochemistry, *Reviews in mineralogy and geochemistry,* **47**, 247-317

Graham D.W., Zindler A., Kurz M.D., Jenkins W.J., Batiza R., Staudigel H. (1988) He, Pb, Sr and Nd isotope constraints on magma genesis and mantle heterogeneity beneath young pacific seamounts. *Contributions to Mineralogy and Petrology,* **99**, 446-463

Graham D.W., Lupton J., Albarède F., Condomines M. (1990) Extreme temporal homogeneity of helium isotopes at Piton de la Fournaise, Réunion Island. *Nature,* **347**, 545-548

Graham D.W., Humpris S.E., Jenkins W.J., Kurz M.D. (1992a) Helium isotope geochemistry of some volcnic rocks from Saint Helena. *Earth and Planetary Science Letters*, **110**, 121-131

Graham D.W., Jenkins W.J., Schilling J-G., Thompson G., Kurz M.D., Humpris S.E. (1992b) Helium isotope geochemistry of mid-ocean ridge basalts from the South Atlantic. *Earth and Planetary Science Letters*, **110**, 133-147

Graham D.W., Christie D.M., Harpp K.S., Lupton J.E. (1993) Mantle plume helium in submarine basalts from the Galapagos platform. *Science*, **262**, 2023-2026

Graham D.W., Hoernle K.A., Lupton J.E., Schmincke H.-U. (1996) Helium isotope variations in volcanic rocks from the Canary Islands and Madiera. *Chapman Conference: Shallow level processes in Ocean island magmatism*, American Geophysical Union (publ.) pp.13-14

Graham D.W., Larsen L.M., Hanan B.B., Storey M., Pedersen A.K. and Lupton J.E. (1998) Helium isotope composition of the early Iceland mantle plume inferred from the Tertiary picrites of West Greenland. *Earth and Planetary Science Letters*, **160**, 241-255

Graham D.W., Johnson K.T.M., Douglas Priebe L., Lupton J.E. (1999) Hotspot-ridge interaction along the Southeast Indian Ridge near Amsterdam and St. Paul Islands: helium isotope evidence. *Earth and Planetary Science Letters*, **167**, 297-310

Graham D.W., Lupton J.E., Spera F.J., Christie D.M. (2001) Upper-mantle dynamics revealed by helium isotope variations along the southeast Indian ridge. *Nature*, **409**, 701-703

Green D.H. (1970) A review of experimental evidence on the origin of basaltic and nephelinitic magmas. *Physics of the Earth and Planetary Interiors*, **3**, 221-235

Green T.H., Blundy J.D., Adam J., Yaxley G.M. (2000) SIMS determination of trace element partition coefficients between garnet, clinopyroxene and hydrous basaltic liquids at 2-7.5GPa and 1080-1200 degrees C. *Lithos*, **53**, 165-187

Gregg T.K.P., Fornari D.J., Perfit M.R., Ridley W.I., Kurz M.D. (2000) Using submarine lava pillars to record mid-ocean ridge eruption dynamics. *Earth and Planetary Science Letters*, **178**, 195-214

Gregory R.T., Taylor H.P. (1981) An oxygen isotope profile in a section of Cretaceous oceanic crust, Samail ophiolite, Oman: Evidence for $\delta^{18}O$ buffering of the oceans by deep (>5km) seawater hydrothermal circulation at mid-ocean ridges. *Journal of geophysical research*, **86**, 2737-2755

Griselin M., Arndt N.T., Baragar W.R.A. (1997) Plume-lithosphere interaction and crustal contamination during formation of Coppermine River basalts, Northwest Territories, Canada. *Canadian Journal of Earth Sciences*, **34**, 958-975

Guillou H., Carracedo J.C., Pérez Torrado F., Badiola E.R. (1996) K-Ar ages and magnetic stratigraphy of a hotspot-induced, fast grown oceanic island: El Hierro, Canary Islands. *Journal of Volcanology and Geothermal Research*, **73**, 141-155

Guillou H., Carracedo J.C., Day S.J. (1998) Dating of the Upper Pleistocene-Holocene volcanic activity of La Palma using the unspiked K-Ar technique. *Journal of Volcanology and Geothermal Research*. **86**, 137-149

Guillou H., Carracedo J.C., Duncan R. (2001) K-Ar, ^{40}Ar-^{39}Ar ages and magnetostratigraphy of Brunhes and Matuyama lava sequences from La Palma Island. *Journal of Volcanological and Geothermal Research*, **106**, 175-194

Halliday A.N., Lee D.-C., Tommasini S., Davies G.R., Paslick C.R., Fitton J.G., James D.E. (1995) Incompatible trace elements in OIB and MORB and source enrichment in the sub-oceanic mantle. *Earth and Planetary Science Letters*, **133**, 379-395

Hamilton M.A., Pearson D.G., Thompson R.N., Kelley S.P., Emeleus C.H. (1998) Rapid eruption of Skye lavas inferred from precise U-Pb and Ar-Ar dating of the Rum and Cuillin plutonic complexes. *Nature*, **394**, 260-263

Hanan B.B., Graham D.W. (1996) Lead and helium isotope evidence from oceanic basalts for a common deep source of mantle plumes. *Science*, **272**, 991-995

Hanski E., Walker R.J., Huhma H., Suominen I. (2001) The Os and Nd isotopic systematics of c. 2.44Ga Akanvaara and Koitelainen mafic layered intrusions in northern Finland. *Precambrian Research*, **109**, 73-102

Hansteen T.H., Anderson T., Neumann E.-R., Jelsma H. (1991) Fluid and silicate glass inclusions in ultramafic and mafic xenoliths from Hierro, Canary Islands: implications for mantle metasomatism. *Contributions to Mineralogy and Petrology,* **107**, 242-254

Hansteen T.H., Troll V.R. (2003) Oxygen isotope composition of xenoliths from the oceanic crust and volcanic edifice beneath Gran Canaria (Canary Islands): consequences for crustal contamination of ascending magmas. *Chemical Geology,* **193**, 181-193

Hanyu T., Kaneoka I. (1997) The uniform and low $^{3}He/^{4}He$ ratios of HIMU basalts as evidence for their origin as recycled materials. *Nature,* **390**, 273-276

Hanyu T., Kaneoka I. (1998) Open system behaviour of helium in the case of the HIMU source area. *Geophysical Research Letters,* **25**, 687-690

Hanyu T., Dunai T.J., Davies G.R., Kaneoka I., Nohda S., Uto K. (2001) Noble gas study of the Reunion hotspot: evidence for less-degassed mantle sources. *Earth and Planetary Science Letters,* **193**, 83-98

Harmon R.S., Hoefs J. (1995) Oxygen isotope heterogeneity of the mantle deduced from global ^{18}O systematics of basalts from different geotectonic settings. *Contributions to Mineralogy and Petrology,* **120**, 95-114

Harris C., Smith H.S., le Roux A.P. (2000) Oxygen isotope composition of phenocrysts from Tristan da Cuhna and Gough Island lavas: variations with fractional crystallisation and evidence for assimilation. *Contributions to mineralogy and petrology,* **138**, 164-175

Harrison J.C., de Frietas T. (1998) Bedrock geology, Bathurst Island group, District of Franklin, Northwest Territories (Nunavut); NTS 68H, 68G, 69A, 69B. *Geological Survey of Canada,* open file **2881**.

Harrison J.C., Mayr U., McNeil D.H., Sweet A.R., McIntyre D.J., Eberle J.J., Harington C.R., Chalmers J.A., Dam G., Nøhr-Hansen H. (1999) Correlation of Cenozoic sequences of the Canadian Arctic region and Greenland; implications for the tectonic history of northern North America. *Bulletin of Canadian Petroleum Geology,* **47**, 223-254

Hart S.R. (1984) A large scale anomaly in the Southern Hemisphere mantle. *Nature,* **309**, 753-757

Hart S.R. (1988) Heterogeneous mantle domains: signatures, genesis and mixing chronologies. *Earth and Planetary Science Letters,* **90**, 273-296

Hart S.R., Kinloch E.D. (1989) Osmium isotope systematics in Witwatersrand and Bushveld ore deposits. *Economic Geology,* **84**, 1651-1655

Hart S.R., Hauri E.H., Oschmann L.A., Whitehead J.A. (1992) Mantle plumes and entrainment; isotopic evidence. *Science,* **256**, 517-520

Hart S.R., Ravizza G. (1996) Os partitioning in phases from lherzolite and basalt. ***In:*** Basu A., Hart S.R. (Eds.) *Earth Processes: Reading the Isotopic code.* American Geophysical Union, Geophysical Monograph, **95**, 123-134

Hart W.K., Carlson R.W., Shirey S.B. (1997) Radiogenic Os in primitive basalts from the northwestern USA: Implications for petrogenesis. *Earth and Planetary Science Letters,* **150**, 103-116

Hartnady C.J.H., le Roux A.P. (1985) Southern ocean hotspot tracks and the Cenozoic absolute motion of the African, Antarctic, and South American plates. *Earth and Planetary Science Letters,* **75**, 245-257

Hattori K., Muehlenbachs K. (1982) Oxygen isotopic ratios of the Icelandic crust. *Journal of Geophysical Research,* **87**, 6559-6565

Hauri E.H. (1996) Major-element variability in the Hawaiian mantle plume. *Nature,* **382**, 415-419

Hauri E.H. (2002) Osmium isotopes and mantle convection. *Philosophical Transactions of the Royal Society of London, A,* **360**, 2371-2382

Hauri E.H., Hart S.R. (1993) Re-Os isotope systematics of HIMU and EMII oceanic island basalts from the South Pacific Ocean, *Earth and Planetary Science Letters,* **114**, 353-371

Hauri E.H., Hart S.R. (1997) Rhenium abundances and systematics in oceanic basalts. *Chemical Geology,* **139**, 185-205

Hauri E.H., Whitehead J.A., Hart S.R. (1994) Fluid dynamic and geochemical aspects of entrainment in mantle plumes. *Journal of Geophysical Research,* **99**, 24275-24300

Hauri E.H., Lassiter J.C., DePaolo D.J. (1996) Osmium isotope systematics of drilled lavas from Mauna Loa, Hawaii. *Journal of Geophysical Research,* **101**, 11793-11806

Hawkesworth C.J., Erlank A.J., Marsh J.S., Menzies M.A., van Calsteren P. (1983) Evolution of the continental lithosphere: evidence from volcanics and xenoliths from southern Africa. In: Hawkesworth C.J., Norry M.J. (Eds.) *Continental basalts and mantle xenoliths,* Shiva press, 111-138

Hawkesworth C.J., Mantovani M.S.M., Peate D. (1988) Lithospheric remobilisation during Parana CFB magmatism. **In:** Menzies M.A., Cox K.G. (Eds.) Oceanic and continental lithosphere: similarities and differences. *Journal of Petrology special volume,* 205-223

Hawkesworth C.J., Erlank A.J., Kempton P.D., Waters F.G. (1990) Mantle metasomatism: isotope and trace element trends in xenoliths from Kimberly, South Africa. *Chemical Geology,* **85**, 19-34

Hawkesworth C.J., Gallagher K., Kelly S., Mantovani M., Peate D.W., Regelous M., Rogers N.W. (1992) Parana magmatism and the opening of the South Atlantic. ***In:*** Storey B.C., Alabaster T., Pankhurst R.J (Eds.) *Magmatism and the causes of continental break-up.* Geological Society of London Special Publication, **68**, 221-240

Hawkesworth C.J., Kelley S., Turner S., leRoux A., Storey B. (1999) Mantle processes during Gondwana break-up and dispersal. *Journal of African Earth Sciences,* **28**, 239-261

Hawkesworth C.J., Blake S., Evans P., Hughes R., Macdonald R., Thomas L.E., Turner S.P., Zellmer G. (2000) Time scales of crystal fractionation in magma chambers – integrating physical, isotopic and geochemical perspectives. *Journal of Petrology,* **41**, 991-1006

Helmberger D.V., Wen L., Ding X. (1998) Seismic evidence that the source of the Iceland hotspot lies at the core-mantle boundary. *Nature,* **396**, 251-255

Hemond C., Condomines M., Fourcade S., Allègre C.J. Oskarsson N., Javoy M. (1988) Thorium, strontium and oxygen isotope geochemistry in recent tholeiites from Iceland: Crustal influence on mantle-derived magmas. *Earth and Planetary Science Letters,* **87**, 273-285

Hemond C., Arndt N.T., Lichtenstein U., Hofmann A.W. Oskarsson N. and Steinthorsson S. (1993) The heterogeneous Iceland plume: Nd-Sr-O isotopes and trace element constraints. *Journal of Geophysical Research,* **98**, 15833-15850

Hernandéz-Pacheco A. (1982) Sobra una posible erupcion en 1793 en la isla de El Hierro (Canarias). *Estudios Geologicos,* **31**, 15-25

Hernandéz-Pacheco A., Valls M.C. (1982) The historic eruptions of La Palma Island (Canarias). *Arquipelago, Review University of Azores Series C. Nat,* **3**, 83-94

Hildenbrand A., Gillot P.Y., Soler V., Lahitte P. (2003) Evidence for persistent uplifting of La Palma (Canary Islands), inferred from morphological and radiometric data. *Earth and Planetary Science Letters,* **210,** 277-289

Hill R.I., Campbell I.H., Davies G.F., Griffiths R.W. (1992) Mantle plumes and continental tectonics. *Science,* **256**, 187-191

Hilton D.R., Grönvold K., O'Nions R.K., Oxburgh E.R. (1990) Regional distribution of ^{3}He anomalies in the Icelandic crust. *Chemical Geology,* **88**, 53-67

Hilton D.R., Hoogewerff J.A., van Bergen M.J., Hammerschmidt K. (1992) Mapping magma sources in the east Sunda-Banda arcs, Indonesia: Constraints from helium isotopes. *Geochimica et Cosmochimica Acta,* **56**, 851-859

Hilton D.R., Hammerschmidt K., Loock G., Friedrichsen H. (1993) Helium and argon isotope systematics of the central Lau Basin and Valu Fa Ridge: Evidence of crust/mantle interactions in a back-arc basin. *Geochimica et Cosmochimica Acta,* **57**, 2819-2841

Hilton D.R., Hammerschmidt K., Teufel S., Freidrichsen H (1993) Helium isotope characteristics of Andean geothermal fluids and lavas, *Earth and Planetary Science Letters,* **120**, 265-282

Hilton D.R., Barling J., Wheller G.E. (1995) Effect of shallow-level contamination on the helium isotope systematics of ocean-island lavas. *Nature,* **373**, 330-333

Hilton D.R., McMurtry G.M., Kreulen R. (1997a) Evidence for extensive degassing of the Hawaiian mantle plume from helium-carbon relationships at Kilauea volcano. *Geophysical Research Letters,* **24 (23)**, 3065-3068

Hilton D.R., McMurtry G.M., Goff F. (1997b) Large variations in vent fluid $CO_2/^3He$ ratios signal rapid changes in magma chemistry at Loihi seamount, Hawaii. *Nature,* **396**, 359-362

Hilton D.R., Grönvold K., Macpherson C.G., Castillo P.R. (1999) Extreme $^3He/^4He$ ratios in northwest Iceland: constraining the common component in mantle plumes. *Earth and Planetary Science Letters,* **173**, 53-60

Hilton D.R., Macpherson C.G., Elliott T.R. (2000a) Helium isotope ratios in mafic phenocrysts and geothermal fluids from La Palma, the Canary islands (Spain): Implications for HIMU mantle sources. *Geochimica et Cosmochimica Acta,* **64**, 2119-2132

Hilton D.R., Thirlwall M.F., Taylor R.N., Murton B.J. and Nichols A. (2000b) Controls on magmatic degassing along the Reykjanes Ridge with implications for the helium paradox. *Earth and Planetary Science Letters,* **183**, 43-50

Hilton D.R., Porcelli D. (2003) Noble Gases as Mantle Tracers. *Treatise on Geochemistry,* **2**, 1-42

Hinkley T.K., Lamothe P.J., Wilson S.A., Finnegan D.L., Gerlach T.M. (1999) Metal emissions from Kilauea, and a suggested revision of the estimated worldwide metal output by quiescent degassing of volcanoes. *Earth and Planetary Science Letters,* **170**, 315-325

Hirose K., Kushiro I. (1993) Partial melting of dry peridotites at high pressures: determination of compositions of melts segregated from peridotites using aggregates of diamonds. *Earth and Planetary Science Letters,* **114**, 477-489

Hirschmann M.M., Stolper E.M. (1996) A possible role for garnet pyroxenite in the origin of the "garnet signature" in MORB. *Contributions to mineralogy and petrology,* **124**, 185-208

Hirschmann M.M., Renne P.R., McBirney A.R. (1997) $^{40}Ar/^{39}Ar$ dating of the Skaergaard intrusion. *Earth and Planetary Science Letters,* **146**, 645-658

Hirschmann M.M., Kosigo T., Baker M.B., Stolper E.M. (2003) Alkalic magmas generated by partial melting of garnet pyroxenite. *Geology,* **31**, 481-484

Hoefs J. (1973) *Stable isotope geochemistry.* Springer-Verlag: Berlin, 140pp.

Hoernle K. (1998) Geochemistry of Jurassic oceanic crust beneath Gran Canaria (Canary Islands): implications for crustal recycling and assimilation. *Journal of Petrology,* **39**, 859-880

Hoernle K., Tilton G, Schmincke H.-U. (1991) Sr-Nd-Pb isotopic evolution of Gran Canaria: Evidence for shallow enriched mantle beneath the Canary Islands. *Earth and Planetary Science Letters,* **106**, 44-63

Hoernle K., Schmincke H.-U. (1993a) The petrology of the tholeiites through melilitite nephelinites on Gran Canaria, Canary Islands: crystal fractionation, accumulation and depths of melting. *Journal of Petrology,* **34**, 573-597

Hoernle K., Schmincke H.-U. (1993b) The role of partial melting in the 15-Ma geochemical evolution of Gran Canaria: A blob model for the Canary hotspot. *Journal of Petrology,* **34**, 599-626

Hoernle K., Zhang Y.-U., Graham D. (1995) Seismic and geochemical evidence for large-scale mantle upwellings beneath the eastern Atlantic and western and central Europe. *Nature,* **374**, 34-39

Hofmann P.F. (1980) Wopmay orogen: a Wilson cycle of Early Proterozoic age in the northwest of the Canadian Shield. ***In:*** Strangway D.W. (Ed.) *The continental crust and its mineral deposits.* Geological Association of Canada Special Paper, **20**, 523-552

Hofmann A.W., White W.M. (1982) Mantle plumes form ancient oceanic crust. *Earth and Planetary Science Letters,* **57**, 421-436

Hofmann A.W. (1997) Mantle geochemistry: the message from oceanic volcanism. *Nature,* **385**, 219-229

Hoke L., Lamb S., Hilton D.R., Poreda R.J. (2000a) Southern limit of mantle derived geothermal helium emissions in Tibet: implications for lithospheric structure. *Earth and Planetary Science Letters*, **180**, 297-308

Hoke L., Poreda R., Reay A., Weaver S.D. (2000b) The subcontinental mantle beneath southern New Zealand, Characterised by helium isotopes in intraplate basalts and gas-rich springs. *Geochimica et Cosmochimica Acta*, **64**, 2489-2507

Holmes A., Harwood H.F. (1937) The petrology of the volcanic area of Bufumbira. *Memoir of the geological survey of Uganda,* **3**, 1-300, part II

Honda M., McDougall I., Patterson D.B. (1993) Solar noble gases in the Earth: the systematics of helium-neon isotopes in mantle derived samples. *Lithos*, **30**, 257-265

Honda M., Phillips D., Harris J.W., Yatsevich I. (2004) Unusual noble gas compositions in polycrystalline diamonds: preliminary results from the Jwaneng kimberlite, Botswana. *Chemical Geology,* **203**, 347-358

Horan M.F., Morgan J.W., Grauch R.I., Coveney R.M., Murowchick J.B., Hulbert L.J. (1994) Rhenium and osmium isotopes in black shales and Ni-Mo-PGE-rich sulphide layers, Yukon Territory, Canada, and Hunan and Guizhou provinces, China. *Geochimica et Cosmochimica Acta,* **58**, 257-265

Horan M.F., Walker R.J., Fedorenko V.A., Czamanske G.K. (1995) Osmium and neodymium isotope constraints on the temporal and spatial evolution of Siberian flood basalt sources. *Geochimica et Cosmochimica Acta,* **59**, 5159-5168

Horan M.F., Morgan J.W., Walker R.J., Cooper R.W. (2001) Re-Os isotopic constraints on magma mixing in the Peridotite zone of the Stillwater complex, Montana, USA. *Contributions to Mineralogy and Petrology,* **141**, 446-457

Hulbert L.J., Gregoire D.C. (1993) Re-Os isotope systematics of the Rankin Inlet Ni ores: an example of the application of ICP-MS to investigate Ni-Cu-PGE mineralization, and the potential use of Os isotopes in mineral exploration. *The Canadian Mineralogist.* **31**, 861-876

Hulbert L., Williamson B., Theriautt R. (1993) Geology of middle Proterozoic Mackenzie diabase suites from Saskatchewan: an overview and their potential to host Noril'sk-type Ni-Cu-PGE mineralization. *Saskatchewan Energy and Mines Miscellaneous Report.* **93-4,** 112-126

Hutchinson D.R., White R.S., Cannon W.F., Schulz K.J. (1990) Keweenaw hotspot: geophysical evidence for a 1.1Ga mantle plume beneath the Midcontinent rift system. *Journal of Geophysical Research,* **95**, 10869-10884

Irvine T.N. (1970) Crystallisation sequences in the Muskox intrusion and other layered intrusions-I. Olivine-pyroxene-plagioclase relations. *Geological Society of Africa Special Publication,* **1**, 441-476

Irvine T.N. (1975) Crystallization sequences in the Muskox intrusion and other layered intrusions-II. Origin of chromitite layers and similar deposits of other magmatic ores. *Geochimica et Cosmochimica Acta,* **39**, 991-1020

Irvine T.N. (1977) Origin of chromitite layers in the Muskox intrusion and other stratiform intrusions: A new interpretation. *Geology,* **5**, 273-277

Irvine T.N. (1980) Magmatic infiltration metasomatism, double-diffusive fractional crystallisation, and adcumulus growth in the Muskox intrusion and other layered intrusions. ***In:*** Hargraves R.B. (Ed.) *Physics of magmatic processes.* Princeton University Press, Princeton, NJ, 325-383

Irvine T.N. (1988) Muskox Intrusion, Northwest Territories. ***In:*** Hulbert L.J., Duke J.M., Eckstrand O.R., Lydon J.W., Scoates R.F.J., Cabri L.J. (eds.) *Geological environments of the platinum group elements.* Geological Survey of Canada Open File, **1440**, 25-39

Irvine T.N., Smith C.H. (1967) The ultramafic rocks of the Muskox Intrusion. ***In:*** Wyllie P.J. (Ed.) *Ultramafic and related rocks.* John Wiley and Son. Inc. New York

Irvine T.N., Baragar W.R.A. (1972) Muskox intrusion and Coppermine River lavas, Northwest Territories, Canada. XXIV International Geology Congress (Montreal) Excursion A29. 70pp.

Irvine G.J., Pearson D.G., Carlson R.W. (2001) Lithospheric mantle evolution of the Kaapvaal craton: a Re-Os isotope study of peridotite xenoliths from Lesotho kimberlites. *Geophysical Research Letters,* **28**, 2505-2508

Irvine G.J., Pearson D.G., Kjarsgaard B.A., Carlson R.W., Kopylova M.G., Dreibus G. (2003) A Re-Os and PGE study of kimberlite-derived peridotite xenoliths from Somerset Island and a comparison to the Slave and Kaapvaal cratons. *Lithos,* **71**, 461-488

Ito E., White W.M. and Göpel C. (1987) The O, Sr, Nd and Pb isotope geochemistry of MORB. *Chemical Geology,* **62**, 157-176

Jackson E.D. (1961) Primary textures and mineral associations in the Ultramafic zone of the Stillwater complex, Montana. *US Geological Survey Professional Paper,* **358**, 106pp.

Jamtveit B., Brooker R., Brooks K., Larsen L.M., Pedersen T. (2001) The water contents of olivines from the North Atlantic Volcanic Province. *Earth and Planetary Science Letters,* **186**, 401-415

Janney P.E., le Roux A.P., Carlson R.W., Viljoen K.S. (2002) A chemical and multi-isotope study of the Western Cape olivine melilitite province, South Africa: Implications for the sources of kimberlites and the origin of the HIMU signature in Africa. *Journal of Petrology,* **43**, 2339-2370

Janney P.E., le Roux A.P., Carlson R.W., Bell D.R. (2003) Os and Hf isotopic constraints on the sources of olivine melilitites from western South Africa. *Proceedings of the 8th International Kimberlite Conference.*

Javoy M., Stillman C.J., Pineau F. (1986) Oxygen and hydrogen isotope studies of the basal complexes of the Canary Islands: implications on the conditions of their genesis. *Contributions to Mineralogy and Petrology,* **92**, 225-235

Jochum K.P., Seufert H.M. and Thirlwall M.F. (1990) High sensitivity Nb analysis by Spark Source Mass Spectrometry (SSMS) and calibration of XRF Nb and Zr. *Chemical Geology,* **81**, 1-16

Johansen T.S., Hauff F., Hoernle K., Kokfelt T.F. (2003) Geochemical and isotopic investigations of the Cumbre Vieja Rift zone, La Palma (Canary Islands). *Geophysical Research Abstracts,* 5, 10524

Jónnason K. (1994) Rhyolite volcanism in the Krafla central volcano, north-east Iceland. *Bulletin of Volcanology,* **56**, 516-528

Jung Y.D., Naslund H.R., McBirney A.R. (2001) The differentiation trend of the Skaergaard intrusion and the timing of magnetite crystallisation: iron enrichment revisited. *Earth and Planetary Science Letters,* **189**, 189-196

Kaban M.K., Flovenz O.G., Palmason G. (2002) Nature of the crust-mantle transition zone and the thermal state of the upper mantle beneath Iceland from gravity modelling. *Geophysical Journal International,* **149**, 281-299

Kato T., Ringwood A.E., Irifune T. (1988) Experimental determination of element partitioning between silicate perovskites, garnets and liquids: constraints on early differentiation of the mantle. *Earth and Planetary Science Letters,* **89**, 123-145

Keays R.R. (1995) The role of komatiitic and picritic magmatism and S-saturation in the formation of ore deposits. *Lithos,* **34**, 1-18

Kellogg L.H., Wasserburg G.J. (1990) The role of plumes in mantle helium fluxes. *Earth and Planetary Science Letters,* **99**, 276-289

Kempton P.D., Fitton J.G., Saunders A.D., Nowell G.M., Taylor R.N., Hardarson B.S. and Pearson G. (2000) The Iceland plume in space and time: a Sr-Nd-Pb-Hf study of the North Atlantic rifted margin. *Earth and Planetary Science Letters,* **177**, 255-271

Kennedy G.C. (1948) Equilibrium between volatiles and iron oxides in igneous rocks. *American Journal of Science,* **246**, 529-549

Kent A.J.R., Norman M.D., Hutcheon I.D., Stolper E.M. (1999) Assimilation of seawater-derived components in an oceanic volcano: evidence from matrix glasses and glass inclusions from Loihi seamount, Hawaii. *Chemical Geology,* **156**, 299-319

Kerans C. (1983) Timing of emplacement of the Muskox Intrusion: constraints from Coppermine homocline cover strata. *Canadian Journal of Earth Sciences.* **20**, 673-683

Kerans C., Ross G.M., Donaldson J.A., Geldsetzer H.J. (1981) Tectonism and depositional history of the Helikian Hornby Bay and Dismal Lake Groups, District of Mackenzie. ***In:*** Campbell F.H.A. (Ed.) *Proterozoic Basins of Canada.* Geological Survey of Canada, Paper **81-10**, 157-182

Kerr J.W. (1974) Geology of Bathurst Island group and Byam Martin Island, Arctic Canada. *Geological Survey of Canada memoir,* **378**, 1-152

Kerr A.C., Arndt N.T (2001) A note on IUGS reclassification of the high-Mg and picritic volcanic rocks. *Journal of Petrology,* **42**, 2169-2172

Keshav S., Gudfinnsson G.H., Sen G., Fei Y. (2004) High-pressure melting experiments on garnet clinopyroxenite and the alkalic to tholeiitic transition in ocean-island basalts. *Earth and Planetary Science Letters,* **223**, 365-379

King S.D., and Anderson D.L. (1995) An alternative mechanism of flood basalt formation. *Earth and Planetary Science Letters,* **136**, 269-279

Klitgord K.D., Schouten H. (1986) Plate kinematics of the central Atlantic. ***In:*** Vogt P.R., Tucholke B.E. (Eds.) *The Geology of North America,* volume, *The Western North Atlantic Region.* Pp. 351-378, Geological Society of America, Boulder, Colorado

Klugel A. (2001a) Reactions between mantle xenoliths and host magma beneath La Palma (Canary Islands): constraints on magma ascent rates and crustal reservoirs. *Contributions to Mineralogy and Petrology,* **131**, 237-257

Klugel A. (2001b) Comment on "Silicic melts produced by reaction between peridotite and infiltrating basaltic magmas: ion probe data on glasses and minerals in veined xenoliths from La Palma, Canary Islands" by Wulff-Pedersen *et al. Contributions to Mineralogy and Petrology,* **141**, 505-510

Klugel A., Hansteen T.H., Schmincke H.-U. (1997) Rates of magma ascent and depths of magma reservoirs beneath La Palma (Canary Islands). *Terra Nova,* **9**, 117-121

Klugel A., Hoernle K., Schmincke H.-U., White J.D.L. (2000) The chemically zoned 1949 eruption on La Palma (Canary Islands): Petrological evolution and magma supply dynamics of a rift zone eruption. *Journal of Geophysical Research,* **105**, 5997-6016

Kosigo T., Hirschmann M.M., Frost D.J. (2003) High-pressure partial melting of garnet pyroxenite: possible mafic lithologies in the source of ocean island basalts. *Earth and Planetary Science Letters,* **216**, 603-617

Kosigo T., Hirschmann M.M., Reiners P.W. (2004) Length scales of mantle heterogeneities and their relationship to ocean island basalt geochemistry. *Geochimica et Cosmochimica Acta,* **68**, 345-360

Kreuzer H., Müller P., Wissmann G., Reinecke T. (1984) Petrography and K-Ar dating of Mazagan granodiorite. *Deep Sea Drilling Project Leg 79, Holes 544A and 547B, initial report DSDP 79, Us Government Printing Office, Washington,* 543-549

Kurz M.D., Jenkins W.J., Hart S.R. (1982) Helium isotope systematics of oceanic islands and mantle heterogeneity. *Nature,* **297**, 43-47

Kurz M.D., W.J. Jenkins., S.R. Hart and Clague D. (1983) Helium isotopic variations in Loihi Seamount and the island of Hawaii. *Earth and Planetary Science Letters,* **66**, 388-406

Kurz M.D., Meyer P.S., Sigurdsson H. (1985) Helium isotopic systematics within the neovolcanic zones of Iceland. *Earth and Planetary Science Letters,* **74**, 291-305

Kurz M.D. (1986) Cosmogenic helium in a terrestrial igneous rock. *Nature,* **320**, 435-439

Kurz M.D., Kenna T.C., Lassiter J.C., DePaolo D.J. (1996) Helium isotopic evolution of Mauna Kea Volcano: First results from the 1km drill core. *Journal of Geophysical Research,* **101**, 11781-11791

Kurz M.D., Geist D. (1999) Dynamics of the Galapagos hotspot from helium isotope geochemistry. *Geochimica et Cosmochimica Acta,* **63**, 4139-4156

Lambert D.D., Morgan J.W., Walker R.J., Shirey S.B., Carlson R.W., Zientek M.L., Koski M.S. (1989) Rhenium-osmium and samarium-neodymium isotopic studies of the Stillwater Complex. *Science,* **244**, 1169-1174

Lambert D.D., Walker R.J., Morgan J.W., Shirey S.B., Carlson R.W., Zientek M.L., Lipin B. R., Koski M.S., Cooper R.L. (1994) Re-Os and Sm-Nd isotope geochemistry of the Stillwater Complex Montana: Implications for the petrogenesis of the J-M Reef. *Journal of Petrology,* **35**, 1717-1753

Lambert D.D., Foster J.G., Frick L.R., Hoatson D.M., Purvis A.C. (1998) Application of the Re-Os isotopic system to the study of Precambrian magmatic sulphide deposits of Western Australia. *Australian Journal of Earth Sciences,* **45**, 265-284

Lambert D.D., Foster J.G., Frick L.R., Li C., Naldrett A.J. (1999) Re-Os isotopic systematics of the Voisey's Bay Ni-Cu-Co magmatic ore system, Labrador , Canada. *Lithos,* **47**, 69-88

Lambert D.D., Foster J.G., Frick L.R., Ripley E.M. (2000) Re-Os isotope geochemistry of magmatic sulphide ore systems. *Reviews in Economic Geology,* **12**, 29-58

Larsen L.M., Pedersen A.K., Sundvoll B., Frei R. (2003) Alkali picrites formed by melting of old metasomatised lithospheric mantle: Manîtdlat member, Vaigat formation, Palaeocene of West Greenland. *Journal of Petrology,* **44**, 3-38

Lassiter J.C. (2003) Rhenium volatility in subaerial lavas: constraints from subaerial and submarine portions of the HSDP-2 Mauna Kea drillcore. *Earth and Planetary Science Letters,* **214**, 311-325

Lassiter J.C., DePaolo D.J. (1997) Plume/lithosphere interaction in the generation of continental and oceanic flood basalts: chemical and isotopic constraints. ***In:*** Mahoney J.J., Coffin M.F. (eds) *Large Igneous Provinces: Continental, Oceanic and Planetary Flood Volcanism.* Geophysical Monograph, American Geophysical Union **100**, 335-355

Lassiter J.C., Hauri E.H. (1998) Osmium-isotope variations in Hawaiian lavas: evidence for recycled oceanic lithosphere in the Hawaiian plume. *Earth and Planetary Science Letters,* **164**, 483-496

Lassiter J.C., Hauri E.H., Reiners P.W., Garcia M.O. (2000) Generation of Hawaiian post-erosional lavas by melting of a mixed lherzolite/pyroxenite source. *Earth and Planetary Science Letters,* **178**, 269-284

LeBas M.J. (2000) IUGS reclassification of the high-Mg and picritic volcanic rocks. *Journal of Petrology,* **41**, 1467-1470

LeBas M.J. (2001) Reply to comments by Kerr and Arndt. *Journal of Petrology,* **42**, 2173-2174

Le Maitre R.W. (Ed.) *A classification of igneous rocks and a glossary of terms.* Blackwell Scientific Publications, Oxford. 193pp.

le Roux A.P. (1986) Geochemical correlations between southern African kimberlites and South Atlantic hotspots. *Nature,* **324**, 243-245

le Roux A.P., Cliff R.A., Adair B.J.I. (1990) Tristan da Cuhna, South Atlantic: geochemistry and petrogenesis of a basanite-phonolite lava series. *Journal of Petrology,* **31**, 779-812

le Roux A.P., Lanyon R. (1998) Isotope and trace element geochemistry of Cretaceous Damaraland lamprophyres and carbonatites, north western Namibia: evidence for plume lithosphere interactions. *Journal of Petrology,* **39**, 1117-1146

LeCheminant A.N., Heaman L.M. (1989) Mackenzie igneous events, Canada: Middle Proterozoic hotspot magmatism associated with ocean opening. *Earth and Planetary Science Letters,* **96**, 38-48

Lee C., Yin Q., Rudnick R.L., Chesley J.T., Jacobsen S.B. (2000) Osmium isotope evidence for Mesozoic removal of lithospheric mantle beneath the Sierra Nevada, California. *Science,* **289**, 1912-1916

Lesher C.M., Stone W.E. (1996) Exploration geochemistry of Komatiites. ***In:*** Wyman D (Ed.) *Igneous trace element geochemistry: applications for massive sulphide ore exploration.* Geological association of Canada short course notes. **12**, 153-204

Lightfoot P.C., Hawkesworth C.J. (1997) Flood basalts and magmatic Ni, Cu, and PGE sulphide mineralization: comparative geochemistry of the Noril'sk (Siberian Traps) and West Greenland sequences. ***In:*** Mahoney J., Coffin M. (Eds.) *Large igneous provinces: Continental, Oceanic and Planetary Flood Basalt volcanism.* The American Geophysical Union, Monograph, WA, **100**, 357-380

Luck J.M. Turekian K.K. (1983) Osmium-187/Osmium-186 in manganese nodules and the Cretaceous-Tertiary boundary. *Science*, **222**, 613-615

Ludwig K. (2003) Isoplot 3.0 add-in for Microsoft Excel. Berkeley Geochronological Centre, CA.

Lupton J.E., Graham D.W., Delaney J.R., Johnson H.P. (1993) Helium isotope variations in Juan de Fuca ridge basalts. *Geophysical Research Letters*, **20**, 1851-1854

Lyell C. (1855) *A manual of elementary geology II*, London, 498pp.

Macpherson C.G. (1994/5) New analytical approaches to the oxygen and carbon stable isotope geochemistry of some subduction-related lavas. *Unpublished PhD thesis, Royal Holloway, University of London.* 206pp.

Macpherson C.G., Mattey D.P. (1998) Oxygen isotope variations in Lau Basin Lavas. *Chemical Geology*, **144**, 177-194

Macpherson C.G., Hilton D.R., Sinton J.M., Poreda R.J., Craig H. (1998) High $^{3}He/^{4}He$ ratios in the Manus back-arc basin. *Geology*, **26**, 1007-1010

Macpherson C.G., Hilton D.R., Mattey D.P. and Sinton J.M. (2000) Evidence for an ^{18}O depleted mantle plume from contrasting $^{18}O/^{16}O$ ratios of back-arc lavas from the Manus Basin and Mariana Trough. *Earth and Planetary Science Letters*, **176**, 171-183

Marcantonio F., Zindler A., Reisberg L., Mathez E.A. (1993) Re-Os isotopic systematics in chromitites from the Stillwater Complex, Montana, USA. *Geochimica et Cosmochimica Acta*, **57**, 4029-4037

Marcantonio F., Reisberg L., Zindler A., Wyman D., Hulbert L. (1994) An isotopic study of the Ni-Cu-PGE-rich Wellgreen intrusion of the Wrangellia Terrane: evidence for hydrothermal mobilisation of rhenium and osmium. *Geochimica et Cosmochimica Acta*, **58**, 1007-1017

Marcantonio F., Zindler A., Elliot T., Staudigel H. (1995) Os isotope systematics of La Palma, Canary Islands: Evidence for recycled crust in the mantle source of HIMU ocean islands. *Earth and Planetary Science Letters*, **133**, 397-410

Marques J.C., Ferreira Filho C.F., Carlson R.W., Pimentel M.M. (2003) Re-Os and Sm-Nd isotope and trace element constraints on the origin of the chromite deposit of the Ipueira-Medrado sill, Bahia, Brasil. *Journal of Petrology*, **44**, 659-678

Marsh J.S. (1989) Geochemical constraints on coupled assimilation and fractional crystallisation involving upper crustal compositions and continental tholeiitic magma. *Earth and Planetary Science Letters*, **92**, 70-80

Martin C.E. (1989) Re-Os isotopic investigation of the Stillwater Complex, Montana. *Earth and Planetary Science Letters*, **93**, 336-344

Martin C.E., Carlson R.W., Shirey S.B., Frey F.A., Chen C.-Y. (1994) Os isotopic variation in basalts from Haleakala Volcano, Maui, Hawaii: a record of magmatic processes in oceanic mantle and crust. *Earth and Planetary Science Letters*, **128**, 287-301

Marty B., Trull T., Lussiez P., Basile I. and Tanguy J-C. (1994) He, Ar, O, Sr and Nd isotope constraints on the origin and evolution of Mount Etna magmatism. *Earth and Planetary Science Letters*, **126**, 23-39

Marty B., Pik R., Gezahegn Y. (1996) Helium isotope variations in Ethiopian plume lavas: nature of magmatic sources and limit on lower mantle contribution. *Earth and Planetary Science Letters*, **144**, 223-237

Marty B., Upton B.G.J., Ellam R.M. (1998) Helium isotopes in early Tertiary basalts, north-east Greenland: evidence for 58Ma plume activity in the North Atlantic-Iceland volcanic province. *Geology*, **26**, 407-410

Matsumoto T., Honda M., McDougall I. and O'Reilly S. (1998) Noble gases in anhydrous lherzolites from the Newer volcanics, south eastern Australia: A MORB-like reservoir in the subcontinental mantle. *Geochimica et Cosmochmica Acta*, **62**, 2521-2533

Matsumoto T., Honda M., McDougall I., O'Reilly S., Norman M. and Yaxley G. (2000) Noble gases in pyroxenites and metasomatised peridotites from the Newer volcanics, south eastern Australia: implications for mantle metasomatism. *Chemical Geology*, **168**, 49-73

Matsumoto T., Chen Y., Matsuda J-i. (2001) Concomitant occurrence of primordial and recycled noble gases in the Earth's mantle. *Earth and Planetary Science Letters,* **185**, 35-47

Mattey D.P., Lowry D., Macpherson C. (1994) Oxygen isotope composition of mantle peridotite. *Earth and Planetary Science Letters,* **128**, 231-241

McBirney A.R., Creaser R.A. (2003) The Skaergaard Layered Series, Part VII: Sr and Nd isotopes. *Journal of Petrology,* **44**, 757-771

McCallum I.S., Thurber M.W., O'Brien H.E., Nelson B.K. (1999) Lead isotopes in sulfides from the Stillwater Complex, Montana: evidence for subsolidus remobilisation. *Contributions to Mineralogy and Petrology,* **137**, 206-219

McCandless T.E., Ruiz J. (1991) Osmium isotopes and crustal sources for platinum-group mineralization in the Bushveld Complex, South Africa. *Geology,* **19**, 1225-1228

McCandless T.E., Ruiz J., Adair I., Freydier C. (1999) Re-Os isotope and Pd/Ru variation in chromitites form the Critical zone, Bushveld Complex, South Africa. *Geochimica et Cosmochimica Acta,* **63**, 911-923

McDaniel D.K., Walker R.J., Hemming S.R., Horan M.F., Becker H., Grauch R.I. (2004) Sources of osmium in modern day oceans: New evidence from the ^{190}Pt-^{186}Os system. *Geochimica et Cosmochimica Acta,* **68**, 1243-1252

McDonough W.F. (1990) Constraints on the composition of the continental lithospheric mantle. *Earth and Planetary Science Letters,* **101**, 1-18

McDonough W.F., Sun S.-s. (1995) The composition of the Earth. *Chemical Geology,* **120**, 223-253

McIver J.R., Ferguson J. (1979) Kimberlitic, melilititic, trachytic and carbonatite eruptives at Saltpetre Kop, Sutherland, South Africa. ***In:*** Meyer H.O.A., Boyd F.R. (eds.) *Kimberlites, Diatremes and Diamonds: their geology, petrology and geochemistry.* American Geophysical Union, Washington, DC. 111-128

McInnes B.I.A., McBride J.S., Evans N.J., Lambert D.D., Andrew A.S. (1999) Osmium isotope constraints on ore metal recycling in subduction zones. *Science,* **286**, 512-516

McKenzie D. (1989) Some remarks on the movement of small melt fractions in the mantle. *Earth and Planetary Science Letters,* **95**, 53-72

McKenzie D., O'Nions R.K. (1983) Mantle reservoirs and oceanic basalts. *Nature,* **301**, 229-331

McKenzie D., O'Nion R.K. (1991) Partial melt distributions from inversion of rare-earth element concentrations. *Journal of Petrology,* **32**, 1021-1091

Meibom A., Frei R. (2002) Evidence for an ancient osmium isotopic reservoir in Earth. *Science,* **296**, 516-518

Meibom A., Anderson D.L. (2003) The statistical upper mantle assemblage. *Earth and Planetary Science Letters,* **217**, 123-139

Meibom A., Sleep N.H., Chamberlain C.P., Coleman R.G., Frei R., Hren M.T., Wooden J.L. (2002) Re-Os isotopic evidence for long-lived heterogeneity and equilibrium processes in the Earth's upper mantle. *Nature,* **419**, 705-708

Meibom A., Anderson D.L., Sleep N.H., Frei R., Chamberlain C.P., Hren M.T., Wooden J.L. (2003) Are high $^{3}He/^{4}He$ ratios in oceanic basalts an indicator of deep-mantle plume components? *Earth and Planetary Science Letters,* **208**, 197-204

Meisel T., Walker R.J., Morgan J.W. (1996) The osmium isotopic composition of the Earth's primitive upper mantle. *Nature,* **383**, 517-520

Meisel T., Walker R.J., Irving A.J., Lorand J.-P. (2001) Osmium isotopic compositions of mantle xenoliths: a global perspective. *Geochimica et Cosmochimica Acta,* **65**, 1311-1323

Menzies M.A., Halliday A.N., Palacz Z., Hunter R., Upton B., Aspen P., Hawkesworth C.J. (1987) Evidence from mantle xenoliths for an enriched lithospheric keel under the outer Hebrides. *Nature,* **325**, 44-47

Menzies M., Halliday A. (1988) Lithospheric mantle domains beneath Archean and Proterozoic crust of Scotland. *Journal of Petrology,* **special lithosphere issue**, 275-302

Menzies M.A., Dupuy C. (1991) Orogenic massifs: protolith, process and provenance. *Journal of Petrology special issue, Orogenic lherzolites and mantle processes*, 1-16

Menzies M.A., Xu Y. (1998) Geodynamics of the North China craton. ***In:*** Flower M., Chung S.L., Lo C.H., Lee T.Y (Eds.) *Mantle dynamics and plate interactions in East Asia*, **27**, 155-165, American Geophysical Union

Mitchell R.H., Platt R.G. (1983) Primitive nephelinitic volcanism associated with rifting and uplift in the Canadian Arctic. *Nature,* **303**, 609-612

Mitchell R.H., Platt R.G. (1984) The Freemans Cove volcanic suite: field relations, petrochemistry, and tectonic setting of nephelinite-basanite volcanism associated with rifting in the Canadian Arctic Archipelago. *Canadian Journal of Earth Sciences,* **21**, 428-436

Mitchell R. H. (1995) *Kimberlites, Orangeites and related rocks*. Plenum press, New York

Molnar P., England P.C., Martinod J (1993) Mantle dynamics, uplift of the Tibetan plateau and the Indian monsoon, *Reviews in Geophysics,* **31**, 357-396

Molzahn M., Reisberg L., Wörner G. (1996) Os, Sr, Nd, Pb, O isotope and trace element data from the Ferrar flood basalts, Antarctica: evidence for an enriched subcontinental lithospheric source. *Earth and Planetary Science Letters,* **144**, 529-546

Monani S., Valley J.W. (2001) Oxygen isotope ratios of zircon: magma genesis of low $\delta^{18}O$ granites from the British Tertiary Igneous Province, western Scotland. *Earth and Planetary Science Letters,* **184**, 377-392

Moore J.G., Clague D.A. (1992) Volcano growth and evolution of the island of Hawaii. *Geological Society of America Bulletin,* **104**, 1471-1484

Moore A.E. (1979) *The geochemistry of the olivine melilitites and related rocks of Namaqualand-Bushmanland, South Africa*. Ph.D. thesis, University of Cape Town, SA

Moore A.E., Erlank A.J. (1978) Unusual olivine zoning – evidence for complex physio-chemical changes during the evolution of olivine melilitite and kimberlite magmas. *Contributions to Mineralogy and Petrology,* **70**, 391-405

Moore A.E., Verwoerd W.J. (1985) The olivine melilitite-"kimberlite"-carbonatite suite of Namaqualand and Bushmanland, South Africa. *Transactions of the Geological Society of South Africa.* **88**, 281-294

Moriera M., Allègre C-J. (1998) Helium-neon systematics and the structure of the mantle. *Chemical Geology,* **147**, 53-59

Moriera M., Allègre C-J. (2002) Rare gas systematics of Mid Atlantic Ridge (37-40 North). *Earth and Planetary Science Letters*, **198**, 401-416

Moreira M., Sarda P. (2000) Noble gas constraints on degassing processes. *Earth and Planetary Science Letters,* **176**, 375-386

Moriera M., Doucelance R., Kurz M.D., Dupre B., Allègre C.J. (1999) Helium and lead isotope geochemistry of the Azores archipelago. *Earth and Planetary Science Letters*, **169**, 189-205

Morgan W.J. (1971) Convection plumes in the lower mantle. *Nature,* **230**, 42-43

Morgan W.J. (1981) Hotspot tracks and the opening of the Atlantic and Indian oceans. ***In:*** Emiliani C (Ed.) *The Sea*. John Wiley, New York

Morgan W.J. (1983) Hotspot tracks and the early rifting of the Atlantic. *Tectonophysics,* **94**, 123-139

Morgan J.W. (1986) Ultramafic xenoliths: clues to Earth's late accretionary history. *Journal of Geophysical Research,* **91**, 12375-12387

Morgan J.W., Wandless G.A., Petrie R.K., Irving A.J. (1981) Composition of the Earth's upper mantle I: Siderophile trace elements in ultramafic nodules. *Tectonophysics,* **75**, 47-67

Morgan J.W., Horan M.F., Walker R.J., Grossman J.N. (1995) Rhenium-osmium concentration and isotope systematics in group IIAB iron meteorites. *Geochimica et Cosmochimica Acta,* **59**, 2331-2344

Morgan J.W., Walker R.J., Horan M.F., Beary E.S., Naldrett A.J. (2002) ^{190}Pt-^{186}Os and ^{187}Re-^{187}Os systematics of the Sudbury Igneous Complex, Ontario. *Geochimica et Cosmochimica Acta,* **66**, 273-290

Muehlenbachs K. (1986) Alteration of the oceanic crust and the ^{18}O history of seawater. ***In:*** Valley J.W., Taylor H.P.J., O'Neill J.R. (Eds.) *Stable isotopes in high temperature geological processes*, 425-444, Mineralogical Society of America

Natland J.H. (2003) Capture of helium and other volatiles during the growth of olivine phenocrysts in picritic basalts from the Juan Fernandez Islands. *Journal of Petrology,* **44**, 421-456

Neal C.R., Taylor L.A., Davidson J.P., Holden P., Halliday A.N., Nixon P.H., Paces J.B., Clayton R.N., Mayeda T.K. (1990) Eclogites with oceanic crustal and mantle signatures from the Bellsbank kimberlite, South Africa, part 2: Sr, Nd and O isotope geochemistry. *Earth and Planetary Science Letters,* **99**, 362-379

Niedermann S., Bach W., Erzinger J. (1997) Noble gas evidence for a lower mantle component in MORBs from the southern East Pacific Rise: Decoupling of helium and neon isotope systematics. *Geochimica et Cosmochimica Acta.* **61**, 2697-2715

Nichols A.R.L., Carroll M.R., Hoskuldsson A. (2002) Is the Iceland hot spot also wet? Evidence from the water contents of undegassed submarine and subglacial pillow basalts. *Earth and Planetary Science Letters,* **202**, 77-87

Nikogosian I.K., Elliott T., Touret J.L.R. (2002) Melt evolution beneath thick lithosphere: a magmatic inclusion study of La Palma, Canary Islands. *Chemical Geology,* **183**, 169-193

Niu Y., O'Hara M.J. (2003) Origin of ocean island basalts: A new perspective from petrology, geochemistry, and mineral physics considerations. *Journal of Geophysical Research,* **108**, doi: 10.1029/2002JB002048

Nixon P.H. (1987) *Mantle xenoliths,* Wiley, Chichester

Norman M.D., Garcia M.O., Bennett V.C. (2004) Rhenium and chalcophile elements in basaltic glasses from Ko'olau and Molokai volcanoes: Magmatic outgassing and composition of the Hawaiian plume. *Submitted to Geochimica et Cosmochimica Acta*

Nowell G., Parrish R.R. (2001) Simultaneous acquisition of isotope compositions and parent/daughter ratios by non-isotope dilution-mode plasma ionisation multi-collector mass spectrometry (PIMMS). ***In:*** Holland J.G., Tanner S.D. (eds.) *Plasma Source Mass Spectrometry, The New Millenium.* Royal Society of Chemistry Special Publication, 298-310

Nowell G.M., Pearson D.G., Ottley C.J., Schweiters J., Dowall D. (2003) Long-term performance characteristics of a plasma ionisation multi-collector mass spectrometer (PIMMS): the Thermo Finnigan Neptune ***In:*** Holland J.G and Tanner S.D. (eds.) *Plasma Source Mass Spectrometry, Applications and Emerging Technologies.* Royal Society of Chemistry Special Publication, 307-320

Olive V., Ellam R.M., Harte B. (1997) A Re-Os isotope study of ultramafic xenoliths from the Matsoku kimberlite. *Earth and Planetary Science Letters*, **150**, 129-140

Osborn E.F. (1959) Role of oxygen pressure in the crystallisation and differentiation of basaltic magmas. *American Journal of Science,* **257**, 609-647

Ovchinnikova G. V., Belyatskii B. V., Vasileva I. M., Levskii L. K., Grachev A. F., Arana V., Mitjavila I. J. (1995) Sr-Nd-Pb isotope of mantle sources of basalts from the Canary Islands, *Petrologiya*, **3**, 195-206

Oyarzun R., Doblas M., López-Ruiz J., Cebriá J.M. (1997) Opening of the central Atlantic and asymmetric mantle up welling phenomena: Implications for long-lived magmatism in western North-Africa and Europe. *Geology,* **25**, 727-730

Ottley C.J., Pearson D.G., Irvine G.I. (2003) A routine method for the dissolution of geological samples for the analysis of REE and trace elements via ICP-MS. ***In:*** Holland J.G and Tanner S.D. (eds.) *Plasma Source Mass Spectrometry, Applications and Emerging Technologies.* Royal Society of Chemistry Special Publication, 221-230

Palmer M.R., Turekian K.K. (1986) $^{187}Os/^{186}Os$ in marine manganese nodules and the constraints on the crustal geochemistries of rhenium and osmium. *Nature,* **319**, 216-220

Palmer M.R., Kenison Falkner K., Turekian K.K., Calvert K.E. (1988) Sources of osmium isotopes in manganese nodules. *Geochimica et Cosmochimica Acta*, **52**, 1197-1202

Pasteels P., Villeneuve M., DePaepe P., Klerkx J. (1989) Timing of the volcanism of the Southern Kivu province. Implications for the evolution of the western branch of the East African rift system. *Earth and Planetary Science Letters*, **94**, 353-363

Peach C.L., Mathez E.A., Keays R.R. (1990) Sulphide melt- silicate melt distribution coefficients for noble metals and other chalcophile elements as deduced from MORB: Implications for partial melting. *Geochimica et Cosmochimica Acta*, **54**, 3379-3389

Peach C.L., Mathez E.A., Keays R.R., Reaves R.J. (1994) Experimentally determined sulphide melt-silicate melt partition coefficients for Ir and Pd. *Chemical Geology*, **117**, 361-377

Pearson D.G. (1999) The age of continental roots, *Lithos*, **48**, 171-194

Pearson D.G., Woodland S.J. (2000) Solvent extraction/ anion exchange separation and determination of PGEs (Os, Ir, Pt, Pd, Ru) and Re-Os isotopes in geological samples by isotope dilution ICP-MS. *Chemical Geology*, **165**, 87-107

Pearson D.G., Nowell G.M. (2002) The continental lithospheric mantle: characteristics and significance as a mantle reservoir. *Philosophical transactions of the Royal Society of London*, **360**, 2383-2410

Pearson D.G., Nowell G.M. (2004) Re-Os and Lu-Hf isotopic constraints on the origin and age of pyroxenites from the Beni Bousera peridotite massif: implications for mixed peridotite-pyroxenite mantle sources. *Journal of Petrology*, **45**, 439-455

Pearson D.G., Davies G.R., Nixon P.H., Greenwood P.B., Mattey D.P. (1991) Oxygen isotope evidence for the origin of pyroxenites in the Beni Bousera peridotite massif N. Morocco: derivation from subducted oceanic lithosphere. *Earth and Planetary Science Letters*, **102**, 289-301

Pearson D.G., Davies G.R., Nixon P.H. (1993) Geochemical constraints on the petrogenesis of diamond facies pyroxenites from Beni Bousera peridotite massif, North Morocco. *Journal of Petrology*, **34**, 125-172

Pearson D.G., Snyder G.A., Shirey S.B., Taylor L.A., Carlson R.W., Sobolev N.V (1995a) Archaean Re-Os age for Siberian eclogites and constraints on Archaean tectonics. *Nature*, **374**, 711-713

Pearson D.G., Shirey S.B., Carlson R.W., Boyd F.R., Pokhilenko N.P., Shimizu N. (1995b) Re-Os, Sm-Nd, and Rb-Sr isotope evidence for thick Archaean lithospheric mantle beneath the Siberian craton modified by multistage metasomatism. *Geochimica et Cosmochimica Acta*, **59**, 959-977

Pearson D.G., Carlson R.W., Shirey S.B., Boyd F.R., Nixon P.H. (1995c) Stabilisation of Archaean lithospheric mantle: A Re-Os isotope study of peridotite xenoliths from the Kaapvaal Craton. *Earth and Planetary Science Letters*, **134**, 341-357

Pearson D.G., Emeleus C.H., Kelley S.P. (1996) Precise $^{40}Ar/^{36}Ar$ ago for the initiation of Palaeogene volcanism in the inner Hebrides and its regional significance. *Journal of the Geological Society of London*, **158**, 815-818

Pearson D.G., Larsen L., Walker R.J., Woodland S.J., Pederson A.K., Carlson R.W., Shirey S.B. (1999) The deep sources of plumes: Re-Os and Pt-Os isotope and PGE systematics of high $^{3}He/^{4}He$ West Green land picrites. *Proceedings of the 9th Annual Goldschmidt Conference*, 223.

Pearson D.G., Canil D., Shirey S. (2003) Mantle samples included in volcanic rocks: Xenoliths and diamonds. *Treatise on Geochemistry*, **2**, 1-106

Pearson D.G., Irvine G.J., Ionov D.A., Boyd F.R., Dreibus G.E. (2004) Re-Os isotope systematics and Platinum Group Element fractionation during mantle melt extraction: a study of peridotite xenoliths from the N. Lesotho and S. Namibian kimberlites, the Vitim volcanic field and massif peridotites from Beni Bousera. *Chemical Geology Special Volume: Highly Siderophile Elements*, in the press

Peate D.W., Baker J.A., Blichert-Toft J., Hilton D.R., Storey M., Kent A.J.R., Brooks C.K., Hansen A., Pedersen A.K., Duncan R.A. (2003) The Prinsen of Wales Bjerge Formation lavas, East Greenland: the transition from tholeiitic to alkalic magmatism during Palaeogene continental break-up. *Journal of Petrology*, **44**, 279-304

Pegram W.J., Allègre C.J. (1992) Osmium isotopic compositions from oceanic basalts. *Earth and Planetary Science Letters,* **111**, 59-68

Pepin R.O., Porcelli D. (2002) Origin of noble gases in the terrestrial planets. *Reviews in Mineralogy and Geochemistry,* **47**, 191-246

Perez N.M., Wakita H., Nakai S., Sano Y., William S.N. (1994) $^{3}He/^{4}He$ isotopic ratios in volcanic-hydrothermal discharges from the Canary Islands, Spain: implications on the origin of volcanic activity. *Mineralogical Magazine,* **58a**, 709-710

Perez N.M., Nakai S., Wakita H., Hernandez P.A., Salazar J.M. (1996) Helium-3 emission in and around Teide volcano, Tenerife, Canary Islands, Spain. *Geophysical Research Letters,* **23**, 3531-3534

Porcelli D.R., O'Nions R.K. and O'Reilly S.Y. (1986) Helium and strontium isotopes in ultramafic xenoliths. *Chemical Geology,* **54**, 237-249

Porcelli D.R., Stone J.O.H., O'Nions R.K. (1987) Enhanced $^{3}He/^{4}He$ ratios and cosmogenic helium in ultramafic xenoliths. *Chemical Geology,* **64**, 25-33

Porcelli D., Ballentine C.J. (2002) Models for the distribution of terrestrial noble gases and the evolution of the atmosphere. *Reviews in mineralogy and geochemistry,* **47**, 412-480

Porcelli D., Halliday A.N. (2001) The core as a possible source of mantle helium. *Earth and Planetary Science Letters,* **192**, 45-56

Porcelli D. and Wasserburg G.J (1995) Mass transfer of helium, neon, argon and xenon through a steady state upper mantle. *Geochimica et Cosmochimica Acta,* **59**, 4921-4937

Poreda R.J., Craig H., Arnorsson S., Welhan J.A. (1992) Helium isotopes in Icelandic geothermal systems: I. ^{3}He, gas chemistry and ^{13}C relations. *Geochimica et Cosmochimica Acta,* **56**, 4221-4228

Poreda R.J., Farley K.A. (1992) Rare gases in Samoan xenoliths. *Earth and Planetary Science Letters,* **113**, 129-144

Potts P.J. (1987) *A handbook of silicate rock analysis.* Blackie, Glasgow. Chapter 1, pp1-46

Puchtel I.S., Brügmann G.E., Hofmann A.W. (1999) Precise Re-Os mineral isochron and Pb-Nd-Os isotope systematics of a mafic-ultramafic sill in the 2.0Ga Onega plateau (Baltic Shield). *Earth and Planetary Science Letters,* **170**, 447-461

Puchtel I.S., Brügmann G.E., Hofmann A.W., Kulikov V.S., Kulikova V.V. (2001) Os isotope systematics of komatiitic basalts from the Vetreny belt, Baltic Shield: evidence for a chondritic source of the 2.45Ga plume. *Contributions to Mineralogy and Petrology,* **140**, 588-599

Puchtel I.S., Brandon A.D., Humayun M. (2004) Precise Pt-Re-Os isotope systematics of the mantle from 2.7-Ga Komatiites. *Earth and Planetary Science Letters,* in the press

Rachdi H., Berrahma M., Delaloye M., Faure-Muret A., Dahmani M. (1997) Le volcanisme tertiare du Rekkame (Maroc): pétrologie, géochemie et geochronologie. *Journal of African Earth Sciences,* **24**, 259-269

Rampino M.R., Stothers R.B. (1988) Flood basalt volcanism during the 250Myrs. *Science,* **241**, 663-666

Ramsey M.H. (1997) Sampling and sample preparation ***In:*** Gill R. *Modern analytical geochemistry.* Longman, pp12-28

Rehkämper M., Halliday A.N. (1997) Development and application of new ion-exchange techniques for the separation of the platinum group and other siderophile elements from geological samples. *Talanta,* **44**, 663-672

Rehkämper M., Halliday A.N., Wentz R.F. (1998) Low-blank digestion of geological samples for platinum-group element analysis using a modified Carius tube design. *Fresenius Journal of Analytical Chemistry,* **361**, 217-219

Reid M.R. and Graham D.W. (1996) Resolving lithospheric and sub-lithospheric contributions to helium isotope variations in basalts from the southwestern US. *Earth and Planetary Science Letters,* **144**, 213-222

Reisberg L., Allègre C.J., Luck J.-M. (1991) The Re-Os systematics of the Ronda ultramafic complex of Southern Spain. *Earth and Planetary Science Letters,* **105**, 196-213

Reisberg L., Zindler A., Marcantonio F., White W., Wyman D., Weaver B. (1993) Os isotope systematics in ocean island basalts. *Earth and Planetary Science Letters,* **120**, 149-167

Reisberg L., Lorand J.-P. (1995) Longevity of sub-continental mantle lithosphere from osmium isotope systematics in orogenic peridotite massifs. *Nature,* **376**, 159-162

Reiss W. (1861) Die Diabas- und Laven formation del Insel Palma. *Kreidel, Wiesbaden*, 11-20

Renne P. R., Swisher C. C., Deino A. L., Karner D. B., Owens T. L., DePaolo D. J., (1998) Intercalibration of standards, absolute ages and uncertainties in $^{40}Ar/^{39}Ar$ dating. *Chemical Geology,* **145**, 117-152

Revillon S., Chauvel C., Arndt N.T., Pik R., Martineau F., Fourcade S., Marty B (2002) Heterogeneity of the Caribbean plateau mantle source: Sr, O and He isotopic compositions from Gorgona Island. *Earth and Planetary Science Letters*, **205**, 91-106

Richard D., Marty B., Chaussidon M., Arndt N. (1996) Helium isotopic evidence for a lower mantle component in depleted Archean komatiite. *Science,* **273**, 93-95

Richardson S.H., Gurney J.J., Erlank A.J., Harris J.W. (1984) Origin of diamonds in ole enriched mantle. *Nature,* **310**, 198-202

Ripley E.M., Lambert D.D., Frick L.R. (1998) Re-Os, Sm-Nd and Pb isotopic constraints on mantle and crustal contributions to magmatic sulphide mineralization in the Duluth complex. *Geochimica et Cosmochimica Acta,* **62**, 3349-3365

Ripley E.M., Park Y.-R., Li C., Naldrett A.J. (1999) Sulfur and oxygen isotopic evidence of country rock contamination in the Voisey;s Bay Ni-Cu-Co deposit, Labrador, Canada. *Lithos,* **47**, 53-68

Ripley E.M., Park Y.-R., Lambert D.D., Frick L.R. (2001) Re-Os isotopic variations in carbonaceous pelites hosting the Duluth Complex: Implications for metamorphic processes associated with mafic magma chambers. *Geochimica et Cosmochimica Acta,* **65**, 2965-2978

Ringwood A.E., Kesson S.E., Hibberson W., Ware N. (1992) Origin of kimberlites and related magmas. *Earth and Planetary Science Letters,* **113**, 521-538

Rison W., Craig H. (1983) Helium isotopes and mantle volatiles in Loihi seamount and Hawaiian Island basalts and xenoliths. *Earth and Planetary Science Letters,* **66**, 407-426

Ritsema J., Allen R.M. (2003) The elusive mantle plume. *Earth and Planetary Science Letters,* **207**, 1-12

Robertson I.D.M., Dyson M, Hudson E.G., Crabb J.F., Willing M.J. and Hart M.K.W (1996) A case-hardened, low contamination ring-mill for multi-element geochemistry. *Journal of Geochemical Exploration,* **57**, 153-158

Roddick J.C. (1988) *The assessment of errors in $^{40}Ar/^{39}Ar$ dating.* ***In:*** Radiogenic Age and Isotopic Studies, Report 2. Geological Survey of Canada, Paper 88-2, pp. 7–16

Roeser H.A. (1982) Magnetic anomalies in the magnetic quite zone off Morocco. ***In:*** Rad U., Hinz K., Sarnthien M., Seibold E. (Eds.) *Geology of the Northwest African Continental Margin,* pp 61-68, Springer-Verlag, New York

Roest W.R., Dañobeitia J.J., Verhoef J., Collette B.J. (1992) Magnetic anomalies in the Canary Basin and the Mesozoic evolution of the central North Atlantic. *Marine and Geophysical Research,* **14**, 1-24

Rogers N.W., Hawkesworth C.J., Palacz Z.A. (1992) Phlogopite in the generation of olivine-melilitites from Namaqualand, South Africa and implications for element fractionation processes in the upper mantle. *Lithos,* **28**, 347-365

Rosenbaum J.M. (1994) Stable isotope fractionation between carbon dioxide and calcite at 900°C. *Geochimica et Cosmochimica Acta,* **58**, 3747-3753

Rossman K.J.R. and Taylor P.D.P. (1998) Isotopic compositions of the elements 1997. *Pure and applied chemistry.* **70**, 217-236

Roy-Barman M., Allègre C.J. (1994) $^{187}Os/^{186}Os$ ratios of mid-ocean ridge basalts and abyssal peridotites. *Geochimica et Cosmochimica Acta,* **58**, 5043-5054

Roy-Barman M., Allègre C.J. (1995) $^{187}Os/^{186}Os$ in oceanic island basalts: Tracing oceanic crust recycling in the mantle. *Earth and Planetary Science Letters,* **129**, 145-161

Roy-Barman M., Wasserburg G.J., Papanastassiou D.A., Chaussidon M. (1998) Osmium isotopic compositions and Re-Os concentrations in sulphide globules from basaltic glasses. *Earth and Planetary Science Letters,* **154**, 331-347

Rudnick R.L. (1995) Making continental crust. *Nature,* **378**, 571-578

Saal A.E., Rudnick R.L., Ravizza G.E., Hart S.R. (1998) Re-Os isotope evidence for the composition, formation and age of the lower crust. *Nature,* **393**, 58-61

Salters V.J.M., White W.M. (1998) Hf isotope constraints on mantle evolution. *Chemical Geology,* **145**, 447-460

Sasaki A. (1969) Sulphur isotope study of the Muskox intrusion, District of Mackenzie. *Geological Survey of Canada Paper,* **68-46**, 68pp.

Saunders A.D., Fitton J.G., Kerr A.C., Norry M.J., Kent R.W. (1997) The North Atlantic Igneous Province. ***In:*** Mahoney J.J., Coffin M.F. (eds) *Large Igneous Provinces: Continental, Oceanic and Planetary Flood Volcanism. Geophysical Monograph, American Geophysical Union* **100**, 45-93

Scaillet S. (2000) Numerical error analysis in $^{40}Ar/^{39}Ar$ dating. *Chemical Geology* **162**, 269–298

Scarsi P. (2000) Fractional extraction of helium by crushing of olivine and clinopyroxene phenocrysts: Effects on the $^{3}He/^{4}He$ measured ratio. *Geochimica et Cosmochimica Acta,* 64, 3751-3762

Schaefer B.F., Parkinson I.J., Hawkesworth C.J. (2000a) Deep mantle plume osmium isotope signatures from West Greenland Tertiary Picrites. *Earth and Planetary Science Letters,* **175**, 105-118

Schaefer B.F., Turner S.P., Rogers N.W., Hawkesworth C.J., Williams H.M., Pearson D.G., Nowell G.M. (2000b) Re-Os isotope characteristics of postorogenic lavas: Implications for the nature of young lithospheric mantle and its contributions to basaltic magmas. *Geology,* **28**, 563-566

Schaefer B.F., Turner S., Parkinson I., Rogers N., Hawkesworth C. (2002) Evidence for recycled Archaean oceanic mantle lithosphere in the Azores plume. *Nature,* **420**, 304-307

Schersten A., Elliott T., Hawkesworth C., Norman M. (2004) Tungsten isotope evidence that mantle plumes contain no contribution from the Earth's core. *Nature,* **427**, 234-237

Schiano P., Birck J.-L., Allegre C.J. (1997) Osmium-strontium-neodymium-lead isotopic convariations in mid-ocean ridge basalt glasses and the heterogeneity of the upper mantle. *Earth and Planetary Science Letters,* **150**, 363-379

Schiano P., Burton K.W., Dupre B., Birck J.-L., Guille G., Allègre C.J. (2001) Correlated Os-Pb-Nd-Sr isotopes in the Austral-Cook chain basalts: the nature of mantle components in plume sources. *Earth and Planetary Science Letters,* **186**, 527-537

Schiffman P., Staudigel H (1994) Hydrothermal alteration of a seamount complex, La Palma, Canary Islands: Implications for metamorphism in accreted terranes. *Geology,* **22**, 151-154

Schilling J.-G. (1973) Iceland mantle plume: Geochemical evidence along the Reykjanes Ridge, *Nature,* **242**, 565-571

Schilling J.-G., Meyer P.S., Kingsley R.H. (1982) Evolution of the Iceland hotspot. *Nature,* **296**, 313-320

Schilling J.-G., Kingsley R., Fontignie D., Poreda R., Xue S. (1999) Dispersion of the Jan Mayen and Iceland mantle plumes in the Arctic: a He-Pb-Nd-Sr isotope tracer study of basalts from the Kolbeinsey, Mohns and Knipovich ridges. *Journal of Geophysical Research,* **104**, 10543-10569

Schmidberger S.S., Simonetti A., Francis D. (2001) Sr-Nd-Pb isotope systematics of mantle xenoliths from Somerset island kimberlites: Evidence for lithosphere stratification beneath Arctic Canada. *Geochimica et Cosmochimica Acta,* **65**, 4243-4255

Schmincke H.-U., Klügel A., Hansteen T.H., Hoernle K., Bogaard P., van den. (1998) Samples from the Jurassic ocean crust beneath Gran Canaria, La Palma and Lanzarote (Canary Islands). *Earth and Planetary Science Letters,* **163**, 343-360

Schoenberg R., Kruger F.J., Nägler T.F., Meisel T., Kramers J.D. (1999) PGE enrichment in chromitite layers and the Merensky Reef of the Bushveld Complex; a Re-Os and Rb-Sr isotope study. *Earth and Planetary Science Letters,* **172**, 49-64

Schulze D.J (1989) Constraints on the abundance of eclogite in the upper mantle. *Journal of Geophysical Research,* **94**, 4205-4212

Schulze D.J., Valley J.W., Spicuzza M.J. (2000) Coesite eclogites from the Roberts Victor kimberlite, South Africa. *Lithos,* **54**, 23-32

Sclater J.G., Parsons B., Jaupart C. (1981) Oceans and continents: similarities and differences in the mechanisms of heat loss. *Journal of Geophysical Research,* **86**, 11535-11552

Seth B., Day J., Thirlwall M., Hilton D., Gronvold K., Macpherson C. (2004) Multi-isotopic constraints on magma sources in central Iceland. *Geochimica et Cosmochimica Acta,* **68**, A589

Shen J.J., Papanastassiou D., Wasserburg G.J. (1996) Precise Re-Os determinations and systematics of iron meteorites. *Geochimica et Cosmochimica Acta,* **60**, 2887-2900

Shen Y., Solomon S.C., Bjarnason I.T., Wolfe C.J. (1998) Seismic evidence for a lower-mantle origin of the Iceland plume, *Nature*, **395**, 62-65

Shirey S.B. (1997) Re-Os isotopic composition of Midcontinent rift system picrites: implications for plume-lithosphere interaction and enriched mantle sources. *Canadian Journal of Earth Sciences,* **34**, 489-503

Shirey S.B., Walker R.J. (1995) Carius tube digestion for low-blank rhenium-osmium analysis. *Analytical Chemistry,* **67**, 2136-2141

Shirey S.B., Walker R.J. (1998) The Re-Os isotope system in cosmochemistry and high-temperature geochemistry. *Annual Reviews of Earth and Planetary Sciences,* **26**, 423-500

Skinner E.M.W., Clement C.R., Gurney J.J., Apter D.B., Hatton C.J. (1992) The distribution and tectonic setting of South African kimberlites. *Russian Geology and Geophysics.* **33**, 26-31

Skovgaard A., Storey M., Baker J., Blusztajn J. and Hart S.R. (2001) Osmium-oxygen isotopic evidence for a recycled and strongly depleted component in the Iceland mantle plume. *Earth and Planetary Science Letters,* **194**, 259-275

Sleep N.H. (1990) Hotspots, mantle plumes: some phenomenology. *Journal of Geophysical Research,* **95**, 6715-6736

Smit Y. (2001) *The Snaefellsnes Transect: A geochemical cross-section through the Iceland plume.* Unpublished PhD thesis, Open University, UK, 246pp.

Smith C.B. (1983) Pb, Sr and Nd isotopic evidence for the sources of southern African Cretaceous kimberlites. *Nature,* **304**, 51-54

Smith A.D. (2003) Critical evaluation of Re-Os and Pt-Os isotopic evidence on the origin of intraplate magmatism. *Journal of Geodynamics,* **36**, 469-484

Smith C.H., Kapp H.E. (1963) The Muskox Intrusion , a recently discovered layered intrusion in the Coppermine River Area, Northwest Territories, Canada. *Mineralogical Society of America Special Paper,* **1**, 30-35

Smoliar M.I., Walker R.J., Morgan J.W. (1996) Re-os ages of Group IIA, IIIA, IVA and IVB iron meteorites. *Science,* **271**, 1099-1102

Snow J.E., Reisberg L. (1995) Os isotopic systematics of the MORB mantle: results from altered abyssal peridotites. *Earth and Planetary Science Letters,* **133**, 411-421

Spencer A.B. (1969) Alkalic Igneous rocks of the Balcones province, Texas. *Journal of Petrology,* **10**, 272-306

Spriggs A.J. (1988) *An isotopic and geochemical study of kimberlites and associated alkaline rocks from Southern Namibia.* Ph.D. thesis, University of Leeds, UK

Staudacher T and Allégre C.J. (1988) Recycling of oceanic crust and sediments: the noble gas subduction barrier. *Earth and Planetary Science Letters,* **89**, 173-183

Staudigel H. (1981) *Der basale Komplex von La Palma, submarine vulkanische prozesse, petrologie, geochemie und sekundare prozesse in herausgehobenen, submarinen teil einer ozean-ischen insel.* Dissertation. Ruhr Universitätat, Buchum, Germany, 1-357

Staudigel H., Schmincke H.-U. (1984) The Pliocene Seamount Series of La Palma, Canary Islands. *Journal of Geophysical Research,* **89**, 11195-11215

Staudigel H., Féraud G., Giannerini G. (1986) The history of intrusive activity of the island of La Palma (Canary Islands). *Journal of Volcanology and Geothermal Research,* **27**, 299-322

Stewart B.W., DePaolo D.J. (1992) Diffusive isotopic contamination of mafic magma be coexisting silicic liquid in the Muskox intrusion. *Science,* **255**, 708-711

Storey M., Duncan R.A., Pedersen A.K., Larsen L.M., Larsen H.C. (1998) $^{40}Ar/^{39}Ar$ geochronology of the West Greenland Tertiary volcanic province. *Earth and Planetary Science Letters,* **160**, 569-586

Stuart F.M., Ellam R.M., Harrop P.J., Fitton J.G. and Bell B.R. (2000) Constraints on mantle plumes from helium isotopic composition of basalts from the British Tertiary Igneous Province. *Earth and Planetary Science Letters,* **177**, 273-285

Stuart F.M., Lass-Evans S., Fitton J.G., Ellam R.M. (2003) High $^{3}He/^{4}He$ ratios in picritic basalts from Baffin Island and the role of a mixed reservoir in mantle plumes. *Nature,* **424**, 57-59

Sturm M.E., Klien E.M., Graham D.W., Karsten J. (1999) Age constraints on crustal recycling to the mantle beneath the southern Chile ridge: He-Pb-Sr-Nd isotope systematics. *Journal of Geophysical Research.* **104**, 5097-5114

Sun S.-S. (1980) Lead isotopic study of young volcanic rocks from mid-ocean ridges, ocean islands and island arcs. *Philosophical transactions of the Royal society of London.* **A297**, 409-44545

Sun. S.-S., Hanson G.N. (1975) Evolution of the mantle: geochemical evidence from alkali basalt *Geology,* **3**, 297-302

Sun W., Bennett V.C., Eggins S.M., Arculus R.J., Perfit M.R. (2003a) Rhenium systematics in submarine MORB and back-arc basin glasses.: Laser ablation ICP-MS results. *Chemical Geology,* **196**, 259-281

Sun W., Bennett V.C., Eggins S.M., Kamenetsky V.S., Arculus R.J. (2003b) Enhanced mantle-to-crust rhenium transfer in undegassed arc magmas. *Nature,* **422**, 294-297

Sun W., Arculus R.J., Bennett V.C., Eggins S.M., Binns R.A. (2000c) Evidence for rhenium enrichment in the mantle wedge from submarine arc-like volcanic glasses (Papua New Guinea). *Geology,* **31**, 845-848

Sun S.-s. and McDonough W.F. (1989) Chemical and isotopic systematics of oceanic basalts: implications for mantle compositions and processes. ***In:*** Saunders A.D. and Norry M.J. (Eds.) *Magmatism in the Ocean Basins.* Geological Society Special Publication, **42**, 313-345

Szérémata N., Laj C., Guillou H., Kissel C., Mazaud A., Carracedo J.C. (1999) Geomagnetic paleosecular variation in the Bruhnes period, from the Island of El Hierro (Canary Islands). *Earth and Planetary Science Letters,* **165**, 241-253

Takahashi E., Shimazaki Y., Tsuzaki Y., Yoshida H. (1993) Melting study of a peridotite KLB-1 to 6.5GPa and the origin of basaltic magmas. *Philosophical Transactions of the Royal Society of London, Series A,* **342**, 105-120

Taylor H. P. Jr., Forester R.W. (1971) Low-O^{18} igneous rocks from the intrusive complexes of Skye, Mull, and Ardnamurchan, Western Scotland. *Journal of Petrology,* **12**, 465-498

Tegner C., Duncan R.A., Bernstein S., Brooks C.K., Bird D.K., Storey M. (1994) ^{40}Ar-^{39}Ar geochronology of Tertiary mafic intrusions along the East Greenland rifted margin: relation to flood basalts and the Iceland hotspot track. *Earth and Planetary Science Letters,* **156**, 75-88

Tepley F.J., Davidson J.P. (2003) Mineral-scale Sr-isotope constraints on magma evolution and chamber dynamics in the Rum layered intrusion, Scotland. *Contributions to Mineralogy and Petrology,* **145**, 628-641

Thirlwall M.F. (1997) Pb isotopic and elemental evidence for OIB derivation from young HIMU mantle. *Chemical Geology,* **139**, 51-74

Thirlwall M.F., Upton B.G.J., Jenkins C (1994) Interaction between continental lithosphere and the Iceland plume. – Sr-Nd-Pb isotope geochemistry of Tertiary basalts, NE Greenland. *Journal of Petrology,* **35**, 839-879

Thirlwall M.F., Jenkins C., Vroon P.Z., Mattey D.P. (1997) Crustal interaction during construction of ocean islands: Pb-Sr-Nd-O isotope geochemistry of the shield basalts of Gran Canaria, Canary Islands. *Chemical Geology,* **135**, 233-262

Thirlwall M.F., Taylor R.N., Mattey D.P., Macpherson C.G., Gee M.A.M., Murton B.J. (1999) Oxygen isotope systematics of Reykjanes ridge MORB: Constraints in the origin and composition of Icelandic plume mantle. *Ninth Annual V.M. Goldschmidt Conference, Lunar and Planetary Institute Contribution* **971**, 296-297

Thirlwall M.F., Singer B.F., Marriner G.F. (2000) ^{39}Ar-^{40}Ar ages and geochemistry of the basaltic shield stage of Tenerife, Canary Islands, Spain. *Journal of Volcanology and Geothermal Research,* **103**, 247-297

Thirlwall M.F., Gee M.A.M., Taylor R.N., Murton B.J. (2004) Mantle components in Iceland and adjacent ridges investigated using double-spike Pb isotope ratios. *Geochimica et Cosmochimica Acta,* **68**, 361-386

Thompson R.N. (1982) Magmatism of the British Tertiary Volcanic Province. *Scottish Journal of Geology,* **18**, 49-107

Thompson R.N., Morrison M.A., Dickin A.P., Hendry G.L. (1983) Continental flood basalts ... arachnids rule ok? In: Hawkesworth C.J., Norry M.J. (eds) *Continental Basalts and Mantle xenoliths.* Nantwich, UK: Shiva, 158-185

Todt W., Cliff R.A., Hanser A., Hofmann A.W. (1996) Evaluation of a ^{202}Pb-^{205}Pb double spike for high precision lead isotope analysis. ***In:*** (Hart S.R., Basu A.) *Earth Processes: Reading the Isotopic code.* American geophysical union. **95**, 429-437

Tolstikhin I.N., Kamensky I.L., Marty B., Nivin V.A., Vetrin V.R., Balganskaya E.G., Ikorsky S.V., Gannibal M.A., Weiss D., Verhulst A., Demaiffe D. (2002) Rare gas isotopes and parent trace elements in the ultrabasic-alkaline-carbonatite complexes, Kola peninsula: Identification of lower mantle component. *Geochimica et Cosmochimica Acta,* **66**, 881-901

Trull T.W., Kurz M.D. (1993) Experimental measurements of ^{3}He and ^{4}He mobility in olivine and clinopyroxene at magmatic temperatures. *Geochimica et Cosmochimica Acta,* **57**, 1313-1324

Turner S., Hawkesworth C. (1995) The nature of the sub-continental mantle: constraints from the major-element composition of continental flood basalts. *Chemical Geology,* **120**, 295-314

Turner S.P., Hawkesworth C., Gallagher K., Stewart K., Peate D., Mantovani M. (1996) Mantle plumes, flood basalts and thermal models for melt generation beneath continents: assessment of a conductive heating model and application to the Parana. *Journal of Geophysical Research,* **101**, 11503-11518

Upton B.G.J., Emeleus C.H., Heaman L.M., Goodenough K.M., Finch A. (2003) Magmatism of the mid-Proterozoic Gardar province, South Greenland: chronology, petrogenesis and geological setting. *Lithos,* **68**, 43-65

Ussing N.V. (1911) Geology of the country around Julianehaab, Greenland. *Meddelelser om Grønvold,* pp1-376

Valbracht P.J., Staudigel H., Honda M., McDougall I., Davies G.R. (1996) Isotopic tracing of volcanic source regions from Hawaii: decoupling of gaseous from lithophile magma components. *Earth and Planetary Science Letters,* **144**, 185-19

Valley J.W., Kitchen N., Kohn M.J., Niendorf C.R., Spicuzza M.J. (1995) UWG-2, a garnet standard for oxygen isotope ratios: strategies for high precision and accuracy with laser heating. *Geochimica et Cosmochimica Acta,* **59**, 5223-5231

van der Hilst R.D., Widiyantoro S., Engdahl E.R. (1997) Evidence for deep mantle circulation from global tomography. *Nature,* **386**, 578-584

Van Keken P.E., Hauri E.H., Ballentine C.J. (2002) Mantle mixing: the generation, preservation and destruction of chemical heterogeneity. *Annual Reviews in Earth and Planetary Sciences,* **30**, 493-525

Vance D., Stone J.O.H., O'Nions R.K. (1989) He, Sr and Nd isotope in xenoliths from Hawaii and other oceanic islands. *Earth and Planetary Science Letters,* **96**, 147-160

Verhoef J., Collette B.J., Dañobeitia J.J., Roeser H.A., Roest W.R. (1991) Magnetic anomalies off West-Africa (20-38°N). *Marine and Geophysical Research,* **13**, 81-103

Verwoerd W.J. (1990) The Saltpetre Kop ring structure, Cape Province, South Africa. *Tectonophysics.* **171**, 275-285

Viljoen K.S. (1988) Petrology of the Sutherland Commonage Melilitite intrusives. *MSc. Thesis,* University of Cape Town.

Villeneuve M.E., MacIntyre D.G. (1997) Laser $^{40}Ar/^{39}Ar$ ages of the Babine porphyries and Newman Volcanics, Fulton Lake map area, west-central British Columbia. ***In:*** *Radiogenic Age and Isotopic Studies,* Report 10. Geological Survey of Canada, Current Research 1997-F, pp.131–139

Villeneuve M.E., Sandeman H.A., Davis W.J. (2000) A method for the intercalibration of U-Th-Pb and $^{40}Ar/^{39}Ar$ ages in the Phanerozoic. *Geochimica et Cosmochimica Acta,* **64**, 4017-4030

Völkening J., Walczyk T., Heumann K.G. (1991) Osmium isotope ratio determination by negative thermal ionisation mass spectrometry. *International Journal of Mass Spectrometry and Ion Processes,* **105**, 139-147

Von Buch L. (1825) *Physikalische Beschriebungen der Canarischen Inseln.* Berlin, 201pp.

Wager L.R. (1960) The major element variation of the Layered Series of the Skaergaard intrusion and re-estimation of the average composition of the hidden layered series and of the successive residual magma. *Journal of Petrology,* **1**, 364-398

Wager L.R., Brown G.M. (1968) *Layered Igneous Rocks,* Oliver and Boyd, Ltd. Edinburgh

Wager L.R., Brown G.M., Wadsworth W.J. (1960) Types of igneous cumulates. *Journal of Petrology,* **1**, 73-85

Walker R.J., Carlson R.W., Shirey S.B., Boyd F.R. (1989) Os, Sr, Nd and Pb isotope systematics of southern African peridotite xenoliths: Implications for the chemical evolution of subcontinental mantle. *Geochimica et Cosmochimica Acta,* **53**, 1583-1595

Walker R.J., Morgan J.W., Horan M.F., Czamanske G.k., Krogstad E.J., Fedorenko V.A., Kunilov V.E. (1994) Re-Os isotopic evidence for an enriched-mantle source for Noril'sk-type, ore bearing intrusions, Siberia. *Geochimica et Cosmochimica Acta,* **58**, 4179-4197

Walker R.J., Morgan J.W., Horan M.F. (1995) Osmium-187 enrichment in some plumes: evidence for core-mantle interaction? *Science,* **269**, 819-822

Walker R.J., Morgan J.W., Hanski E.J., Smolkin V.F. (1997) Re-Os systematics of Early Proterozoic ferropicrites, Penchenga Complex, north western Russia: evidence for ancient ^{187}Os-enriched plumes. *Geochimica et Cosmochimica Acta,* **61**, 3145-3160

Walker R.J., Storey M., Kerr A.C., Tarney J., Arndt N.T. (1999) Implications of ^{187}Os isotopic heterogeneities in a mantle plume: evidence from Gorgona Island and Curacao. *Geochimica et Cosmochimica Acta,* **63**, 713-728

Walker R.J., Horan M.F., Morgan J.W., Becker H., Grossman J.N., Rubin A.E. (2002) Comparative ^{187}Re-^{187}Os systematics of chondrites: Implications regarding early solar system processes. *Geochimica et Cosmochimica Acta,* **66**, 4137-4201

Walker R.J., Prichard H.M., Ishiwaratari A., Pimentel M. (2002) The osmium isotopic composition of convecting upper mantle deduced from ophiolite chromites. *Geochimica et Cosmochimica Acta,* **66**, 329-345

Wallace M.E., Green D.H. (1988) An experimental determination of primary carbonatite magma composition. *Nature,* **335**, 343-346

Wallace M.E., Green D.H. (1991) The effect of bulk rock composition on the stability of amphibole in the upper mantle: Implications for solidus position and mantle metasomatism. *Contributions to Mineralogy and Petrology,* **44**, 1-19

Weaver B.L. (1991a) The origin of ocean island basalt end-member compositions: Trace element and isotopic constraints. *Earth and Planetary Science Letters,* **104**, 381-397

Weaver B.L (1991b) Trace element evidence for the origin of ocean-island basalts. *Geology,* **19**, 123-126

White W.M. (1985) Sources of oceanic basalts: Radiogenic isotope evidence. *Geology,* **13**, 115-118

Whitehouse M.J., Neumann E.-R. (1995) Sr-Nd-Pb isotope data for ultramafic xenoliths from Hierro, Canary Islands: Melt infiltration processes in the upper mantle. *Contributions to Mineralogy and Petrology,* 119, 239-246

Widom E., Shirey S.B. (1996) Os isotope systematics in the Azores: implications for mantle plume sources. *Earth and Planetary Science Letters*, **142**, 451-465

Widom E., Hoernle K.A., Shirey S.B., Schminke H.-U. (1999) Os isotope systematics in the Canary Islands and Madiera: Lithospheric contamination and mantle plume signatures. *Journal of Petrology*, **40**, 279-296

Widom E., Farquhar J. (2002) Oxygen isotope signatures in olivines from São Miguel (Azores) basalts: implications for crustal and mantle processes. *Chemical Geology,* **193**, 237-255

Wignall P.B. (2001) Large igneous provinces and mass extinctions. *Earth Science Reviews,* **53**, 1-33

Williams H.M., Turner S.P., Pearce J.A., Kelley S.P., Harris N.B.W. (2004) Nature of the source regions for post-collisional, potassic magmatism in southern and northern Tibet from geochemical variations and inverse trace element modelling. *Journal of Petrology,* **45**, 555-608

Wilson J.T. (1963) A possible origin of the Hawaiian islands. *Canadian Journal of Physics,* **41**, 863-870

Wilson M., Downes H. (1991) Tertiary-Quaternary extension-related alkaline magmatism in western and central Europe. *Journal of Petrology,* **32**, 811-849

Wilson M., Rosenbaum J.M., Dunworth E.A. (1995) Melilitites: partial melts of the thermal boundary layer? *Contributions to Mineralogy and Petrology,* **119**, 181-196

Wilson A.H., Shirey S.B., Carlson R.W. (2003) Archaean ultra-depleted Komatiites formed by hydrous melting of cratonic mantle. *Nature,* **423**, 858-860

Wolfe C.J., Bjarnasson I.T., VanDecar J.C., Solomon S.C. (1997) Seismic structure of the Iceland mantle plume. *Nature,* **385**, 245-247

Wooden J.L., Czamanske G.K., Federenko V.A., Arndt N.T., Chauvel C., Bouse R.M., King B.W., Knight R.J., Siems D.F. (1993) Isotopic and trace-element constraints on mantle and crustal contributions to Siberian continental flood-basalts, Noril'sk area, Siberia. *Geochimica et Cosmochimica Acta,* **57**, 3677-3704

Woodhead J.D., Greenwood P., Harmon R.S., Stoffers P. (1993) Oxygen isotope evidence for recycled crust in the source of EM-type oceanic island basalts. *Nature,* **362**, 809-813

Woodhead J.D. (1996) Extreme HIMU in an oceanic setting: the geochemistry of Mangaia Island (Polynesia), and temporal evolution of the Cook-Austral hotspot. *Journal of Volcanology and Geothermal Research,* **72**, 1-19

Woodland S.J. (1999) Development of ICP-MS isotope dilution preconcentration techniques for determination of platinum group elements in volcanic rocks. *Unpublished PhD thesis, The University of Durham.* 384pp.

Woodland S.J., Pearson D.G. (1999) Platinum group element analysis of geological samples using isotope dilution: a comparison of fire assay and anion-exchange chromatography, preconcentration techniques. **In:** Holland G., Tanner S.D. (Eds.) *Plasma Source Mass Spectrometry: New Developments and Applications. Royal Society of Chemistry Special Publication.* 267-276

Woodland S.J., Pearson D.G., Thirlwall M.F. (2002) A platinum group element and Re-Os isotope investigation of siderophile element recycling in subduction zones: comparison of Grenada, Lesser Antilles Arc and the Izu-Bonin arc. *Journal of Petrology,* **43**, 171-198

Wulff-Pedersen E., Neumann E.-H., Jensen B.B. (1996) The upper mantle under La Palma, Canary Islands: formation of Si-K-Na-rich melt and its importance as a metasomatic agent. *Contributions to Mineralogy and Petrology,* **125**, 113-139

Yin Q.Z., Jacobsen S.B., Lee C.-T., McDonough W.F., Rudnick R.L., Horn I. (2001) A gravimetric K_2OsCl_6 standard: Application to precise and accurate Os spike calibration. *Geochimica et Cosmochimia Acta,* **65**, 2113-2127

Zheng Y-F. (1990) Calculation of oxygen isotope fractionation in anhydrous silicate minerals. *Geochimica et Cosmochimica Acta.* **57**, 1079-1091

Zindler A., Hart S.R. (1986) Chemical geodynamics. *Annual Reviews in Earth and Planetary Sciences,* **14**, 493-571

Appendix A - Locations and petrographical descriptions of samples

List of mineralogical data abbreviations for appendix A

Ol	-	olivine
Cpx	-	clinopyroxene (commonly augite unless stated)
Opx	-	orthopyroxene (commonly hypersthene unless stated)
Gnt	-	garnet
Fd	-	feldspar
Pl	-	plagioclase feldspar
Ne	-	nepheline
Me	-	melilite
Le	-	leucite
Sd	-	sanidine
Or	-	orthoclase
Ao	-	anorthoclase
Qtz	-	quartz
Sp	-	spinel
Sh	-	sphene
Ap	-	apatite
Hy	-	hauyne
Ep	-	epidote
Mt	-	Fe-Ti oxide such as magnetite
Cpy	-	chalcopyrite
Cr	-	chromite
Pv	-	perovskite
Il	-	ilmenite
Zr	-	zircon
Hbl	-	hornblende
Am	-	amphibole
Ph	-	phlogopite mica
Bi	-	biotite mica
Mu	-	muscovite mica
Chl	-	chlorite
Chlr	-	chloritoid
Tr-Ac	-	tremolite-actinolite
Ser	-	serpentinite
C	-	clay alteration minerals (e.g. sericite)
CC	-	calcite/dolomite
Z	-	zeolite
Gl	-	glass

Modal percentage of phenocrysts as a function of the whole rock matrix are estimated to be accurate to ±20%

Table A.1 *Central and Northern Iceland locations (Chapter 2)*

Sample	Location	Lat (°N)	Lon (°W)	Lithology
KVK-147	Hvannalindir	64.52	16.21	Subglacial basalt glass (Gp3)
KVK-168	Jardfraedingslod	64.46	16.38	Subglacial basalt glass (Gp3)
NAL-357	Upptyppingar	65.02	16.14	Subglacial basalt glass (Gp3)
KVK-169	Jardfraedingslod	64.46	16.30	Subglacial basalt glass (Gp2)
NAL-355	Upptyppingar	65.02	16.14	Subglacial basalt glass (Gp2)
NAL-356	Upptyppingar	65.02	16.14	Subglacial basalt glass (Gp2)
NAL-355/6	Upptyppingar	65.02	16.14	Subglacial basalt glass (Gp2)
NAL-239	Ketildyngia	65.27	16.43	Subglacial basalt glass (Gp2)
Herdubried	Herdubried	65.10	16.21	Subglacial basalt glass (Gp1)
SAL-306	Bardarbunga	64.42	17.35	Subglacial basalt glass (Gp1) NAL-496 Gaesahruikir 64.46 17.29 Subglacial basalt glass (Gp1)
SAL-575	South Lowlands	63.32	19.23	Subglacial basalt glass (Gp1)
NAL-688	Eggert	65.15	16.29	Picrobasalt pillow lava (Gp1) **P**
NAL-626	Fjallsendi	65.03	17.05	Basalt **P**
TH-29	Theistareykir	65.53	16.50	Picrite
NAL-611	Kistufell	64.48	17.10	Picrite
NAL-625	Vadalda	64.56	16.28	Picrobasalt **P**
PJOR	Pjorsardalur	64.08	20.10	Picrite
9613	Odadahruan	65.09	16.32	Picrite
TRO-53	Trolladyngia	64.54	17.06	Picrite

P *= Petrographical description in table A.2 - Gp1, Gp2, Gp3 = Groupings defined in chapter 2 for Icelandic basalts. Location names are from Langmailingar Islands (1981): map sheets 5 (midausterland), 7 (nordausterland) and 8 (mid-island).*

Table A.2 *Petrography of selected Icelandic lavas (Chapter 2)*

	Modal % phenocrysts					Groundmass	Comments
Sample	Ol	Cpx	Opx	Feld	Sp		
NAL-688	10	-	-	-	<0.5	Gl Pl Sp	pillow lava - skeletal strained Ol - red chrome Sp
NAL-626	-	5	-	30	-	Gl Pl Ol Cpx Mt	vesicular - glomeroporphyritic, complex zoned labradorite, with inclusion-rich cores
NAL-625	10	10	5	-	-	Pl Cpx Ol Gl	vesicular – strained olivine megacrysts – reaction rims on Ol and Cpx, not Opx – Sp inclusions

Table A.3 *Petrography of an ugandite, Bumfumbira, East Africa (Chapter 3)*

	Modal % phenocrysts		Groundmass	Comments
Sample	Ol	Cpx		
PHN2902A	8	16	Ne Cpx Gl Mt Cr	vesicular – strong resorbtion textures – zoned Cpx with rotten cores and Cr inclusions – mixing boundary evidence (MBE)

Table A.4 *Petrography of a eclogite, 79Ma Roberts Victor kimberlite pipe, South Africa (Chapter 3)*

	Modal % mineralogy		Interstices	Comments
Sample	Gnt	Cpx		
RV2000	35	65	Cpx Mt Opx Ep Chl Tr-Ac Ser Bi	pyrope-almandine Gnt (fresh) - omphacite px, zoned, inc. epidote (~40% crystals unaltered) – complex reaction histories

Table A.5 *South African olivine melilitite locations and ages (Chapter 3)*

Sample	Location	Age (Ma)	Dating method and reference	
KSV-256	Sutherland, Western Cape	75.8±1.3	K-Ar	Duncan *et al.*, 1978
KSV-266	Sutherland, Western Cape	75.8±1.3	K-Ar	Duncan *et al.*, 1978
SPK-1	Salt Petre Kop, Western Cape	73.9±1.3	K-Ar	Duncan *et al.*, 1978
SPK-2	Salt Petre Kop, Western Cape	73.9±1.3	K-Ar	Duncan *et al.*, 1978
SPK-3	Salt Petre Kop, Western Cape	73.9±1.3	K-Ar	Duncan *et al.*, 1978
ROB-10	Robertson, Western Cape	63.7±1.3	K-Ar	Duncan *et al.*, 1978
ROB-11	Robertson, Western Cape	63.7±1.3	K-Ar	Duncan *et al.*, 1978
ZW-1	Zwartheuwel, NBW	77	K-Ar	Moore & Verwoerd, 1985
BKB-10	Bruinkop pipe B, NBW	72	Ar-Ar	G. Kiviets, unpubl, 2000
BKA-10	Bruinkop pipe A, NBW	72	Ar-Ar	G. Kiviets, unpubl, 2000
WK-1	Wolfkraal, NBW	72	Ar-Ar	G. Kiviets, unpubl, 2000
HO-5	Hoedkop, NBW	80	K-Ar	Moore & Verwoerd, 1985
SP-3	Spioenkop, NBW	75	Ar-Ar	G. Kiviets, unpubl, 2000
SP-4	Spioenkop, NBW	75	Ar-Ar	G. Kiviets, unpubl, 2000

Table A.6 *Petrography of Western Cape Province (WCMP) and Namaqualand-Bushmanland-Warmbad (NBW) olivine melilitites and proto-kimberlites (Chapter 3)*

	Modal % Ol phenocrysts		Groundmass	Comments
Sample	megacrysts	microcrysts		
SPK-1	5	35	Ol Me Mt Cpx Ao Pv Ph Z	microporphyritic – blue cored melilite - <10% Ol strained, inclusion-rich rims barren cores
SPK-2	6	40	Ol Me Mt Cpx Ao Pv Ph Chl C CC	<10% strained Ol – blue cored melilite – Ao interstitial late - Ol skeletal or zoned - MBE
SPK-3	4	40	Ol Me Mt Cpx Ao Pv Ph Chl C	Ol zoned, inclusion rich microporphyritic
ROB-10	1	20	Ol Mt Cpx Ao Ser	<10% strained Ol – Ao interstitial – no Me or Pv Ol orientated? – Cpx laths
ROB-11	2	20	Ol Mt Cpx Ao Ph CC Qtz	ghost structure of Mt core Ao to Or, Qtz and CC
ZW-1	5	40	Ol Pv Mt Cpx Ao C Chl Z	strained and unstrained Ol Qtz+Fd ghost structure

BKB-10	3	45	Ol Pv Mt Cpx Ph Chl Ao	exsolution lamellae in Cpx
BKA-10	3	40	Ol Il Pv Mt Cpx Chl C Ser	as BKB-10 lacks Me or Fd due to alteration?
WK-1	3	35	Ol Il Mt Pv Me Cpx Ao Bi Chl	Il macrocryst – ghost structure Fd+Mt+Bt+Chl – Me not cored strained and unstrained Ol
HO-5	15	10	Ol Pv Mt Ph C Z Ser	megacrysts zoned, strained or aggregate Ol - highly altered Matrix
SP-3	4	40	Ol Mt Pv Cpx Me Ao Ph Chl Ser	Fe-rich Chl blebs ($Fe(OH)^{-}$) and Ph masses – <10% Strained Ol
SP-4	2	40	Ol Mt Pv Cpx Me Ao Z Ph Chl	Fe-rich Chl blebs – altered Me <5% Strained Ol

Here the distinction of micro-phenocrysts and phenocrysts or megacrysts is based upon an arbitrary grain-size threshold of 1mm

Table A.7 *Skye and East Greenland sample locations (Chapter 2)*

Sample	Location[#]	BGS Grid Reference[§]	Lithology[§]
SK266	SMLS	NG 248 487	Olivine porphyritic basalt lava
BB1	SMLS	NG 328 302	Olivine-spinel phyric basalt lava
LL1	SMLS	NG 442 679	Olivine porphyritic basalt lava
SK291	SMLS	NG 384 641	Olivine porphyritic basalt lava
INV1	LMS	NG 521 606	Olivine dolerite sill
BH1	LMS	NG 371 717	Picrite sill
SR81	LMS	NG 371 718	Picrite dyke
SK056	SDS	NG 450 192	Feldspathic Peridotite
SK057	SDS	NG 451 190	Feldspathic Peridotite
SK204	SDS	NG 426 180	Feldspathic Peridotite
SK208	CC	NG 449 200	Bytownite Troctolite
EG2240	PWF	-	Olivine phyric basalt lava
EG2244	PWF	-	Olivine phyric basalt lava
EG3359	PWF	-	Olivine phyric basalt lava

[#]SMLS = Skye Main Lava Series, LMS = Little Minch Sills, SDS = Skye Dyke Swarm, CC = Cuillin Complex, PWF = Prinsen Af Wales Fm., East Greenland. [§]Data from Stuart et al. (2000)

Table A.8 *Freemans Cove Complex sample location - lithology (Chapter 3)*

Sample	Lat (°N)	Lon (°W)	Lithology	^{40}Ar-^{39}Ar (Ma) ±2σ
KIA99-BI-1	751580	980194	Nephelinite dyke	
KIA99-BI-2	751400	980200	Olivine gabbro	
KIA99-BI3a	751714	982285	Melilitite-rich breccia pipe	
KIA99-BI4	751123	982205	Basanite	
KIA99-BI5	750975	981931	Nephelinite	
KIA99-BI6	750968	981857	Basanite	
KIA99-BI7	750936	981962	Basanite dyke	
KIA99-BI8	750575	982711	Basanite	
KIA99-BI9	750554	983059	Trachyte	54.5±0.4 (Sanidine)

KIA99-BI10A	750089	982304	Basanite block	
KIA99-BI10B	750089	982304	Basanite block (with pyroxene comb-layered vein)	
KIA99-BI10C	750089	982304	Basanite dyke	
KIA99-BI10D	750089	982304	Nephelinite dyke	
KIA99-BI10E	750089	982304	Basanite dyke	
KIA99-BI10F	750089	982304	Basanite block	
KIA99-BI10G	750089	982304	Basanite dyke	
KIA99-BI11A	750205	982038	Nephelinite	
KIA99-BI11B	750205	982038	Alkali Gabbro	
KIA99-BI11C	750205	982038	Basanite	
KIA99-BI11D	750205	982038	Nephelinite	
KIA99-BI11E	750205	982038	Basanite	
KIA99-BI11F	750205	982038	Basanite	56.5±0.5 (Biotite)
KIA99-BI12	750718	980841	Alkali Gabbro sill	
C246-149	750716	980525	Olivine melilitite	
C311-456	751214	982404	Basanite	
C311-515	752317	980068	Olivine Gabbro	55.8±0.4 (Biotite)
C311-458	750810	982541	Mafic Phonolite	
C311-455	751214	981910	Mafic Phonolite	
C311-443	751686	982757	Nephelinite	

^{40}Ar-^{39}Ar data for the Freemans Cove Complex can be found in Appendix D

Table A.9 *Petrography of Freemans Cove Complex volcanics (Chapter 3)*

	Modal % phenocrysts			Groundmass	Comments
Sample	Ol	Cpx	Fd		
KIA99-BI-1	2	2	1	Ne Ao Cpx Bt Mt CC C Ser	skeletal Ol with altered rims - Cpx glomeroporphyrtic zoned inclusion rich – 1 disequilibrium plagioclase
KIA99-BI-2	-	-	-	Pl Ol Cpx Mt Sp Bt C	Aphyric – Rare zoned and complex twinned plagioclase – andesine to labradorite compositions
KIA99-BI3a	-	-	-	Cpx Gl Ao CC Z Qt Mu	Cpx crystals in vesicular Gl – small Ao laths – Full of sediment $CaCO_3$ (fossiliferous) and conglomerate
KIA99-BI4	1	0.5	0	Ol Cpx Ao Mt Gl	<5% strained Ol – zoned Cpx – microphenocrystic - MBE
KIA99-BI5	1	1	0	Cpx Ol Ao Mt CC Ser	<5% strained Ol – zoned CPX - microphenocrystic
KIA99-BI6	0	1	0	Cpx Bt Mt Ao CC	microphenocrystic - glomeroporphyritic Cpx
KIA99-BI7	3	8	0	Cpx Ol Mt Pl CC Ser Z	zoned Cpx – Ol heavily alt – Some Mt + CC + Cpx blebs Cpx aggregates
KIA99-BI8	3	1	0	Cpx Ol Mt Ne (Ao)?	zoned Cpx phenocrysts in micro-phenocryst matrix – strained Ol 1 Mt megacryst (<0.5% total)

KIA99-BI9	0	0	5	Sd	groundmass so fine grained Mineralogy is impossible
KIA99-BI10A	4	0	0	Ol Cpx Ne Ao Mt	10% strained Ol (all megacrysts) otherwise microphenocrystal
KIA99-BI10B	0	1	0	Cpx CC Mt Bt Sp Pl Ser	highly altered – ghost Ol now CC vug filled used to be up to 8%
KIA99-BI10C	4	1	0	Ol Cpx Mt CC Ser C Z	megacrystal Ol all strained – Altered Me ghost structures – Z plus CC filled vugs
KIA99-BI10D	8	1	0	Ol Cpx Mt Ao Pl	megacrystal Ol all strained and skeletal – Cpx zoned
KIA99-BI10E	4	1	0	Ol Cpx Mt Sp Ser CC	megacrystal Ol all strained - Aphanitic groundmass – rare Sp
KIA99-BI10F	2	1	0	Ol Cpx Ne Ao Bt	microphenocrystal - >20% Ol population strained as rest of 10 series – Cpx zoned
KIA99-BI10G	3	1	0	Ol Cpx Pl Ser C Z CC	highly altered – as much as 12% originally Ol phenocrysts
KIA99-BI11A	0	1	0 (50)	Cpx Pl Mt Ser C Bt Chl	massive glomeroporphyritic Cpx heavily altered – Pl is andesine to labradorite – microphenocrystic Pl - ol completely serpentinised
KIA99-BI11B	0	1	0 (50)	Cpx Pl Mt Ser C Bt Chl	very similar to BI 11 A great deal of pl and haematite
KIA99-BI11C	0.5	8	0	Cpx Ol Mt Ser C CC	altered groundmass and most Ol replaced by Ser + $Fe(OH)^+$ - Cpx zoned - microphenocrystic
KIA99-BI11D	1	8	0	Cpx Ol Mt Pl C Ser	xenocrystic Ol + Cpx in a trachytic textured groundmass mainly andesine composition Pl
KIA99-BI11E	0	8	0	Cpx Mt Pl CC Z Ser	similar to BI11D but more glomeroporphyritic Cpx – $Fe(OH)^+$
KIA99-BI11F	3	5	0	Ol Cpx Mt Ne Bt Z Ser CC C	despite alteration some fresh Ol - Bt appears primary
KIA99-BI12	0	0	0	Ol Cpx Pl Mt	microphenocrystic – strained Ol and Cpx which is also zoned andesine to labradorite – some polycrystalline Ol and Cpx aggregates
C246-149	8	2	0	Ol Cpx Me Ne Ao Cr Mt	polycrystalline strained Ol abundant Me, very fresh zoned Cpx
C311-456	5	20	0	Cpx Ol Mt Ao Ser Bt	zoned Cpx dominant – iddingsite alteration to Ol – Cpx-rich

					enclaves
C311-515	-	-	-	Cpx Pl Mt Bt Ap Ser Chl C	similar to previous dolerite/basalt altered Ol – labradorite to sanidine large Mt – Bt primary + 2ndry
C311-458	0.5	2	5	Sd Cpx Ol Or Pl Ser Mt Bt Am	Ol highly altered – Cpx as poly-crystalline aggregates and zoned - abundant hydrous phases
C311-455	0	1	10	Sd Le Or CC Mt Cpx Am Bt	green Am, Sd, Cpx and Le as phenocrysts - altered Bt
C311-443	7	10	0	Cpx Ser CC Gl Mt C	0.5cm^3 calc-silicate crustal fragments -

Table A.10 *El Hierro sample location, height, lithology, unit (Chapter 4)*

Sample	Lat (°N)	Lon (°W)	Height	Lithology	Unit‡
			metres ASL		
JMDDEH01	274522	180854	60	Vesicular ankaramite flow	PFE
JMDDEH02	274537	180837	46	Alkali basalt flow A 'a spatter cone	PFE
JMDDEH03	274736	175528	724	Vesicular basanite flow	Tinõr
JMDDEH04	274747	175515	749	Alkali basalt flow Thin (<15cm) xenolith laden flow	Tinõr
JMDDEH05	274748	175515	757	Alkali basalt flow Thin (<10cm) xenolith laden flow	Tinõr
JMDDEH06	274608	175518	180	Hawaiite flow	Tinõr
JMDDEH07	274608	175517	195	Ankaramite flow	Tinõr
JMDDEH08	274605	175511	153	Basanite flow	Tinõr
JMDDEH09	274753	175833	575	Trachytic flow	UEGS
JMDDEH10	274758	175850	650	Ankaramite flow	CFE
JMDDEH11	274759	175850	680	Alkali basalt flow	CFE
JMDDEH12	274802	175849	733	Alkali basalt flow Highly vesicular	CFE
JMDDEH13	274804	175848	728	Ankaramite flow	CFE
JMDDEH14	274749	175856	470	Alkali basalt flow Highly vesicular	UEGS
JMDDEH15	274739	175901	410	Ankaramite flow	UEGS
JMDDEH16	274727	175912	275	Basanite flow	LEGS
JMDDEH17	273956	175940	339	Alkali basalt flow Vesicular	PFE
JMDDEH18	274846	175302	29	Ankaramite flow	PFE

‡ PFE = Platform forming eruption, CFE = Cliff forming eruption, UEGS = Upper El Golfo Series, LEGS = Lower El Golfo Series, Tinõr = Oldest preserved series

Table A.11 *Petrography of El Hierro lavas and xenoliths (Chapter 4)*

Sample	Phenocrysts				Mineral Phases	Comments
	Ol	Px	Mt	Fd		
JMDDEH01	10	22	4	-	Cr, Ol, Cpx, Mt, Pl, Gl	Very large zoned augite, Large Mt Highly vesiculated, very fresh, 4th Order birefringence Ol

JMDDEH02	- 2 - -	Cpx, Pl, Fe-Ti, Gl, Ol	Very fresh, vesiculated with Trachytic texture, Skeletal Ol Glomeroporphyritic zoned Cpx
JMDDEH03	9 8 - -	Cr, Ol, Cpx, Mt, Pl, Gl	Porphyritic texture, very fine Groundmass Pl, Mt, Cpx, Gl Skeletal Cpx and Ol phenocrysts Zoned
JMDDEH04a	- - - -	Ol, Cpx, Mt, Pl, Gl	Highly vesiculated basalt, small Bubbles – Contains xenolith (below)
JMDDEH04a	Cpx xenolith	Cpx, Ol, Opx, Gl	Frozen melt textures, metasomatic Opx, Cpx strained, Complex melt texture at boundary with host lava
JMDDEH04b	- 4 - -	Cpx, Ol, Mt, Pl, Gl	Very similar to EH04a – more Included xenolithic material
JMDDEH04b	Cpx xenolith	Cpx, Opx, Ol, Mt, Gl	Contains abundant Mt by contrast With EH04a, Large number of melt Inclusions with chatter mark Textures
JMDDEH04Ci	- - - -	Cr, Ol, Cpx, Mt, Pl, Gl	Highly vesiculated, abundant strained Ol and resorbed Cpx
JMDDEH04Ci	Cpx xenolith	Cpx, Ol, Mt	Strained Cpx, melt veins preserved Interstitially
JMDDEH04Cii	- - - -	Cr, Ol, Cpx, Mt, Pl, Gl	Highly vesiculated, Abundant Mt
JMDDEH04Cii	Dunite Xenolith	Cr, Ol, Cpx	Large chromite within heavily Strained Ol, Not as much Interaction with basalt as Cpx Xenoliths
JMDDEH04Ciii	2 - - -	Ol, Cpx, Mt, Pl, Gl	Highly vesiculated, some bubbles Quite large
JMDDEH04Ciii	Websterite Xeno	Cr, Ol, Cpx, Mt	Incredible melt textures, highly Rounded by eruption process Badly strained Ol and Cpx
JMDDEH04d	1 2 - -	Ol, Cpx, Mt, Pl, Gl	Again vesiculated, glomerporphy Blebs of Cpx/Pl/Mt/Gl Fe-Ti Oxide
JMDDEH04d	Dunite Xenolith	Cr, Ol, Cpx, Mt, Sp, Gl	Dihedral angles on crystal faces
JMDDEH05	2 - - -	Ol, Cr, Cpx, Mt, Pl, Gl	Vesicles not as rounded as EH04 Series
JMDDEH05	Gabbro Xenolith	Mt, Cpx, Pl, Sp, Fe(OH)	Labradorite Pl, Heavily zoned and Altered Cpx, Melt inclusions in Cpx

JMDDEH05	Dunite Xenolith	Ol, Cpx, Cr, Mt	Very similar to EH04 Dunites
JMDDEH06	- 2 1 24	Cpx, Pl, Mt, Fe(OH), Ol	Stellate Pl in groundmass Dominated by Pl, Pl and Cpx Zoned, Pl Andesine composition Highly altered Ol to Fe(OH)
JMDDEH07	7 7 - -	Ol, Cpx, Pl, Mt, Gl	Porphyritic Ol is resorbed to extent Incredible zoning in Augite
JMDDEH08	4 15 1 -	Cr, Ol, Cpx, Mt, Pl, Fe(OH), Gl	Strongly zoned Cpx (Xenocrystic) Glomeroporphyritic Cpx, Pl Inclusion-rich rims or cores, Vesicular
JMDDEH09	- - - -	Pl, Mt, Cpx, Fe(O)	Mt-Fe(O) clusters after Am Trachytic Pl texture
JMDDEH10	10 10 2 -	Cr, Ol, Cpx, Mt, Pl	Large, often strained, Ol, Cpx is Also large Cpx often vesiculated Porphyritic and vesicular
JMDDEH11	7 10 2 -	Cr, Ol, Cpx, Mt, Pl	Cpx contain large Mt, obvious Zones – exsolution related? Again Porphyritic and vesicular textures
JMDDEH12	8 2 - -	Cr, Ol, Cpx, Mt, Pl	Abundant Mt in strongly Porphyritic and vesicular lava Some Ol with exsolution to Mt Others remain unexsolved.
JMDDEH13	16 22 4 -	Ol, Cpx, Mt, Pl	Massively porphyritic, Abundant Mt
JMDDEH14	4 3 1 -	Cr, Ol, Cpx, Mt, Pl	Glomeroporphyritic Cpx, Trachytic flow textures revealed by Pl
JMDDEH15	9 4 - -	Cr, Ol, Cpx, Mt, Pl	Strained Ol, Mafic pods also Present, Vesicular
JMDDEH16	6 10 - -	Ol, Cpx, Mt, Pl, Gl	Vesicular and porphyritic, large Zoned Cpx
JMDDEH17	3 - - -	Ol, Cpx, Mt, Pl, Gl	Skeletal Ol, Slightly vesiculated – Gl around outside of vesicles
JMDDEH18	3 4 - -	Cr, Ol, Cpx, Mt, Pl, Gl	Large zoned Cpx, Sympletic Mt Vesiculated

Table A.12 *La Palma sample location, height, lithology, unit (Chapter 4)*

Sample	Lat (°N)	Lon (°W)	Height	Lithology	Unit†
			metres ASL		
JMDDLP01	284546	174917	1400	Ankaramite Flow	Garafia
JMDDLP02	284552	174904	1400	Ankaramite Flow	Garafia
JMDDLP03	284048	175502	203	Picrite pillow lava Serpentinised	US

JMDDLP04	284617	175157	1862	Ankaramite Flow Vesiculated		LT
JMDDLP05	284614	175153	1905	Ankaramite Flow Vesiculated		LT
JMDDLP06	284613	175153	1954	Hawaiite ankaramite flow		LT
JMDDLP07	284606	175153	2025	Ankaramite Flow		LT
JMDDLP08	284123	175221	1710	Alkali basalt Flow		BV
JMDDLP09	284118	175207	1555	Amphibole Tephrite Flow		BV
JMDDLP10	284905	174948	438	Ankaramite flow		UT
JMDDLP11	284911	174950	473	Basanite flow		UT
JMDDLP12	284918	174950	490	Ankaramite		UT
JMDDLP13a	283837	175630	10	Olivine Clinopyroxenite Xenolith		CFE
JMDDLP13b	283839	175631	8	Olivine Clinopyroxenite Xenolith		CFE
JMDDLP14	283526	175428	120	Basanite flow		CFE
JMDDLP15	283531	175438	139	Basanite flow	1949 SJ	PFE
JMDDLP16	283314	175204	761	Basanite flow	1712	PFE
JMDDLP17	283512	175248	621	Basanite flow Contains phonolite xenoliths	1585RJ	PFE
JMDDLP18	283439	175015	1794	Basanite flow	1949 LL	PFE
JMDDLP19	283656	155041	1585	Basanite flow	6Ka BF	PFE
JMDDLP20a	283503	175222	746	Phonolite Pyroclastic flow	RJ	PFE
JMDDLP20b	283503	175222	746	Phonolite Block flow	RJ	PFE
JMDDLP21	282901	175106	634	Basanite spatter cone Xenolith-rich	SA	PFE
JMDDLP22	282852	175123	410	Phonolite	RT	PFE
JMDDLP23	282734	175055	44	Basanite flow	1971	PFE
JMDDLP24	282825	175138	81	Basanite flow	1677	PFE
JMDDLP25	283126	174907	760	Basanite flow	1646	PFE

† PFE = Platform Forming Eruptions (RT = Roques de Teneguia; BF = Biragoyo flow; LL = Lava lake; RJ= Roques de Jedey; SJ = San Juan), CFE = Cliff Forming Eruption, BV = Benejado Volcano, UT = Upper Taburiente, LT = Lower Taburiente, US = Pliocene Seamount

Table A.13 *Petrography of La Palma lavas and xenoliths (Chapter 4)*

Sample	Phenocrysts Ol Px Mt Fd Am	Mineral Phases	Comments
JMDDLP01	5 8 - - -	Cr, Ol, Cpx, Mt, Pl, Gl	Large zoned and vesiculated Cpx Ol very fresh, in places clustered And zoned, Porphyritic and vesiculated
JMDDLP02	3 9 - - -	Ol, Cpx, Mt, Pl, Gl, Fe(O)	Massive zoned and vesiculated Cpx, Porphyritic and vesicular Mafic pods within flow
JMDDLP03	30 - - - -	Cr, Ol, Cpx, Mt, Ser, C CC	Some of the Ol remains Remarkably fresh, Zeolite Greenschist facies
JMDDLP04	2 3 - - -	Ol, Cpx, Mt, Pl	Some of the most extraordinary Zoned and vesiculated Cpx Vesicular flow

JMDDLP05	3 7 - - -	Cr, Ol, Cpx, Mt, Pl	Zoned Cpx that is vesiculated on Outside, Strained Ol
JMDDLP06	- 4 1 - -	Mt, Cpx, Pl	Strongly zoned Cpx, Large Mt, Moderately vesicular
JMDDLP07	3 8 - - -	Ol, Cpx, Mt, Pl, Gl	Ol strained and Cpx zoned and Vesiculated – porphyritic texture And lava is vesicular
JMDDLP08	- 3 1 - 3	Cpx, Hbl, Ap, Mt, Pl	Euhedral acicular laths of Hbl, Ap is hexagonal and included in Hbl, Hbl and Cpx are zoned
JMDDLP09	4 6 - - -	Ol, Cpx, Mt, Pl, Fe(OH)	Highly vesicular, Cpx zoned and Vesiculated, Clusters of Cpx and Ol – similar to cumulate growth, Fine grained groundmass Mt, Pl, Cpx
JMDDLP10	15 20 - - -	Ol, Cpx, Mt, Pl, Fe(O), Fe(OH)	Large cluster of Ol and Cpx (xenolith), Fine grained ground Mass which is vesiculated
JMDDLP11	3 4 - - -	Cr, Ol, Cpx, Mt, Pl, Gl	Strained high birefringence Ol Cpx are zoned and vesiculated Vesculated lava of Pl, Cpx, Mt, Gl
JMDDLP12	- - 1 - -	Mt, Ol, Cpx, Ap, Pl,	Fresh Ol in lava, altered Ser Ol in Augite – zoned and vesiculated Vesicular flow
JMDDLP13a(1)	Cpx xenolith	Ol, Cpx, Mt, Fe(OH)	Irregular strained Ol crystals, Cpx strongly zoned, abundant Mt
JMDDLP13a(2)	Cpx xenolith	Ol, Cpx, Mt	Similar but larger crystals Compared to (1)
JMDDLP13b(1)	Cpx xenolith	Ol, Cpx, Mt	Polycrystalline Ol aggregates, Zoned Cpx, Masses of Mt
JMDDLP13b(2)	Cpx xenolith	Ol, Cpx, Mt	Polycrystalline Ol aggregates and Zoned Cpx appear to partition – Lots of Mt
JMDDLP14	- - - - -	Ol, Cpx, Mt, Pl, Gl	Aphanitic, Strongly zoned and resorbed Cpx, Mt and Gl rich groundmass
JMDDLP15	4 6 - - -	Cr, Ol, Cpx, Mt, Pl, Gl	Ol contain Cr and are strained, Zoned Cpx, Large quantity of Opaques around Ol – vesiculated
JMDDLP16	3 7 1 - -	Ol, Cpx, Mt, Pl, Gl	Large fresh Ol, zoned Cpx, very Fine grained groundmass, Cpx Glomeroporphyritic pod – highly Vesiculated flow

JMDDLP17	- 2 - - 1	Ol, Cpx, Mt, Pl, Hbl, Fe(OH)	Hbl with resorbed Fe(OH) rims, Highly vesiculated
JMDDLP18	- - - - -	Ol, Cpx, Mt, Pl, Gl	Highly vesiculated bomb with Zoned Cpx
JMDDLP19	- - - - 1	Ol, Cpx, Hbl, Pl, Fe(OH) Mt	Hbl with resorbed Fe(OH) rims Vesiculated and fine grained
JMDDLP19	Hbl xenolith	Hbl, Cpx, Mt, Fe(OH), Pl	Large quantity of xenolith now Opaque Fe(OH) and indicates Massive resorbtion of Hbl
JMDDLP19	Ap xenolith	Ap, Hbl, Cpx, Mt, Gl	Massive Ap and Hbl crystals Ap enclosed within Hbl and Cpx
JMDDLP20a	- - - 10 1	Pl, Hbl, Hy, Am, Cpx Or, Sd	Bright blue Hy, Two Am, Large zoned Pl, Trachytic texture, less Alkali-rich Am pod within plug
JMDDLP20bi	- - - 11 1	Pl, Hbl, Hy, Am, Or, Ao Mt	Hy present, large zoned Pl and Am also zoned, No flow texture
JMDDLP20bii	- - - 9 1	Pl, Hbl, Hy, Am, Or, Ao Mt	Complex and oscillatory zoned Pl Hy blue internally
JMDDLP21a	- 2 - - 1	Hbl, Cpx, Ol, Cr, Mt	Aphanitic and highly vesicular Basalt with abundant xenoliths
JMDDLP21a	Hbl xenolith	Hbl, Ap, Cpx, Mt, Ol, Gl	Large Hbl, containing Ap and Gl Large quantity of Mt
JMDDLP21a	Hbl xenolith	Hbl, Cpx, Mt, Ap	Large Hbl and Cpx dominated Xenolith with zoned Cpx
JMDDLP21bi	Hbl xenolith	Hbl, Ol, Cpx, Mt, Ap, Fe(OH), Pl	Strongly resembles disaggregated xenolith with zoned Cpx and Strained Ol
JMDDLP21bii	Gabbro xenolith	Pl, Cpx, Hbl, Mt	Dominated by Pl, with speckled And twinned Cpx
JMDDLP21biii	Hbl xenolith	Hbl, Cpx, Mt, Ap	Loads of interstitial Ap (crystallise At same time as not included in Hbl?
JMDDLP21biv	Hbl xenolith	Hbl, Cpx, Mt, Cr, Ol, Ap	More included Cpx in Hbl than biii Vesiculated with zoned Cpx
JMDDLP22	- - - - -	An, Or, Hy, Hbl, Am, Fe(OH)	Zoned Am, Hbl and Fd Quite fine grained phonolite
JMDDLP23	3 2 - - -	Cr, Ol, Cpx, Mt, Hbl, Fe(OH)	Ol surrounded by Cpx surrounded by Hbl-Fe(OH) rim, astounding Aphanitic groundmass, vesiculated
JMDDLP24	3 3 - - -	Ol, Cpx, Hbl, Mt, Fe(OH) Pl, Gl	Strained Ol and zoned Cpx, single Fe(OH) encrusted Am, vesiculated

JMDDLP25	- 2 - - -	Cpx, Ol, Mt, Pl	Glomeroporphyritic and zoned Cpx, minor strained Ol, FeO Dominate matrix

Table A.14 *Coppermine River Continental Flood Basalts location, lithology and optical freshness (Chapter 5)*

Sample	DFB(m) True Thickness	Formation	Lithology	Alteration
HDB-98-125	4387	Husky Creek	Basalt	Weak
HDB-98-126	4260	Husky Creek	Basalt	Weak
HDB-98-127	3964	Husky Creek	Basalt	Weak
HDB-98-130A	3434	Husky Creek	Basalt	Weak
HDB-98-124	2914	Copper Creek	Basalt	Weak
HDB-98-89A	2457	Copper Creek	Basalt	Moderate
HDB-98-87	2379	Copper Creek	Basalt	Moderate
HDB-98-82	2131	Copper Creek	Basalt	Fresh
HDB-98-75	1850	Copper Creek	Basalt	Fresh
HDB-98-70	1598	Copper Creek	Basalt	Fresh
HDB-98-64	1437	Copper Creek	Basalt	Fresh
HDB-98-61B	1286	Copper Creek	Basalt	Fresh
HDB-98-60	1269	Copper Creek	Basalt	Fresh
HDB-98-55	1024	Copper Creek	Basalt	Fresh
HDB-98-51	865	Copper Creek	Basalt	Moderate
HDB99-CM19B	498	Copper Creek	Basaltic-Andesite	Very Fresh
HDB99-CM19C	498	Copper Creek	Basaltic-Andesite	Very Fresh
HDB-98-109	484	Copper Creek	Picrite	Weak
HDB-99-CM35B	459	Copper Creek	Picro-basalt	Weak
HDB-99-CM36	459	Copper Creek	Picro-basalt	Weak
HDB-98-119B	454	Copper Creek	Picrite	Weak
HDB-98-119A	454	Copper Creek	Picro-basalt	Weak
HDB-96-67		Copper Creek	Picrite	Weak
HDB-96-70		Copper Creek	Picrite	Weak
HDB-98-176	413	Copper Creek	Basalt	Moderate
HDB-98-170A	161	Copper Creek	Basalt	Moderate
HDB-98-170B	161	Copper Creek	Basalt	Moderate
HDB-98-94	31	Copper Creek	Basalt	Fresh
HDB-98-91	5	Copper Creek	Basalt	Fresh
HDB-98-90B	0	Copper Creek	Basalt	Fresh

Table A.15 *Petrography of the Coppermine River Continental Flood Basalts (Chapter 5)*

Sample	Phenocrysts	Mineral Phases	Comments
HDB-98-125	Ol (Ser) <0.5%	Cpx, Pl, Mt, Ser, C Chl, Fe(OH)	Glomeroporphyric zones of Cpx-Pl, Large Mt, Few Ol altered to Ser
HDB-98-126		Pl, Cpx, Mt, Ser, C Z	Large Mt, Amygdales (<0.5%), Pl shows

			preferred orientation
HDB-98-127		Pl, Cpx, Mt, Opx, Z Ser, C	Fine grained zone with Z, Mt interstitial
HDB-98-130A	Ol (Ser) <0.5%	Pl, Cpx, Mt, Opx, Ser, C, Fe(OH)	Very fine grained, Ser as a vein, Glomeroporphyritic Cpx-Pl
HDB-98-124		Pl, Mt, Cpx, C, Chl, Ser	Pigeonite, Upto 10% Mt Fine grained
HDB-98-89A		Pl, Cpx, Mt, C, Chl, Z	Some glomeroporphyritic Texture, Mt primary and Interstitial
HDB-98-87	Ol (Ser) <0.5%	Pl, Cpx, Mt, Ser, Opx, Z Fe(OH)	Zoned Cpx, Interlocking Pl crystal framework, Apparent Pl crystal Orientation
HDB-98-82	Ol (Ser) <0.5%	Pl, Cpx, Mt, Ser, C	Pl definitely aligned, Cpx Very small crystal Aggregates, Large Mt Blebs
HDB-98-75		Pl, Cpx, Mt, Z, C	Two populations of Cpx Two populations of Pl Abundant small Mt blebs
HDB-98-70		Pl, Cpx, Mt, Fe(OH)	Two zones one coarse Unoriented the other fine With oriented Pl crystals
HDB-98-64		Pl, Cpx, Mt, Chl, Fe(OH)	Oriented Pl crystals, Abundant, fine Mt and Oriented zones of altered Material
HDB-98-60	Ol (Ser/Fe(OH) <0.5%	Pl, Cpx, Mt, Z, Fe(OH) Ser, CC, Qtz	Larger Pl zoned, CC-Qtz vein, Interesting textures
HDB-98-55	Glomeroporphyritic <20%	Pl, Cpx, Mt, Opx, C, Mu	Glomeroporphyritic Cpx - Pl-Opx, no Mt, rest of flow very fine grained
HDB-98-51		Pl, Mt, Cpx, Qtz, Fe(OH)	Vein of Mt, Colour from Fe(OH) in section, 10% Mt, very fine grained
HDB-96-70		Ol, Pl, Cpx, Opx, Mt, Z Chl	Ol, Pl and Cpx fresh Surrounded by large Px Intergrowth, minor Mt, Green colour from Z/Chl
HDB-96-67		Ol, Cpx, Pl, Opx, Mt, Z Ser, Chl, Fe(OH)	Ol ~20% and fresh, Again Px encasing other Phases, Fresh flow

HDB-99-CM19B		Cr, Opx, Ol, Pl, Gl, Mt	Unbelievably fresh, Skeletal Pl/Ol, spherulitic Texture developed, Cr-Mt <0.25%, developed helix Structure of crystals in Gl
HDB-99-CM19C		Cr, Opx, Ol, Pl, Gl, Mt	Greater concentration of Crystals than CM19B, Skeletal Pl and harrisitic Ol
HDB-98-109	Ol (15%)	Cr, Ol, Cpx. Pl, Opx, Bt, Mt, Chl, C, Z	Ol ~30% altered to Bt-Chl Fe(OH), Ophitic Px
HDB-99-CM36	Opx (10%)	Opx, Pl, Cpx, Mt, Z, CC Fe(OH)	Glomeroporphyritic clumps of Opx in fine Grained Cpx-Pl-Mt Groundmass
HDB-98-119B	Ol (15%)	Ol, Cpx, Pl, Opx, Mt, Ser Z, Fe(OH)	Although altered, some Ol remains fresh, Ophitic Px, Ser vein
HDB-98-176		Pl, Cpx, Mt, CC, Z, Fe(OH), Chl	Alteration after Ol?, Abundant Z, Mt common
HDB-98-170A	Cpx (C/Z ~10%)	Pl, Cpx, Mt, Z, Mu, Fe(OH), C, Ser	Some fresh Cpx that is zoned, Abundant v.fine Mt
HDB-98-170B	Cpx (Ser ~10%)	Pl, Cpx, Mt, Ser, Z, Fe(OH), C, CC	Liesegang Fe(OH), Abundant Mt, Highly Altered
HDB-98-94		Cpx, Pl, Mt	Ultra-fine grained basalt Z and CC filled cracks Similar to trachyte cracks Mt oriented into 1st phase Cracks
HDB-98-91		Cpx, Pl, Mt, Z, Ser CC	Very fine grained, ultra-Fine partitions within
HDB-98-90B		Cpx, Pl, Mt, Z, C, CC	Coarser grained than 91 Crystals layer parallel to Flow top and base

Table A.16 *Muskox Intrusion North diamond drill hole samples, depth, unit, and lithology (Chapter 5) - 67°05'30''N 115°16'30''W*

Sample	DFB(m) True Thickness	Lithology	Cyclic Unit	Layer	Comments
DDH-MX-N1	1880.74	Hornby Bay Sst	-	-	Roof Rock
DDH-MX-N3	1878.00	Granophyric gabbro	25	35	Top Border Zone
DDH-MX-N11	1834.72	Granophyric gabbro	25	35	-
DDH-MX-N14	1821.31	Picritic Websterite	25	34	Mid-layer 34
DDH-MX-N18	1800.88	Gabbro	24	33	-

DDH-MX-N27	1746.33	Gabbro	24	33	-
DDH-MX-N35	1700.31	Feldspathic Websterite	23	31	-
DDH-MX-N46	1633.56	Feldspathic Websterite	23	31	-
DDH-MX-N54	1571.38	Websterite	22	29	Base layer 29
DDH-MX-N55	1568.22	Websterite	21	27	Top layer 27
DDH-MX-N56	1564.43	Websterite	21	27	Mid layer 27
DDH-MX-N59	1542.73	Feldspathic peridotite	21	26	Mid layer 26
DDH-MX-N66	1505.24	Feldspathic peridotite	20	24	-
DDH-MX-N75	1458.31	Dunite	19	21	Top layer 21
DDH-MX-N85	1397.35	Peridotite	18	20	Top layer 20
DDH-MX-N97	1333.95	Peridotite	17	18	Top layer 18
DDH-MX-N100	1307.33	Olivine clinopyroxenite	16	17	Top layer 17
DDH-MX-N101	1302.45	Olivine clinopyroxenite	16	17	Mid layer 17
DDH-MX-N104	1288.24	Dunite	16	16	Mid layer 16
DDH-MX-N111	1232.16	Dunite	15	14	Base layer 14
DDH-MX-N115	1214.48	Dunite	14	12	-
DDH-MX-N122	1171.81	Dunite	14	12	-
DDH-MX-N129	1061.48	Dunite	12	12	-
DDH-MX-N141	990.77	Dunite	11	12	-
DDH-MX-N151	936.51	Troctolitic Peridotite	8	11	Mid layer 11
DDH-MX-N159	893.54	Olivine clinopyroxenite	7	8	Mid layer 8

Table A.17 *Petrography of the Muskox Intrusion North diamond drill hole (Chapter 5)*

Sample	Texture	Mineral Phases	Comments
DDH-MX-N1	Statically Recrystallised	Qtz, Chl, Mu, C	C after Fd, 95% Qtz – peppery text Variation in Qtz crystal sizes, Strange Qtz intergrowths
DDH-MX-N3	Coarsely Crystalline Granophyric	K-Fd, Qtz, Mt, Chl C, Ep	C after K-Fd, 8% Mt, 15% Chl 60% K-Fd, 15% Qtz, Lacks Crystallographic orientation
DDH-MX-N11	Crystalline Granophyric	K-Fd, Opx, Cpx, Ol Mt, Pl, Qtz, Bt, Chl, C Ser	Qtz exsolution, disequilibrium assemblage, Cpx-Opx exsolution
DDH-MX-N14	Granophyric	Ser, C, Chl, Sh, Ep Ilm?, Qtz, (Cr?)	Cleavage parallel micro-inclusions Mg-rich chlorite, Sh appears Primary, Ghost Ol, Cpx. V. Green!
DDH-MX-N18	Heterocumulate (Crystals oriented)	Pl, Cpx, Opx, Mt, Bt, C Qtz, Mu	Exsolution of Qtz, Px exsolution Px enclose Plag as orthocumulate
DDH-MX-N27	Granophyric	Pl, Cpx, Opx, Qtz, Mt, C Chl, Bt	Exsolution of Qtz, Px, Mt also As with all roof rocks, highly Altered!
DDH-MX-N35	Granophyric	Pl, Cpx, Mt, Ser, C	Pl early crystallising phase Zoned Cpx, Ser after Ol Very large single Cpx

DDH-MX-N46	Granophyric	Pl, Cpx, Opx, Mt, Ep C, Bt (minor)	Px exsolution, Ser veins Granular texture similar to N35
DDH-MX-N54	Orthocumulate	Opx, Cpx, Ser, C, Mt Bit of Pl?	Opx initial crystallisation phase Ophitic texture with Cpx (Augite) Exsoln. of interstitial Cpx
DDH-MX-N55	Mesocumulate	Cpx, Opx, Mt, Ser, C Bt	Px exsolution in Cpx Interstitial completely altered Texture almost granular
DDH-MX-N56	Granular	Cpx, Opx, Pl, C	Pl interstitial, Px exsolution, Ser vein, Fresher than N55/N54
DDH-MX-N59	Orthocumulate	Ser, Cpx, Ol, Cr Chl, Baddeleyite?	Almost totally serpentinised, Rounded ghost olivines, 0.5-1.5mm, Fairly consistent size, Cr first crystallisation phase
DDH-MX-N66	Orthocumulate	Ser, Cpx, Cr, Mt Opx, Chl, Ol	Mt/Cr exsolution from Ol, Ophitic Cpx (as N59), Cr primary phase, Cpx exsolution lamellae, 7% oxide Network of orientated fabrics
DDH-MX-N75	Mesocumulate	Cr, Ser, Chl, Mu, Fe(OH)	Orthocumulate patch – odd Nearly adcumulate, mostly ser After Ol – lots of Cr (2-3%)
DDH-MX-N85	Mesocumulate	Ser, Cr, Mt, Bt, Cpx	Strongly coloured Bt, Crystal Supported texture, Ophitic Cpx Still preserved, Crystal orientation? 8% Fe-Cr-Ti oxides
DDH-MX-N97	Mesocumulate	Ser, Cr, Mt, Chl	Mr-rich Chl, vivid lilac, 10-15% Fe-Cr-Ti oxides
DDH-MX-N100	Adcumulate	Cpx, Ser, Ol, Mt	Cpx (>80%), Interlocking Cpx Grains surrounding Ol, Fresh Cpx, Slight exsolution, ~3mm diameter
DDH-MX-N101	Adcumulate	Cpx, Ser, Ol, Cr (in Ol)	Cpx (>70%), Interlocking Cpx Cr within Ol which are altered to Ser, Some exsolution in Cpx
DDH-MX-N104	Adcumulate/ Mesocumulate	Ser, Cpx, Cr, Mt	Ophitic texture in places, adcumulate in others - Cr in Ol And in Cpx, 8% Fe-Cr-Ti
DDH-MX-N111	Adcumulate/ Mesocumulate	Ser, Cpx, Cr, Mt, Bt, Chl	Less Cr than N104, Ophitic texture Apparent crystal alignment and Fluid-flow patches, 3% Fe-Cr-Ti
DDH-MX-N115	Mesocumulate	Ser, Cr, Cpx, Mt, Bt	Again beautiful textures, 2% Mt-Cr-Ti Oxide
DDH-MX-N122	Mesocumulate/ Adcumulate	Ser, Mt, Cr, Bt, Chl	Large variation in olivine ghost structure diameters compared With previously described

			Dunite. ~2% Mt-Cr-Ti
DDH-MX-N129	Mesocumulate	Ser, Mt, Cr, Chl, Fe(OH)	~5-7% Fe-Cr-Ti oxide Which are interstitial! Network interstitial texture
DDH-MX-N141	Adcumulate	Ser, Mt, Cr, Fe(OH), Sh, Chl	Network of Mt-rich veins pervades structure – response to Adcumulate structure? – Inclusion Of Garnet?
DDH-MX-N151	Orthocumulate	Ser, Cpx, Ol, Pl, C	Pl interstitial, Some Ol fresh – No Fe-Ti oxides present
DDH-MX-N157	Orthocumulate	Cpx, Ser, Mt Minor Chl	Mt veins in and around Ol, Cpx Exsolution – Interlocking Crystal fabric

Table A.18 *Muskox Intrusion South diamond drill hole samples, depth, unit, and lithology (Chapter 5) - 67°00'30''N 115°13'00''W*

Sample	DFB(m) True Thickness	Lithology	Cyclic Unit	Layer	Comments
DDH-MX-S44	845.37	Dunite (Ser)	7	7	-
DDH-MX-S51	803.01	Dunite (Ser)	7	7	-
DDH-MX-S60	759.12	Dunite	6	5	-
DDH-MX-S69	704.26	Dunite	6	5	-
DDH-MX-S76	662.20	Dunite	6	5	-
DDH-MX-S85	606.73	Dunite	5	5	-
DDH-MX-S93	557.66	Dunite	5	5	-
DDH-MX-S102	502.19	Dunite	4	5	-
DDH-MX-S110	454.64	Dunite	4	5	-
DDH-MX-S121	391.24	Dunite	3	3	Base layer 3
DDH-MX-S123	387.17	Olivine clinopyroxenite	2	2	Mid layer 2
DDH-MX-S124	383.21	Olivine clinopyroxenite	2	2	Base layer 2
DDH-MX-S128	363.81	Dunite	2	1	-
DDH-MX-S133	333.33	Dunite	2	1	-
DDH-MX-S137	308.95	Dunite	2	1	-
DDH-MX-S143	272.07	Dunite	2	1	-
DDH-MX-S144	266.78	Dunite	2	1	-
DDH-MX-S151	223.61	Dunite	2	1	-
DDH-MX-S154	205.33	Dunite	2	1	-
DDH-MX-S156	193.13	Dunite	2	1	-
DDH-MX-S160	174.24	Peridotite	2	MZ	Marginal zone
DDH-MX-S164	151.99	Feldspathic peridotite	2	MZ	-
DDH-MX-S171	110.54	Feldspathic peridotite	2	MZ	-
DDH-MX-S182	52.63	Picrite	1	MZ	-
DDH-MX-S192	0.20	Bronzite gabbro	1	MZ	-
DDH-MX-S195	-2.10	Paragniess	-	-	Basement

Table A.19 *Petrography of the Muskox Intrusion South diamond drill hole (Chapter 5)*

Sample	Texture	Mineral Phases	Comments
DDH-MX-S44	Adcumulate	Ser, Mt, Fe(OH), Cr, Chl	Mt surrounds ghost Ol crystals Very brown, heavily serpentinised High Mg Chl, 0.5% Fe-Cr-Ti
DDH-MX-S51	Mesocumulate	Ser, Mt, Fe(OH), Cr, Chl Cpx	Interstitial Cpx (not much), Some adcumulate some Mesocumulate, ~0.5mm diameter 0.5% Fe-Cr-Ti
DDH-MX-S60	Adcumulate	Ser, Fe(OH), Mu, Chl, Mt, Sh	~1% Fe-Ti oxide, No Cr, Sh within Ser, Very brown as S44, 51, 69 and 76.
DDH-MX-S69	Adcumulate/ Mesocumulate	Ser, Fe(OH), Chl, Mt Cr, Sh	~1% Fe-Cr-Ti Oxide, Similar CSD Some Ser veins
DDH-MX-S76	Adcumulate	Ser, Ol, Cr, Mt, Chl Fe(OH)	Clear fluidised texture, Some Ol preserved - ~2% Fe-Cr-Ti oxide
DDH-MX-S85	Mesocumulate	Ol, Ser, Cr, Mt, Fe(OH) Chl (Cpx and Opx?)	Increasingly freshly preserved Ol Large Ser vein illustrating beautiful Relationship of alteration and Preservation of original crystals ~1% Fe-Cr-Ti oxide
DDH-MX-S93	Adcumulate	Ol, Cr, Ser, Mt, Chl C	C after minor interstitial Cpx – Fresh Ol with Ser in cracks, ~1% Cr-Ti-Fe oxides
DDH-MX-S102	Orthocumulate	Ol, Cpx, Ser, Cr, Mt, Fe(OH), Chl, Bt	Fluidised texture, Ser veins filled with Mt, Ophitic Cpx, generally Fresh
DDH-MX-S110	Mesocumulate	Ol, Cpx, Ser, Cr, Bt, Mt, Chl, Fe(OH)	Bt in some cases so laced with Fe Mt exsolution occurs (common) Px exsolution - <0.5% Fe-Cr-Ti
DDH-MX-S121	Adcumulate	Ol, Cpx, Pl, Cr, Mt, Bt Ser, Fe(OH), Chl	Cpx minor and ophitic, Granular addition of Ol, Large Cr and Mt grains - ~1% Cr-Fe-Ti
DDH-MX-S123	Mesocumulate	Cpx, Ol, Mt, Fe(OH) Sh?, Chl	Large Ophitic Cpx, Spectacular granular texture, Fe-Ti <0.5%
DDH-MX-S124	Mesocumulate	Cpx, Ol, Mt, Bt, Opx Ser, Chl, Bt, Fe(OH)	Px Exsolution, Spectacular intergranular textures, Veins of Alteration pervade section
DDH-MX-S128	Adcumulate	Ol, Cr, Mt Fe(OH) Chl, Bt	Very fresh Ol, Heteradcumulate of Wager *et al.* (1960) - Two Ol and Cr populations (~1% Cr)

DDH-MX-S133	Mesocumulate /Adcumulate	Ol, Cpx, Cr, Mt, Fe(OH) Chl, Bt	Similar to S128 but with Cpx surrounding Ol clusters ophitically (~1% Cr)
DDH-MX-S137	Adcumulate	Ol, Cpx, Cr, Mt, Bt, Fe(OH)	Large Cpx crystal in adcumulate Ol. Ophitic textures, abundant Interstitial Bt
DDH-MX-S144	Adcumulate	Ol, Cpx, Opx, Cr, Mt, Bt, Ser, Fe(OH), Chl	Fracture running through section alteration around fracture, again Ophitic and individual Cpx and Opx crystal, 2 populations Ol – Cr
DDH-MX-S151	Mesocumulate	Ol, Cpx, Cr, Mt, Fe(OH)	Strong ophitic texture and vein Fracture around Cpx intergrowth Larger Ol in Ophitic enclosures
DDH-MX-S154	Mesocumulate/ Adcumulate	Ol, Cpx, Opx, Cr, Mt, Bt Fe(OH)	Strong ophitic texture, abundant fracture, fresh Ol, two or three Populations of Ol and Cr
DDH-MX-S156	Mesocumulate	Ol, Cpx, Opx, Cr, Mt, Bt Fe(OH)	Greater fracture than S154 but similar mineralogy and textures Even Ol within Cpx/Opx enclosure Show fracture
DDH-MX-S160	Mesocumulate	Ol, Cpx, Pl, Cr, Mt, Bt, Fe(OH), Chl	Small grains of Pl (interstitial) otherwise texture very similar to S156. ~2% Fe-Cr-Ti
DDH-MX-S164	Orthocumulate	Ol, Cpx, Pl, Opx, Cr, Mt Bt, Chl	Strong fracture and Mt-Bt partition Large enclosing Cpx (minor Opx) And Pl - ~5% Fe-Cr-Ti
DDH-MX-S171	Orthocumulate	Ol, Cpx, Pl, Opx, Cr, Mt Bt, Chl, C	Perhaps some crystallographic orientation, very similar fracture And features to S164
DDH-MX-S182	Orthocumulate	Cpx, Opx, Ol, Pl, Mt, Cr Bt, Chl, Ser	Alteration of Ol to Ser Possible crystallographic Orientation – 3% Fe-Cr-Ti
DDH-MX-S192	Granophyre	Cpx, Opx, Qtz, C, Bt, Mt, Cpy	Strong orientation of crystals parallel to the cooling surface Alteration of Fd to C
DDH-MX-S195	Crystalline Banded	Fd, Qtz, Opx, Mt, Fe(OH) Bt, Zr	Strong banding and red colouration from Fe(OH)

Table A.20 *Petrography of the Muskox Intrusion Main Chromitite Reef (Chapter 5)*

Sample	Mineral Phases	Comments
HDB-2000-MX24C (i)	Cr, Cpx, Opx, Pl, Ser	Rafts of Cpx surrounded by Cr enclosed in Cpx and Opx – Cpx>Cr>Opx>Pl Crystallisation – 30% Cr
HDB-2000-MX24C (ii)	Cr, Opx, Pl, Mt, Cpx, Ser	Ser after Ol, Cr forced into gaps by later Opx crystallisation phase, Plag interstitial to Opx – 10% Cr
HDB-2000-MX24C (iii)	Cr, Opx, Pl, Cpx, Ser, Bt	Again forcing of Cr into veins, clearly did Not crystallise synchronously with Opx or Pl – 5% Cr – Cpx-Opx below

Table A.21 *Petrography of the Muskox Intrusion "keel" feeder dyke (Chapter 5)*

HDB-2001-MX5	Crystalline	Ol, Pl, Cpx, Opx, Cr, Mt, Bt, Ser, Fe(OH), Chl	Large Opx crystals, fresh Ol Minor Ser, Ol poikilitically Enclosed in Opx, Cr with Fe-Ti Rims

Appendix B - Sample preparation, major and trace element concentration analytical techniques

B.1 Sample preparation – crushing and powdering

Volcanic and intrusive rocks are susceptible to weathering after emplacement near or at the Earth's surface. Care was taken during all forms of sample preparation to ensure that the least post-emplacement altered material was made available for analysis. When analyzing geological materials a number of guidelines must be followed for its initial preparation before dissolution or digestion by acid attack or direct analysis. The difficulty is that 'rules' differ between institutions (e.g., departments), groups (e.g., environmental vs. geo- and cosmo-chemists) and individuals. For this reason it seems that the best approach by an individual should be to document their methodology which should broadly follow institutional guidelines, and should be followed with every sample prepared until such time as the system is modified.

Rock samples can be contaminated in three principle ways during their preparation. They can be contaminated by equipment used to split and crush, during preparation in the laboratory environment and from analytical reagents used in the chemical preparation of the samples. When analyzing samples for PGEs or any very low level elemental abundance or isotopic work it is advisable to design a sample preparation technique that represents a minimal contaminative risk to the analysis. For this reason a method suitable for the crushing suite at the Department of Earth Sciences, University of Durham is described here.

First, weathered rinds, veins, amygdales and xenoliths were removed from lavas and adhering material was either avoided or removed from xenolith samples using a water-cooled steel bladed Diamond Periphery Norton Clipper leaving fresh blocks of sample approximately 100-300g in mass. All weathered cuts were retained either to 'pre-contaminate' the rock reducing equipment, or for future reference. The water in the clipper reservoir is generally changed before use and only samples with similar characteristics are sawn in a session (an extreme example would be that sulphide ore would not be sawn in the same session as basalt). The sawn block was then thoroughly washed with distilled water.

Samples were thoroughly buffed using corundum paper to remove any permanent marker pen, whose ink contains trace metals, and saw marks left on the blocks. A rock splitter is not recommended for two main reasons, first the desegregation of samples leaves visible metal marks that are almost impossible to remove, second the splitting method does not allow a choice of surface and is inefficient often resulting in loss of some sample, whilst the work surface and instrument are generally dirty and difficult to clean. A sawn block of proportions to fit in the crusher are better suited for very low level elemental and isotopic work.

Before using the crusher the room surfaces were cleaned and adequate ventilation was provided to remove the acetone vapour and rock dust to prevent dust settling on pristine sample. Notes were made of the order of sample grinding and crushing to look for possible cross-contamination trends. At Durham a Fritch Pulverette (Type 01-704) reciprocating jaw rock crusher with an adapted vacuum system is used to disaggregate samples. The jaws are manganese steel composites and are thought to provide very limited blank to the sample. Evans *et al.* (unpublished) found that of the crushers they tested a Mn steel jaw crusher gave the least metal contamination with measured values for Pt and Au at 0.1ppb, Pd and Ru at 0.05ppb, Rh at 0.01ppb and Ir at 0.006ppb (measurements are non-I.D) – never the less these values still swamp basaltic abundances of some of these elements. It should be noted that the lab in which these tests were conducted regularly disaggregates sulphide ores which does not take place at Durham. The crusher was thoroughly cleaned before usage and a rough sample passed through to 'flush' the system. The sample was subsequently passed through and after each sample the crusher was thoroughly scrubbed and then cleaned with distilled water and acetone/ethanol.

The course crush sample was coned and quartered on chemically untreated paper. The crush generated chunks less than $1cm^3$ and an 80g aliquot was prepared for milling. The mill used at Durham was a Fritch Planetary Agate ball mill. An agate ceramic is recommended for ultra-trace work leading to the least metal contamination (Robertson *et al.*, 1996; Evans *et al.*, unpublished). Contamination is inherent to most geological analyses because grinding contributes some of the mill material to the sample. Evans *et al.* (unpublished) found that only 0.008ppb Ir and 0.08ppb Au contamination occurs at worst in samples whilst Pt, Pd, Ru and Rh are below detection limits for their measurement technique. The only other powdering

process recommended would be a ceramic shatter box which also has very low blanks associated with desegregation of the sample. Tungsten Carbide swing mills or TEMAs should be avoided at all costs as they will result in heavy metal Ti, Co, Ta and Os and Pt contamination via isobaric interference from W. There are four main mill types the first of which are hardened steel mills which are cheapest but contaminate samples heavily with Fe, Cr, Ni Co, Mo, Mn and V. These include Mn-steel, Cr-steel, Ketos steel (an oil hardened steel) and a K 1045 mill (Robertson *et al.*, 1996). Such mills are adequate for metal or sulphides analyzed for major elemental data and for rough mining results and are shown to contribute less contamination with reduced run times (Robertson *et al.*, 1996). Tungsten carbide mills are also used and can be used for high concentration sulfides or low precision work but contribute noticeable quantities of Co, Ta, Sc, W and trace Nb (Jochum *et al.*, 1990; Ramsey, 1997). Alumina ceramics are becoming increasingly popular in Re-Os and PGE isotopic studies, however these are often brittle and contaminate with large quantities of Al and also trace amounts of Li, B, Ti, Mn, Fe, Co, Cu, Zn, Ga, Zr and Ba. In this study only agate mills were used for rock samples.

The mill and the agates were thoroughly cleaned and dried using distilled water and acetone/ethanol. Clean low trace sand was milled in the agates for 5 minutes to remove all trace of the previous sample and the agates were cleaned with water and dried with ethanol once more. The agates were then pre-contaminated with the crushed reject material from the sample for 10 minutes and were again washed and dried. This was performed every time a new sample was introduced to the agate. The sample was then added to the jars and milled for 25mins at a high torque (increased RPM) to produce a very fine rock flour that was then carefully bagged or placed in pre-cleaned glass or polyethylene storage vessels. All samples are bagged, even whole rock hand specimen samples, to avoid cross contamination. Although effectively 'clean', the agate contains geoids with the potential for contamination (especially Pb, F, Cu), they are also fragile and must be handled with care, and have long milling times due to their relatively low density compared to metal mills (Ramsey, 1997). Agates have also been shown to contaminate up to 2.3ppm B and 3.9ppm Cu (Potts, 1987) but the chalcedony is relatively pure silica. Milling in any of the mills described above is likely to oxidize the sample and can cause volatilization (Fitton and Gill 1970). Fitton and Gill (1970) showed that considerable

oxidation of Fe^{2+} to Fe^{3+} can take place if samples are mechanically ground for longer than about 1 minute. Clearly, this is not sufficient time to adequately powder the material, so consideration should be made for FeO and Fe_2O_3 analyses of samples after milling. Specific consideration of relative FeO and Fe_2O_3 content of samples analysed in this thesis does not form a part of this study.

B.2 Major element preparation and analysis by X-Ray Fluorescence (XRF)

Major element preparation and analysis by XRF were performed at the Geological Survey of Canada (GSC) for the Freemans Cove Complex (Chapter 3), the Muskox Intrusion (Chapter 5) and the Coppermine volcanics (Chapter 5) and at the University of Leicester for the Western Canary Island volcanics (Chapter 4). Methods for analysis by XRF of Western Cape Melilitite Province and Namaqualand-Bushmanland-Warmbad melilitites (Chapter 3) are presented in Janney *et al.* (2002).

Powders are dried overnight in an oven at 100 to 110°C to drive off surface moisture. Then ~2g of dried powder is weighed into a ceramic crucible. The crucible is then placed in a furnace at 900°C in order to remove water of crystallisation. The 'ignited' powders are then reweighed to determine the loss on ignition (LOI). The major element are measured as weight percentages determined by XRF by means of fusion disk 'charges' which are generally prepared by introducing lithium tetraborate flux with ignited powder in an agate mill to facilitate through mixing. The charge is then fused in a Pt crucible at a temperature of 1050°C for ~20 minutes. The charge is poured into a graphite mould whilst molten and pressed with an aluminium plunger to form the disk. The fusion disks are analysed using the X-ray fluorescence spectrometers at the institutions and the calibration and correction factors and operating conditions specific to the instrumentation and institution. Loss on ignition was measured by gravimetric analysis at 900°C.

B.3 Trace element preparation and analysis by Inductively Coupled Plasma Mass Spectrometry (ICP-MS)

B.3.1 Introduction

Trace element data for this study were obtained using the Perkin-Elmer Sciex Elan 6000 quadrupole inductively coupled plasma mass spectrometer (ICP-MS) at Durham University. Janney *et al.* (2002) quotes procedures for trace elements of the Western Cape Melilitite Province and Namaqualand-Bushmanland-Warmbad lineation melilitites studied in Chapter 3. A detailed description of pre-concentration chemistry, instrument operating conditions and data reduction considerations for this technique is contained in Ottley *et al.* (2003). A summary is provided below.

B.3.2 Sample digestion, spiking and dilution

Samples were usually processed in batches of 20-40, including 3-4 blanks in each batch. All acids used were SPA grade or equivalent. 0.1 ± 0.001g of sample powder was weighed into 22ml Savillex PFA beakers. 1mL of 16N SPA HNO_3 was carefully added to each beaker, allowing any reaction with carbonate which may evolve CO_2 to go to completion. The beaker was then gently agitated by hand to ensure the powder was fully wetted. 4mL of 29N SPA HF was added to each beaker. The beakers were sealed and placed on a hotplate and allowed to reflux at ~150°C for 48 hours. After this initial digestion step, the samples were dried down to a moist residue in a clean-air environment. It was important to ensure that the samples did not dry out completely, at which point they will start to oxidise. A further 2mL of 16N SPA HNO_3 was then added to each beaker and allowed to dry down on the hotplate. 2.5mL of 16N SPA HNO_3 was then added to each beaker, diluted to approximately 10mL with 18.3MΩ de-ionised water. The beakers were sealed and returned to the hotplate overnight at 100-120°C. Once cooled, each beaker was spiked with 1mL of a 1ppm Re-1ppm Rh ICP-MS solution. The sample was then diluted to 50ml in 18.3MΩ MQ. 1mL of this sample solution was then further diluted into a polypropylene test-tube at a 1:10 ratio, to produce a 11mL volume for analysis and a 5500 dilution of the digested rock matrix in the resultant solution.

B.3.3 ELAN 6000 Instrumental parameters

The sample solution was introduced into the plasma using a cross-flow nebuliser assembly and a Scott double-pass spray chamber. Nebuliser Ar flow rate was typically set at 0.8-0.9 litres per minute to optimise signal intensity. A daily check solution was run before each analysis session to ensure that instrument sensitivity, oxide levels and molecular interferences were at acceptable levels. During each analysis session the response of the instrument is calibrated using a set of solutions prepared from international rock standards.

The typical solution uptake rate is ~1mL per minute, with analysis for a full suite of trace elements requiring ~180 seconds for completion. Data is acquired by peak hopping, with a dwell time of approximately 10-60ms, depending on individual elemental detection limits (Ottley et al., 2003). The mass spectrum is swept 25 times for each reading, and two replicate readings are obtained for each analysis. Each sample is allowed to wash in for 50 seconds prior to the analysis commencing, and the instrument is allowed to aspirate a 0.8M HNO_3 wash solution for 180 seconds between samples.

B.3.4 Checks on data quality

The quality of the trace element analyses produced using this procedure is monitored in a number of ways:

- Analysis of total procedural blanks provides a check on levels of contamination introduced into the sample during the chemical procedure.
- Inclusion of the Re-Rh internal standard allows sample loss during dilution and variability in instrument sensitivity during analysis to be corrected for.
- Use of international rock standards during the analysis session permits accurate calibration of the machine response during each individual session.
- Multiple analyses of blanks and standards during a session (e.g. at start, mid-way, and end of run) allow any drift in the instrument calibration to be detected. Reproducibility of elemental concentrations in standards run in this manner is almost always better than 5% (relative standard deviation), and often <3% (Ottley *et al.*, 2003).

B.4 Mineral separation and purification for O and He isotope analysis

Sample crush was wet sieved to coarse, 500μm and 200μm fractions and then dried at 110°C overnight. The sieved fractions were then examined under a binocular microscope and fresh minerals were hand separated. Glasses were hand picked straight from crush without sieving. Around 20mg of phenocryst or glass was separated for oxygen isotope analysis by laser fluorination and normally ~0.1g of glass and between 0.2 and 2g of clinopyroxene or olivine separate was prepared for He isotope analysis. Glass separates were cleaned ultrasonically in distilled water and then ethanol prior to drying in an oven at 110°C. Olivine and clinopyroxene separates were cleaned in 2.5N HCl in an ultrasonic bath at 50°C for 70 minutes prior to washing in distilled water in an ultrasonic bath and treatment in ethanol and drying in an oven at 110°C. After chemical treatment mineral separates were re-picked to remove any adhering matrix or altered sample. This mineral separate was purified a third time prior to O or He isotope analysis.

Appendix C - Techniques for He, O, Sr, Nd, Pb and Re-Os isotope analysis

C.1 Re-Os isotope analysis (AHIGL)

The Arthur Holmes Isotope Geology Laboratory (AHIGL) took possession of a Thermo Triton® Thermal Ionisation Mass Spectrometer (TIMS) and a Thermo Neptune® Plasma Ionisation Multi-collector Mass-Spectrometer (PIMMS) in the summer of 2001. The entire Os isotope and concentration analyses quoted in this thesis were collected on the Triton® in negative ion mode (N-TIMS) by the author. Re concentration measurements by isotope dilution (I.D) were obtained by the author using either the AHIGL Neptune® PIMMS or the ELAN 6000® ICP-MS which is also housed at the AHIGL.

The methods employed for the analysis of Re and the platinum group elements (PGE) have been described in detail by Woodland (1999), Pearson and Woodland (2000) and Day *et al.* (2003). The following techniques section describes modifications to the procedures outlined in previous AHIGL publications and the techniques, blanks and standard data for obtaining highly precise Os concentrations and $^{187}Os/^{188}Os$ ratios on the AHIGL Triton®.

C.1.1 Re-Os preparation

One to two grams of homogenised whole rock powder (see Appendix B) were introduced using a pre-cleaned Teflon funnel into a single-use, annealed, Pyrex™ boro-silicate Carius tube pre-cleaned in inverse aqua regia and 18.3MΩ MQ and cooled externally to -10°C using an ethanol-water mixture. An enriched multi-element spike designed for basaltic and picritic rocks, SPA (Super-purity acid) 16N HNO_3 (5-6mL) and 12M TD HCl (2mL) were also introduced into the Carius tube. Although an old chemical digestion technique (Carius, 1865), Carius tube digestions have become a widely used technique for Re-Os isotope work on geological samples (Shirey and Walker, 1995) because of the low blanks that can be obtained using this technique (Table C.1. Rehkämper *et al.*, 1998; Pearson and Woodland, 2000).

Sealed Carius tubes were encapsulated in stainless steel sleeves, and placed into an oven heated to 220-230°C for in excess of 72 hours prior to slow cooling. The

reaction between the sample and the inverse aqua regia does not completely digest silicate phases but it is highly effective at releasing the PGE and Re from their matrices and in generating volatile OsO_4 which is effectively retained in the Pyrex™ boro-silicate tube (Pearson and Woodland, 2000). The reaction is also exceptionally effective at equilibrating the spike solution with the sample-acid mixture. This work confirms this observation on the basis of replicate analyses for both Re and Os in standards (Table C.6) and samples (e.g., Chapter 4). Blanks for Carius tubes in this study for Re (Table C.1) compare favourably with those measured previously at Durham and elsewhere (Rehkämper *et al.*, 1998).

OsO_4 is extracted from the inverse aqua regia by cooling the Carius tube and breaking the seal prior to adding CCl_4, a non-polar organic solvent, which is triply extracted (4, 3 and 2mL aliquots) from the acid to ensure a high yield of Os from the acid solution (Cohen and Waters, 1996). The CCl_4 solution was then added to 4ml of UPA (Ultra-purity acid) 9N HBr in a teflon vessel, thoroughly shaken, and left overnight. The high partition coefficient of Os in HBr means a high Os yield using this procedure (Cohen and Waters, 1996). The HBr solution was then extracted and placed into a rocket vial and slowly dried (<100°C) under clean, HEPA-scrubbed, air conditions.

In order to purify the Os-bearing residue for N-TIMS analysis a micro-distillation procedure based on the work of Birck *et al.* (1997) was employed. The residue was either (i) taken-up in 5μL of UPA HBr and placed onto a cap of a 9N HBr-cleaned rocket vial and dried down or (ii) taken up directly in 20μL of 12M H_2SO_4. 20μL of Cr_2O_3 was added to the bead and the inverted rocket vial was sealed and placed, wrapped in silver foil, on an 85°C hotplate with 20μl of 9N UPA HBr in the base to capture the oxidised Os species to reduce Os to $OsBr_6$ form. After precisely 120mins the micro-distillation was taken off the heat, the Cr_2O_3 was checked for oxidation state and the HBr fraction in the base was dried down prior to loading for Os isotope analysis by N-TIMS.

Table C.1: Re and Os concentration and Os isotope data for Arthur Holmes Isotope Geology Laboratory blanks (this study unless stated)

Sample	Spike (g)	Re (pg/g)	Os (pg/g)	$^{187}Os/^{188}Os_m$	±	1σ	Cleaning
Cl-18.3Ω	-	*bdl*	-	-		-	
Cl-18.3Ω I.D	0.0001	0.08	-	-		-	
TD HCl	-	*bdl*	-	-		-	
TD HCl I.D	0.0001	0.15	-	-		-	
Resin [c]	-	*1.00*	-	-		-	
03/07/03 Resin	-	0.04	-	-		-	
Column blank[d]	-	3.50	-	-		-	
CTB Durham [c]	-	*2.00*	-	-		-	Cold AqR[a]
CTB 1	-	0.14	-	-		-	AqR boil[b]
CTB 2	-	0.20	-	-		-	AqR boil
TPBa [c]	-	*3.00*	*7.80*	-		-	Cold AqR
TPBb [c]	-	*2.30*	*9.14*	-		-	Cold AqR
TPBc [c]	-	*5.10*	*2.10*	-		-	AqR boil
TPB 1 I.D	0.0055	0.84	0.26	-		-	AqR boil
TPB 2 I.D	0.0055	6.31	0.56	-		-	AqR boil
TPB 3	-	0.85	0.08	0.29250	±	0.00100	AqR boil
TPB 4	-	-	0.07	0.15781	±	0.00083	AqR boil
TPB 5	-	0.45	0.00	-		-	AqR boil
TPB 6	-	1.66	1.41	-		-	AqR boil
TPB 7	-	2.70	0.84	0.19384	±	0.00018	AqR boil
TPB 8	-	2.23	0.08	0.26908	±	0.10035	AqR boil
TPB 9	-	5.00	0.19	0.20993	±	0.00066	AqR boil
TPB 10	-	4.30	0.06	0.21748	±	0.00132	AqR boil
Durham Av.		**2.90**	**0.49**	**0.22147**	**±**	**0.05127**	

[a] Cold aqua regia boil

[b] Boiled in inverse aqua regia

[c] From Woodland (1999)

[d] New AHIGL clean laboratory column blank (April 2004)

Re aliquots from the same sample analysed for Os will remain in the inverse aqua regia solution after CCl_4 extraction along with Ir, Pt, Pd and some Ru. The inverse aqua regia solution was placed into a Teflon vial and dried down (all dry downs under clean air conditions) prior to addition of 1mL 29N TD HF and 2mL 16N SPA HNO_3 to fully digest the silicate phases. The Re and PGE aliquot was then dried down and a further 1mL of 16N SPA HNO_3 was added and dried down to remove fluoride salt species. 3mL of 12M TD HCl was added and dried down prior to taking

the solution up in 1M TD HCl and either (i) chlorination prior to centrifuging and loading onto anion exchange columns or (ii) centrifuging and direct loading onto anion exchange columns.

1cm^3 of rigorously pre-cleaned Bio-Rad® AG1 X8 100-200# resin was used for anion-exchange chromatography and Re was taken off using 4N SPA HNO_3 employing a total procedural volume of TD or SPA and 18.3MΩ MQ solutions of only 48ml for Re columns and 120mL for full PGE columns (Ir, Pt, Re and a further 20mls for Pd). The 20mL Re cut was dried down prior to solution analysis by PIMMS or ICP-MS.

C.1.1.1 Quantification of preparation blanks for Re and Os

The main source of blank contribution for Re and Os concentration and $^{187}Os/^{188}Os$ isotope work come from the Carius tube, the acids and, for Re, the anion exchange resin. Routine analysis of Teflon lab-ware showed that the rigorous cleaning method employed ensured no cross-contamination of samples and blanks were at background levels in all cases. Additionally analysis of the resins used in this study indicated Re blank contributions of less than 1pg. Reagents used in this study were either 16N SPA HNO_3 (<1pg Re), 29N TD HF (<1pg Re) and TD HCl which was measured using I.D. methodologies (Table C.1) and found to be <150fg. Samples analysed using the chlorination method may also be susceptible to contamination by the Cl-gas which is likely to heavily corrode its pressurised gas tank. However, I.D measurement of the blank contribution for Re was found to be less than 80fg and was at background levels for non I.D. measurements.

Large blank contributions have been reported by Rehkämper *et al.* (1998) for PGE and were also found to be quite high for cold aqua-regia cleaned boro-silicate tubes for Re by Woodland (1999; Table C.1). The inverse aqua-regia cleaning method employed at AHIGL appears to be highly effective at stripping Re (and other PGE) from the tube with blanks as low a 140fg for a full-volume (264cm^3) Carius tube. Total procedural blanks confirm the low blank contribution even to blanks prepared with high concentration Re and Os samples analysed for Chapter 5 of this study (Table C.1). The average blank for this study was measured at <2.9pg Re, <0.49pg Os with a $^{187}Os/^{188}Os$ ratio of 0.221±0.051 (Table C.1).

C.1.2 Os isotope analysis by Negative Thermal Ionisation Mass Spectrometry (N-TIMS)

The micro-distilled Os residue was taken-up in 0.5µl of ultra-low blank 9N UPA HBr (Table C.2) and dried onto 99.999% pure Cross™ or ESPI™ Pt filament ribbon using a hot lamp under HEPA filtered air. The filament ribbon was generally pre-cleaned using 8N SPA HNO_3 and was gently fused to finished- and H_2O_2 pre-cleaned single filament armatures. Detailed analysis of filament blanks for Os and for interfering Re species show that fusion using $KHSO_4$ and out-gassing or pre-heating are unnecessary to lower the Os (or Re) blank contributions. Cross™ Pt filament blanks, including the activator, were all less than 15fg and were regularly as low, or lower than 0.5fg for different filament batches and at different operating currents. Re blanks were lower than 6pg with one batch as low as 140fg. ESPI™ and PureTech™ Pt filament ribbon blanks, although generally low, were never found to be as routinely low as those for Cross™ cleaned using a simple nitric washing procedure (Table C.2; Fig. C.1).

0.5µL of an activator solution was applied to the dried HBr. Barium nitrate was firstly used as an activator but was found to provide less stable ionisation of the samples and standards so a switch was made to a barium hydroxide activator in the second N-TIMS session. The Os blank contributions also appear to be higher in the barium nitrate than the barium hydroxide activators (Table C.2). Filaments were loaded into a 21 carousel magazine into a pre-cleaned source housing and pumped down overnight to at least 1×10^{-7} Torr.

A small oxygen bleed was provided during analysis to aid ionisation and the filaments had current applied slowly over an hour or more (~15mA/min). Samples and most standards were measured in peak-hopping mode on the secondary electron multiplier (Table C.3), using ion-counting, with integration times on ^{188}Os, ^{187}Os and ^{186}Os of 4, 8 and 4 seconds respectively. Typical count rate of 500k were aimed for on the spike isotope ^{190}Os for samples and varied for ^{192}Os in the standards according to samples measured with them (Table C.3). Peak shapes and focussing were carefully monitored. Application of slow current resulted in steady or slightly growing beams during analysis.

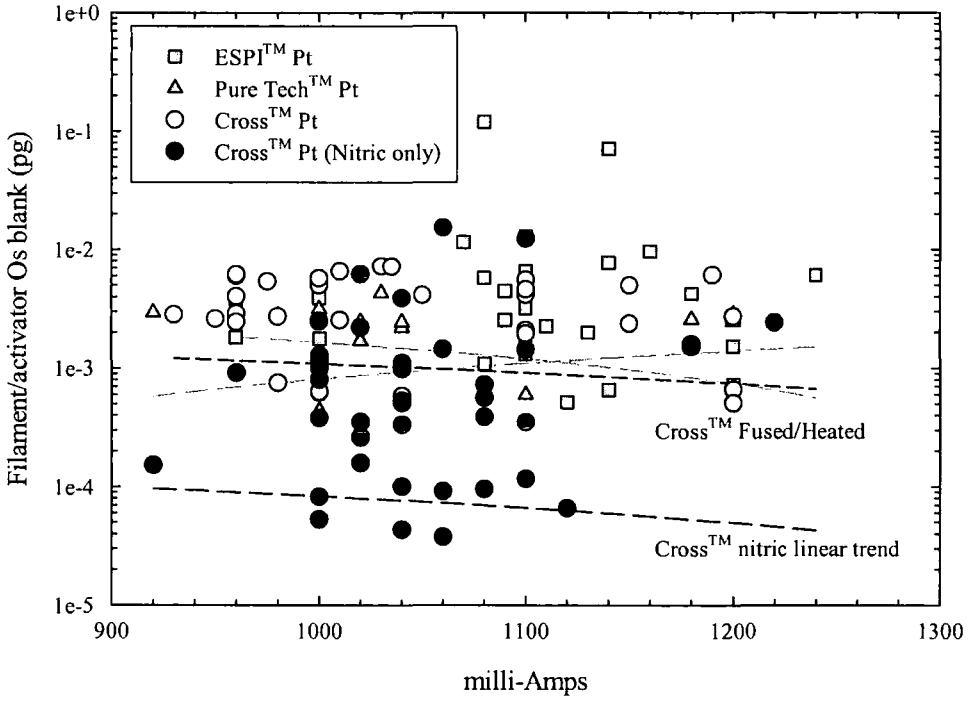

Fig. C.1: Comparison of Cross™, ESPI™ and PureTech™ 99.999% pure Pt filament and $Ba(NO_3)_3$ or $Ba(OH)_2$ activator Os blanks run during the course of this study versus currents applied during measurement. Linear trends indicate nitric washed Cross™ Pt filaments are an order of magnitude cleaner, on average, than by other fusing or heating purification methods or other manufactured filament ribbons.

Os was measured as OsO_4^- and online Os corrections were applied to account for ReO_4^- interference on ^{187}Os. This correction was rarely applied because of the low Re interferences – the Re comes almost exclusively from the Pt filament which was effectively stripped of Re using the HNO_3 cleaning methodology (Table C.2). When counts on mass 233 are observed there are often no corrections applied to $^{187}Os/^{188}Os$ and $^{189}Os/^{188}Os$ indicating the interference is unlikely to be Re. All peaks were centred before analysis (except 233). Sample analysis consisted of 100 cycles of data and lasted ~70 minutes meaning that individual Os isotope analyses lasted for a total generally in excess of 180 minutes. Standards run over the 18 month period of analysis for this study are presented in Tables C.3, C.4 and C.5. External precision for $^{187}Os/^{188}Os$ using the SEM for the AHIGL Triton® is better than 2.14‰ (2σ) for

Table C2: Filament and activator blanks run during the course of this thesis Re and Os concentration data for Arthur Holmes Isotope Geology Laboratory Blanks

Sample	Filament Type (manufacturer)	Cleaning method[a]	Activator[b]	Amperage (mA)	Re (pg/g)[c]	Os (pg/g)[d]
OSEFH1(12)	ESPI™	F N H	$Ba(NO_3)_2$	1080	-	**0.1200**
				1140	-	**0.0712**
OSEFH21 (12)	ESPI™	F N H	$Ba(NO_3)_2$	1090	-	**0.0025**
				1110	-	**0.0023**
				1130	-	**0.0020**
OSEFH13 (13)	ESPI™	F N H	$Ba(NO_3)_2$	*960*	-	**0.0038**
				1000	-	**0.0039**
				1100	-	**0.0032**
				1200	-	**0.0015**
OSEFH14 (13)	ESPI™	F N H	$Ba(NO_3)_2$	*960*	-	**0.0018**
				1000	-	**0.0018**
				1100	-	**0.0013**
OSEF13 (14)	ESPI™	F N H	$Ba(NO_3)_2$	1080	-	**0.0011**
				1100	-	**0.0015**
				1200	-	**0.0015**
OSEF14 (14)	ESPI™	F N H	$Ba(NO_3)_2$	1120	-	**0.0005**
				1140	-	**0.0007**
				1200	-	**0.0007**
OSEF3 (12)	ESPI™	F N	$Ba(NO_3)_2$	1070	-	**0.0116**
				1100	-	**0.0129**
				1160	-	**0.0097**
RSEF4 (12)	ESPI™	F N	$Ba(NO_3)_2$	980	**1.49**	-
OSEFH5 (12)	ESPI™	N H	$Ba(NO_3)_2$	1080	-	**0.0058**
				1100	-	**0.0066**
				1180	-	**0.0042**
OSEFH6 (12)	ESPI™	N H	$Ba(NO_3)_2$	1090	-	**0.0045**
				1140	-	**0.0078**
				1240	-	**0.0061**
RSEF7 (12)	ESPI™	N H	$Ba(NO_3)_2$	980	**2.13**	-
				1020	**2.12**	-

Sample	Filament Type (manufacturer)	Cleaning method[a]	Activator[b]	Amperage (mA)	Re (pg/g)[c]	Os (pg/g)[d]
OSCFH11 (12)	Cross™	F N H	$Ba(NO_3)_2$	1010	-	**0.0065**
				1030	-	**0.0072**
				1190	-	**0.0061**
OSCFH11 (13)	Cross™	F N H	$Ba(NO_3)_2$	*960*	-	**0.0060**
				1000	-	**0.0050**
				1100	-	**0.0041**
				1200	-	**0.0027**
OSCFH12 (13)	Cross™	F N H	$Ba(NO_3)_2$	*960*	-	**0.0029**
				1000	-	**0.0025**
				1100	-	**0.0021**
OSCF15 (14)	Cross™	F N H	$Ba(NO_3)_2$	1000	-	**0.0006**
				1040	-	**0.0006**
				1200	-	**0.0007**
OSCF8 (12)	Cross™	F N	$Ba(NO_3)_2$	1035	-	**0.0072**
				1100	-	**0.0056**
				1150	-	**0.0050**
OSCF9 (12)	Cross™	F N	$Ba(NO_3)_2$	960	-	**0.0040**
				975	-	**0.0054**
				1050	-	**0.0041**
OSCF10 (12)	Cross™	F N	$Ba(NO_3)_2$	930	-	**0.0028**
				950	-	**0.0026**
				1150	-	**0.0024**
RSCF15 (12)	Cross™	F N	$Ba(NO_3)_2$	960	**2.62**	-
				980	**2.82**	-
RSCF16 (12)	Cross™	F N	$Ba(NO_3)_2$	960	**3.00**	-
				1000	**3.91**	-
RSCF17 (12)	Cross™	F N	$Ba(NO_3)_2$	950	**3.95**	-
				990	**3.57**	-
OSCNH14 (12)	Cross™	N H	$Ba(NO_3)_2$	980	-	**0.0027**
				1010	-	**0.0025**
				1180	-	**0.0015**

Sample	Filament Type (manufacturer)	Cleaning method[a]	Activator[b]	Amperage (mA)	Re (pg/g)[c]	Os (pg/g)[d]
OSCNH14 (12)	Cross™	N H	$Ba(NO_3)_2$	980	-	**0.0027**
				1010	-	**0.0025**
				1180	-	**0.0015**
OSCNH9 (13)	Cross™	N H	$Ba(NO_3)_2$	*960*	-	**0.0061**
				1000	-	**0.0057**
				1100	-	**0.0046**
OSCNH10 (13)	Cross™	N H	$Ba(NO_3)_2$	*960*	-	**0.0024**
				1000	-	**0.0025**
				1100	-	**0.0019**
OSCNH18 (15)	Cross™	N H	$Ba(NO_3)_2$	980	-	**0.0008**
				1000	-	**0.0006**
				1200	-	**0.0005**
OSCN12 (12)	Cross™	N 2001	$Ba(NO_3)_2$	1000	-	**0.0025**
				1020	-	**0.0022**
				1180	-	**0.0016**
OSCN13 (12)	Cross™	N 2001	$Ba(NO_3)_2$	1020	-	**0.0062**
				1040	-	**0.0039**
				1220	-	**0.0024**
RSCN18 (12)	Cross™	N 2001	$Ba(NO_3)_2$	935	**0.40**	-
				1020	**0.40**	-
RSCN18 (12)	Cross™	N 2001	$Ba(NO_3)_2$	980	**2.15**	
				1000	**2.11**	
RSCN20 (12)	Cross™	N 2001	$Ba(NO_3)_2$	960	**5.14**	-
				980	**5.11**	-
OSCN13 (51)	Cross™	N 2001	$Ba(NO_3)_2$	*1000*	-	**0.0008**
OSCN14 (51)	Cross™	N 2001	$Ba(OH)_2$	*1000*	-	**0.0010**
OSCN11 (52)	Cross™	N 2001	$Ba(OH)_2$	*1000*	-	**0.0010**
OSCN17 (54)	Cross™	N 2001	$Ba(OH)_2$	1040	-	**0.0005**
				1080	-	**0.0006**
OSCN18 (54)	Cross™	N 2001	$Ba(OH)_2$	1000	-	**0.0013**
				1000	-	**0.0012**
				1040	-	**0.0011**
OSCN21 (55)	Cross™	N*	$Ba(OH)_2$	1060	-	**0.0153**
				1100	-	**0.0124**

Sample	Filament Type (manufacturer)	Cleaning method[a]	Activator[b]	Amperage (mA)	Re (pg/g)[c]	Os (pg/g)[d]
OSCN17 (56)	Cross™	N 21/03/02	$Ba(OH)_2$	1020	-	**0.0003**
				1020	-	**0.0003**
				1100	-	**0.0003**
OSCN18 (56)	Cross™	N 21/03/02	$Ba(OH)_2$	1020	-	**0.0003**
				1020	-	**0.0004**
RSCN19 (56)	Cross™	N 21/03/02	$Ba(OH)_2$	1005	**5.72**	-
				1020	**5.80**	-
OSCN18 (57)	Cross™	N 21/03/02	$Ba(OH)_2$	1060	-	**0.0014**
				1100	-	**0.0014**
RSCN19 (57)	Cross™	N 21/03/02	$Ba(OH)_2$	1020	**0.26**	-
OSCN18 (60)	Cross™	N 22/08/02	$Ba(OH)_2$	1040	-	**0.0003**
OSCN19 (60)	Cross™	N 22/08/02	$Ba(OH)_2$	1040	-	**0.0005**
RSCN20 (60)	Cross™	N 22/08/02	$Ba(OH)_2$	980	**0.59**	-
OSCN17 (61)	Cross™	N 22/08/02	$Ba(OH)_2$	1080	-	**0.0007**
OSCN18 (61)	Cross™	N 22/08/02	$Ba(OH)_2$	1080	-	**0.0004**
RSCN21 (61)	Cross™	N 22/08/02	$Ba(OH)_2$	980	**4.52**	-
OSCN20 (62)	Cross™	N*	$Ba(OH)_2$	1040	-	**0.0010**
RSCN21 (62)	Cross™	N 07/12/02	$Ba(OH)_2$	1000	**0.14**	-
OSCN5 (64)	Cross™	N 09/01/03	$Ba(OH)_2$	1000	-	**0.0004**
OSCN20 (117)	Cross™	N 09/01/03	$Ba(OH)_2$	920	-	**0.0002**
				960	-	**0.0009**
				1000	-	**0.0001**
OSCN21 (117)	Cross™	N 09/01/03	$Ba(OH)_2$	1020	-	**0.0002**
				1060	-	**0.0001**
OSCN3 (118)	Cross™	N 12/05/03	$Ba(OH)_2$	1080	-	**0.0001**
				1120	-	**0.0001**
OSCN4 (118)	Cross™	N 12/05/03	$Ba(OH)_2$	1000	-	**0.0001**
				1040	-	**0.0000**

Sample	Filament Type (manufacturer)	Cleaning method[a]	Activator[b]	Amperage (mA)	Re (pg/g)[c]	Os (pg/g)[d]
OSCN7 (123)	Cross™	N 21/06/03	$Ba(OH)_2$	1040	-	**0.0001**
OSCN8 (123)	Cross™	N 21/06/03	$Ba(OH)_2$	1060	-	**0.0000**
OSCN17 (125)	Cross™	N 21/06/03	$Ba(OH)_2$	1100	-	**0.0001**
RECN19 (125)	Cross™	N 21/06/03	$Ba(OH)_2$	950	**2.17**	-
OSPT14 (15)	Puretech™	N	$Ba(NO_3)_2$	980	-	**0.0028**
				1020	-	**0.0025**
				1200	-	**0.0029**
OSPT15 (15)	Puretech™	N	$Ba(NO_3)_2$	1020	-	**0.0017**
				1040	-	**0.0022**
				1200	-	**0.0025**
OSPT16 (15)	Puretech™	N	$Ba(NO_3)_2$	1000	-	**0.0032**
				1040	-	**0.0024**
				1200	-	**0.0026**
OSPT17 (15)	Puretech™	N	$Ba(NO_3)_2$	920	-	**0.0029**
				960	-	**0.0027**
				1180	-	**0.0026**
OSPT15 (51)	Puretech™	N	$Ba(NO_3)_2$	*1000*	-	**0.0012**
OSPT6 (53)	Puretech™	N	$Ba(OH)_2$	1030	-	**0.0043**
OSPT7 (53)	Puretech™	N	$Ba(OH)_2$	1000	-	**0.0004**
				1100	-	**0.0006**
HBr Blank A	Cross™	N 12/05/03	$Ba(OH)_2$	1040	-	**0.0001**
				1080	-	**0.0001**
HBr Blank B	Cross™	N 09/01/03	$Ba(OH)_2$	1080	-	**0.0001**
HBr Blank C	Cross™	N 21/06/03	$Ba(OH)_2$	1100	-	**0.0001**
HBr Re Blank	Cross™	N 21/06/03	$Ba(OH)_2$	1100	**0.606**	-

[a] F = Fused using $KHSO_4$; N = Cleaned in 8N SPA HNO_3; H = Pre-heated at 1.2mA for 120S

[b] 0.5µl of activator solution added in every case

[c] 0.5µl of DTM dilute spike solution 94-4-35

[d] 0.5µl of DTM dilute spike solution 94-4-43

* Cleaned in 4N SPA HNO_3

60 Cycles of ^{192}Os, ^{190}Os, ^{188}Os data were taken for each measurment quoted in this table

both UMCP (7000 to 17.5pg loads; Table C.3, Fig. C.2) and DTM standards (2500pg; Table C.5, Fig. C.3). Better than 0.23% (2σ) and 0.14% (2σ) reproducibility for $^{190}Os/^{188}Os$ and $^{189}Os/^{188}Os$ respectively were also measured for standards measured on the SEM; measurements of these ratios were even better from static Faraday experiments (Table C.4, Fig. C.4). Comparison with published values for UMCP and DTM standards shows that the standard averages for this study are within 30ppm of Faraday measurements of the UMCP standard ($^{187}Os/^{188}Os$ = 0.113819±0.000243, 2σ, *n*=273 versus 0.113791±0.000020, 2σ, *n*=15 Shirey and Walker, 1995) and better than 60ppm for SEM measurements of the DTM standard at the Open University ($^{187}Os/^{188}Os$ = 0.174021±0.000273, 2σ, *n*=21 versus 0.173963±0.000171, 2σ, *n*=140).

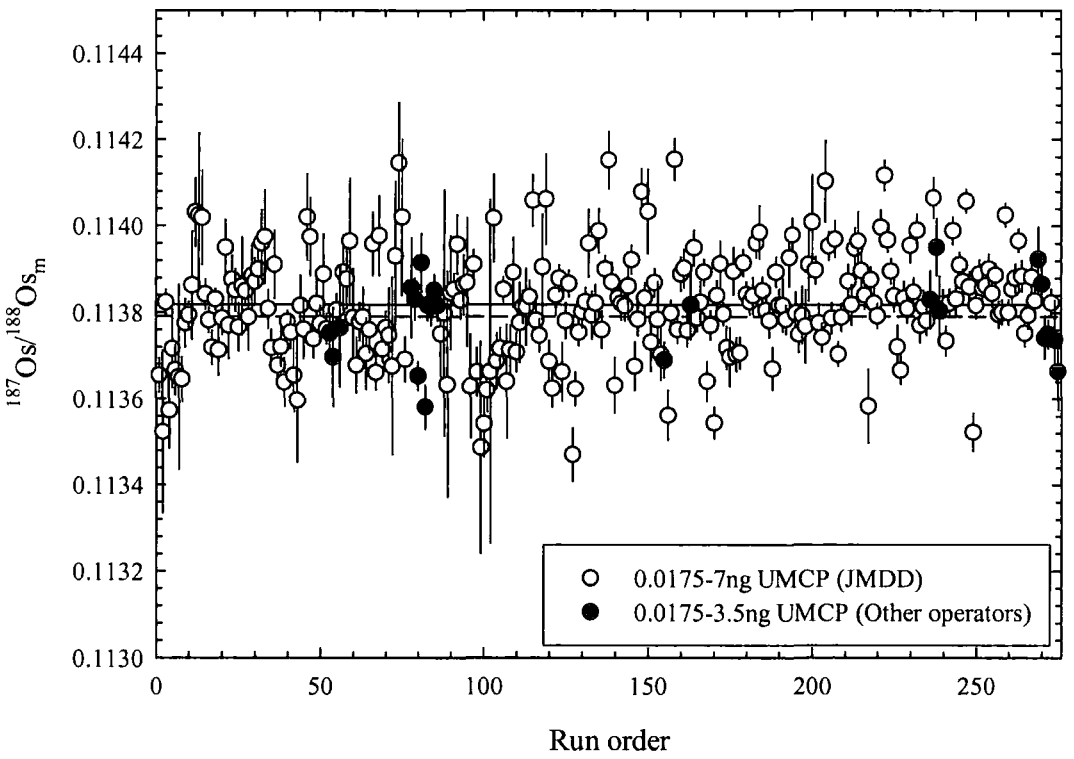

Fig. C.2: Results of 273 variable size UMCP Johnson Matthey standards against run order (an 18 month period in total). The external reproducibility is expressed as the long-term standard deviation (2σ) and is 0.113819±0.000242 (solid line). Also shown on the Fig. is a dashed line representing the measured Faraday value quoted in Shirey and Walker (1998) Data from Table C.3

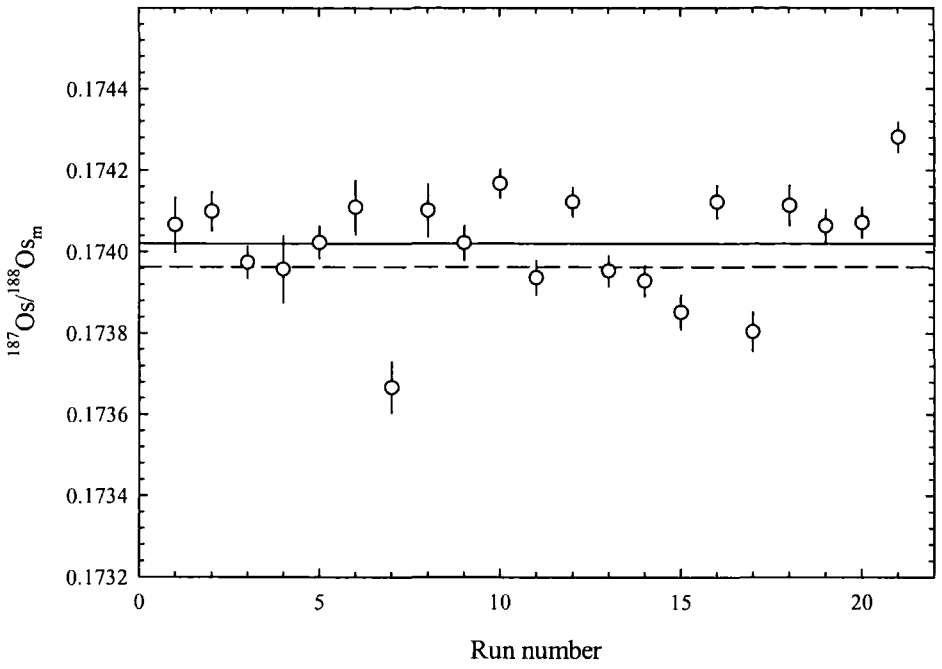

Fig. C.3: Results of 21 2.5ng DTM standards run over an 8 month period. The external reproducibility is expressed as the the long-term standard deviation (2σ) and is 0.17402±0.00027 (solid line). Also shown on the Fig. is a dashed line representing the measured SEM values for the Open University Finnigan MAT 261 quoted in Schaefer et al. (2002). Data from Table C.5

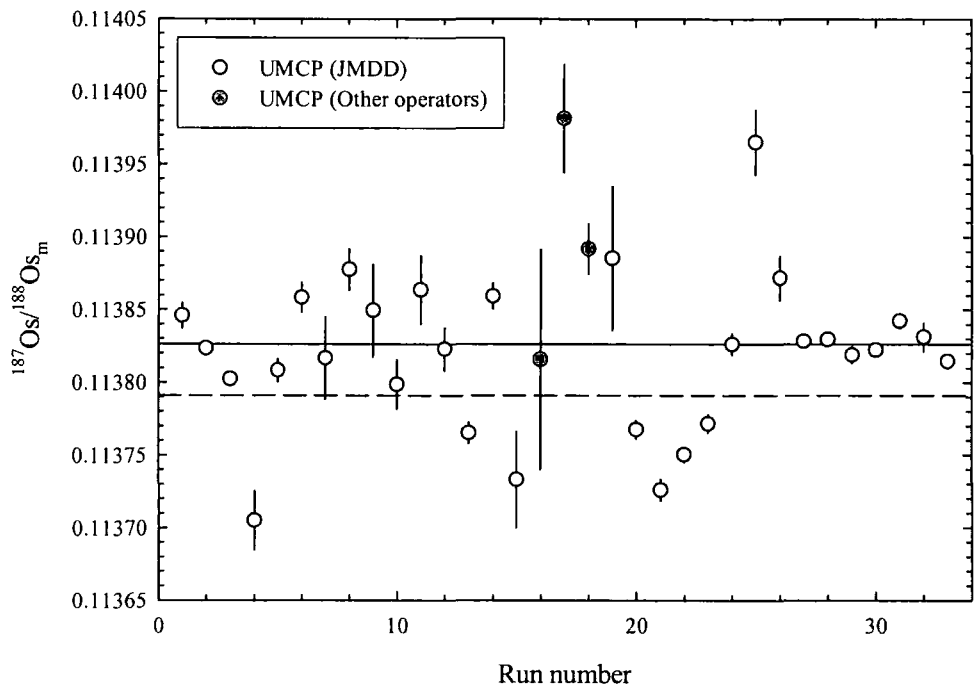

Fig. C.4: Results of 33 concentrated to 0.175ng UMCP Johnson Matthey standards run over an 8 month period. The external reproducibility is expressed as the long-term standard deviation (2σ) and is 0.113826±0.000118 (solid line). Also shown on the Fig. is the measured Faraday value quoted in Shirey and Walker (1998). Data from Table C.4

Table C.3: 273 UMCP Standards generated by SEM on the AHIGL TRITON over the period of 02/2002 until 09/2003

Std.	Mag.	Size (ng)	Op.	Run date	^{192}Os (kcps)	$^{190}Os/^{188}Os_m$	± 1σ	$^{189}Os/^{188}Os_m$	± 1σ	$^{187}Os/^{188}Os_m$	± 1σ
FIRST N-TIMS SESSION											
UMCP1	13	C.	JMDD	25/02/02	317	1.98424	± 48	1.21991	± 23	0.11365	± 4
UMCP1	13	C.	JMDD	25/02/02	13	1.98323	± 183	1.22078	± 133	0.11352	± 19
UMCP1	13	C.	JMDD	25/02/02	701	1.98591	± 31	1.21969	± 16	0.11382	± 3
UMCP1	13	C.	JMDD	25/02/02	59	1.98935	± 81	1.21964	± 53	0.11357	± 9
UMCP1	13	C.	JMDD	25/02/02	46	1.98965	± 98	1.22092	± 56	0.11372	± 9
UMCP2	13	1.75	JMDD	22/02/02	123	1.98430	± 66	1.21928	± 35	0.11367	± 6
UMCP2	13	1.75	JMDD	22/02/02	11	1.98616	± 211	1.21866	± 130	0.11365	± 21
UMCP2	13	1.75	JMDD	21/02/02	246	1.98435	± 51	1.21962	± 31	0.11365	± 5
UMCP2	13	1.75	JMDD	21/02/02	229	1.98364	± 48	1.22038	± 27	0.11378	± 6
UMCP2	13	1.75	JMDD	21/02/02	446	1.98309	± 40	1.21999	± 21	0.11379	± 3
UMCP2	13	1.75	JMDD	21/02/02	32	1.98355	± 126	1.21827	± 68	0.11386	± 12
UMCP2	13	1.75	JMDD	23/02/02	76	1.98631	± 90	1.21632	± 48	0.11403	± 8
UMCP2	13	1.75	JMDD	23/02/02	11	1.99306	± 202	1.22055	± 133	0.11402	± 19
UMCP2	13	1.75	JMDD	23/02/02	35	1.99004	± 130	1.21950	± 81	0.11402	± 11
UMCP2	13	1.75	JMDD	23/02/02	291	1.98626	± 45	1.21986	± 27	0.11384	± 3
UMCP2	13	1.75	JMDD	24/02/02	517	1.98497	± 36	1.21954	± 21	0.11378	± 3
UMCP2	13	1.75	JMDD	24/02/02	389	1.98582	± 40	1.21956	± 23	0.11372	± 4
UMCP2	13	1.75	JMDD	24/02/02	661	1.98581	± 28	1.21989	± 19	0.11383	± 2
UMCP2	13	1.75	JMDD	24/02/02	174	1.98601	± 55	1.21953	± 31	0.11371	± 6
UMCP3	14	0.175	JMDD	07/03/02	262	1.98406	± 51	1.22361	± 28	0.11379	± 4
UMCP3	14	0.175	JMDD	07/03/02	96	1.98192	± 95	1.21893	± 44	0.11395	± 6
UMCP3	14	0.175	JMDD	08/03/02	72	1.98464	± 84	1.21926	± 50	0.11377	± 8
UMCP3	14	0.175	JMDD	09/03/02	112	1.98295	± 78	1.21935	± 40	0.11388	± 5
UMCP3	14	0.175	JMDD	09/03/02	261	1.98361	± 47	1.21968	± 23	0.11385	± 5
UMCP3	14	0.175	JMDD	11/03/02	379	1.98417	± 57	1.22011	± 38	0.11377	± 5
UMCP3	14	0.175	JMDD	11/03/02	29	1.98506	± 129	1.22134	± 79	0.11386	± 11
UMCP3	14	0.175	JMDD	12/03/02	540	1.98386	± 41	1.21937	± 26	0.11385	± 3
UMCP3	14	0.175	JMDD	12/03/02	73	1.98357	± 81	1.22041	± 49	0.11379	± 8
UMCP3	14	0.175	JMDD	13/03/02	108	1.98527	± 73	1.21936	± 44	0.11389	± 7
UMCP3	14	0.175	JMDD	13/03/02	115	1.98519	± 66	1.21985	± 38	0.11387	± 5
UMCP3	14	0.175	JMDD	13/03/02	464	1.98476	± 39	1.21949	± 21	0.11390	± 4
UMCP3	14	0.175	JMDD	13/03/02	54	1.98523	± 109	1.22039	± 63	0.11396	± 8
UMCP3	14	0.175	JMDD	13/03/02	48	1.98574	± 103	1.21885	± 60	0.11398	± 11
UMCP2	14	1.75	JMDD	04/03/02	231	1.98420	± 46	1.22050	± 29	0.11381	± 4
UMCP2	14	1.75	JMDD	04/03/02	218	1.98428	± 40	1.21979	± 30	0.11372	± 4
UMCP2	14	1.75	JMDD	05/03/02	85	1.98269	± 93	1.21909	± 51	0.11391	± 8
UMCP2	14	1.75	JMDD	06/03/02	345	1.98383	± 43	1.21941	± 22	0.11368	± 3
UMCP2	14	1.75	JMDD	06/03/02	264	1.98498	± 50	1.22063	± 29	0.11372	± 4
UMCP2	14	1.75	JMDD	06/03/02	120	1.98394	± 65	1.21956	± 40	0.11364	± 6
UMCP2	14	1.75	JMDD	28/02/02	596	1.98409	± 29	1.21893	± 15	0.11378	± 2
UMCP2	14	1.75	JMDD	28/02/02	301	1.98446	± 43	1.22053	± 24	0.11375	± 4
UMCP2	14	1.75	JMDD	28/02/02	60	1.98370	± 102	1.21975	± 53	0.11365	± 8
UMCP2	14	1.75	JMDD	28/02/02	22	1.98159	± 145	1.21910	± 93	0.11360	± 14
UMCP2	14	1.75	JMDD	01/03/02	71	1.98494	± 80	1.22024	± 46	0.11382	± 7
UMCP2	14	1.75	JMDD	01/03/02	106	1.98365	± 71	1.22003	± 45	0.11376	± 7
UMCP2	14	1.75	JMDD	27/02/02	41	1.98677	± 130	1.21727	± 71	0.11402	± 10
UMCP2	14	1.75	JMDD	27/02/02	50	1.98570	± 119	1.21998	± 65	0.11398	± 9
UMCP2	14	1.75	JMDD	27/02/02	231	1.98600	± 51	1.21939	± 27	0.11374	± 4

Std.	Mag.	Size (ng)	Op.	Run date	^{192}Os (kcps)	$^{190}Os/^{188}Os_m$	± 1σ	$^{189}Os/^{188}Os_m$	± 1σ	$^{187}Os/^{188}Os_m$	± 1σ
UMCP2	14	1.75	JMDD	10/03/02	212	1.98331	± 80	1.22058	± 41	0.11382	± 6
UMCP2	14	1.75	JMDD	10/03/02	250	1.98472	± 50	1.22080	± 29	0.11378	± 4
UMCP2	14	1.75	JMDD	10/03/02	68	1.98399	± 90	1.22011	± 48	0.11389	± 9
UMCP2	14	1.75	JMDD	10/03/02	412	1.98379	± 37	1.22046	± 22	0.11376	± 4
UMCP2	15	1.75	DGP	18/03/02	287	1.98427	± 40	1.22044	± 25	0.11375	± 4
UMCP2	15	1.75	DGP	18/03/02	38	1.98053	± 115	1.22060	± 879	0.11370	± 11
UMCP2	15	1.75	JMDD	22/03/02	247	1.98671	± 47	1.22030	± 31	0.11381	± 4
UMCP3	15	0.175	DGP	20/03/02	27	1.98495	± 117	1.21896	± 95	0.11377	± 14
UMCP3	15	0.175	JMDD	25/03/02	58	1.98313	± 99	1.22073	± 75	0.11389	± 8
UMCP3	15	0.175	JMDD	25/03/02	87	1.98353	± 73	1.21901	± 45	0.11388	± 7
UMCP2	15	1.75	JMDD	26/03/02	17	1.98506	± 165	1.22048	± 132	0.11397	± 14
UMCP2	15	1.75	JMDD	26/03/02	41	1.98625	± 116	1.22155	± 86	0.11379	± 11
UMCP2	15	1.75	JMDD	26/03/02	101	1.98440	± 68	1.22018	± 49	0.11368	± 6
UMCP2	15	1.75	JMDD	26/03/02	254	1.98429	± 39	1.22016	± 30	0.11378	± 4
UMCP2	15	1.75	JMDD	26/03/02	245	1.98427	± 79	1.22010	± 51	0.11379	± 7
UMCP2	16	1.75	JMDD	02/04/02	60	1.98379	± 92	1.21873	± 62	0.11371	± 8
UMCP2	16	1.75	JMDD	02/04/02	196	1.98491	± 68	1.22041	± 46	0.11376	± 5
UMCP2	16	1.75	JMDD	04/04/02	114	1.98671	± 59	1.22026	± 55	0.11396	± 7
UMCP2	16	1.75	JMDD	05/04/02	309	1.98906	± 45	1.21965	± 30	0.11366	± 4
UMCP2	16	1.75	JMDD	08/04/02	74	2.00194	± 98	1.22006	± 61	0.11398	± 9
UMCP2	16	1.75	JMDD	08/04/02	434	1.99055	± 36	1.22059	± 22	0.11372	± 3
UMCP2	16	1.75	JMDD	08/04/02	299	1.98791	± 44	1.22035	± 33	0.11377	± 4
UMCP3	16	0.175	JMDD	06/04/02	30	1.98482	± 148	1.21782	± 111	0.11375	± 11
UMCP3	16	0.175	JMDD	06/04/02	23	1.98488	± 226	1.22008	± 144	0.11368	± 20
UMCP3	16	0.175	JMDD	06/04/02	17	1.98522	± 175	1.21702	± 122	0.11393	± 17
UMCP3	16	0.175	JMDD	07/04/02	22	1.97981	± 157	1.21932	± 100	0.11415	± 14
UMCP3	16	0.175	JMDD	07/04/02	11	1.98478	± 193	1.21791	± 139	0.11402	± 18
UMCP2	16	1.75	JMDD	07/04/02	224	1.98476	± 54	1.22034	± 31	0.11369	± 5
SECOND N-TIMS SESSION											
UMCP2	51	0.175	DGP	05/08/02	36	1.98041	± 129	1.21720	± 91	0.11386	± 11
UMCP2	51	0.175	DGP	05/08/02	162	1.98435	± 66	1.22015	± 42	0.11383	± 5
UMCP2	51	0.175	DGP	05/08/02	456	1.98438	± 34	1.21983	± 28	0.11365	± 3
UMCP2	51	0.175	DGP	05/08/02	101	1.98172	± 74	1.21822	± 47	0.11392	± 7
UMCP2	51	0.175	DGP	05/08/02	495	1.98446	± 65	1.22025	± 40	0.11358	± 5
UMCP1	52	3.5	DGP	08/08/02	535	1.98225	± 52	1.21915	± 28	0.11382	± 4
UMCP2	52	0.175	DGP	08/08/02	241	1.98554	± 67	1.21982	± 38	0.11381	± 4
UMCP1	52	3.5	DGP	08/08/02	329	1.98320	± 59	1.21930	± 33	0.11385	± 4
UMCP1	52	3.5	DGP	08/08/02	355	1.98314	± 50	1.21888	± 28	0.11382	± 4
UMCP2	53	1.75	JMDD	22/08/02	59	1.98348	± 124	1.22022	± 69	0.11375	± 10
UMCP3	53	0.175	JMDD	22/08/02	7	1.97739	± 425	1.22085	± 240	0.11380	± 28
UMCP3	53	0.175	JMDD	22/08/02	5	1.98291	± 380	1.21604	± 244	0.11363	± 26
UMCP3	53	0.175	JMDD	22/08/02	32	1.98507	± 142	1.22039	± 87	0.11385	± 13
UMCP3	53	0.175	JMDD	22/08/02	364	1.98317	± 37	1.21931	± 30	0.11385	± 4
UMCP2	53	1.75	JMDD	22/08/02	110	1.98335	± 100	1.21829	± 43	0.11396	± 7
UMCP2	53	1.75	JMDD	22/08/02	262	1.98319	± 61	1.22006	± 30	0.11383	± 4
UMCP2	53	1.75	JMDD	22/08/02	99	1.98232	± 84	1.21864	± 43	0.11387	± 7
UMCP2	53	3.5	JMDD	22/08/02	28	1.98191	± 189	1.21797	± 92	0.11387	± 15
UMCP2	53	3.5	JMDD	22/08/02	35	1.98318	± 160	1.21856	± 88	0.11363	± 12
UMCP2	53	3.5	JMDD	22/08/02	418	1.98282	± 48	1.21935	± 28	0.11391	± 3
UMCP2	54	3.5	JMDD	02/09/02	137	1.98382	± 93	1.21949	± 51	0.11366	± 6
UMCP3	54	0.175	JMDD	02/09/02	8	1.97947	± 361	1.21975	± 163	0.11349	± 25
UMCP2	54	3.5	JMDD	02/09/02	72	1.98185	± 85	1.22073	± 63	0.11354	± 8

Std.	Mag.	Size (ng)	Op.	Run date	^{192}Os (kcps)	$^{190}Os/^{188}Os_m$	± 1σ	$^{189}Os/^{188}Os_m$	± 1σ	$^{187}Os/^{188}Os_m$	± 1σ
UMCP2	54	3.5	JMDD	02/09/02	269	1.98495	± 59	1.22021	± 36	0.11362	± 5
UMCP3	54	0.175	JMDD	02/09/02	3	1.97774	± 507	1.22165	± 297	0.11366	± 40
UMCP3	54	0.175	JMDD	02/09/02	47	1.98191	± 136	1.21793	± 83	0.11402	± 10
UMCP3	54	3.5	JMDD	02/09/02	79	1.98431	± 92	1.21882	± 47	0.11369	± 6
UMCP3	54	3.5	JMDD	02/09/02	238	1.98331	± 64	1.22078	± 39	0.11372	± 5
UMCP2	54	3.5	JMDD	02/09/02	586	1.98221	± 37	1.21934	± 22	0.11385	± 3
UMCP2	55	1.75	JMDD	19/09/02	20	1.98074	± 200	1.21968	± 110	0.11364	± 13
UMCP2	55	1.75	JMDD	19/09/02	159	1.98436	± 69	1.21933	± 37	0.11371	± 6
UMCP2	55	3.5	JMDD	19/09/02	59	1.98452	± 122	1.22148	± 74	0.11389	± 8
UMCP2	55	3.5	JMDD	19/09/02	252	1.98284	± 52	1.21932	± 29	0.11371	± 4
UMCP2	55	3.5	JMDD	19/09/02	67	1.98250	± 123	1.22059	± 63	0.11378	± 9
UMCP2	55	3.5	JMDD	19/09/02	439	1.98343	± 40	1.21985	± 24	0.11381	± 4
UMCP2	55	1.75	JMDD	19/09/02	67	1.98628	± 124	1.22042	± 74	0.11381	± 9
UMCP2	55	1.75	JMDD	19/09/02	369	1.98228	± 41	1.21972	± 30	0.11384	± 4
UMCP2	55	1.75	JMDD	19/09/02	139	1.98198	± 68	1.21845	± 44	0.11406	± 6
UMCP2	55	3.5	JMDD	19/09/02	173	1.98499	± 73	1.21963	± 38	0.11378	± 5
UMCP2	55	3.5	JMDD	19/09/02	384	1.98443	± 43	1.21992	± 27	0.11375	± 4
UMCP3	55	0.175	JMDD	19/09/02	28	1.98219	± 165	1.21910	± 92	0.11391	± 12
UMCP3	55	0.175	JMDD	19/09/02	45	1.98357	± 150	1.21887	± 87	0.11406	± 10
UMCP2	55	7	JMDD	19/09/02	192	1.98334	± 60	1.22029	± 34	0.11369	± 5
UMCP2	55	7	JMDD	19/09/02	214	1.98467	± 73	1.21974	± 35	0.11362	± 4
UMCP2	56	1.75	JMDD	06/10/02	216	1.98433	± 64	1.22037	± 43	0.11384	± 4
UMCP2	56	1.75	JMDD	06/10/02	547	1.98302	± 33	1.21954	± 25	0.11388	± 3
UMCP2	56	1.75	JMDD	06/10/02	100	1.98420	± 83	1.22049	± 52	0.11366	± 7
UMCP2	56	1.75	JMDD	06/10/02	379	1.98252	± 45	1.21958	± 27	0.11378	± 4
UMCP2	56	1.75	JMDD	06/10/02	596	1.98291	± 36	1.22005	± 21	0.11387	± 3
UMCP2	56	7	JMDD	06/10/02	115	1.98568	± 74	1.22037	± 40	0.11347	± 6
UMCP2	56	7	JMDD	06/10/02	293	1.98323	± 53	1.22000	± 37	0.11362	± 4
UMCP2	56	7	JMDD	06/10/02	504	1.98274	± 41	1.21954	± 22	0.11376	± 3
UMCP2	56	7	JMDD	06/10/02	443	1.98328	± 39	1.22002	± 25	0.11380	± 4
UMCP2	56	7	JMDD	06/10/02	404	1.98236	± 41	1.21943	± 26	0.11383	± 3
UMCP3	57	0.175	JMDD	13/10/02	79	1.98118	± 95	1.21785	± 68	0.11396	± 8
UMCP3	57	0.175	JMDD	13/10/02	252	1.98354	± 61	1.21946	± 41	0.11379	± 5
UMCP3	57	0.175	JMDD	13/10/02	275	1.98335	± 59	1.22007	± 30	0.11382	± 4
UMCP2	57	1.75	JMDD	13/10/02	485	1.98287	± 77	1.21968	± 36	0.11399	± 5
UMCP2	57	1.75	JMDD	13/10/02	257	1.98345	± 51	1.21972	± 25	0.11376	± 4
UMCP2	57	1.75	JMDD	13/10/02	444	1.98148	± 46	1.21893	± 23	0.11390	± 3
UMCP4	57	0.018	JMDD	13/10/02	95	1.98049	± 95	1.21874	± 53	0.11415	± 7
UMCP4	57	0.018	JMDD	13/10/02	238	1.98478	± 59	1.22055	± 38	0.11387	± 4
UMCP2	57	1.75	JMDD	13/10/02	98	1.98447	± 98	1.22283	± 53	0.11363	± 6
UMCP2	57	1.75	JMDD	13/10/02	551	1.98291	± 35	1.21991	± 20	0.11383	± 3
UMCP2	57	1.75	JMDD	13/10/02	622	1.98364	± 51	1.21934	± 27	0.11382	± 4
UMCP2	57	1.75	JMDD	13/10/02	501	1.98233	± 45	1.21921	± 22	0.11382	± 3
UMCP2	57	3.5	JMDD	13/10/02	79	1.98155	± 98	1.21898	± 58	0.11386	± 8
UMCP2	57	3.5	JMDD	13/10/02	498	1.98210	± 40	1.21926	± 22	0.11392	± 3
UMCP2	57	3.5	JMDD	13/10/02	226	1.98655	± 68	1.22084	± 39	0.11368	± 6
UMCP2	57	3.5	JMDD	13/10/02	487	1.98274	± 44	1.21974	± 21	0.11379	± 4
UMCP2	58	1.75	JMDD	25/10/02	430	1.97952	± 66	1.21852	± 32	0.11408	± 5
UMCP2	58	1.75	JMDD	25/10/02	391	1.98244	± 57	1.21985	± 33	0.11383	± 3
UMCP2	58	1.75	JMDD	25/10/02	383	1.98153	± 99	1.21913	± 47	0.11403	± 10
UMCP3	58	1.75	JMDD	25/10/02	122	1.98046	± 79	1.21935	± 49	0.11373	± 7
UMCP3	58	1.75	JMDD	25/10/02	521	1.98315	± 41	1.21928	± 21	0.11387	± 3

Std.	Mag.	Size (ng)	Op.	Run date	^{192}Os (kcps)	$^{190}Os/^{188}Os_m$	± 1σ	$^{189}Os/^{188}Os_m$	± 1σ	$^{187}Os/^{188}Os_m$	± 1σ
UMCP3	58	1.75	JMDD	25/10/02	65	1.98284	± 112	1.21915	± 63	0.11378	± 9
UMCP3	58	1.75	JMDD	25/10/02	132	1.98202	± 81	1.21865	± 43	0.11370	± 6
UMCP2	59	1.75	DGP	27/10/02	316	1.98294	± 51	1.21943	± 29	0.11369	± 4
UMCP2	59	1.75	JMDD	27/10/02	204	1.98480	± 84	1.22008	± 44	0.11356	± 6
UMCP2	59	1.75	JMDD	27/10/02	526	1.98245	± 40	1.21950	± 23	0.11380	± 3
UMCP3	59	0.175	JMDD	27/10/02	236	1.98273	± 68	1.21958	± 42	0.11415	± 5
UMCP3	59	0.175	JMDD	27/10/02	412	1.98309	± 42	1.21982	± 23	0.11376	± 3
UMCP3	59	0.175	JMDD	27/10/02	462	1.98394	± 42	1.22012	± 22	0.11389	± 4
UMCP2	59	1.75	JMDD	27/10/02	319	1.98293	± 61	1.22001	± 30	0.11390	± 4
UMCP2	59	1.75	JMDD	27/10/02	389	1.98383	± 45	1.21949	± 25	0.11376	± 4
UMCP2	59	3.5	DGP	27/10/02	73	1.98285	± 110	1.21910	± 60	0.11382	± 8
UMCP3	59	0.175	JMDD	27/10/02	438	1.98246	± 55	1.21947	± 29	0.11395	± 4
UMCP3	59	0.175	JMDD	27/10/02	409	1.98356	± 53	1.21973	± 27	0.11379	± 3
UMCP2	59	3.5	JMDD	27/10/02	178	1.98306	± 61	1.21904	± 31	0.11382	± 5
UMCP2	59	3.5	JMDD	27/10/02	510	1.98281	± 39	1.21926	± 20	0.11389	± 3
UMCP2	60	1.75	JMDD	10/11/02	321	1.98335	± 51	1.21998	± 33	0.11364	± 5
UMCP2	60	1.75	JMDD	10/11/02	542	1.98398	± 48	1.21967	± 26	0.11377	± 3
UMCP2	60	1.75	JMDD	10/11/02	323	1.98386	± 64	1.21975	± 38	0.11355	± 4
UMCP2	60	1.75	JMDD	10/11/02	558	1.98281	± 36	1.21982	± 21	0.11384	± 3
UMCP3	60	0.175	JMDD	10/11/02	209	1.98401	± 69	1.21973	± 33	0.11391	± 5
UMCP3	60	0.175	JMDD	10/11/02	611	1.98466	± 32	1.22015	± 21	0.11380	± 3
UMCP3	60	0.175	JMDD	10/11/02	214	1.98441	± 61	1.21944	± 37	0.11372	± 5
UMCP3	60	0.175	JMDD	10/11/02	86	1.98139	± 77	1.21910	± 49	0.11370	± 7
UMCP3	60	0.175	JMDD	10/11/02	135	1.98415	± 78	1.21997	± 38	0.11390	± 5
UMCP4	60	0.018	JMDD	10/11/02	341	1.98455	± 59	1.21963	± 25	0.11370	± 4
UMCP4	60	0.018	JMDD	10/11/02	322	1.98325	± 41	1.22035	± 33	0.11371	± 4
UMCP2	60	1.75	JMDD	10/11/02	516	1.98233	± 38	1.21904	± 21	0.11392	± 3
UMCP2	60	1.75	JMDD	10/11/02	469	1.98213	± 43	1.21973	± 22	0.11384	± 3
UMCP2	60	1.75	JMDD	10/11/02	562	1.98294	± 36	1.21942	± 24	0.11383	± 3
UMCP2	61	1.75	JMDD	23/11/02	260	1.98308	± 82	1.21958	± 40	0.11384	± 4
UMCP2	61	1.75	JMDD	23/11/02	480	1.98254	± 35	1.22064	± 22	0.11396	± 3
UMCP3	61	0.175	JMDD	23/11/02	148	1.98299	± 79	1.22007	± 42	0.11399	± 6
UMCP3	61	0.175	JMDD	23/11/02	458	1.98315	± 49	1.21972	± 24	0.11385	± 3
UMCP3	61	0.175	JMDD	23/11/02	374	1.98381	± 47	1.21962	± 27	0.11381	± 3
UMCP4	61	0.018	JMDD	23/11/02	338	1.98457	± 81	1.21984	± 38	0.11378	± 4
UMCP4	61	0.018	JMDD	23/11/02	269	1.98540	± 56	1.22066	± 33	0.11367	± 5
UMCP3	61	0.175	JMDD	23/11/02	423	1.98196	± 51	1.21962	± 25	0.11389	± 3
UMCP2	61	1.75	JMDD	23/11/02	377	1.98382	± 47	1.21934	± 22	0.11382	± 4
UMCP2	61	1.75	JMDD	23/11/02	126	1.98578	± 82	1.21997	± 55	0.11382	± 6
UMCP2	62	1.75	JMDD	08/12/02	361	1.98260	± 45	1.21951	± 28	0.11379	± 3
UMCP2	62	1.75	JMDD	08/12/02	154	1.98306	± 65	1.21941	± 41	0.11393	± 7
UMCP3	62	0.175	JMDD	08/12/02	352	1.98319	± 50	1.22005	± 28	0.11398	± 4
UMCP3	62	0.175	JMDD	08/12/02	163	1.98426	± 66	1.21979	± 42	0.11380	± 5
UMCP3	62	0.175	JMDD	08/12/02	224	1.98270	± 58	1.21946	± 31	0.11375	± 4
UMCP3	62	0.175	JMDD	08/12/02	117	1.98095	± 92	1.21993	± 47	0.11379	± 7
UMCP3	62	0.175	JMDD	08/12/02	62	1.98299	± 118	1.21855	± 67	0.11377	± 8
UMCP4	62	0.175	JMDD	08/12/02	55	1.98430	± 120	1.21818	± 85	0.11391	± 8
UMCP4	62	0.175	JMDD	08/12/02	31	1.98543	± 143	1.21929	± 84	0.11401	± 11
UMCP2	62	1.75	JMDD	08/12/02	457	1.98322	± 47	1.21963	± 24	0.11390	± 3
UMCP2	62	1.75	JMDD	08/12/02	250	1.98223	± 52	1.21933	± 34	0.11378	± 4
UMCP2	62	1.75	JMDD	08/12/02	436	1.98239	± 40	1.21987	± 23	0.11374	± 3
UMCP2	63	1.75	JMDD	17/12/02	62	1.98438	± 117	1.22007	± 68	0.11410	± 9

Std.	Mag.	Size (ng)	Op.	Run date	^{192}Os (kcps)	$^{190}Os/^{188}Os_m$	± 1σ	$^{189}Os/^{188}Os_m$	± 1σ	$^{187}Os/^{188}Os_m$	± 1σ
UMCP2	63	1.75	JMDD	17/12/02	438	1.98256	± 45	1.21981	± 27	0.11395	± 3
UMCP2	63	1.75	JMDD	17/12/02	313	1.98341	± 52	1.21928	± 25	0.11379	± 4
UMCP2	63	1.75	JMDD	17/12/02	340	1.98228	± 64	1.21852	± 35	0.11397	± 4
UMCP2	63	1.75	JMDD	17/12/02	531	1.98242	± 36	1.21927	± 21	0.11370	± 3
UMCP2	63	1.75	JMDD	17/12/02	469	1.98405	± 38	1.21985	± 26	0.11379	± 3
THIRD N-TIMS SESSION											
UMCP2	116	1.75	JMDD	14/05/03	435	1.98237	± 41	1.21932	± 24	0.11387	± 4
UMCP2	116	1.75	JMDD	14/05/03	280	1.98126	± 62	1.21926	± 33	0.11382	± 5
UMCP2	117	1.75	JMDD	16/05/03	596	1.98285	± 50	1.21927	± 26	0.11395	± 5
UMCP4	117	0.018	JMDD	16/05/03	153	1.98610	± 71	1.21940	± 46	0.11397	± 7
UMCP3	117	0.175	JMDD	16/05/03	358	1.97994	± 48	1.21898	± 27	0.11390	± 4
UMCP3	117	0.175	JMDD	16/05/03	358	1.97758	± 46	1.21754	± 28	0.11384	± 3
UMCP4	117	0.018	JMDD	16/05/03	94	1.98424	± 96	1.22042	± 61	0.11358	± 9
UMCP3	117	0.175	JMDD	16/05/03	471	1.98198	± 47	1.21930	± 25	0.11388	± 3
UMCP2	117	1.75	JMDD	16/05/03	477	1.98586	± 45	1.22022	± 22	0.11382	± 3
UMCP2	117	1.75	JMDD	16/05/03	528	1.98589	± 47	1.22022	± 24	0.11379	± 3
UMCP3	118	0.175	JMDD	22/05/03	598	1.98065	± 48	1.21907	± 28	0.11400	± 4
UMCP3	118	0.175	JMDD	22/05/03	477	1.97576	± 45	1.21739	± 23	0.11412	± 3
UMCP2	119	1.75	JMDD	25/05/03	744	1.98104	± 38	1.21930	± 21	0.11397	± 3
UMCP2	119	0.175	JMDD	25/05/03	540	1.97904	± 45	1.21889	± 20	0.11390	± 3
UMCP3	119	0.175	JMDD	25/05/03	558	1.98325	± 44	1.21987	± 23	0.11384	± 4
UMCP3	119	0.175	JMDD	25/05/03	175	1.98596	± 61	1.22015	± 31	0.11372	± 5
UMCP3	119	0.175	JMDD	25/05/03	532	1.98652	± 41	1.22057	± 24	0.11367	± 3
UMCP2	119	1.75	JMDD	25/05/03	437	1.98609	± 53	1.22045	± 30	0.11383	± 4
UMCP2	119	1.75	JMDD	25/05/03	438	1.98528	± 41	1.22038	± 24	0.11381	± 3
UMCP2	120	1.75	JMDD	02/06/03	486	1.98103	± 60	1.21877	± 30	0.11396	± 4
UMCP2	120	1.75	JMDD	02/06/03	547	1.98320	± 45	1.21957	± 25	0.11385	± 3
UMCP3	120	0.175	JMDD	02/06/03	407	1.98091	± 47	1.21912	± 25	0.11399	± 4
UMCP3	120	0.175	JMDD	02/06/03	390	1.98236	± 39	1.21980	± 28	0.11377	± 4
UMCP2	120	1.75	JMDD	02/06/03	364	1.98343	± 40	1.21985	± 24	0.11381	± 4
UMCP2	120	1.75	JMDD	02/06/03	369	1.98300	± 49	1.22016	± 26	0.11378	± 3
UMCP2	121	1.75	DGP	08/06/03	146	1.98591	± 85	1.22089	± 41	0.11383	± 7
UMCP3	121	0.175	JMDD	08/06/03	331	1.98089	± 57	1.21944	± 39	0.11406	± 5
UMCP3	121	0.175	DGP	08/06/03	136	1.98197	± 84	1.21881	± 57	0.11395	± 6
UMCP2	121	1.75	DGP	08/06/03	73	1.98261	± 103	1.22049	± 70	0.11380	± 8
UMCP2	122	1.75	JMDD	15/06/03	469	1.98244	± 40	1.21954	± 23	0.11382	± 3
UMCP2	122	1.75	JMDD	15/06/03	455	1.98341	± 46	1.22002	± 30	0.11374	± 3
UMCP3	122	0.175	JMDD	15/06/03	574	1.98374	± 40	1.21980	± 25	0.11382	± 3
UMCP2	122	1.75	JMDD	15/06/03	523	1.98270	± 47	1.21934	± 22	0.11399	± 3
UMCP2	122	1.75	JMDD	15/06/03	505	1.98304	± 41	1.22022	± 24	0.11383	± 4
UMCP2	123	1.75	JMDD	22/06/03	590	1.98327	± 34	1.21961	± 20	0.11391	± 3
UMCP2	123	1.75	JMDD	22/06/03	575	1.98290	± 43	1.21991	± 17	0.11387	± 3
UMCP2	123	1.75	JMDD	22/06/03	610	1.98122	± 39	1.21852	± 22	0.11406	± 3
UMCP2	123	1.75	JMDD	22/06/03	358	1.98367	± 52	1.22023	± 26	0.11386	± 3
UMCP2	123	1.75	JMDD	22/06/03	334	1.98363	± 60	1.22034	± 36	0.11352	± 4
UMCP2	123	1.75	JMDD	22/06/03	434	1.98118	± 44	1.21970	± 26	0.11382	± 3
UMCP2	123	1.75	JMDD	22/06/03	607	1.98269	± 37	1.22007	± 17	0.11389	± 3
UMCP2	123	1.75	JMDD	22/06/03	347	1.98301	± 45	1.21985	± 31	0.11386	± 4
UMCP3	123	0.175	JMDD	22/06/03	619	1.98202	± 47	1.21887	± 25	0.11386	± 3
UMCP2	124	1.75	JMDD	01/07/03	467	1.98234	± 55	1.21997	± 24	0.11390	± 3
UMCP2	124	1.75	JMDD	01/07/03	550	1.98340	± 38	1.21991	± 21	0.11385	± 3
UMCP2	124	1.75	JMDD	01/07/03	589	1.98206	± 31	1.21989	± 20	0.11389	± 3

Std.	Mag.	Size (ng)	Op.	Run date	^{192}Os (kcps)	$^{190}Os/^{188}Os_m$	±	1σ	$^{189}Os/^{188}Os_m$	±	1σ	$^{187}Os/^{188}Os_m$	±	1σ
UMCP2	124	1.75	JMDD	01/07/03	601	1.98331	±	39	1.21940	±	26	0.11380	±	3
UMCP2	125	1.75	JMDD	07/07/03	438	1.98341	±	39	1.21977	±	21	0.11380	±	3
UMCP3	125	0.175	JMDD	07/07/03	718	1.98296	±	32	1.21984	±	19	0.11403	±	3
UMCP3	125	0.175	JMDD	07/07/03	508	1.98395	±	39	1.22000	±	24	0.11380	±	3
UMCP2	125	1.75	JMDD	07/07/03	527	1.98313	±	50	1.21915	±	26	0.11385	±	3
UMCP2	125	1.75	JMDD	07/07/03	527	1.98330	±	38	1.21984	±	26	0.11388	±	3
UMCP3	125	0.175	JMDD	07/07/03	631	1.98167	±	44	1.21953	±	22	0.11397	±	3
UMCP2	126	1.75	JMDD	13/07/03	647	1.98245	±	43	1.21938	±	27	0.11388	±	4
UMCP2	126	1.75	JMDD	13/07/03	490	1.98254	±	41	1.21961	±	23	0.11375	±	3
UMCP2	126	1.75	JMDD	13/07/03	557	1.98352	±	47	1.21988	±	26	0.11379	±	3
UMCP2	126	1.75	JMDD	13/07/03	611	1.98267	±	42	1.21956	±	25	0.11388	±	4
UMCP2	126	1.75	JMDD	13/07/03	723	1.98304	±	35	1.21958	±	21	0.11383	±	3
UMCP3	127	0.175	DGP	28/07/03	93	1.98292	±	93	1.21954	±	60	0.11392	±	7
UMCP2	127	1.75	DGP	29/07/03	326	1.98397	±	70	1.22007	±	36	0.11387	±	4
UMCP2	127	1.75	DGP	31/07/03	257	1.98959	±	47	1.22220	±	38	0.11374	±	5
UMCP3	128	0.175	DGP	15/09/03	485	1.98432	±	59	1.22024	±	30	0.11375	±	3
UMCP3	128	0.175	JMDD	15/09/03	540	1.98263	±	45	1.21980	±	24	0.11382	±	3
UMCP4	128	0.018	DGP	15/09/03	61	1.98403	±	127	1.21957	±	69	0.11374	±	9
UMCP4	128	0.018	DGP	15/09/03	70	1.98403	±	127	1.21957	±	69	0.11366	±	9
Average						**1.98363**			**1.21966**			**0.11382**	**±**	**12**
2*St Dev						**0.00454**			**0.00170**			**0.00024**		
2σ‰ varn.												**2.14**		
Shirey and Walker (1995) n=15 (UMCP on 30ng aliquots)												0.11379	±	2
‰ difference between AHIGL analyses and quoted literature data												0.03		

Table C.4: 33 UMCP Standards measured statically on the AHIGL TRITON over the period of 02/2002 until 10/2002

Standard	Mag.	Size (ng)	Op.	Run date	^{192}Os (volts)	$^{190}Os/^{188}Os_m$	±	1σ	$^{189}Os/^{188}Os_m$	±	1σ	$^{187}Os/^{188}Os_m$	±	1σ
UMCP1	13	C.	JMDD	25/02/02	**0.6**	1.98379	±	4	1.21972	±	2	0.11385	±	1
UMCP1	13	C.	JMDD	25/02/02	**2.6**	1.98375	±	2	1.21970	±	1	0.11382	±	0
UMCP1	13	C.	JMDD	25/02/02	**2.6**	1.98374	±	2	1.21969	±	1	0.11380	±	0
UMCP1	13	C.	JMDD	25/02/02	**0.4**	1.98371	±	9	1.21969	±	4	0.11371	±	2
UMCP1	13	C.	JMDD	25/02/02	**1.0**	1.98380	±	3	1.21970	±	2	0.11381	±	1
UMCP1	13	C.	JMDD	25/02/02	**1.4**	1.98377	±	3	1.21970	±	2	0.11386	±	1
UMCP2	13	1.75	JMDD	21/02/02	**0.3**	1.98371	±	7	1.21958	±	4	0.11382	±	3
UMCP2	13	1.75	JMDD	23/02/02	**0.5**	1.98380	±	8	1.21969	±	3	0.11388	±	1
UMCP2	13	1.75	JMDD	23/02/02	**0.4**	1.98368	±	8	1.21961	±	6	0.11385	±	3
UMCP2	13	1.75	JMDD	24/02/02	**0.4**	1.98375	±	6	1.21976	±	3	0.11380	±	2
UMCP2	14	1.75	JMDD	04/03/02	**0.4**	1.98377	±	5	1.21972	±	4	0.11386	±	2
UMCP2	14	1.75	JMDD	13/03/02	**0.7**	1.98383	±	9	1.21969	±	3	0.11382	±	1
UMCP2	14	1.75	JMDD	10/03/02	**1.1**	1.98378	±	7	1.21976	±	2	0.11377	±	1
UMCP2	14	1.75	JMDD	10/03/02	**1.2**	1.98373	±	5	1.21970	±	2	0.11386	±	1
UMCP2	15	1.75	JMDD	22/03/02	**0.2**	1.98415	±	10	1.21967	±	6	0.11373	±	3
UMCP1	51	3.5	DGP	05/08/02	**0.2**	1.98370	±	10	1.21965	±	6	0.11382	±	8
UMCP1	51	3.5	DGP	05/08/02	**0.2**	1.98430	±	9	1.21977	±	57	0.11398	±	4
UMCP1	51	3.5	DGP	05/08/02	**0.4**	1.98363	±	6	1.21964	±	4	0.11389	±	2
UMCP2	54	3.5	JMDD	02/09/02	**0.2**	1.98362	±	13	1.21959	±	7	0.11389	±	5
UMCP2	54	3.5	JMDD	02/09/02	**1.1**	1.98375	±	2	1.21972	±	1	0.11377	±	1
UMCP3	54	3.5	JMDD	02/09/02	**1.1**	1.98371	±	13	1.21973	±	4	0.11373	±	1
UMCP3	54	3.5	JMDD	02/09/02	**1.6**	1.98372	±	7	1.21972	±	2	0.11375	±	1
UMCP2	54	3.5	JMDD	02/09/02	**1.4**	1.98369	±	13	1.21971	±	4	0.11377	±	1
UMCP2	55	1.75	JMDD	19/09/02	**1.5**	1.98377	±	14	1.21968	±	5	0.11383	±	1
UMCP2	55	1.75	JMDD	19/09/02	**0.4**	1.98409	±	16	1.21961	±	7	0.11397	±	2
UMCP2	55	3.5	JMDD	19/09/02	**0.9**	1.98372	±	8	1.21969	±	3	0.11387	±	2
UMCP2	55	3.5	JMDD	19/09/02	**2.8**	1.98370	±	8	1.21970	±	3	0.11383	±	0
UMCP2	55	7	JMDD	19/09/02	**4.4**	1.98373	±	11	1.21972	±	3	0.11383	±	0
UMCP2	55	7	JMDD	19/09/02	**3.6**	1.98370	±	13	1.21969	±	4	0.11382	±	1
UMCP2	55	7	JMDD	19/09/02	**4.1**	1.98370	±	7	1.21972	±	2	0.11382	±	0
UMCP2	56	1.75	JMDD	06/10/02	**2.2**	1.98371	±	9	1.21972	±	3	0.11384	±	0
UMCP2	56	7	JMDD	06/10/02	**0.8**	1.98370	±	6	1.21971	±	3	0.11383	±	1
UMCP2	56	7	JMDD	06/10/02	**2.4**	1.98372	±	10	1.21973	±	3	0.11381	±	0
Average						**1.98377**			**1.21969**			**0.11383**	**±**	**6**
2*St Dev						**0.00028**			**0.00009**			**0.00012**		
2σ‰ varn.												**1.04**		
Shirey and Walker (1995) n=15 (UMCP on 30ng aliquots)												0.11379	±	2
‰ difference between AHIGL analyses and quoted literature data												0.04		

Table C.5: 21 DTM Standards generated during the course of this thesis by J.M.D.D

Standard	Mag.	Size (ng)	Op.	Run date	^{192}Os (kcps)	$^{190}Os/^{188}Os_m$	±	1σ	$^{189}Os/^{188}Os_m$	±	1σ	$^{187}Os/^{188}Os_m$	±	1σ
01OS03	**61**	2.5	JMDD	23/11/02	177	1.98429	±	74	1.21942	±	42	0.17407	±	7
01OS03	**61**	2.5	JMDD	23/11/02	443	1.98202	±	41	1.21934	±	24	0.17410	±	5
01OS03	**61**	2.5	JMDD	23/11/02	540	1.98379	±	40	1.21933	±	24	0.17397	±	4
01OS03	**62**	2.5	JMDD	08/12/02	107	1.98440	±	83	1.21966	±	49	0.17396	±	8
01OS03	**62**	2.5	JMDD	08/12/02	466	1.98324	±	41	1.21967	±	25	0.17402	±	4
01OS03	**119**	2.5	JMDD	25/05/03	483	1.98431	±	56	1.21949	±	32	0.17411	±	7
01OS03	**119**	2.5	JMDD	25/05/03	280	1.98934	±	60	1.22103	±	30	0.17367	±	6
01OS03	**122**	2.5	JMDD	15/06/03	420	1.98333	±	66	1.21970	±	26	0.17410	±	6
01OS03	**122**	2.5	JMDD	15/06/03	514	1.98357	±	34	1.21967	±	21	0.17402	±	4
01OS03	**123**	2.5	JMDD	22/06/03	500	1.98277	±	39	1.21954	±	20	0.17417	±	4
01OS03	**123**	2.5	JMDD	22/06/03	511	1.98296	±	35	1.21935	±	23	0.17394	±	4
01OS03	**123**	2.5	JMDD	22/06/03	500	1.98222	±	37	1.21971	±	23	0.17412	±	4
01OS03	**124**	2.5	JMDD	01/07/03	564	1.98488	±	39	1.22006	±	22	0.17395	±	4
01OS03	**124**	2.5	JMDD	01/07/03	583	1.98452	±	37	1.22022	±	22	0.17393	±	4
01OS03	**124**	2.5	JMDD	01/07/03	427	1.98356	±	48	1.22035	±	26	0.17385	±	4
01OS03	**125**	2.5	JMDD	07/07/03	549	1.98314	±	39	1.21919	±	22	0.17412	±	4
01OS03	**125**	2.5	JMDD	07/07/03	343	1.98407	±	52	1.22011	±	29	0.17380	±	5
01OS03	**125**	2.5	JMDD	07/07/03	431	1.98370	±	48	1.21944	±	28	0.17411	±	5
01OS03	**125**	2.5	JMDD	07/07/03	422	1.98113	±	44	1.21902	±	24	0.17406	±	4
01OS03	**125**	2.5	JMDD	07/07/03	547	1.98309	±	32	1.21943	±	20	0.17407	±	4
01OS03	**126**	2.5	JMDD	13/07/03	500	1.98219	±	40	1.21948	±	24	0.17428	±	4
Average						**1.9836**			**1.2197**			**0.17402**	±	**14**
2*St Dev						**0.0032**			**0.0009**			**0.00027**		
2σ‰ varn.												**1.57**		
Schaefer *et al.* (2002) n=140 (Open University, Feb 1997 until Oct 2000)												0.17396	±	9
‰ difference between AHIGL analyses and quoted literature data												0.06		

C.1.3 Re analysis

Re aliquots from anion exchange chromatography were taken up in 2ml of 0.8N SPA HNO_3 in micro-centrifuge tubes prior to solution analysis. The basic methods for analysis are outlined in Pearson and Woodland (2000) and Day *et al.* (2003) for ICP-MS and PIMMS and are presented here with modifications.

C.1.3.1 Re analysis by ICP-MS

Some of the samples analysed for Re in this study were measured using an ELAN 6000 ICP-MS housed at the AHIGL. The method is described in Pearson and Woodland (2000) and uses a standard cross-flow nebuliser with an uptake of *ca.* 1mL/min. This nebuliser has very low memory effect for Re and produced oxide isobaric interferences of *ca.* 0.8 to 2.5% as metal-oxide to metal ratios. Prior to analysis 10ppb solutions of Yb were measured to estimate oxide production to correct for possible YbO interference on Re. Re standard solutions of equivalent

concentrations to sample solutions, were interspersed regularly (1 standard for every 2 samples) to monitor sensitivity as well as mass bias drift, which was found to be negligible. A comparison between ICP-MS and PIMMS techniques is made in section C.1.3.3

C.1.3.2 Re analysis by PIMMS

I.D Re isotopic compositions were measured for the majority of samples using a Thermo Neptune® PIMMS, a double focusing magnetic sector ICP-MS in the AHIGL at the University of Durham. For samples and Re-Ir standard solution measurements, an ESI™ PFA-50 nebuliser and a dual cyclonic Scott double pass quartz spray chamber (CSDP) were utilised. This inlet combination has the advantage of faster washout times compared with the Cetac Aridus micro concentric desolvating nebuliser. Although the Re standard solutions washed to very low background levels, it was found that samples and standards run using the Aridus showed persistent background. For experiments with Re, the standard Finnigan "H" cone was used and comparison of cone performance is given elsewhere in Nowell *et al.* (2003).

The AHIGL PIMMS is equipped with one fixed and eight moveable Faraday collectors plus an SEM detector. Re was analysed in the peak-jumping mode on the SEM. Re mass bias was corrected for by measuring Ir in a static configuration. In addition to correction for mass fractionation, analysis of the ^{193}Ir isotope in each sequence during peak-hopping allows correction for plasma fluctuation. A $^{193}Ir/^{191}Ir$ ratio of 1.69205 was used for normalization and was derived by mass fractionation correcting the measured $^{193}Ir/^{191}Ir$ to a $^{187}Re/^{185}Re$ isotope ratio of 1.67392. Re was measured in blocks 20 cycles with 4.194 second integration times. Re was corrected for mass bias using an exponential law, and correction coefficients derived from the Ir static measurement.

C.1.3.3 Comparison of Re analysis by ICP-MS and PIMMS

ICP-MS has become the preferred method of trace element analysis in geochemistry and is ideally suited to the determination of PGEs by isotope dilution (Rehkämper and Halliday, 1997; Pearson and Woodland, 2000). The Elan 6000 ICP-MS at Durham University has been routinely used to measure Re concentrations by isotope dilution at the ppt level (Woodland and Pearson, 1999; Pearson and Woodland,

2000). The effects of memory, isobaric interferences and other analytical protocols are outlined elsewhere (Pearson and Woodland, 2000). It will be illustrated here that Re analyses by ICP-MS are highly precise. However, the AHIGL Thermo Neptune® PIMMS instrument has greater than one hundred times the sensitivity of the quadrupole ICP-MS and thus can measure the isotopic ratio of small samples with greater accuracy. In addition, the multi-collector capability allows simultaneous collection on large beams of an element used to correct for mass bias, whilst simultaneously being able to measure very small analyte beams on the secondary electron multiplier (SEM). Hence, the PIMMS offers the potential for accurate mass bias corrections for Re.

C.1.3.3.1 Analysis of Re standard solutions

Replicate analyses (n = 134) of 0.001 to 10ppb Re standard solutions doped with 10-20ppb natural Ir, were carried out over six sessions from August 2001 to June 2004. These combined results yield a long-term reproducibility for fractionation corrected $^{187}Re/^{185}Re$ of 1.67728±990 (5.9‰; 2.S.D.; Fig. C.5). The small differences seen in average $^{187}Re/^{185}Re$ observed between data collected over different sessions are within error. Sessions i-iv in Fig. C.5 were run without correction for plasma flicker whilst sessions v to vi were corrected for plasma flicker which is reflected in the better standard reproducibility. It is important to note that all standard analyses were performed under operating conditions similar to those for analysis of samples and standards, i.e., interspersed with isotope dilution analyses of rocks with $^{187}Re/^{185}Re$ ratios ranging 0.01-1.4. Re sample aliquots were either (i) not doped with Ir and were mass bias corrected using corrected with reference to an average standard value or (ii) doped with Ir that swamped any potential interference from the ^{191}Ir spike whose yield in the Re chemistry was found to be minimal. The excellent reproducibility of the standard data demonstrates the efficiency of washing out small background signals which depended upon the isotope composition of the memory approaching a stable value.

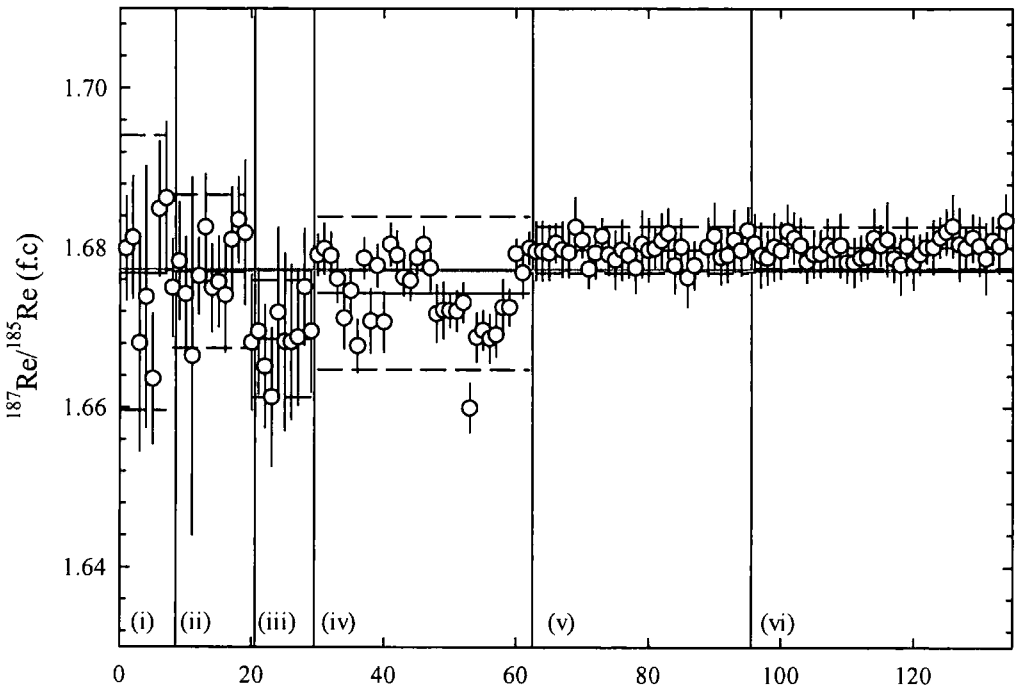

Fig. C.5: Replicate analyses of standard solutions of natural Re doped with Ir to monitor mass fractionation. Individual errors are the internal precision (2.s.e) from each analysis. Individual and combined external reproducibility's for each analytical session are (i) 1.6768±86, (ii) 1.677±48, (iii) 1.6686±37, (iv) 1.6743±47, (v) 1.6798±29, (vi) 1.6801±26. The horizontal, thick stippled line represents $^{187}Re/^{185}Re$ calculated from Rosman and Taylor (1998).

Re data were obtained from the Elan 6000 ICP-MS at Durham and were corrected for mass bias using sample-standard bracketing without an external Ir admixture. Fig. C.6 shows the PIMMS and ICP-MS data relative to the natural Re isotopic value (1.673939, Rosman and Taylor, 1998). Points in Fig. C.6 represent nine ICP-MS and six PIMMS analytical sessions with 20-40 Re standard analyses per session of standard solutions which were interspersed with spiked samples. Standards were measured on the Elan 6000 using both cross flow and Aridus nebulisers. For the Elan 6000, external reproducibility of $^{187}Re/^{185}Re$ was 1.6947±230 (1.33%; 2.s.d) for 0.1 to 10ng/ml standards versus 1.6773±99 (0.75%; 2.s.d.) for all PIMMS standards. Errors are larger for the ICP-MS method and the average standard ICP-MS value is 1.28% higher than the fractionation corrected value determined by PIMMS. This is attributed to the lower sensitivity of the ICP-MS, intra-element mass fractionation (using Ir for PIMMS), and preferential analysis of the heavier Re isotope during analysis.

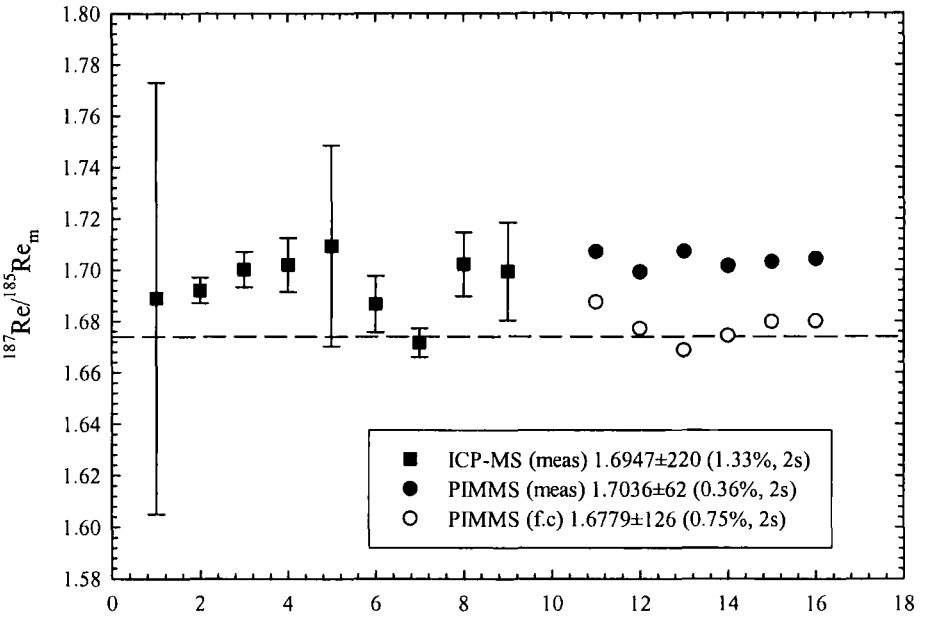

Fig. C.6: Comparison of natural Re standard solutions by ICP-MS and PIMMS (Errors for PIMMS are smaller than symbols). Re standards analysed by PIMMS are doped with Ir for mass bias corrections (f.c.). The dashed line represents the natural $^{187}Re/^{185}Re$ of 1.673939 (Rosman and Taylor, 1998).

C.1.3.3.2 Comparison of Re analyses by ID-ICP-MS and ID-PIMMS

Re concentrations of samples from a number of different geological environments were determined by isotope dilution using the Elan 6000 ICP-MS and the Neptune PIMMS. Different splits of the same solutions were used in all cases. Re concentrations of samples obtained by PIMMS and ICP-MS are compared in Fig. C.7. The straight line regression of (R^2=0.9996) indicates that both methods give highly precise and reproducible data for Re concentrations. Such a relationship is encouraging and illustrates the power of plasma source mass spectrometry in measuring low concentration PGEs by isotope dilution.

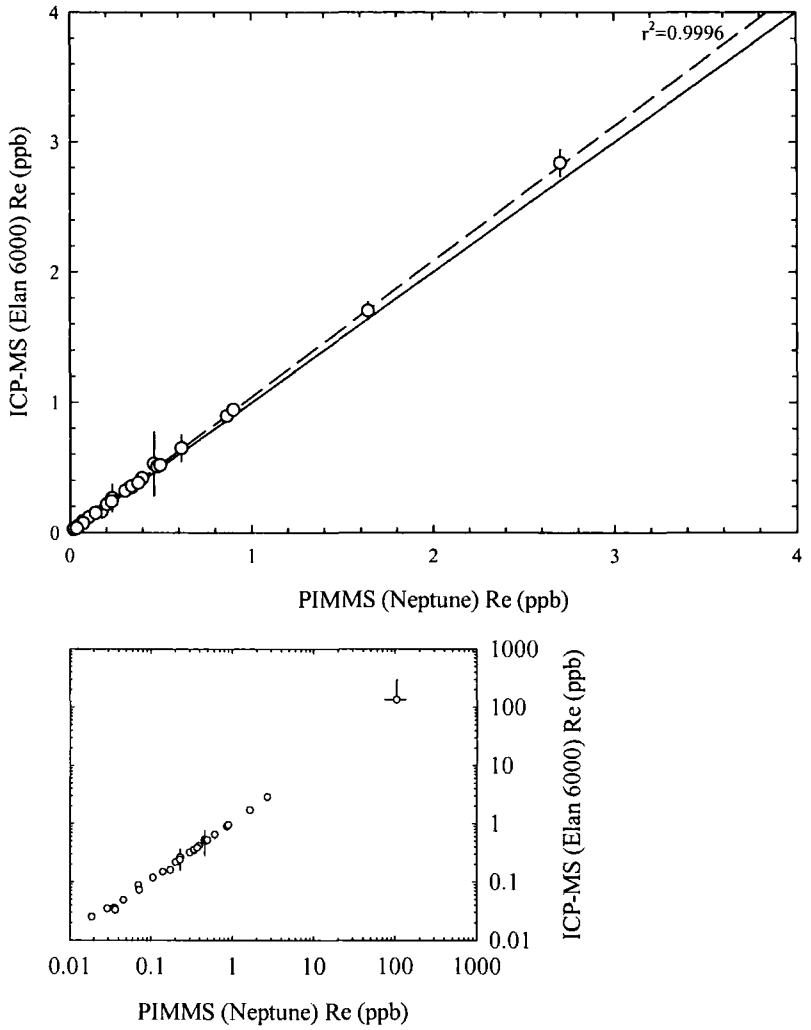

Fig. C.7: Comparison of Re-concentrations determined by PIMMS and ICP-MS. PIMMS and ICP-MS analyses for the same sample solutions agree to within 7.3% on average (2σ) and 21% in the worst case (High concentration sample in expanded plot).

C.1.4 Calibration of the Durham picrite (and peridotite) spikes

The abundances of ^{185}Re in the Durham picrite spike and ^{190}Os in the Durham picrite and peridotite spikes were calibrated by the author relative to DTM standards 94-4-37 (Re = 55.1643ng/g) and 94-4-27 (Os = 24.444ng/g) respectively. Os and Re calibrations were performed separately by homogenising standard and spike in a sealed Pyrex™ borosilicate Carius tube with 3mL of inverse aqua regia at 240°C for 72Hrs. For Os calibrations the OsO_4 was extracted using a typical solvent extraction (Cohen and Waters, 1996) and micro-distillation (Birck *et al.*, 1997) procedure prior to analysis by N-TIMS. Re calibrations were purified by CCl_4 extraction of interfering Os species in the mixed spike. The inverse aqua regia was dried down and

16M UPA HNO_3 was added to breakdown organic compounds within the residue. Re calibrations were analysed as 0.8M HNO_3 solutions on the Thermo Neptune® by sample-standard bracketing in peak-hopping mode on the Faraday collectors.

The concentration of ^{185}Re in the Durham picrite spike is equal to 0.02933mol/g (±0.00011, 1σ) with an in-run analytical precision of 0.75% (2σ). The concentration of ^{190}Os in the Durham picrite spike is equal to 0.03125mol/g (±0.00004, 1σ) and in the Durham peridotite spike is equal to 0.21946mol/g (±0.00027, 1σ). Both the Durham picrite and peridotite ^{190}Os spike calibrations were measured with in-run precisions of better than 0.25% (2σ). The Os spike used in this study was calibrated with ammonium hexachloroosmate salt upon which the stoichiometry is no better than ±3%, so the Durham picrite and peridotite spikes are limited to accuracy of ±3% as outlined in Morgan *et al.* (1995) and subsequently in Walker *et al.* (2002). Yin *et al.* (2001) found that potassium hexachloroosmate salt for calibration may yield better accuracy (±0.2%) because, unlike $(NH_4)_2OsCl_6$, K_2OsCl_6 is not hygroscopic and does not decompose during heating. However, the accuracy of the $(NH_4)_2OsCl_6$ spike calibration is entirely adequate for isochron work performed in this study (Chapter 5).

C.1.5 Offline correction of Re and Os data

$^{187}Re/^{185}Re$ ratios for sample solutions were corrected for mass bias using the deviation for the standard average run on the day over the natural $^{187}Re/^{185}Re$. The mass bias corrected ratios were then blank corrected. The blank correction for Re was less than 2% in most cases and was 8.2% at worst. A customised sheet was designed for $^{187}Os/^{188}Os$ ratio and Os concentration corrections was employed. The sheet firstly oxide corrects all the Os isotopes using values for $^{16}O/^{18}O$ and $^{17}O/^{18}O$ of 0.0003708 and 0.002045 respectively (Nier, 1950). An iterative fractionation correction is then applied using a $^{192}Os/^{188}Os$ ratio =3.082614 (Volkening *et al.* 1991). A penultimate ^{190}Os spike subtraction was performed prior to an Os blank subtraction. The blank correction for Os was less than 0.5% in most cases (typically <0.005% for Chromitite, high Os abundance samples, <0.01% for peridotites, <0.5% for basaltic lavas) and was 4.6% at worst for the standard EN026 10D-3.

C.1.6 Re-Os data for rock standards GP13 and EN026 10D-3 and inter-lab comparison

To assess the reproducibility of the analytical procedure five replicate analyses of peridotite standard GP-13 and four replicate analyses of basalt standard EN026 10D-3 were performed during the course of this study. GP-13 is an orogenic peridotite from the Beni-Bousera massif emplaced into the Betic-Rif orogen ~22Ma (Pearson *et al.*, 2004c). EN026 10D-3 is a mid-ocean ridge basalt dredged from the Mohns Ridge, Greenland Sea.

External reproducibility of the standard GP13, including the standard spiked with the Leoben University spike (supplied by T. Meisel) is expressed as two times the relative standard deviation of the mean and was 3.2% for Os and 4.4% for Re. This external standard reproducibility using the Durham picrite and Leoben multi-isotopic spikes compares well with repeat dissolutions using the Durham peridotite spike (6.1% Re, 8.8% Os), to measurements at Leoben University using a high pressure asher (6.4% Re, 1.7% Os), and to Chicago #000531 (2.8% Os; Puchtel *et al.*, 2004). The results for Os for GP13 in this study are on average 11%, 7% and 3% lower than Leoben, Durham peridotite and Chicago spike estimates. Analysis of a single GP13 aliquot using the Leoben spike at Durham was 7.6% higher for Re and 4% higher for Os. Accurate calibration of the Durham picrite spike and documented change in the concentration for the Durham peridotite spike (section C.1.4) may account for the 7% difference between the Durham peridotite spike. In this study the $^{187}Os/^{188}Os$ ratio of GP13 was also precisely measured and gives a ratio of 0.12632 (±0.00009, 1σ, n=5). This estimate compares favourably with the one quoted isotopic measurement of GP13 of 0.1262 in Pearson *et al.* (2004c).

External reproducibility of the standard EN026-10D3 for Re, expressed as two times the relative standard deviation of the mean, was 0.22%. The first three analyses of EN026-10D3 for Os listed in Table C.1 give a mean RSD of 0.36%. It was found that one of the analyses of EN026-10D3 yielded an Os concentration 7 times greater than the other three analyses which were in the 8ppt range. This result is not attributed to blank. This is because the blank contributions were regularly monitored during analyses and were found to be routinely less than 0.5fg (or <5% of the total analysis of EN026-10D3). This result is confirmed by the reproducibility on the first three analyses of EN026-10D3 for Os concentration and $^{187}Os/^{188}Os$ in Table C.6

which would not be expected with a poorly constrained blank. Interestingly the replicate analyses of EN026-10D3 generate an isochronous relationship suggesting standard heterogeneity which is not observed in GP13. The isochron yields an age of 2.2±0.8Ma with a $^{187}Os/^{188}Os$ initial of 0.1246±0.0074 (Fig. C.8). Interestingly, the $^{187}Os/^{188}Os$ initial of EN026-10D3 is very close to the measured isotopic ratios of abyssal peridotites (Brandon *et al.*, 2000).

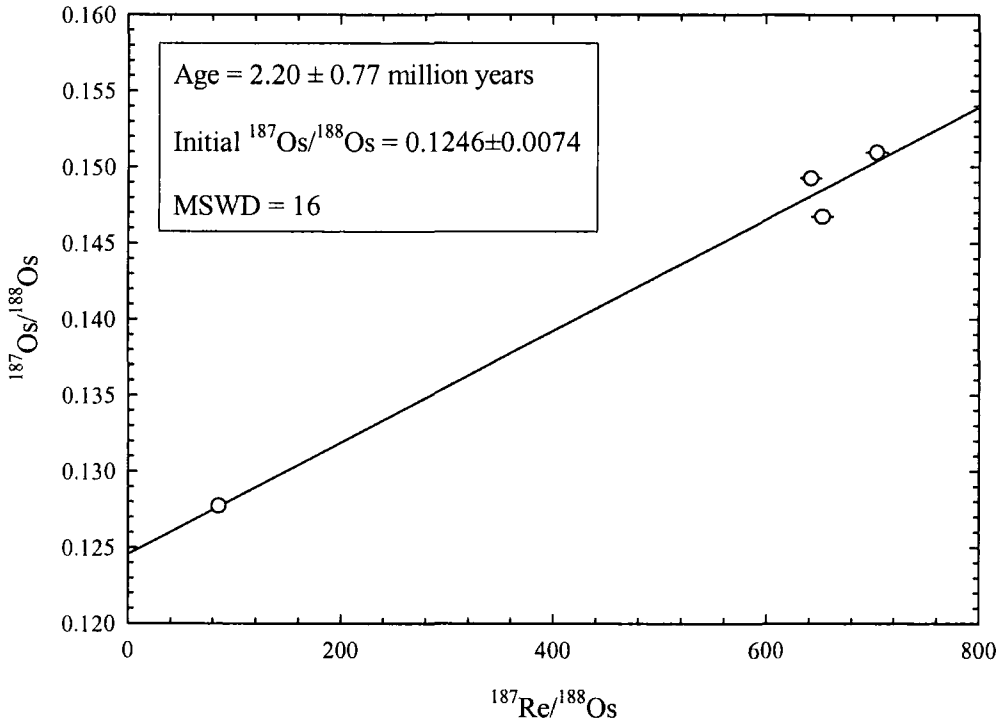

Fig. C.8: $^{187}Re/^{188}Os$-$^{187}Os/^{188}Os$ plot of replicate analyses of EN026-10D3 analysed throughout the course of this study. Errors on the $^{187}Os/^{188}Os$ ratio are smaller than symbols. The isochron was fitted using ISOPLOT 3.0 (Ludwig, 2003).

PGE standard heterogeneity is most likely to occur due to the 'nugget-effect' where PGE-alloys, especially IPGE (Os, Ir, Ru)-alloys cause sample heterogeneity. This heterogeneity would be expected to cause systematic fractionation and variation of Re/Os generating isochronous relationships for geologically old samples (>1Ma) as observed in EN026-10D3 (Fig. C.8). No isochronous relationship is observed in GP13, instead a negative correlation between $^{187}Re/^{188}Os$-$^{187}Os/^{188}Os$ (Fig. C.9) is observed and is probably caused through analytical artefacts or possible disturbance at outcrop in recent times (Pearson *pers. Comm.).*

EN026-10D3 loads had a 33% failure rate during sample digestion (2 of 6 exploded in the oven). This failure rate is exceptionally high with failure normally caused by poor annealing accounting for around 1 failure in ~40 loads. EN026-10D3 is a standard dredged from the Mohns ridge and is likely to contain a large quantity of carbonate and excess H_2O. Therefore it also appears that EN026-10D3 is susceptible to de-carbonisation and de-volatilisation in the Carius tube.

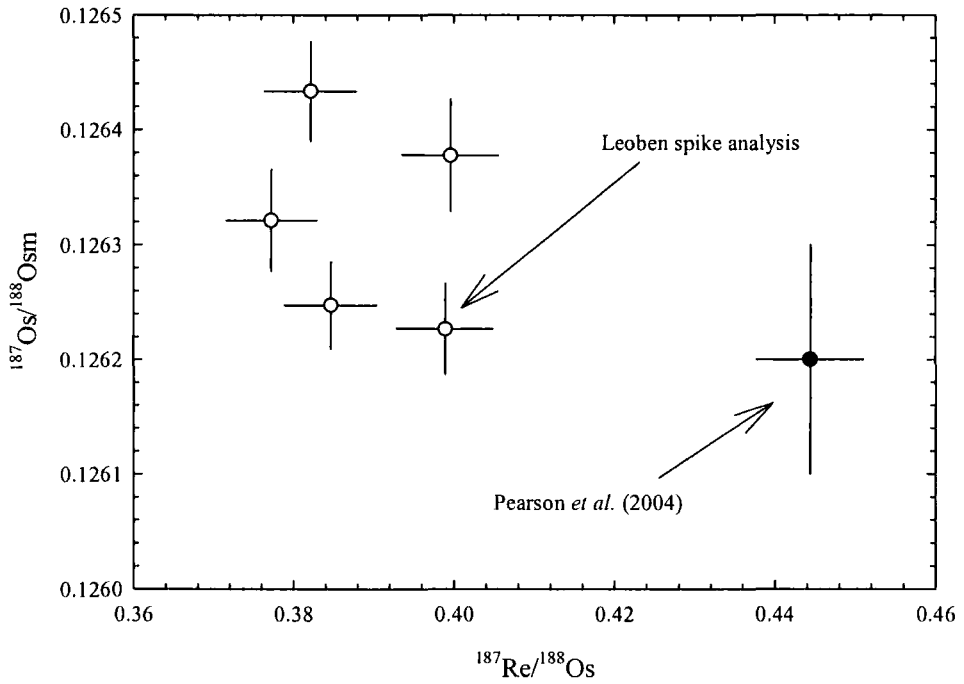

Fig. C.9: $^{187}Re/^{188}Os$-$^{187}Os/^{188}Os$ plot of replicate analyses of GP13 analysed throughout the course of this study.

Table C.6: Standards prepared and analysed during the course of this thesis by J.M.D.D Re and Os concentration and Os isotopic data for in house Durham and Rhode Island Standards

Sample	Re (ppb)	±2σ	Os (ppb)	±2σ	$^{187}Re/^{188}Os$[a]	$^{187}Os/^{188}Os_m$	± 2σ	$\gamma Os_{(t)}$[b]
GP13 a	0.296	7	3.737	13	0.38	0.12643	± 8	-0.89
GP13 b	0.291	8	3.509	12	0.40	0.12638	± 10	-0.94
GP13c	0.274	1	3.501	12	0.38	0.12632	± 8	-0.97
GP13d	0.285	1	3.565	12	0.38	0.12625	± 8	-1.03
GP13e[c]	0.309	1	3.727	13	0.40	0.12623	± 8	-1.05
Average	***0.291***		***3.608***			***0.12632***		***-0.98***
St Dev	***0.013***		***0.116***			***0.00009***		***0.07***
Durham (n=8)	0.330	20	3.870	340				
Leoben (n=3)	0.312	20	4.060	70				
Chicago (n=5)	-	-	3.620	100				
EN026 10D-3	1.062	2	0.0073	3	700.20	0.15096	± 30	-1.77
EN026 10D-3	1.113	2	0.0084	3	638.49	0.14926	± 26	-1.33
EN026 10D-3	1.177	2	0.0088	3	649.41	0.14674	± 26	-3.62
EN026 10D-3	1.044	2	0.0591	21	85.07	0.12773	± 12	-2.31
Average	***1.099***		***0.008***			***0.14899***		***-2.24***
St Dev	***0.060***		***0.001***			***0.00212***		***1.21***

[a]*The 2σ error in this ratio is 0.33% (Re) and 0.57% (Os) and is a function of spike uncertainty* [b]*Age corrected γOs values. γOs is the percentage difference between the age corrected $^{187}Os/^{188}Os$ ratio and the $^{187}Os/^{188}Os$ ratio of a chondritic mantle where the present-day chondritic mantle had $^{187}Os/^{188}Os$=0.12757 and $^{187}Re/^{188}Os$=0.3972 (Walker et al., 1989).* [c]*Using Leoben Spike*

C.2 **O isotope analysis** (Royal Holloway University of London)

Mineral and glasses phases were separated (appendix B) for oxygen isotope analysis by laser fluorination at the Department of Geology, Royal Holloway, University of London. Sample preparation and data processing protocols can be found in Macpherson and Mattey (1998). In contrast to that work, an automated extraction system employing a CO_2 laser was used to promote the fluorination reaction in a BrF_5 reagent and isotope ratios were measured on oxygen gas rather than CO_2 on an OPTIMA mass spectrometer. All analyses yielded 95±5% of the expected volume of O_2.

Replicate analyses of internal standards over the period of analysis gave the following results: San Carlos olivine 1, +4.84±0.10‰ (1σ, n=27), San Carlos olivine 2, +5.22±0.08‰ (1σ, n=19), NBS 30 biotite, +5.08±0.08‰ (1σ, n=8), UW-GMG2 garnet, +5.71±0.09‰ (1σ, n=22). These average standard values are within error of the long-term standard reproducibility for the OPTIMA (San Carlos olivine 1, +4.83±0.11‰ [2*RSD = 4.6%, n=77], San Carlos olivine 2, +5.23‰ [2*RSD = 3.7%, n=82], NBS 30 biotite, +5.00±0.11‰ [2*RSD = 4.5%, n=9], UW-GMG II garnet, +5.71±0.08‰ [2*RSD = 2.9%, n=82]. Results for San Carlos Olivine 1 are

also within error of the value quoted by Mattey *et al.* (1994) and Macpherson and Mattey (1998) of +4.88±0.09‰ (n=26). For UW-GMG II garnet values the standard precision and reproducibility compares favourably with published values of 5.8±0.1‰ (Anderson *et al.*, 1971) and 5.75±0.06‰ (Eiler *et al.*, 1996). Minor within-run drift was corrected by monitoring results for the 4 standards each day (i.e. per 12 samples). Precision and accuracy within runs were similar to the overall standard results.

C.3 **He isotope analysis** (Scripps Institution of Oceanography)

Mineral and glasses phases were separated (appendix B) for helium isotope analysis at the Fluid and Volatiles laboratory, Geoscience Research Division, Scripps Institution of Oceanography. Helium trapped in inclusions of olivine and clinopyroxene phenocrysts and the vesicles of glasses were released by crushing *in vacuo*. Separates free of adhering matrix were ultrasonically cleaned in ethanol and dried prior to loading into two on-line crushing devices (Scarsi, 2000). Blanks were obtained by operating the crusher (~70 beats per minute) for the same amount of time used for crushing (150s). Short crush times avoided the release of extraneous He contained in crystal lattice sites (Hilton *et al.*, 1993; Graham *et al.* 1998; Scarsi, 2000). The average vacuum line blank represented on average 0.26% and 2% of measured sample ^{3}He and ^{4}He respectively. At worst the total blank represented 2% and 10% of the measured sample ^{3}He and ^{4}He respectively. He liberated by crushing was expanded into a stainless steel preparation line and sequentially exposed for a total of 30 minutes to a Ti getter at 750°C – decreasing to 400°C, a liquid N-cooled charcoal trap, a SAES© Zr-Al getter operated at room temperature and a liquid He-cooled charcoal trap to isolate helium from neon. Following this, helium was expanded into a split-tube, dual collection He-isotope mass spectrometer (GAD) for $^{3}He/^{4}He$ analysis using peak-jumping protocols as described by Hilton *et al.* (2000a). Raw helium isotope were normalised using standard aliquots from Murdering Mudpots, Yellowstone National Park (= $16.45R_A$) and SIO Pier air (= $1R_A$). Ne was monitored on every run to correct $^{3}He/^{4}He$ ratios for the effects of air contamination (<2% for all samples).

Raw data was corrected offline for blank substitution, concentration, and error calculations. Concentrations calculations were performed relative to the Air standard whose pipetted He volume is precisely known.

C.4 Sr, Nd, Pb isotope analysis (AHIGL)

Sr, Nd and Pb isotope analysis was performed on single dissolutions of whole rock powders from the Western Canary Islands. All steps in the preparation of these whole rock powders was performed under clean air conditions at AHIGL.

C.4.1 Chemical preparation of samples prior to Sr, Nd, Pb isotope analysis

~100mg of powder was digested in 1mL 16N SPA HNO_3 and 4mL of 29N TD HF for 72Hrs on a hotplate at 150°C in Savillex Teflon beakers. This step was dried down and the residue was taken up and sequentially digested and dried-down in a series of steps using 2mL of 16N SPA HNO_3, 1mL 12M TD HCl and 2mL 1M TD HCl. The solutions were then centrifuged and $1/3^{rd}$ was aliquotted for the Sr and Pb column procedure with the remaining solution preserved for the Nd column procedure. The Sr-Pb aliquot was dried down and taken up in 3N UPA HNO_3, dried down and taken up once more in 3N UPA HNO_3 to change this solution into a nitric form. Rationale for this digestion technique is provided in Dowall *et al.* (2003).

Nd solutions were loaded onto cation-exchange resin columns using Bio-Rad® AG50W-X8 resin. Procedures for obtaining Nd-bearing fractions from this column procedure are outlined in Dowall *et al.* (2003). Sr- and Pb-bearing fractions were obtained using a micro-scale column procedure using Sr-specification resin and designed for Sr-drill microanalysis at AHIGL. The Sr-bearing fraction was collected in 0.35mL 0.05N TD HNO_3 whilst Pb was removed using 0.5mL of 6M UPA HCl. Column chromatography in this way removed elements which may cause isobaric or matrix interferences during analysis (e.g. ^{87}Rb on ^{87}Sr).

C.4.2 Sr, Nd, Pb isotope analysis by Plasma Ionisation Multicollector Mass-Spectrometry (PIMMS)

All isotopic measurements on samples processed for Sr, Nd and Pb isotopes were made using the Thermo Neptune® PIMMS instrument at AHIGL. Once collected

from the ion-exchange columns, the Sr, Nd and Pb fractions are evaporated to dryness and taken up in 1mL 0.8N HNO_3 solution. Sample solutions are introduced into the plasma using an Elemental Scientific Inc. (ESI) PFA-50 microflow nebuliser and an ESI dual cyclonic Scott double pass (CSDP) quartz spray chamber. Typical sample uptake rates were 70-100μL/min. Each analysis is based on the average of 50 measurement cycles with an integration time of 4.1 seconds per cycle. The Neptune® is equipped with 9 Faraday detectors and standard cup configurations for Sr and Nd are presented in Dowall *et al.* (2003).

One of the main sources of isobaric interference during isotopic analysis of Nd and Sr arises from spectral overlaps from the parent elements of the analyte, i.e. Sm on Nd and Rb on Sr. There are also other isobaric overlaps to account for, namely Hg on Pb, Ce on Nd and Kr on Sr. The correction for ^{86}Kr is particularly critical because instrumental mass bias during Sr analyses is measured using the $^{86}Sr/^{88}Sr$ ratio. Since Rb is not completely separated from Sr, Sm and Nd are not resolved at all by the chemistry, and some Hg is present as ambient background in Pb solution chemistry, corrections are required on measured $^{87}Sr/^{86}Sr$ and $^{143}Nd/^{144}Nd$ and $^{206}Pb/^{204}Pb$, $^{207}Pb/^{204}Pb$ and $^{208}Pb/^{204}Pb$ ratios. At present these are performed externally to the data acquisition routine. Detailed descriptions of the correction procedures adopted for isobaric interferences on Nd and Sr are given in Nowell and Parrish (2001) and Nowell *et al.* (2003). Examples of the general principles of the correction routines for Nd and Sr are given in Dowall *et al.* (2003).

To ensure that sample data is of consistently high quality during isotope ratio measurement it is essential to regularly monitor the accuracy and reproducibility of isotopic values in a standard reference material. The long-term reproducibility of the $^{143}Nd/^{144}Nd$ and $^{87}Sr/^{86}Sr$ ratios for appropriate standard solutions during the first two years of operation of the Durham Neptune is presented in Nowell *et al.* (2003). Average measured values for these ratios are within error of the accepted values. For Western Canary Island data collection sessions $^{143}Nd/^{144}Nd$ and $^{87}Sr/^{86}Sr$ for 200ppb J&M and NBS987 standards were 0.511107±14 (2σ, n=13) and 0.710257±11 (2σ, n=17). Samples ratios are normalised to accepted values of these standards (0.511111 and 0.710250 respectively, Nowell *et al.,* 2003). Blank and yield data for Sr and Nd preparation chemistry can be found in Dowall *et al.* (2003).

Pb data were measured using a Tl spike procedure on the Neptune® PIMMS. Pb isotope ratios were corrected for mass bias by doping sample liquids with a pure 50ppb Tl solution using a $^{205}Tl/^{203}Tl$ ratio of 2.388. This ratio has been derived by mass bias correcting $^{205}Tl/^{203}Tl$ to an accepted NBS 981 $^{207}Pb/^{208}Pb$ isotope ratio of 0.914585 (Todt *et al.*, 1996). NBS 981 results for the analytical session of 16.9372±7, 15.4930±7 and 36.705±3 for $^{206}Pb/^{204}Pb$, $^{207}Pb/^{204}Pb$ and $^{208}Pb/^{204}Pb$ respectively (2σ; n=20). The NBS 981 are significantly more heavy-isotope enriched than those of Todt *et al.* (1996), resulting in sample $\Delta^{207}Pb$ and $\Delta^{208}Pb$ values respectively 251 and 122ppm higher than for data normalised to the values of Todt *et al.* (1996). Such results are similar to results quoted in other laboratories using Tl, double-spike, or triple-spike methodologies (e.g. Thirlwall *et al.*, 2004). ^{204}Pb is subject to isobaric interferences from Hg. A peak stripping correction procedure was employed to correct for this interference which determines how much of the signal intensity measured at a particular mass is due to ^{204}Pb and how much is due to ^{204}Hg. $^{202}Hg/^{204}Hg$ is mass-bias corrected before peak stripping. Blank and yield data for Sr and Nd preparation chemistry for Pb can be found in Charlier *et al.* (in preparation, 2004).

Appendix D - ^{40}Ar-^{39}Ar techniques and results for Freemans Cove Complex volcanics

$^{40}Ar/^{39}Ar$ analysis of phenocrysts of sanidine and biotite were performed by standard mineral separation techniques, including hand-picking of clear, unaltered crystals in the size range 0.5 to 1 mm. Individual mineral separates were loaded into aluminum foil packets along with co-loaded Fish Canyon Tuff Sanidine (FCT-SAN) to act as flux monitor (apparent age = 28.03 ± 0.28 Ma; Renne *et al.*, 1998). The sample packets were arranged radially inside an aluminum can. The samples were then irradiated for 12 hours at the research reactor of McMaster University in a fast neutron flux of approximately $3x10^{16}$ neutrons/cm^2.

Laser $^{40}Ar/^{39}Ar$ step-heating analysis was carried out at the Geological Survey of Canada laboratories in Ottawa, Ontario. Upon return from the reactor, samples were split into several aliquots and loaded into individual 1.5 mm-diameter holes in a copper planchet. The planchet was then placed in the extraction line and the system evacuated. Heating of individual sample aliquots in steps of increasing temperature was achieved using a Merchantek MIR10 10W CO_2 laser equipped with a 2 mm x 2 mm flat-field lens. The released Ar gas was cleaned over getters for ten minutes, and then analyzed isotopically using the secondary electron multiplier system of a VG3600 gas source mass spectrometer; details of data collection protocols can be found in Villeneuve and MacIntyre (1997) and Villeneuve *et al.* (2000). Error analysis on individual steps follows numerical error analysis routines outlined in Scaillet (2000); error analysis on grouped data follows algebraic methods of Roddick (1988).

Corrected argon isotopic data are listed in Table D.1, and presented below both as spectra of gas release (Fig. D.1a-c). Each gas-release spectrum is normalized to the total volume of ^{39}Ar released. Such plots provide a visual image of heating profiles, evidence for Ar-loss in the low temperature steps, and the error and apparent age of each step.

Neutron flux gradients throughout the sample canister were evaluated by analyzing the sanidine flux monitors included with each sample packet and interpolating a linear fit against calculated J-factor and sample position. The error on

individual J-factor values is conservatively estimated at ±0.6% (2σ). Because the error associated with the J-factor is systematic and not related to individual analyses, correction for this uncertainty is not applied until calculation of dates from isotopic correlation diagrams (Roddick, 1988). No evidence for excess ^{40}Ar was observed in any of the samples and, therefore, all regressions are assumed to pass through the $^{40}Ar/^{36}Ar$ value for atmospheric air (295.5). All errors are quoted at the 2σ level of uncertainty.

Table D.1: Ar-Ar data for Freemans Cove Complex samples

Power[a]	Volume ^{39}Ar x10^{-11} cc	$^{36}Ar/^{39}Ar$	$^{37}Ar/^{39}Ar$	$^{38}Ar/^{39}Ar$	$^{40}Ar/^{39}Ar$	$\%^{40}Ar$ ATM	$*^{40}Ar/^{39}Ar$	f_{39}[b] (%)	Apparent Age Ma[c]
C/311/515 Biotite; J=.0028911 Freemans Cove Complex (Z7694; 75.3881°N 98.0189°E)									
2.4	0.211	0.0700±0.0077	0.277±0.017	0.074±0.016	30.398±1.385	68.9	9.441±1.800	0.6	48.58±9.14
2.8	0.7239	0.0108±0.0029	0.078±0.004	0.017±0.011	13.621±0.302	20.6	10.818±0.756	1.9	55.56±3.83
3.0	2.4724	0.0048±0.0007	0.051±0.003	0.007±0.011	12.165±0.090	10.7	10.866±0.172	6.6	55.80±0.87
3.5	3.4188	0.0018±0.0005	0.021±0.001	0.003±0.011	11.294±0.068	4.0	10.846±0.124	9.1	55.70±0.63
3.9	4.2644	0.0013±0.0004	0.018±0.001	0.005±0.011	11.165±0.061	2.9	10.846±0.100	11.3	55.70±0.51
4.2	4.6215	0.0010±0.0004	0.015±0.001	0.009±0.011	11.048±0.050	2.0	10.827±0.101	12.3	55.61±0.51
4.6	6.3005	0.0006±0.0006	0.015±0.001	0.043±0.011	11.062±0.056	1.9	10.850±0.103	16.7	55.72±0.52
5.0	6.3914	0.0006±0.0005	0.015±0.000	0.041±0.011	11.013±0.049	1.7	10.829±0.097	17	55.61±0.49
6.0	5.5999	0.0005±0.0006	0.019±0.001	0.041±0.011	11.006±0.087	1.5	10.837±0.113	14.9	55.66±0.57
12.0	3.7117	0.0010±0.0009	0.014±0.001	0.046±0.011	11.177±0.081	3.0	10.838±0.158	9.8	55.66±0.80
KIA99-BI/11/F Biotite; J=.0028898 Freemans Cove Complex (z7696; 75.0345°N 98.3436°E)									
2.8	0.8188	0.0098±0.0026	1.027±0.026	0.030±0.011	14.609±0.242	18.4	11.926±0.522	3.3	61.13±2.63
3.0	1.3824	0.0030±0.0016	0.125±0.009	0.029±0.011	11.757±0.141	6.4	11.002±0.325	5.5	56.47±1.64
3.5	2.5828	0.0018±0.0009	0.044±0.002	0.027±0.011	11.453±0.109	3.8	11.014±0.216	10.3	56.53±1.09
3.9	2.7896	0.0012±0.0008	0.071±0.001	0.030±0.011	11.310±0.101	2.5	11.027±0.176	11.1	56.59±0.89
4.2	3.0721	0.0011±0.0008	0.142±0.003	0.033±0.011	11.119±0.076	2.3	10.859±0.168	12.2	55.74±0.85
4.6	2.3472	0.0003±0.0010	0.041±0.001	0.034±0.011	11.087±0.081	0.0	11.085±0.204	9.3	56.88±1.03
5.0	2.2686	0.0014±0.0010	0.032±0.002	0.032±0.011	11.267±0.086	3.0	10.933±0.199	9	56.12±1.01
6.0	3.5104	0.0007±0.0006	0.007±0.001	0.032±0.011	11.162±0.069	1.4	11.009±0.130	13.9	56.50±0.66
12.0	6.4167	0.0005±0.0005	0.004±0.001	0.028±0.011	11.034±0.073	1.0	10.922±0.145	25.5	56.06±0.74
KIA99-BI/9 Sanidine; J=.0028884 Freemans Cove Complex (Z7695; 75.0983°N 98.5164°E)									
2.8	2.0359	0.0097±0.0012	0.038±0.004	0.008±0.011	13.234±0.151	20.5	10.527±0.331	8.9	54.04±1.68
3.0	1.9063	0.0001±0.0010	0.029±0.002	0.004±0.011	10.627±0.072	0.2	10.602±0.189	8.4	54.42±0.96
3.5	5.3883	0.0003±0.0003	0.020±0.001	-0.005±-0.011	10.577±0.062	0.0	10.574±0.076	23.7	54.28±0.39
3.9	2.119	0.0003±0.0009	0.025±0.001	-0.002±-0.011	10.620±0.072	0.4	10.583±0.186	9.3	54.32±0.94
4.2	0.2461	0.0008±0.0068	0.083±0.011	0.038±0.011	11.108±0.330	2.0	10.881±1.318	1.1	55.83±6.66
5.0	2.9417	0.0007±0.0006	0.025±0.001	-0.004±-0.011	10.631±0.058	0.6	10.568±0.126	12.9	54.24±0.64
6.0	2.2548	0.0001±0.0005	0.028±0.002	0.000±0.011	10.604±0.055	0.1	10.597±0.131	9.9	54.39±0.66
12.0	5.8688	0.0033±0.0003	0.021±0.002	-0.004±-0.011	11.484±0.073	7.9	10.578±0.082	25.8	54.29±0.42

a: As measured by laser in % of full nominal power (10W)

b: Fraction 39Ar as percent of total run

c: Errors are analytical only and do not reflect error in irradiation parameter J

d: Nominal J, referenced to FCT-SAN=28.03 Ma (Renne et al., 1998)

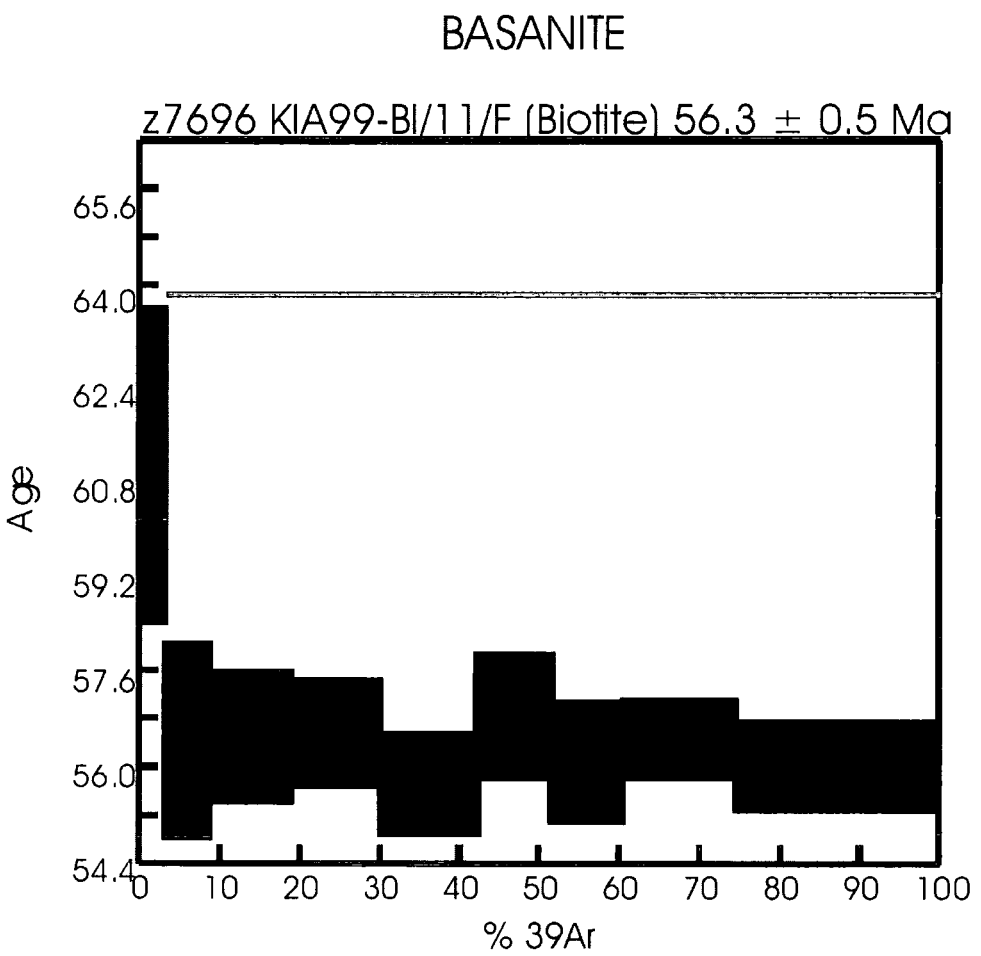

Fig. D.1 - Spectra of gas release for KIA99-BI/11/F biotite

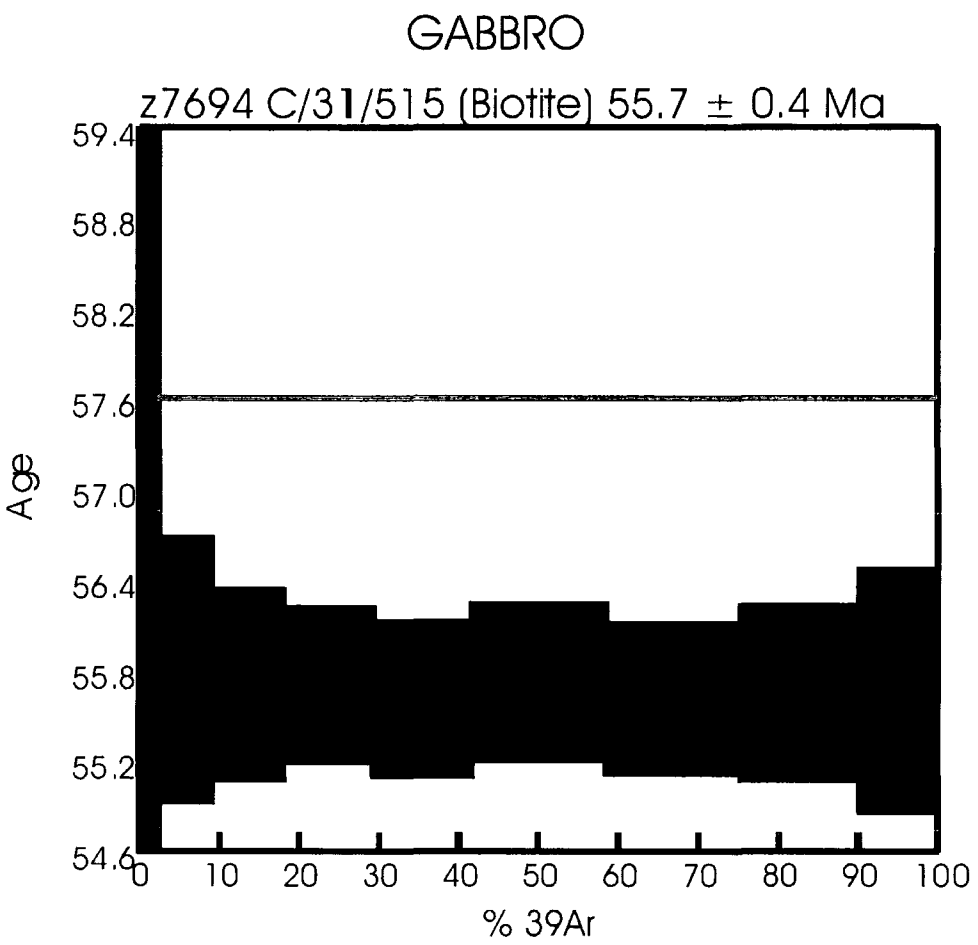

Fig. D.2 - Spectra of gas release for C/31/515 biotite

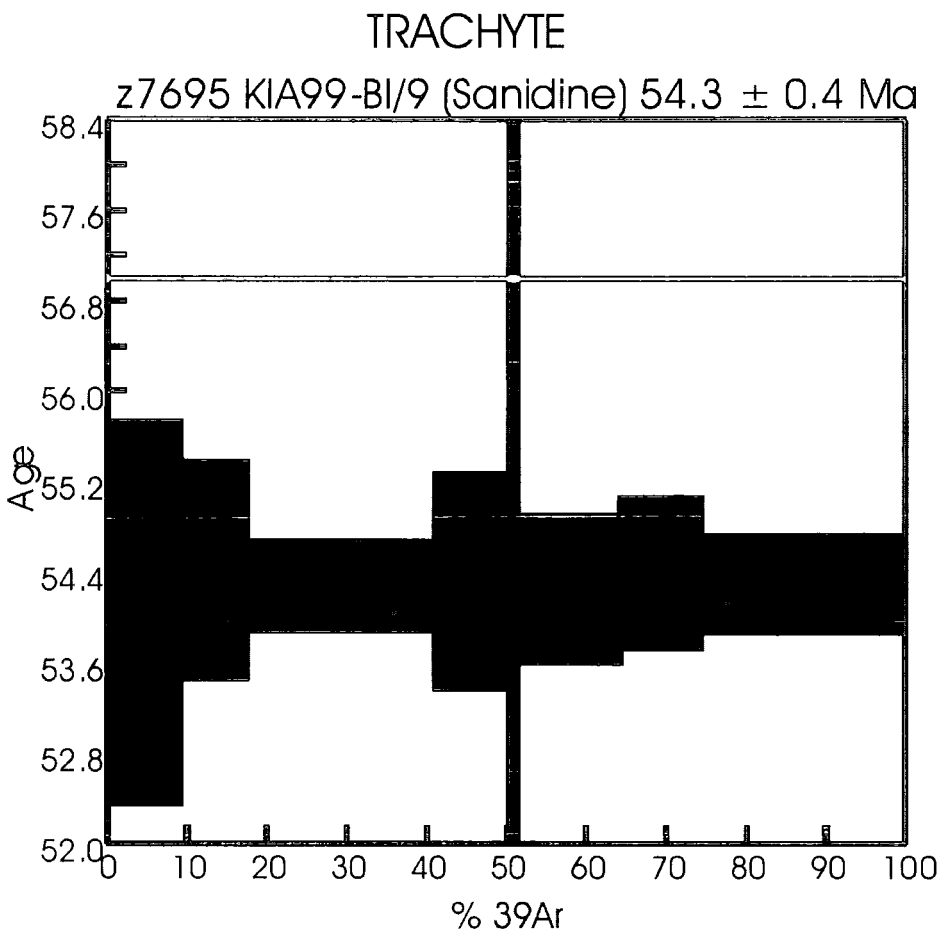

Fig. D.3 - Spectra of gas release for KIA99-BI/9 sanidine

Appendix E - North Atlantic Igneous Province and Central Iceland datasets (Chapter 2)

Appendix E contains major and trace element data for central Icelandic lavas relevant to *"Chapter 2: $^{18}O/^{16}O$ compositions of central Icelandic and North Atlantic Igneous Province magmatism; source mixing versus crustal contamination for the origin of extreme $^{3}He/^{4}He$ variation in volcanic rocks"*.

Major element analyses were performed at the Nordic Volcanological Institute using the protocol of Breddam (2002). Trace elements were determined using a Perkin Elmer ELAN 6000 inductively coupled plasma mass spectrometer (ICP-MS) at the University of Durham. Trace element analytical protocols are documented in Appendix A. Data for NAL 611 is published in Breddam (2002).

Table E.1: Major element and selected trace element data for central Iceland lavas

Sample	Th-29*	Nal-239	Herdubried	NAL-626	NAL-355	NAL-356
Location	Theistareykir	Ketildyngia	Herdubried	Fjallsendi	Upptyppingar	Upptyppingar
Lithology	Picrite	Basalt	Glass pillow	Basalt	Glass pillow	Glass pillow
wt. %						
SiO_2	47.47	50.71	48.06	48.03	48.16	47.90
TiO_2	0.50	1.53	1.31	0.75	1.95	2.19
Al_2O_3	13.41	14.33	16.05	15.45	15.74	13.40
Fe_2O_3	0.91					
FeO	7.16	11.19	11.30	9.54	9.91	11.10
MgO	15.73	6.72	12.45	9.27	8.42	7.17
MnO	0.16	0.19	0.18	0.16	0.16	0.14
CaO	12.50	12.34	9.20	14.65	12.44	13.10
Na_2O	1.13	2.29	1.91	1.88	2.46	2.30
K_2O	0.01	0.15	0.15	0.07	0.36	0.42
P_2O5	0.02	0.27	0.12	0.08	0.25	0.23
LOI	0.34	0.34				
Total	99.34	100.06	100.73	99.88	99.85	97.95
Mg-no.	77.90	51.69	66.25	63.39	60.22	53.51
ppm						
Sc	4.00	37.37	41.49	-	36.02	36.55
V	207.00	304.03	300.09	-	312.65	307.66
Cr	2176.00	418.98	331.97	-	240.39	284.00
Co	63.00	56.10	51.27	-	48.48	49.87
Ni	559.00	215.75	147.20	-	120.37	134.23
Cu	95.00	120.59	123.33	-	110.87	115.90
Ga	50.00	17.30	16.20	-	17.15	17.07
Rb	0.24	4.75	2.90	-	5.86	6.20
Sr	51.00	226.12	175.11	-	260.79	259.92
Y	14.10	24.24	20.33	-	23.38	23.06
Zr	19.10	102.94	65.17	-	98.86	96.68
Nb	0.47	12.16	6.50	-	12.81	12.38
Cs	-	0.05	0.03	-	0.07	0.07
Ba	3.67	67.41	42.31	-	88.01	90.47
La	0.54	8.60	4.86	-	9.01	8.67
Ce	1.84	20.55	12.04	-	21.60	20.74
Pr	0.36	3.07	1.87	-	3.28	3.14
Nd	2.31	14.52	9.19	-	15.48	14.92
Sm	1.00	3.83	2.59	-	3.99	3.82
Eu	0.45	1.38	0.99	-	1.45	1.41
Gd	1.72	4.49	3.34	-	4.67	4.43
Tb	0.32	0.72	0.56	-	0.74	0.70
Dy	2.20	4.29	3.47	-	4.28	4.14
Ho	0.48	0.87	0.73	-	0.84	0.82
Er	1.41	2.30	1.97	-	2.19	2.13
Tm	0.22	0.37	0.33	-	0.36	0.35
Yb	1.45	2.16	1.96	-	2.05	1.98
Lu	0.23	0.35	0.32	-	0.32	0.32
Hf	0.62	2.63	1.72	-	2.64	2.56
Ta	0.04	0.79	0.42	-	0.83	0.80
Pb	-	0.58	0.37	-	0.51	0.78
Th	0.02	0.61	0.34	-	0.71	0.71
U	0.01	0.18	0.10	-	0.21	0.20

* XRF and ICP-MS data from Skovgaard *et al.* (2001).

Table E.1: Major element and selected trace element data for Central Iceland lavas (continued)

Sample	Nal-355/6	Nal-357	Nal-625	Tro-53	KVK-147	NAL-611**
Location	Upptyppingar	Upptyppingar	Vadalda	Trolladyngia	Hvannalindir	Kistufell
Lithology	Glass pillow	Glass pillow	Picrite	Picro-basalt	Glass pillow	Picro-basalt
wt. %						
SiO_2	48.16	50.83	-	46.37	47.86	47.91
TiO_2	1.95	2.38	-	0.87	2.64	1.06
Al_2O_3	15.74	15.62	-	18.33	13.24	16.01
Fe_2O_3			-			
FeO	9.91	11.97	-	7.92	14.09	9.54
MgO	8.42	12.00	-	11.13	6.43	10.45
MnO	0.16	0.16	-	0.13	0.22	0.16
CaO	12.44	4.12	-	13.69	11.83	12.69
Na_2O	2.46	1.95	-	1.25	2.69	1.89
K_2O	0.36	0.48	-	0.08	0.47	0.08
P_2O5	0.25	0.37	-	0.09	0.40	0.09
LOI						
Total	99.85	99.87	-	99.86	99.87	99.88
Mg-no.	60.22	64.11	-	71.46	44.85	66.12
ppm						
Sc	34.99	38.48	35.31	33.10	39.12	37.40
V	290.74	384.44	215.36	190.00	433.93	257.00
Cr	394.57	41.15	1645.06	390.00	44.07	384.00
Co	55.56	49.18	87.18	48.00	44.55	49.60
Ni	213.94	34.49	882.23	211.00	32.14	223.00
Cu	106.09	118.41	15.51	116.00	98.51	111.00
Ga	16.37	20.41	12.53	-	21.06	-
Rb	5.69	11.44	0.68	-	11.20	1.37
Sr	246.56	238.85	194.28	159.00	236.27	239.00
Y	21.86	34.67	15.48	15.00	39.80	18.10
Zr	91.35	189.16	68.52	46.00	207.21	47.80
Nb	11.73	20.32	8.20	-	23.07	3.00
Cs	0.06	0.12	0.01	-	0.12	0.05
Ba	85.26	126.07	21.29	29.00	127.31	50.00
La	8.15	15.90	6.87	-	17.37	2.69
Ce	19.45	37.53	15.76	-	41.04	7.26
Pr	2.95	5.60	2.25	-	6.16	1.08
Nd	14.00	25.79	10.49	-	28.41	5.82
Sm	3.64	6.34	2.71	-	7.02	2.01
Eu	1.34	2.12	0.98	-	2.36	0.81
Gd	4.22	7.07	3.14	-	7.94	2.60
Tb	0.68	1.11	0.50	-	1.24	0.45
Dy	3.92	6.33	2.84	-	7.11	3.06
Ho	0.78	1.24	0.56	-	1.41	0.71
Er	2.04	3.18	1.40	-	3.65	1.75
Tm	0.33	0.51	0.22	-	0.58	0.29
Yb	1.88	2.93	1.24	-	3.36	1.86
Lu	0.31	0.47	0.19	-	0.54	0.32
Hf	2.40	4.74	1.90	-	5.04	-
Ta	0.75	1.31	0.55	-	1.48	0.22
Pb	0.60	1.01	0.36	-	1.09	-
Th	0.66	1.47	0.51	-	1.47	0.13
U	0.19	0.42	0.09	-	0.42	0.02

** XRF and ICP-MS data from Breddam (2002)

Table E.1: Major element and selected trace element data for Central Iceland lavas (continued)

Sample	Nal-496	KVK-168	KVK-169	SAL-306	NAL-688	NAL-688
Location	Gaesahruiker	Jardfraedinga..	Jardfraedinga..	Bardarbunga	Eggert	Eggert
Lithology	Glass pillow	Glass pillow	Glass pillow	Glass pillow	Picro-basalt	Glass Rind
wt. %						
SiO_2	-	50.50	51.43	49.61	-	-
TiO_2	-	3.33	2.83	1.32	-	-
Al_2O_3	-	12.97	13.45	14.33	-	-
Fe_2O_3	-				-	-
FeO	-	13.94	13.59	10.68	-	-
MgO	-	5.05	5.03	7.78	-	-
MnO	-	0.22	0.22	0.17	-	-
CaO	-	9.87	9.44	13.50	-	-
Na_2O	-	2.83	2.80	2.17	-	-
K_2O	-	0.66	0.61	0.16	-	-
P_2O5	-	0.42	0.32	0.17	-	-
LOI						
Total	-	99.79	99.72	99.89	-	-
Mg-no.	-	39.23	39.74	56.49	-	-
ppm						
Sc	45.73	36.92	39.33	46.16	33.16	44.45
V	317.16	474.83	322.87	302.87	174.42	238.29
Cr	159.84	15.12	227.50	237.80	2300.68	993.79
Co	51.22	49.01	48.23	49.52	90.69	63.22
Ni	88.32	24.41	80.18	94.00	1176.13	459.30
Cu	148.34	92.61	127.97	132.50	47.80	109.55
Ga	16.35	21.33	18.06	15.26	8.50	11.87
Rb	2.70	11.01	6.57	2.49	0.45	0.60
Sr	153.64	235.41	225.74	147.94	36.02	49.17
Y	23.36	40.76	24.83	22.82	10.50	15.18
Zr	74.43	210.69	117.31	72.56	14.05	20.15
Nb	6.60	23.66	12.98	6.56	0.64	0.83
Cs	0.03	0.12	0.07	0.02	0.00	0.01
Ba	34.42	126.42	83.55	31.87	4.97	6.56
La	5.21	17.96	9.99	5.20	0.56	0.73
Ce	12.99	42.30	23.70	12.90	1.64	2.28
Pr	2.07	6.25	3.58	2.03	0.28	0.39
Nd	10.06	28.58	16.67	10.02	1.82	2.60
Sm	2.94	7.09	4.22	2.91	0.75	1.07
Eu	1.09	2.36	1.49	1.09	0.31	0.46
Gd	3.73	7.97	4.82	3.77	1.23	1.81
Tb	0.64	1.26	0.77	0.64	0.24	0.35
Dy	4.02	7.30	4.42	3.93	1.61	2.36
Ho	0.83	1.47	0.89	0.82	0.37	0.54
Er	2.24	3.87	2.29	2.21	1.05	1.54
Tm	0.36	0.62	0.37	0.36	0.18	0.27
Yb	2.18	3.60	2.13	2.14	1.11	1.61
Lu	0.36	0.57	0.34	0.35	0.18	0.27
Hf	2.04	5.32	2.95	1.97	0.56	0.66
Ta	0.45	1.52	0.85	0.44	0.07	0.06
Pb	0.45	1.17	0.98	0.36	0.75	0.16
Th	0.43	1.55	0.81	0.42	0.06	0.07
U	0.13	0.44	0.23	0.12	0.02	0.02

Table E.1: Major element and selected trace element data for Central Iceland lavas (continued)

Sample	Pjor
Location	Pjorsardalur
Lithology	Picro-basalt
wt. %	
SiO_2	-
TiO_2	-
Al_2O_3	-
Fe_2O_3	-
FeO	-
MgO	-
MnO	-
CaO	-
Na_2O	-
K_2O	-
P_2O5	-
LOI	
Total	-
Mg-no.	-
ppm	
Sc	21.60
V	149.58
Cr	2075.79
Co	109.19
Ni	1653.34
Cu	17.29
Ga	8.43
Rb	1.15
Sr	76.07
Y	11.33
Zr	45.80
Nb	4.38
Cs	0.04
Ba	10.16
La	3.25
Ce	8.24
Pr	1.29
Nd	6.28
Sm	1.75
Eu	0.61
Gd	2.07
Tb	0.34
Dy	1.99
Ho	0.40
Er	1.07
Tm	0.17
Yb	1.00
Lu	0.16
Hf	1.38
Ta	0.32
Pb	0.90
Th	0.29
U	0.10

Appendix F - Continental Lithospheric Mantle (CLM) and Continental Intraplate Alkaline Volcanic (CIAV) dataset (Chapter 3)

Appendix F contains major, trace element and Sr-Nd isotope data pertaining to *"Chapter 3: Does a high time integrated $^{3}He/(U+Th)$ reservoir exist in the upper mantle? Evidence from continental lithospheric mantle xenoliths and intraplate alkaline volcanics"*.

For the Freemans Cove Complex and Ugandite PHN2902A, major element analyses were performed at the Geological Survey of Canada and the analytical protocols are outlined in Appendix B. Trace elements were determined using a Perkin Elmer ELAN 6000 inductively coupled plasma mass spectrometer (ICP-MS) at the University of Durham. Trace element analytical protocols are documented in Appendix B. Sr and Nd data for the Freemans Cove Complex were performed at the Arthur Holmes Isotope Geology Laboratory (analytical techniques in Appendix C) and are presented in Barker *et al.* (2002).

Major and trace element and Sr-Nd isotope analytical techniques for the Western Cape Melilitite Province and Namaqualand-Bushmanland-Warmbad province are presented in Janney *et al.* (2002). Elemental and isotopic data for these provinces is reproduced by kind permission of P.E. Janney.

Table F.1: Major trace element data for CIAV from Canada and South Africa

Sample	C246149	BI-5	BI-10-B	BI-4-1	BI-8	BI-10-C	BI-10-E
Province	FCC	FCC	FCC	FCC	FCC	FCC	FCC
Lithology	Ol Mel Neph Diatreme	Neph Dyke	Neph	Basan Dyke	Basan Dyke	Basan Dyke	Basan Dyke
wt. %							
SiO_2	39.41	39.52	39.86	41.84	41.50	40.13	38.70
TiO_2	1.44	1.64	1.64	1.89	2.09	1.62	1.62
Al_2O_3	8.08	10.52	10.71	11.93	11.55	10.64	10.36
Fe_2O_3	4.63	5.40	6.35	5.91	5.95	6.46	5.71
$FeO^{\dagger}$	6.10	6.10	5.50	6.10	6.50	5.00	5.70
Fe_2O_{3T}	10.27	10.96	11.21	11.42	11.85	10.81	10.84
MgO	18.72	13.53	14.72	12.51	14.26	14.77	14.94
MnO	0.17	0.18	0.15	0.18	0.18	0.15	0.15
CaO	14.09	15.07	13.52	13.18	12.68	12.96	13.55
Na_2O	2.76	2.93	3.43	3.47	3.01	1.89	2.54
K_2O	0.75	0.97	0.85	1.23	0.97	0.68	0.49
P_2O5	0.66	1.21	0.52	0.72	0.56	0.64	0.64
$S^{\ddagger}$	-	0.02	0.04	0.02	0.03	0.15	0.06
$H_2O_T^{\dagger}$	2.50	1.10	1.30	0.70	1.10	4.40	3.50
$CO_{2T}^{\dagger}$	0.40	1.60	1.30	0.40	0.10	1.00	1.60
LOI	2.73	2.44	2.30	0.72	0.81	5.13	5.11
Total	99.08	98.97	98.91	99.09	99.46	99.42	98.94
Mg-no.	78.3	71.0	72.2	68.5	70.5	73.0	73.2
ppm							
$F^{\dagger}$	987	899	851	880	851	857	902
$Cl^{\dagger}$	3800	1229	2855	834	279	239	6054
Sc	31.57	25.44	25.77	27.15	29.34	25.64	25.48
V	195.47	198.67	224.43	236.61	248.48	214.01	216.66
Cr	1506.27	459.26	502.84	391.76	464.28	465.19	495.82
Co	63.40	53.66	59.82	55.28	61.03	58.39	56.60
Ni	593.86	384.38	421.97	293.47	369.22	424.45	426.31
Cu	73.05	86.85	64.08	71.10	77.82	71.62	68.90
Ga	10.46	13.46	14.18	15.90	15.97	14.29	13.32
Rb	25.32	21.28	26.76	43.96	19.59	24.13	19.64
Sr	1199.24	1464.22	1111.60	1076.50	775.98	681.44	1102.12
Y	20.30	35.36	23.64	34.09	26.32	32.97	32.79
Zr	114.44	132.17	142.23	170.15	159.78	146.74	139.45
Nb	76.45	107.43	100.80	93.31	76.06	91.26	92.81
Cs	0.21	0.30	0.51	0.54	0.47	1.33	0.60
Ba	1207.90	1552.17	1112.45	1107.61	715.48	1315.67	1094.30
La	74.26	144.95	80.20	86.58	51.20	74.68	76.25
Ce	122.89	261.29	141.56	149.39	94.38	133.82	135.04
Pr	13.68	25.02	16.18	16.83	11.28	15.23	15.50
Nd	48.50	84.53	57.54	60.19	43.32	55.42	56.34
Sm	7.52	11.28	8.76	9.05	7.37	8.47	8.64
Eu	2.16	3.21	2.55	2.68	2.26	2.47	2.48
Gd	5.71	8.77	7.24	7.60	6.56	7.16	7.15
Tb	0.76	1.07	0.92	0.99	0.88	0.92	0.90
Dy	3.92	5.14	4.57	4.95	4.44	4.60	4.47
Ho	0.72	0.91	0.81	0.89	0.80	0.84	0.82
Er	1.72	2.16	1.97	2.14	1.88	1.99	1.94
Tm	0.25	0.31	0.29	0.31	0.27	0.30	0.29
Yb	1.44	1.71	1.60	1.76	1.52	1.65	1.59
Lu	0.23	0.27	0.25	0.27	0.24	0.25	0.24
Hf	2.59	2.74	3.02	3.71	3.69	3.17	3.02
Ta	3.54	3.77	4.35	4.43	4.03	4.09	4.19
Pb	4.71	8.94	4.36	4.67	3.12	4.70	4.92
Th	9.51	19.44	9.52	10.74	6.40	8.96	8.87
U	1.91	3.67	1.97	2.41	1.40	1.90	1.80

Table F.1: Major trace element data for CIAV from Canada and South Africa (cont.)

Sample	BI-11-F	BI-10-G	BI-12	PHN2902A
Province	FCC	FCC	FCC	Bufumbira
Lithology	Basan	Pic-Bas	Alk Gab	Bas
	Diatreme	Dyke	Sill	Lava
wt. %				
SiO_2	40.29	39.13	46.70	42.80
TiO_2	1.85	1.62	1.96	2.88
Al_2O_3	11.31	10.02	13.40	8.71
Fe_2O_3	6.31	6.37	4.56	-
$FeO^{\dagger}$	5.50	5.40	8.60	-
Fe_2O_{3T}	11.18	11.13	12.70	12.00
MgO	12.88	15.50	9.30	17.10
MnO	0.15	0.15	0.20	0.19
CaO	14.14	13.59	11.10	11.20
Na_2O	2.78	0.75	3.07	2.03
K_2O	0.41	0.83	0.85	2.53
P_2O5	0.95	0.63	0.53	0.44
$S^{\ddagger}$	0.06	0.04	0.02	0.02
$H_2O_T^{\dagger}$	3.30	5.80	1.20	-
$CO_{2T}^{\dagger}$	0.60	1.00	0.10	-
LOI	3.61	6.15	0.84	-
Total	99.55	99.50	100.65	99.88
Mg-no.	69.5	73.4	59.2	73.8
ppm				
$F^{\dagger}$	947	782	532	-
$Cl^{\dagger}$	2508	129	804	-
Sc	28.85	26.26	22.71	28.64
V	223.00	208.51	183.27	278.70
Cr	368.67	513.79	232.71	1418.96
Co	53.11	60.77	48.91	70.96
Ni	266.28	497.27	196.40	422.83
Cu	64.30	65.83	56.38	49.62
Ga	15.22	12.68	18.01	13.65
Rb	9.47	29.40	20.96	77.19
Sr	973.64	1897.55	793.58	799.71
Y	30.34	29.51	30.34	18.91
Zr	156.96	141.74	124.05	202.79
Nb	90.92	89.33	47.44	88.50
Cs	0.92	0.31	0.33	0.66
Ba	1025.43	475.65	708.02	991.04
La	90.49	74.77	53.55	63.34
Ce	157.63	133.11	92.36	120.23
Pr	17.84	15.23	10.38	14.58
Nd	64.36	55.59	38.43	53.96
Sm	9.60	8.47	6.68	8.26
Eu	2.77	2.45	2.11	2.25
Gd	8.06	6.91	6.50	6.11
Tb	1.03	0.89	0.94	0.76
Dy	5.16	4.47	5.04	3.72
Ho	0.94	0.80	0.95	0.67
Er	2.27	1.90	2.34	1.61
Tm	0.33	0.28	0.35	0.25
Yb	1.86	1.54	1.96	1.39
Lu	0.28	0.24	0.31	0.22
Hf	3.36	3.09	3.03	4.81
Ta	3.80	4.05	2.08	5.42
Pb	5.32	4.66	3.49	4.20
Th	11.10	8.46	5.97	9.00
U	2.17	1.73	1.21	1.57

Table F.1: Major trace element data for CIAV from Canada and South Africa (cont.)

Sample	KSV-256	KSV-266	SPK-1	SPK-2	SPK-3	ROB-11	ZW-1
Province	WCMP	WCMP	WCMP	WCMP	WCMP	WCMP	NBW
Lithology	Ol Mel Diatreme	Ol Mel Diatreme	Ol Mel Diatreme	Ol Mel Diatreme	Ol Mel Diatreme	Ol Mel Diatreme	Ol Mel Diatreme
wt. %							
SiO_2	36.40	31.55	33.95	35.20	34.41	37.59	35.39
TiO_2	3.47	2.98	2.29	2.19	2.33	4.36	5.28
Al_2O_3	7.84	6.93	7.79	7.59	7.44	7.23	4.82
Fe_2O_3	-	-	-	-	-	-	-
$FeO^{\dagger}$	-	-	-	-	-	-	-
Fe_2O_{3T}	12.83	13.81	11.09	10.98	11.31	16.56	15.82
MgO	18.39	19.17	17.18	16.88	17.10	17.00	19.64
MnO	0.21	0.31	0.19	0.19	0.20	0.20	0.20
CaO	14.85	18.15	18.08	17.03	17.24	12.50	13.02
Na_2O	3.30	3.11	3.46	3.28	3.56	2.05	1.76
K_2O	1.93	1.31	1.80	1.86	1.76	1.85	1.53
P_2O5	0.92	1.78	1.42	1.33	1.37	0.77	1.31
$S^{\ddagger}$	-	-	-	-	-	-	-
$H_2O_T^{\dagger}$	0.07	0.12	0.42	0.37	0.35	-	0.25
$CO_{2T}^{\dagger}$	-	-	-	-	-	-	-
LOI	0.21	0.87	2.06	2.35	2.18	0.35	0.19
Total	100.35	99.97	99.31	98.88	98.90	100.46	98.96
Mg-no.	74.0	73.3	75.4	75.3	75.0	67.0	71.1
ppm							
$F^{\dagger}$	-	-	-	-	-	-	-
$Cl^{\dagger}$	-	-	-	-	-	-	-
Sc	30.00	28.00	28.38	28.66	31.51	25.00	26.60
V	273.00	182.00	191.00	231.00	201.00	292.00	307.30
Cr	831.00	837.00	830.00	841.00	856.00	691.00	742.83
Co	-	-	-	-	-	-	-
Ni	565.09	524.47	493.00	495.00	502.00	562.00	827.58
Cu	-	-	-	-	-	-	-
Ga	-	-	-	-	-	-	-
Rb	63.97	39.05	69.37	50.00	46.01	54.94	52.47
Sr	1221.65	1780.74	1476.98	1272.00	1506.57	789.68	1037.03
Y	25.45	34.26	26.20	24.40	28.50	25.75	28.34
Zr	319.58	324.36	139.00	179.00	312.00	476.00	375.48
Nb	124.03	208.87	149.49	-	160.61	107.37	115.06
Cs	0.88	0.62	1.38	-	0.87	0.52	0.34
Ba	1411.31	1121.40	1644.54	2167.00	2573.01	571.60	706.87
La	73.70	145.75	190.54	-	182.18	62.50	86.13
Ce	143.88	277.03	307.63	-	301.05	128.90	180.58
Pr	16.81	31.98	31.53	-	31.25	16.10	22.66
Nd	64.26	116.73	106.00	-	105.06	63.70	89.28
Sm	11.38	18.87	15.81	-	15.37	12.12	16.22
Eu	3.24	5.30	4.29	-	4.13	3.29	4.36
Gd	8.18	12.85	10.48	-	10.07	9.33	11.89
Tb	1.08	1.63	1.32	-	1.29	1.22	1.52
Dy	5.34	7.72	6.12	-	6.14	5.87	7.01
Ho	0.87	1.22	0.94	-	0.99	1.00	1.15
Er	1.99	2.70	1.98	-	2.16	2.32	2.54
Tm	0.25	0.35	0.24	-	0.26	0.28	0.30
Yb	1.40	1.85	1.17	-	1.31	1.56	1.59
Lu	0.19	0.25	0.15	-	0.17	0.20	0.20
Hf	6.60	5.55	3.06	-	6.05	11.59	8.44
Ta	-	-	-	-	-	-	7.47
Pb	2.28	4.75	15.44	-	49.31	2.62	2.50
Th	9.30	25.10	27.10	26.90	29.20	7.83	8.30
U	2.53	5.94	5.54	-	7.04	1.85	2.13

Table F.1: Major trace element data for CIAV from Canada and South Africa (cont.)

Sample	BKB-10	WK-1	HO-5	SP-4
Province	NBW	NBW	NBW	NBW
Lithology	Ol Mel Diatreme	Ol Mel Diatreme	Ol Mel Diatreme	Ol Mel Diatreme
wt. %				
SiO_2	35.98	33.55	40.78	35.51
TiO_2	6.27	6.72	3.62	6.02
Al_2O_3	4.69	5.06	5.64	4.48
Fe_2O_3	-	-	-	-
$FeO^{\dagger}$	-	-	-	-
Fe_2O_{3T}	16.40	16.42	12.76	16.90
MgO	20.76	18.03	19.10	20.33
MnO	0.19	0.19	0.18	0.20
CaO	10.93	13.69	10.10	12.42
Na_2O	0.96	1.44	2.59	1.68
K_2O	1.07	1.98	2.30	1.31
P_2O5	0.54	1.06	0.68	1.04
$S^{\ddagger}$	-	-	-	-
$H_2O_T^{\dagger}$	0.51	0.38	0.56	0.33
$CO_{2T}^{\dagger}$	-	-	-	-
LOI	0.88	0.59	1.81	0.31
Total	98.67	98.74	99.56	100.20
Mg-no.	71.5	68.5	74.8	70.4
ppm				
$F^{\dagger}$	-	-	-	-
$Cl^{\dagger}$	-	-	-	-
Sc	27.05	28.54	-	-
V	322.37	351.34	191.07	321.92
Cr	719.90	504.39	752.01	727.57
Co	-	-	-	-
Ni	829.10	658.85	691.89	900.34
Cu	-	-	-	-
Ga	-	-	-	-
Rb	60.87	80.79	116.42	47.17
Sr	659.14	946.94	1087.37	904.65
Y	21.40	24.78	34.95	25.32
Zr	330.39	373.70	301.57	293.56
Nb	135.00	138.10	158.18	-
Cs	0.38	0.70	1.67	-
Ba	743.25	667.48	1386.28	555.75
La	82.61	83.87	113.85	70.78
Ce	170.22	173.97	213.69	154.27
Pr	20.89	21.26	24.99	18.05
Nd	80.91	82.87	93.87	72.10
Sm	14.44	14.88	16.37	13.45
Eu	3.92	3.94	4.17	3.95
Gd	10.66	10.79	11.90	9.73
Tb	1.35	1.36	1.58	1.25
Dy	6.14	6.28	7.65	5.76
Ho	1.00	1.03	1.31	-
Er	2.17	2.27	3.14	2.27
Tm	0.25	0.27	0.41	-
Yb	1.30	1.40	2.32	1.39
Lu	0.16	0.18	0.32	-
Hf	8.16	9.08	7.04	-
Ta	10.09	9.47	8.80	-
Pb	2.93	8.50	11.78	-
Th	10.17	10.07	20.49	9.23
U	2.32	2.63	4.38	-

Table F.2: Sr and Nd isotopic data for CIAV (Chapter 3)

Sample	Lithology	$^{87}Rb/^{86}Sr$	$^{87}Sr/^{86}Sr_i$	2σ	$^{147}Sm/^{144}Nd$	$^{143}Nd/^{144}Nd_i$	2σ	εNd_i
Western Cape Melilitite Province, South Africa								
ROB 10	Ol Mel		0.703180			0.512755		3.9
ROB 11	Ol Mel		0.703163			0.512754		3.9
KSV-256	Ol Mel		0.703323			0.512753		4.1
KSV-266	Ol Mel		0.703539			0.512746		3.9
SPK-1	Ol Mel		0.704253			0.512635		1.8
SPK-3	Ol Mel		0.704231			0.512647		2.1
Namaqualand-Bushmanland-Warmbad Province, South Africa								
ZW-1	Ol Mel		0.703247			0.512725		3.55
WK-1	Ol Mel		0.703291			0.512729		3.41
BKB-10	Ol Mel		0.703251			0.512705		3.12
SP-4	Ol Mel		0.703280			0.512706		3.2
HO-5	Ol Mel		0.704692			0.512692		2.55
HO-5	Ol Mel		0.704692			0.512692		2.55
Freemans Cove Complex, Nunavut, Canada								
BI1-1a	Neph	0.064	0.704091	18	0.102	0.512718	17	1.6
BI1-1b	Neph	0.064	0.704100	17	0.102	0.512722	18	1.6
BI11C	Basanite	0.044	0.704180	17	0.101	0.512673	17	0.7
BI11E	Basanite	0.124	0.703962	19	0.107	0.512711	18	1.4
BI11F	Basanite	0.027	0.703959	18	0.094	0.512658	17	0.4
BI2-1	Ol. Gabbro	0.116	0.704240	17	0.128	0.512655	19	0.3
BI4-1	Basanite	0.115	0.703972	17	0.095	0.512671	18	0.6
C311462	Phonolite	2.647	0.703844	15	0.102	0.512728	18	1.8
C311462	Phonolite	2.647	0.703812	15	0.102	0.512730	17	1.8
C311463	Phonolite	2.148	0.709200	15	0.100	0.512720	17	1.6
C311465	Phonolite	4.103	0.705938	15	0.108	0.512724	17	1.7
C311472	Phonolite	2.598	0.705800	15	0.102	0.512725	20	1.7
C311458	Mafic Pho	0.167	0.703868	14	0.084	0.512654	16	0.3
C311455	Mafic Pho	0.424	0.703619	16	0.095	0.512720	16	1.6
BI-2	Ol. Gabbro	0.116	0.704119	15	0.128	0.512626	17	-0.2
C311443	Neph	0.049	0.704077	15	0.083	0.512543	16	-1.9
C311473	Phonolite	0.084	0.703865	16	0.121	0.512671	16	0.6
C311465	Phonolite	4.103	0.704112	15	0.108	0.512736	17	1.9
BI-11C	Basanite	0.044	0.704082	15	0.101	0.512646	16	0.2
C311458	Mafic Pho	0.167	0.703841	14	0.084	0.512638	16	0.0

Data for WCMP and NBW reproduced by permission of P.E. Janney

Data for FCC from Barker et al., 2002 (for analytical details see Appendix C)

Appendix G - Western Canary Island dataset (Chapter 4)

G.1 Geology, stratigraphy and evolution of La Palma

La Palma has been the most volcanically active of the Canary Islands in historic times with eruptions recorded in ~1440, 1585, 1646, 1677, 1712, 1949 and 1971 (Hernandez-Pacheco and Valls, 1982; Fig. 4.2). La Palma has experienced intense geological study since the early 19th century when the large central depression in the island became the type locale for a 'caldera' (Von Buch, 1825; Lyell, 1855; Reiss, 1861). This feature has now been recognised as the surface expression of a debris avalanche collapse scar and not the result of a massive evacuating eruption(s) causing central edifice subsidence, as the term now implies. La Palma lies to the west of the M25 palaeo-magnetic anomaly on the youngest oceanic lithosphere of all the Canary Islands and rises ~6500m above the seafloor to a maximum elevation of 2426m above present-day sea level. The island has the approximate shape of a tear-drop, oriented north-south with a surface area of 706km^2. La Palma is made up of two poly-genetic volcanic edifices, the Northern Shield and the Cumbre Vieja Ridge (Fig. 4.2). The overall volume of the edifice can be estimated to be in excess of 14000km^3 based upon the basal area and height of the edifice.

The geology of La Palma can be separated into distinct units based upon their ages and stratigraphic positions (Fig. 4.2). The oldest exposed parts of La Palma form part of the Northern Shield and are located within the deeply incised 'Caldera de Taburiente'. Previously termed the 'basal complex', these Pliocene submarine volcanics and associated plutonics have been interpreted as an uplifted submarine seamount (Staudigel, 1981; Staudigel and Schmincke, 1984). The seamount is composed of uplifted and deformed sequences of oceanic sediments, a thick sequence of basaltic to picritic pillow lavas and hyaloclastites, a basaltic dyke swarm and a substantial plutonic intrusive complex of keratophyres (trachytic and phonolitic compositions) and gabbros, all of which have suffered moderate to intense hydrothermal alteration up to hornfels facies metamorphism with a metamorphic gradient of ~200 to 300°C/km (Staudigel and Schmincke, 1984; Schiffman and Staudigel, 1994).

The seamount series is between 4 and 2.9Ma (Staudigel, 1981; Staudigel *et al.*, 1986). It is separated from the overlying subaerial volcanics by a distinct angular and erosive unconformity, and represents a near-complete 3.6km thick cross-section through a seamount. The uplifted seamount is obviously at an abnormal elevation. The minimum uplift rate to account for its current sub-aerial configuration is ~0.5mm/yr (Staudigel and Schmincke, 1984). This uplift rate is considered to be persistent to the present day (Hildenbrand *et al.*, 2003), so that unlike many ocean Islands, La Palma has experienced positive vertical movements rather than subsidence during its ~4Ma history.

The first sub-aerial volcanism in La Palma formed the Northern shield volcano which disconformably overlies the Pliocene Seamount series. The oldest Garafia series lavas outcrop in deeply incised barrancos and include fresh ankaramite flows even though the Garafia series is extensively pervaded by later alkali basalt dyke swarms. Garafia flows are dated between 1.77 and 1.21Ma by K-Ar and $^{40}Ar/^{39}Ar$ (Carracedo *et al.*, 2001). Volcanic activity in the northern shield continued without significant interruption until 0.4Ma. The separation of the Garafia and subsequent upper and lower Taburiente series lavas is made because in areas there is angular or erosive discordance, probably due to major structural collapse of the southern flank of the Northern shield ~1.2Ma subsequently forming a 'central plateau' (Carracedo *et al.*, 2001) (Fig. 4.2).

The Taburiente series can be sub-divided in to the lower and upper Taburiente series on the basis of the change in eruptive styles from shield-vent eruptions to well-defined axi-symmetrical rift-zone eruptions (Carracedo *et al.*, 2001). Lower Taburiente series lavas range in age from 1.12 to 0.83Ma and are dominated by cyclic-units of ankaramites, alkali basalts and trachytes with abundant, interspersed tephra and scoria horizons. The earliest Lower Taburiente series eruptions were phreato-magmatic pyroclastics and lahars and indicate a change in the degree of water-magma interaction with time (Carracedo *et al.*, 2001). Upper Taburiente lavas erupted from 0.8 to 0.4Ma and mantle the Northern shield showing similar trends of ankaramite to trachyte volcanism to the Lower Taburiente series lavas (Carracedo *et al.*, 1999).

The Benejado volcano represents a continuation of upper Taburiente series volcanism and in-fills another major structural collapse around 0.5Ma which

exposed the Pliocene seamount series and formed the 'Caldera de Taburiente' (Carracedo *et al.*, 2001). The formation of the Benejado was extremely rapid and K-Ar and ^{40}Ar-^{39}Ar ages show a restricted range of 0.58 to 0.49Ma for this volcano (Carracedo *et al.*, 2001).

The last and most recent volcanism on La Palma has taken place exclusively in the last 0.123Ma and has extended sub-aerial volcanism southward in the form of the Cumbre Vieja ridge (Guillou *et al.*, 1998; Carracedo *et al.*, 1999). Volcanism has occurred to form a dorsal ridge by southward propagation of the volcanic rift system and ranges from alkali basalt and basanites through to tephritic and phonolitic compositions. Based on physiological and geochronological criteria Cumbre Vieja volcano can be divided into cliff-forming eruptions (CFE), platform-forming eruptions (PFE), dated prehistoric eruptions and historic eruptions. CFE and PFE are distinguished by the fact that CFE correspond to the lowest sea level stand at 125-80Ka and PFE to the modern day relative high sea level stand beginning ~20ka. All of the historic eruptions in La Palma have occurred in the southernmost part of the Island and throughout this thesis will be grouped with the PFE and CFE. The majority of peridotite-pyroxenite-gabbro xenolith-bearing lava occurrences on La Palma occur in the basanite flows of the Cumbre Vieja. Interaction with groundwater is common during eruption of these lavas, and most of the recent eruptions exhibit phreato-magmatic eruption features (Klügel *et al.*, 1999). Combined sub-aerial volumes and age constraints of the Northern Garafia and Taburiente Volcanoes and Cumbre Vieja suggest eruptive rates in the region of 0.2 and 0.9km^3/Ka, respectively (Carracedo *et al.*, 2002); by comparison average magma supply rates for the Island of Hawaii are estimated in the order of 20km^3/Ka (Moore and Clague, 1992).

G.2 Stratigraphy and evolution of El Hierro

Discounting San Boróndon, El Hierro is the smallest (287km^2) and youngest Island in the Canarian archipelago. Unlike La Palma, El Hierro is geologically speaking, relatively unstudied. There is a paucity of historical eruptions on the Island with a questionable record of eruption at Lomo Negro volcano in 1793 (Hernández Pacheco, 1982). El Hierro lies to the east of the M25 palaeo-magnetic anomaly and is in the form of a tri-lobate rift structure due to three-branched rift zone development (Carracedo *et al.*, 1994, 1996). El Hierro rises ~5500m above the

seafloor to a maximum elevation of 1501m a.s.l. (Fig. 4.3) making it one of the steepest oceanic shield volcanoes in the world (Carracedo *et al.*, 2001). The volume of the El Hierro edifice is estimated at 5500km^3 based upon the basal area and height of the edifice.

A seamount series has not been recognised on El Hierro and the oldest known subaerial lavas are ~1.12Ma (Guillou *et al.*, 1996). The Tiñor volcanic series forms the first of three observed stages of growth on El Hierro and consists of thin, steeply dipping flows and the Ventejís volcano group which are the only xenolith-bearing lava flows on the Island. The Tiñor volcanic series range from 0.88 to 1.12Ma and are terminated by a major structural collapse at 0.88Ma (Guillou *et al.*, 1996; Carracedo *et al.*, 2001). The second phase of volcanism is known as the El Golfo series volcanics which developed and in-filled the embayment of the Tiñor volcanic collapse. The El Golfo edifice existed from ~0.55Ma and is terminated by differentiated trachytic units at around 0.176Ma. The El Golfo volcanic series can be subdivided into a lower (LEGS) and upper (UEGS) sub-series. This sub-division is made because LEGS lavas are predominantly made up of surtseyan and strombolian pyroclastics and are cut by numerous later dykes and UEGS predominantly consisting of lava flows (Guillou *et al.*, 1996; Carracedo *et al.*, 2001). The most recent stages of volcanism are controlled by rifting and can be subdivided into CFE and PFE just as on the Island of La Palma. Aligned monogenetic cinder cone clusters are interpreted as the surface expression of volcanic rift zones feeding CFE and PFE (Fuster *et al.*, 1993; Carracedo, 1994).

The geomorphology of the island, as with that of La Palma, is controlled by a competition of constructive and destructive processes with the formation of tri-lobate volcanic rift zones and structural instability resulting in major collapses. These collapse have formed the large vertical cliffs of Las Playas (900m) and El Golfo (1100m) which allow dissection and sampling of the entire sub-aerial stratigraphy of El Hierro. Combined sub-aerial volume and age constraints on the Island of El Hierro suggests a magma supply rate of ~0.1km^3/Ka, however debris avalanche deposits account for large volumes (>1000km^3 sub-aerial and submarine) of the edifice and magma supply rates are therefore likely to be larger than estimated and more akin to those on La Palma. A comparison of the stratigraphic units of La Palma and El Hierro and their ages is presented in Fig. 4.4.

Table G.1: Major element and selected trace element data for El Hierro lavas

Sample	JMDD EH01	JMDD EH03	JMDD EH04	JMDD EH07	JMDD EH08	JMDD EH10
Series	PFE	Tinõr	Tinõr	Tinõr	Tinõr	CFE
Lithology	Ankaramite	Basanite	Alkali Basalt	Ankaramite	Basanite	Ankaramite
wt. %						
SiO_2	39.83	42.74	41.25	43.71	43.11	41.40
TiO_2	5.39	3.47	6.05	3.30	4.65	5.23
Al_2O_3	9.21	11.46	11.94	11.18	12.94	9.35
Fe_2O_{3T}	16.83	14.86	15.74	13.57	14.26	17.77
MgO	14.22	12.82	10.48	11.74	9.27	14.22
MnO	0.21	0.21	0.20	0.20	0.21	0.21
CaO	10.68	10.93	11.08	11.08	10.47	10.00
Na_2O	1.84	2.37	2.67	2.14	2.79	2.23
K_2O	0.77	0.76	0.86	1.02	1.17	0.75
P_2O5	0.47	0.54	0.99	0.64	0.77	0.67
LOI	-0.54	-0.46	-0.45	0.63	0.50	-0.76
Total	98.91	99.69	100.82	99.21	100.12	101.07
Mg-no.	63.38	63.87	57.70	63.92	57.13	62.11
ppm						
Sc	38.57	38.11	29.88	35.50	31.96	34.92
V	425.45	366.63	375.54	317.74	349.05	385.15
Cr	729.83	638.93	393.03	662.84	350.51	700.33
Co	86.40	76.11	61.71	64.68	58.45	91.22
Ni	133.89	106.81	80.21	97.30	65.04	135.46
Cu	110.44	60.66	97.71	100.08	69.43	108.63
Ga	20.96	20.84	23.22	19.81	24.00	21.09
Rb	19.99	18.39	21.96	25.18	30.36	17.14
Sr	635.46	685.72	912.03	842.60	912.46	742.69
Y	26.48	29.65	34.14	28.95	36.11	30.32
Zr	277.27	279.67	327.54	351.45	441.86	316.43
Nb	48.98	54.50	64.79	157.34	75.17	60.01
Cs	0.26	0.14	0.29	0.17	0.36	0.24
Ba	230.06	244.21	315.41	310.18	304.66	238.40
La	31.19	37.32	49.56	79.03	49.04	42.94
Ce	68.65	79.15	103.68	160.37	107.56	91.62
Pr	9.70	10.54	13.99	18.41	14.75	12.33
Nd	43.87	45.50	61.17	66.55	64.13	53.28
Sm	9.32	9.25	12.56	10.61	12.56	10.66
Eu	2.87	2.86	3.89	3.08	3.83	3.28
Gd	8.12	8.20	10.97	8.58	10.63	9.14
Tb	1.11	1.15	1.47	1.15	1.44	1.27
Dy	5.45	5.77	7.07	5.68	7.22	6.15
Ho	0.95	1.04	1.21	1.00	1.27	1.07
Er	2.13	2.45	2.75	2.32	2.99	2.41
Tm	0.28	0.35	0.36	0.32	0.41	0.32
Yb	1.59	2.02	2.04	1.87	2.43	1.83
Lu	0.24	0.31	0.30	0.27	0.36	0.27
Hf	6.65	6.32	7.38	7.86	9.44	7.05
Ta	2.84	3.18	3.63	8.49	4.33	3.41
Pb	2.30	2.06	2.62	3.39	2.88	2.20
Th	3.42	3.51	4.65	8.11	4.74	3.89
U	0.86	0.79	1.15	1.48	1.26	1.03

Table G.1: Major element and selected trace element data for El Hierro lavas (continued)

Sample	JMDD EH11	JMDD EH12	JMDD EH13	JMDD EH14	JMDD EH15	JMDD EH16
Series	CFE	CFE	CFE	UEGS	UEGS	LEGS
Lithology	Alkali Basalt	Alkali Basalt	Ankaramite	Alkali Basalt	Ankaramite	Basanite
wt. %						
SiO_2	41.63	42.08	40.91	42.67	42.27	43.11
TiO_2	5.43	3.72	5.15	5.61	3.02	4.03
Al_2O_3	10.52	10.74	8.92	13.38	8.94	10.36
Fe_2O_{3T}	16.28	14.67	17.19	15.16	15.86	14.55
MgO	11.49	13.49	14.24	8.03	17.57	11.70
MnO	0.22	0.20	0.21	0.22	0.19	0.21
CaO	10.78	10.79	10.45	10.20	9.21	12.42
Na_2O	2.57	2.41	2.33	3.61	1.72	2.42
K_2O	1.01	0.68	0.58	1.13	0.48	0.81
P_2O5	0.63	0.47	0.51	0.92	0.30	0.75
LOI	-0.42	-0.06	-0.35	-0.63	-0.27	0.17
Total	100.14	99.18	100.14	100.30	99.29	100.53
Mg-no.	59.12	65.33	62.93	52.06	69.41	62.24
ppm						
Sc	35.17	36.07	36.75	26.19	36.28	38.49
V	375.31	335.80	407.25	339.35	307.09	368.88
Cr	438.74	711.81	715.22	238.99	1056.68	733.82
Co	73.32	74.21	86.41	52.10	94.96	67.20
Ni	91.48	136.28	126.48	41.27	195.76	94.02
Cu	101.73	118.01	66.72	65.42	107.36	130.37
Ga	22.33	19.37	22.14	24.28	16.52	22.23
Rb	25.74	16.26	17.49	27.33	11.53	23.72
Sr	797.90	582.26	735.21	1067.62	453.66	911.88
Y	33.44	25.90	28.95	37.76	21.73	32.17
Zr	367.99	216.27	327.08	360.31	169.15	346.92
Nb	70.39	54.34	61.39	87.24	35.31	67.91
Cs	0.24	0.18	0.33	0.29	0.14	0.40
Ba	307.43	225.82	279.50	394.71	143.55	290.30
La	46.03	28.92	41.85	56.87	19.84	43.70
Ce	96.74	61.97	88.27	116.59	42.25	95.06
Pr	13.14	8.39	11.92	15.50	5.82	13.19
Nd	57.06	36.75	51.53	65.82	26.12	58.20
Sm	11.50	7.64	10.40	13.14	5.85	12.14
Eu	3.48	2.44	3.18	4.03	1.89	3.72
Gd	9.74	6.98	8.88	11.17	5.60	10.27
Tb	1.35	1.00	1.21	1.53	0.81	1.41
Dy	6.72	5.06	5.95	7.69	4.16	6.80
Ho	1.18	0.90	1.02	1.33	0.75	1.16
Er	2.73	2.12	2.29	3.12	1.79	2.63
Tm	0.37	0.29	0.30	0.43	0.25	0.35
Yb	2.14	1.69	1.71	2.45	1.46	1.95
Lu	0.32	0.25	0.25	0.36	0.22	0.29
Hf	8.25	5.02	7.56	8.09	4.11	7.90
Ta	4.00	3.11	3.48	4.87	2.06	3.88
Pb	2.94	1.74	2.55	3.55	1.30	2.71
Th	4.77	2.56	4.46	5.91	1.93	4.15
U	1.18	0.67	1.13	1.38	0.50	1.05

Table G.1: Major element and selected trace element data for El Hierro lavas (continued)

Sample	JMDD EH17	JMDD EH18
Series	PFE	PFE
Lithology	Alkali Basalt	Ankaramite
wt. %		
SiO_2	41.06	41.99
TiO_2	4.34	5.41
Al_2O_3	10.27	11.30
Fe_2O_{3T}	15.61	15.34
MgO	13.31	10.88
MnO	0.21	0.21
CaO	11.07	10.09
Na_2O	2.68	3.18
K_2O	0.91	0.98
P_2O5	0.83	0.64
LOI	-0.75	0.10
Total	99.54	100.14
Mg-no.	63.61	59.23
ppm		
Sc	32.20	32.15
V	357.93	362.47
Cr	577.93	494.45
Co	71.97	67.08
Ni	111.16	80.85
Cu	102.48	71.00
Ga	21.14	21.93
Rb	23.06	27.75
Sr	898.73	893.65
Y	31.25	34.06
Zr	314.43	362.32
Nb	69.37	73.85
Cs	0.30	0.22
Ba	330.66	315.87
La	52.99	46.01
Ce	108.17	99.46
Pr	14.09	13.76
Nd	59.27	60.04
Sm	11.52	11.87
Eu	3.55	3.61
Gd	9.95	10.08
Tb	1.35	1.38
Dy	6.49	6.90
Ho	1.10	1.21
Er	2.46	2.84
Tm	0.33	0.39
Yb	1.86	2.27
Lu	0.27	0.34
Hf	7.06	8.23
Ta	3.90	4.26
Pb	2.80	3.03
Th	4.89	5.17
U	1.19	1.01

Table G.2: Major element and selected trace element data for La Palma lavas

Sample	JMDD LP01	JMDD LP02	JMDD LP03	JMDD LP04	JMDD LP05	JMDD LP07
Series	Garafia	Garafia	Picrite	Ankaramite	Oceanite	Ankaramite
Lithology	Ankaramite	Ankaramite	Seamount	L. Taburiente	L. Taburiente	L. Taburiente
wt. %						
SiO_2	44.05	44.56	39.04	43.51	41.32	42.44
TiO_2	3.20	3.65	1.40	4.87	3.97	3.84
Al_2O_3	10.30	12.85	5.40	14.06	10.72	11.62
Fe_2O_{3T}	13.63	13.26	14.47	13.56	15.36	14.23
MgO	13.43	9.43	28.66	7.90	12.20	9.79
MnO	0.20	0.20	0.22	0.21	0.21	0.20
CaO	11.40	10.60	4.16	10.72	11.20	12.47
Na_2O	2.07	2.96	-0.03	3.35	2.40	2.75
K_2O	0.78	1.22	0.05	1.34	0.77	1.15
P_2O5	0.39	0.62	0.19	0.77	0.56	0.62
LOI	-0.24	-0.28	6.29	-0.23	0.01	-0.29
Total	99.21	99.06	99.84	100.06	98.71	98.83
Mg-no.	66.88	59.30	80.24	54.41	61.94	58.50
ppm						
Sc	35.16	28.76	17.65	24.13	31.96	33.80
V	292.67	330.36	132.82	309.52	366.54	352.74
Cr	814.13	358.01	1235.76	267.05	543.44	405.26
Co	66.69	52.90	113.29	46.02	72.83	59.35
Ni	471.14	182.31	1126.12	130.62	308.87	196.41
Cu	94.49	79.28	67.78	67.87	121.28	129.95
Ga	16.43	20.43	7.32	21.09	20.60	19.72
Rb	23.28	38.66	5.24	35.98	30.94	36.13
Sr	613.47	883.63	95.22	947.21	744.76	774.22
Y	21.97	30.31	10.75	32.79	27.38	26.80
Zr	185.47	331.69	83.16	323.81	286.55	258.39
Nb	42.16	68.49	19.95	77.80	71.58	63.19
Cs						
Ba	269.56	410.62	75.58	430.10	363.77	397.62
La	26.53	62.60	13.65	51.25	45.43	44.91
Ce	56.42	128.78	28.76	105.06	91.56	90.89
Pr	7.85	16.25	3.79	14.15	12.16	12.10
Nd	34.21	62.54	16.20	59.57	50.97	50.37
Sm	7.09	10.79	3.26	11.32	9.84	9.68
Eu	2.19	3.10	0.97	3.43	2.98	2.82
Gd	6.43	9.33	3.12	9.88	8.54	8.65
Tb	0.88	1.20	0.39	1.30	1.14	1.11
Dy	4.44	6.08	2.09	6.64	5.72	5.59
Ho	0.82	1.15	0.42	1.20	1.01	1.02
Er	1.89	2.64	0.92	2.78	2.28	2.26
Tm	0.26	0.38	0.13	0.38	0.31	0.31
Yb	1.52	2.18	0.80	2.22	1.77	1.74
Lu	0.23	0.33	0.12	0.33	0.26	0.26
Hf	4.59	7.74	1.95	7.05	6.60	6.11
Ta	6.50	4.03	1.15	4.55	4.26	3.69
Pb	1.70	3.35	0.81	2.46	2.26	3.04
Th	2.20	5.49	1.38	4.24	4.31	4.27
U	0.50	1.39	0.35	1.00	1.07	1.00

Table G.1: Major element and selected trace element data for La Palma lavas (continued)

Sample	JMDD LP09	JMDD LP10	JMDD LP11	JMDD LP14	JMDD LP15	JMDD LP19
Series	Tephrite	Ankaramite	Basanite	Basanite	Basanite	Tephrite
Lithology	Benejado	U. Taburiente	U. Taburiente	CFE	1949 San Juan	Birigoyo
wt. %						
SiO_2	42.04	43.78	42.97	43.16	43.23	44.30
TiO_2	3.29	2.97	3.71	3.67	3.76	4.03
Al_2O_3	10.98	9.98	12.70	11.75	12.47	15.05
Fe_2O_{3T}	13.76	14.06	14.53	13.49	13.33	13.07
MgO	13.45	14.80	8.92	11.46	10.54	6.87
MnO	0.19	0.20	0.20	0.19	0.19	0.21
CaO	10.89	10.46	11.16	10.81	10.96	10.33
Na_2O	2.26	1.68	2.26	3.26	3.38	4.49
K_2O	0.93	0.61	0.94	1.30	1.59	2.08
P_2O5	0.50	0.33	0.56	0.95	0.76	1.04
LOI	0.43	0.29	0.57	-0.40	-0.20	-0.57
Total	98.73	99.16	98.50	99.65	99.99	100.90
Mg-no.	66.70	68.32	55.72	63.50	61.85	51.85
ppm						
Sc	26.05	37.05	30.39	25.71	26.86	23.45
V	291.69	252.25	342.89	307.58	316.70	305.10
Cr	646.80	939.90	308.22	492.78	588.32	222.94
Co	66.80	75.95	60.22	62.23	57.09	43.74
Ni	409.33	481.07	176.19	322.50	259.14	96.00
Cu	98.79	89.72	123.64	103.72	121.91	83.32
Ga	19.05	16.13	20.45	20.34	20.39	23.47
Rb	25.47	12.67	29.25	39.89	39.57	53.86
Sr	712.56	505.25	698.09	1095.34	971.66	1290.93
Y	22.46	26.23	28.08	32.24	30.73	36.82
Zr	225.83	196.22	278.51	268.43	296.04	370.69
Nb	71.92	45.10	58.58	84.52	88.03	110.63
Cs						
Ba	427.56	221.40	347.69	570.29	535.04	653.18
La	37.02	31.37	40.73	81.87	73.80	85.22
Ce	73.52	60.70	84.25	150.17	135.21	157.08
Pr	9.74	8.37	11.33	18.44	16.56	19.42
Nd	41.47	35.53	47.89	72.33	64.50	77.14
Sm	8.28	7.10	9.36	12.77	11.38	13.88
Eu	2.50	2.14	2.82	3.65	3.29	4.00
Gd	7.47	6.70	8.28	10.51	9.67	11.62
Tb	0.96	0.90	1.12	1.36	1.26	1.50
Dy	4.76	4.57	5.73	6.70	6.28	7.38
Ho	0.85	0.87	1.03	1.18	1.14	1.34
Er	1.88	2.02	2.42	2.64	2.61	3.12
Tm	0.26	0.29	0.34	0.35	0.36	0.44
Yb	1.43	1.66	1.93	1.99	2.11	2.54
Lu	0.21	0.26	0.30	0.29	0.32	0.39
Hf	5.36	4.79	6.47	6.08	6.40	8.10
Ta	4.05	2.67	3.49	4.72	4.90	6.23
Pb	2.18	1.50	2.24	3.45	4.07	4.86
Th	3.76	2.81	3.50	7.86	8.22	9.12
U	0.94	0.72	0.90	2.04	2.10	2.63

Table G.1: Major element and selected trace element data for La Palma lavas (continued)

Sample	JMDD LP24	LPF 96-66	LP 96-46	LP 96-41	LPF 96-63	LP 96-48
Series	Basanite	Ankaramite	Basanite	Basanite	Basanite	Basanite
Lithology	1677	U. Taburiente	U. Taburiente	U. Taburiente	U. Taburiente	U. Taburiente
wt. %						
SiO_2	43.37	44.61	44.80	45.40	45.00	44.10
TiO_2	3.93	2.52	3.07	3.31	3.56	3.82
Al_2O_3	13.28	9.80	11.90	12.10	11.40	12.70
Fe_2O_{3T}	13.68	12.98	13.80	13.49	13.09	13.81
MgO	8.58	15.54	11.4	11.68	11.81	9.48
MnO	0.20	0.18	0.18	0.18	0.17	0.19
CaO	11.64	11.33	11.06	10.45	10.70	11.10
Na_2O	3.70	1.65	2.59	2.61	2.68	3.32
K_2O	1.70	0.65	0.85	1.12	1.41	0.79
P_2O5	0.90	0.32	0.51	0.49	0.45	0.68
LOI	-0.53	-0.09	-0.50	-0.60	-0.20	0.00
Total	100.46	99.50	100.16	100.83	100.27	99.99
Mg-no.	56.25	71.05	62.87	63.96	64.90	58.45
ppm						
Sc	28.30	38.00	32.35	29.90	30.94	30.70
V	334.10	289.42	299.21	307.07	343.90	340.45
Cr	353.70	1014.27	571.59	662.11	621.07	391.40
Co	53.12	77.47	65.97	67.78	65.43	57.51
Ni	151.51	454.60	337.49	382.74	398.05	218.06
Cu	104.78	55.24	21.38	18.00	31.82	114.99
Ga	22.14	16.03	19.91	20.25	20.73	21.26
Rb	42.89	14.09	16.92	23.87	33.41	10.93
Sr	1212.49	473.36	610.16	673.21	621.83	938.43
Y	37.22	22.48	27.39	28.75	27.75	31.03
Zr	325.62	170.95	217.33	256.13	235.67	333.25
Nb	99.09	40.58	50.37	62.64	52.09	82.59
Cs		0.09	0.12	0.19	0.27	0.42
Ba	610.08	223.07	299.38	333.52	371.06	392.80
La	90.01	27.46	37.87	42.99	31.56	56.41
Ce	165.63	56.13	78.60	86.93	66.85	113.37
Pr	20.34	7.37	10.35	11.36	9.21	14.81
Nd	79.46	30.70	42.17	46.18	39.49	60.39
Sm	13.89	6.22	8.20	9.03	8.37	11.21
Eu	4.04	1.98	2.64	2.82	2.64	3.39
Gd	11.79	5.98	7.82	8.25	7.99	9.42
Tb	1.51	0.84	1.08	1.13	1.12	1.28
Dy	7.51	4.44	5.50	5.82	5.68	6.43
Ho	1.36	0.81	0.98	1.04	1.01	1.14
Er	3.07	1.95	2.33	2.46	2.34	2.66
Tm	0.42	0.29	0.34	0.37	0.35	0.40
Yb	2.46	1.62	1.86	2.03	1.87	2.17
Lu	0.37	0.24	0.28	0.31	0.27	0.33
Hf	7.38	4.21	5.35	6.09	5.91	7.65
Ta	5.67	2.37	2.95	3.75	3.15	4.97
Pb	4.29	3.23	3.14	2.72	4.47	2.98
Th	9.24	2.64	3.26	4.14	2.84	5.15
U	2.36	0.62	0.63	1.02	0.61	1.19

Table G.1: Major element and selected trace element data for La Palma lavas (continued)

Sample	LP 96-14	LP 96-22	LP 96-83	LP69A	LP 113	LP 107
Series	Basanite	Basanite	Basanite	Basanite	Basanite	Basanite
Lithology	U. Taburiente	U. Taburiente	U. Taburiente	1949	U. Taburiente	U. Taburient
wt. %						
SiO_2	42.60	43.00	42.70	43.96	45.18	44.12
TiO_2	3.79	3.32	3.36	3.35	3.31	2.64
Al_2O_3	12.20	11.20	11.30	13.87	14.27	9.30
Fe_2O_{3T}	14.94	14.65	14.78	13.71	13.10	13.48
MgO	10.32	11.58	11.31	8.35	8.27	15.50
MnO	0.19	0.19	0.19	0.19	0.19	0.18
CaO	11.54	12.76	12.37	10.83	10.09	10.86
Na_2O	3.21	2.54	2.66	3.47	3.34	1.78
K_2O	0.77	0.49	0.65	1.27	1.33	0.65
P_2O5	0.59	0.39	0.40	0.70	0.77	0.41
LOI	0.40	-0.10	-0.20	0.00	0.00	0.30
Total	100.14	100.11	99.71	99.70	99.85	98.92
Mg-no.	58.60	61.83	61.06	55.52	56.40	70.21
ppm						
Sc	29.91	44.41	41.93	27.30		
V	383.27	409.24	387.42	296.00	272.00	277.00
Cr	364.22	533.40	602.77	307.00	293.00	1048.00
Co	65.78	71.81	69.05	52.40	58.00	100.00
Ni	243.46	237.00	228.91	122.00	152.00	539.00
Cu	27.57	33.56	25.99		86.00	89.00
Ga	23.39	21.45	20.28			
Rb	14.41	28.65	21.26	27.00	28.50	13.00
Sr	859.44	633.06	612.27	930.47	827.00	500.00
Y	29.65	27.86	26.57	32.00	32.50	22.70
Zr	285.54	232.42	222.45	290.97	341.00	192.00
Nb	74.92	59.27	57.24	70.79	73.90	36.00
Cs	0.64	0.27	0.26	0.39		
Ba	485.10	334.57	325.88	415.58	376.19	197.05
La	47.54	41.77	40.68	51.58	47.00	27.00
Ce	96.01	84.92	81.80	126.00	113.00	60.00
Pr	12.88	11.03	10.71			
Nd	53.22	44.62	43.49	60.00	52.00	29.00
Sm	10.55	8.58	8.37	11.80	10.60	
Eu	3.30	2.69	2.60	3.63		
Gd	9.45	8.01	7.72			
Tb	1.27	1.09	1.04	1.55		
Dy	6.27	5.61	5.35			
Ho	1.09	1.01	0.96			
Er	2.49	2.39	2.25			
Tm	0.35	0.35	0.33			
Yb	1.87	1.93	1.86	2.22		
Lu	0.27	0.29	0.28	0.33		
Hf	6.70	5.85	5.50	8.93	9.30	4.90
Ta	4.31	3.40	3.27	4.62		
Pb	5.47	3.60	3.59	3.21	2.51	1.30
Th	4.47	4.06	3.97	5.89	5.25	
U	1.10	0.92	0.92	1.65	1.55	

Table G.1: Major element and selected trace elem

Sample	LP 110	LP 134
Series	Basanite	Gabbro
Lithology	U. Taburient	Seamount
wt. %		
SiO_2	43.58	44.44
TiO_2	3.42	3.41
Al_2O_3	12.52	12.07
Fe_2O_{3T}	14.33	12.84
MgO	9.81	10.30
MnO	0.19	0.18
CaO	11.73	11.15
Na_2O	2.47	2.71
K_2O	0.94	1.30
P_2O5	0.52	0.53
LOI	0.60	1.30
Total	99.51	98.92
Mg-no.	58.38	62.18
ppm		
Sc		
V	354.00	311.00
Cr	386.00	497.00
Co	69.00	67.00
Ni	204.00	229.00
Cu	132.00	112.00
Ga		
Rb	25.90	27.60
Sr	662.00	640.00
Y	28.00	26.90
Zr	249.00	255.00
Nb	49.60	51.00
Cs		
Ba	295.58	313.49
La	30.00	32.00
Ce	79.00	74.00
Pr		
Nd	39.00	39.00
Sm		7.67
Eu		
Gd		
Tb		
Dy		
Ho		
Er		
Tm		
Yb		
Lu		
Hf	6.60	6.70
Ta		
Pb	2.15	
Th		2.95
U		0.96

Appendix H - Mackenzie Large Igneous Province dataset (Chapter 5)

H.1 Description of Muskox intrusion stratigraphy

The Muskox intrusion is divided into four parts: the keel dyke, the marginal zones, a layered series, and a granophyric roof zone (figure 5.14). The Keel dyke shows a symmetrical zonation of rock types from gabbro norites at the margins to picritic gabbro norites in the centre. This zonation has previously been attributed to flow differentiation and not fractional crystallisation processes (Bhattacharji and Smith, 1964). Field relationships indicate that the Keel dyke is older than the main intrusion above, suggesting that a previously formed dyke was expanded and was fed laterally from the north where much of the intrusion is preserved under younger Proterozoic and Phanerozoic cover. The marginal zones line the inward-dipping footwall contacts, are ~130-230m thick and generally grade from bronzite gabbro at the contact, through picrite, feldspathic peridotite to peridotite similarly to the Keel dyke. Unlike the Keel dyke, the marginal zone gabbro norites contain more orthopyroxene and contain more included and melted patches of country rock, consistent with a greater degree of assimilation of upper crustal rocks in the marginal zones (Francis, 1994). The marginal zones were sampled, for the purpose of this study, at the base of the intrusion.

The layered series, occupying the trough formed by the marginal zones, is about 1800m thick and comprises 42 discernable layers of 18 different rock types (figure 5.14). The layers range in thickness from 3 to 350m, are sharply defined, show little internal layering or structure other than planer lamination, and are laterally continuous from marginal zone boundaries. The layers dip 3-5° to the North in keeping with the regional structure seen in the older Helikian Sequence. This suggests that the tilting came after emplacement of the Mackenzie LIP. Some layers can be traced for more than 25km and from drill hole intersections it is apparent that many have aerial extents in excess of 250km^2. The succession of rock types in the layered series is from dunite at the base through peridotite, pyroxenite and gabbros. The roof zone is characterised by granophyric gabbros and granophyres which are extensively charged with roof rock xenoliths. There are three thin layers of >50%

cumulus chromite identified within the intrusion. Two are closely spaced at ~1500m in the stratigraphy (figure 5.14) and are probably laterally continuous for more than 100km^2 in extent. The third chromitite has been newly recognised and is 'cryptic' being recognised only from its chemical fingerprint in the drill core section. This lower chromitite lies within the main layer 2 dunite horizon and is termed the 'Hulbert reef'.

Perhaps the most spectacular features of the Muskox intrusion layered series is the dominance of olivine cumulates and the repetition of rock types (Irvine, 1980). Olivine makes up more than 50% of the layered series and is typically accompanied by >1% cumulus chromite. The amounts of olivine and chromite are grossly disproportionate to the apparent composition of the parental liquid which is assessed to be a silica-saturated tholeiite with only 19 wt% normative olivine (15 Wt % MgO) and only 0.25 wt% chromium trioxide (Smith and Kapp, 1963; Irvine, 1980). Part of the explanation to this discrepancy may be that the chilled gabbro from which these parental magma compositions were calculated may only be the residuum of more primitive parent magma after fractionation of olivine and chromite (Irvine, 1988). The repetition of rock types evidently reflects the crystallisation order of cumulus minerals from their parental liquids (Irvine and Smith, 1967; Irvine, 1970). The layered series has been divided into 25 cyclic units, so-called after the sub-division of the Stillwater ultramafic zone by Jackson (1961). The cyclic units have been interpreted as at least 25 replenishments of fresh liquid during accumulation of the layered series, with concurrent displacement and removal of the residual differentiated liquid, possibly as volcanic eruptions (Irvine and Smith, 1967; Irvine and Baragar, 1972). It is notable that the roof of the intrusion is composed of Helikian rocks whereas the sidewalls are Wopmay orogen lithologies; this relationship strongly suggest the level of neutral buoyancy for the intrusion was reached at this crustal intersection and explains the ponding of the proto-Muskox intrusion magmas.

H.2 Petrology of Muskox Intrusion cyclic units and country rocks

The Muskox intrusion layered series, marginal rocks, keel dyke, chromitites and country rocks have been described in Findlay and Smith (1965). Classic studies of sulphide and native metal distributions and properties have also been undertaken on

Muskox intrusion rocks (Chamberlain *et al.*, 1965; Chamberlain, 1967; Sasaki, 1969). Petrographic descriptions of samples used in this study are provided in appendix A and are for drill core material apart from the chromitite horizon and keel dyke samples which were collected on ground surveys.

Two crustal rocks have been examined from the footwall and hanging wall of the intrusion to constrain potential contaminants. The hanging wall country rock is metamorphosed Hornby Bay sandstone (DDH-MX-N1), part of the Helikian sequence. It is a thermally metamorphosed quartzite with recrystallised and composed dominantly of quartz with minor chlorite, muscovite and calcite after K-feldspar. The footwall rock is a Wopmay ortho-paragneiss (DDH-MX-S195) which is banded and composed of K-feldspar, quartz, hypersthene and minor magnetite, iron hydroxide, biotite and zircon. Keel-dyke samples are represented by HDB-2001-MX5 which is a gabbro norite containing fresh olivine phenocrysts and large orthopyroxene oikocrysts enclosing the olivines.

For the purpose of describing the cumulates within the Muskox intrusion the classification of Wager *et al.* (1960) is adopted. Rocks formed by crystal accumulation in the Muskox intrusion are orthocumulates in the marginal zones near to the footwall contacts (e.g., DDH-MX-S171) and grade to mesocumulates in the lower and middle parts of the layered series (e.g., DDH-MX-S156); these variations probably reflect preservation of primary cumulus textures in the margins which did not suffer excessive post-cumulus modification. Some of the pyroxenite layers are adcumulates (e.g., DDH-MX-N100) as are most of the olivine gabbro in the middle layered series. Dunites tend to be mesocumulates and adcumulates but trend to hetero-adcumulates (e.g., DDH-MX-S128). Gabbro and granophyre classification in the uppermost parts of the intrusion are less definite, due to uncertainty in distinguishing post-cumulus material, but these appear to be mostly mesocumulates grading to orthocumulates. Dunite dominates the stratigraphy and is generally fresh in the lowermost parts of the intrusion with olivine, chromite, magnetite and rare plagioclase (peridotite) but becomes heavily serpentinised in the heavily reducing central zone of the intrusion which contains native metals and depletions in sulphides as noted by Chamberlain and co-workers (1965; 1967). Serpentinised units with Mg-rich chlorite grade into iron-hydroxide rich layers above suggesting increasing oxygen fugacity (fO_2) in the uppermost portions of the intrusion. The

chromitites are composed of between 5 and 50% chromite which crystallised before the enclosing silicates (orthopyroxene, clinopyroxene, and plagioclase) and has been forced into melt 'gaps' between silicate minerals or has become enclosed within the silicates as rafts of chromite.

Roof rocks are dominantly granophyres and gabbros (DDH-MX-N3 through to DDH-MX-N46) and are dominated by plagioclase and k-feldspar, orthopyroxene, clinopyroxene and quartz with a large variation in crystal sizes as well as alteration and post-cumulus phases (e.g., magnetite). The roof rocks are often visibly charged with crustal xenoliths; however these have not been intersected in any of the available drill core material. The marginal zone rocks (DDH-MX-S192 through to DDH-MX-S160) are composed of feldspathic peridotite, peridotite, picrites and bronzite-gabbro. The bronzite gabbro contains abundant chalcopyrite; this is typical of the marginal zone rocks which host the majority of the sulphides located within the intrusion (Chamberlain, 1967; Sasaki, 1969).

Table H.1: Major element and selected trace element data for Coppermine continental flood basalts

Sample	HDB-98-90B	HDB-98-91	HDB-98-94	HDB-98-170	HDB-98-176	HDB-98-119A
Height (M)	0.1	5.4	31.5	161.4	413.2	454.0
Lithology	Basalt	Basalt	Basalt	Basalt	Picritic Flow	Picritic Flow
wt. % annhydrous corrected						
SiO_2	54.85	50.88	49.57	54.20	49.20	47.74
TiO_2	1.85	1.57	1.31	1.76	1.00	0.70
Al_2O_3	12.78	13.34	13.92	10.55	12.22	8.30
FeO_c	9.76	10.05	9.85	9.79	9.81	10.84
Fe_2O_{3c}	1.21	1.24	1.22	1.21	1.21	1.34
MgO	7.88	8.47	10.09	8.43	12.86	20.71
MnO	0.12	0.17	0.18	0.23	0.16	0.19
CaO	7.91	11.77	9.93	9.85	11.50	8.95
Na_2O	1.97	1.65	3.12	1.95	1.37	0.62
K_2O	1.42	0.60	0.56	1.74	0.40	0.23
P_2O5	0.17	0.16	0.12	0.16	0.09	0.06
Mg-no.	56.53	57.56	62.25	58.09	67.84	75.45
ppm						
Sc	27.00	38.39	42.63	28.99	33.00	32.52
V	260.00	326.56	320.25	289.97	250.00	213.23
Cr	373.99	546.03	670.59	702.53	832.30	1694.77
Co	44.00	51.65	53.53	53.10	59.00	91.12
Ni	114.27	311.99	241.65	228.03	305.53	208.48
Cu	98.69	166.46	141.05	98.58	40.03	65.16
Zn		78.26	74.46	91.88		73.53
Ga	19.00	17.74	16.50	17.68	15.00	9.73
Rb	31.00	8.36	8.73	34.41	10.00	6.98
Sr	270.00	242.96	454.42	232.00	110.00	78.91
Y	24.00	24.09	20.97	23.18	18.00	11.51
Zr	140.00	115.64	96.10	150.37	66.00	43.05
Nb	11.00	8.06	5.60	11.01	3.90	2.63
Cs	0.29	0.41	0.40	0.41	0.33	1.89
Ba	400.00	214.68	467.80	552.29	94.00	74.04
La	18.00	12.32	8.41	17.75	6.80	3.99
Ce	42.00	28.35	19.91	38.89	16.00	9.25
Pr	5.50	4.03	2.89	5.44	2.20	1.33
Nd	23.00	18.53	13.64	24.06	10.00	6.23
Sm	5.20	4.40	3.46	5.34	2.80	1.65
Eu	1.80	1.47	1.12	1.65	0.91	0.57
Gd	5.30	4.82	3.93	5.31	3.20	2.02
Tb	0.83	0.76	0.64	0.80	0.53	0.34
Dy	4.30	4.38	3.75	4.38	3.20	2.00
Ho	0.84	0.87	0.78	0.85	0.64	0.41
Er	2.10	2.28	2.03	2.13	1.70	1.09
Tm	0.31	0.37	0.32	0.33	0.25	0.17
Yb	2.00	2.15	1.93	1.90	1.70	1.03
Lu	0.28	0.34	0.31	0.29	0.24	0.16
Hf	3.90	3.13	2.35	3.95	1.90	1.20
Ta	0.70	0.53	0.38	0.74	0.26	0.21
Pb		5.32	3.43	6.60		1.26
Th	3.20	2.10	1.40	3.43	1.00	0.69
U	0.81	0.54	0.34	1.01	0.31	0.18

Table H.1: Major element and selected trace element data for Coppermine continental flood basalts (continued)

Sample	HDB-98-119B	HDB99-CM36	HDB99CM35B	HDB-98-109	HDB99CM19B	HDB-98-51
Height (M)	454.1	459.3	459.3	483.9	497.5	864.6
Lithology	Picritic Flow	Picritic contact	Picritic contact	Picritic Flow	Andesite	Basalt
wt. % annhydrous corrected						
SiO_2	47.42	54.15	59.93	47.32	62.66	54.22
TiO_2	0.58	0.99	0.85	0.64	0.83	1.99
Al_2O_3	8.13	12.09	12.26	7.49	14.23	13.78
FeO_c	10.89	8.89	7.91	11.03	6.11	11.00
Fe_2O_{3c}	1.34	1.10	0.98	1.36	0.75	1.36
MgO	21.48	9.97	8.92	21.10	4.93	5.45
MnO	0.20	0.16	0.14	0.20	0.12	0.19
CaO	8.74	9.37	4.09	9.83	6.21	7.70
Na_2O	0.63	1.63	1.25	0.31	2.23	2.76
K_2O	0.18	1.34	3.04	0.29	1.42	1.32
P_2O5	0.06	0.09	0.10	0.06	0.12	0.21
Mg-no.	76.05	64.35	64.49	75.48	56.50	44.38
ppm						
Sc	33.92	29.00	23.00	32.84	19.23	34.00
V	212.75	238.00	228.00	212.65	146.67	380.00
Cr	1989.77	1320.67	3427.44	1893.76	2494.23	41.86
Co	94.70	48.00	35.00	90.94	24.44	44.00
Ni	720.12	222.48	178.64	679.50	93.79	73.52
Cu	53.46	114.80	47.78	64.89	44.08	50.03
Zn	69.97			73.89	118.03	
Ga	9.84	14.00	17.00	9.93	17.97	23.00
Rb	5.77	36.00	84.00	7.70	41.82	32.00
Sr	79.74	150.00	110.00	87.27	347.38	230.00
Y	11.13	21.00	27.00	11.36	30.73	36.00
Zr	37.94	97.00	160.00	41.45	169.40	150.00
Nb	2.12	6.00	11.00	2.38	12.69	11.00
Cs	1.22	0.55	1.90	1.30	36.24	0.38
Ba	53.46	310.00	440.00	80.24	556.53	310.00
La	3.50	15.00	31.00	3.77	36.04	18.00
Ce	8.39	32.00	64.00	9.03	68.94	42.00
Pr	1.23	3.80	7.30	1.28	8.36	5.80
Nd	5.96	15.00	26.00	6.29	30.97	26.00
Sm	1.63	3.40	5.00	1.65	5.85	6.30
Eu	0.57	0.92	1.00	0.57	1.15	2.10
Gd	1.96	3.50	4.60	2.00	5.37	7.00
Tb	0.32	0.58	0.74	0.33	0.86	1.10
Dy	1.93	3.50	4.50	1.96	5.14	6.20
Ho	0.40	0.70	0.94	0.40	1.06	1.20
Er	1.06	1.90	2.50	1.09	2.89	3.20
Tm	0.17	0.29	0.39	0.17	0.49	0.46
Yb	1.00	1.90	2.70	1.01	2.91	3.00
Lu	0.16	0.29	0.39	0.16	0.47	0.44
Hf	1.08	2.50	4.00	1.16	4.58	4.60
Ta	0.14	0.49	0.77	0.16	1.09	0.75
Pb	1.04			1.04	32.36	
Th	0.64	4.70	11.00	0.68	13.91	2.70
U	0.16	1.20	2.70	0.18	3.28	0.72

Table H.1: Major element and selected trace element data for Coppermine continental flood basalts (continued)

Sample	HDB-98-55	HDB-98-60	HDB-98-61B	HDB-98-64	HDB-98-70	HDB-98-75
Height (M)	1024.4	1268.8	1286.5	1437.1	1598.4	1850.0
Lithology	Basalt	Basalt	Basalt	Basalt	Basalt	Basalt
wt. % annhydrous corrected						
SiO_2	50.23	50.50	49.14	48.30	49.38	50.75
TiO_2	2.10	2.45	3.09	3.74	3.18	2.99
Al_2O_3	14.19	13.01	12.93	12.51	12.50	11.38
FeO_c	12.57	13.05	13.99	14.66	14.35	14.70
Fe_2O_{3c}	1.55	1.61	1.73	1.81	1.77	1.81
MgO	5.31	6.08	6.25	4.98	5.17	5.40
MnO	0.40	0.24	0.29	0.32	0.24	0.31
CaO	9.93	10.02	9.48	10.09	9.75	8.35
Na_2O	2.25	2.17	2.17	2.34	2.46	2.87
K_2O	1.26	0.60	0.61	0.79	0.79	1.12
P_2O5	0.19	0.25	0.29	0.45	0.39	0.31
Mg-no.	40.47	42.87	41.82	35.36	36.71	37.17
ppm						
Sc	37.59	36.00	36.51	38.71	37.87	37.00
V	493.69	430.00	468.97	493.40	501.26	490.00
Cr	105.91	79.52	84.54	47.31	51.13	31.78
Co	53.72	48.00	52.44	51.86	50.24	45.00
Ni	172.27	72.29	24.06	60.38	68.29	54.34
Cu	99.48	568.03	38.21	395.91	302.74	164.04
Zn	148.46		138.74	150.03	130.98	
Ga	22.56	21.00	22.51	24.36	22.52	22.00
Rb	16.98	12.00	15.91	20.28	24.25	31.00
Sr	239.50	220.00	291.42	300.93	260.24	210.00
Y	34.30	36.00	37.74	55.12	48.66	44.00
Zr	166.26	170.00	213.70	337.06	269.87	190.00
Nb	13.02	14.00	19.24	32.19	24.52	18.00
Cs	0.18	0.12	0.35	0.17	0.41	0.66
Ba	204.40	160.00	163.73	224.60	222.35	450.00
La	13.22	16.00	18.52	30.89	24.16	20.00
Ce	32.91	39.00	45.34	73.63	57.30	49.00
Pr	4.96	5.50	6.72	10.82	8.47	6.70
Nd	23.39	26.00	31.37	49.40	39.00	31.00
Sm	5.96	6.70	7.55	11.54	9.30	7.80
Eu	1.97	2.10	2.47	3.37	2.84	2.40
Gd	6.59	7.40	7.96	11.79	9.91	9.10
Tb	1.06	1.10	1.26	1.79	1.55	1.40
Dy	6.13	6.70	7.02	10.21	8.88	8.00
Ho	1.24	1.30	1.38	2.00	1.78	1.50
Er	3.26	3.30	3.51	5.13	4.60	4.10
Tm	0.53	0.47	0.52	0.81	0.74	0.58
Yb	3.02	3.20	3.21	4.70	4.29	4.00
Lu	0.49	0.46	0.50	0.73	0.68	0.60
Hf	4.44	4.70	5.55	8.63	7.07	5.50
Ta	0.85	0.86	1.23	2.07	1.60	1.10
Pb	6.29		6.51	6.70	3.32	
Th	1.63	1.60	1.96	3.26	2.65	1.80
U	0.47	0.45	0.53	0.88	0.69	0.50

Table H.1: Major element and selected trace element data for Coppermine continental flood basalts (continued)

Sample	HDB-98-82	HDB-98-87	HDB-98-89A	HDB-98-124	HDB-98-130A	HDB-98-127
Height (M)	2130.5	2379.2	2456.7	2913.5	3434.0	3963.7
Lithology	Basalt	Basalt	Basalt	Basalt	Basalt	Basalt
wt. % annhydrous corrected						
SiO_2	51.48	49.84	50.28	50.32	50.28	50.34
TiO_2	1.79	1.50	2.44	2.47	1.18	1.29
Al_2O_3	13.80	13.10	12.75	13.17	14.35	13.28
FeO_c	12.10	11.53	12.59	13.33	10.62	11.84
Fe_2O_{3c}	1.49	1.42	1.55	1.65	1.31	1.46
MgO	7.15	8.33	7.97	6.44	7.95	9.15
MnO	0.21	0.21	0.34	0.26	0.17	0.32
CaO	8.12	9.95	7.89	8.76	11.81	10.12
Na_2O	2.80	3.82	3.11	2.57	1.76	1.65
K_2O	0.81	0.12	0.77	0.74	0.41	0.40
P_2O5	0.23	0.14	0.27	0.26	0.12	0.12
Mg-no.	48.74	53.75	50.46	43.74	54.64	55.44
ppm						
Sc	41.00	42.44	43.00	45.69	46.00	51.09
V	330.00	409.80	420.00	461.66	310.00	366.65
Cr	75.76	139.95	134.77	66.23	206.49	114.65
Co	50.00	52.52	52.00	55.65	49.00	54.54
Ni	62.27	97.59	92.27	74.60	102.21	88.96
Cu	69.54	49.79	155.50	177.17	134.22	28.34
Zn		93.29		113.25		103.50
Ga	22.00	17.62	20.00	20.84	16.00	16.33
Rb	22.00	3.37	22.00	12.94	5.70	4.48
Sr	200.00	336.96	180.00	202.40	140.00	139.48
Y	38.00	26.33	35.00	41.70	26.00	26.18
Zr	150.00	110.69	170.00	197.75	82.00	83.80
Nb	13.00	10.01	18.00	18.74	6.10	8.86
Cs	0.49	0.12	0.46	0.38	0.45	0.17
Ba	270.00	109.78	260.00	214.16	110.00	186.92
La	17.00	9.43	16.00	17.81	6.40	6.79
Ce	39.00	23.61	39.00	42.29	16.00	17.10
Pr	5.30	3.55	5.70	6.13	2.30	2.60
Nd	25.00	16.78	26.00	28.20	11.00	12.64
Sm	5.90	4.28	6.40	6.79	3.10	3.40
Eu	1.90	1.45	1.90	2.14	1.10	1.19
Gd	6.70	4.89	7.00	7.62	4.00	4.13
Tb	1.10	0.81	1.10	1.23	0.66	0.71
Dy	6.30	4.72	6.10	7.19	4.10	4.31
Ho	1.30	0.96	1.20	1.49	0.87	0.93
Er	3.40	2.51	3.00	3.99	2.40	2.57
Tm	0.51	0.41	0.42	0.65	0.35	0.43
Yb	3.50	2.41	2.90	3.85	2.50	2.62
Lu	0.52	0.38	0.42	0.63	0.37	0.43
Hf	4.20	2.90	4.40	5.12	2.10	2.28
Ta	0.81	0.65	1.10	1.22	0.38	0.56
Pb		2.70		3.33		0.99
Th	2.00	1.00	1.30	2.06	0.50	0.59
U	0.45	0.25	0.37	0.53	0.13	0.15

Table H.1: Major element and selected trace elemen

Sample	HDB-98-126	HDB-98-125
Height (M)	4260.1	4387.1
Lithology	Basalt	Basalt
wt. % annhydrous corrected		
SiO_2	51.96	50.77
TiO_2	1.75	1.10
Al_2O_3	13.41	13.84
FeO_c	12.22	11.12
Fe_2O_{3c}	1.51	1.37
MgO	8.65	9.87
MnO	0.20	0.30
CaO	5.85	6.66
Na_2O	3.35	3.23
K_2O	0.88	1.57
P_2O5	0.19	0.11
Mg-no.	53.27	58.82
ppm		
Sc	52.00	52.01
V	380.00	363.60
Cr	115.24	205.74
Co	52.00	56.96
Ni	82.77	116.80
Cu	115.24	57.80
Zn		87.94
Ga	17.00	15.82
Rb	11.00	18.89
Sr	250.00	543.84
Y	32.00	28.07
Zr	100.00	83.73
Nb	10.00	6.83
Cs	0.28	0.39
Ba	850.00	5042.82
La	8.90	6.22
Ce	22.00	15.99
Pr	3.40	2.50
Nd	16.00	12.24
Sm	4.20	3.43
Eu	1.60	1.09
Gd	5.10	4.48
Tb	0.85	0.73
Dy	5.20	4.57
Ho	1.10	0.99
Er	3.00	2.68
Tm	0.45	0.45
Yb	3.20	2.66
Lu	0.50	0.43
Hf	2.90	2.29
Ta	0.61	0.43
Pb		1.53
Th	0.50	0.53
U	0.13	0.13

Table H.2: Major element and selected trace element data for the Muskox intrusion

Sample	N-1	N-3	N-11	N-14	N-18	N-27
DFB (m)	1880.7	1878.0	1834.7	1821.3	1800.9	1746.3
Lithology	Hornby Bay	Grano. gabbro	Grano. gabbro	Pic. Webs	Gabbro	Gabbro
Cyclic Unit	Sst	25	25	25	24	24
wt. % annhydrous corrected						
SiO_2	89.83	58.09	52.54	42.71	51.42	50.52
TiO_2	0.06	2.40	1.56	1.66	0.84	0.73
Al_2O_3	3.56	12.33	14.76	14.05	14.19	15.46
Fe_2O_{3t}	3.16	13.35	10.49	17.70	8.65	7.98
MgO	2.94	4.01	7.62	22.97	9.35	10.01
MnO	0.01	0.10	0.15	0.14	0.15	0.12
CaO	0.21	4.10	8.60	0.54	12.79	12.76
Na_2O	0.00	1.94	1.63	0.00	1.41	1.72
K_2O	0.17	3.35	2.51	0.04	1.14	0.63
P_2O5	0.05	0.34	0.14	0.17	0.06	0.07
Mg-no.	65.64	38.07	59.81	72.67	68.88	71.99
ppm						
S	1071.00	7070.00	283.00	638.00	321.00	508.00
Sc	0.85	29.13	25.68	35.24	34.61	25.78
V	46.49	333.72	284.04	289.75	248.33	182.13
Cr	13.45	9.26	114.42	834.94	75.30	479.22
Co	37.49	32.64	40.56	66.81	42.69	41.25
Ni	5.71	31.90	124.31	225.73	138.57	175.76
Cu	5.44	29.93	148.07	27.24	54.54	155.95
Ga	3.98	21.61	17.24	18.33	15.01	14.65
Rb	8.34	68.58	42.51	0.65	26.90	15.90
Sr	39.45	358.53	294.95	14.64	252.73	226.86
Y	6.13	51.87	19.01	21.12	13.87	10.78
Zr	73.21	310.62	118.79	108.61	57.58	49.48
Nb	2.84	17.24	10.03	7.18	3.55	3.21
Cs	0.40	0.30	0.72	0.23	0.44	0.56
Ba	52.26	866.12	331.75	8.85	171.71	125.16
La	39.87	39.00	13.50	31.18	5.88	5.33
Ce	52.01	81.70	29.34	59.85	13.32	11.92
Pr	4.88	11.28	4.04	6.98	1.93	1.70
Nd	17.06	48.67	17.47	26.93	9.04	7.72
Sm	2.97	11.13	3.96	4.66	2.33	1.89
Eu	0.51	2.86	1.39	0.95	0.81	0.68
Gd	2.23	11.08	4.02	4.03	2.74	2.12
Tb	0.28	1.68	0.62	0.62	0.43	0.33
Dy	1.27	9.63	3.45	3.60	2.58	1.93
Ho	0.22	1.89	0.68	0.78	0.50	0.39
Er	0.55	4.87	1.75	2.19	1.27	0.99
Tm	0.09	0.78	0.28	0.37	0.20	0.15
Yb	0.54	4.48	1.61	2.44	1.15	0.92
Lu	0.09	0.70	0.25	0.41	0.19	0.15
Hf	2.00	8.29	3.14	2.97	1.64	1.37
Ta	0.23	1.22	0.65	0.49	0.31	0.24
Pb	8.29	22.87	5.51	11.40	4.49	5.89
Th	8.29	11.90	2.20	2.28	1.11	1.04
U	3.82	3.11	0.58	0.69	0.29	0.27

Table H.2: Major element and selected trace element data for the Muskox intrusion (continued)

Sample	N-35	N-46	N-54	N-55	N-56	N-57
DFB (m)	1700.3	1633.6	1571.4	1560.0	1555.0	1550.0
Lithology	Flds. Web	Flds. Web	Opx-Webs	Opx-Webs	Opx-Webs	Opx-Webs
Cyclic Unit	23	23	22	21	21	21
wt. % annhydrous corrected						
SiO_2	51.92	51.82	51.77	51.33	53.35	53.71
TiO_2	0.86	0.54	0.68	0.72	0.58	0.54
Al_2O_3	10.34	10.59	3.82	4.02	4.59	4.69
Fe_2O_{3t}	9.44	8.27	14.98	9.54	8.78	10.88
MgO	11.73	13.66	23.86	17.90	18.11	24.35
MnO	0.15	0.15	0.22	0.18	0.17	0.20
CaO	13.79	13.42	4.23	15.94	13.67	4.90
Na_2O	1.21	1.11	0.30	0.30	0.60	0.50
K_2O	0.47	0.40	0.07	0.03	0.12	0.15
P_2O5	0.08	0.04	0.06	0.04	0.04	0.08
Mg-no.	71.80	77.20	76.55	79.36	80.88	82.10
ppm						
S	2989.00	165.00	3257.00	181.00	111.00	199.00
Sc	39.32	36.37	24.28	48.28	44.86	26.00
V	229.51	188.67	165.59	243.57	216.17	140.00
Cr	862.83	816.88	2509.17	2894.31	3080.85	2400.00
Co	59.84	49.88	120.33	61.95	57.71	71.00
Ni	769.01	342.38	1242.03	437.67	438.75	390.00
Cu	1369.67	41.22	679.47	38.65	19.65	130.00
Ga	11.79	11.19	6.15	6.62	7.05	6.90
Rb	12.88	10.47	3.27	1.82	2.97	4.30
Sr	166.32	175.29	51.24	28.61	81.47	70.00
Y	13.21	8.72	8.57	11.57	10.03	7.90
Zr	50.74	27.03	46.50	36.14	26.77	42.00
Nb	3.51	1.72	3.05	2.42	1.74	2.30
Cs	0.40	0.33	0.66	0.21	0.11	0.16
Ba	141.48	87.56	47.50	11.00	39.47	92.00
La	5.75	2.89	4.77	3.84	2.73	4.40
Ce	13.04	6.66	11.06	9.06	6.60	11.00
Pr	1.87	1.01	1.59	1.33	1.02	1.50
Nd	8.74	4.83	7.10	6.60	5.16	6.60
Sm	2.23	1.35	1.69	1.85	1.53	1.40
Eu	0.78	0.53	0.43	0.60	0.52	0.38
Gd	2.66	1.67	1.85	2.28	1.93	1.40
Tb	0.43	0.27	0.28	0.36	0.31	0.22
Dy	2.46	1.60	1.60	2.16	1.86	1.40
Ho	0.47	0.31	0.31	0.43	0.37	0.27
Er	1.22	0.80	0.79	1.10	0.95	0.74
Tm	0.19	0.12	0.12	0.17	0.15	0.11
Yb	1.09	0.71	0.78	0.98	0.86	0.76
Lu	0.18	0.11	0.12	0.15	0.13	0.12
Hf	1.44	0.78	1.27	1.05	0.80	1.10
Ta	0.28	0.17	0.25	0.16	0.14	0.10
Pb	7.14	5.09	5.89	2.54	2.10	1.00
Th	1.00	0.48	0.93	0.68	0.48	0.78
U	0.26	0.12	0.24	0.18	0.12	0.22

Table H.2: Major element and selected trace element data for the Muskox intrusion (continued)

Sample	N-59	N-66	N-75	N-85	N-97	N-100
DFB (m)	1542.7	1505.2	1458.3	1397.3	1334.0	1311.0
Lithology	Peridotite	Fsp. peridotite	Dunite	Peridotite	Peridotite	Ol. Cpxenite
Cyclic Unit	21	20	19	18	17	16
wt. % annhydrous corrected						
SiO_2	44.01	42.38	40.48	42.01	41.14	51.62
TiO_2	0.21	0.34	0.21	0.30	0.12	0.27
Al_2O_3	4.32	2.42	1.73	3.43	1.38	1.83
Fe_2O_{3t}	13.19	16.36	15.50	13.59	15.33	7.33
MgO	34.95	35.55	41.85	39.89	41.71	21.16
MnO	0.18	0.21	0.20	0.16	0.17	0.16
CaO	3.09	2.66	0.02	0.56	0.13	17.29
Na_2O	0.00	0.00	0.00	0.00	0.00	0.31
K_2O	0.02	0.07	0.00	0.03	0.00	0.01
P_2O5	0.02	0.03	0.01	0.03	0.02	0.01
Mg-no.	84.45	81.66	84.69	85.75	84.80	85.54
ppm						
S	378.00	192.00	1441.00	942.00	4258.00	80.00
Sc	11.67	11.31	6.49	6.92	6.76	52.36
V	75.73	87.87	61.45	61.24	44.74	238.92
Cr	3412.74	3243.22	4241.38	3462.47	1656.30	3882.63
Co	124.19	120.14	115.99	124.93	164.62	61.64
Ni	1358.30	1750.65	2102.04	1863.02	3388.11	411.07
Cu	46.35	44.29	327.47	111.51	1133.51	3.33
Ga	4.29	3.45	2.51	3.39	1.35	2.89
Rb	0.89	2.43	0.29	1.68	0.19	0.56
Sr	10.63	27.70	0.51	2.84	1.93	13.21
Y	2.72	4.54	1.02	3.37	1.54	6.12
Zr	6.41	15.78	4.54	13.59	4.39	4.45
Nb	0.36	1.19	0.72	0.78	0.26	0.09
Cs	0.21	0.11	0.03	0.09	0.02	0.18
Ba	7.90	29.31	2.22	9.22	1.56	6.03
La	0.74	2.02	0.22	1.62	0.45	0.37
Ce	1.76	4.59	0.56	3.48	1.02	1.26
Pr	0.27	0.66	0.09	0.49	0.15	0.27
Nd	1.31	3.03	0.41	2.24	0.72	1.74
Sm	0.38	0.75	0.12	0.56	0.20	0.69
Eu	0.16	0.23	0.05	0.19	0.06	0.24
Gd	0.49	0.90	0.14	0.62	0.26	1.04
Tb	0.08	0.14	0.02	0.10	0.04	0.18
Dy	0.49	0.84	0.16	0.60	0.25	1.13
Ho	0.10	0.17	0.03	0.12	0.05	0.23
Er	0.25	0.43	0.10	0.31	0.14	0.58
Tm	0.04	0.07	0.02	0.05	0.02	0.09
Yb	0.25	0.41	0.14	0.31	0.16	0.52
Lu	0.04	0.07	0.03	0.05	0.03	0.08
Hf	0.20	0.47	0.14	0.37	0.14	0.20
Ta	0.08	0.15	0.14	0.12	0.09	0.05
Pb	2.96	1.48	3.99	4.62	1.46	1.30
Th	0.13	0.38	0.08	0.27	0.09	0.04
U	0.03	0.09	0.04	0.06	0.02	0.01

Table H.2: Major element and selected trace element data for the Muskox intrusion (continued)

Sample	N-101	N-104	N-111	N-115	N-122	N-129
DFB (m)	1305.0	1288.2	1232.2	1214.5	1171.8	1061.5
Lithology	Ol. Cpxenite	Peridotite	Dunite	Dunite	Dunite	Dunite
Cyclic Unit	16	16	15	14	14	12
wt. % annhydrous corrected						
SiO_2	51.76	42.34	42.87	41.74	41.44	37.98
TiO_2	0.27	0.20	0.17	0.18	0.21	0.14
Al_2O_3	1.85	1.78	1.58	1.82	1.80	3.37
Fe_2O_{3t}	7.19	16.49	14.74	15.13	16.62	16.83
MgO	21.36	35.49	38.90	40.18	39.11	41.43
MnO	0.16	0.21	0.18	0.16	0.18	0.19
CaO	17.40	3.47	1.54	0.75	0.52	0.01
Na_2O	0.00	0.00	0.00	0.00	0.00	0.00
K_2O	0.00	0.00	0.01	0.02	0.09	0.04
P_2O5	0.01	0.02	0.02	0.02	0.03	0.01
Mg-no.	85.89	81.52	84.39	84.48	82.83	83.46
ppm						
S	165.00	146.00	346.00	540.00	251.00	3572.00
Sc	54.07	20.96	12.57	8.32	4.59	6.57
V	236.27	151.65	52.52	49.59	53.18	120.97
Cr	4730.58	9723.56	2449.73	3379.39	3029.15	18829.49
Co	72.98	161.09	140.00	131.89	100.70	165.46
Ni	513.72	2141.06	1111.16	1483.48	1787.00	4359.77
Cu	3.69	15.85	75.56	106.67	14.30	70.17
Ga	3.21	3.67	1.65	1.77	2.51	4.34
Rb	0.03	0.53	0.88	1.41	3.44	2.12
Sr	12.60	4.20	3.66	2.17	2.42	0.78
Y	6.47	3.33	2.54	2.31	2.65	1.00
Zr	3.64	6.89	10.42	12.04	16.60	6.14
Nb	0.04	0.36	0.55	0.65	0.88	0.10
Cs	0.01	0.02	0.04	0.08	0.16	0.07
Ba	3.53	5.27	6.35	7.49	21.71	9.41
La	0.25	0.70	0.98	0.87	0.93	0.05
Ce	1.05	1.73	2.27	2.10	2.57	0.33
Pr	0.25	0.28	0.32	0.31	0.41	0.02
Nd	1.67	1.44	1.55	1.45	1.93	0.33
Sm	0.75	0.45	0.40	0.37	0.47	0.09
Eu	0.25	0.16	0.13	0.11	0.11	0.02
Gd	1.09	0.58	0.47	0.43	0.51	0.13
Tb	0.19	0.10	0.08	0.07	0.08	0.02
Dy	1.19	0.61	0.45	0.41	0.47	0.16
Ho	0.24	0.12	0.09	0.08	0.10	0.03
Er	0.60	0.32	0.23	0.22	0.27	0.10
Tm	0.09	0.06	0.04	0.03	0.04	0.02
Yb	0.55	0.31	0.23	0.23	0.27	0.12
Lu	0.09	0.05	0.04	0.03	0.05	0.02
Hf	0.20	0.21	0.28	0.33	0.43	0.14
Ta	0.05	0.03	0.12	0.11	0.12	0.01
Pb	0.49	2.83	2.86	2.23	1.83	1.93
Th	0.01	0.09	0.16	0.21	0.39	0.06
U	0.00	0.03	0.04	0.05	0.10	0.02

Table H.2: Major element and selected trace element data for the Muskox intrusion (continued)

Sample	N-141	N-151	N-157	S-44	S-51	S-60
DFB (m)	990.8	936.5	893.5	845.4	803.0	759.1
Lithology	Dunite	Fs Ol Px-Troc	Ol. Cpxenite	Dunite (ser)	Dunite (ser)	Dunite
Cyclic Unit	11	8	7	7	7	6
wt. % annhydrous corrected						
SiO_2	40.30	42.13	50.04	40.45	41.69	39.61
TiO_2	0.03	0.01	0.21	0.05	0.12	0.05
Al_2O_3	0.58	9.48	1.46	0.47	0.93	0.47
Fe_2O_{3t}	15.78	10.70	8.03	13.72	14.21	16.29
MgO	43.09	32.08	25.33	44.82	42.14	43.03
MnO	0.18	0.11	0.17	0.19	0.22	0.21
CaO	0.02	5.45	14.77	0.30	0.66	0.29
Na_2O	0.00	0.00	0.00	0.00	0.00	0.00
K_2O	0.00	0.03	0.00	0.00	0.01	0.04
P_2O5	0.01	0.01	0.00	0.01	0.02	0.01
Mg-no.	84.84	86.01	86.61	87.01	85.87	84.41
ppm						
S	243.00	136.00	77.00	25.00	88.00	92.00
Sc	4.82	4.31	44.86	6.21	11.57	3.59
V	31.95	13.89	211.06	28.52	49.15	14.81
Cr	2247.78	711.17	3325.71	2759.02	1976.49	1231.22
Co	127.59	128.68	66.11	125.83	118.78	127.53
Ni	2559.11	1410.09	644.79	1781.45	1825.85	1363.22
Cu	7.21	78.34	41.01	6.25	37.22	4.19
Ga	0.78	5.38	2.01	0.91	1.05	0.49
Rb	0.41	2.69	0.09	0.25	0.86	1.48
Sr	0.91	117.78	10.41	2.09	3.09	2.78
Y	0.30	0.23	4.76	0.60	2.17	0.37
Zr	0.98	0.52	3.06	2.18	7.24	1.85
Nb	0.04	0.03	0.03	0.17	0.50	0.08
Cs	0.02	0.77	0.02	0.03	0.13	0.08
Ba	2.13	36.19	2.82	0.69	3.41	5.08
La	0.07	0.13	0.28	0.26	0.74	0.06
Ce	0.14	0.25	1.05	0.58	1.81	0.15
Pr	0.02	0.03	0.23	0.08	0.27	0.03
Nd	0.07	0.12	1.37	0.34	1.24	0.17
Sm	0.02	0.03	0.54	0.08	0.33	0.04
Eu	0.00	0.04	0.18	0.02	0.09	0.01
Gd	0.02	0.04	0.81	0.09	0.37	0.05
Tb	0.00	0.01	0.14	0.01	0.06	0.01
Dy	0.04	0.04	0.86	0.09	0.40	0.05
Ho	0.01	0.01	0.18	0.02	0.08	0.01
Er	0.03	0.02	0.45	0.06	0.21	0.04
Tm	0.01	0.00	0.07	0.01	0.03	0.01
Yb	0.06	0.03	0.42	0.07	0.21	0.07
Lu	0.01	0.00	0.06	0.01	0.03	0.01
Hf	0.03	0.02	0.15	0.06	0.19	0.05
Ta	0.10	0.08	0.05	0.02	0.11	0.10
Pb	3.00	2.38	1.25	0.68	2.33	2.77
Th	0.03	0.02	0.01	0.07	0.17	0.04
U	0.01	0.00	0.00	0.02	0.04	0.02

Table H.2: Major element and selected trace element data for the Muskox intrusion (continued)

Sample	S-69	S-76	S-85	S-93	S-102	S-110
DFB (m)	704.3	662.2	606.7	557.7	502.2	454.6
Lithology	Dunite	Dunite	Dunite	Dunite	Dunite	Dunite
Cyclic Unit	6	6	5	5	4	4
wt. % annhydrous corrected						
SiO_2	40.14	40.36	40.47	40.48	40.73	40.89
TiO_2	0.10	0.08	0.12	0.17	0.16	0.20
Al_2O_3	1.08	0.94	1.36	1.78	1.51	1.51
Fe_2O_{3t}	13.14	14.87	13.57	15.00	14.12	14.35
MgO	44.62	43.01	42.97	40.84	42.19	41.27
MnO	0.14	0.17	0.17	0.19	0.17	0.17
CaO	0.69	0.54	1.30	1.47	1.06	1.54
Na_2O	0.00	0.00	0.00	0.00	0.00	0.00
K_2O	0.08	0.01	0.02	0.05	0.04	0.03
P_2O5	0.01	0.01	0.02	0.02	0.02	0.03
Mg-no.	87.43	85.56	86.65	84.80	85.96	85.49
ppm						
S	130.00	138.00	74.00	66.00	57.00	67.00
Sc	3.61	6.11	4.65	6.51	6.03	9.94
V	19.60	23.80	23.68	51.40	33.00	77.15
Cr	1780.20	1560.75	1884.08	3362.18	2101.93	5270.91
Co	109.64	125.04	113.41	137.71	133.43	123.10
Ni	1959.94	2442.06	2129.85	2746.46	2249.24	2366.61
Cu	2.96	41.30	20.78	38.71	26.79	34.40
Ga	0.73	0.66	1.03	2.05	1.84	2.85
Rb	3.45	0.96	1.55	3.49	2.62	2.44
Sr	3.57	2.85	27.45	48.07	23.52	24.45
Y	1.03	1.32	1.72	2.28	2.29	2.64
Zr	3.72	3.79	6.41	9.94	12.51	11.55
Nb	0.22	0.22	0.35	0.68	0.72	0.89
Cs	0.39	0.14	0.12	0.28	0.20	0.13
Ba	8.92	7.48	32.35	61.15	27.53	27.27
La	0.25	0.65	0.72	1.07	1.24	1.34
Ce	0.78	1.70	1.69	2.35	2.79	3.03
Pr	0.13	0.24	0.25	0.34	0.39	0.44
Nd	0.60	1.00	1.10	1.50	1.71	1.93
Sm	0.15	0.23	0.27	0.39	0.42	0.48
Eu	0.03	0.07	0.08	0.11	0.11	0.14
Gd	0.18	0.26	0.30	0.44	0.44	0.53
Tb	0.03	0.04	0.05	0.07	0.07	0.08
Dy	0.19	0.24	0.32	0.40	0.41	0.48
Ho	0.04	0.05	0.06	0.08	0.08	0.09
Er	0.10	0.13	0.17	0.21	0.21	0.25
Tm	0.02	0.02	0.03	0.03	0.03	0.04
Yb	0.12	0.13	0.16	0.22	0.21	0.24
Lu	0.02	0.02	0.03	0.04	0.04	0.04
Hf	0.10	0.11	0.17	0.27	0.31	0.31
Ta	0.08	0.09	0.09	0.11	0.13	0.07
Pb	3.13	3.43	3.76	5.78	2.13	1.93
Th	0.08	0.07	0.16	0.23	0.30	0.27
U	0.02	0.02	0.04	0.06	0.08	0.07

Table H.2: Major element and selected trace element data for the Muskox intrusion (continued)

Sample	S-121	S-123	S-124	S-128	S-133	S-137
DFB (m)	391.2	378.0	372.0	363.8	333.3	309.0
Lithology	Dunite	Ol. Cpxenite	Ol. Cpxenite	Dunite	Dunite	Dunite
Cyclic Unit	3	2	2	2	2	2
wt. % annhydrous corrected						
SiO_2	40.06	41.92	44.61	39.43	39.77	40.10
TiO_2	0.19	0.20	0.25	0.15	0.24	0.23
Al_2O_3	1.25	1.54	1.92	1.05	1.56	1.87
Fe_2O_{3t}	17.74	15.93	13.53	17.98	17.91	17.91
MgO	39.17	36.08	31.54	40.07	38.79	37.78
MnO	0.22	0.21	0.19	0.22	0.22	0.21
CaO	1.29	4.07	7.86	1.05	1.33	1.68
Na_2O	0.00	0.00	0.00	0.00	0.10	0.00
K_2O	0.05	0.04	0.06	0.02	0.06	0.19
P_2O5	0.03	0.02	0.03	0.02	0.02	0.03
Mg-no.	81.90	82.28	82.70	82.04	81.62	81.21
ppm						
S	77.00	80.00	74.00	25.00	90.00	1106.00
Sc	6.91	18.41	28.63	8.73	9.35	6.98
V	48.01	112.49	144.91	91.88	106.15	60.93
Cr	1863.00	3892.92	2530.04	6259.57	6681.22	2500.25
Co	142.19	142.20	110.42	164.69	158.10	152.50
Ni	1630.42	1672.22	1311.29	2154.28	2131.45	2257.82
Cu	25.54	20.93	27.99	35.57	34.80	56.17
Ga	1.82	2.85	2.67	2.84	3.40	2.29
Rb	2.85	2.69	3.28	2.43	3.04	6.54
Sr	32.09	31.22	46.44	34.70	28.79	26.05
Y	2.62	2.93	4.66	1.96	2.50	3.03
Zr	13.41	8.70	10.23	9.32	11.87	13.18
Nb	0.90	0.61	0.61	0.66	0.83	0.89
Cs	0.22	0.25	0.28	0.19	0.21	0.41
Ba	30.13	29.33	55.35	41.95	30.85	36.50
La	1.31	0.85	1.08	0.99	1.22	1.24
Ce	3.13	2.16	2.68	2.36	2.97	3.03
Pr	0.45	0.30	0.44	0.30	0.39	0.46
Nd	2.06	1.62	2.24	1.53	1.93	2.12
Sm	0.50	0.46	0.69	0.37	0.46	0.54
Eu	0.12	0.15	0.22	0.11	0.14	0.14
Gd	0.50	0.52	0.89	0.38	0.48	0.59
Tb	0.08	0.09	0.15	0.06	0.08	0.10
Dy	0.47	0.52	0.84	0.36	0.46	0.55
Ho	0.09	0.10	0.17	0.07	0.09	0.11
Er	0.24	0.28	0.44	0.19	0.24	0.29
Tm	0.04	0.04	0.06	0.03	0.04	0.04
Yb	0.23	0.28	0.41	0.18	0.24	0.27
Lu	0.04	0.05	0.06	0.03	0.04	0.04
Hf	0.37	0.26	0.32	0.25	0.31	0.37
Ta	0.13	0.04	0.17	0.05	0.06	0.13
Pb	1.01	1.88	2.67	2.09	2.26	1.36
Th	0.29	0.17	0.17	0.21	0.26	0.28
U	0.07	0.04	0.04	0.06	0.07	0.07

Table H.2: Major element and selected trace element data for the Muskox intrusion (continued)

Sample	S-143	S-144	S-151	S-154	S-156	S-160
DFB (m)	272.1	264.0	223.6	205.3	193.1	174.2
Lithology	Dunite	Dunite	Dunite	Dunite	Dunite	Peridotite
Cyclic Unit	2	2	2	2	2	2
wt. % annhydrous corrected						
SiO_2	39.92	40.23	40.20	40.31	40.31	40.45
TiO_2	0.22	0.22	0.30	0.33	0.36	0.36
Al_2O_3	1.57	1.81	1.97	2.18	2.11	2.24
Fe_2O_{3t}	17.98	16.91	17.97	17.97	18.47	18.73
MgO	38.62	38.85	37.46	36.97	36.56	35.94
MnO	0.21	0.21	0.22	0.22	0.22	0.21
CaO	1.39	1.60	1.71	1.77	1.77	1.87
Na_2O	0.00	0.00	0.00	0.10	0.00	0.00
K_2O	0.06	0.13	0.11	0.10	0.15	0.15
P_2O5	0.03	0.03	0.04	0.04	0.05	0.04
Mg-no.	81.49	82.48	81.03	80.82	80.23	79.72
ppm						
S	78.00	63.00	158.00	147.00	107.00	1946.00
Sc	8.90	8.74	7.40	8.13	82.37	10.47
V	130.00	85.78	93.79	96.28	976.21	114.53
Cr	5900.00	5091.63	4614.46	4159.42	37976.78	4591.33
Co	140.00	147.29	140.52	142.86	1395.54	156.85
Ni	1900.00	2067.49	1914.11	2040.85	18982.00	1519.63
Cu	44.00	2.64	95.50	75.60	463.87	879.74
Ga	3.30	3.02	3.34	3.40	35.22	4.34
Rb	3.30	5.74	4.47	3.52	53.29	6.13
Sr	22.00	28.40	37.33	34.33	332.97	38.83
Y	2.90	2.76	3.76	4.08	46.52	4.58
Zr	16.00	14.82	19.91	19.05	261.04	23.81
Nb	1.00	0.95	1.37	1.42	20.16	1.88
Cs	0.19	0.50	0.23	0.12	1.76	0.35
Ba	24.00	31.30	46.80	35.01	425.75	50.75
La	1.70	1.00	2.19	2.23	27.27	2.62
Ce	3.50	2.59	4.97	5.13	62.76	6.05
Pr	0.51	0.38	0.71	0.74	8.93	0.84
Nd	2.10	1.87	3.13	3.27	40.01	3.81
Sm	0.47	0.49	0.74	0.77	9.41	0.90
Eu	0.13	0.12	0.21	0.22	2.33	0.24
Gd	0.59	0.53	0.76	0.81	10.10	0.91
Tb	0.09	0.09	0.12	0.13	1.48	0.14
Dy	0.47	0.51	0.68	0.74	8.56	0.80
Ho	0.09	0.10	0.14	0.15	1.65	0.16
Er	0.26	0.26	0.35	0.38	4.29	0.42
Tm	0.05	0.04	0.05	0.06	0.64	0.07
Yb	0.28	0.25	0.33	0.36	4.12	0.40
Lu	0.04	0.04	0.05	0.06	0.68	0.06
Hf	0.38	0.38	0.54	0.52	6.87	0.63
Ta	0.10	0.13	0.15	0.16	2.12	0.15
Pb	3.00	0.76	4.11	1.32	10.22	2.21
Th	0.26	0.31	0.41	0.39	5.30	0.55
U	0.07	0.09	0.10	0.09	1.33	0.14

Table H.2: Major element and selected trace element data for the Muskox intrusion (continued)

Sample	S-164	S-171	S-182	S-192	S-195
DFB (m)	152.0	110.5	52.6	0.2	-2.1
Lithology	Fsp peridotite	Fsp peridotite	Picrite	Bronzite gab	Wopmay
Cyclic Unit	2	2	1	1	Paragneiss
wt. % annhydrous corrected					
SiO_2	41.02	43.08	44.23	49.46	47.07
TiO_2	0.48	0.63	0.64	0.71	0.35
Al_2O_3	3.08	5.15	6.73	8.52	9.69
Fe_2O_{3t}	17.96	16.90	14.81	20.94	29.98
MgO	34.39	28.73	27.35	12.12	6.79
MnO	0.21	0.20	0.18	0.24	2.84
CaO	2.50	4.56	5.17	5.45	1.16
Na_2O	0.11	0.41	0.52	1.16	0.60
K_2O	0.19	0.27	0.29	1.33	1.45
P_2O5	0.05	0.07	0.07	0.07	0.08
Mg-no.	79.69	77.69	79.09	54.26	31.69
ppm					
S	158.00	199.00	216.00	46800.00	5769.00
Sc	13.03	17.49	19.43	37.76	16.97
V	132.95	178.54	165.56	465.53	135.82
Cr	4341.85	4252.40	3237.25	679.45	144.18
Co	142.88	129.66	111.02	475.54	64.06
Ni	566.41	1543.16	403.66	1778.61	136.20
Cu	62.22	120.31	83.34	1286.65	882.50
Ga	5.09	7.59	8.07	12.13	16.06
Rb	6.81	9.09	10.66	40.88	74.81
Sr	68.85	89.26	87.26	144.86	167.08
Y	6.23	7.21	9.05	20.14	15.55
Zr	34.40	38.41	45.89	76.96	52.12
Nb	2.43	3.33	3.60	6.69	5.40
Cs	0.30	0.25	1.22	1.06	7.76
Ba	67.03	79.89	78.54	209.71	588.52
La	3.81	4.09	4.93	8.04	12.27
Ce	8.58	9.24	10.80	23.40	25.11
Pr	1.20	1.24	1.48	3.77	2.91
Nd	5.30	5.75	6.54	17.56	11.22
Sm	1.22	1.33	1.56	3.91	2.20
Eu	0.34	0.45	0.47	0.65	0.69
Gd	1.29	1.45	1.66	3.59	2.19
Tb	0.20	0.23	0.28	0.57	0.37
Dy	1.12	1.32	1.57	3.34	2.38
Ho	0.22	0.26	0.32	0.70	0.52
Er	0.57	0.69	0.87	1.99	1.53
Tm	0.08	0.11	0.13	0.32	0.28
Yb	0.53	0.65	0.83	2.11	1.83
Lu	0.09	0.11	0.13	0.35	0.31
Hf	0.90	1.02	1.21	2.20	1.58
Ta	0.22	0.22	0.28	0.51	0.43
Pb	2.89	1.90	2.39	12.73	23.67
Th	0.68	0.79	1.06	7.68	5.56
U	0.18	0.21	0.27	1.75	1.47

Table H.2: Major element and selected trace element data for the Muskox intrusion (continued)

Sample	MX-04a	MX-26a	MX-40a
Lithology	Chromitite	Chromitite	Chromitite
Cyclic Unit	Main Reef	Main Reef	Main Reef
wt. % annhydrous corrected			
SiO_2	27.43	33.79	22.40
TiO_2	2.82	1.95	3.14
Al_2O_3	10.07	10.51	15.21
Fe_2O_{3t}	35.65	29.41	32.90
MgO	15.11	18.40	17.70
MnO	0.27	0.26	0.28
CaO	8.20	5.06	8.20
Na_2O	0.32	0.45	0.10
K_2O	0.13	0.16	0.08
P_2O5	0.00	0.00	0.00
Mg-no.	46.48	56.18	52.43
ppm			
S			
Sc	23.87	20.27	16.68
V	1141.39	524.80	1210.51
Cr	89081.60	37975.71	112012.16
Co	131.81	106.21	148.88
Ni	1711.51	1564.35	895.43
Cu	5949.49	2348.39	312.25
Ga	26.79	14.67	41.49
Rb	2.46	2.71	1.48
Sr	31.13	54.08	40.25
Y	5.87	5.44	4.34
Zr	17.13	18.60	14.44
Nb	1.23	1.14	1.07
Cs	0.12	0.18	0.09
Ba	39.18	53.72	25.69
La	1.75	2.02	1.47
Ce	4.32	4.74	3.36
Pr	0.66	0.68	0.50
Nd	3.38	3.23	2.45
Sm	0.97	0.87	0.67
Eu	0.32	0.31	0.32
Gd	1.20	1.03	0.83
Tb	0.19	0.16	0.13
Dy	1.11	0.97	0.80
Ho	0.21	0.19	0.16
Er	0.56	0.53	0.41
Tm	0.08	0.08	0.06
Yb	0.50	0.50	0.38
Lu	0.07	0.08	0.06
Hf	0.52	0.51	0.46
Ta	0.08	0.08	0.08
Pb	4.34	4.23	2.65
Th	0.29	0.34	0.18
U	0.07	0.08	0.05

Table H.2: Major element and selected trace element data for the Muskox intr

Sample	MU 033.241.21	MU 033.252.76	HDB-2001-MX5
Lithology	Gabbro Norite	Gabbro Norite	Gabbro Norite
Cyclic Unit	The Keel	The Keel	The Keel
wt. % annhydrous corrected			
SiO_2	45.65	45.90	46.53
TiO_2	0.52	0.50	0.58
Al_2O_3	8.44	8.86	8.17
Fe_2O_{3t}	12.69	12.26	12.50
MgO	23.67	22.92	22.45
MnO	0.18	0.18	0.18
CaO	7.96	8.50	8.43
Na_2O	0.64	0.64	0.81
K_2O	0.21	0.21	0.31
P_2O5	0.04	0.04	0.05
Mg-no.	79.26	79.30	78.64
ppm			
S			
Sc	26.99	25.92	32.36
V	175.49	161.08	196.66
Cr	2851.27	2640.95	2334.92
Co	96.21	89.95	97.91
Ni	327.12	303.36	268.15
Cu	85.06	67.86	146.54
Ga	8.62	8.57	9.01
Rb	7.02	6.00	9.66
Sr	107.53	114.00	106.51
Y	8.67	7.81	11.72
Zr	32.35	26.87	42.61
Nb	2.01	1.72	2.43
Cs	0.35	0.30	0.54
Ba	60.22	69.09	84.44
La	3.53	3.08	4.55
Ce	8.00	7.00	10.03
Pr	1.13	1.00	1.40
Nd	5.16	4.63	6.29
Sm	1.31	1.15	1.64
Eu	0.46	0.44	0.53
Gd	1.54	1.38	1.88
Tb	0.24	0.23	0.32
Dy	1.46	1.35	1.94
Ho	0.30	0.28	0.40
Er	0.81	0.74	1.10
Tm	0.12	0.11	0.17
Yb	0.80	0.73	1.05
Lu	0.12	0.12	0.17
Hf	0.86	0.74	1.15
Ta	0.17	0.15	0.21
Pb	1.97	6.60	8.08
Th	0.67	0.55	1.02
U	0.17	0.14	0.26